East European Journal of Physics. 1. 9–19 (2025)
DOI: 10.26565/2312-4334-2025-1-01 ISSN 2312-4334

RECONSTRUCTION OF KANIADAKIS HOLOGRAPHIC DARK ENERGY MODEL IN SELF CREATION THEORY OF GRAVITY

Y. Aditya[a], **D. Tejeswararao**[a], **U.Y. Divya Prasanthi**[b,*], **D. Ram Babu**[a]
[a] *Department of Basic Sciences and Humanities, GMR Institute of Technology, Rajam-532127, India*
[b] *Department of Statistics & Mathematics, College of Horticulture, Dr. Y.S.R. Horticultural University, Parvathipuram-535502, India*
[*] *Corresponding Author e-mail: divyaaug24@gmail.com*

Received November 12, 2024; revised January 6, 2025; accepted January 25, 2025

The primary objective of this paper is to examine a Kaniadakis holographic dark energy universe of Bianchi type-*II* within the framework of self-creation gravity theory. In this dark energy model, the Hubble horizon is used as the infrared cutoff, following Kaniadakis' holographic dark energy concept. We calculate various dynamical parameters in this model, including the statefinder (r, s) plane, the deceleration parameter q, the equation of state (ω_{de}), the square speed of sound, and the $\omega_{de} - \omega'_{de}$ plane. A graphical analysis of these parameters is provided across a range of free parameter values. The results reveal that the deceleration parameter demonstrates the universe's smooth transition from an early decelerated phase to the current accelerated expansion, while the equation of state parameter suggests a phantom phase. The $\omega_{de} - \omega'_{de}$ plane reaches the thawing region, and the statefinder plane aligns with both the phantom model and Chaplygin gas. The current values of the parameters are consistent with existing observational data, and the strong energy conditions are found to be violated.

Keywords: *Bianchi type-II model; Kaniadakis holographic dark energy; Self creation Theory; Dark energy; Modified theory of gravity*

PACS: 98.80.-k, 95.36.+x

1. INTRODUCTION

One of the most astonishing findings in modern cosmology is that the universe is not only expanding but accelerating. Today, multiple independent observational sources support this accelerating behavior of the cosmos [1]-[3]. Explanations for this observed phenomenon fall broadly into two main approaches. In the framework of the General Theory of Relativity (GTR), the universe appears dominated by an enigmatic, negative-pressure component known as dark energy (DE), as evidenced by CMBR and LSS analyses. Alternatively, the acceleration could be explained by altering the law of gravity itself through modifications of the GTR action, known as modified gravity theories. Among these are the well-known $f(R)$ gravity [4] and Gauss-Bonnet gravity, which involves the Gauss-Bonnet invariant [5]. Other approaches include $f(R,T)$ gravity [6], as well as scalar-tensor theories like Brans-Dicke (BD) [7] and Saez-Ballester (SB) [8], along with the self-creation theory of gravitation. Barber [9] introduced two continuous creation theories: one as a variation of the BD theory and the other modifying GTR to accommodate continuous matter creation in alignment with observational data. These theories suggest a universe generated by self-contained gravitational and matter fields. Barber's second self-creation theory has inspired extensive study into diverse cosmological models (Ref. [10]-[14]). The theory provides a framework where the cosmological constant can emerge naturally from the dynamics of the gravitational field and matter. It offers a novel approach to explain cosmic acceleration and dark energy without relying on a constant energy density. Essentially, the theory proposes a self-creation of gravity, which modifies both the gravitational field equations and the evolution of the universe. For a thorough exploration of DE and modified gravity theories, please refer to the sources cited in [15]-[28].

Alternatively, some theoretical approaches attempt to resolve the DE problem by introducing novel types of matter or modified equations of state [29]-[30]. Another promising avenue is Holographic DE (HDE), rooted in the holographic principle [31, 32]. When applied to the universe, the vacuum energy associated with this principle can be interpreted as DE, or specifically HDE, as proposed by Cohen et al. [33]. Over recent decades, various entropy formulations have been applied to develop and examine cosmological models. This has led to several innovative HDE models, such as the Tsallis HDE [34, 35], Sharma-Mittal HDE (SMHDE) [36], and Renyi HDE model [37]. Numerous researchers have evaluated cosmological models based on these new HDE concepts [38]- [42]. Recently, Kaniadakis statistics have been utilized as a generalized measure of entropy [43]- [45] to investigate various gravitational and cosmological phenomena. Kaniadakis entropy modifies the standard thermodynamics, allowing for non-linearities that account for a broader range of behaviors in dark energy. It provides a more generalized equation of state, enabling flexibility in describing the evolution of dark energy over cosmic time. The generalized $\mathcal{K}$-entropy, or Kaniadakis entropy, which characterizes black hole entropy, can be expressed with a single free parameter [46].

$$S_{\mathcal{K}} = \frac{1}{\mathcal{K}} sinh(\mathcal{K}\, S_{BH}) \tag{1}$$

Cite as: Y. Aditya, D. Tejeswararao, U.Y.D. Prasanthi, D. Ram Babu, East Eur. J. Phys. 1, 9 (2025), https://doi.org/10.26565/2312-4334-2025-1-01

where $\mathcal{K}$ is an unknown parameter. Thus, by using the concept of entropy and the notion of HDE, a novel model of DE called Kaniadakis HDE (KHDE) is proposed [46], which exhibits significant characteristics. Jawad and Sultan [47], Sharma [48], and Drepanou et al. [49] have examined KHDE models inside various gravitational theories. The dynamic structures of HDE, as investigated by Sadeghi et al. [50], have been analyzed within the context of BD's theory of gravity, using the Tsallis and Kaniadakis approaches. Rao et al. [51] explored KHDE model in GTR. The integration of KHDE within Barber's second self-creation theory of gravitation enhances both the theoretical framework for gravity and DE. It provides a dynamic, thermodynamically consistent solution to cosmological problems such as the cosmological constant and cosmic acceleration. By linking gravity's evolution with a generalized, non-linear description of DE, this combination could offer deeper insights into the structure of the universe and the nature of its expansion.

Several studies provide information about how the large-scale structure we see today might have developed from tiny anisotropies. The conditions of the early universe before it attained the isotropic state can be modeled using Binachi type(BT)-*II* space-time. For theories explaining how the universe changed from a highly anisotropic state to its current isotropic state, this is essential. Potential anisotropies and abnormalities in the CMB are studied using Bianchi models, such as type-*II*. These investigations aid in determining the effect of anisotropic expansion on the CMB and evaluating the universe's isotropy. The discussion above makes it evident that a number of authors have looked into KHDE models of the universe. The BT-*II* KHDE model has not yet been studied in the literature in relation to the self-creation theory of gravity. In this work, we consider the self-creation theory of gravity in the setting of the BT-*II* universe, which includes matter and KHDE.

With this motivation, in this work we construct Bianchi type-*II* KHDE model with Hubble horizon as IR cutoff in self-creation theory of gravitation. The following is how the paper has been arranged: The field equations in self creation theory of gravity pertaining to the KHDE source are formulated along with their solution in section-2. Section-3 provides cosmological parameters and their physical discussion. Final remarks are presented in section-4.

2. FIELD EQUATIONS AND MODEL

We consider BT-II metric of the form

$$ds^2 = -dt^2 + R(t)^2dx^2 + S(t)^2dy^2 + 2S(t)^2xdydz + (S(t)^2x^2 + R(t)^2)dz^2. \tag{2}$$

The self-creation theory field equations are as follows:

$$R_{ij} - \frac{1}{2}Rg_{ij} = \frac{-8\pi}{\phi}(T_{ij} + \overline{T}_{ij}), \tag{3}$$

$$\Box\phi = \phi^{;v}_{;v} = \frac{8\pi\mu}{3}(T + \overline{T}). \tag{4}$$

In this context, the symbols have their usual meaning. The stress-energy tensors for matter distribution is as follows.

$$T_{ij} = diag[0, 0, 0, -1]\rho_m, \quad \overline{T}_{ij} = diag[\omega_{de}, \omega_{de} + \gamma, \omega_{de}, -1]\rho_{de}. \tag{5}$$

The field equations for the space-time (2), using the comoving coordinate system and the above equations (3) and (4), may be represented as:

$$\frac{\ddot{S}}{S} + \frac{\ddot{R}}{R} + \frac{\dot{R}}{R}\frac{\dot{S}}{S} + \frac{S^2}{4R^4} = \frac{-8\pi\omega_{de}\rho_{de}}{\phi} \tag{6}$$

$$\frac{\dot{R}^2}{R^2} + \frac{2\ddot{R}}{R} - \frac{3S^2}{4R^4} = \frac{-8\pi(\omega_{de} + \gamma)\rho_{de}}{\phi} \tag{7}$$

$$\frac{\ddot{R}}{R} + \frac{\ddot{S}}{S} + \frac{\dot{S}}{S}\frac{\dot{R}}{R} + \frac{S^2}{4R^4} = -8\pi\omega_{de}\rho_{de} \tag{8}$$

$$\frac{2\dot{R}\dot{S}}{RS} + \frac{\dot{R}^2}{R^2} - \frac{S^2}{4R^4} = \frac{8\pi[\rho_m + \rho_{de}]}{\phi} \tag{9}$$

$$\dot{\phi}\left(\frac{\dot{S}}{S} + \frac{2\dot{R}}{R}\right) + \ddot{\phi} = \frac{8\pi\mu(T + \overline{T})}{3}. \tag{10}$$

Differentiation with respect to time t is represented by a dot above a variable in this notation. We can solve this system appropriately with the use of assumptions which connects unknowns in the field equations. Because of this, we take into account the following physically plausible circumstances:

$$R = S^k \tag{11}$$

Here, k denotes a constant (Collins et al. [55]). Observations of velocity-redshift from extragalactic sources indicate that the Hubble expansion of the present universe is isotropic to within 30% [52]-[54]. Additionally, redshift surveys place a constraint on $\frac{\sigma}{H} \leq 0.3$ within our current Galaxy.

Additionally, it is common in the literature to assume a power-law relationship between ϕ and the average scale factor $a(t)$, expressed as [56, 57]: $\phi \propto [a(t)]^n$, where n is the power index. Various researchers have explored different properties of scalar fields following this relationship. Considering the physical relevance of this relationship, we adopt following assumption

$$\phi(t) = \phi_0[a(t)]^n. \tag{12}$$

Using the relations (11) and (12) in Eqs. (6) and (7), we obtain the metric potentials as

$$R = (b_3 e^{\gamma_0 t} + b_4)^{\frac{1}{k+2}} \tag{13}$$

and

$$S = (b_3 e^{\gamma_0 t} + b_4)^{\frac{k}{k+2}} \tag{14}$$

where $b_3 = \frac{(k+2)b_1}{\gamma_0}$, $b_4 = (k+2)b_2$, b_1 and b_2 are integrating constants. The scalar field of the model is

$$\phi = \phi_0 \left(b_3 e^{\gamma_0 t} + b_4\right)^{\frac{n}{3}}. \tag{15}$$

Now metric (2), with the aid of Eqs. (13) and (14), can be written as

$$\begin{aligned} ds^2 = -dt^2 + (b_3 e^{\gamma_0 t} + b_4)^{\frac{2}{k+2}} dx^2 + (b_3 e^{\gamma_0 t} + b_4)^{\frac{2k}{k+2}} dy^2 + 2(b_3 e^{\gamma_0 t} + b_4)^{\frac{2k}{k+2}} xdydz \\ +((b_3 e^{\gamma_0 t} + b_4)^{\frac{2k}{k+2}} x^2 + (b_3 e^{\gamma_0 t} + b_4)^{\frac{2}{k+2}}) dz^2. \end{aligned} \tag{16}$$

Equation (16) describes a anisotropic BT-*II* KHDE model within the context of self-creation gravity theory, with the following physical parameters. The model's average scale factor $a(t)$ and volume $V(t)$ are defined as follows:

$$V(t) = a(t)^3 = (b_3 e^{\gamma_0 t} + b_4). \tag{17}$$

The expressions for the mean Hubble H and the expansion scalar θ parameters are derived as follows:

$$H = 3\theta = \frac{b_3 \gamma_0 e^{\gamma_0 t}}{3\, b_3 e^{\gamma_0 t} + 3\, b_4}. \tag{18}$$

The average anisotropic parameter A_h and shear scalar σ^2 are given by

$$\sigma^2 = \frac{(k-1)^2 b_3^2 \gamma_0^2 e^{2\gamma_0 t}}{(k+2)^2 \left(b_3 e^{\gamma_0 t} + b_4\right)^2}\ ;\ \ A_h = \frac{2(k-1)^2}{(k+2)^2}. \tag{19}$$

From the aforementioned parameters, it is evident that both the spatial volume of the universe demonstrate its exponential expansion. Moreover, during the initial epoch, all values become finite. However, as t tends to infinity, they diverge. Notably, when $k = 1$, the model achieves shear-free and isotropic characteristics, as indicated by the conditions $\sigma^2 = 0$ and $A_h = 0$.

According to the HDE theory, for DE is responsible for the accelerated expansion, the total vacuum energy contained within a region of size $\mathcal{L}$ must be less than or equal to the energy of a black hole of the same size, as governed by the Kaniadakis black hole entropy equation (Eq. (1)). This leads to the following condition:

$$\Lambda^4 \equiv \rho_{de} \propto \frac{\mathcal{S}_{\mathcal{K}}}{\mathcal{L}^4} \tag{20}$$

for the energy density ρ_{de}. Now, IR cutoff is taken as Hubble horizon (i.e., $\mathcal{L} = \frac{1}{H};\ A = \frac{4\pi}{H^2}$),

$$\rho_{de} = \frac{3c^2 H^4}{\mathcal{K}} sinh\left(\frac{\pi \mathcal{K}}{H^2}\right) \tag{21}$$

in this formulation, the constant c^2 remains unknown, $\mathcal{K}$ is a real-valued parameter, and the Hubble parameter is given by $H = \frac{\dot{a}}{a}$. It follows that, as $k \to 0$, we retrieve the well-established Bekenstein entropy-based HDE expression, $\rho_{de} \to \frac{3c^2H^4}{\mathcal{K}}$. In addition, we account for a pressureless fluid with energy density ρ_m and a DE component with pressure p_{de} and density ρ_{de}.

Using $H(t)$ in the above Eq. (21), we get the energy density of KHDE of the model as

$$\rho_{de} = \frac{3c^2 {b_3}^4 {\gamma_0}^4 \left(e^{\gamma_0 t}\right)^4}{\left(3\, b_3 e^{\gamma_0 t} + 3\, b_4\right)^4 \mathcal{K}} \sinh\left(\frac{\pi \mathcal{K} \left(3\, b_3 e^{\gamma_0 t} + 3\, b_4\right)^2}{{b_3}^2 {\gamma_0}^2 \left(e^{\gamma_0 t}\right)^2}\right). \tag{22}$$

Using Eqs. (13)-(15) and (22) in Eq. (9), we get the energy density of matter as

$$\begin{aligned} \rho_m \;=\; & \frac{\phi_0 \left(b_3 e^{\gamma_0 t} + b_4\right)^{n/3}}{8\pi} \left[\frac{{b_3}^2 {\gamma_0}^2 \left(e^{\gamma_0 t}\right)^2}{(k+2)^2 \left(b_3 e^{\gamma_0 t} + b_4\right)^2} + \frac{2 {b_3}^2 {\gamma_0}^2 \left(e^{\gamma_0 t}\right)^2 k}{(k+2)^2 \left(b_3 e^{\gamma_0 t} + b_4\right)^2}\right. \\ & \left. - \frac{\left(b_3 e^{\gamma_0 t} + b_4\right)^{\frac{2k}{k+2}}}{4 \left(b_3 e^{\gamma_0 t} + b_4\right)^{\frac{4}{k+2}}}\right] - \frac{3c^2 {b_3}^4 {\gamma_0}^4 \left(e^{\gamma_0 t}\right)^4}{\left(3\, b_3 e^{\gamma_0 t} + 3\, b_4\right)^4 \mathcal{K}} \sinh\left(\frac{\pi \mathcal{K} \left(3\, b_3 e^{\gamma_0 t} + 3\, b_4\right)^2}{{b_3}^2 {\gamma_0}^2 \left(e^{\gamma_0 t}\right)^2}\right). \end{aligned} \tag{23}$$

Using Eqs. (13)-(15), (21) in Eq. (6), we obtain the EoS parameter of KHDE as

$$\begin{aligned} \omega_{de} \;=\; & -\frac{\phi_0 \left(b_3 e^{\gamma_0 t} + b_4\right)^{n/3} \left(3\, b_3 e^{\gamma_0 t} + 3\, b_4\right)^4 \mathcal{K}}{24\pi\, c^2 {b_3}^4 {\gamma_0}^4 \left(e^{\gamma_0 t}\right)^4} \left(\frac{{b_3}^2 {\gamma_0}^2 \left(e^{\gamma_0 t}\right)^2 + (k+2)\, b_3 b_4 {\gamma_0}^2 e^{\gamma_0 t}}{(k+2)^2 \left(b_3 e^{\gamma_0 t} + b_4\right)^2}\right. \\ & + \frac{k^2 {b_3}^2 {\gamma_0}^2 \left(e^{\gamma_0 t}\right)^2 + k\,(k+2)\, b_3 b_4 {\gamma_0}^2 e^{\gamma_0 t}}{(k+2)^2 \left(b_3 e^{\gamma_0 t} + b_4\right)^2} + \frac{{b_3}^2 {\gamma_0}^2 \left(e^{\gamma_0 t}\right)^2 k}{(k+2)^2 \left(b_3 e^{\gamma_0 t} + b_4\right)^2} \\ & \left. + \frac{1}{4\left(\left(b_3 e^{\gamma_0 t} + b_4\right)^{4(k+2)^{-1}}\right)} \left(b_3 e^{\gamma_0 t} + b_4\right)^{\frac{k}{k+2}}\right) \left(\sinh\left(\frac{\pi \mathcal{K} \left(3\, b_3 e^{\gamma_0 t} + 3\, b_4\right)^2}{{b_3}^2 {\gamma_0}^2 \left(e^{\gamma_0 t}\right)^2}\right)\right)^{-1}. \end{aligned} \tag{24}$$

The skewness parameter is determined as

$$\begin{aligned} \gamma \;=\; & \frac{\phi_0 \left(b_3 e^{\gamma_0 t} + b_4\right)^{n/3} \left(3\, b_3 e^{\gamma_0 t} + 3\, b_4\right)^4 \mathcal{K}}{24\pi\, c^2 {b_3}^4 {\gamma_0}^4 \left(e^{\gamma_0 t}\right)^4} \left(\left(b_3 e^{\gamma_0 t} + b_4\right)^{\frac{2k-4}{k+2}} - \frac{{\gamma_0}^2 (1-k)\, b_3 e^{\gamma_0 t}}{(k+2)\left(b_3 e^{\gamma_0 t} + b_4\right)}\right) \\ & \times \left(\sinh\left(\frac{\pi \mathcal{K} \left(3\, b_3 e^{\gamma_0 t} + 3\, b_4\right)^2}{{b_3}^2 {\gamma_0}^2 \left(e^{\gamma_0 t}\right)^2}\right)\right)^{-1}. \end{aligned} \tag{25}$$

3. COSMOLOGICAL PARAMETERS AND PHYSICAL DISCUSSION

In this section, we investigate the expansion of the universe by scrutinizing various cosmological parameters. These parameters include the energy conditions, the scalar field ($\phi(t)$), the EoS (ω_{de}), the squared sound speed (v_s^2), the deceleration (q) parameters, as well as cosmic planes like $\omega_{de} - \omega'_{de}$ and statefinder planes for the anisotropic KHDE model.

Scalar field: Fig. 1 illustrates the evolution of the scalar field with time. The scalar field maintains a positive value and demonstrates a consistent decrease over time. This declining trend of the scalar field suggests a concurrent increase in kinetic energy within the model. Additionally, it has been observed that as the parameter k rises, the scalar field exhibits a decreasing behavior.

EoS parameter (ω): It serves as a crucial tool for categorizing the various phases in the expanding universe. It is expressed as $\omega = \frac{p}{\rho}$, representing the relationship between pressure (p) and energy density (ρ) within a given matter distribution. Different phases, characterized by deceleration or acceleration, correspond to specific ranges of ω:

Deceleration phases encompass intervals such as those involving cold dark matter or dust fluid (ω equals zero), indicating the radiation era when ω lies between 0 and $1/3$, and the fluid is classified as stiff for $\omega = 1$. The accelerating phase, akin to the cosmic constant/vacuum period (ω equals -1), corresponds to the quintessence period when $-1 < \omega < -1/3$, and it's known as the phantom era when $\omega < -1$. This signifies a quintom period characterized by a combination of both quintessence and phantom components.

The EoS parameter of KHDE with the Hubble horizon cutoff is provided in Eq. (24). Fig. 2 illustrates the evolution of the EoS parameter ω_{de} concerning cosmic time t. Initially, as depicted in Fig. 2, ω_{de} originates from the DE era, transitioning through the aggressive phantom region ($\omega_{de} << -1$) and into the phantom region ($\omega_{de} < -1$) and quintessence as well as ΛCDM model for three values of c respectively. With decreasing values of the parameter c, our model is progressively enters the quintessence region.

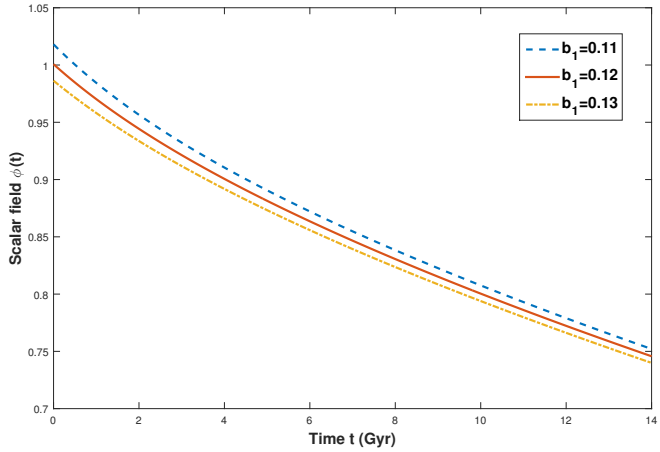

Figure 1. Scalar field Vs. t for $\gamma_0 = 0.178$, $k = 0.97$, $n = -0.28$, $b_2 = -0.34$ and $\phi_0 = 1$.

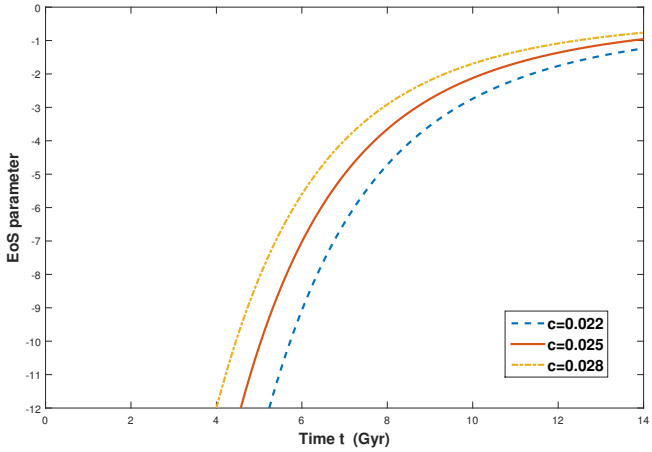

Figure 2. EoS parameter Vs. t for $\gamma_0 = 0.178$, $k = 0.97$, $n = -0.28$, $b_2 = -0.34$, $\phi_0 = 1$, $b_1 = 0.12$ and $\mathcal{K} = 0.007$.

Squared sound speed: It is derived as

$$v_s^2 = \frac{\dot{p}_{de}}{\dot{\rho}_{de}} = \omega_{de} + \frac{\rho_{de}}{\dot{\rho}_{de}}\,\dot{\omega}_{de}. \tag{26}$$

The sign of v_s^2 is crucial in assessing the stability of DE models. A positive signature of v_s^2 indicates model stability, while a negative signature suggests instability. By substituting the energy density and EoS parameter from equations (22) and (24) into the equation for squared sound speed (v_s^2) provided by equation (26), we conduct a graphical analysis of v_s^2 for our model. As illustrated in Fig. 3, the trajectories are negative at initial epoch and consistently exhibit positive behavior at later stages of the evolution of the model. Consequently, this indicates that our model is unstable at initial epoch whereas it becomes stable at present and late-times.

ω_{de}–ω'_{de} plane: We examine the $\omega_{de} - \omega'_{de}$ plane, where ω'_{de} represents the rate of change of the EoS parameter ω_{de} with respect to $\ln(a(t))$ [58]. It has also been found that the $\omega_{de} - \omega'_{de}$ plane can be split into two regions: thawing ($\omega_{de} < 0$, $\omega'_{de} > 0$) and freezing ($\omega_{de} < 0$, $\omega'_{de} < 0$). The freezing region corresponds to a phase of faster cosmic acceleration compared to the thawing region.

Fig. 4 illustrates the relationship between the $\omega_{de} - \omega'_{de}$ plane and different values of c. It shows that the $\omega_{de} - \omega'_{de}$ plane predominantly corresponds to the thawing region, irrespective of the specific parameter values. Moreover, the current values of ω_{de} and ω'_{de} align well with present observational data.

Energy conditions: The Raychaudhuri equations initiated the exploration of energy conditions, playing a crucial role in analyzing the alignment of null and time-like geodesics. The energy conditions are used to illustrate other universal

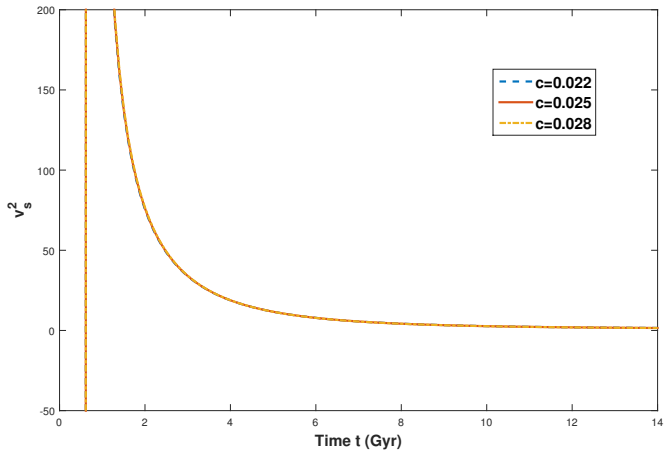

Figure 3. v_s^2 Vs. t for $\gamma_0 = 0.178$, $k = 0.97$, $n = -0.28$, $b_2 = -0.34$, $\phi_0 = 1$, $b_1 = 0.12$ and $\mathcal{K} = 0.007$.

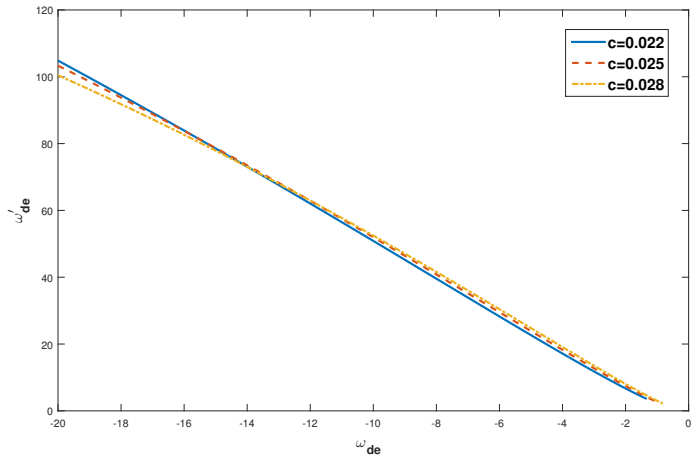

Figure 4. ω_{de}–ω'_{de} plane for $\gamma_0 = 0.178$, $k = 0.97$, $b_1 = 0.12$, $n = -0.28$, $b_2 = -0.34$, $\phi_0 = 1$ and $\mathcal{K} = 0.007$.

principles about the dynamics of intense gravitational fields. The often observed energy conditions are as follows:

Dominant energy condition (DEC): $\rho_{de} \geq 0$, $\rho_{de} \pm p_{de} \geq 0$.

Strong energy conditions (SEC) : $\rho_{de} + p_{de} \geq 0$, $\rho_{de} + 3p_{de} \geq 0$,

Null energy conditions (NEC): $\rho_{de} + p_{de} \geq 0$,

Weak energy conditions (WEC): $\rho_{de} \geq 0$, $\rho_{de} + p_{de} \geq 0$,

Fig. 5 illustrates the energy conditions of our KHDE model. It is evident that the WEC is satisfied, as $\rho_{de} \geq 0$. However, the SEC $\rho_{de} + 3p_{de} \geq 0$ is not met. This observation, reflecting the universe's acceleration in its later stages, is consistent with contemporary observational evidence.

Deceleration parameter: The expansion of the universe is often described using deceleration parameter (DP). Positive values of the DP indicate that the model exhibits a decelerating expansion in the usual sense. When $q = 0$, the universe expands at a constant rate. Accelerated expansion takes place when q lies between -1 and 0, while super-exponential expansion occurs when q is less than -1. The DP can be calculated as follows:

$$q = -1 + \frac{d}{dt}\left(\frac{1}{H(t)}\right) = -1 - \frac{3b_4}{b_3 e^{\gamma_0 t}}. \tag{27}$$

Fig. 6 depicts the evolution of the DP q as a function of time t. Notably, our model shows a transition from the early decelerating phase to the current accelerating era, in agreement with recent observational data. Furthermore, the current value of the DP ($q_0 \approx -0.86$) closely matches contemporary observational results.

Statefinder parameters: Various DE models have emerged in recent years, aiming to elucidate the accelerating expansion of the universe. Interestingly, these models often yield identical values for the current Hubble and deceleration

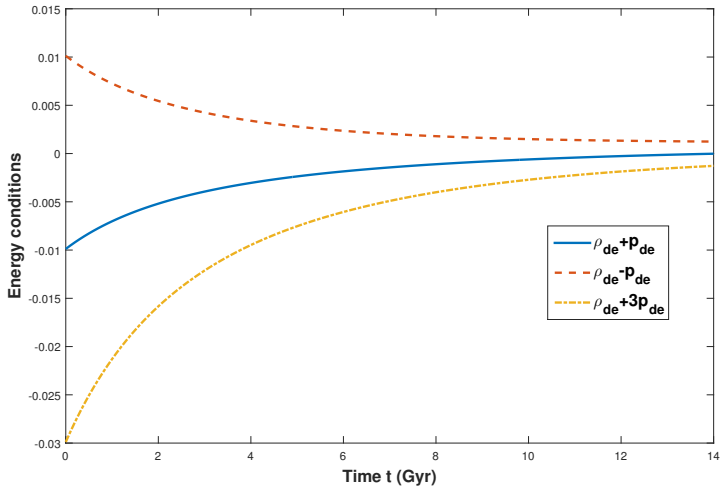

Figure 5. Energy conditions Vs. t for $\gamma_0 = 0.178$, $k = 0.97$, $n = -0.28$, $b_1 = 0.12$, $c = 0.025$, $b_2 = -0.34$, $\phi_0 = 1$, $c = 0.028$ and $\mathcal{K} = 0.007$.

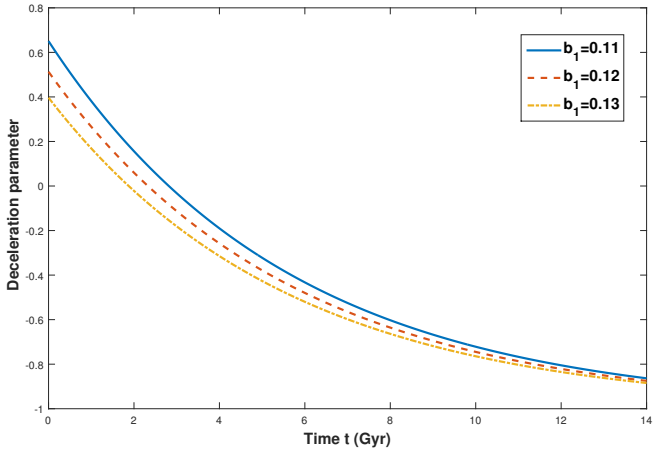

Figure 6. q Vs. t for $\gamma_0 = 0.178$, $k = 0.97$, $n = -0.28$ and $b_2 = -0.34$.

parameters, making them practically indistinguishable from one another. Sahni et al. [59] proposed a merger of the deceleration and Hubble parameters, expressed as:

$$r=\frac{\dddot{a}}{aH^3}, \quad s=\frac{r-1}{3(q-1/2)}. \tag{28}$$

The statefinder parameters for our model are

$$r = 1+\frac{9{b_4}^2}{{b_3}^2\left(e^{\gamma_0 t}\right)^2} \tag{29}$$

$$s = \frac{{b_4}^2}{{b_3}^2\left(e^{\gamma_0 t}\right)^2}\left(-\frac{1}{2}-\frac{b_4}{b_3 e^{\gamma_0 t}}\right)^{-1} \tag{30}$$

The regions shown below are defined by these statefinders: ΛCDM for $(r, s) = (1, 0)$ and CDM model for $(r, s) = (1, 1)$; $r< 1$ gives quintessence and $s> 0$ gives phantom DE phases; $r> 1$ with $s< 0$ establishes the Chaplygin gas model. Fig. 7 depicts the $r - s$ plane's trajectory. The $r - s$ plane resembles to the quintessence as well as phantom regions it its evolution.

Comparative analysis: Here, we compare our work with recent studies on this subject and discuss its alignment with observational data.

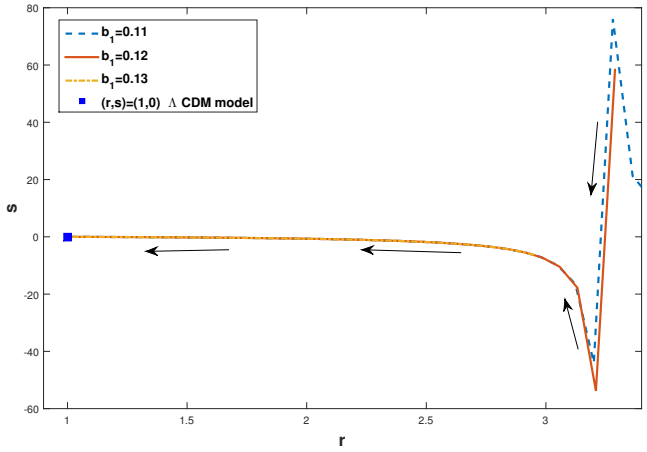

Figure 7. Statefinder parameters for $\gamma_0 = 0.178$, $k = 0.97$, $n = -0.28$, $b_1 = 0.12$ and $b_2 = -0.34$.

Rao and Prasanthi [60] conducted an investigation into BT-*I* and BT-*III* DE models within the framework of SB theory. These models evolve from the phantom region and gradually transition into the quintessence region. Similarly, Rao et al. [39] examined a universe filled with holographic Ricci DE. Their model sees the EoS parameter evolve from a matter-dominated state to the phantom region, crossing the phantom divide line and ultimately progressing towards the quintessence region as time advances. Sadri and Vakili [61] explored the FRW new HDE model within the BD gravity. Their findings revealed that the EoS parameter could enter the phantom era without requiring any interaction between DE and dark matter. Aditya and Reddy [62] studied BT-I universe within the SB scalar–tensor theory and it begins in the matter-dominated era, progresses through the quintessence region, crosses the phantom divide line, and ultimately stabilizes in the phantom region. Prasanthi and Aditya [63] delved into BT-VI$_0$ RHDE models in GTR, where they observed the universe exhibiting both quintom and phantom behaviors. Naidu et al. [64] analyzed the FRW-type DE cosmological models within the SB gravity. Aditya [65] examined the BT-I RHDE model in SB theory and determined that it demonstrated quintom behavior while aligning with observational data. Aditya and Prasanthi [66] looked into the dynamics of SMHDE in the BD gravity, finding that their model starts in the matter-dominated era, crosses the phantom divide line, and ultimately stabilizes in the aggressive phantom region. Dasunaidu et al. [67] explored FRW-type DE models in SB's theory, observing that the models evolve from the matter-dominated era, pass through the quintessence DE phase, and finally approach vacuum DE and the phantom era. Rao et al. [51] studied the BT-VI$_0$ KHDE model in GTR, asserting that the model starts in the matter-dominated era, evolves through the quintessence region, and eventually becomes the ΛCDM model. Aditya et al. [68] explored BT-VI$_0$ space-time within the SMHDE framework in the BD theory of gravitation, concluding that the model accurately characterizes both the quintessence and vacuum regions of the universe. Prasanthi et al. [69] investigated the KHDE model within the BD gravity, particularly in the Kantowski-Sachs space-time. Murali et al. [70] explored the BT-I universe KHDE model within SB theory, claiming that these models closely resemble the ΛCDM limit at late times and match recent observational data. In comparison to these studies, our models align with existing results in the literature. The analysis of the EoS parameter shows that our model begins in the aggressive phantom region ($\omega_{de} \ll -1$) and eventually transitions into the ΛCDM model ($\omega_{de} = -1$), exhibiting behavior that closely mirrors the models discussed above. Furthermore, the observational data from the Planck mission, as presented by Aghanim et al. [71], provide constraints on the EoS parameter of DE, with the following ranges: $\omega_{de} = -1.56^{+0.60}_{-0.48}$ (Planck + TT + lowE); $\omega_{de} = -1.58^{+0.52}_{-0.41}$ (Planck + TT, TE, EE + lowE); $\omega_{de} = -1.57^{+0.50}_{-0.40}$ (Planck + TT, TE, EE + lowE + lensing); and $\omega_{de} = -1.04^{+0.10}_{-0.10}$ (Planck + TT, TE, EE + lowE + lensing + BAO) at a 95% confidence level. As shown in Fig. 2, the EoS parameter of our model lies comfortably within these observational limits, further reinforcing the consistency of our results with cosmological data.

Moreover, the trajectories of the $\omega_{de} - \omega'_{de}$ plane derived from our model intersect with the observational data reported by various studies [73, 74]. Specifically, the values of ω_{de} and ω'_{de} obtained from our model fall within the ranges provided by observations from the Planck mission: $\omega_{de} = -1.13^{+0.24}_{-0.25}$, $\omega'_{de} < 1.32$ (Planck + WP + BAO); and $\omega_{de} = -1.34 \pm 0.18$, $\omega'_{de} = 0.85 \pm 0.7$ (WMAP + eCAMB + BAO + H_0). This alignment further affirms the credibility of our model's predictions and its consistency with observational data. Finally, the current values of the deceleration parameter q from our model align well with those derived from observational data—$q = -0.930 \pm 0.218$ (BAO + Masers + TDSL + Pantheon + H_z) and $q = -1.2037 \pm 0.175$ (BAO + Masers + TDSL + Pantheon + H_0 + H_z) as reported by Capozziello et al. [72]. This alignment underscores the reliability and accuracy of our model's predictions, indicating that our KHDE model is more viable than the DE models proposed by several other authors.

4. CONCLUSIONS

A cosmological reconstruction of the second self-creation gravity has been studied in this study using the KHDE model. Both the geometric and matter components are considered to have contributed to the acceleration of the expansion of the Universe. The BT-II Universe with a pressure-less matter contribution as cosmic fluid configuration has been studied and the associated field equations have been derived. Using energy conditions, deceleration parameters, and the EoS, the reconstruction of the KHDE model has been examined for its evolutionary behavior. We also investigated the (r, s) and $\omega_{de} - \omega'_{de}$ cosmic planes to learn more about how the model changed over time. Here are the main takeaways from our research.

i. According to Fig. 2 (the EoS parameter trajectory), the model begins in the aggressive phantom region and eventually approaches the ΛCDM model and the phantom phase of the Universe.

ii. The model smoothly moves from the early decelerated epoch to the present accelerated era of the Universe when the DP evolves against cosmic time (Fig. 6). According to Fig. 7, the statefinder diagnostic plane of our rebuilt model aligns with both the phantom and Chaplygin gas models.

iii. The thawing region is depicted by the track in the $\omega_{de} - \omega'_{de}$ plane (Fig. 4). According to Fig. 3, our model is unstable at the first period but becomes stable over the present and late times. The energy conditions shown in Fig. 5 are from our KHDE model. While the SEC has not been satisfied, the WEC has been satisfied. Therefore, according to modern observational evidence (Fig. 5), the cosmos is expanding at an accelerated rate in its latter phases.

Acknowledgment: Y. Aditya expresses gratitude to the National Board for Higher Mathematics, Department of Atomic Energy, Government of India, for their financial support under grant No: 02011/8/2023 NBHM(R.P.)/R & D II/3073.

ORCID

Y. Aditya, https://orcid.org/0000-0002-5468-9697; **D. Tejeswararao**, https://orcid.org/0000-0003-3508-346X; **U.Y. Divya Prasanthi**, https://orcid.org/0009-0004-5397-050X; **D. Ram Babu**, https://orcid.org/0009-0008-7791-5977

REFERENCES

[1] S. Perlmutter, et al., Astrophys. J. **517**, 565 (1999). https://doi.org/10.1086/307221

[2] A. G. Riess, et al., Astron. Soc. Pac. **112**, 1284 (2000). https://doi.org/10.1086/316624

[3] M. Tegmark, et al., Phys. Rev. D, **69**, 103501 (2004). https://doi.org/10.1103/PhysRevD.69.103501

[4] M. Sharif, and Z.J. Yousaf, Astropart. Phys. **56**, 19 (2014). https://doi.org/10.1016/j.astropartphys.2014.02.006

[5] S. Nojiri, and S. Odintsov, Phys. Lett. B. **631**, 1 (2005). https://doi.org/10.1016/j.physletb.2005.10.010

[6] T. Harko, and F.S.N. Lobo, Int. J. Mod. Phys. D, **21**, 1242019 (2012). https://doi.org/10.1142/S0218271812420199

[7] C. Brans, and R.H., Dicke, Phys. Rev. **124**, 925 (1961). https://doi.org/10.1103/PhysRev.124.925

[8] D. Saez, and V.J. Ballester, Phys. Lett. A, **113**, 467 (1986). https://doi.org/10.1016/0375-9601(86)90121-0

[9] G.A. Barber, Gen. Relativ. Gravit. **14**, 117 (1982). https://doi.org/10.1007/BF00756918

[10] T. Singh, and T. Singh, Astrophys. Space Sci. **102**, 67 (1984). https://doi.org/10.1007/BF00651062

[11] D.R.K. Reddy, Astrophys. Space Sci. **133**, 389 (1987). https://doi.org/10.1007/BF00642496

[12] V.U.M. Rao, et al., Astrophys Space Sci. **317**, 83 (2008). https://doi.org/10.1007/s10509-008-9859-7

[13] R.L. Naidu, et al.: Astrophys Space Sci. **358**, 23 (2015). https://doi.org/10.1007/s10509-015-2421-5

[14] V.U.M. Rao, and U.Y.D. Prasanthi, Can. J. Phys. **95(6)**, 554 (2017). https://doi.org/10.1139/cjp-2017-0014

[15] R.R. Caldwell, and M. Kamionkowski, Ann. Rev. Nucl. Part. Sci. **59**, 397 (2009). https://doi.org/10.1146/annurev-nucl-010709-151330

[16] K. Bamba, et al., Astrophys. Space Sci. **342**, 155 (2012). https://doi.org/10.1007/s10509-012-1181-8

[17] S. Nojiri, et al., Phys. Rept. **692**, 1 (2017). https://doi.org/10.1016/j.physrep.2017.06.001

[18] Y. Aditya, and D.R.K. Reddy, Eur. Phys. J. C, **78**, 619 (2018). https://doi.org/10.1140/epjc/s10052-018-6074-8

[19] V.U.M. Rao, et al., Results in Physics, **10**, 469 (2018). https://doi.org/10.1016/j.rinp.2018.06.027

[20] Y. Aditya, et al., Eur. Phys. J. C, **79**, 1020 (2019). https://doi.org/10.1140/epjc/s10052-019-7534-5

[21] U.K. Sharma, et al., IJMPD, **31**, 2250013 (2022). https://doi.org/10.1142/S0218271822500134

[22] U.Y.D. Prasanthi, and Y. Aditya, Results of Physics **17**, 103101 (2020). https://doi.org/10.1016/j.rinp.2020.103101

[23] U.Y.D. Prasanthi, and Y. Aditya, Physics of the dark universe **31**, 100782 (2021). https://doi.org/10.1016/j.dark.2021.100782

[24] Y. Aditya, and D.R.K. Reddy, Astrophys. Space Sci. **363**, 207 (2018). https://doi.org/10.1007/s10509-018-3429-4

[25] Y Aditya, et al., Results in Physics, **12**, 339 (2019). https://doi.org/10.1016/j.rinp.2018.11.074

[26] Y. Aditya, et al. Astrophys. Space Sci. **364**, 190 (2019). https://doi.org/10.1007/s10509-019-3681-2

[27] Y. Aditya, et al., Int. J. Mod. Phys. A, **37**, 2250107 (2022). https://doi.org/10.1142/S0217751X2250107X
[28] A. Jawad, et al., Symmetry, **10**, 635 (2018). https://doi.org/10.3390/sym10110635
[29] A. Riess, et al., Astron. J. **116**, 1009 (1998). https://doi.org/10.1086/300499
[30] B. Jain, and A. Taylor, Phys. Rev. Lett. **91**, 141302 (2003). https://doi.org/10.1103/PhysRevLett.91.141302
[31] L. Susskind, J. Math. Phys. **36**, 6377 (1994). https://doi.org/10.1063/1.531249
[32] R. Bousso, JHEP, **07**, 004 (1999). https://doi.org/10.1088/1126-6708/1999/07/004
[33] A. Cohen, et al.: Phys. Rev. Lett. **82**, 4971 (1999). https://doi.org/10.1103/PhysRevLett.82.4971
[34] M. Tavayef, et al., Phys. Lett. B, **781**, 195 (2018). https://doi.org/10.1016/j.physletb.2018.04.001
[35] C. Tsallis, and L.J.L. Cirto, Eur. Phys. J. C, **73**, 2487 (2013). https://doi.org/10.1140/epjc/s10052-013-2487-6
[36] A.S. Jahromi, et al., Phys. Lett. B, **780**, 21 (2018). https://doi.org/10.1016/j.physletb.2018.02.052
[37] H. Moradpour, et al., Eur. Phys. J. C, **78**, 829 (2018). https://doi.org/10.1140/epjc/s10052-018-6309-8
[38] Y. Aditya, and D.R.K. Reddy, Eur. Phys. J. C, **78**, 619 (2018). https://doi.org/10.1140/epjc/s10052-018-6074-8
[39] V.U.M. Rao, et al., Results in Physics, **10**, 469 (2018). https://doi.org/10.1016/j.rinp.2018.06.027
[40] M.V. Santhi, et al., Int. J. Theor. Phys. **56**, 362 (2017). https://doi.org/10.1007/s10773-016-3175-8
[41] Y. Aditya, et al., Eur. Phys. J. C, **79**, 1020 (2019). https://doi.org/10.1140/epjc/s10052-019-7534-5
[42] A. Iqbal, A. Jawad, Physics of the Dark Universe, **26**, 100349 (2019). https://doi.org/10.1016/j.dark.2019.100349
[43] G. Kaniadakis, Physica A: Stat. Mech. and its Appl. **296**(3-4), 405 (2001). https://doi.org/10.1016/S0378-4371(01)00184-4
[44] M. Masi, Phys. Lett. A, **338**, 217 (2005). https://doi.org/10.1016/j.physleta.2005.01.094
[45] E.M. Abreu, et al., EPL (Europhysics Letters), **124**, 30003 (2018). https://doi.org/10.1209/0295-5075/124/30003
[46] H. Moradpour, et al. Eur. Phys. J. C, **80**, 1 (2020). https://doi.org/10.1140/epjc/s10052-020-8307-x
[47] A. Jawad, and A.M. Sultan, Adv. High Energy Phys. **2021**, 5519028 (2021). https://doi.org/10.1155/2021/5519028
[48] U.K. Sharma, et al., IJMPD, **31**, 2250013 (2022). https://doi.org/10.1142/S0218271822500134
[49] N. Drepanou, et al., Eur. Phys. J. C, **82**, 449 (2022). https://doi.org/10.1140/epjc/s10052-022-10415-9
[50] J. Sadeghi, et al., arXiv:2203.04375 (2022). https://doi.org/10.48550/arXiv.2203.04375
[51] B.G. Rao, et al., East Eur. J. Phys. (1), 43 (2024). https://doi.org/10.26565/2312-4334-2024-1-03
[52] K.S. Thorne, Astrophys. J. **148**, 51 (1967). http://dx.doi.org/10.1086/149127
[53] R. Kantowski, and R.K. Sachs, J. Math. Phys. **7**, 433 (1966). https://doi.org/10.1063/1.1704952
[54] J. Kristian, and R.K. Sachs, Astrophys. J. **143**, 379 (1966). https://doi.org/10.1086/148522
[55] C.B. Collins, et al., Gen. Relativ. Gravit. **12**, 805 (1980). https://doi.org/10.1007/BF00763057
[56] V.B. Johri, and R. Sudharsan, Australian Journal of Physics **42(2)**, 215 (1989). https://doi.org/10.1071/PH890215
[57] V.B. Johri, and K. Desikan, Gen Relat Gravit **26**, 1217 (1994). https://doi.org/10.1007/BF02106714
[58] R. Caldwell, and E.V. Linder, Phys. Rev. Lett. **95**, 141301 (2005). https://doi.org/10.1103/PhysRevLett.95.141301
[59] V. Sahni, et al., J. Exp. Theor. Phys. Lett. **77**, 201 (2003). https://doi.org/10.1134/1.1574831
[60] V.U.M. Rao, and U.Y.D. Prasanthi, The European Physical Journal Plus, **132**, 64 (2017). https://doi.org/10.1140/epjp/i2017-11328-9
[61] E. Sadri, B. Vakili, Astrophysics and Space Science **363**, 13 (2018). https://doi.org/10.1007/s10509-017-3237-2
[62] Y. Aditya, and D.R.K. Reddy, Astrophys. Space Sci. **363**, 207 (2018). https://doi.org/10.1007/s10509-018-3429-4
[63] U.Y. Divya Prasanthi, and Y. Aditya, Results Phys. **17**, 103101 (2020). https://doi.org/10.1016/j.rinp.2020.103101
[64] R.L. Naidu, et al., New Astronomy, **85**, 101564 (2021). https://doi.org/10.1016/j.newast.2020.101564
[65] Y. Aditya, Bulgarian Astronomical Journal **40**, 95 (2024). https://astro.bas.bg/AIJ/issues/n40/YAditya.pdf
[66] Y. Aditya, and U.Y.D. Prasanthi, Bulgarian Astronomical Journal **38**, 52 (2023). https://astro.bas.bg/AIJ/issues/n38/YAditya.pdf
[67] K. Dasunaidu, et al., Bulgarian Astronomical Journal **39**, 72 (2023). https://astro.bas.bg/AIJ/issues/n39/KDasunaidu.pdf
[68] Y. Aditya, et al., East Eur. J. Phys. (1), 85 (2024). https://doi.org/10.26565/2312-4334-2024-1-06
[69] A. V. Prasanthi, et al., East Eur. J. Phys. (2), 10 (2024). https://doi.org/10.26565/2312-4334-2024-2-01
[70] K. Murali, et al., Mod. Phys. Let. A, **39**, 2450106 (2024). https://doi.org/10.1142/S0217732324501062
[71] N. Aghanim, et al., A&A **641**, A6 (2020). https://doi.org/10.1051/0004-6361/201833910
[72] S. Capozziello, et al., MNRAS, **484**, 4484 (2019). https://doi.org/10.1093/mnras/stz176
[73] P.A.R. Ade, et al., Astrophys. **571**, A16 (2014). https://doi.org/10.1051/0004-6361/201321591
[74] G.F. Hinshaw, et al., Astrophys. J. Suppl. **208**, 19 (2018). https://doi.org/10.1088/0067-0049/208/2/19

РЕКОНСТРУКЦІЯ ГОЛОГРАФІЧНОЇ МОДЕЛІ ТЕМНОЇ ЕНЕРГІЇ КАНІАДАКІСА В ТЕОРІЇ САМОСТВОРЕННЯ ГРАВІТАЦІЇ

Ю. Адітья[a], **Д. Техесварарао**[a], **Ю.Й. Дів'я Прасанті**[b], **Д. Рам Бабу**[b]

[a] *Департамент фундаментальних і гуманітарних наук, Технологічний інститут GMR, Раджам-532127, Індія*

[b] *Департамент статистики і математики, Коледж садівництва, Доктор Ю.С.Р. Університет садівництва, Парватіпурам-535502, Індія*

Основною метою цієї статті є дослідження голографічного всесвіту темної енергії Каніадакіса типу Б'янкі *II* в рамках теорії гравітації самостворення. У цій моделі темної енергії горизонт Хаббла використовується як межа інфрачервоного випромінювання відповідно до голографічної концепції темної енергії Каніадакіса. Ми обчислюємо різні динамічні параметри в цій моделі, включаючи площину вимірювача стану (r, s), параметр сповільнення q, рівняння стану (ω_{de}), квадрат швидкості звуку та площина $\omega_{de} - \omega'_{de}$. Графічний аналіз цих параметрів надається в діапазоні безкоштовних значень параметрів. Результати показують, що параметр уповільнення демонструє плавний перехід Всесвіту від ранньої уповільненої фази до поточного прискореного розширення, тоді як рівняння параметра стану свідчить про фантомну фазу. Площина $\omega_{de} - \omega'_{de}$ досягає області розморожування, а площина вимірювача стану вирівнюється як з фантомною моделлю, так і з газом Чаплигіна. Поточні значення параметрів узгоджуються з наявними даними спостережень, а сильні енергетичні умови виявляються порушеними.

Ключові слова: *Модель Б'янкі типу II; голографічна темна енергія Каніадакіса; теорія самостворення; темна енергія; модифікована теорія гравітації*

East European Journal of Physics. **1.** 20-28 (2025)
DOI:10.26565/2312-4334-2025-1-02 ISSN 2312-4334

ACCELERATING THE COSMOLOGICAL MODEL WITH ZERO-MASS SCALAR FIELD IN LYRA'S GEOMETRY

M. Krishna[a], K. Sobhan Babu[b], R. Santhikumar[c]*
[a]*Raghu Engineering College, Visakhapatnam, Andhra Pradesh, India*
[b]*University Collage of Engineering, Narasaraopeta, Andhra Pradesh, India*
[c]*Aditya Institute of Technology and Management, Tekkali, Srikakulam Dist. Andhra Pradesh-India*
**Corresponding author email: skrmahanthi@gmail.com*
Received October 10, 2024; revised December 15, 2024; in final form December 26, 2024; accepted January 8, 2025

Examining Bianchi's type-III cosmological model involves incorporating a zero-mass scalar field in the context of Lyra's geometry. The source of energy-momentum tensor is supposed to be a bulk viscous fluid. A barotropic equation of state is applied to characterize the Pressure and density, seeking a specific solution to the field equations. This solution is derived using the distinctive variation principle for Hubble's parameter proposed by [M.S. Berman, Il Nuovo Cimento B, 74, 182 (1983)]. The ensuing analysis delves into the physical properties inherent in this model.
Keywords: *Accelerating; Cosmology; Lyra's geometry*
PACS: 4.50.Kd, 03.30.+p, 98.80.Bp, 66.20.-d, 98.80Cq

INTRODUCTION

The advancement of general relativity was profoundly influenced by the groundbreaking contributions of Einstein and Hilbert [2–4], leaving an indelible mark on cosmology, physics, and mathematics. The works of both Hilbert and Einstein extensively employed Riemannian geometry [5], a framework where space-time is equipped with a metric and an affine structure. These key components are delineated by $g_{\mu\nu}$ and a connection represented by $\Gamma^{\alpha}_{\mu\nu}$, respectively.

The geometric and gravitational characteristics of space-time find expression in the curvature tensor $R^{\mu}{}_{\nu\sigma\lambda}$ and its contraction, providing the foundation for the construction of the Einstein tensor.

Several modifications to Riemannian geometry have been proposed to unify the universe's gravitation, the electromagnetic field, and other fundamental interactions. Weyl [6] made one such attempt by trying to unify gravitation and electromagnetism within a single space-time geometry. However, Weyl's theory faced criticism due to its reliance on the non-integrability of length transfer. Later, Lyra [7] introduced a further modification to Riemannian geometry by incorporating a gauge function into a less manifold structure, thereby eliminating the issue of non-integrability in length transfer. This modification naturally gave rise to a displacement vector. Building on Lyra's work, Sen [8] and Sen and Dunn [9] developed a new scalar-tensor theory of gravitation and formulated an analogy of the Einstein field equations based on Lyra's geometry. Halford [10] noted that the constant vector displacement field ϕ_i Lyra's geometry functions similarly to the cosmological constant Λin conventional general relativity. Furthermore, Halford [11] demonstrated that the scalar-tensor theory derived from Lyra's geometry yields predictions consistent with observational limits, matching the results of Einstein's theory.

Cosmological models of Bianchi [12] exhibit both homogeneity and anisotropy, providing a framework for investigating the gradual isotropization of the universe over time. Additionally, from a mathematical and theoretical perspective, anisotropic universes offer greater generality than isotropic Friedmann-Robertson-Walker (FRW) models.

Exploring interacting fields, particularly involving a zero-mass scalar field, is essential to address the unresolved challenge of unifying gravitational and quantum theories. This study delves into the intricate problem of reconciling these fundamental aspects of physics.

Furthermore, examining viscous mechanisms in cosmology is pivotal in elucidating the high entropy observed at present. This investigation contributes valuable insights into understanding the thermodynamic properties and evolution of the cosmos.

This paper is framed within the context of previous research studies. Reddy et al. [13-14] investigated Bianchi type-III models incorporating bulk viscous coefficients. Katore et al. [15] explored solutions for zero-mass cosmological models with bulk viscous coefficients within the Lyra geometry. Halford [16] provided an overview of Lyra's geometry, and Singh [17] further delved into the same topic. Santhikumar [18] focused on accelerating cosmological models, while Santhikumaret al. [19] explored Lyra's geometry heat flow cosmological models. Krishna [20] also examined plane-symmetric cosmological models within Lyra's geometry. Numerous authors have extended their research within Lyra's geometry, laying the foundation for future research. By Motivation from these studies, this paper presents a novel contribution: a Bianchi type-III cosmological model incorporating a zero-mass scalar field and perfect fluid and bulk viscous effects in Lyra's geometry.

Cite as: M. Krishna, K.S. Babu, R. Santhikumar, East Eur. J. Phys. 1, 20 (2025), https://doi.org/10.26565/2312-4334-2025-1-02

The structure of this paper is organized as follows: Section 2 examines the metric and field equations within the Bianchi type-III cosmological model, incorporating a zero-mass scalar field in Lyra's Geometry. Section 3 is dedicated to deriving the solutions to the field equations. In Section 4, we focus on explaining the physical properties of the models. Section 5 provides a detailed discussion, and Section 6 concludes the paper.

METRIC AND FIELD EQUATIONS

The Bianchi type-III metric is

$$ds^2 = dt^2 - A^2(t)dx^2 - B^2(t)e^{-2x}dy^2 - C^2(t)dz^2, \tag{1}$$

where $A, B\&C$ are cosmic scale factors.

The field equations in standard gauge for Lyra's geometry, as obtained by Sen [8], are

$$\left(R_{ij} - \frac{1}{2}g_{ij}R\right) + \left(\frac{3}{2}\phi_i\phi_j - \frac{3}{4}g_{ij}\phi_k\phi^k\right) = \kappa T_{ij} + \left(\psi_{;i}\psi_{;j} - \frac{1}{2}g_{ij}\psi_{,k}\psi^{,k}\right). \tag{2}$$

In the Einstein field equations, κ(kappa) is a constant related to the gravitational constant 'G' and the speed of light 'C' Specifically, $\kappa = \frac{8\pi}{c^4}G$, in natural units, where c=1 κ reduces to 8π, so $\kappa = 8\pi G$. It simplifies the Einstein field equations to avoid explicitly carrying around the constant, making focusing on the functional relationships between variables easier. We consider $\kappa = 1$, (*the n*atural units $G = 1$, $8\pi G = 1$)).

Here $\phi_i = (0,0,0,\beta(t))$ is the displacement vector,

Consider

$$\bar{T}_{ij} = \left(\frac{3}{2}\phi_i\phi_j - \frac{3}{4}g_{ij}\phi_k\phi^k\right) = \begin{cases} \frac{3}{4}\beta^2(t), for\ i = j = 0\ (Time - time) \\ -\frac{3}{4}g_{ij}g^{00}\beta^2(t)\ , for\ i = j\ \neq 0\ (spatial\ components for\ i = j = 1,2,3) \end{cases}, \tag{3}$$

so, we have

$$\bar{T}_0^0 = \frac{3}{4}\beta^2(t), \bar{T}_1^1 =, \bar{T}_2^2 = \ \bar{T}_3^3 = -\frac{3}{4}\beta^2(t) \tag{4}$$

$$\bar{\Psi}_{ij} = \left(\psi_{;i}\psi_{;j} - \frac{1}{2}g_{ij}\psi_{,k}\psi^{,k}\right) = \begin{cases} \frac{1}{2}\dot{\psi}^2\ , for\ i = i = 0\ (Time - time) \\ -\frac{1}{2}g_{ij}\dot{\psi}^2, for\ i = j \neq 0\ (spatial\ components for\ i = j = 1,2,3) \end{cases}, \tag{5}$$

so, we have

$$\bar{\Psi}_0^0 = \frac{1}{2}\dot{\psi}^2\ , \bar{\Psi}_1^1 = \bar{\Psi}_2^2 = \bar{\Psi}_3^3 = -\frac{1}{2}\dot{\psi}^2 \tag{6}$$

T_{ij} is the energy-momentum tensor for bulk viscous and zero-mass scalar fields as

$$T_{ij} = (\rho + \overline{p})u_i u_j - \overline{p}g_{ij} \tag{7}$$

Together with

$$u^i u_i = 1, \overline{p} = p - \eta u^i_{;i} = p - 3\eta H \tag{8}$$

Where u_i is the four-velocity vector of the distribution,

p is the Pressure,$\overline{p}$ is the adequate Pressure,

η is the bulk viscosity coefficient, and ψ is the zero-mass scalar field.

The non-vanishing energy-momentum tensor components are

Here

$$T_0^0 = \rho, T_1^1 = T_2^2 = T_3^3 = -\overline{p}. \tag{9}$$

Introducing a barotropic equation of state into the discussion

$$p = (\gamma - 1)\rho, 0 \leq \gamma \leq 2 \tag{10}$$

Employing co-moving coordinates, the field equations (1) – (8)

$$-\frac{\dot{A}\dot{C}}{AC} - \frac{\dot{B}\dot{C}}{BC} - \frac{\dot{A}\dot{B}}{AB} + \frac{1}{A^2} + \frac{3}{4}\beta^2 = \left(\rho + \frac{1}{2}\dot{\psi}^2\right), \tag{11}$$

$$\frac{\ddot{B}}{B}+\frac{\ddot{C}}{C}+\frac{\dot{B}\dot{C}}{BC}+\frac{3}{4}\beta^2=\left(\overline{p}+\frac{1}{2}\dot{\psi}^2\right) \tag{12}$$

$$\frac{\ddot{A}}{A}+\frac{\ddot{C}}{C}+\frac{\dot{A}\dot{C}}{AC}+\frac{3}{4}\beta^2=\left(\overline{p}+\frac{1}{2}\dot{\psi}^2\right) \tag{13}$$

$$\frac{\ddot{A}}{A}+\frac{\ddot{B}}{B}+\frac{\dot{A}\dot{B}}{AB}-\frac{1}{A^2}+\frac{3}{4}\beta^2=\left(\overline{p}+\frac{1}{2}\dot{\psi}^2\right) \tag{14}$$

$$\frac{\dot{A}}{A}-\frac{\dot{B}}{B}=0 \tag{15}$$

The scalar field ψ complies with the following equation.

$$\psi^{i}_{;i}=0 \tag{16}$$

Hence, the semi-colon $(;)$ indicates covariant differentiability
By using the equations(14), which yields that

$$\ddot{\psi}+\dot{\psi}\left[\frac{\dot{A}}{A}+\frac{\dot{B}}{B}+\frac{\dot{C}}{C}\right]=0 \tag{17}$$

And conservation of L.H.S of Eq.(2) leads that

$$\left(R^{j}_{i}-\frac{1}{2}g^{j}_{i}R\right)_{;j}+\left[\frac{3}{2}(\phi_i\phi^j)_{;j}-\frac{3}{4}\left(\phi_k\phi^k g^{j}_{i}\right)_{;j}\right]=0 \tag{18}$$

$$\frac{3}{2}\phi_i\left[\frac{\partial\phi^j}{\partial x^j}+\phi^l\Gamma^{\mathrm{j}}_{\mathrm{lj}}\right]+\frac{3}{2}\phi^j\left[\frac{\partial\phi_i}{\partial x^j}-\phi_l\Gamma^{\mathrm{l}}_{\mathrm{ij}}\right]-\frac{3}{4}g^{j}_{i}\phi_k\left[\frac{\partial\phi^k}{\partial x^j}+\phi^l\Gamma^{\mathrm{k}}_{\mathrm{lj}}\right]-\frac{3}{4}g^{j}_{i}\phi^k\left[\frac{\partial\phi_k}{\partial x^j}-\phi_l\Gamma^{\mathrm{l}}_{\mathrm{kj}}\right]=0. \tag{19}$$

Eq. (19) leads that

$$\frac{3}{2}\beta\dot{\beta}+\frac{3}{2}\beta^2\left(\frac{\dot{A}}{A}+\frac{\dot{B}}{B}+\frac{\dot{C}}{C}\right)=0 \tag{20}$$

The Solution to The Field Equations

Integrating eq. (13), we get

$$B=kA \tag{21}$$

Take $k=1$, without loss of generality, So we have

$$B=A \tag{22}$$

By using Equation (16) in Equations (9)-(12) reduced to

$$-2\frac{\dot{A}\dot{C}}{AC}-\left(\frac{\dot{A}}{A}\right)^2+\frac{1}{A^2}+\frac{3}{4}\beta^2=\left(\rho+\frac{1}{2}\dot{\psi}^2\right), \tag{23}$$

$$\frac{\ddot{A}}{A}+\frac{\ddot{C}}{C}+\frac{\dot{A}\dot{C}}{AC}+\frac{3}{4}\beta^2=\left(\overline{p}+\frac{1}{2}\dot{\psi}^2\right), \tag{24}$$

$$2\frac{\ddot{A}}{A}+\left(\frac{\dot{A}}{A}\right)^2-\frac{1}{A^2}+\frac{3}{4}\beta^2=\left(\overline{p}+\frac{1}{2}\dot{\psi}^2\right). \tag{25}$$

The relation between average scale factor 'a' and Volume 'V' are

$$V=\sqrt{-g}=A(t)B(t)C(t)e^{-x} and\ a(t)=(V)^{1/3}=(A(t)B(t)C(t)e^{-x})^{1/3}. \tag{26}$$

The average Hubble parameter is

$$H=\frac{1}{3}\left(H_x+H_y+H_z\right)=\frac{\dot{a}}{a} \tag{27}$$

where $H_x=\frac{\dot{A}}{A}, H_y=\frac{\dot{B}}{B}, H_z=\frac{\dot{C}}{C}$.
The scalar expansion is

$$\theta = u^{i}_{;i} = 2\frac{\dot{A}}{A} + \frac{\dot{C}}{C} \tag{28}$$

The shear scalar is

$$\sigma^2 = \frac{1}{2}\sigma_{ik}\sigma^{ik} = \frac{1}{2}\left[2\left(\frac{\dot{A}}{A}\right)^2 + \left(\frac{\dot{C}}{C}\right)^2 - \frac{1}{3}\left(2\frac{\dot{A}}{A} + \frac{\dot{C}}{C}\right)^2\right] \tag{29}$$

The mean anisotropic parameter is

$$A_\alpha = \frac{1}{3}\sum_{i=1}^{3}\left(\frac{\Delta H_i}{H}\right)^2 = \frac{1}{3H^2}\left[{H_x}^2 + {H_y}^2 + {H_z}^2 - \frac{1}{9}\left(H_x + H_y + H_z\right)^2\right] \tag{30}$$

where $\Delta H_i = H_i - H$, for $i = 1,2,3$

Since Eqs.$(23) - (25)$equations are highly non-linear equations. Hence, to derive a definitive solution, it is imperative to consider the following requisite conditions.

(i) Utilizing the variation of Hubble's parameter proposed by Berman [1], we obtain models of the universe characterized by the constant decelerating parameter

$$q = \frac{-a\ddot{a}}{\dot{a}^2} = \text{constant.} \tag{31}$$

The solutions of Eq. (31) yields that

$$a = [k_1 t + k_2]^{\frac{1}{(q+1)}} \tag{32}$$

This equation indicates that the criterion for accelerated expansion is$(1 + q) > 0$.

(ii) Since, $\theta^2 \propto \sigma^2$Collin et al. [21]
which gives us

$$A = C^n, \text{ for } n \neq 1 \tag{33}$$

By Equations (22), (31), (32) and (33)
We obtain metric coefficients, which are

$$A = B = [k_4 t + k_5]^{\frac{3n}{(1+q)(2n+1)}} \tag{34}$$

$$C = [k_4 t + k_5]^{\frac{3}{(1+q)(2n+1)}}. \tag{35}$$

Using Eq. (22) and (33), the Eqs. (23)-(25) reduces to

$$-(2n + n^2)\left(\frac{\dot{C}}{C}\right)^2 + C^{-2n} + \frac{3}{4}\beta^2(t) = \rho + \frac{1}{2}\dot{\psi}^2, \tag{36}$$

$$(n+1)\frac{\ddot{C}}{C} + n^2\left(\frac{\dot{C}}{C}\right)^2 + \frac{3}{4}\beta^2(t) = \bar{p} + \frac{1}{2}\dot{\psi}^2 \tag{37}$$

$$2n\frac{\ddot{C}}{C} + n(2n-1)\left(\frac{\dot{C}}{C}\right)^2 - C^{-2n} + \frac{3}{4}\beta^2(t) = \bar{p} + \frac{1}{2}\dot{\psi}^2. \tag{38}$$

By substituting the values A, B and C in (2), we get

$$ds^2 = dt^2 - [k_4 t + k_5]^{\frac{6n}{(1+q)(2n+1)}}[dx^2 + e^{-2x}dy^2] - [k_4 t + k_5]^{\frac{6}{(1+q)(2n+1)}}dz^2. \tag{39}$$

Some Physical Properties of the Model

Eq. (39) describes the Bianchi type-III cosmological model featuring bulk viscous effects and a zero-mass scalar field under Lyra's geometry.
The Spatial volume is

$$V = (k_4 t + k_5)^{\frac{3(n+1)}{1+q}} e^{-x} \tag{40}$$

The Hubble's parameter is

$$H = \frac{k_4}{(1+q)(k_4 t + k_5)} \tag{41}$$

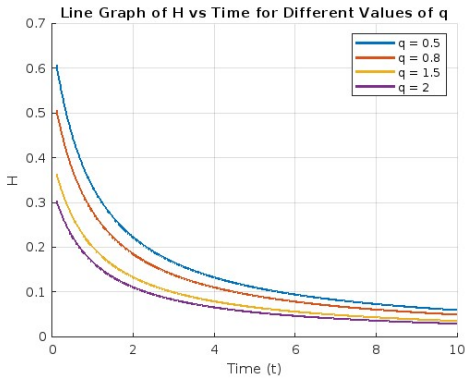

Figure 1. Hubble's Parameter H V$_{s.}$ time t
Parameters used $k_4 = 1$; $k_5 = 1$

The scalar expansion is

$$\theta = \frac{3k_4}{(1+q)(k_4t+k_5)}. \tag{42}$$

The shear scalar is

$$\sigma^2 = 3(n^2+n-1)\left(\frac{k_4}{(2n+1)(1+q)(k_4t+k_5)}\right)^2. \tag{43}$$

Clearly

$$\lim_{t\to\infty}\frac{\sigma^2}{\theta^2} = \frac{(n^2+n-1)}{3(2n+1)^2} \neq 0. \tag{44}$$

Hence, the model approaches anisotropy for large values of t
The mean anisotropic parameter is

$$A_\alpha = \frac{(1-4n)}{3(2n+1)^2}. \tag{45}$$

By Solving Equation. (17) the zero-mass scalar field is

$$\psi(t) = C_3(k_4t+k_5)^{\left(\frac{q-2}{1+q}\right)} + C_2, \tag{46}$$

where $C_2 = \frac{C_1(1+q)}{k_4(1+q-3)}$, $C_1 and\ C_2$ are integration constants

By solving equation (20) with the help of Eqs. (34) and (35), we have
The displacement vector $\beta(t)$ is

$$\beta(t) = \frac{C_4}{(k_4t+k_5)^{\left(\frac{3}{1+q}\right)}}. \tag{47}$$

Where $C_4$is integration constant
Using Eqs. (34) and (35) in Eqs.(36)-(38) , we get
The density of the model is

$$\rho = \left(\frac{-9(n^2+2n)}{(2n+1)^2(1+q)^2}\right)\left(\frac{k_4}{k_4t+k_5}\right)^2 + \frac{1}{(k_1t+k_2)^{\frac{6n}{(1+q)(2n+1)}}} + \frac{3}{4}\left(\frac{C_4}{(k_4t+k_5)^{\left(\frac{3}{1+q}\right)}}\right)^2 - \frac{1}{2}\left(\frac{C_1}{(k_1t+k_2)^{\frac{3}{1+q}}}\right) \tag{48}$$

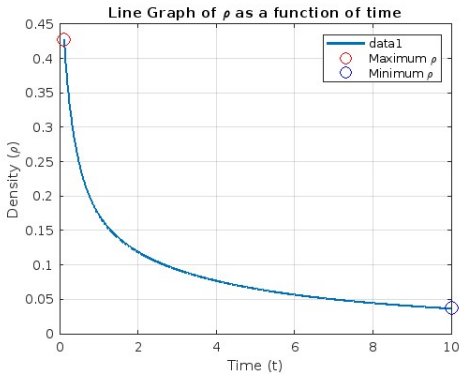

Figure 2. Density Vs. time
Parameters used n = 2; q = 1; $k_1 = 1$; $k_2 = 1$; $k_4 = 1$; $k_5 = 1$; $C_1 = 1$; C4 = 1

The Adequate Pressure of the model is

$$\overline{p} = \left(\frac{9(n^2+n+1)-3(2n+1)(1+q)}{(2n+1)^2(1+q)^2}\right)\left(\frac{k_4}{k_4t+k_5}\right)^2 + \frac{3}{4}\left(\frac{C_4}{(k_4t+k_5)^{\left(\frac{3}{1+q}\right)}}\right)^2 - \frac{1}{2}\left(\frac{C_1}{(k_1t+k_2)^{\frac{3}{1+q}}}\right). \tag{49}$$

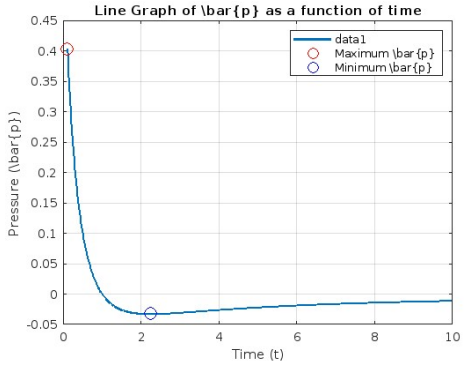

Figure 3. Adequate Pressure Vs. time
Parameters used n = 2; q = 1; k_1 = 1; k_2 = 1; k_4 = 1; k_5 = 1; C_1 = 1; C4 = 1

The Pressure of the model is

$$p = (\gamma-1)\left[\left(\frac{-9(n^2+2n)}{(2n+1)^2(1+q)^2}\right)\left(\frac{k_4}{k_4t+k_5}\right)^2 + \frac{1}{(k_1t+k_2)^{\frac{6n}{(1+q)(2n+1)}}} + \frac{3}{4}\left(\frac{C_4}{(k_4t+k_5)^{\left(\frac{3}{1+q}\right)}}\right)^2 - \frac{1}{2}\left(\frac{C_1}{(k_1t+k_2)^{\frac{3}{1+q}}}\right)\right]. \tag{50}$$

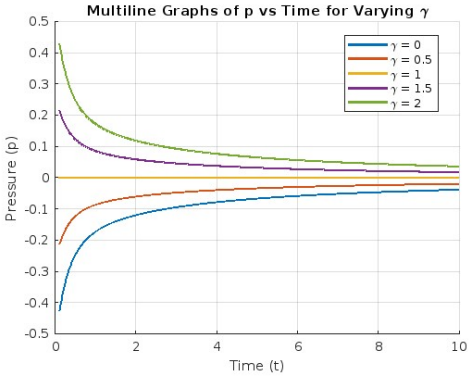

Figure 4. Pressure Vs. time
Parameters used n = 2; q = 1; k_1 = 1; k_2 = 1; k_4 = 1; k_5 = 1; C_1 = 1; C4 = 1, $0 \leq \gamma \leq 2$

The Coefficient of Bulk Viscosity of the model is

$$\eta = \frac{(1+q)(k_4t+k_5)}{3k_4}\left[\begin{array}{l}\left(\frac{-9(\gamma-1)(n^2+2n)-\left(\frac{9(n^2+n+1)-3(2n+1)(1+q)}{(2n+1)^2(1+q)^2}\right)}{(2n+1)^2(1+q)^2}\right)\left(\frac{k_4}{k_4t+k_5}\right)^2 \\ + \frac{(\gamma-1)}{(k_1t+k_2)^{\frac{6n}{(1+q)(2n+1)}}} + \frac{3(\gamma-2)}{4}\left(\frac{C_4}{(k_4t+k_5)^{\left(\frac{3}{1+q}\right)}}\right)^2 - \frac{1}{2}\left(\frac{(\gamma-2)C_1}{(k_1t+k_2)^{\frac{3}{1+q}}}\right)\end{array}\right]. \tag{51}$$

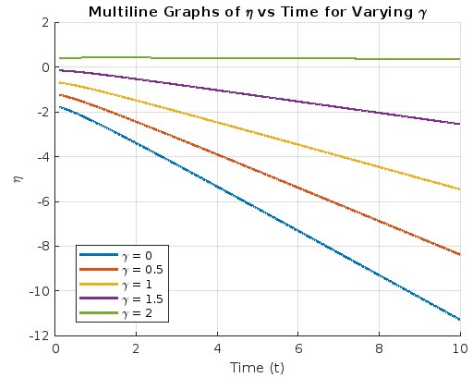

Figure 5. Bulk viscous Coefficient Vs. time t Parameters used n = 2; q = 1; k_1 = 1; k_2 = 1; k_4 = 1; k_5 = 1; C_1 = 1; C4 = 1, $0 \leq \gamma \leq 2$

The Density parameter of the model is

$$\Omega = \frac{1}{3}\left(\frac{(1+q)(k_4t+k_5)}{k_4}\right)^2\left[\left(\frac{-9(n^2+2n)}{(2n+1)^2(1+q)^2}\right)\left(\frac{k_4}{k_4t+k_5}\right)^2 + \frac{1}{(k_1t+k_2)^{\frac{6n}{(1+q)(2n+1)}}} + \frac{3}{4}\left(\frac{C_4}{(k_4t+k_5)^{\left(\frac{3}{1+q}\right)}}\right)^2 - \frac{1}{2}\left(\frac{C_1}{(k_1t+k_2)^{\frac{3}{1+q}}}\right)\right]. \quad (52)$$

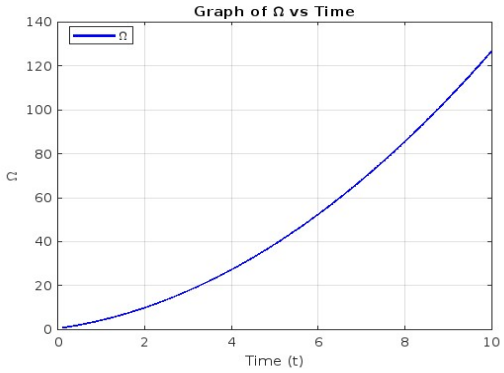

Figure 6. Density Parameter Vs. time t
Parameters used n = 2; q = 1; k_1 = 1; k_2 = 1; k_4 = 1; k_5 = 1; C_1 = 1; C4 = 1

From Eqs. (40) to (52), we observed that at t=0, the spatial volume and zero mass scalar are zero, increasing with cosmic time, showing the late-time accelerated expansion of the universe. Also, at t=0, the parameters $H, \theta, \rho, p, \bar{p}, \eta, \Omega$ are diverse while they vanish for infinitely large values of t. The mean anisotropic parameter is uniform throughout the whole evolution of the universe, which shows that the dynamics of the mean anisotropic parameter do not depend on cosmic time t. Also, since $\lim_{t\to\infty}\frac{\sigma^2}{\theta^2}$ It is constant; the model does not approach isotropy through the whole evolution of the universe. It may also be observed that the model Eq. (39) has no initial singularity.

Discussions for Physical Properties of the Model

Here, we can discuss the three physical models based on the value of $\gamma = 0, 2, \frac{4}{3}$ respectively

False Vacuum model

When $\gamma = 0$equals zero, the model embodies the false vacuum model with an Equation of State given by $p = -\rho$, characterizing both the 'false vacuum' and 'degenerate vacuum.' The explicit form and physical properties of this model are then delineated

$$p = -\rho = -\left[\left(\frac{-9(n^2+2n)}{(2n+1)^2(1+q)^2}\right)\left(\frac{k_4}{k_4t+k_5}\right)^2 + \frac{1}{(k_1t+k_2)^{\frac{6n}{(1+q)(2n+1)}}} + \frac{3}{4}\left(\frac{C_4}{(k_4t+k_5)^{\left(\frac{3}{1+q}\right)}}\right)^2 - \frac{1}{2}\left(\frac{C_1}{(k_1t+k_2)^{\frac{3}{1+q}}}\right)\right]. \quad (53)$$

$$\eta = \frac{(1+q)(k_4t+k_5)}{3k_4}\left[\left(\frac{-9(n^2+2n)-\left(\frac{9(n^2+n+1)-3(2n+1)(1+q)}{(2n+1)^2(1+q)^2}\right)}{(2n+1)^2(1+q)^2}\right)\left(\frac{k_4}{k_4t+k_5}\right)^2 + \frac{1}{(k_1t+k_2)^{\frac{6n}{(1+q)(2n+1)}}} - \frac{3}{2}\left(\frac{C_4}{(k_4t+k_5)^{\left(\frac{3}{1+q}\right)}}\right)^2 + \left(\frac{C_1}{(k_1t+k_2)^{\frac{3}{1+q}}}\right)\right] \quad (54)$$

The Equation of State parameter is

$$\omega = \frac{p}{\rho} = -1 \quad (55)$$

Zel'dovish fluid model (Stiff fluid model)

At $\gamma = 2$, $p = \rho$, representing a Zel'dovich fluid distribution. Then, the explicit form of the physical properties inherent in this model is detailed.

$$p = \rho = \left[\left(\frac{-9(n^2+2n)}{(2n+1)^2(1+q)^2}\right)\left(\frac{k_4}{k_4t+k_5}\right)^2 + \frac{1}{(k_1t+k_2)^{\frac{6n}{(1+q)(2n+1)}}} + \frac{3}{4}\left(\frac{C_4}{(k_4t+k_5)^{\left(\frac{3}{1+q}\right)}}\right)^2 - \frac{1}{2}\left(\frac{C_1}{(k_1t+k_2)^{\frac{3}{1+q}}}\right)\right] \quad (56)$$

$$\eta = \frac{(1+q)(k_4t+k_5)}{3k_4}\left[\left(\frac{-9(n^2+2n)-\left(\frac{9(n^2+n+1)-3(2n+1)(1+q)}{(2n+1)^2(1+q)^2}\right)}{(2n+1)^2(1+q)^2}\right)\left(\frac{k_4}{k_4t+k_5}\right)^2 + \frac{1}{(k_1t+k_2)^{\frac{6n}{(1+q)(2n+1)}}}\right] \quad (57)$$

$$\omega = \frac{p}{\rho} = 1 \quad (58)$$

Radiating model

When $\gamma = \frac{4}{3}$, then$p = \frac{\rho}{3}$. This representation corresponds to a matter distribution with disordered radiation, signifying the universe where the predominant portion of energy density exists, like radiation. Consequently, the model is termed a radiation-dominated universe or a radiating model. The explicit form of the physical properties inherent in this model is then elaborated.

$$p = \frac{1}{3}\rho = \frac{1}{3}\left[\left(\frac{-9(n^2+2n)}{(2n+1)^2(1+q)^2}\right)\left(\frac{k_4}{k_4t+k_5}\right)^2 + \frac{1}{(k_1t+k_2)^{\frac{6n}{(1+q)(2n+1)}}} + \frac{3}{4}\left(\frac{C_4}{(k_4t+k_5)^{\left(\frac{3}{1+q}\right)}}\right)^2 - \frac{1}{2}\left(\frac{C_1}{(k_1t+k_2)^{\frac{3}{1+q}}}\right)\right] \quad (59)$$

$$\eta = \frac{(1+q)(k_4t+k_5)}{3k_4}\left[\left(\frac{-3(n^2+2n)-\left(\frac{9(n^2+n+1)-3(2n+1)(1+q)}{(2n+1)^2(1+q)^2}\right)}{(2n+1)^2(1+q)^2}\right)\left(\frac{k_4}{k_4t+k_5}\right)^2 + \frac{1}{3(k_1t+k_2)^{\frac{6n}{(1+q)(2n+1)}}} - \frac{1}{2}\left(\frac{C_4}{(k_4t+k_5)^{\left(\frac{3}{1+q}\right)}}\right)^2 + \frac{1}{3}\left(\frac{C_1}{(k_1t+k_2)^{\frac{3}{1+q}}}\right)\right] \quad (60)$$

$$\omega = \frac{p}{\rho} = \frac{1}{3} \quad (61)$$

Our observations show that the model described by equation (39) exhibits no singularity, specifically at t=0. The zero-mass scalar field displays divergence at t=0 but diminishes for larger t values. The spatial volume undergoes expansion with increasing t, as indicated by the positivity of 1+q, portraying accelerated universe expansion. Additionally, θ, σ^2, and H tend towards infinity at t=0 and converge towards zero for larger t values. The constancy of the average anisotropy parameter signifies its uniformity throughout the universe's evolution. However, since $\frac{\sigma^2}{\theta^2}$Remains unalter, indicating a sustained anisotropic nature. It is observed that for the closed universe, when ω_D It is a decreasing function of time and an increasing function of time for open and flat universes. Universe is Closed, open, and flat universes are varying in quintessence ($\omega_D > -0.5$), phantom ($-3 < \omega_D < -1$), and super phantom ($\omega_D < -0.3$) regions, respectively.

Scientific Comparison

Compared to the model proposed by B. Misra et al. (2015) [22], the current framework is more streamlined, with time dependence primarily expressed through power-law terms. It adopts a more phenomenological perspective on density evolution over time, featuring reduced complexity in its dependencies. This approach indicates an alternative or simplified cosmological paradigm, offering a distinct interpretation of ρ that could imply processes such as dissipation, decay, or energy loss. K.P. Singh et al. (2018) [23] explored cosmological models within the framework of Lyra's geometry, utilizing the Bianchi type III metric, with particular emphasis on the interaction between the Van der Waals fluid and Lyra's manifold, as well as its contribution to the generation of dark energy. In contrast, the current model focuses on deriving solutions involving a zero-mass scalar field and a bulk viscous fluid characterized by a barotropic equation of state. These two models adopt different approaches and interpretations, highlighting their distinct objectives and methodologies.

CONCLUSIONS

In this investigation, we explored the characteristics of a Bianchi type-III cosmological model incorporating a zero-mass scalar within Lyra's geometry, with the energy-momentum tensor sourced by bulk viscous fluid. We observed that at t = 0, the spatial volume and zero mass scalar are zero, increasing with cosmic time, showing the late-time accelerated expansion of the universe. Also, at t = 0, the parameters $H, \theta, \rho, p, \bar{p}, \eta, \Omega$ are diverse while they vanish for infinitely large values of t. The mean anisotropic parameter is uniform throughout the whole evolution of the universe, which shows that the dynamics of the mean anisotropic parameter do not depend on cosmic time t. Also, since $\lim_{t\to\infty} \frac{\sigma^2}{\theta^2}$ It is constant; the model does not approach isotropy through the whole evolution of the universe. It may also be observed that the model Eq. (39) has no initial singularity.

Notably, our findings reveal that the model is non-singular, exhibits shearing and non-rotating properties, and does not tend towards isotropy for large values of cosmic time t. The spatial volume displays an increasing trend with time (as 1+q > 0), suggesting the possibility of cosmic re-collapse in the finite future. This dynamic evolution entails phases of inflation, deceleration, and subsequent acceleration. Consequently, the model emerges as an accelerating cosmological model featuring a zero-mass scalar under Lyra's geometry. We have discussed the physical models corresponding to the False Vacuum, Stiff fluid, and radiating. These cosmological models are anisotropic and have no initial singularity. Hence,zero-mass scalar field and bulk viscosity are expected to play an essential role in the universe's early evolution. Therefore, the model presented here better understands the evaluation of the universe.

Acknowledgment

The authors wish to place on record their sincere thanks to the referee whose valuable comments and suggestions have helped improve this manuscript's quality.

ORCID
M. Krishna, https://orcid.org/0000-0003-1975-8930; **K. Sobhan Babu,** https://orcid.org/0000-0002-2991-7651
R. Santhikumar, https://orcid.org/0000-0001-5122-3800

REFERENCES

[1] M.S. Berman, "A Special Law of Variation for Hubble's Parameter," Il Nuovo Cimento B, **74**, 182-186 (1983). http://dx.doi.org/10.1007/BF02721676
[2] A. Einstein, Preussische Akademie der Wissenschaften, Sitzungsberichte, (Berlin, 1915). pp. 831-839.
[3] D. Hilbert, "Nachrichten von der Gesellschaft der Wissenschaftenzu Göttingen," Math. Phys. Klasse, **3**, 395 (1915).
[4] A. Einstein, "The Foundation of the General Theory of Relativity," Annalen der Physik, **49,** 769-822 (1916) http://dx.doi.org/10.1002/andp.19163540702
[5] B. Riemann, Habilitationsschrift, Abhandlungen der Königlichen Gesellschaft der Wissenschaftenzu Göttingen, **13**(1), 1854 (1867).
[6] H. Weyl, *Sitzungsberichte der Königlich Preussischen Akademie der Wissenschaften zu Berlin*, **465**, (1918). https://www.biodiversitylibrary.org/bibliography/42231
[7] G. Lyra, "Über eine Modifikation der Riemannschen Geometrie," Math. Z. **54**, 52-64 (1951). https://doi.org/10.1007/BF01175135
[8] D.K. Sen, "A Static Cosmological Model," Zeitschriftfur Physik A Hadrons and Nuclei, **149**(3), 311-323 (1957).
[9] D.K. Sen, and K.A. Dunn, J. Math. Phys. **12**, 578 (1971). https://doi.org/10.1063/1.1665623
[10] W.D. Halford, "Cosmological theory based on Lyra's geometry," Australian Journal of Physics, **23**(5), 863-870 (1970). https://doi.org/10.1071/PH700863
[11] W.D. Halford, "Scalar-tensor theory of gravitation in a Lyra manifold," J. Math. Phys. **13**, 1699–1703, (1972). https://doi.org/10.1063/1.1665894
[12] L. Bianchi, *Sugli spazí a tre dimensioni che ammettono un gruppo continuo di movimenti: memoria*, vol. **11**, (Tipografia della R. Academia dei Lincei, 1898).
[13] D.R.K. Reddy, R. Santhikumar, and T.V. Pradeepkumar, "Bianchi type-III Dark Energy Model in f(R,T) Gravity," Int. J. Theor. Physics. **52**, 1 239 (2013). https://doi.org/10.1007/s10773-012-1325-1
[14] D.R.K. Reddy, R. Santikumar, and R.L. Naidu, "Bianchi type-III cosmological model in f(R, T) theory of gravity," Astrophys. Space Sci. **342**, 249–252 (2012). https://doi.org/10.1007/s10509-012-1158-7
[15] K.S. Adhav, S.D. Katore, R.S. Rane, et al., "Zero mass scalar field with bulk viscous cosmological solutions in Lyra geometry," Astrophys. Space Sci. **323**, 87–90 (2009). https://doi.org/10.1007/s10509-009-0042-6
[16] W.D. Halford, "Cosmological Theory Based on Lyra's Geometry," Aust. J. Phys. **23**, 863-870 (1970). https://doi.org/10.1071/PH700863
[17] G.P. Singh, and K. Desikan, "A new class of cosmological models in Lyra geometry," Pramana – J. Phys. **49**, 205–212 (1997). https://doi.org/10.1007/BF02845856
[18] R.S. Kumar, and B. Satyannarayana, "Accelerating anisotropic cosmological model in f(R, T) theory of gravity," Indian J. Phys. **91**, 1293–1296 (2017). https://doi.org/10.1007/s12648-017-1017-z
[19] S. Rajamahanthi, S. Bora, S.P.S. Komu, *et al*., "Bianchi-type cosmological models with heat flow in Lyra's geometry," J. Pure Appl. Math. **7**(1), 37-44 (2023). https://doi.org/10.37532/2752-8081.23.7(1).01-09
[20] M. Krishna, S. Koppala, and R.S. Rajamahanthi, "Accelerating plane-symmetric cosmological model with bulk viscous and cosmic Strings in Lyra's geometry," Indian J. Phys. **98**, 3733–3740 (2024). https://doi.org/10.1007/s12648-024-03100-y
[21] C.B. Collins, E.N. Glass, and D.A. Wilkinson, "Exact Spatially Homogeneous Cosmologies," General Relativity and Gravitation, **12**, 805-823 (1980). http://dx.doi.org/10.1007/BF00763057
[22] B. Mishra, P.K. Sahoo, and Ch.B.S. Varma, "Dark Energy Cosmological Model for Bianchi Type III Space-Time with Perfect Fluid," International Journal of Pure and Applied Mathematics, **99**, 1 109-121 (2015). http://dx.doi.org/10.12732/ijpam.v99i1.9
[23] K.P. Singh, and M.R. Mollah, "Bianchi Type III Cosmological Model with Hybrid Scale Factor in the Presence of Van der Waals Fluid in Lyra Manifold," International Journal of Modern Physics A, **33**, 1850207 (2018). https://doi.org/10.1142/S0217751X1850207X

ПРИСКОРЕННЯ КОСМОЛОГІЧНОЇ МОДЕЛІ ЗІ СКАЛЯРНИМ ПОЛЕМ НУЛЬОВОЇ МАСИ У ГЕОМЕТРІЇ ЛІРИ

М. Крішна[a], К. Собхан Бабу[b], Р. Сантікумар[c]
[a]Інженерний коледж Рагу, Вісакхапатнам, штат Андхра-Прадеш, Індія
[b]Університетський інженерний коледж, Нарасараопета, Андхра-Прадеш, Індія
[c]Інститут технології та менеджменту Адітя, Теккалі, округ Шрікакулам. Андхра-Прадеш-Індія

Вивчення космологічної моделі III типу Б'янкі передбачає включення скалярного поля з нульовою масою в контексті геометрії Ліри. Джерелом тензора енергії-імпульсу вважається об'ємна в'язка рідина. Баротропне рівняння стану використовується для характеристики тиску та густини, шукаючи конкретний розв'язок рівнянь поля. Це рішення отримано з використанням принципу відмінної варіації для параметра Хаббла, запропонованого [M.S. Berman, Il Nuovo Cimento B, 74, 182 (1983)]. Подальший аналіз заглиблюється в фізичні властивості, притаманні цій моделі.

Ключові слова: *прискорення; космологія; геометрія Ліри*

EAST EUROPEAN JOURNAL OF PHYSICS. 1. 29–43 (2025)
DOI: 10.26565/2312-4334-2025-1-03 ISSN 2312-4334

FLRW COSMOLOGICAL MODEL WITH QUADRATIC FUNCTIONAL FORM IN $f(R,T)$ THEORY OF GRAVITY

Chandra Rekha Mahanta, Kankana Pathak, Dibyajyoti Das*
Department of Mathematics, Gauhati University, Gopinath Bordoloi Nagar, Jalukbari, 781014, Assam, India
*Corresponding Author e-mail: dasdibyajyoti07@gauhati.ac.in
Received December 31, 2024; revised January 29, 2025; accepted February 4, 2025

This work investigates a spatially homogeneous and isotropic flat Friedmann-Lemaître-Robertson-Walker (FLRW) universe within the context of $f(R,T)$ gravity as introduced by Harko, *et al*., [Phys. Rev. D, 84, 024020 (2011)]. The present work deals with the functional form $f(R,T) = f_1(R) + f_2(T)$ with $f_1(R) = R + \lambda_1 R^2$ and $f_2(T) = 2\lambda_2 T$ where λ_1 and λ_2 are arbitrary constants, R and T being the Ricci scalar and the trace of the stress-energy tensor T_{ij} respectively. We present a novel cosmological model in the framework of $f(R,T)$ gravity, exploring the dynamics of the FLRW universe through an exact solution to the gravitational field equations. By employing an innovative ansatz for the Hubble parameter, $H = \alpha\left(1+\frac{1}{t}\right)$ where α is a positive constant, we capture a evolutionary history of the universe. This approach provides a natural pathway to investigate key cosmological parameters, such as the scale factor, deceleration parameter, jerk, snap, lerk parameters and energy conditions, revealing intriguing insights into the universe's expansion dynamics. We also discuss the statefinder diagnostic. Our results offer a deeper understanding of cosmic evolution within the $f(R,T)$ gravity framework.

Keywords: *$f(R,T)$ gravity; FLRW metric; Hubble parameter; Statefinder diagnostic*

PACS: 04.50.kd, 98.80.-k, 04.20.jb

1. INTRODUCTION

Late time cosmic acceleration is one of the most significant and challenging discoveries in cosmology which might revolutionize the theories of gravitation and cosmology in near future. Over the last few decades, several crucial cosmological and astrophysical observations from high redshift supernovae type Ia (SNIa) [1–3], Wilkinson Microwave Anisotropy Probe (WMAP) [4–8], Large Scale Structure (LSS) [9], Cosmic Microwave Background (CMB) [10, 11] etc. have been providing strong evidence that the universe is currently undergoing a phase of accelerated expansion. As there is no theoretical explanation for this observed acceleration in the rate of expansion of the universe, many theories have been proposed in the literature to understand the cause behind it. The General Theory of Relativity has provided the foundation for numerous attempts with a prominent hypothesis that the acceleration is driven by Dark energy, an enigmatic form of energy with a high negative pressure, which itself significantly challenges conventional cosmology as cosmological origin and the true nature of dark energy have not been determined yet. In addition, according to the observational data, more than 95% of the total matter-energy budget of the universe is comprised of two dark components - dark energy (DE) and dark matter (DM) - the contributions from DE and DM being about 68.3% and 26.8% respectively. The characteristics of these two dark components are not distinctly recognized. However, the nature of dark matter appears to be partially known [12] as it can be inferred to exist from its gravitational effects on ordinary baryonic matter which contributes only about 4.9% of the total content of the universe. Dark energy, therefore, becomes one of the biggest mysteries and a challenging topic of research in modern cosmology.

The cosmological constant Λ is the most widely discussed candidate for dark energy. However, it encounters two significant theoretical challenges: Cosmic Coincidence Problem and Fine-Tuning Problem.

To address these issues, several candidates of dark energy such as quintessence, k-essence, tachyon, phantom, Chaplygin gas models, Holographic dark energy models etc. are proposed in the literature. Another approach to understand the true cause behind the presence of dark sector in the universe and the mechanism behind the cosmic acceleration in the recent past is the modification of Einstein's theory of gravity. Several modifications of General Theory of Relativity are available in the literature, popularly known as modified theories of gravity, which are extremely attractive. Some important modified theories of gravity are: $f(R)$ theory of gravity [13], where R is the Ricci scalar, the action of which is constructed by replacing R by an arbitrary function $f(R)$ in the Einstein-Hilbert Lagrangian. $f(R,T)$ theory of gravity [14], a generalization of $f(R)$ theory by introducing an arbitrary function $f(R,T)$ of R and T, where T is the trace of the stress-energy of tensor, Brans Dicke theory of gravity [15] in which gravity couples with a time-varying scalar field through a coupling parameter. $f(T)$ gravity theory [16], which uses the torsion scalar in place of the Ricci scalar. $f(G)$ theory of gravity [17] where G is the Gauss-Bonnet invariant. $f(Q)$ gravity [18] where Q is the non-metricity scalar.

Cite as: C.R. Mahanta, K. Pathak, D.J. Das, East Eur. J. Phys. 1, 29 (2025), https://doi.org/10.26565/2312-4334-2025-1-03

Some other modified theories of gravity are $f(R,G)$ gravity [19], $f(Q,T)$ gravity [20] etc. By exploring these diverse approaches, researchers aim to gain a deeper understanding of the fundamental nature of the universe and its evolution with an accelerated rate of expansion.

Harko *et al.* introduced the $f(R,T)$ theory of gravity and obtained the gravitational field equations for three explicit forms of the functional $f(R,T)$ viz. $f(R,T) = R + 2f(T)$, $f(R,T) = f_1(R) + f_2(T)$ and $f(R,T) = f_1(R) + f_2(R)f_3(T)$. Houndjo [21] developed the cosmological reconstruction of $f(R,T)$ theory of gravity for the functional $f(R,T) = f_1(R) + f_2(T)$ and discussed the transition of matter dominated era with decelerated expansion to the current era with an accelerated expansion. Since then many authors have explored various aspects of this theory in different contexts as this theory can be best applied to study several issues of current interest and also takes care of the early time inflation as well as the late time accelerated expansion. Bhattacharjee and Sahoo [22] studied redshift drift in $f(R,T)$ theory of gravity where they have used the functional $f(R,T) = R + \lambda T$. Pradhan *et al.* [23] studied FLRW model in $f(R,T)$ gravity using $f(R,T) = R + 2\lambda T$.

In the present work, we consider the functional form $f(R,T) = f_1(R) + f_2(T)$ with $f_1(R) = R + \lambda_1 R^2$ and $f_2(T) = \lambda_2 T$ where λ_1 and λ_2 are arbitrary constants. Starobinsky's work [24] motivates us to consider the functional form $f_1(R) = R + \lambda_1 R^2$. The Starobinsky model follow the cosmological observational test and successfully predicts a spectrum of nearly scale-invariant curvature perturbations. The R^2 term in the functional form $f(R) = R + \alpha R^2$, α is a constant, in Starobinsky's original work demonstrates that the R^2 term could naturally drive inflation due to a slow-roll regime, leading to a nearly de Sitter expansion. This mechanism does not require an explicit scalar field as the additional degrees of freedom from the R^2 term behave like a scalar field.

A number of researchers also considered the functional form $f(R,T)$ of the type $f(R,T) = R + \lambda_1 R^2 + \lambda_2 T$ in various contexts. Zubair and Noureen [25] studied evolution of axially symmetric anisotropic sources, Noureen *et al.* [26] investigated shear-free condition and dynamical instability, Sahoo *et al.* [27,28] proposed a model of wormholes and also $f(R,T)$ gravity model as alternatives to cosmic acceleration by constructing three cosmological models that arise from the three different choices for $f_1(R)$, viz, $f_1(R) = R + \alpha R^2 - \frac{\mu^4}{R}$, $f_1(R) = R + k\ln(\gamma R)$ and $f_1(R) = R + me^{[-nR]}$ with α, μ, k, γ, m and n all free parameters. Vinuthaa and Kavya [29] studied Bianchi type cosmological models in $f(R,T)$ theory with quadratic functional form. Bishi *et al.* [30] studied domain walls and quark matter cosmological models in $f(R,T) = R + aR^2 + kT$ gravity. These studies affirm $f(R,T)$ gravity as a versatile and promising framework, capable of providing insights into a wide array of phenomena, from exotic matter distributions to cosmic expansion, while accommodating both isotropic and anisotropic configurations.

In this study, we consider a flat Friedmann-Lemaître-Robertson-Walker (FLRW) universe filled with a perfect fluid within the framework of $f(R,T)$ gravity with the functional form $f(R,T) = R + \lambda_1 R^2 + \lambda_2 T$, where λ_1, λ_2 are arbitrary constants. The outline of the present work is as follows: In section 2, we provide a concise overview of the metric formalism of $f(R,T)$ theory of gravity and present the basic equations. In section 3, we derive the gravitational field equations in terms of the Hubble parameter H. In section 4, we solve the field equations by choosing an ansatz for the Hubble parameter. In Section 5, we discuss the physical and kinematical properties of the model by plotting the cosmological parameters against cosmic time t and redshift parameter z. In Section 6, we analyze and discuss the jerk, snap and lerk parameters, the statefinder diagnostic and the energy conditions of our model. Finally, in Section 7, we conclude the paper with a summary of our findings and key insights.

2. $f(R,T)$ GRAVITY THEORY: BASIC EQUATIONS

The action of $f(R,T)$ gravity theory proposed by Harko *et al.* [14] is given by

$$S = \int \left[\frac{1}{16\pi} f(R,T) + L_m\right] \sqrt{-g}\, d^4x \tag{1}$$

where $f(R,T)$ is an arbitrary function of the Ricci Scalar R and the trace T of the stress-energy tensor and L_m is the matter Lagrangian density.

The stress-energy tensor of matter is defined as

$$T_{ij} = \frac{-2}{\sqrt{-g}} \frac{\delta(\sqrt{-g}L_m)}{\delta g^{ij}} \tag{2}$$

and the trace T is given by $T = g^{ij}T_{ij}$. Considering the metric tensor components g_{ij} to be the sole ones influencing the amount L_m of matter and not its derivatives, the stress-energy tensor T_{ij} is obtained as

$$T_{ij} = g_{ij}L_m - 2\frac{\partial L_m}{\partial g^{ij}} \tag{3}$$

By varying the action (1) with respect to the metric tensor components g^{ij}, the field equations of $f(R,T)$ gravity are obtained as

$$f_R(R,T)R_{ij} - \frac{1}{2}f(R,T)g_{ij} + (g_{ij}\Box - \bigtriangledown_i\bigtriangledown_j)f_R(R,T) = 8\pi T_{ij} - f_T(R,T)T_{ij} - f_T(R,T)\Theta_{ij} \tag{4}$$

where, $f_R(R,T) = \frac{\partial f(R,T)}{\partial R}$, $f_T(R,T) = \frac{\partial f(R,T)}{\partial T}$ and the covariant derivative with regard to the symmetric connection Γ associated to the metric g is represented by the operator $\bigtriangledown_i$.

Here, Θ_{ij} is obtained by specifying the variation of T with respect to the metric tensor

$$\frac{\delta(g^{\alpha\beta}T_{\alpha\beta})}{\delta g^{ij}} = T_{ij} + \Theta_{ij} \tag{5}$$

For a known matter Lagrangian L_m, Θ_{ij} can be calculated as

$$\Theta_{ij} = -2T_{ij} + g_{ij}L_m - 2g^{lk}\frac{\partial^2 L_m}{\partial g^{ij}\partial g^{lk}} \tag{6}$$

For a perfect fluid, the stress-energy tensor of matter is provided by

$$T_{ij} = (\rho + p)u_iu_j - pg_{ij} \tag{7}$$

where ρ is the energy density, p is the pressure and the four velocity u_i satisfies the conditions $u_iu^i = 1$ and $u^i \bigtriangledown_j u_i = 0$. The matter Lagrangian can be written as $L_m = -p$. Using eq (6), we get the expression for Θ_{ij} for the modification of stress-energy tensor of perfect fluid as

$$\Theta_{ij} = -2T_{ij} - pg_{ij} \tag{8}$$

Assuming

$$f(R,T) = f_1(R) + f_2(T) \tag{9}$$

where $f_1(R)$ and $f_2(T)$ are arbitrary functions of R and T respectively, from equation (4), if the matter source is a perfect fluid, then the field equations of $f(R,T)$ gravity become

$$f_1^{'}(R)R_{ij} - \frac{1}{2}f_1(R)g_{ij} + (g_{ij}\Box - \bigtriangledown_i\bigtriangledown_j)f_1^{'}(R) = 8\pi T_{ij} + f_2^{'}(T)T_{ij} + \left[f_2^{'}(T)p + \frac{1}{2}f_2(T)\right]g_{ij} \tag{10}$$

where the prime denotes differentiation with respect to the argument.

For the choice of $f_1(R) = R + \lambda_1R^2$ and $f_2(T) = 2\lambda_2T$, where λ is a constant, the gravitational field equations of $f(R,T)$ gravity from eq (10) are obtained as

$$R_{ij} - \frac{1}{2}Rg_{ij} + 2\lambda_1R\left(R_{ij} - \frac{1}{4}Rg_{ij}\right) + (g_{ij}\Box - \bigtriangledown_i\bigtriangledown_j)(1 + 2\lambda_1R) = 8\pi T_{ij} + \lambda_2\left[2T_{ij} + (\rho - p)g_{ij}\right] \tag{11}$$

3. THE METRIC AND GRAVITATIONAL FIELD EQUATIONS

We consider the flat Friedmann-Lemaître-Robertson-Walker metric given by

$$ds^2 = dt^2 - a^2(dx^2 + dy^2 + dz^2) \tag{12}$$

where a is a function of cosmic time t only. Using comoving coordinates, the field equations (11) for the metric (12) are obtained as

$$\frac{\ddot{a}}{a} + \frac{1}{2}\frac{\dot{a}^2}{a^2} + 6\lambda_1G_1(a,\dot{a},\ddot{a},\dddot{a},\ddddot{a}) = -4\pi p + \frac{\lambda_2}{2}(\rho - 3p) \tag{13}$$

$$\frac{\dot{a}^2}{a^2} + 6\lambda_1G_2(a,\dot{a},\ddot{a},\dddot{a}) = \frac{8\pi}{3}\rho + \lambda_2\left(\rho - \frac{p}{3}\right) \tag{14}$$

where

$$G_1(a,\dot{a},\ddot{a},\dddot{a},\ddddot{a}) = -\frac{3}{2}\left[\left(\frac{\dot{a}}{a}\right)^4 + \frac{\ddot{a}^2}{a^2}\right] - 2\left[\frac{\dot{a}\dddot{a}}{a^2} - 3\frac{\dot{a}^2\ddot{a}}{a^3}\right] - \frac{\ddddot{a}}{a}$$

$$G_2(a,\dot{a},\ddot{a},\dddot{a}) = -2\left(\frac{\dot{a}}{a}\right)^2\left[\frac{\dddot{a}}{\dot{a}} + \frac{\ddot{a}}{a} - \frac{3}{2}\left(\frac{\dot{a}}{a}\right)^2\right] + \left(\frac{\ddot{a}}{a}\right)^2$$

In terms of the Hubble parameter H, defined by $H = \frac{\dot{a}}{a}$, equations (13) and (14) can be expressed as

$$\dot{H} + \frac{3}{2}H^2 + 6\lambda_1 G_1(a,\dot{a},\ddot{a},\dddot{a},\ddddot{a}) = -4\pi p + \frac{\lambda_2}{2}(\rho - 3p) \tag{15}$$

$$H^2 + 6\lambda_1 G_2(a,\dot{a},\ddot{a},\dddot{a}) = \frac{8\pi}{3}\rho + \lambda_2\left(\rho - \frac{p}{3}\right) \tag{16}$$

where

$$G_1(H,\dot{H},\ddot{H},\dddot{H}) = -\left(\dddot{H} + 6H\ddot{H} + 9H^2\dot{H} + \frac{9}{2}\dot{H}^2\right)$$

$$G_2(H,\dot{H},\ddot{H}) = \dot{H}^2 - 6H^2\dot{H} - 2H\ddot{H}$$

The Ricci scalar curvature is

$$R = -\left(6\dot{H} + 12H^2\right) \tag{17}$$

where an overhead dot denotes differentiation with respect to t.

From equations (15) and (16), we get

$$\rho = \frac{1}{(8\pi+4\lambda_2)(4\pi+\lambda_2)}\Big[12\pi H^2 + \lambda_2(3H^2 - \dot{H}) + 72\pi\lambda_1(\dot{H}^2 - 6H^2\dot{H} - 2H\ddot{H}) + 3\lambda_1\lambda_2(2\dddot{H} + 18\dot{H}^2 - 6H\ddot{H} - 36H^2\dot{H})\Big] \tag{18}$$

$$p = \frac{1}{(8\pi+4\lambda_2)(4\pi+\lambda_2)}\Big[-(8\pi+3\lambda_2)\dot{H} - 3(4\pi+\lambda_2)H^2 + 24\pi\lambda_1\left(2\dddot{H} + 12H\ddot{H} + 18H^2\dot{H} + 9\dot{H}^2\right) + 18\lambda_1\lambda_2(\ddot{H} + 5\dot{H}^2 + 5H\ddot{H} + 6H^2\dot{H})\Big] \tag{19}$$

4. EXACT SOLUTION OF THE FIELD EQUATIONS

To find an exact solution of the field equations, we consider the following ansatz for the Hubble parameter H:

$$H = \alpha\left(1 + \frac{1}{t}\right) \tag{20}$$

where $\alpha > 0$ is an arbitrary constant.

The Hubble parameter H is an observable parameter. It measures the rate of cosmic expansion. Using the definition $H = \frac{\dot{a}}{a}$, from equation (20), we obtain the scale factor a as

$$a(t) = a_0(te^t)^\alpha \tag{21}$$

where $a_0 > 0$ is a constants.

Then from equations (18) and (19), the energy density ρ and the pressure p are obtained as

$$\rho(t) = \frac{3\alpha^2}{8\pi+4\lambda_2} + \frac{\alpha}{(8\pi+4\lambda_2)(4\pi+\lambda_2)}\left[\frac{(24\pi+6\lambda_2)\alpha}{t} + \frac{\lambda_2 + 3\alpha(4\pi+\lambda_2)(1+36\lambda_1\alpha)}{t^2} + \frac{108\lambda_1\lambda_2\alpha^2 + 36\lambda_1\alpha(3\alpha-1)(8\pi+\lambda_2)}{t^3} + \frac{18\lambda_1(2\alpha-1)(12\pi\alpha+\lambda_2(3\alpha+2))}{t^4}\right] \tag{22}$$

$$p(t) = \frac{-3\alpha^2}{8\pi+4\lambda_2} + \frac{\alpha}{(8\pi+4\lambda_2)(4\pi+\lambda_2)}\left[\frac{-(24\pi+6\lambda_2)\alpha}{t} + \frac{(8\pi+3\lambda_2) - (4\pi+\lambda_2)(3\alpha+108\lambda_1\alpha^2)}{t^2} + \frac{36\lambda_1\alpha((16\pi+5\lambda_2) - \alpha(24\pi+6\lambda_2))}{t^3} + \frac{18\lambda_1(\alpha(44\pi+15\lambda_2) - \alpha^2(24\pi+6\lambda_2) - (16\pi+6\lambda_2))}{t^4}\right] \tag{23}$$

The equation of state (EoS) parameter is defined as the ratio of pressure to energy density: $\omega = \frac{p}{\rho}$. This parameter is crucial in understanding the nature of the universe's energy content.

Therefore, the equation of state parameter ω is obtained as

$$\omega(t) = \frac{\begin{array}{c}-3\alpha t^4 - (24\pi + 6\lambda_2)\alpha t^3 + \left\{(8\pi + 3\lambda_2) - (4\pi + \lambda_2)(3\alpha + 108\lambda_1\alpha^2)\right\} t^2 + \\ 36\lambda_1\alpha\left\{(16\pi + 5\lambda_2) - \alpha(24\pi + 6\lambda_2)\right\} t + 18\lambda_1\left\{\alpha(44\pi + 15\lambda_2) - \alpha^2(24\pi + 6\lambda_2) - (16\pi + 6\lambda_2)\right\}\end{array}}{\begin{array}{c}3\alpha t^4 + (24\pi + 6\lambda_2)\alpha t^3 + \left\{\lambda_2 + 3\alpha(4\pi + \lambda_2)(1 + 36\lambda_1\alpha)\right\} t^2 + \\ \left\{108\lambda_1\lambda_2\alpha^2 + 36\lambda_1\alpha(3\alpha - 1)(8\pi + \lambda_2)\right\} t + 18\lambda_1(2\alpha - 1)\left\{12\pi\alpha + \lambda_2(3\alpha + 2)\right\}\end{array}} \tag{24}$$

The deceleration parameter q, a dimensionless measure of the cosmic expansion, is defined by the relation $q = -\frac{a\ddot{a}}{\dot{a}^2}$. Thus, q is related to the Hubble parameter H by the relation $q = -1 + \frac{d}{dt}\left(\frac{1}{H}\right)$. For our model, we obtain

$$q = -1 + \frac{1}{\alpha(1+t)^2} \tag{25}$$

The deceleration parameter exhibits the universe's expansion. For $q < 0$, it undergoes accelerated expansion and for $q > 0$, it undergoes decelerated expansion. Recent observations reveal that the universe transitioned from the decelerated expansion phase to an accelerated expansion phase in the recent past and currently passing through a phase of accelerated expansion. According to current observational data, $-1 \leq q < 0$.

5. PHYSICAL AND KINEMATICAL PROPERTIES OF THE MODEL

We aim to investigate the physical and kinematical properties of the model by studying the bahaviour of some cosmological parameters as the universe evolves. Cosmological parameters describe the kinematic properties of the universe's expansion and are essential for understanding its dynamic evolution. To develop a cosmological model that transitions from a decelerating phase to an accelerating phase, we focus on the range $0 < \alpha < 1$, as recommended by the equation (25). This range aligns with models that match observed cosmic acceleration patterns.

For our analysis, we consider four specific values of α viz $\alpha = 0.3, 0.4, 0.5$ and 0.6. These values allow us to explore how slight variations in α influence the behavior of the universe's expansion. Additionally, we set the arbitrary constants as $\lambda_1 = 0.2$ and $\lambda_2 = 0.1$.

Using these values, we compute and plot the behaviour of various cosmological parameters. These plots help us to visualize and analyze how the universe's expansion evolves over time and assess whether the model aligns with the expected transition from a decelerated expansion to an accelerated expansion phase. This transition is a critical feature of modern cosmological theories that explain the role of dark energy in driving the accelerated expansion of the universe.

The scale factor a measures the relative size of the universe at a given time. As the universe expands, the scale factor increases. In the context of cosmology, the volume V of the universe is directly related to the scale factor, as $V \propto a^3$, meaning that as the scale factor increases, the volume increases significantly.

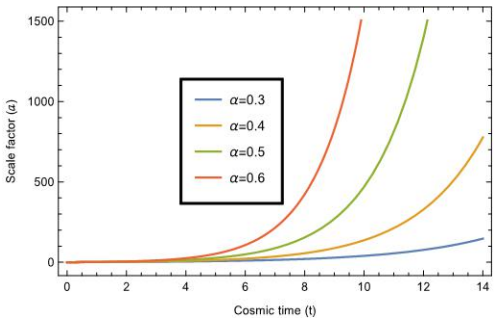

Figure 1. Variation of the scale factor a versus cosmic time t with $a_0 = 1$ and different values of α.

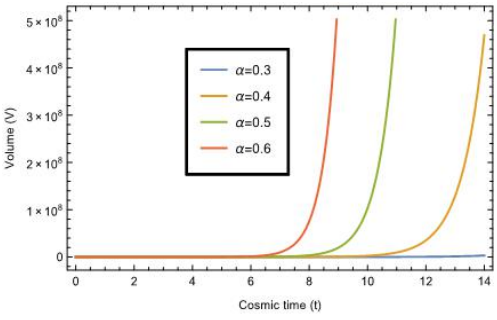

Figure 2. Variation of the volume V versus cosmic time t with different α.

From Figures 1 and 2, we see that the scale factor and volume grow significantly over time, especially in the late universe. This rapid increase in volume suggests that the universe's expansion has accelerated, particularly after a certain point. This acceleration can be attributed to the influence of dark energy, which became dominant in recent cosmic history, driving the universe's expansion at an increasingly rapid pace.

In order to have a better understanding of the properties of the universe corresponding to our model, it will be of great help if we also study the evolutionary behaviour of some cosmological parameters versus redshift z.

REDSHIFT AND COSMIC TIME RELATION

The redshift z is related to the scale factor $a(t)$ by:

$$z = \frac{a_0}{a(t)} - 1$$

which implies

$$a(t) = \frac{a_0}{1+z}$$

Substituting this into equation (21), we get

$$a_0(te^t)^\alpha = \frac{a_0}{1+z}$$

To isolate te^t, we take the α-th root of both sides and get

$$te^t = (1+z)^{-1/\alpha}$$

The equation $te^t = C$, where $C = (1+z)^{-1/\alpha}$, is solved using the Lambert W function. The Lambert W function satisfies: $W(x)e^{W(x)} = x$

Thus, we can obtain the time-redshift relation as:

$$t = W\left[(1+z)^{-\frac{1}{\alpha}}\right] \tag{26}$$

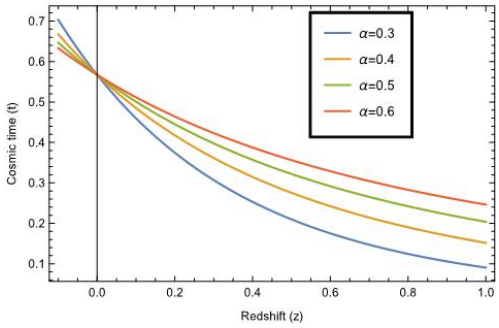

Figure 3. Variation of cosmic time t versus redshift z for different values of α.

The Hubble parameter and deceleration parameter in terms of redshift lead to

$$H(z) = \alpha\left[1 + \frac{1}{W\left[(1+z)^{-\frac{1}{\alpha}}\right]}\right] \tag{27}$$

$$q(z) = -1 + \frac{1}{\alpha\left(1 + W\left[(1+z)^{-\frac{1}{\alpha}}\right]\right)^2} \tag{28}$$

Using eqn (26), the expressions for the energy density (ρ), the pressure (p) and Equation of State (EoS) parameter ω in terms of redshift (z) are obtained as:

$$\rho(z) = \frac{3\alpha^2}{8\pi+4\lambda_2} + \frac{\alpha}{(8\pi+4\lambda_2)(4\pi+\lambda_2)}\left[\frac{(24\pi+6\lambda_2)\alpha}{W\left[(1+z)^{-\frac{1}{\alpha}}\right]} + \frac{\lambda_2+3\alpha(4\pi+\lambda_2)(1+36\lambda_1\alpha)}{W\left[(1+z)^{-\frac{1}{\alpha}}\right]^2} + \frac{108\lambda_1\lambda_2\alpha^2+36\lambda_1\alpha(3\alpha-1)(8\pi+\lambda_2)}{W\left[(1+z)^{-\frac{1}{\alpha}}\right]^3} + \frac{18\lambda_1(2\alpha-1)(12\pi\alpha+\lambda_2(3\alpha+2))}{W\left[(1+z)^{-\frac{1}{\alpha}}\right]^4}\right] \tag{29}$$

$$p(z) = \frac{-3\alpha^2}{8\pi+4\lambda_2} + \frac{\alpha}{(8\pi+4\lambda_2)(4\pi+\lambda_2)}\left[\frac{-(24\pi+6\lambda_2)\alpha}{W\left[(1+z)^{-\frac{1}{\alpha}}\right]} + \frac{(8\pi+3\lambda_2)-(4\pi+\lambda_2)(3\alpha+108\lambda_1\alpha^2)}{W\left[(1+z)^{-\frac{1}{\alpha}}\right]^2} + \frac{36\lambda_1\alpha((16\pi+5\lambda_2)-\alpha(24\pi+6\lambda_2))}{W\left[(1+z)^{-\frac{1}{\alpha}}\right]^3} + \frac{18\lambda_1(\alpha(44\pi+15\lambda_2)-\alpha^2(24\pi+6\lambda_2)-(16\pi+6\lambda_2))}{W\left[(1+z)^{-\frac{1}{\alpha}}\right]^4}\right] \tag{30}$$

$$\omega(z) = \frac{-3\alpha W\left[(1+z)^{-\frac{1}{\alpha}}\right]^4 - (24\pi+6\lambda_2)\alpha W\left[(1+z)^{-\frac{1}{\alpha}}\right]^3 + \left\{(8\pi+3\lambda_2)-(4\pi+\lambda_2)(3\alpha+108\lambda_1\alpha^2)\right\}W\left[(1+z)^{-\frac{1}{\alpha}}\right]^2 + 36\lambda_1\alpha\left\{(16\pi+5\lambda_2)-\alpha(24\pi+6\lambda_2)\right\}W\left[(1+z)^{-\frac{1}{\alpha}}\right] + 18\lambda_1\left\{\alpha(44\pi+15\lambda_2)-\alpha^2(24\pi+6\lambda_2)-(16\pi+6\lambda_2)\right\}}{3\alpha W\left[(1+z)^{-\frac{1}{\alpha}}\right]^4 + (24\pi+6\lambda_2)\alpha W\left[(1+z)^{-\frac{1}{\alpha}}\right]^3 + \left\{\lambda_2+3\alpha(4\pi+\lambda_2)(1+36\lambda_1\alpha)\right\}W\left[(1+z)^{-\frac{1}{\alpha}}\right]^2 + \left\{108\lambda_1\lambda_2\alpha^2+36\lambda_1\alpha(3\alpha-1)(8\pi+\lambda_2)\right\}W\left[(1+z)^{-\frac{1}{\alpha}}\right] + 18\lambda_1(2\alpha-1)\left\{12\pi\alpha+\lambda_2(3\alpha+2)\right\}} \tag{31}$$

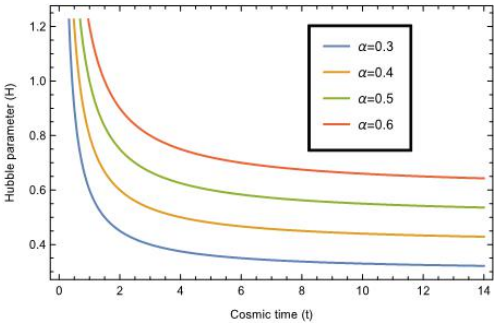

Figure 4. Variation of Hubble parameter H versus cosmic time t with different values of α.

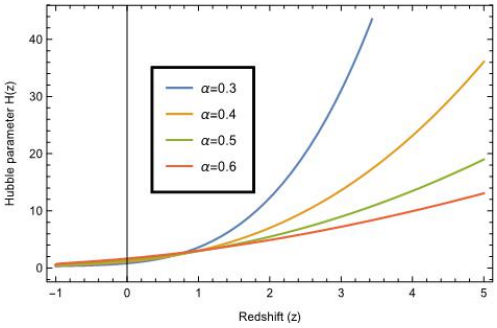

Figure 5. Variation of Hubble parameter H versus redshift z with different α.

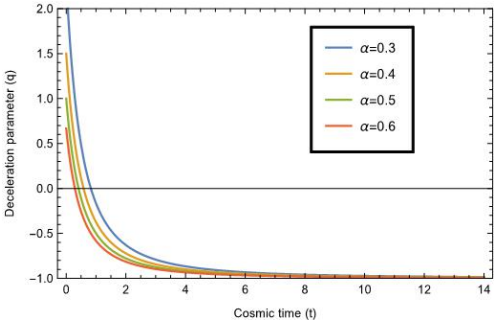

Figure 6. Variation of deceleration parameter q versus cosmic time t with different α.

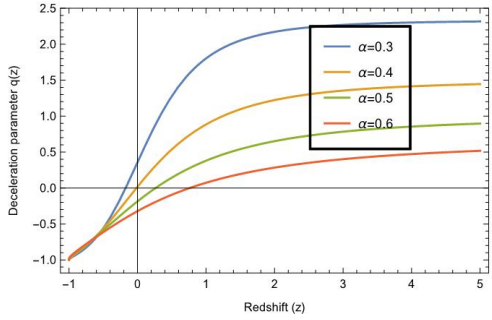

Figure 7. Variation of deceleration parameter q versus redshift z with different α.

From Figures 4 and 5, we observe that in the early universe, the Hubble parameter (H) is very large, and keeps decreasing as the universe evolves. This is consistent with the Big Bang theory, according to which the universe started from an extremely hot and dense state, and then began to expand. As time progresses, the value of H decreases, reflecting the fact that the rate of expansion slows down due to the gravitational pull of matter in the universe. In cosmological terms, redshift (z) corresponds to looking at the universe in the past. The Hubble parameter decreases with redshift (z). The decrease of H with respect to z refers to how the expansion rate of the universe slows down as the universe ages.

Figures 6 and 7 show that at the start of the universe, $q > 0$, meaning that the expansion was slowing down. As time progressed, due to the influence of matter and radiation, the deceleration continued for a long period. Initially, the universe is decelerating, but as the value of q moves toward negative values, the expansion switches to an accelerating phase. This matches observations of the current expansion rate, where the universe is observed to be accelerating due to the influence of dark energy.

From the above graphs, we see that the choice of $\alpha = 0.5$ reflects a best model where the deceleration parameter transitions smoothly into the accelerating phase. We choose this value for the plots of other cosmological parameters.

The energy density (ρ) of the universe consists of contributions from matter-energy content of the universe. Figure 8 shows that at the beginning of the universe (near time $t = 0$), the energy density is extremely high, exhibiting thereby that the universe was incredibly dense and compact. This is consistent with the idea of a hot, dense Big Bang origin. As the universe expands, the energy density decreases. This behaviour is expected in the standard cosmological model, where both matter and radiation contribute to the energy density but becomes less dense as the universe expands. The energy density asymptotically approaches zero as time progresses towards infinity, reflecting the fact that, although the

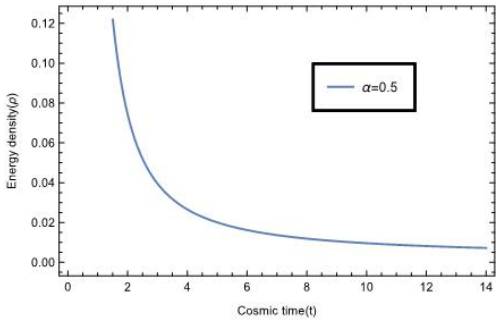

Figure 8. Variation of energy density ρ versus cosmic time t with $\alpha = 0.5$.

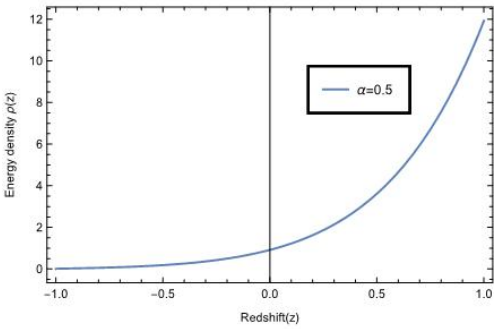

Figure 9. Variation of energy density ρ versus redshift (z) with $\alpha = 0.5$.

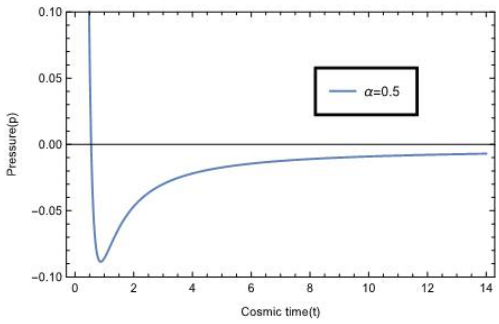

Figure 10. Variation of pressure p versus cosmic time t with $\alpha = 0.5$.

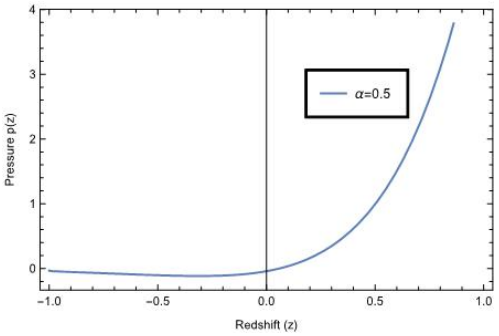

Figure 11. Variation of pressure p versus redshift (z) with $\alpha = 0.5$.

universe continues to expand, the contributions of matter and radiation become negligible over time, and dark energy (which remains constant or evolves slowly) dominates. From Figure 9, we see that the energy density ρ decreases against redshift z. This decrease in ρ describes how different components of the universe's energy content (like matter, radiation and dark energy) evolve as the universe expands.

The pressure (p) in the universe varies with time and plays an essential role in understanding the dynamics of the universe. In Figure 10, for $\alpha = 0.5$, the pressure is initially positive, which is typical for a matter dominated universe. However, as the universe expands, the pressure becomes negative. Negative pressure is associated with dark energy, which causes the accelerated expansion of the universe. This transition from positive to negative pressure is one of the signatures of the onset of the dark energy dominated phase. From Figure 11, we see that the pressure p decreases against redshift z.

In Figures 12 and 13, we observe that the value of ω lies between -1 and 1. This range is significant because $\omega \approx 0$ corresponds to matter domination, $\omega = \frac{1}{3}$ corresponds to radiation domination and $\omega \approx -1$ corresponds to a universe dominated by dark energy, as dark energy is modeled to have $\omega = -1$ in the simplest cosmological models.

Since ω lies within this range, it suggests that the universe is currently undergoing accelerated expansion, dominated by dark energy, which fits well with current cosmological observations of an accelerated expanding universe.

6. PHYSICAL ACCEPTABILITY OF THE SOLUTIONS

For the validity of the solution, we should check that our model is physically acceptable.

6.1. Jerk, snap and lerk parameters

In cosmological models, understanding the evolution of the universe's expansion is crucial for predicting its future behaviour and unraveling the underlying forces shaping its dynamics. While the deceleration parameter provides a foundational insight into how the expansion rate of the universe is changing, higher-order time derivatives of the scale factor such as the jerk, snap, and lerk offer a more detailed and refined understanding of the universe's expansion.

These parameters are derived from the Taylor series expansion of the scale factor $a(t)$, which describes the size of the universe as a function of time (t). By examining the higher derivatives of the scale factor, more complex aspects of the universe's expansion, such as changes in acceleration and the rate at which these changes are occurring can be captured.

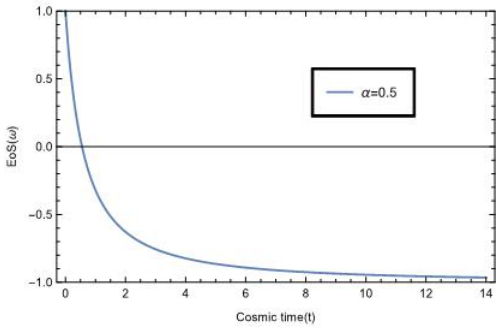

Figure 12. Variation of EoS parameter (ω) versus cosmic time t with $\alpha = 0.5$.

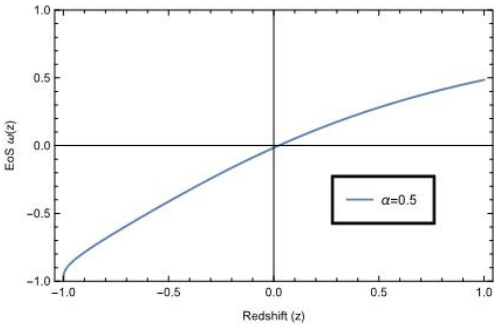

Figure 13. Variation of EoS parameter (ω) versus redshift (z) with $\alpha = 0.5$.

These higher-order derivatives - jerk, snap, and lerk are essential for predicting the future evolution of the universe and for understanding its past behavior with greater precision.

Jerk parameter

The jerk parameter is the third time derivative of the scale factor $a(t)$, denoted by $j(t)$. It measures the rate of change of the acceleration of the universe's expansion. In other words, it provides insight into whether the rate of acceleration is itself increasing or decreasing over time. The jerk parameter is particularly important because it helps predict the future behaviour of the expansion. If the jerk is positive, it indicates that the expansion is accelerating at an increasing rate. Conversely, a negative jerk suggests that the acceleration is decreasing.

Mathematically, the jerk parameter is expressed as:

$$j(t) = \frac{a^2}{\dot{a}^3}\frac{d^3a}{dt^3}$$

For our model, it is obtained as

$$j(t) = 1 - \frac{3}{\alpha(1+t)^2} + \frac{2}{\alpha^2(1+t)^3} \tag{32}$$

This equation reflects how the second derivative of the scale factor (acceleration) changes over time.

Snap parameter

The snap parameter is the fourth time derivative of the scale factor $a(t)$, denoted by $s(t)$. It measures how the jerk parameter *i.e* the rate of change of acceleration evolves over time. It is a higher-order derivative that provides even finer details about the acceleration of the universe's expansion. The snap is essential for identifying subtle transitions in the universe's expansion, such as shifts between accelerating and decelerating phases of expansion.

The snap parameter is mathematically defined as:

$$s(t) = \frac{a^3}{\dot{a}^4}\frac{d^4a}{dt^4}$$

For our model, it is obtained as

$$s(t) = 1 - \frac{6}{\alpha(1+t)^2} + \frac{8}{\alpha^2(1+t)^3} + \frac{3\alpha - 6}{\alpha^3(1+t)^4} \tag{33}$$

This equation reflects the evolving nature of the jerk parameter, which helps us understand the changing nature of the universe's acceleration in even greater detail.

Lerk parameter

The lerk parameter is the fifth time derivative of the scale factor $a(t)$, denoted by $l(t)$. As the fifth derivative, the lerk parameter measures how the snap parameter, the rate of change of the jerk parameter is changing over time. The lerk parameter provides the most detailed information about the expansion of the universe, capturing extremely subtle shifts in the acceleration and deceleration rates.

Mathematically, the lerk parameter is defined as:

$$l(t) = \frac{a^4}{\dot{a}^5}\frac{d^5a}{dt^5}$$

For our model, it is obtained as

$$l(t) = 1 - \frac{10}{\alpha(1+t)^2} + \frac{20}{\alpha^2(1+t)^3} + \frac{15\alpha - 30}{\alpha^3(1+t)^4} + \frac{24 - 20\alpha}{\alpha^4(1+t)^5} \tag{34}$$

This equation provides the highest level of detail regarding the changing behaviour of the universe's expansion, offering important insights into the acceleration dynamics that may not be immediately apparent from the jerk or snap parameter alone.

For our model, the expressions for jerk, snap and lerk parameter in terms of redshift (z) are obtained as:

$$j(z) = 1 - \frac{3}{\alpha\left(1 + W\left[(1+z)^{-\frac{1}{\alpha}}\right]\right)^2} + \frac{2}{\alpha^2\left(1 + W\left[(1+z)^{-\frac{1}{\alpha}}\right]\right)^3} \tag{35}$$

$$s(z) = 1 - \frac{6}{\alpha\left(1 + W\left[(1+z)^{-\frac{1}{\alpha}}\right]\right)^2} + \frac{8}{\alpha^2\left(1 + W\left[(1+z)^{-\frac{1}{\alpha}}\right]\right)^3} + \frac{3\alpha - 6}{\alpha^3\left(1 + W\left[(1+z)^{-\frac{1}{\alpha}}\right]\right)^4} \tag{36}$$

$$l(z) = 1 - \frac{10}{\alpha\left(1 + W\left[(1+z)^{-\frac{1}{\alpha}}\right]\right)^2} + \frac{20}{\alpha^2\left(1 + W\left[(1+z)^{-\frac{1}{\alpha}}\right]\right)^3} + \frac{15\alpha - 30}{\alpha^3\left(1 + W\left[(1+z)^{-\frac{1}{\alpha}}\right]\right)^4} + \frac{24 - 20\alpha}{\alpha^4\left(1 + W\left[(1+z)^{-\frac{1}{\alpha}}\right]\right)^5} \tag{37}$$

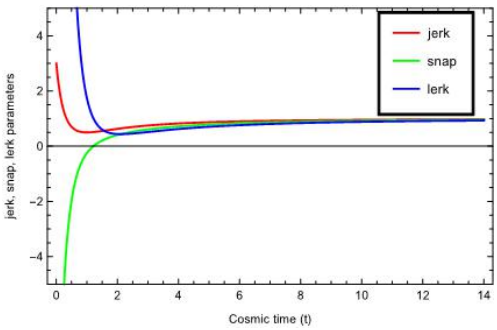

Figure 14. Variation of jerk, snap and lerk parameter versus cosmic time t with $\alpha = 0.5$

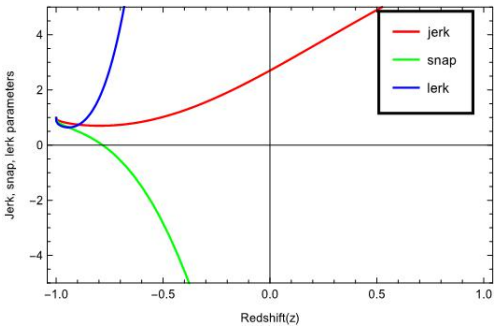

Figure 15. Variation of jerk, snap and lerk parameter versus redshift z with $\alpha = 0.5$

From Figures 14 and 15, we observe that the jerk and lerk parameters remain positive throughout the evolution of the universe. They exhibit diminishing tendencies as seen in the figures. The snap parameter has negative value in the beginning and occurs positive value at late cosmic time. This denotes an accelerated expansion of the universe.

6.2. Statefinder diagnostic

Statefinder parameter is a crucial geometrical diagnostic tool used to differentiate between different dark energy models. The two parameters of statefinder $\{r, s\}$ are dimensionless and geometrical since they are generated from the cosmic scale factor $a(t)$ alone, however they may be reconstructed in terms of dark energy and dark matter.

In table 1, various forms of statefinder pairs are displayed. Here, r measures the third derivative of the scale factor normalized by the Hubble parameter, quantifying jerk or snap and s provides a diagnostic to distinguish between dark energy models by normalizing r using q. ΛCDM model serves as the baseline: standard cosmological constant with cold dark matter model. Quintessence dark energy model represents a scalar field with varying energy density that drives the accelerated expansion of the universe. Phantom dark energy model is the model where the dark energy equation of state is $\omega < -1$, leading to super-accelerated expansion. Chaplygin gas model is a unified dark matter-energy model. Interacting Models are models involving interactions between dark energy and other components of the universe like cold dark matter.

Table 1. Statefinder diagnostic

Parameter	Definition
Deceleration Parameter (q)	$q = -\frac{\ddot{a}a}{\dot{a}^2}$
Statefinder Pair $\{r, s\}$	$r = \frac{\dddot{a}}{aH^3}$, $s = \frac{r-1}{3(q-\frac{1}{2})}$
ΛCDM Model	$\{r, s\}$= $\{1, 0\}$
Quintessence	$r < 1, s > 0$
Phantom Dark Energy	r, s vary based on parameters
Chaplygin Gas	$r > 1, s < 0$
Interacting Models	$r \neq 1$, $s \neq 0$

The statefinder pair $\{r, s\}$ [32] for our model are obtained as

$$r = \frac{a^2}{\dot{a}^3}\frac{d^3a}{dt^3} = 1 - \frac{3}{\alpha(1+t)^2} + \frac{2}{\alpha^2(1+t)^3} \tag{38}$$

$$s = \frac{r-1}{3\left(q-\frac{1}{2}\right)} = \frac{4 - 6\alpha(1+t)}{6\alpha(1+t) - 9\alpha^2(1+t)^3} \tag{39}$$

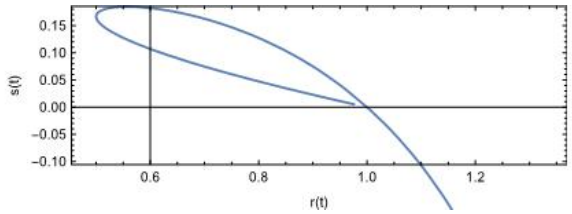

Figure 16. Variation of statefinder pair $\{r, s\}$

For our model, the statefinder pair $\{r, s\}$ has a present value of $\{r, s\}$= $\{0.976, 0.0054\}$ for $\alpha = 0.5$. Since, from Figure 16, we find $r < 1$ and $s > 0$, therefore, our model aligns with a quintessence dark energy model. Quintessence differs from the cosmological constant (Λ) as it evolves over time, leading to unique dynamics captured by the statefinder parameters. At late times, our model will behave like the ΛCDM model.

6.3. Energy Conditions

Energy conditions are sets of mathematical inequalities imposed on the energy-momentum tensor T_{ij}, which describes the matter and energy content of the universe in the framework of general relativity. These conditions provide a way to ensure the physical viability of a cosmological model and impose constraints on the behavior of matter and energy under gravitational interactions.

1. Null Energy Condition (NEC): The Null Energy Condition requires: $\rho + p \geq 0$. The NEC ensures that the energy density observed by a light-like observer (null vector) is non-negative. It is the most fundamental of all energy conditions, as the violation of the NEC often leads to unphysical scenarios such as exotic matter or superluminal signals. In an expanding universe, the NEC is closely linked to the second law of thermodynamics and the avoidance of unphysical singularities.

2. Weak Energy Condition (WEC): The Weak Energy Condition requires: $\rho \geq 0, \quad \rho + p \geq 0$. The WEC ensures that the energy density observed by any time like observer is non-negative. This condition is fundamental for a physically reasonable distribution of matter and energy. Satisfying the WEC indicates that matter behaves normally (e.g., no negative energy densities). It guarantees the normal gravitational attraction of matter and aligns with the observed dynamics of galaxies and cosmic structures.

3. Dominant Energy Condition (DEC): The Dominant Energy Condition requires: $\rho \geq |p|$. The DEC ensures that the flow of energy and momentum is causal, meaning that energy cannot propagate faster than the speed of light. Additionally, it implies that the energy density dominates over pressure contributions. Models satisfying the DEC respect causality and prevent the occurrence of unphysical faster-than-light phenomena. It is critical in describing the large-scale structure of the universe and the evolution of density perturbations.

4. Strong Energy Condition (SEC): The Strong Energy Condition requires: $\rho + 3p \geq 0$, $\rho + p \geq 0$. The SEC ensures that gravity is always attractive, implying that the combined effects of energy density and pressure act as a source

of gravitational pull. The SEC is rooted in classical general relativity, where gravity is inherently attractive. In standard cosmology, the SEC is satisfied during the matter-dominated and radiation-dominated phases. However, during the accelerated expansion of the universe (e.g., the inflationary epoch or the current dark energy-dominated era), the SEC is violated. This violation is necessary to explain repulsive gravitational effects, such as the ones driving the universe's accelerated expansion.

For our model,

$$\rho(t)+p(t)=\frac{\alpha}{(4\pi+\lambda_2)t^4}\left[t^2+36\lambda_1\left(-1+2\alpha+\alpha t\right)\right] \tag{40}$$

$$\rho(t)-p(t)=\frac{6\alpha^2}{(8\pi+4\lambda_2)(4\pi+\lambda_2)}+\frac{\alpha}{(8\pi+4\lambda_2)t^4}\left[12\alpha t^3+(6\alpha+216\lambda_1\alpha^2-2)t^2+216\lambda_1\alpha(2\alpha-1)t+36\lambda_1(6\alpha^2-7\alpha+2)\right] \tag{41}$$

$$\rho(t)+3p(t)=\frac{\alpha}{(4\pi+2\lambda_2)(4\pi+\lambda_2)t^4}\left[-3\alpha t^4-(24\pi+6\lambda_2)\alpha t^3+\left\{(12\pi+5\lambda_2)-3\alpha(4\pi+\lambda_2)(1+36\lambda_1\alpha)\right\}t^2+36\lambda_1\alpha t\left\{(20\pi+7\lambda_2)-6\alpha(4\pi+\lambda_2)\right\}+18\lambda_1\left\{\alpha(60\pi+23\lambda_2)-(24\pi+10\lambda_2)-\alpha^2(24\pi+6\lambda_2)\right\}\right] \tag{42}$$

In terms of redshift, we obtain

$$\rho(z)+p(z)=\frac{\alpha}{(4\pi+\lambda_2)W\left[(1+z)^{-\frac{1}{\alpha}}\right]^4}\left[W\left[(1+z)^{-\frac{1}{\alpha}}\right]^2+36\lambda_1\left(-1+2\alpha+\alpha W\left[(1+z)^{-\frac{1}{\alpha}}\right]\right)\right] \tag{43}$$

$$\rho(z)-p(z)=\frac{6\alpha^2}{(8\pi+4\lambda_2)(4\pi+\lambda_2)}+\frac{\alpha}{(8\pi+4\lambda_2)W\left[(1+z)^{-\frac{1}{\alpha}}\right]^4}\left[12\alpha W\left[(1+z)^{-\frac{1}{\alpha}}\right]^3+(6\alpha+216\lambda_1\alpha^2-2)W\left[(1+z)^{-\frac{1}{\alpha}}\right]^2+216\lambda_1\alpha(2\alpha-1)W\left[(1+z)^{-\frac{1}{\alpha}}\right]+36\lambda_1(6\alpha^2-7\alpha+2)\right] \tag{44}$$

$$\rho(z)+3p(z)=\frac{\alpha}{(4\pi+2\lambda_2)(4\pi+\lambda_2)W\left[(1+z)^{-\frac{1}{\alpha}}\right]^4}\left[-3\alpha W\left[(1+z)^{-\frac{1}{\alpha}}\right]^4-(24\pi+6\lambda_2)\alpha W\left[(1+z)^{-\frac{1}{\alpha}}\right]^3+\left\{(12\pi+5\lambda_2)-3\alpha(4\pi+\lambda_2)(1+36\lambda_1\alpha)\right\}W\left[(1+z)^{-\frac{1}{\alpha}}\right]^2+36\lambda_1\alpha W\left[(1+z)^{-\frac{1}{\alpha}}\right]\left\{(20\pi+7\lambda_2)-6\alpha(4\pi+\lambda_2)\right\}+18\lambda_1\left\{\alpha(60\pi+23\lambda_2)-(24\pi+10\lambda_2)-\alpha^2(24\pi+6\lambda_2)\right\}\right] \tag{45}$$

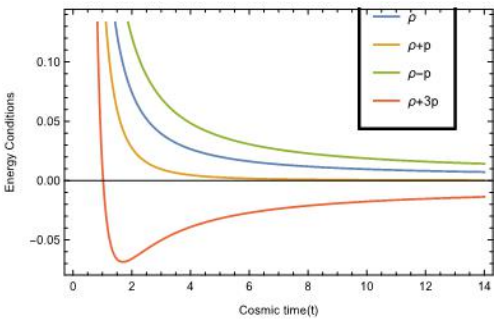

Figure 17. Variation of Energy Conditions versus cosmic time t with $\alpha = 0.5$.

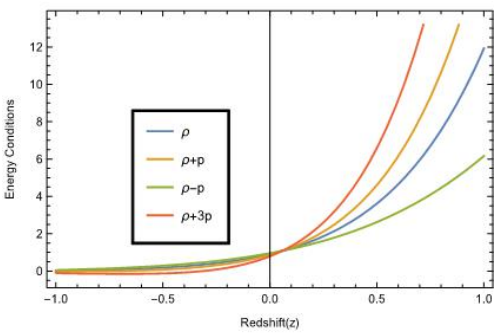

Figure 18. Variation of Energy Conditions versus redshift z with $\alpha = 0.5$.

From figures 17 and 18, we observe that the WEC, NEC, DEC are well satisfied whereas the SEC gets violated at approximately $t \approx 1$ and $z \approx 0.08$. This violation results in the accelerated expansion of the universe for our model.

7. CONCLUSIONS

In this study, we explore flat Friedmann-Lemaître-Robertson-Walker (FLRW) cosmological model within the context of an extended gravitational theory known as $f(R,T)$ gravity. By solving the non-linear field equaitons derived from this theory using the Hubble parameter as $H = \alpha\left(1+\frac{1}{t}\right)$; $\alpha > 0$, we aim to understand the evolution of the universe and its expansion dynamics. Our findings provide several critical insights into the Hubble parameter, deceleration parameter, energy density, and other higher-order cosmological parameters. Furthermore, we evaluate the model's compatibility with standard cosmology, particularly the ΛCDM model, and test its consistency with various energy conditions.

The key features of the cosmological model corresponding to the solution obtained in Section 4 are as follows:

The Hubble parameter H, which quantifies the universe's expansion rate, exhibits significant changes over cosmic time: At the early stages of the universe ($t = 0$), H is exceptionally high, reflecting a rapid expansion. As time progresses, H decreases monotonically, consistent with the gradual slowing of expansion during the matter-dominated era, followed by a phase of accelerated expansion at late times driven by dark energy. When expressed in terms of redshift (z), H increases as z increases. This is a natural consequence of the relation between redshift and scale factor, where higher redshifts correspond to earlier cosmic epochs with faster expansion rates.

The deceleration parameter q is a critical quantity that describes the acceleration or deceleration of the universe's expansion: Initially, the universe is in a decelerating phase, dominated by the gravitational pull of matter and radiation. The model shows a transition from deceleration to acceleration at a specific point in cosmic time, corresponding to the dominance of dark energy or a similar repulsive component. For lower values of the model parameter α, this transition to acceleration occurs earlier (at lower redshifts), highlighting the sensitivity of the model to its parameters. At very late times ($t \to \infty$), the deceleration parameter asymptotically approaches -1, indicating a de Sitter like state with a constant rate of accelerated expansion, typical of dark energy-dominated cosmologies.

The behavior of the energy density ρ and pressure p in the model reveals key characteristics of the universe's evolution: At $t = 0$, the energy density ρ is extremely high, consistent with a big bang-type singularity, where the universe begins in a state of infinite density. Over time, ρ decreases monotonically but never reaches zero, even p as $t \to \infty$. This ensures that $\rho > 0$ throughout the evolution, satisfying fundamental physical requirements. The pressure is negative at all times, a crucial feature for explaining the observed accelerated expansion. Negative pressure is a hallmark of dark energy or similar components driving the late-time acceleration of the universe.

The study also examines the higher-order parameters derived from the scale factor: the jerk, snap, and lerk parameters (representing the third, fourth, and fifth derivatives of $a(t)$, respectively) which provide additional insights into the universe's expansion dynamics. These parameters show trends consistent with a universe transitioning from deceleration to acceleration, further validating the model's description of cosmic evolution.

Our analysis shows that the model behaves like a quintessence dark energy scenario at present times. Quintessence is a dynamic form of dark energy driven by a scalar field with a time-dependent equation of state, as opposed to the constant equation of state in the standard cosmological constant (Λ) model. At late times, the model aligns with the ΛCDM framework, suggesting that it can reproduce the well-observed behavior of the universe while providing additional flexibility in earlier epochs.

To evaluate the physical viability of the model, we tested it against the four standard energy conditions. In our model, initially the Strong Energy Condition (SEC) is satisfied but later it is violated. This is a typical feature of models describing an accelerating universe.

The presence of a point-type singularity at $t = 0$ is consistent with the Big Bang scenario, marking the universe's origin in a state of infinite density and temperature. As time progresses, the volume of the universe increases monotonically, reflecting the ongoing cosmic expansion. The model captures the key features of late-time acceleration, aligning with observations of the universe's current phase of accelerated expansion driven by dark energy. Its compatibility with quintessence-like behavior and eventual convergence to ΛCDM at late times ensures that it is consistent with the observational data for both current and early-universe.

By successfully explaining the transition from deceleration to acceleration, the evolution of energy density and pressure, and the higher-order cosmological parameters, this model demonstrates the potential of $f(R,T)$ gravity to serve as a viable extension of general relativity. The framework offers flexibility to accommodate a range of observational phenomena while maintaining consistency with fundamental physical laws.

Acknowledgments

The authors express their profound gratitude to the esteemed referee for his/her valuable comments and suggestions which helped to improve the quality of this paper in the present form.

ORCID

Chandra Rekha Mahanta, https://orcid.org/0000-0002-8019-8824; **Kankana Pathak**, https://orcid.org/0009-0004-0353-809X; **Dibyajyoti Das**, https://orcid.org/0009-0007-0927-0903

REFERENCES

[1] Riess, A. G., Filippenko, A. V., Challis, P. *et al.*, Observational evidence from supernovae for an accelerating universe and a cosmological constant, Astron. J. **116**, 1009 (1998). https://doi.org/10.1086/300499

[2] Perlmutter, S., Aldering, G., Valle, M. D., Deustua, S., Ellis, R. S., Fabbro, S., Fruchter, A. *et al.*, Discovery of a supernova explosion at half the age of the Universe, Nature **391**, 51 (1998). https://doi.org/10.1038/34124

[3] Perlmutter, S., Aldering, G., Goldhaber, G. *et al.*, Measurements of Ω and Λ from 42 high-redshift supernovae, Astrophys. J. **517**, 565 (1999). https://doi.org/10.1086/307221

[4] Bennett, C. L., Halpern, M., Hinshaw, G. *et al.*, First-Year Wilkinson Microwave Anisotropy Probe (WMAP)* Observations: Preliminary Maps and Basic Results, Astrophys. J. Suppl. Ser. **148**, 1 (2003). https://doi.org/10.1086/377253

[5] Bennett, C. L., Larson, D., Weiland, J. L. *et al.*, Nine-Year Wilkinson Microwave Anisotropy Probe (WMAP) Observations: Final Maps and Results, Astrophys. J. Suppl. Ser. **208**, 20 (2013). https://doi.org/10.1088/0067-0049/208/2/20

[6] Spergel, D. N., Verde, L., Peiris, H. V. *et al.*, First Year Wilkinson Microwave Anisotropy Probe (WMAP) Observations: determination of cosmological parameters, Astrophys. J. Suppl. Ser. **148**, 175 (2003). https://doi.org/10.1086/377226

[7] Spergel, D. N., Bean, R., Doré, O. *et al.*, Three-year Wilkinson Microwave Anisotropy Probe (WMAP) observations: implications for cosmology, Astrophys. J. Suppl. Ser. **170**, 377 (2007). https://doi.org/10.1086/513700

[8] Hinshaw, G. *et al.*, Nine year wilkinson microwave anisotropy probe observations: cosmological parameter results, Astrophys. J. Suppl. Ser. **208**, 19 (2013). https://doi.org/10.1088/0067-0049/208/2/19

[9] Tegmark, M., Strauss, M. A., Blanton, M. R. *et al.*, Cosmological parameters from SDSS and WMAP, Phys. Rev. D, **69**, 103501 (2004). https://doi.org/10.1103/PhysRevD.69.103501

[10] Caldwell, R. R., Doran, M., Cosmic microwave background and supernova constraints on quintessence: Concordance regions and target models, Phys. Rev. D, **69**, 103517 (2004). https://doi.org/10.1103/PhysRevD.69.103517

[11] Huang, Z.−Y., Wang, B., Abdalla, E., Su, R.−K., Holographic explanation of wide-angle power correlation suppression in the Cosmic Microwave Background Radiation, J. Cosmo. Astropart. Phys. **5**, 013 (2006). https://doi.org/10.1088/1475-7516/2006/05/013

[12] Zwicky, F., The redshift of extragalactic nebulae, Helvetica Physica Acta, **6**, 110 (1933). http://doi.org/10.48550/arxiv.1711.01693

[13] Carroll, S.M., Duvvuri, V., Trodden, M., Turner, M.S., Is cosmic speed-up due to new gravitational physics?, Phys. Rev. D, **70**, 043528 (2004). https://doi.org/10.1103/PhysRevD.70.043528

[14] Harko, T., Lobo, F. S. N., Nojiri, S., Odintsov, S. D., $f(R,T)$ gravity, Phys. Rev. D **84**, 024020 (2011). https://doi.org/10.1103/PhysRevD.84.024020

[15] Brans, C., Dicke, R. H., Mach's Principle and a Relativistic Theory of Gravitation, Phys. Rev. D, **124**, 925 (1961). https://doi.org/10.1103/PhysRev.124.925

[16] Ferraro, R., Fiorini, F., Modified teleparallel gravity: Inflation without an inflaton, Phys. Rev. D, **75**, 084031 (2007). https://doi.org/10.1103/PhysRevD.75.084031

[17] Carroll, S.M., Felice, A.D., Duvvuri, V., Easson, D.A., Trodden, M., Turner, M.S., Cosmology of generalized modified gravity models, Phys. Rev. D, **71**, 063513 (2005). https://doi.org/10.1103/PhysRevD.71.063513

[18] Jiménez, J. B., Heisenberg, L., Koivisto, T., Coincident general relativity, Phys. Rev. D, **98**, 044048 (2018). https://doi.org/10.1103/PhysRevD.98.044048

[19] Bamba, K. *et al.*, Finite-time future singularities in modified Gauss-Bonnet and $F(R,G)$ gravity and singularity avoidance, Eur. Phys. J. C **67**, 295 (2010). https://doi.org/10.1140/epjc/s10052-010-1292-8

[20] Xu, Y., Li, G., Harko, T., Liang, S., $f(Q,T)$ gravity, Eur. Phys. J. C, **79**, 708 (2019). https://doi.org/10.1140/epjc/s10052-019-7207-4

[21] Houndjo, M. J. S., Reconstruction of $f(R,T)$ gravity describing matter dominated and accelerated phases, Int. J. Mod. Phys. D **21**, 1250003 (2012). https://doi.org/10.1142/S0218271812500034

[22] Bhattacharjeea, S. and Sahoo, P. K., Redshift Drift in $f(R,T)$ Gravity, New Astron. **81**, 101425 (2020). https://doi.org/10.1016/j.newast.2020.101425

[23] Pradhan, A., Goswami, G., Rani R., Beesham, A., An $f(R,T)$ gravity based FLRW model and observational constraints, Astronomy and Computing **44**, 100737 (2023). https://doi.org/10.1016/j.ascom.2023.100737

[24] Starobinsky, A. A., A new type of isotropic cosmological models without singularity, Phys. Lett. B **91**, 99 (1980). https://doi.org/10.1016/0370-2693(80)90670-X

[25] Zubair, M., Noureen, I., Evolution of axially symmetric anisotropic sources in $f(R,T)$ gravity, Eur. Phys. J. C **75**, 265 (2015). https://doi.org/10.1140/epjc/s10052-015-3496-4

[26] Zubair, M., Noureen, I., Bhatti, A.A., Abbas, G., Shear-free condition and dynamical instability in $f(R,T)$ gravity, Eur. Phys. J. C, **75**, 323 (2015). https://doi.org/10.1140/epjc/s10052-015-3547-x

[27] Sahoo, P.K., Moraes, P. H. R. S., Sahoo, P., Wormholes in R^2-gravity within the $f(R,T)$ formalism, Eur. Phys. J. C, **78**, 46 (2018). https://doi.org/10.1140/epjc/s10052-018-5538-1

[28] Sahoo, P.K., Moraes, P. H. R. S., Sahoo, P., Bishi, B. K., $f(R,T) = f(R) + \lambda T$ gravity models as alternatives to cosmic acceleration, Eur. Phys. J. C, **78**, 736 (2018). https://doi.org/10.1140/epjc/s10052-018-6211-4

[29] Vinutha, T., Kavya, K. S., Bianchi type cosmological models in $f(R,T)$ theory with quadratic functional form, Eur. Phys. J. Plus, **135**, 306 (2020). https://doi.org/10.1140/epjp/s13360-020-00309-8

[30] Bishi, B. K. *et al.*, Domain Walls and Quark Matter Cosmological Models in $f(R,T) = R + aR^2 + kT$ gravity, Iran. J. Sci. Technol. Trans. Sci. **45**, 1835 (2021). https://doi.org/10.1007/s40995-021-01113-4

[31] Hassan, A. *et al.*, An Interacting Two-Fluid Scenario for Dark Energy in an FRW Universe, Chinese Phys. Lett. **28**, 039801 (2011). https://doi.org/10.1088/0256-307X/28/3/039801

[32] Sahni, V. *et al.*, Statefinder - a new geometrical diagnostic of dark energy, JETP Lett. **77**, 201 (2003). https://doi.org/10.1134/1.1574831

КОСМОЛОГІЧНА МОДЕЛЬ FLRW ІЗ КВАДРАТИЧНОЮ ФУНКЦІОНАЛЬНОЮ ФОРМОЮ У $f(R,T)$ ТЕОРІЇ ГРАВІТАЦІЇ

Чандра Рекха Маханта, **Канкана Патхак**, **Діб'яджйоті Дас**

Департамент математики, Університет Гаухаті, Гопінат Бордолой Нагар, Джалукбарі, 781014, Ассам, Індія

У цій роботі досліджується просторово однорідний та ізотропний плоский всесвіт Фрідмана-Лемаître-Робертсона-Уокера (FLRW) у контексті гравітації $f(R,T)$, представленої Harko, *et al*., [Phys. Rev. D, 84, 024020 (2011)]. У цій роботі розглядається функціональна форма $f(R,T) = f_1(R) + f_2(T)$ з $f_1(R) = R + \lambda_1 R^2$ і $f_2(T) = 2\lambda_2 T$ де λ_1 і λ_2 довільні константи, R і T є скаляром Річчі та слідом тензора енергії напруги T_{ij} відповідно. Ми представляємо нову космологічну модель у рамках гравітації $f(R,T)$, досліджуючи динаміку Всесвіту FLRW через точне рішення рівнянь гравітаційного поля. Використовуючи інноваційний анзац для параметра Хаббла, $H = \alpha\left(1+\frac{1}{t}\right)$, де α — додатна константа, ми фіксуємо еволюційну історію Всесвіту. Цей підхід забезпечує природний шлях для дослідження ключових космологічних параметрів, таких як масштабний фактор, параметр уповільнення, ривок, стрибок, параметри lerk та енергетичні умови, відкриваючи інтригуючу інформацію про динаміку розширення Всесвіту. Ми також обговорюємо діагностику вимірювача стану. Наші результати пропонують глибше розуміння космічної еволюції в рамках $f(R,T)$ гравітації.

Ключові слова: *$f(R,T)$ гравітація; метрика FLRW; параметр Хаббла; діагностика вимірювача стану*

East European Journal of Physics. 1. 44–58 (2025)
DOI: 10.26565/2312-4334-2025-1-04 ISSN 2312-4334

THERMODYNAMICS OF HOMOGENEOUS AND ISOTROPIC UNIVERSE FOR VARIOUS DARK ENERGY CONDITIONS

Neeru Goyal[a], **Anil Kumar Yadav**[b], **Tensubam Alexander Singh**[c], **Aditya Sharma Ghrera**[a], **Asem Jotin Meitei**[d,e], **Kangujam Priyokumar Singh**[e*]

[a] *Department of Applied Sciences, The NorthCap University, Gurugram - 122017, India*
[b] *Department of Physics, United College of Engineering and Research,Greater Noida - 201310, India*
[c] *Department of Mathematical Sciences, Bodoland University, Kokrajhar-783370, Assam, India*
[d] *Department of Mathematics, Pravabati College, Mayang Imphal-795132, Manipur, India*
[e] *Department of Mathematics, Manipur University, Canchipur, Imphal-795003, Manipur, India*
[*] *Corresponding Author e-mail: pk_mathematics@yahoo.co.in*

Received October 10, 2024; revised January 01, 2025; accepted January 30, 2025

The thermodynamic properties of homogeneous and isotropic universe for various dark energy conditions with decaying cosmological term $\Lambda(t)$ are investigated. To obtain the explicit solution of Einstein's field equations, we have considered a linearly varying deceleration parameter in the form of $q = -\alpha t + m - 1$ with α and m as scalar constants. We have constrained the model parameters H_0 and m as 68.495 km/s/Mpc and 1.591 respectively by bounding the derived model with combined pantheon compilation of SN Ia and H(z) data sets. Furthermore, we have studied the time varying dark energy states for two different assumptions i) $\Lambda = \Lambda_1 t^{-2}$ and ii) $\Lambda \propto [R(t)]^{-2n}$. For a specific assumption, our models indicate a dark energy like behaviour in in open, flat and closed space - time geometry. The temperature and entropy density of the model remain positive for both the cases i) $\Lambda = \Lambda_1 t^{-2}$ and ii) $\Lambda \propto [R(t)]^{-2n}$.. Some physical properties of the universe are also discussed.

Keywords: *FRW Model; Homogeneous; Thermodynamics; Pantheon; Dark energy*

PACS: 98.80.-K; 98.80Jk.

1. INTRODUCTION

Most of the studies in the recent years suggest that the understanding of the fate of the accelerating expansion of the universe in view of Type Ia Supernova [1, 2, 3, 4] is a very challenging and interesting field for the present research in Cosmology. Various studies have been done to explain this special discovery out of which [5, 6] can be mentioned. It is an interesting component that considered as dark energy possessing a negative pressure and is recommended to understand the accelerating expansion of the universe. The current simplest candidate for a standard model of cosmology and a good understanding with most observations [7, 8] is the ΛCDM model which is required due to two major problems as fine-tuning or why so small and coincidence [9, 10, 11]. There are mainly three different methods to express the dark energy problem i.e., dynamical dark energy [5], the anthropic principle [9] and interacting dark energy [12, 13]. Out of which, dynamical dark energy has an hypothetical form called as Quintessence which is reported as a scalar field minimally connected to gravity which can fall to the late time inflation accelerating cosmological expansion for some particular form of potential, Also, due to these particular potentials it lighten the cosmological coincidence model [11]. In this paper, we have intended to focus on this quintessence and phantom phase models since the role of thermodynamics in cosmology remain essential to study the transverse of irreversible energy flow from gravitational field to matter creation that can helps to transform space-time into matter as suggested by [14]. Also, the irreversible matter creation, the big-bang initial singularity remain unstable. This dissipative process of the Einstein field equation leads to the possibility of cosmological model from empty space to creation of matter and entropy. Gravitational entropy remain meaningful as associated with the entropy which is necessary to produce matter. This extend signifies the possibility of impact fullness of third law of thermodynamics. As the source of dark energy of the current phase of universe can modify the horizon entropy, so its thermodynamics in both cosmological as well as gravitational set ups have more impaction [15, 16, 17, 18, 21, 23, 24]. Also, it seems that the properties of such modifications to the thermodynamics are in line with non-extensive thermodynamics of space-time and the current universe. Here, we investigated the mutual relationship between the thermodynamic laws with the Einstein field equations (EFE) with the concept of Einstein theory of gravitation. In order to study the model here we apply the thermodynamical laws of Apparent Horizon of FRW universe as FRW metric is an exact solution of EFE of general relativity, which describes an isotropic homogeneous and expanding universe. The solution of this model can proved its generic properties that are different from dynamical FL Model which are specific solutions for scale factor $R(t)$ that assumes the only contribution to stress energy, cold matter, radiation and cosmological constant.

Cite as: N. Goyal, A.K. Yadav, T.A. Singh, A.S. Ghrera, A.J. Meitei, K.P. Singh, East Eur. J. Phys. 1, 44 (2025), https://doi.org/10.26565/2312-4334-2025-1-04

It is worthwhile to mention that there was a major breakthrough after results of Supernovae type Ia project [25]. A new type of fluid with negative pressure, called dark energy, leads cosmic acceleration of the universe at present epoch. In the recent past, many cosmological modes have been investigated to describe the nature of dark energy [26, 27, 28, 29, 30, 31, 32, 33, 34, 35, 36, 37]. The most suitable candidate of dark energy is a time varying cosmological constant term $\Lambda(t)$ but it suffers few problems on the theoretical scale namely fine tuning and cosmic coincidence problems. In order to alleviate cosmological constant problems, one can refer the following Refs. [38, 39, 40, 41, 42, 43, 44]. Up to now, the dark energy and its physical nature is still mysterious and unclear, and we only know its some phenomenological properties such as the dark energy is a cosmic fluid with equation of state parameter, numerically equivalent to -1 and it violated strong energy condition. Also, the dark energy is homogeneously permeated in the universe and its clustering property is smaller than dark matter. Some applications of time dependent Λ term are given in the Refs. [45, 46, 47, 48]. The idea of that during the evolution of the universe the energy density of the vacuum decouples into the particles thus the value of cosmological term decreases with age of the universe. As the result one has the creation of particles although the typical rate of the creation is very small. Now, it has been established that the universe is in accelerating phase at present epoch. This acceleration of the universe is usually described by inclusion of dark energy density along with the matter energy density in the Einstein's field equation [38, 39, 49, 52, 51, 52, 53, 37]. The observational estimates suggest that the universe is filled with dark matter with null pressure and dark energy with negative pressure. However, the nature of dark matter and dark energy is still mysterious. In the recent past, some cosmological models have been investigated to explore the problems associated with dark energy and its possible solutions [54, 55, 56, 57, 58]. We also note that some important properties of dark energy in light of the early JWST observations are explored in Ref. [59]. Nunes et al. [60] have investigated the dark sector interactions from the full-shape galaxy power spectrum and described its new features in context of accelerating universe. The soundness of dark energy properties and its applications are given in ref. [61]. Motivated by above investigations, in this paper, we confine ourself to investigate some thermodynamic properties of homogeneous and isotropic universe for various dark energy conditions. The study reveals that the derived models might be a suitable model to describe the dynamics and fate of the universe at present epoch.

The structure of our paper is as follows: In Section 2, we have presented thermodynamical behaviour and entropy of the model where we have expressed the entropy production rate, apparent Horizon and Cui-Kim temperature of the apparent horizon. In Section 3, we derived some basis of Einstein's gravity with detail solutions of FRW metric. Sections 4 and 5 deal with two independent models: i) $\Lambda = \Lambda_1 t^{-2}$ and ii) $\Lambda = \Lambda_2 \left(\frac{t}{2m-\alpha t}\right)^{-\frac{2n}{m}}$ and its physical properties respectively. In Section 6, we summarize our findings in details.

2. THERMODYNAMICAL BEHAVIOUR AND ENTROPY

Thermodynamical study has been an important tool to incept a gravitational theory as pivotal event. Black hole thermodynamics and recent Conformal field theory correspondence shows a strong corelation between gravity and thermodynamics, also it has a great significance on recent observations. From the concept of thermodynamics, the interaction between first and second law of thermodynamics with volume V [14] can be expressed as

$$\tau ds = d(\rho V) + \rho dV, \tag{1}$$

where τ and S represents the temperature and entropy respectively. The above equation can be written as

$$\tau dS = d(p + \rho)V - V dp, \tag{2}$$

to define a perfect fluid as a thermodynamic system an integrability condition is required which can be written as

$$dp = \left(\frac{p + \rho}{\tau}\right) d\tau. \tag{3}$$

Using equations (2) and (3), we have the differential equation

$$dS = \frac{1}{\tau} d(p + \rho)V - (p + \rho)V \frac{d\tau}{\tau^2}. \tag{4}$$

Rewriting above equation

$$dS = d\left[\frac{(p + \rho)V}{\tau}\right]. \tag{5}$$

Therefore, the entropy can be defined as

$$S = \left[\frac{(p + \rho)V}{\tau}\right]. \tag{6}$$

The well known relation between pressure and energy density is read as

$$p = \gamma\rho \tag{7}$$

where $p = \gamma\rho$ and the parameter "γ" stands for equation of state parameter.
Let the entropy density is

$$S_1 = \frac{S}{V} = \frac{p+\rho}{\tau} = \frac{(1+\gamma)\rho}{\tau}. \tag{8}$$

Consider the apparent horizon of the universe for the assumed model appeared at r_A where

$$r_A = \frac{1}{\sqrt{H^2 + \frac{k}{a^2}}}. \tag{9}$$

Then the entropy density in terms of temperature with the help of first law of thermodynamics can be expressed as

$$d(\rho V) + \gamma\rho dV = (1+\gamma)\tau d\left(\frac{\rho V}{\tau}\right), \tag{10}$$

which on integration yields

$$\tau = \rho^{\frac{\gamma}{1+\gamma}}. \tag{11}$$

From equation (3), we obtain

$$S_1 = (1+\gamma)\rho^{\frac{\gamma}{1+\gamma}}. \tag{12}$$

Now the Cui-Kim temperature of the apparent horizon can be obtained as

$$\tilde{T} = \frac{1}{2\pi r_A}. \tag{13}$$

Here, the above equation (6) represents the entropy which does not depends on any individual fluids and is only depends on the isotropic pressure and total matter density of the fluid. Many authors have investigated on thermodynamical aspects of cosmological model using different theories with different fluid contents. Samant et. al [16] have investigated on the validity of second law of thermodynamics using Kaluza-Klein metric with Bulk viscosity in the context of $f(R,T)$ theory and found that the second law of thermodynamics doesn't hold for the assumed model. As we know that the actions of thermodynamic parameters is directly related to the energy density of the universe. Recently, Shekh et.al., [17] investigated thermodynamical aspects of relativistic hydrodynamics in $f(R,G)$ gravity for accelerated spatially homogeneous and isotropic FRW cosmological model with a non-perfect (un-magnetized) fluid in the framework of $f(R,G)$ gravity model by defining entropy density with the condition stated above. Jamil et.al [18] have investigated on Horava-Lifshitz cosmology for thermodynamical validity in different types of universe and found that the model remain valid for closed and flat universe but conditionally valid for open universe which matches to the result obtained during our study.

3. EINSTEIN FIELD EQUATION AND THEIR SOLUTION

The Einstein's field equation can be written as follows

$$R_{\mu\nu} - \frac{1}{2}Rg_{\mu\nu} = T_{\mu\nu}, \tag{14}$$

where $G_{\mu\nu}$ the Einstein tensor, Λ is the cosmological constant which can be regarded as dark energy of the model introduced by Einstein and $T_{\mu\nu}$ is the energy-momentum tensor.

To study the nature of the model universe, it is quiet necessary to consider a metric by which the Einstein field equations can be evaluated and further solutions can be evaluated. Let us consider FRW metric with a maximally symmetric spatial section as

$$ds^2 = -dt^2 + R^2(t)\left[\frac{dr^2}{1-kr^2} + r^2(d\theta^2 + \sin^2\theta d\phi^2)\right], \tag{15}$$

where $R(t)$ the cosmic scale factor and the spatial curvature index $k = -1, 0, +1$ corresponds to spatially open, flat and closed universe respectively.
Now, consider the fluid representation for the energy-momentum tensor which can be written as follows

$$T_{\mu\nu} = [\rho, p, p, p]. \tag{16}$$

In a co-moving coordinate system, the Einstein field equation (13) with the use of equations (14) and (15), we have

$$3H^2 + \frac{3k}{R^2} = \rho + \Lambda, \tag{17}$$

$$3H^2 + \frac{k}{R^2} + 2\dot{H} = -p + \Lambda, \tag{18}$$

where H stands for well-known Hubble parameter.

The above system of equation consists of two equation and four unknowns. To make the system consistent two additional constraints required. So first we have considered the well-known relation between pressure and energy density as described in Eq. (7). The parameter γ in Eq. (7) takes a vital role to model the universe for its different values. For $\gamma = 0, \frac{1}{3}$ and -1 the model represents a dust, radiating and vacuum energy of the fluid. Similarly, for $\gamma < 0$ is considered as an accelerating expansion of the universe in the context of dark energy. Moreover, for different range of γ such as quintessence phase, $-1 < \gamma < 0$, phantom phase $\gamma < -1$ and for cosmological constant cold dark matter ΛCDM universe, we have $\gamma = -1$. Still, it is worthwhile to note that there is no clear understanding on equation of state parameter of dark energy yet.

Furthermore, we also considered a linearly varying deceleration parameter [19, 20, 21, 22] as

$$q = -\alpha t + m - 1 \tag{19}$$

where α and m are scalar constants and $q = -\frac{R\ddot{R}}{\dot{R}^2}$ the deceleration parameter which helps to predict whether the model is accelerating or decelerating in nature.

It is worthwhile to note that the concept of linearly varying deceleration parameter was given in Ref. [19] and later on its observational analysis are presented in Refs. [20, 22]. In this paper, we confine ourself to describe the thermodynamics of the universe for various dark energy conditions on the basis of linearly varying deceleration parameter.

The proposed form of deceleration parameter yields

$$R = a_1 \left(\frac{t}{2m - \alpha t}\right)^{\frac{1}{m}}, \quad \alpha > 0, m > 0. \tag{20}$$

where, $a_1 = k_1{}^{\frac{1}{m}}$ is an arbitrary constant while k_1 denotes an integrating constant.
The Hubble parameter can be calculated by using equation (8) as

$$H = -\frac{2}{t(\alpha t - 2m)}. \tag{21}$$

Hence the apparent horizon for the model is appeared at

$$r_A = \left(\frac{4}{t^2(\alpha t - 2m)^2} + \frac{k}{a_1^2}\left(\frac{\alpha t}{2m - \alpha t}\right)^{-\frac{2}{m}}\right). \tag{22}$$

The energy density and pressure can be calculated as follows

$$\rho = \frac{12}{t^2(\alpha t - 2m)^2} + \frac{3k}{a_1^2}\left(\frac{\alpha t}{2m - \alpha t}\right)^{-\frac{2}{m}} - \Lambda, \tag{23}$$

$$p = \frac{8(m - \alpha t) - 12}{t^2(\alpha t - 2m)^2} - \frac{k}{a_1^2}\left(\frac{\alpha t}{2m - \alpha t}\right) + \Lambda. \tag{24}$$

Now, the equation of state parameter can be calculated on using (18)

$$\gamma = \frac{8(m - \alpha t) + \Lambda t^2(\alpha t - 2m)^2 - \frac{k}{a_1^2}\left(\frac{\alpha t}{2m - \alpha t}\right)^{-\frac{2}{m}} t^2(\alpha t - 2m)^2 - 12}{12 - \Lambda t^2(\alpha t - 2m)^2 + \frac{k}{a_1^2}\left(\frac{\alpha t}{2m - \alpha t}\right)^{-\frac{2}{m}} t^2(\alpha t - 2m)^2}. \tag{25}$$

3.1. Observational confrontation

The red-shift z is read as

$$z = -1 + \frac{R_0}{R} \tag{26}$$

where, R_0 denotes the present value of scale factor and it is taken as 1.
Therefore, Hubble's parameter in term of z is obtained as

$$H(z) = -\frac{1}{1+z}\frac{dz}{dt} \tag{27}$$

Eqs. (20), (26) and (27) lead to

$$H = \frac{H_0}{(1+a_1^m)(1+z)^m}\left[1+a_1(1+z)^m\right]^2 \tag{28}$$

where, H_0 reads the present value of Hubble parameter.

Solving Eqs. (20) and (26), the time - redshift relationship is obtained as

$$t(z) = \frac{2m}{\alpha + [a_1(1+z)]^m} \tag{29}$$

Thus, the deceleration parameter in terms of redshift z is computed as

$$q = -1 + m - \frac{2m\alpha}{\alpha + [a_1(1+z)]^m} \tag{30}$$

It is worthwhile to note that the observational analysis of the linearly varying q in terms of time has been carried out in Refs. [20, 22]. In particular, Akarsu et al. [20] have investigated the kinematics and fate of the universe by confronting observational data for the linearly time-varying deceleration parameter model and its comparison with standard ΛCDM model while Pacif [22] has investigated dark energy cosmological model by considering the linearly time-varying deceleration parameter and constrained the model parameter with observational data. In this paper, we use the recent 1048 pantheon compilation of SN Ia data points [62] and 57 $H(z)$ data sets [63, 64, 65] while in Pacif [22], 580 data points of SN Ia is used. Furthermore, we also estimate H_0 along with model parameters m and a_1 whereas the value of $H_0 = 67.8\ km/s/Mpc$ is taken as prior in Pacif [22].

The χ^2 estimator is read as

$$\chi^2 = \sum_{i=1}^{N}\left[\frac{E_{th}(z_i) - E_{obs}(z_i)}{\sigma_i}\right]^2. \tag{31}$$

where $E_{th}(z_i)$ and $E_{obs}(z_i)$ denote the theoretical and observed values respectively, and σ_i^2 denotes standard deviation of each $E_{obs}(z_i)$. N is the number of data points.
The joint χ^2 estimator is read as

$$\chi^2_{joint} = \chi^2_{OHD} + \chi^2_{Pantheon} \tag{32}$$

The left panel of Fig. 1 depicts the two-dimensional contours in the $H_0 - m$ plane at 1σ, 2σ and 3σ confidence regions while the right panel of Fig.1 shows the two-dimensional contours in the $H_0 - a_1$ plane at 1σ, 2σ and 3σ confidence regions by bounding our model with joint 57 $H(z)$ data sets and pantheon compilation of SN Ia data. We constrained the model parameters H_0, m and a_1 as 68.495 km/s/Mpc, 1.591 and 1.462 respectively. The values of parameters m and a_1 differ slightly from Pacif [22]. That is why, we choose $m = 1.591$ and $a_1 = 1.462$ for graphical analysis of various parameters of the derived model. Fig. 2 depicts the dynamics of deceleration parameter q versus redshift z for $m = 1.591$ and $a_1 = 1.462$. From Fig. 2, we observe that the derived model exhibits a model of transitioning universe from early decelerating phase to current accelerating phase. Furthermore, we obtain the transition redshift and present value of deceleration parameter as $z_t = 0.73$ and $q_0 = -0.535$ respectively. It is worthwhile to note that an useful approach to compare the linearly varying deceleration parameter models with standard ΛCDM model are given in Ref. [20]. The present value of deceleration parameter and transition redshift are reported as $q_0 = -0.556 \pm 0.046$ and $z_t = 0.682 \pm 0.082$ respectively [20]. Moreover, Akarsu et al. [20] have obtained $z_t = 0.733^{+0.148}_{-0.095}$ for linearly varying deceleration parameter with redshift (LVDPz) which is very close to the transition redshift of this paper.

4. MODEL WITH $\Lambda \propto t^{-2}$ *i.e.* $\Lambda = \Lambda_1 t^{-2}$

This case gives the results of the physical parameter of the model as

$$\rho = \frac{12}{t^2(\alpha t - 2m)^2} + \frac{3k}{a_1^2}\left(\frac{t}{2m-\alpha t}\right)^{-\frac{2}{m}} - \Lambda_1 t^{-2}, \tag{33}$$

$$p = \frac{8(m-\alpha t) - 12}{t^2(\alpha t - 2m)^2} - \frac{k}{a_1^2}\left(\frac{t}{2m-\alpha t}\right) + \Lambda_1 t^{-2}, \tag{34}$$

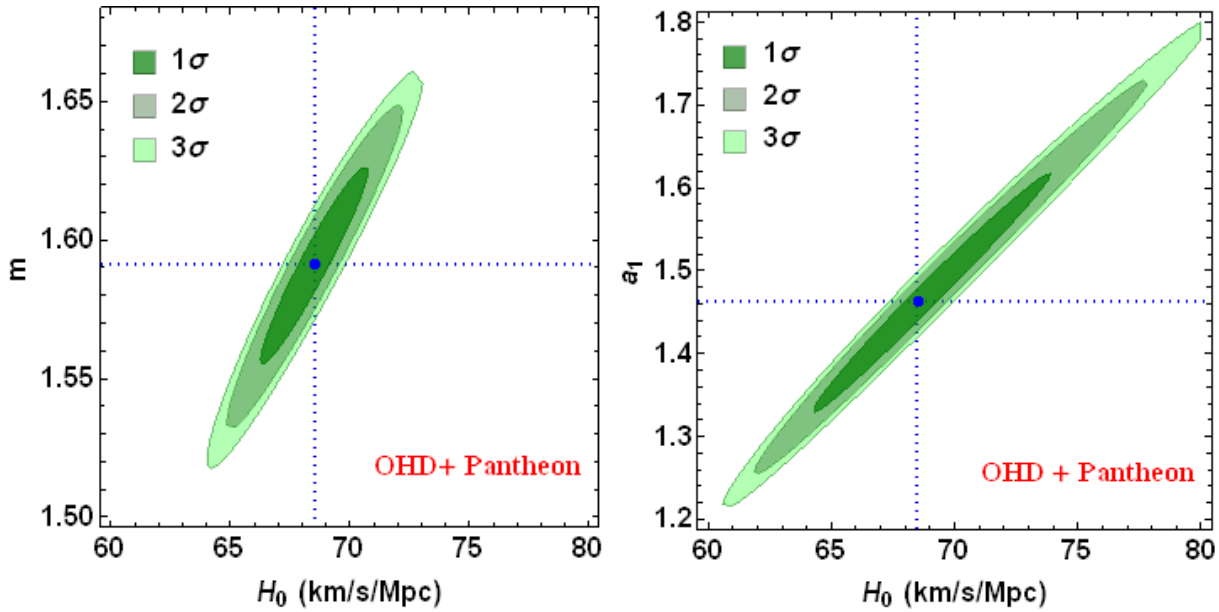

Figure 1. The left panel of Fig. 1 depicts the two-dimensional contours in the $H_0 - m$ plane at 1σ, 2σ and 3σ confidence regions while the right panel of Fig.1 shows the two-dimensional contours in the $H_0 - a_1$ plane at 1σ, 2σ and 3σ confidence regions by bounding our model with OHD + Pantheon compilation of SN Ia data.

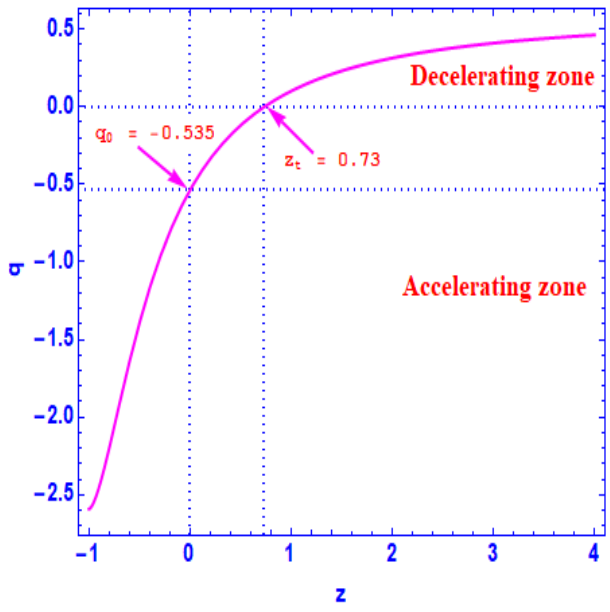

Figure 2. The deceleration parameter q versus z for $m = 1.59$ and $a_1 = 1.462$.

$$\gamma = \frac{8(m-\alpha t)+\Lambda_1 t^2(\alpha t-2m)^2-\frac{k}{a_1^2}\left(\frac{t}{2m-\alpha t}\right)^{-\frac{2}{m}}t^2(\alpha t-2m)^2-12}{12-\Lambda_1 t^2(\alpha t-2m)^2+\frac{k}{a_1^2}\left(\frac{t}{2m-\alpha t}\right)^{-\frac{2}{m}}t^2(\alpha t-2m)^2}. \tag{35}$$

Temperature

$$\tau = \left(\frac{12}{t^2(\alpha t-2m)^2}+\frac{3k}{a_1^2}\left(\frac{t}{2m-\alpha t}\right)^{-\frac{2}{m}}-\Lambda_1 t^{-2}\right)^{\beta}, \tag{36}$$

where

$$\beta = \frac{\frac{8(m-\alpha t)+\Lambda_1 t^2(\alpha t-2m)^2-\frac{k}{a_1^2}\left(\frac{t}{2m-\alpha t}\right)^{-\frac{2}{m}}t^2(\alpha t-2m)^2-12}{12-\Lambda_1 t^2(\alpha t-2m)^2+\frac{k}{a_1^2}\left(\frac{t}{2m-\alpha t}\right)^{-\frac{2}{m}}t^2(\alpha t-2m)^2}}{1+\frac{8(m-\alpha t)+\Lambda_1 t^2(\alpha t-2m)^2-\frac{k}{a_1^2}\left(\frac{t}{2m-\alpha t}\right)^{-\frac{2}{m}}t^2(\alpha t-2m)^2-12}{12-\Lambda_1 t^2(\alpha t-2m)^2+\frac{k}{a_1^2}\left(\frac{t}{2m-\alpha t}\right)^{-\frac{2}{m}}t^2(\alpha t-2m)^2}}. \tag{37}$$

The entropy density

$$S_1 = (1+\gamma)\left(\frac{12}{t^2(\alpha t-2m)^2}+\frac{3k}{a_1^2}\left(\frac{t}{2m-\alpha t}\right)^{-\frac{2}{m}}-\Lambda_1 t^{-2}\right)^{1-\beta}. \tag{38}$$

Moreover, using Eq. (29) in Eqs. (33) - (35), one may compute the energy density ρ and pressure p in terms of redshift z as following

$$\rho(z) = \frac{3k\left[(a_1(z+1))^{-m}\right]^{-2/m}}{a_1^2}+\frac{3(a_1(z+1))^{-2m}\left[\alpha+(a_1(z+1))^m\right]^4}{4m^4}-\frac{\Lambda_1\left[\alpha+(a_1(z+1))^m\right]^2}{4m^2} \tag{39}$$

$$p(z) = \frac{(a_1(z+1))^{-2m}\left({a_1}^2\left(\alpha+(a_1(z+1))^m\right)^2\left(-6\alpha(a_1(z+1))^m+(m(\Lambda_1 m+2)-3)(a_1(z+1))^{2m}-\alpha^2(2m+3)\right)-\zeta\right)}{4{a_1}^2m^4} \tag{40}$$

where $\zeta = 4\alpha k m^4(a_1(z+1))^m$.

Fig.3 and Fig. 4 show the behavior of the universe for energy density ρ and pressure $p$with respect to redshift z respectively. From the above graphical representations, we observe that the the energy density and pressure decrease as $z \to 0$. The variation of EOS parameter $\gamma = \frac{p}{\rho}$ with respect to time has been graphed in Fig. 5. We observe that open, flat and closed model of the universe, the EOS parameter varies as with negative sign, therefore, the derived model in open, flat and closed space - time geometry depicts dark energy EOS parameter like behaviour for $\Lambda = \Lambda_1 t^{-2}$. Furthermore, from Eq. (35), it is clear that the entropy density S_1 is decreasing function of time and at $t \to \infty$, $S_1 \to 0$, which indicates that the second law of thermodynamics remains impact-less on this model of universe.

In general theory of relativity, the energy conditions have significant role to describes the Hawking's Penrose singularity [23] whereas to verify the positive mass theorem, the dominant energy condition (DEC) is required to validate [24]. It consists of a couple of constraints which characterise the nature of the obscurity of lightlike, timelike or spacelike curves. Furthermore, to identify the second law of black hole thermodynamics, null energy condition plays a major role [66]. The four different types of energy conditions are Null energy condition (NEC), Weak energy condition (WEC), Strong energy condition (SEC) and Dominant energy condition (DEC) are respectively (i) $\rho + p \geq 0$ (ii) $\rho + p \geq 0$, $\rho \geq 0$ (iii) $\rho + 3p \geq 0$ (iv) $\rho > |p|$ [67]. The graphical representation of the energy conditions for this case are presented in Fig. 6. In the derived model, WEC, NEC and DEC are validated whereas it violates SEC as expected in dark energy models. Moreover, the SEC is violated for the derived model of the universe which indicates that the universe is accelerating in nature, which supports the results of Shekh et al. [17].

5. MODEL WITH $\Lambda \propto [R(t)]^{-2n}$ *i.e.* $\Lambda = \Lambda_2\left(\frac{t}{2m-\alpha t}\right)^{-\frac{2n}{m}}$

The different parameters of this model are obtained as

$$\rho = \frac{12}{t^2(\alpha t-2m)^2}+\frac{3k}{a_1^2}\left(\frac{t}{2m-\alpha t}\right)^{-\frac{2}{m}}-\Lambda_2\left(\frac{t}{2m-\alpha t}\right)^{-\frac{2n}{m}}, \tag{41}$$

$$p = \frac{8(m-\alpha t)-12}{t^2(\alpha t-2m)^2}-\frac{k}{a_1^2}\left(\frac{t}{2m-\alpha t}\right)^{-\frac{2}{m}}+\Lambda_2\left(\frac{t}{2m-\alpha t}\right)^{-\frac{2n}{m}}, \tag{42}$$

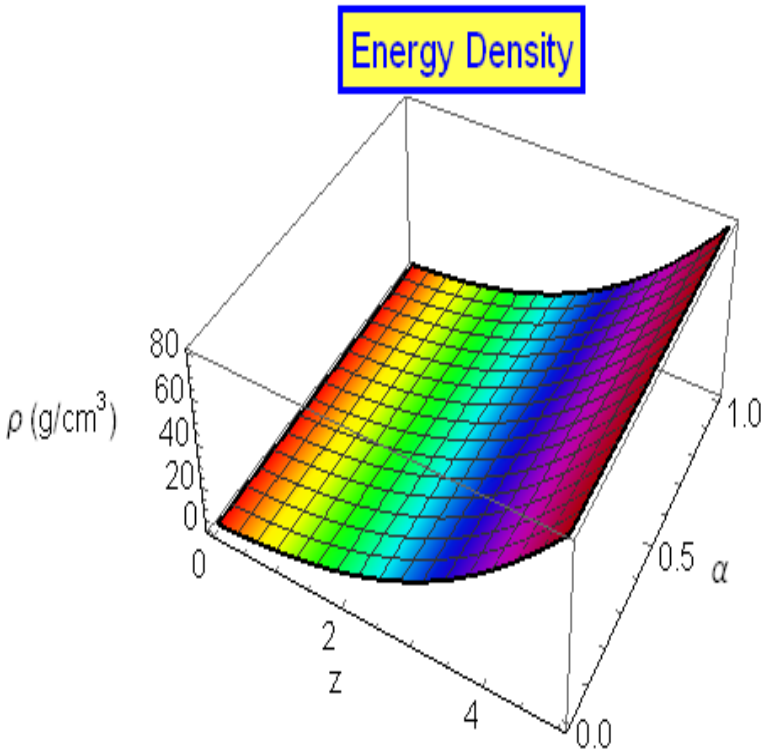

Figure 3. The energy density ρ versus redshift z for $m = 1.591$ and $a_1 = 1.462$ for model $\Lambda = \Lambda_1 t^{-2}$.

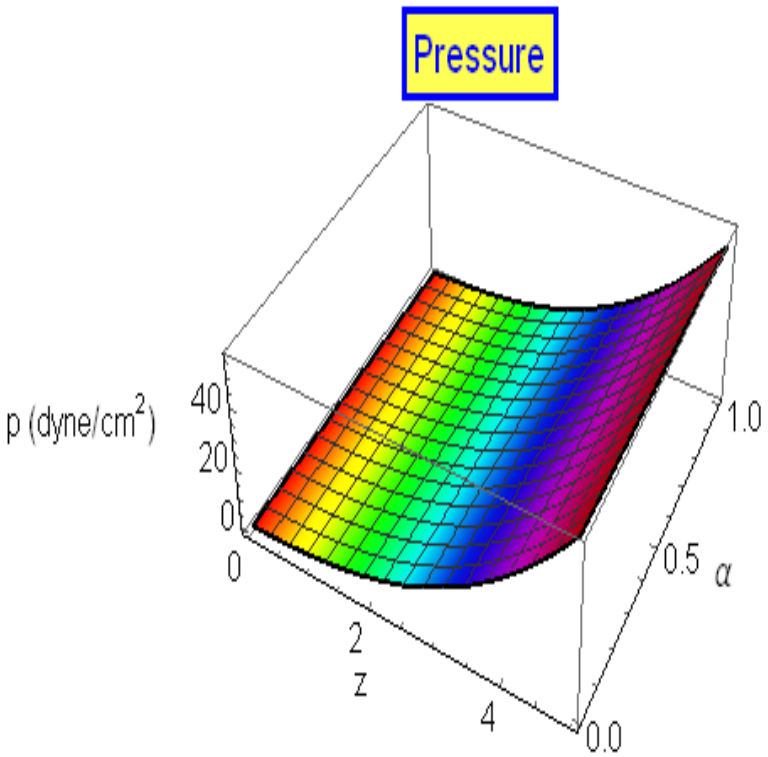

Figure 4. The pressure p versus redshift z for $m = 1.591$ and $a_1 = 1.462$ for model $\Lambda = \Lambda_1 t^{-2}$.

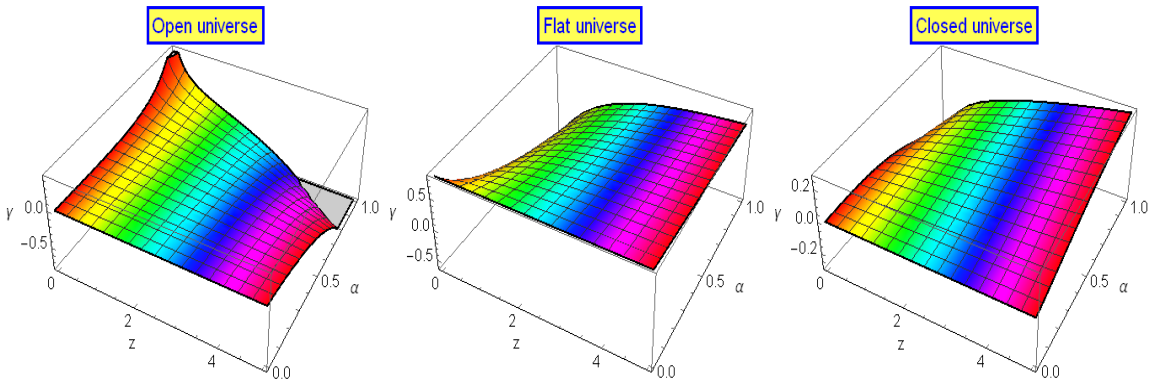

Figure 5. EOS parameter γ versus redshift z for model $\Lambda = \Lambda_1 t^{-2}$ for $m = 1.591$ and $a_1 = 1.462$.

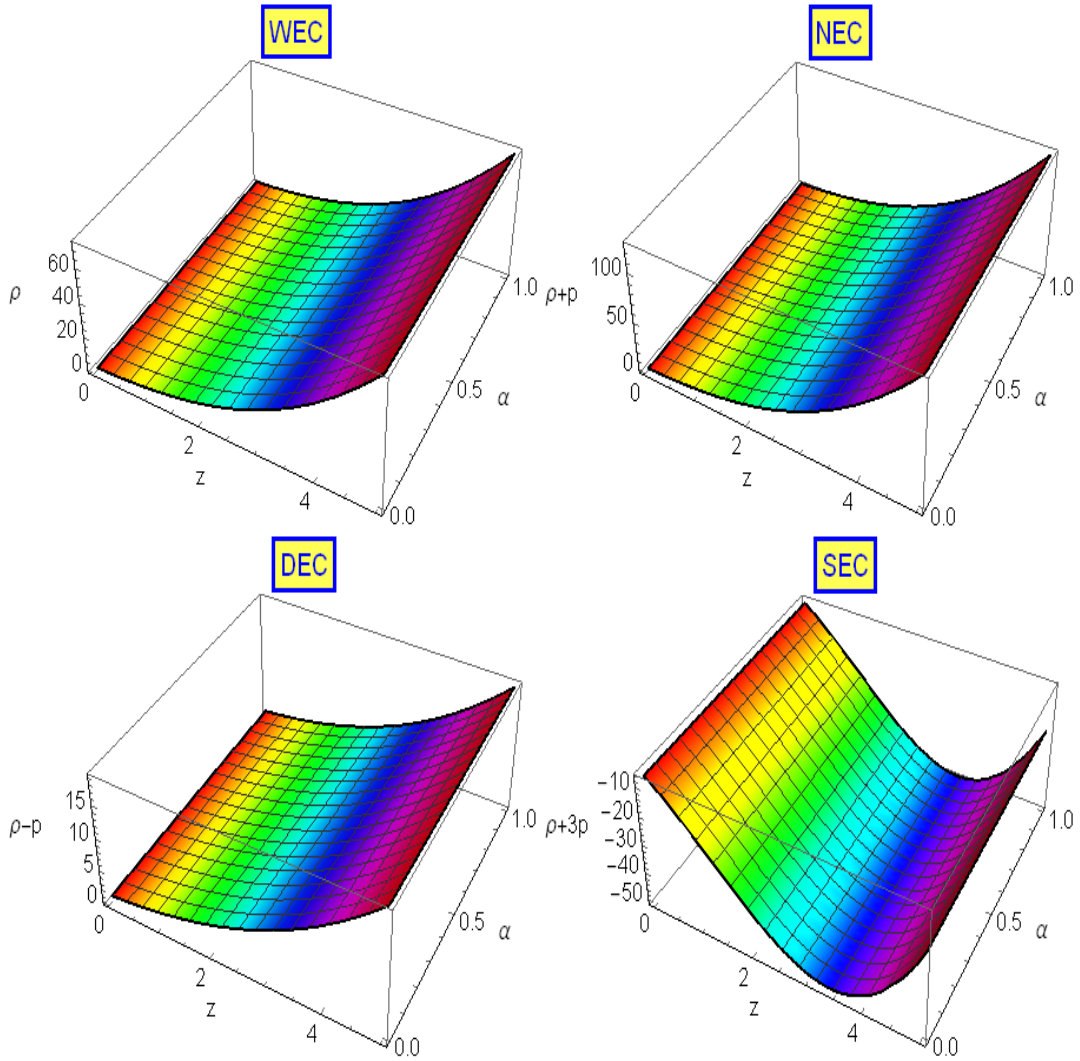

Figure 6. Energy conditions: i) WEC $\rho \geq 0$ ii) NEC $\rho + p \geq 0$ iii) DEC $\rho - p \geq 0$ and iv) SEC $\rho - 3p \leq 0$ for model $\Lambda = \Lambda_1 t^{-2}$.

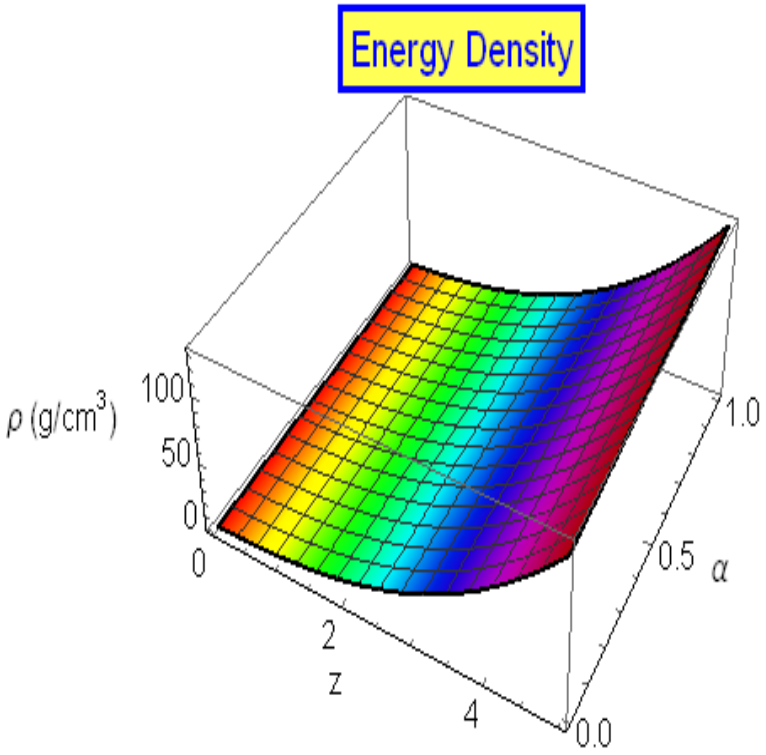

Figure 7. The energy density ρ versus redshift z for $m = 1.591$ and $a_1 = 1.462$. for model $\Lambda = \Lambda_2 \left(\frac{t}{2m-\alpha t}\right)^{-\frac{2n}{m}}$.

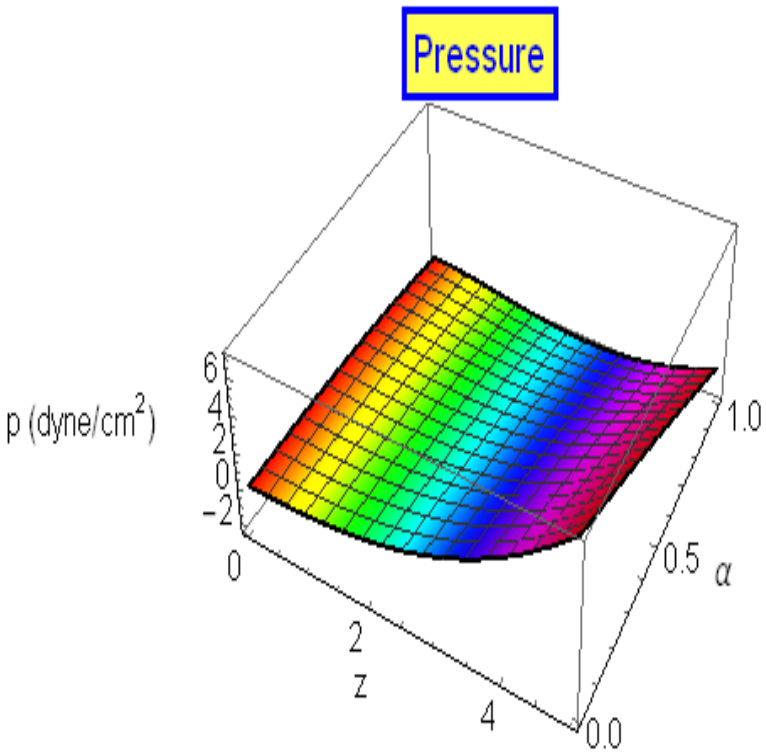

Figure 8. The pressure p versus redshift z for $m = 1.591$ and $a_1 = 1.462$. for model $\Lambda = \Lambda_2 \left(\frac{t}{2m-\alpha t}\right)^{-\frac{2n}{m}}$.

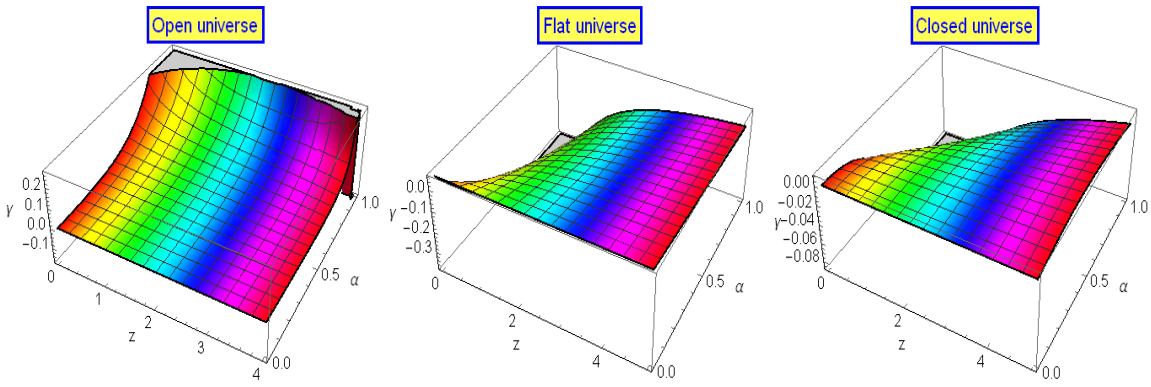

Figure 9. EOS parameter γ versus redshift z for model $\Lambda = \Lambda_2 \left(\frac{t}{2m-\alpha t}\right)^{-\frac{2n}{m}}$ for $m = 1.591$ and $a_1 = 1.462$.

$$\gamma = \frac{8(m-\alpha t) + \Lambda_2 \alpha^2 t^4 \left(\frac{t}{2m-\alpha t}\right)^{-\frac{2(n+m)}{m}} - \frac{k}{a_1^2}\left(\frac{t}{2m-\alpha t}\right)^{-\frac{2}{m}} t^2(\alpha t-2m)^2 - 12}{12 - \Lambda_2 \alpha^2 t^4 \left(\frac{t}{2m-\alpha t}\right)^{-\frac{2(n+m)}{m}} + \frac{k}{a_1^2}\left(\frac{t}{2m-\alpha t}\right)^{\frac{2}{m}} t^2(\alpha t-2m)^2}. \tag{43}$$

The temperature is given by

$$\tau = \left(\frac{12}{t^2(\alpha t-2m)^2} + \frac{3k}{a_1^2}\left(\frac{t}{2m-\alpha t}\right)^{-\frac{2}{m}} - \Lambda_2 \left(\frac{t}{2m-\alpha t}\right)^{-\frac{2n}{m}}\right)^{\eta}, \tag{44}$$

where

$$\eta = \left(\frac{\frac{8(m-\alpha t)+\Lambda_2\alpha^2t^4\left(\frac{t}{2m-\alpha t}\right)^{-\frac{2(n+m)}{m}} - \frac{k}{a_1^2}\left(\frac{t}{2m-\alpha t}\right)^{-\frac{2}{m}} t^2(\alpha t-2m)^2-12}{12-\Lambda_2\alpha^2t^4\left(\frac{t}{2m-\alpha t}\right)^{-\frac{2(n+m)}{m}} + \frac{k}{a_1^2}\left(\frac{t}{2m-\alpha t}\right)^{\frac{2}{m}} t^2(\alpha t-2m)^2}}{1 + \frac{8(m-\alpha t)+\Lambda_2\alpha^2t^4\left(\frac{t}{2m-\alpha t}\right)^{-\frac{2(n+m)}{m}} - \frac{k}{a_1^2}\left(\frac{t}{2m-\alpha t}\right)^{-\frac{2}{m}} t^2(\alpha t-2m)^2-12}{12-\Lambda_2\alpha^2t^4\left(\frac{t}{2m-\alpha t}\right)^{-\frac{2(n+m)}{m}} + \frac{k}{a_1^2}\left(\frac{t}{2m-\alpha t}\right)^{\frac{2}{m}} t^2(\alpha t-2m)^2}}\right). \tag{45}$$

And the entropy density obtained as

$$S_1 = \left(1 + \frac{8(m-\alpha t) + \Lambda_2 \alpha^2 t^4 \left(\frac{t}{2m-\alpha t}\right)^{-\frac{2(n+m)}{m}} - \frac{k}{a_1^2}\left(\frac{t}{2m-\alpha t}\right)^{-\frac{2}{m}} t^2(\alpha t-2m)^2 - 12}{12 - \Lambda_2 \alpha^2 t^4 \left(\frac{t}{2m-\alpha t}\right)^{-\frac{2(n+m)}{m}} + \frac{k}{a_1^2}\left(\frac{t}{2m-\alpha t}\right)^{\frac{2}{m}} t^2(\alpha t-2m)^2}\right)$$
$$\left(\frac{12}{t^2(\alpha t-2m)^2} + \frac{3k}{a_1^2}\left(\frac{t}{2m-\alpha t}\right)^{-\frac{2}{m}} - \Lambda_2 \left(\frac{t}{2m-\alpha t}\right)^{-\frac{2n}{m}}\right)^{1-\eta}. \tag{46}$$

Moreover, using Eq. (29) in Eqs. (41) and (42), we obtain an expression of the energy density ρ and pressure p in terms of redshift z as following

$$\rho(z) = \frac{3k\left[\alpha(a_1(z+1))^{-m}\right]^{-2/m}}{{a_1}^2} + \frac{3(a_1(z+1))^{-2m}\left[\alpha + (a_1(z+1))^m\right]^4}{4m^4} - \Lambda_2\left[\alpha(a_1(z+1))^{-m}\right]^{-\frac{2n}{m}} \tag{47}$$

$$p(z) = \frac{(a_1(z+1))^{-2m}\left(\alpha + (a_1(z+1))^m\right)^3\left(2m\left((a_1(z+1))^m - \alpha\right) - 3\left(\alpha + (a_1(z+1))^m\right)\right)}{4m^4} - \frac{\alpha k (a_1(z+1))^{-m}}{{a_1}^2} +$$
$$\Lambda_2\left(\alpha(a_1(z+1))^{-m}\right)^{-\frac{2n}{m}} \tag{48}$$

The expressions for energy density ρ, pressure p in terms of time are obtained in Eqs. (41) and (42) respectively while Eqs. (47) and (48) exhibit ρ and p in terms of redshift z. The graphical behaviours of energy density, pressure and EOS parameter versus redshift z are shown in Fig. 7, Fig. 8 and Fig. 9 respectively. As in the earlier case here also we can see the same results for energy density and EOS parameter for model $\Lambda = \Lambda_2 \left(\frac{\alpha t}{2m-\alpha t}\right)^{-\frac{2n}{m}}$ for $m = 1.591$ and $a_1 = 1.462$. Moreover, we also obtain here the similar results for energy conditions which indicates that the assumption made

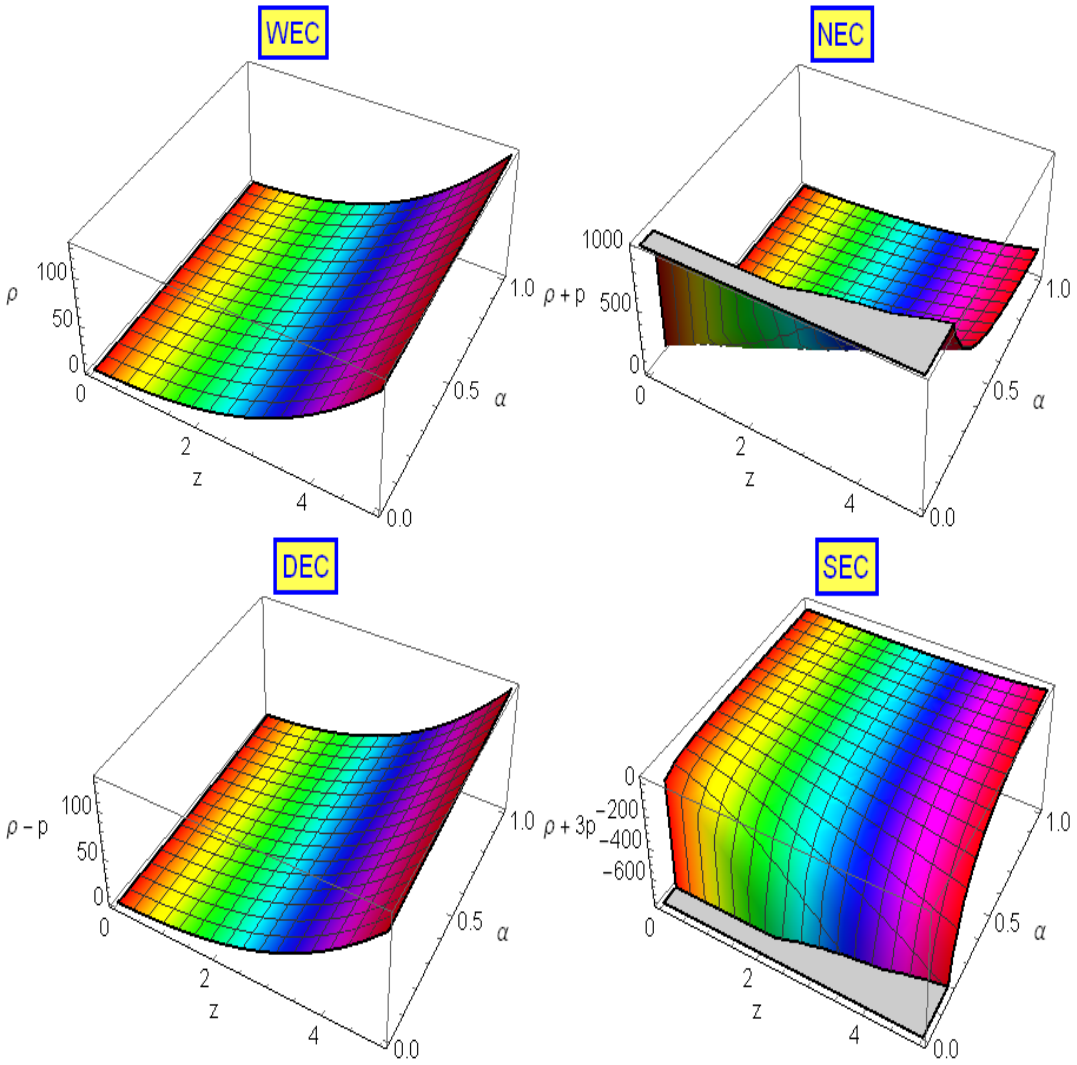

Figure 10. Energy conditions: i) WEC $\rho \geq 0$ ii) NEC $\rho + p \geq 0$ iii) DEC $\rho - p \geq 0$ and iv) SEC $\rho + 3p \leq 0$ for model $\Lambda = \Lambda_2 \left(\frac{t}{2m-\alpha t}\right)^{-\frac{2n}{m}}$.

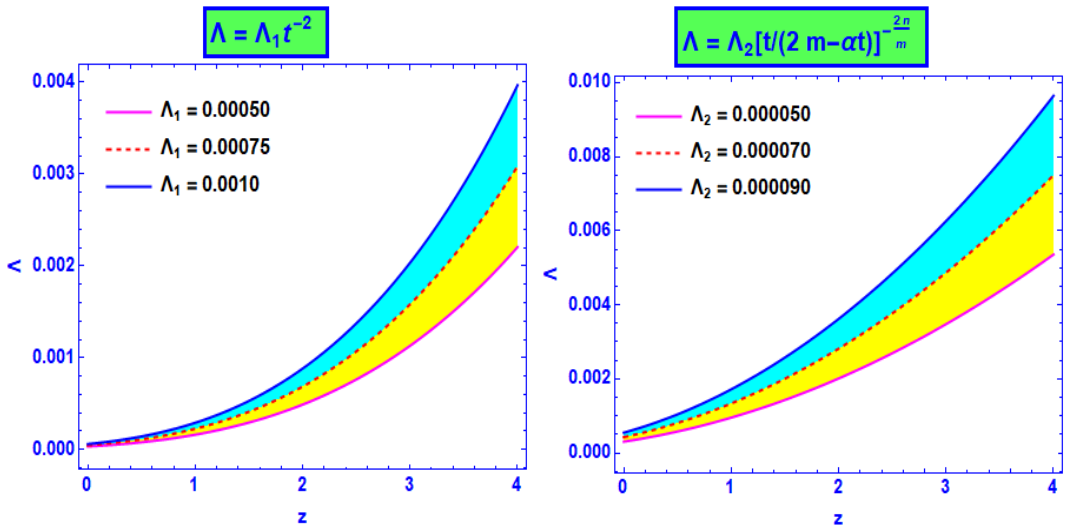

Figure 11. The behaviour of cosmological constant Λ with redshift z for models i) $\Lambda = \Lambda_1 t^{-2}$ (left panel) and ii) $\Lambda = \Lambda_2 \left(\frac{t}{2m-\alpha t}\right)^{-\frac{2n}{m}}$ (right panel) for $m = 1.591$ and $a_1 = 1.462$.

for dark energy in this case remain valid in energy condition aspects. The Fig. 10 describes the graphical representations of energy conditions. We observe that the derived model of the universe validates WEC, NEC and DEC while it violates SEC. The violation of SEC favors the accelerating expansion of the universe. It is worthwhile to note that the entropy density of the model remain positive and it approaches to a small positive value at present epoch.

6. CONCLUSIONS

The present study deals with the phenomenon early stage of the universe and the dynamics of the universe at present epoch with in the framework of isotropic and homogeneous space - time. It is also well established that the mathematical formulation of different cosmological models through the laws of physics becomes an essential component in understanding the nature of the universe. Hence, in this present work, we have investigated FRW cosmological model in the context of Einstein's theory of gravitation. We have studied time varying dark energy states of two different assumptions: i) $\Lambda = \Lambda_1 t^{-2}$ and ii) $\Lambda \propto [R(t)]^{-2n}$. This study reveals that the universe was expanding with positive value of deceleration parameter at early time and it enters into accelerating phase at $z_t = 0.73$. Moreover, we also observed that the Hubble parameter approaches to infinite when time approaches to zero, this indicates that, the universe describes a power law inflation. The temperature and entropy density of the model remain positive for both the cases. In view of energy conditions, the assumptions yields identical results. Our study suggests that the SEC violates for our model which indicates the domination of dark energy type fluid at present epoch. Finally, we conclude that the second law of thermodynamics remain impact-less in both the assumptions. Furthermore, the study suggests that the models of the universe presented in this paper is finite with increasing rate of expansion that leads accelerating phenomenon of the universe at present epoch. The nature of cosmological constant as function of redshift in the derived models have been graphed in Fig. 11. From Fig. 11, we observe that the cosmological constant Λ decrease with redshift z and finally it approaches a small positive value at present epoch ($z = 0$) which is supported by type Ia supernova observations [2, 3, 4].

Declaration of competing interest

In this paper the authors declare that they have no known competing financial interests or personal relationships that could have appeared to influence the work reported.

Acknowledgments

The authors wish to place on record their sincere thanks to the editor and reviewer(s) for illuminating suggestions that have significantly improved the manuscript in terms of research quality.

ORCID

Neeru Goyal, https://orcid.org/0009-0007-0283-0584; **Anil Kumar Yadav**, https://orcid.org/0000-0002-5174-5542; **Tensubam Alexander Singh**, https://orcid.org/0000-0003-2968-9350; **Aditya Sharma Ghrera**, https://orcid.org/0000-0002-2715-5390; **Asem Jotin Meitei**, https://orcid.org/0000-0003-3384-5264; **Kangujam Priyokumar Singh**, https://orcid.org/0000-0002-8784-4091

REFERENCES

[1] J.A.S. Lima, A.S.M. Germano, and L.R.W. Abramo, Phys. Rev. D, **53**, 4287 (1996). https://doi.org/10.1103/PhysRevD.53.4287

[2] S. Permutter, et al., Nature, **391**, 51 (1998). https://doi.org/10.1038/34124

[3] A.G. Riess, et al., Astron. J. **116**, 1009 (1998). https://doi.org/10.1086/300499

[4] S. Perlmutter et al., Astrophys. J. **517**, 565 (1999). https://doi.org/10.1086/307221

[5] E.J. Copeland, M. Sami, and S. Tsujikawa, Int. J. of Mod. Phys. D, **15**, 1753 (2006). https://doi.org/10.1142/S021827180600942X

[6] B. Ratra, M.S. Vogeley, Publ. Astron. Soc. Pacific, **120**(865), 235 (2008). https://doi.org/10.1086/529495

[7] J.A. Frieman, M.S. Turner, and D. Huterer, Annu. Rev. Astron. Astrophys. **46**, 385 (2008). https://doi.org/10.1146/annurev.astro.46.060407.145243

[8] H.K. Jassal, J.S. Bagla, and T. Padmanabhan, Mon. Not. R. Astron. Soc. **405**, 2639 (2010). https://doi.org/10.1111/j.1365-2966.2010.16647.x

[9] S. Weinberg, Rev. Mod. Phys. **61**, 1 (1989). https://doi.org/10.1103/RevModPhys.61.1

[10] I. Zlatev, L. Wang, P. J. Steinhardt, Phys. Rev. Lett. **82**, 896 (1999). https://doi.org/10.1103/PhysRevLett.82.896

[11] Y. Chen, Z.H. Zhu, J. S. Alcaniz, and Y. Gong, Astrophys. J. **711**, 439 (2010). https://doi.org/10.1088/0004-637X/711/1/439

[12] L. Amendola, Phys. Rev. D, **62**, 043511 (2000). https://doi.org/10.1103/PhysRevD.62.043511

[13] G. Caldera-Cabral, R. Maartens, and L.A. Ureña-López, Phys. Rev. D, **79**, 063518 (2009). https://doi.org/10.1103/PhysRevD.79.063518

[14] I. Prigogine, J. Geheniau, E. Gunzig, and P. Nardone, Proc. Natl. Acad. Sci. **85**, 7428 (1988).

[15] H. Moradpour, N. Sadeghnezhad, S. Ghaffari, and A. Jahan, Adv. High Energy Phys. **2017**, 9687976 (2017). https://doi.org/10.1155/2017/9687976

[16] G.C. Samanta, R. Myrzakulov, and P. Shah, Zeitschrift für Naturforsch. A, **72**, 365 (2017). https://doi.org/10.1515/zna-2016-0472

[17] S.H. Shekh, S. Arora, V.R. Chirde, and P.K. Sahoo, Int. J. Geom. Methods Mod. Phys. **17**, 2050048 (2020). https://doi.org/10.1142/S0219887820500486

[18] M. Jamil, D. Momeni, M. Raza, and R. Myrzakulov, Eur. Phys. J. C, **72**, 1999 (2012). https://doi.org/10.1140/epjc/s10052-012-1999-9

[19] Ö. Akarsu, and T. Dereli, Int. J. Theor. Phys. **51**, 612 (2012). https://doi.org/10.1007/s10773-011-0941-5

[20] Ö. Akarsu, T. Dereli, S. Kumar, and L. Xu, Euro. Phys. J Plus, **129**, 22 (2014). https://doi.org/10.1140/epjp/i2014-14022-6

[21] R.N. Patra, A.K. Sethi, B. Nayak, and R.R. Swain, New Astron. **66**, 74 (2019). https://doi.org/10.1016/j.newast.2018.08.001

[22] S.K.J. Pacif, Euro. Phys. J. Plus, **135**, 792 (2020). https://doi.org/10.1140/epjp/s13360-020-00769-y

[23] S.W. Hawking, and G.F.R. Ellis, *The Large Scale Structure of Space-time*, (Press Syndicate of the University of Cambridge, New York, 1973).

[24] R. Schoen, and S.T. Yau, Commun. Math. Phys. **79**, 231 (1981). https://doi.org/10.1007/BF01942062

[25] S. Perlmutter et al., Astrophys. J. **517**, 565 (1999). https://doi.org/10.1086/307221

[26] B. Wang, E. Abdalla, F. Atrio-Barandela, and D. Pavon, Rep. Prog. Phys. **79**, 096901 (2016). https://doi.org/10.1088/0034-4885/79/9/096901

[27] P.J.E. Peebles, and B. Ratra, Rev. Mod. Phys. **75**, 559 (2003). https://doi.org/10.1103/RevModPhys.75.559

[28] T. Padmanabhan, Phys. Rep. **380**, 235 (2003). https://doi.org/10.1016/S0370-1573(03)00120-0

[29] E.J. Copeland, M. Sami, and S. Tsujikawa, Int. J. Mod. Phys. D, **15**, 1753 (2006). http://dx.doi.org/10.1142/S021827180600942X

[30] M. Li, X.D. Li, S. Wang, and Y. Wang, Front. Phys. **8**, 828 (2013). https://doi.org/10.1007/s11467-013-0300-5

[31] S. Weinberg, *Sources and Detection of Dark Matter and Dark Energy in the universe: The cosmological constant problem*, (Springer, 2001), pp. 18–26.

[32] V. Sahni, Classical Quantum Gravity, **19**, 3435 (2002). https://doi.org/10.1088/0264-9381/19/13/304

[33] J. Garriga, and A. Vilenkin, Phys. Rev. D, **64**, 023517 (2001). https://doi.org/10.1103/PhysRevD.64.023517

[34] J.A. Frieman, M.S. Turner, and D. Huterer, Annu. Rev. Astron. Astrophys. **46**, 385 (2008). https://doi.org/10.1146/annurev.astro.46.060407.145243

[35] S. Nojiri, and S.D. Odintsov, Phys. Rep. **505**, 59 (2011). https://doi.org/10.1016/j.physrep.2011.04.001

[36] R. Caldwell, and M. Kamionkowski, Annu. Rev. Astron. Astrophys. **59**, 397 (2009). https://doi.org/10.1146/annurev-nucl-010709-151330

[37] Ö Akarsu, and C.B. Killinc, Gen. Relativ. Gravit. **42**, 763 (2010). https://doi.org/10.1007/s10714-009-0878-7

[38] S. Kumar, and A.K. Yadav, Mod. Phys. Lett. A, **26**, 647 (2011). https://doi.org/10.1142/S0217732311035018

[39] A.K. Yadav, Astrophys. Space Sci. **335**, 565 (2011). https://doi.org/10.1007/s10509-011-0745-3

[40] A.K. Yadav, and L. Yadav, Int. J. Theor. Phys. **50**, 218, (2011). https://doi.org/10.1007/s10773-010-0510-3

[41] S. Nojiri, and S.D. Odintsov, Phys. Rev. D, **70**, 103522 (2004). https://doi.org/10.1103/PhysRevD.70.103522

[42] S. Nojiri, S.D. Odintsov, and S. Tsujikawa, Phys. Rev. D, **71**, 063004 (2005). https://doi.org/10.1103/PhysRevD.71.063004

[43] S. Nojiri, and S.D. Odintsov, Gen. Relativ. Gravit. **38**, 1285 (2006). https://doi.org/10.1007/s10714-006-0301-6

[44] S. Nojiri, and S.D. Odintsov, Phys. Rev. D, **72**, 023003 (2005). https://doi.org/10.1103/PhysRevD.72.023003

[45] J.C. Carvalho, J.A.S. Lima, and I. Waga, Phys. Rev. D, **46**, 2404 (1992). https://doi.org/10.1103/PhysRevD.46.2404

[46] J.M. Salim, and I. Waga, Class. Quant. Grav. **10**, 1767 (1993). https://doi.org/10.1088/0264-9381/10/9/018

[47] M.S. Berman, Phys. Rev. D, **43**, 1075 (1991). https://doi.org/10.1103/PhysRevD.43.1075

[48] A.K. Yadav, Int. J. Theor. Phys. **49**, 1140 (2010). https://doi.org/10.1007/s10773-010-0295-4

[49] A.K. Yadav, Astrophys. and Space Sc. **361**, 1 (2016).

[50] G.K. Goswami, A.K. Yadav, and B. Mishra, Mod. Phys. Lett. A, **35**, 2050224 (2020). https://doi.org/10.1142/S0217732320502247

[51] H. Amirhashchi, A.K. Yadav, N. Ahmad, and V. Yadav, Phys. Dark Uni. **36**, 101043 (2022). https://doi.org/10.1016/j.dark.2022.101043

[52] G.K. Goswami, M. Mishra, A.K. Yadav, and A. Pradhan, Mod. Phys. Lett. A, **33**, 2050086 (2020). https://doi.org/10.1142/S0217732320500868

[53] S. Kumar, and C.P. Singh, Gen. Relativ. Grav. **43**, 1427 (2011). https://doi.org/10.1007/s10714-010-1125-y

[54] E. Abdalla, *et al*., J. High Energy Astrophys. **34**, 49 (2022). https://doi.org/10.1016/j.jheap.2022.04.002

[55] E.D. Valentino, *et al*., Astropart. Phys. **131**, 102605 (2021). https://doi.org/10.1016/j.astropartphys.2021.102605

[56] E.D. Valentino, *et al*., Astropart. Phys. **131**, 102607 (2021). https://doi.org/10.1016/j.astropartphys.2021.102607

[57] E.D. Valentino, *et al*., Astropart. Phys. **131**, 102604 (2021). https://doi.org/10.1016/j.astropartphys.2021.102604

[58] E.D. Valentino, *et al*., Astropart. Phys. **131**, 102606 (2021). https://doi.org/10.1016/j.astropartphys.2021.102606

[59] A.S. Adil, U. Mukhopadhyay, A.A. Sen, and S. Vagnozzi, JCAP **2023(10)**, 072 (2023). https://doi.org/10.1088/1475-7516/2023/10/072

[60] R.C Nunes, S. Vagnozzi, S. Kumar, E.Di Valentino, and O. Mena, Phys. Rev. D, **105**, 123506 (2022). https://doi.org/10.1103/PhysRevD.105.123506

[61] E.D. Valentino, S. Gariazzo, O. Mena, and S. Vagnozzi, JCAP **2020(7)**, 045 (2020). https://doi.org/10.1088/1475-7516/2020/07/045

[62] D.M. Scolnic, *et al*., Astrophys. J. **859**, 101 (2018). https://doi.org/10.3847/1538-4357/aab9bb

[63] G.S. Sharov, and V.O. Vasiliev, Mathematical Modelling and Geometry **6**, 1 (2018). https://mmg.tversu.ru/images/publications/2018-611.pdf

[64] P. Biswas, P. Roy, and R. Biswas, https://doi.org/10.48550/arXiv.1908.00408.

[65] A.K. Yadav, *et al*., J. High Energy Astrophys. **43**, 114 (2024). https://doi.org/10.1016/j.jheap.2024.06.012

[66] S.M. Carroll, *Spacetime and geometry: An introduction to general relativity*, (Carlifonia, USA, 2004)

[67] M. Visser, "Lorentzian Wormholes: From Einstein to Hawking," in: *AIP Series in Computational and Applied Mathematical Physics*, (American Institute of Physics, 1995).

ТЕРМОДИНАМІКА ОДНОРІДНОГО ТА ІЗОТРОПНОГО ВСЕСВІТУ ДЛЯ РІЗНИХ УМОВ ТЕМНОЇ ЕНЕРГІЇ

Ніру Гоял[a], **Аніл Кумар Ядав**[b], **Тенсубам Олександр Сінгх**[c], **Адітя Шарма Грера**[a], **Асем Джотін Мейтей**[d,e], **Кангуджам Прійокумар Сінгх**[d*]

[a] *Департамент прикладних наук, Університет НортКап, Гуруграм - 122017, Індія*

[b] *Департамент фізики, Об'єднаний коледж інженерії та досліджень, Велика Нойда - 201310, Інді*

[c] *Департамент математичних наук, Університет Бодоленд, Кокрайхар-783370, Ассам, Індія*

[d] *Департамент математики, коледж Правабаті, Маянг Імпхал-795132, Маніпур, Індія*

[e] *Департамент математики, Маніпурський університет, Канчіпур, Імфал-795003, Маніпур, Індія*

Досліджено термодинамічні властивості однорідного та ізотропного Всесвіту для різних умов темної енергії з спадаючим космологічним членом $\Lambda(t)$. Щоб отримати явний розв'язок рівнянь поля Ейнштейна, ми розглянули лінійно змінний параметр уповільнення у формі $q = -\alpha t + m - 1$ з α і m як скалярними константами. Ми обмежили параметри моделі H_0 і m як 68, 495 км/с/Мпк і 1, 591 відповідно, обмеживши похідну модель комбінованою компіляцією пантеону наборів даних SN Ia і H(z). Крім того, ми досліджували стани темної енергії, що змінюються в часі, для двох різних припущень: i) $\Lambda = \Lambda_1 t^{-2}$ та ii) $\Lambda \propto [R(t)]^{-2n}$. Для конкретного припущення наші моделі вказують на поведінку, подібну до темної енергії, у відкритому, плоскому та закритому просторі – геометрія часу. Температура та щільність ентропії моделі залишаються додатними для обох випадків: i) $\Lambda = \Lambda_1 t^{-2}$ і ii) $\Lambda \propto [R(t)]^{-2n}$.. Також обговорюються деякі фізичні властивості Всесвіту.

Ключові слова: *модель FRW; однорідний; термодинаміка; пантеон; темна енергія*

EAST EUROPEAN JOURNAL OF PHYSICS. 1. 59-69 (2025)
DOI:10.26565/2312-4334-2025-1-05 ISSN 2312-4334

BIANCHI TYPE VI_0 GENERALIZED GHOST PILGRIMS DARK ENERGY COSMOLOGICAL MODEL IN SAEZ-BALLESTER THEORY OF GRAVITATION

Tenneti Ramprasad[a], M.P.V.V. Bhaskara Rao[b]*, M. Kiran[c], Satyanarayana Bora[d]
[a]*Department of Mathematics, Vasavi College of Engineering(A), Hyderabad, India.*
[b]*Department of Basic Sciences and Humanities, Vignan's Institute of Information Technology (A), Vishakhapatnam, Andhra Pradesh, India*
[c]*Department of Mathematics, MVGR College of Engineering, Vizianagaram(A), India*
[d]*College of Computing and Information Sciences, University of Technology and Applied Sciences, Musandam, PO Box:12, PC: 811, Khasab, Oman*
**Corresponding Author e-mail: mekabhaskar@gmail.com*
Received November 20, 2024; revised February 6, 2025; accepted February 10, 2025

The Generalized Ghost Pilgrim Dark Energy (GGPDE) in the Saez-Ballester Theory of Gravitation (SBTG) and the Bianchi type VI_0 space-time framework serve as the foundation for this work. We used Mishra and Dua's [Astrophys. Space Sci. 366, 6 (2021)] straightforward parameterization of average scale factor $a(t) = exp\{(\alpha t + \beta)^p\}$ to find precise solutions to the field equations. We have looked into the GGPDE and dark matter (DM), both when they interact and when they don't. For both models, some significant and well-known parameters are produced, including the Hubble parameter, the equation of state (EOS) parameter, the deceleration parameter, etc. It is discovered that for both models, the deceleration parameter denotes an accelerated phase and the EOS parameter a cosmological constant. For both the non-interacting and interacting models, the stability analysis and energy conditions are examined.
Keywords: *Hubble parameter; EOS parameter; deceleration parameter; GGPDE; SBTG*
PACS: 95.35.+d, 95.36.+x, 98.80.-k, 98.80.Jk, 98.80.Es, 04.20.Jb

1. INTRODUCTION

According to recent astronomical observations [2-4], we live in an expanding and accelerating Universe. These findings imply that the Universe is dominated by two dark components: dark matter (DM) and dark energy. Dark matter, a pressure less substance, is primarily utilized to explain galaxy curves and the formation of the Universe's structure, whereas DE, an exotic energy with a huge negative pressure, is used to explain the Universe's cosmic acceleration. Researchers are working hard to determine the nature of dark energy, and several ideas have been presented to define it. The cosmological constant with the EOS parameter $\omega = p/\rho = -1$, where p is the pressure andρ is the energy density of DE, is the simplest and most obvious choice for DE. However, it suffers from fine-tuning and cosmic coincidence issues [5]. To address the issue of DE, cosmologists have developed many DE models such as quintessence [6-7], phantom [7-8], tachyon [9], dilaton [10], and so on.

A type of DE known as Veneziano ghost DE has been postulated [11-13] to explain the Universe's current rapid stage. When H is used in place of the Hubble parameter, the energy density of the vacuum ghost field is proportional to 3 QCDH [14-15]. QCDH stands for the QCD mass scale. Because this GDE's energy density DE relies linearly on the Hubble parameter H, as in DE = H, and is connected to the QCD (Quantum Chromo dynamics) mass scale, it has attracted the interest of researchers. The robust interaction in nature is described by QCD. In QCD, the Veneziano ghost field's general vacuum energy has the form $H + O(H^2)$[16]. In the early Universe's evolution, which serves as the early DE, the term H^2has a key place [17]. In comparison to the standard GDE, also known as generalized ghost dark energy (GGDE), one can provide better agreement with observational data by taking the term H^2into consideration [18]. The generalized model's energy density is given by$\rho_{DE} = \tau H + \eta H^2$ where η is a constant. Based on the hypothesis that the strong repulsive force of the type of DE can prevent black hole (BH) creation, Wei [19] presented a new dark energy model dubbed pilgrim DE (PDE). In terms of PDE, GGDE has been changed as$\rho_{DE} = (\tau H + \eta H^2)^u$, where u is a PDE parameter [20].

Scientists have come up with different models to try and understand dark energy. They use these models to explain how the universe is expanding and what might be causing it. One of these models is called GGPDE in the Bianchi type I Universe, which was explored by Santhi et al. [21]. Another model, investigated by Jawad [22], is called GGPDE in the context of a non-flat FRW Universe. Gravitation theory based on Saez-Ballester was used by Garg et al. [23] to study GGPDE. With the aid of a straightforward parameterization of the average scale factor *a(t)*, Mishra and Dua [1] estimated the FLRW Universe in the Brans-Dicke theory. One of the simplest models with an anisotropic background to describe the early phases of the universe's evolution is the Bianchi type model. Bianchi space-times are helpful in creating models of spatially homogenous and anisotropic cosmologies due to the simplicity of the field equations and relative ease of solutions.

We propose a study of the GGPDE in SBTG within the context of Bianchi type VI_0 space-time, which is motivated by the aforementioned recent efforts of various authors [24-26]. The following is the manuscript's structure: Section 2

Cite as: T. Ramprasad, M.P.V.V. Bhaskara Rao, M. Kiran, S. Bora, East Eur. J. Phys. 1, 59 (2025), https://doi.org/10.26565/2312-4334-2025-1-05

discusses metric and field equations. We found the answers to the field equations in Section 3. Sections 4 and Section 5 address the non-interactive and interacting models, respectively. Sections 6 and 7 include descriptions of the stability analysis and energy conditions, respectively. In Section 8, many parameters are illustrated and explained. Section 9's final observations bring the paper to a close.

2. METRIC AND FIELD EQUATIONS:

The spatially homogeneous and anisotropic Bianchi type VI_0 space-time is given by

$$ds^2 = -A^2dx^2 - B^2e^{2x}dy^2 - C^2e^{-2x}dz^2 + dt^2, \tag{1}$$

where A, B, C are the gravitational potentials which are functions of cosmic time *t*.

The Saez-Ballester field equations are given by

$$G_j^i - w\phi^n\left(\phi^{,i}\phi_{,j} - \frac{1}{2}\delta_j^i\phi^{,k}\phi_{,k}\right) = \left(T_j^i + \bar{T}_j^i\right), \tag{2}$$

where G_j^i is Einstein tensor and T_j^i,$\bar{T}_j^i$ are energy momentum tensors of dark matter and GGPDE respectively.

The scalar field ϕ satisfies the equation

$$2\phi^n\phi_{;i}^{,i} + n\phi^{n-1}\phi_{,k}\phi^{,k} = 0. \tag{3}$$

The energy momentum tensor of dark matter (DM) is given by

$$T_j^i = diag[\,0,0,0,\rho_m]. \tag{4}$$

The energy momentum tensor of GGPDE is given by

$$\bar{T}_j^i = diag[-p_{DE}, -p_{DE}, -p_{DE}, \rho_{DE}]. \tag{5}$$

Here scalar field ϕ and the energy momentum tensors components depend only on cosmic time.

The field equation (2) for the metric (1) using equations (4), (5) are obtained as

$$\frac{\ddot{B}}{B} + \frac{\ddot{C}}{C} + \frac{\dot{B}\dot{C}}{BC} + \frac{1}{A^2} - \frac{1}{2}w\phi^n\dot{\phi}^2 = -p_{DE}, \tag{6}$$

$$\frac{\ddot{C}}{C} + \frac{\ddot{A}}{A} + \frac{\dot{C}\dot{A}}{CA} - \frac{1}{A^2} - \frac{1}{2}w\phi^n\dot{\phi}^2 = -p_{DE}, \tag{7}$$

$$\frac{\ddot{A}}{A} + \frac{\ddot{B}}{B} + \frac{\dot{A}\dot{B}}{AB} - \frac{1}{A^2} - \frac{1}{2}w\phi^n\dot{\phi}^2 = -p_{DE}, \tag{8}$$

$$\frac{\dot{A}\dot{B}}{AB} + \frac{\dot{B}\dot{C}}{BC} + \frac{\dot{C}\dot{A}}{CA} - \frac{1}{A^2} + \frac{1}{2}w\phi^n\dot{\phi}^2 = \rho_m + \rho_{DE}, \tag{9}$$

$$\frac{\dot{B}}{B} - \frac{\dot{C}}{C} = 0. \tag{10}$$

From equation (3) we have

$$\ddot{\phi} + \dot{\phi}\left(\frac{\dot{A}}{A} + \frac{\dot{B}}{B} + \frac{\dot{C}}{C}\right) + \frac{n}{2}\frac{\dot{\phi}^2}{\phi} = 0. \tag{11}$$

By integrating equation (10) and assuming integration constant as unity, we get

$$B = C. \tag{12}$$

Now by using (12) in equations (6)-(9),(11) we get

$$\frac{2\ddot{B}}{B} + \frac{\dot{B}^2}{B^2} + \frac{1}{A^2} - \frac{1}{2}w\phi^n\dot{\phi}^2 = -p_{DE}, \tag{13}$$

$$\frac{\ddot{A}}{A} + \frac{\ddot{B}}{B} + \frac{\dot{A}\dot{B}}{AB} - \frac{1}{A^2} - \frac{1}{2}w\phi^n\dot{\phi}^2 = -p_{DE}, \tag{14}$$

$$\frac{\dot{B}^2}{B^2} + 2\frac{\dot{A}\dot{B}}{AB} - \frac{1}{A^2} + \frac{1}{2}w\phi^n\dot{\phi}^2 = \rho_m + \rho_{DE}, \tag{15}$$

$$\ddot{\phi} + \dot{\phi}(3H) + \frac{n}{2}\frac{\dot{\phi}^2}{\phi} = 0. \tag{16}$$

The energy conservation equation is

$$T_{j\ ;i}^{i} + \bar{T}_{j\ ;i}^{i} = 0. \tag{17}$$

From (17) we get

$$\dot{\rho}_m + \dot{\rho}_{DE} + 3H(\rho_m + \rho_{DE} + p_{DE}) = 0. \tag{18}$$

In this article, we have considered both interacting and non-interacting models. The continuity equations of DM and GGPDE through an interaction Q are

$$\dot{\rho}_m + 3H\rho_m = Q, \tag{19}$$

$$\dot{\rho}_{DE} + 3H(\rho_{DE} + p_{DE}) = -Q, \tag{20}$$

where $Q > 0$ shows energy flows from GGPDE to DM and $Q < 0$ means energy flows from DM to GGPDE and$Q = 0$ indicates non interaction model. Wei and Cai [27] proposed the interaction term Qas

$$Q = 3bH\rho_m, \tag{21}$$

where$b > 0$ is a coupling constant.

3. SOLUTIONS OF FIELD EQUATIONS:

Equations (13)-(16) are a system of four field equations in 6 unknowns $A, B, \rho_m, \rho_{DE}, p_{DE}$ and ϕ. To solve these field equations, we need two physical conditions. These are as follows:

(i) The energy momentum tensor of GGPDE is given by

$$\rho_{DE} = (\tau H + \eta H^2)^u, \tag{22}$$

where u is PDE parameter.

(ii) Mishra and Dua [1] proposed a simple parameterization of scale factor (see (31)) as

$$a(t) = exp\{(\alpha t + \beta)^p\}, \tag{23}$$

where $\alpha, \beta > 0$ and $0 < p < 1$ are arbitrary constants.

From equations (13) and (14), we get

$$\frac{\dot{A}}{A} - \frac{\dot{B}}{B} = \frac{k}{V} exp\left(\int \frac{\left(\frac{-2}{A^2}\right)}{\left(\frac{\dot{B}}{B} - \frac{\dot{A}}{A}\right)} dt \right). \tag{24}$$

Where *k* is integration constant and V is the volume of the Universe (see (32))

Following Adhav [28], we assume

$$\frac{\dot{B}}{B} - \frac{\dot{A}}{A} = \frac{2}{A^2}. \tag{25}$$

Using equations (24) and (25), we get

$$\frac{\dot{A}}{A} - \frac{\dot{B}}{B} = \frac{k}{V} e^{-t}. \tag{26}$$

Integrating equation (25),

$$A = lB\, exp\left\{k \int \frac{e^{-t}}{[exp\{(\alpha t+\beta)^p\}]^3} dt\right\}, \tag{27}$$

where *l* is constant of integration.

Now from the above equations the metric potentials are obtained as

$$A = exp\{(\alpha t + \beta)^p\}\, l^{\frac{2}{3}}\, exp\left\{\frac{2k}{3} \int \frac{e^{-t}}{[exp\{(\alpha t+\beta)^p\}]^3} dt\right\}, \tag{28}$$

$$B = exp\{(\alpha t + \beta)^p\}\, l^{\frac{-1}{3}}\, exp\left\{\frac{-k}{3} \int \frac{e^{-t}}{[exp\{(\alpha t+\beta)^p\}]^3} dt\right\}. \tag{29}$$

From equation (16) the Saez-Ballester scalar field is obtained as

$$\phi(t) = \left[\frac{n+2}{2} \phi_0 \int exp(-3(\alpha t + \beta)^p)\, dt + \psi_0\right]^{\left(\frac{2}{n+2}\right)}, \tag{30}$$

where ϕ_0, ψ_0 are integration constants.

3. PHYSICAL AND KINEMATICAL PARAMETERS OF THE MODEL:

The parameters which play a vital role in the discussion of dynamics of the obtained model are as follows,

The average scale factor

$$a(t) = (AB^2)^{\frac{1}{3}} = exp((\alpha t + \beta)^p). \tag{31}$$

The volume V of the universe

$$V = \left(a(t)\right)^3 = AB^2 = exp((\alpha t + \beta)^{3p}). \tag{32}$$

From Fig. (1), the Volume increases as$t \to \infty$.It shows the spatial expansion of the universe.
The Hubble parameter

$$H = \frac{\dot{a}}{a} = \frac{1}{3}\frac{\dot{V}}{V} = \frac{1}{3}\left(\frac{\dot{A}}{A} + \frac{2\dot{B}}{B}\right) = p\alpha(\alpha t + \beta)^{p-1}. \tag{33}$$

The scalar expansion of the universe

$$\theta = 3H = \left(\frac{\dot{A}}{A} + \frac{2\dot{B}}{B}\right) = 3p\alpha(\alpha t + \beta)^{p-1}. \tag{34}$$

The shear scalar of the universe

$$\sigma^2 = \frac{1}{2}\left[\left(\frac{\dot{A}}{A}\right)^2 + 2\left(\frac{\dot{B}}{B}\right)^2\right] - \frac{\theta^2}{6} = k^2\frac{e^{-2t}}{\exp\left((2(\alpha t+\beta)^{3p}\right)}. \tag{35}$$

From Figures (2), (3) and (4), observed that $H, \theta, \sigma^2$are diverge at $t = 0$ and tends small values as $t \to \infty$. Our model exhibits shear free universe at late time.

The average anisotropy parameter

$$A_h = \frac{1}{3H^2}\left(\frac{(H_1-H)^2+2(H_2-H)^2}{H^2}\right) = \frac{2ke^{-2t}}{9\alpha^4p^4(\alpha t+\beta)^{(4p-4)}[exp(\alpha t+\beta)^p]^6}, \tag{36}$$

where $H_1 = \frac{\dot{A}}{A}, H_2 = H_3 = \frac{\dot{B}}{B}$ are directional Hubble parameters**.**

From figure (5), clearly anisotropy exists at early time and decreases and tends to zero at late time. So, our model is anisotropic model and converges to an isotropic model at late time.
The deceleration parameter is

$$q = -\frac{a\ddot{a}}{(\dot{a})^2} = -1 - \left(\frac{p-1}{p}\right)(\alpha t + \beta)^{-p}. \tag{37}$$

Clearly, $q > 0$for $t < \frac{\left(\left(\frac{1}{p}-1\right)^{\frac{1}{p}}-\beta\right)}{\alpha}$and $q < 0$ for $t > \frac{\left(\left(\frac{1}{p}-1\right)^{\frac{1}{p}}-\beta\right)}{\alpha}$ and $q \to -1$ as $t \to \infty$.

So, the present model shows the transition from early deceleration to present acceleration phase of the Universe. From Figure (6), the decelerating parameter is positive (decelerating phase) initially and after some time it moves to negative (acceleration phase). So, our model exhibits both early deceleration and present-day acceleration of the Universe. This is coinciding with the present-day observations.

The jerk parameter is

$$j(t) = q + 2q^2 - \frac{\dot{q}}{H} = 1 + \frac{(p^2-3p+2)(\alpha t+\beta)^{-2p}+(3p^2-3p)(\alpha t+\beta)^{-p}}{p^2}. \tag{38}$$

From figure (7), the jerk parameter is positive throughout evolution of the universe. Cosmologists believe that the positive value of jerk parameter and negative value of decelerating parameter indicates the accelerating phase of expansion of the universe. So the obtained model denotes the present day accelerating phase of expansion of the Universe.
From (22) the energy density of GGPDE is

$$\rho_{DE} = [\tau\alpha p(\alpha t + \beta)^{p-1} + \eta\alpha^2p^2(\alpha t + \beta)^{2p-2}]^u. \tag{39}$$

From Figure (8), observed that the energy density of GGPDE is diminishes w.r.t. cosmic time *t.*

4. NON-INTERACTING MODEL

The energy conservation equation for DM is

$$\dot{\rho}_m + 3H\rho_m = 0 \tag{40}$$

From (40) and (33), we get

$$\rho_m = \frac{\rho_0}{exp(3(\alpha t+\beta)^p)} \tag{41}$$

where ρ_0 is integration constant. Clearly it is decreasing as $t \to \infty$.
The energy conservation equation for GGPDE is

$$\dot{\rho}_{DE} + 3H(\rho_{DE} + p_{DE}) = 0. \tag{42}$$

From (42), (33), (39) and by using $\omega_{DE} = \frac{p_{DE}}{\rho_{DE}}$ the EoS parameter of GGPDE in non-interacting case is obtained as

$$\omega_{DE} = -1 - \frac{1}{3H}\frac{\dot{\rho}_{DE}}{\rho_{DE}},$$

$$\omega_{DE} = -1 - \frac{u(p-1)}{3p(\alpha t+\beta)^{p+1}}\left[\frac{\tau+2\eta p\alpha(\alpha t+\beta)^{p-1}}{\tau+\eta p\alpha(\alpha t+\beta)^{p-1}}\right]. \tag{43}$$

Clearly from figure (9), the non-interacting model denotes a quintessence universe and tends toΛCDM model at late time.i.e.,$\omega_{DE} \to -1$ as $t \to \infty$.

The pressure of GGPDE is obtained as

$$p_{DE} = \omega_{DE}\rho_{DE} = (\alpha t+\beta)^{p-1}\left(-1 - \frac{u(p-1)}{3p(\alpha t+\beta)^{p+1}}\left[\frac{\tau+2\eta p\alpha(\alpha t+\beta)^{p-1}}{\tau+\eta p\alpha(\alpha t+\beta)^{p-1}}\right]\right)([\tau\alpha p + \eta\alpha^2 p^2(\alpha t+\beta)^{p-1}]^u). \tag{44}$$

The overall density parameter of the non-interacting model is

$$\Omega = \Omega_m + \Omega_{DE} = \frac{1}{3H^2}(\rho_m + \rho_{DE}). \tag{45}$$

By using (41), (39) and (33)

$$\Omega = \frac{(\alpha t+\beta)^2\left[\frac{\rho_0}{e^{3(\alpha t+\beta)^p}} + \left(\frac{\tau(\alpha t+\beta)^p p\alpha}{\alpha t+\beta} + \frac{\eta\alpha^2 p^2(\alpha t+\beta)^{2p}}{(\alpha t+\beta)^2}\right)^p\right]}{3\alpha^2 p^2(\alpha t+\beta)^{2p}}. \tag{46}$$

Figure (10), displays that the overall density of the non-interacting model is increases w.r.t. expansion of the universe.

5. INTERACTING MODEL

The energy conservation equation DM is

$$\dot{\rho}_m + 3H\rho_m = 3bH\rho_m. \tag{47}$$

By using (33) in (47),

$$\rho_m = \frac{\rho_1}{exp(3(1-b)(\alpha t+\beta)^p)}, \tag{48}$$

where ρ_1 is integration constant. Clearly the energy density of DM for interacting model decreases w.r.t. time t.

The energy conservation equation for GGPDE is

$$\dot{\rho}_{DE} + 3H(\rho_{DE} + p_{DE}) = -3bH\rho_m. \tag{49}$$

By using (33), (39),(48) in (49), the EoS parameter ω_{DE} of GGPDE is

$$\omega_{DE} = -1 - \frac{u(p-1)}{3p(\alpha t+\beta)^{p+1}}\left[\frac{\tau+2\eta p\alpha(\alpha t+\beta)^{p-1}}{\tau+\eta p\alpha(\alpha t+\beta)^{p-1}}\right] - \frac{b\rho_m}{\rho_{DE}}. \tag{50}$$

Figure (11) displays $-1 < \omega_{DE} < -1/3$initially and $\omega_{DE} \to -1$ for large values of *t.* So initially the interacting model denotes the quintessence model and it tends cosmological constant model (ΛCDMModel) for late time.

The pressure of GGPDE in Interacting case is

$$p_{DE} = \omega_{DE}\rho_{DE} = (\alpha t+\beta)^{p-1}\left(-1 - \frac{u(p-1)}{3p(\alpha t+\beta)^{p+1}}\left[\frac{\tau+2\eta p\alpha(\alpha t+\beta)^{p-1}}{\tau+\eta p\alpha(\alpha t+\beta)^{p-1}}\right] - \frac{b\rho_m}{\rho_{DE}}\right)([\tau\alpha p + \eta\alpha^2 p^2(\alpha t+\beta)^{p-1}]^u). \tag{51}$$

The overall density parameter of the interacting model is

$$\Omega = \Omega_m + \Omega_{DE} = \frac{1}{3H^2}(\rho_m + \rho_{DE}). \tag{52}$$

By using (33),(48) and (39)in (52),

$$\Omega = \frac{(\alpha t+\beta)^2\left[\frac{\rho_1}{e^{(3-3b)(\alpha t+\beta)^p}} + \left(\frac{\tau(\alpha t+\beta)^p p\alpha}{\alpha t+\beta} + \frac{\eta\alpha^2 p^2(\alpha t+\beta)^{2p}}{(\alpha t+\beta)^2}\right)^p\right]}{3\alpha^2 p^2(\alpha t+\beta)^{2p}} \tag{53}$$

The overall density of interacting model increases with time *t* as universe expands. It is shown in figure (12). The both interacting and non-interacting models are tending to cosmological constant at late time and the overall density of both model increases with time.

6. STABILITY ANALYSIS

In this section the stability of both interacting and non-interacting models has discussed. In order to characterize the stability of models, the sign of $v_s{}^2 = \frac{\dot{p}_{DE}}{\dot{\rho}_{DE}}$is crucial. If $v_s{}^2 > 0$shows a table model and if $v_s{}^2 < 0$ shows unstable model [29]. Also, the casualty condition must be satisfied, means that the speed of the sound less than the speed of the light.

The square speed of sound$v_s{}^2$ for non-interacting model is

$$v_s{}^2 = -\left((\alpha t+\beta)\left(+\frac{1}{2}\left(3\tau\left(+\left(\begin{array}{c}\frac{2p^3\eta^2\left(\left(\frac{3t\tau}{2}+\left(\left(u-\frac{1}{2}\right)p-u\right)\eta\right)\alpha+\frac{3\beta\tau}{2}\right)\alpha^2(\alpha t+\beta)^{2p-1}}{3}\\ +p^4(\alpha t+\beta)^{-1+3p}\alpha^3\eta^3\\ \frac{\tau^2(\alpha t+\beta)^2\left((u-1)p-u\right)(\alpha t+\beta)^{-p}}{9}\end{array}\right)p\right)\right)\right)\right)}{\left(p\left(\eta(\alpha t+\beta)^p p\alpha+\frac{\tau(\alpha t+\beta)}{2}\right)\left(\eta(\alpha t+\beta)^p p\alpha+\tau(\alpha t+\beta)\right)^2\right)} \tag{54}$$

The square speed of sound $v_s{}^2$ for interacting model is

$$v_s{}^2 = -\left(3(\alpha t+\beta)\left(+\frac{1}{9}\left(8(p-1)\left(+\tau\left(\begin{array}{c}\frac{\eta^2\alpha^2\left(\left(\eta\left(u-\frac{1}{2}\right)p+\frac{3t\tau}{2}-u\eta\right)\alpha+\frac{3\beta\tau}{2}\right)p^3(\alpha t+\beta)^{2p-1}}{2}\\ +\frac{3p^4(\alpha t+\beta)^{-1+3p}\alpha^3\eta^3}{4}\\ \frac{9p^3(\alpha t+\beta)^{2p}\alpha^2\eta^2}{8}+\frac{\tau^2(\alpha t+\beta)^2\left((u-1)p-u\right)(\alpha t+\beta)^{-p}}{8}\end{array}+\left(\begin{array}{c}\eta\alpha p\left(\left(\eta\left(u-\frac{1}{2}\right)p+\left(-u-\frac{1}{8}\right)\eta+\frac{3t\tau}{2}\right)\alpha+\frac{3\beta\tau}{2}\right)(\alpha t+\beta)^p\\ +\frac{5(\alpha t+\beta)\tau\left(\left(\eta\left(u-\frac{3}{5}\right)p+\left(-u-\frac{1}{5}\right)\eta+\frac{3t\tau}{5}\right)\alpha+\frac{3\beta\tau}{5}\right)}{8}\end{array}\right)p\right)\right)u\right)\right)\right)}{\left(2\left(\eta(\alpha t+\beta)^p p\alpha+\frac{\tau(\alpha t+\beta)}{2}\right)(p-1)up\left(\eta(\alpha t+\beta)^p p\alpha+\tau(\alpha t+\beta)\right)^2\right)} \tag{55}$$

The graphs of square speed of sound for both interacting and non-interacting models are depicted in Figure (13) and Figure (14) respectively. In both models it is negative throughout the evolution of the universe. The negative sign of $v_s{}^2$denotes the unstableness of the model. So, the both interacting and non-interacting models are unstable models.

7. ENERGY CONDITIONS

In this section we discussed the energy conditions for interacting and non-interacting models.

The Energy conditions are given by

(1) $\rho_{DE} \geq 0$ (WEC)

(2)$\rho_{DE} + p_{DE} \geq 0$ (DEC)

(3) $\rho_{DE} + 3p_{DE} \geq 0$ (SEC)

The three energy conditions were plotted by using equations (39), (44) and (51) for both models.

From figure (15) and (16), it is observed that WEC and DEC are satisfied for both interacting and non-interacting models whereas SEC fails in both models. The violation SEC gives anti-gravitational effect for which universe gets jerk. So, the both models exhibit transition from early deceleration to present acceleration. So, the obtained models have good agreement with cosmological observations.

8. GRAPHICAL DISCUSSIONS

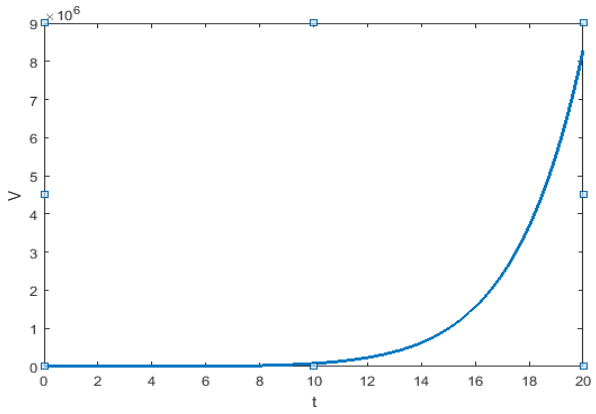

Figure 1.
The plot of V versus t
for $\alpha = 1.4, \beta = 0.2, p = 0.5$.
Clearly the spatial volume increases w.r.t. cosmic time t

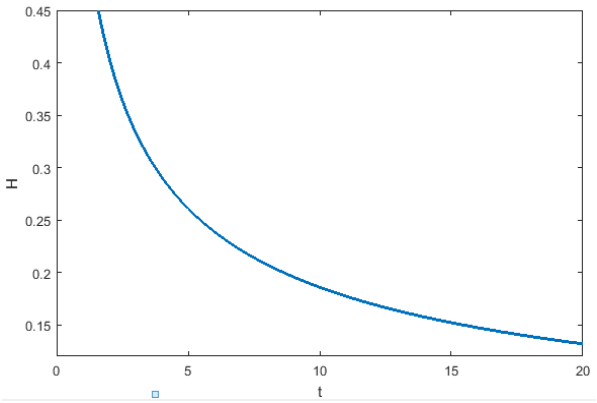

Figure 2.
The plot of H versus t
for $\alpha = 1.4, \beta = 0.2, p = 0.5$.
Clearly H decreases and tend to small value for late time

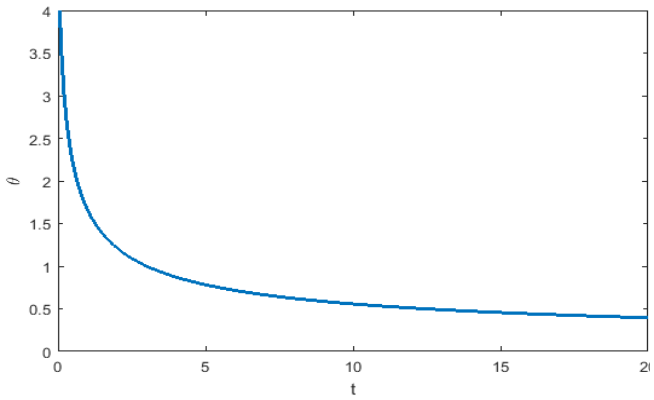

Figure 3.
The plot of θ versus t
for $\alpha = 1.4, \beta = 0.2, p = 0.5$.

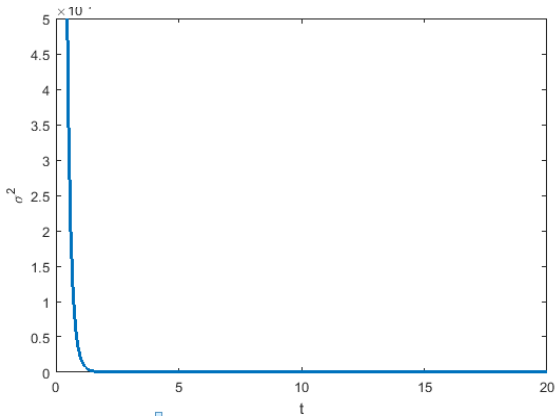

Figure 4.
The plot of σ^2 versus t
for $\alpha = 1.4, \beta = 0.2, p = 0.5, k = 0.03$.
It is observed that our universe is shear free at late time

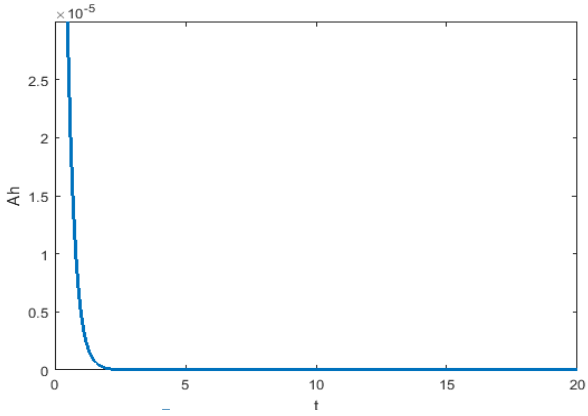

Figure 5.
The plot of A_h versus t
for $\alpha = 1.4, \beta = 0.2, p = 0.5, k = 0.03$.
It shows anisotropic nature in early stage and tends to zero (isotropic) at late lime

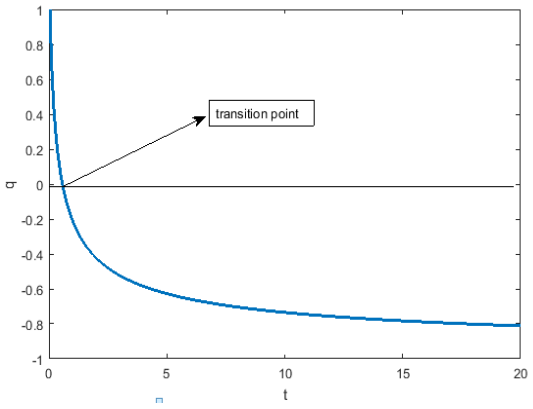

Figure 6.
The plot of q versus t
for $\alpha = 1.4, \beta = 0.2, p = 0.5$.
It is observed that q moves from positive region negative region.so our model denotes both decelerating and present accelerating phase

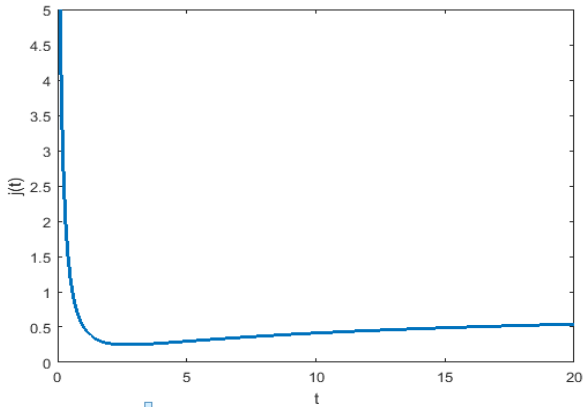

Figure 7.
The plot of j(t) versus t
for$\alpha = 1.4, \beta = 0.2, p = 0.5$.
It is observed that the jerk parameter is positive throughout the evolution of the universe.

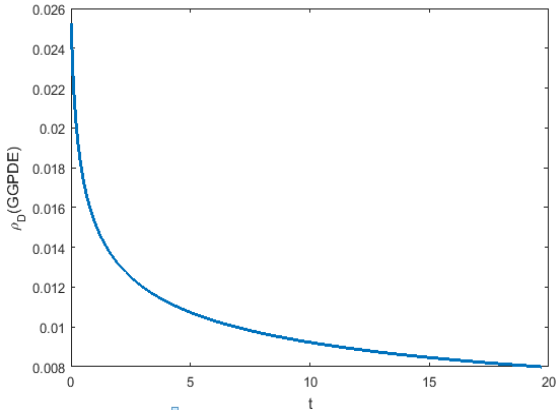

Figure 8.
The plot of ρ_{DE} versus t
for $\alpha = 1.4, \beta = 0.2, p = 0.5, \tau = 0.0004, \eta = 0.0005, u = 0.5$.
It is observed that the energy density of GGPDE is decreasing and tend to zero for large time t.

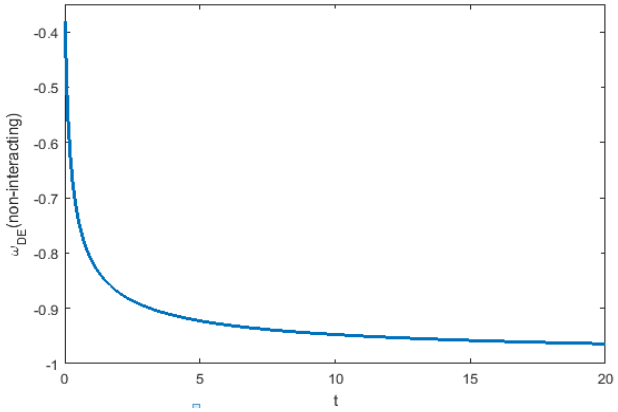

Figure 9.
The plot of EoS parameter ω_{DE} versus cosmic time of non-interacting model
for $\alpha = 1.4, \beta = 0.2, p = 0.5, \tau = 0.0004, \eta = 0.0005, u = 0.5$.
It shows the obtained model is quintessence model and tends to cosmological constant (ΛCDMmodel) as universe expands.

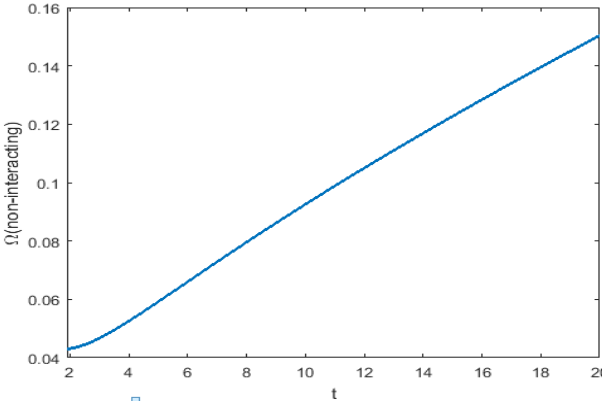

Figure 10.
The plot of overall density Ω versus time t for non-interacting model
for $\alpha = 1.4, \beta = 0.2, p = 0.5, \tau = 0.0004, \eta = 0.0005, u = 0.5, \rho_0 = 1$.
It displays the overall density of non – interacting model increases w.r.t. time t.

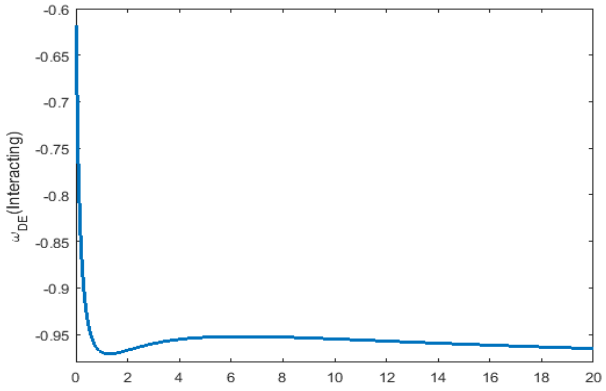

Figure 11.
The plot of EoS parameter ω_{DE} versus cosmic time of interacting model
for $\alpha = 1.4, \beta = 0.2, p = 0.5, \tau = 0.0004, \eta = 0.0005, u = 0.5, b = 0.5, \rho_1 = 0.04$.
It shows, initially $-1 < \omega_{DE} - 1/3$ and $\omega_{DE} \to -1$ as $t \to \infty$.
So the obtained interacting model is quintessence model andit tends to cosmological constant (ΛCDMmodel) as universe expands.

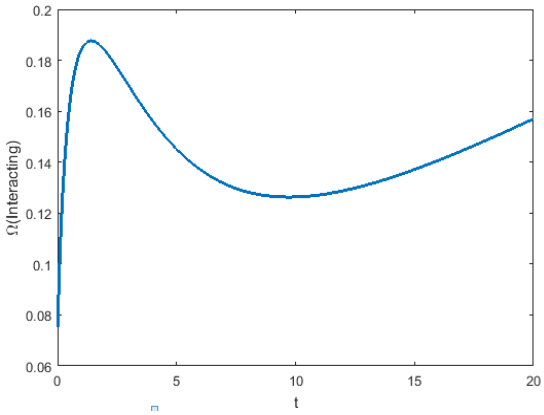

Figure 12.
The plot of overall density Ω versus time t for interacting model
for $\alpha = 1.4, \beta = 0.2, p = 0.5, \tau = 0.0004, \eta = 0.0005, u = 0.5, \rho_1 = 1, b = 0.5$.
The overall density of interacting model initially increases and after some time decreases and finally increases for large time t.

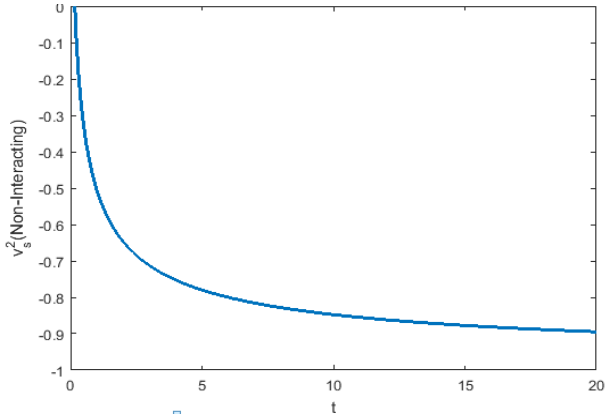

Figure 13.
The plot of v_s^2versus time t
for of non-Interactingmodel with $\alpha = 1.4, \beta = 0.2, p = 0.5, \tau = 0.0004, \eta = 0.0005, u = 0.5$.
It is observed that it is negative throughout the evolution of the universe.

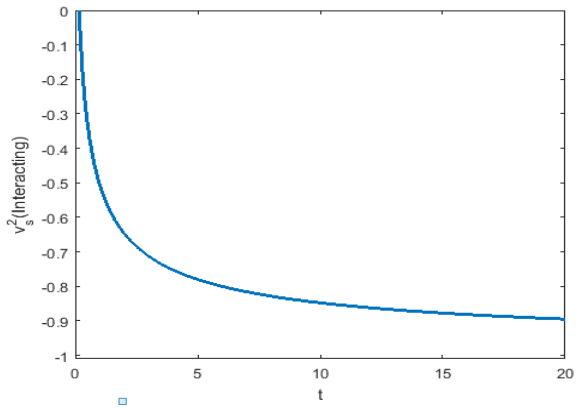

Figure 14.
The plot of v_s^2versus time t
for of Interactingmodel with $\alpha = 1.4, \beta = 0.2, p = 0.5, \tau = 0.0004, \eta = 0.0005, u = 0.5. \rho_1 = 0.04, b = 0.5$
It is observed that it is negative throughout the evolution of the universe.

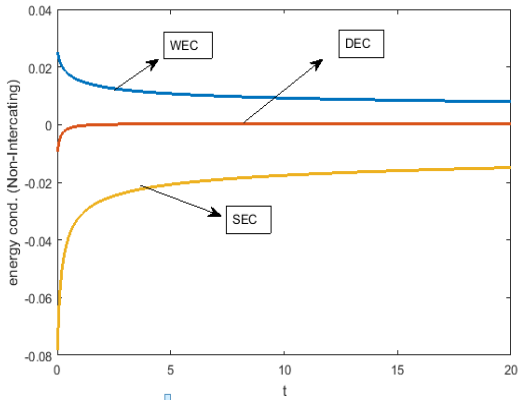

Figure 15.
The plots of energy conditions for non-Interacting model versus time t.

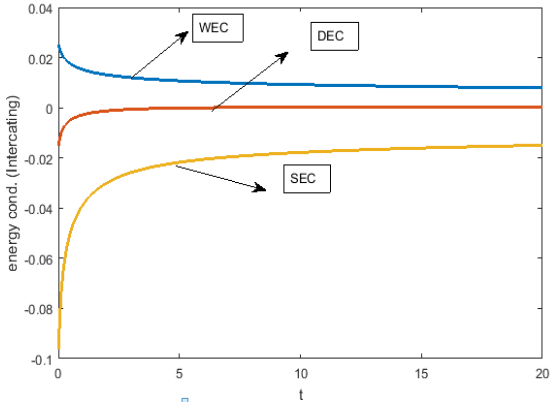

Figure 16.
The plots of energy conditions for Interacting model versus time t.

9. CONCLUSIONS

In this paper we have investigated the spatially homogeneous and anisotropic Bianchi type VI_0 space time with GGPDE in Saez-Ballester theory of gravitation. To obtain the solutions of field equations, the simple parametric form scale factor proposed by Mishra and Dua [1] is used. Both Interacting and non-interacting models have discussed. The findings of those models are given point wise as follows;

- The Spatial volume V is increasing with cosmic time *t.*
- The parameters H, θ, σ^2 are diminishes and approaches to zero as time evolves.
- From figure (5), the anisotropy parameter is diverging initially and decreasing with time and tend to zero at late time. This concludes the model is anisotropic in early universe and becoming isotropic model as $t \to \infty$.
- The decelerating parameter q is depicted in figure (6). The sign of decelerating parameter is changing from positive to negative. So, this model exhibits early deceleration and late time acceleration of the universe.
- The jerk parameter of the model is positive throughout the evolution of the universe. It can be observed from Figure (7).
- The EoS parameter for both models is presented in figures (9) and (11). For both models $\omega \to -1$ as time evolves. The both models behave like ΛCDM model at late time.
- The energy density of GGPDE is decreasing w.r.t. time and tends to a small value for large *t.*
- From the stability analysis of the models, it is observed that v_s^2 is negative for both models. So, the obtained interacting and non-interacting models are unstable.
- The overall density is increasing with time for both interacting and non-interacting models.
- The energy conditions were plotted for both the models. The energy conditions WEC, DEC are satisfied and SEC is violated for both models. So, the both models denote the accelerating expansion of the universe.

Acknowledgement: The authors are thankful to the referee for valuable comments and suggestions.

ORCID

Tenneti Ramprasad, https://orcid.org/0000-0002-5599-1118; **M.P.V.V. Bhaskara Rao,** https://orcid.org/0000-0001-6347-4156
Satyanarayana Bora, https://orcid.org/0000-0001-7019-4873

REFERENCES

[1] R.K. Mishra, and H. Dua, "Evolution of FLRW universe in Brans-Dicke gravity theory," Astrophys. Space Sci. **366**, 6 (2021). https://doi.org/10.1007/s10509-020-03908-0

[2] A.G. Riess, *et al*., "Observational Evidence from Supernovae for an Accelerating Universe and a Cosmological Constant," Astron. J. **116**, 1009–1038 (1998). https://doi.org/10.1086/300499

[3] D.N. Spergel, *et al*., "First Year Wilkinson Microwave Anisotropy Probe (WMAP) Observations: Determination of Cosmological Parameters," Astrophys. J. Suppl. Ser. **148**, 175–194 (2003). https://doi.org/10.1086/377226

[4] M. Tegmark, *et al*., "Cosmological parameters from SDSS and WMAP," Phys. Rev. D, **69**, 10350 (2004); S. Weinberg, "The cosmological constant problem," Rev. Mod. Phys. **61**, 103501 (1989). https://doi.org/10.1103/PhysRevD.69.103501

[5] S. Weinberg, "The cosmological constant problem," Rev. Mod. Phys. **61**, 1 (1989). https://doi.org/10.1103/RevModPhys.61.1

[6] P. Steinhardt, L. Wang, and I. Zlatev, "Cosmological tracking solutions," Phys. Rev. D, **59**, 123504 (1999). https://doi.org/10.1103/PhysRevD.59.123504

[7] R.R. Caldwell, "A phantom menace? Cosmological consequences of a dark energy component with super-negative equation of state," Phys. Lett. B, **545**, 23-29 (2002). https://doi.org/10.1016/S0370-2693(02)02589-3

[8] S. Noijiri, S.D. Odintsov, and S. Tsujikawa, "Properties of singularities in the (phantom) dark energy universe," Phys. Rev. D, **71**, 063004 (2005). https://doi.org/10.1103/PhysRevD.71.063004

[9] T. Padmanabhan, "Accelerated expansion of the universe driven by tachyonic matter," Phys. Rev. D, **66**, 021301(R) (2002). https://doi.org/10.1103/PhysRevD.66.021301

[10] M. Gasperini, F. Piazza, and G. Veneziano, "Quintessence as a runaway dilaton," Phys. Rev. D, **65**, 023508 (2001). https://doi.org/10.1103/PhysRevD.65.023508

[11] F.R. Urban, and A.R. Zhitnitsky, "The cosmological constant from the QCD Veneziano ghost," Phys. Lett. B, **688**(1), 9–12 (2010). https://doi.org/10.1016/j.physletb.2010.03.080

[12] N. Ohta, "Dark energy and QCD ghost," Phys. Lett. B, **695**, 41-44 (2011). https://doi.org/10.1016/j.physletb.2010.11.044

[13] R.G. Cai, Z.L. Tuo, H.B. Zhang, and Q. Su, "Notes on ghost dark energy," Phys. Rev. D, **84**(12), 123501 (2011). https://doi.org/10.1103/PhysRevD.84.123501

[14] A.R. Zhitnitsky, "Gauge fields and ghosts in Rindler space," Phys. Rev. D, **82**(10), 103520 (2010). https://doi.org/10.1103/PhysRevD.82.103520

[15] B. Holdom, "From confinement to dark energy," Phys. Lett. B, **697**(4), 351–356 (2011). https://doi.org/10.1016/j.physletb.2011.02.024

[16] A.R. Zhitnitsky, "Contact Term, its Holographic Description in QCD and Dark Energy," arXiv:1112.3365[hep-ph], Phys. Rev. D, **86**, 045026 (1988). https://doi.org/10.1103/PhysRevD.86.045026

[17] M. Maggiore, L. Hollenstein, M. Jaccard, and E. Mitsou, "Early dark energy from zero-point quantum fluctuations," Phys. Lett. B, **704**(3), 102-107 (2011). https://doi.org/10.1016/j.physletb.2011.09.010

[18] R.G. Cai, Z.L. Tuo, Y.B. Wu, and Y.Y. Zhao, "More on QCD Ghost Dark Energy," arXiv:1201.2494v2[astro-ph.CO], Phys. Rev. D, **86**, 023511 (2012). https://doi.org/10.1103/PhysRevD.86.023511

[19] H. Wei, "Pilgrim Dark Energy," arXiv: 1204.4032v3[gr-qc], Class. Quantum Grav. **29**, 175008 (2012). https://doi.org/10.1088/0264-9381/29/17/175008

[20] M. Sharif, and A. Jawad, "Analysis of generalized ghost version of pilgrim dark energy," Astrophys. Space Sci. **351**, 321-328 (2014). https://doi.org/10.1007/s10509-014-1833-y

[21] M.V. Santhi, V.U.M. Rao, and Y. Aditya, "Anisotropic Generalized Ghost Pilgrim Dark Energy Model in General Relativity," Int. J. Theor. Phys. **56**, 362-371 (2017). https://doi.org/10.1007/s10773-016-3175-8

[22] A. Jawad, "Analysis of Generalized Ghost Pilgrim Dark Energy in Non-flat FRW Universe," arXiv: 1412.4000v1[gr-qc], Eur. Phys. J. C, **74**, 3215 (2014). https://doi.org/10.1140/epjc/s10052-014-3215-6

[23] P. Garg, A. Dixit, and A. Pradhan, "Cosmological models of generalized ghost pilgrim dark energy (GGPDE) in the gravitation theory of Saez-Ballester," arXiv: 2004.11153v1[physics. gen-ph], International Journal of Geometric Methods in Modern Physics, **18**(14), 2150221 (2020). https://doi.org/10.1142/S0219887821502212

[24] R. Bali, and P. Kumari, "Bianchi Type VI_0 inflationary universe with constant declaration parameter and flat potential in General Relativity," Advances in Astrophysics, **2**(2), 67-72 (2017). https://dx.doi.org/10.22606/adap.2017.22001

[25] G.G. Luciano, "Saez–Ballester gravity in Kantowski–Sachs Universe: A new reconstruction paradigm for Barrow Holographic Dark Energy," Physics of the Dark Universe, **41**, 101237 (2023). https://doi.org/10.1016/j.dark.2023.101237

[26] T. Vinutha, and K.V. Vasavi, "The study of accelerating DE models in Saez–Ballester theory of gravitation," Eur. Phys. J. Plus, **137**, 1294 (2022). https://doi.org/10.1140/epjp/s13360-022-03477-x

[27] H. Wei, and R.G. Cai, "Interacting agegraphic dark energy," Eur. Phys. J. C, **59**, 99-105 (2009). https://doi.org/10.1140/epjc/s10052-008-0799-8

[28] K.S. Adhav, "LRS Bianchi Type-I universe with anisotropic dark energy in lyra geometry," Int. J. Astron. Astrophys. 1(4), 204-209 (2011). http://dx.doi.org/10.4236/ijaa.2011.14026

[29] Y.S. Myung, "Instability of holographic dark energy models. Phys. Lett. B, **652**, 223-227 (2007). https://doi.org/10.1016/j.physletb.2007.07.033

УЗАГАЛЬНЕНА GHOST PILGRIMS КОСМОЛОГІЧНА МОДЕЛЬ ТЕМНОЇ ЕНЕРГІЇ Б'ЯНЧІ ТИПУ VI_0 В ТЕОРІЇ ГРАВІТАЦІЇ САЕЗА-БАЛЛЕСТЕРА

Теннеті Рампрасад[a], М.П.В.В. Бхаскара Рао[b], М. Кіран[c], Сатьянараяна Бора[d]

[a]Департамент математики, Інженерний коледж Васаві (А), Хайдарабад, Індія

[b]Департамент фундаментальних і гуманітарних наук Інституту інформаційних технологій Віньяна (А), Вішакхапатнам, Андхра-Прадеш, Індія

[c]Факультет математики, Інженерний коледж MVGR, Візіанагарам (А), Індія

[d]Коледж комп'ютерних та інформаційних наук, Університет технології та прикладних наук, Мусандам, PO Box:12, PC: 811, Хасаб, Оман

Узагальнена Ghost Pilgrim темна енергія (GGPDE) у теорії гравітації Саеза-Баллестера (SBTG) і просторово-часова структура VI_0 типу Бьянчі слугують основою для цієї роботи. Ми використали просту параметризацію середнього масштабного коефіцієнта $a(t) = exp\{(\alpha t+\beta)^n\}$ Мішри та Дуа [Astrophys. Space Sci. 366, 6 (2021)], щоб знайти точні розв'язки рівнянь поля. Ми вивчили GGPDE і темну матерію (DM), як коли вони взаємодіють, так і коли вони не взаємодіють. Для обох моделей виробляються деякі важливі та добре відомі параметри, включаючи параметр Хаббла, параметр рівняння стану (EOS), параметр уповільнення тощо. Виявлено, що для обох моделей параметр уповільнення означає прискорену фазу, а параметр EOS — космологічну константу. Як для невзаємодіючих, так і для взаємодіючих моделей досліджуються аналіз стабільності та енергетичні умови.

Ключові слова: *параметр Хаббла; параметр EOS; параметр уповільнення; GGPDE; SBTG*

EAST EUROPEAN JOURNAL OF PHYSICS. 1. 70-78 (2025)
DOI:10.26565/2312-4334-2025-1-06 ISSN 2312-4334

DYNAMICS OF STRING COSMOLOGICAL MODEL IN $f(R, L_m)$ THEORY OF GRAVITY

S.D. Katore[a], P.R. Agrawal[b], H.G. Paralikar[a], A.P. Nile[b]
[a]*Department of Mathematics, Sant Gadge Baba Amravati University, Amravati 444602, India*
[b]*Department of Mathematics, Brijlal Biyani Science College, Amravati, 444602, India*
Corresponding Author e-mail: katore777@gmail.com, prachi.gadodia@gmail.com, hparalikar05@gmail.com; ankushnile15@gmail.com
Received August 23, 2024; revised October 14, 2024; in final form December 28, 2024; accepted February 4, 2025

The present paper examines the FLRW model with cosmic string within the framework of $f(R,L_m)$ gravity, considering two different forms of $f(R,L_m)$ gravity such as $f(R,L_m)=\frac{R}{2}+L_m^{\eta}+\beta$ and $f(R,L_m)=\Lambda e^{\frac{R}{2\Lambda}+\frac{L_m}{\Lambda}}$, where η,β and Λ are free model parameters. The solutions of the models are obtained using both, the power law and the hybrid expansion law. The resulting physical and dynamical parameters of the models analyzed and presented through graphical representations.
Keywords: $f(R,L_m)$ *gravity; String Cosmological Model; Power law; Hybrid expansion law*
PACS: 04.50.Kd, 98.80.-k, 98.80.Jk

INTRODUCTION

A potentially effective approach to interpret the latest observational findings (Riess *et al.* (1998); Peebles and Ratra (2003)) regarding the Universe's late-time acceleration and dark matter is to propose that Einstein's theory of general relativity may not hold at large scales. Instead, a broader gravitational framework could better describe these phenomena. Harko *et al.* (2010) introduced an advanced form of matter-curvature coupling theories, referred as $f(R,L_m)$ gravity, where f represents a variable function dependent on the matter Lagrangian L_m and the Ricci scalar R. This theory of gravity can be viewed as the most extensive expansion of all the gravitational theories formulated in Riemann space. The trajectory of test particle within this theory deviates from geodesic paths, resulting in an additional force perpendicular to the four-velocity vector.

Functional expressions for $f(R)$ gravity incorporates logarithmic, exponential and power law models, an extension of framework is known as $f(R,L_m)$ gravity which has been recently emerged as $f(R,L_m)=f_1(R)+f_2(R)G(L_m)$, where f_1,f_2 and G are arbitrary functions of the Ricci scalar and the matter Lagrangian density respectively. The gravitational field equations and the equation of motions for a particular, in which the action of gravitational field has an exponential dependence on the standard general realistic Hilbert Einstein density, $f(R,L_m)=\Lambda e^{\frac{R}{2\Lambda}+\frac{L_m}{\Lambda}}$ are also derived. The Kasner-type static, cylindrically symmetric interior string solutions were investigated in the $f(R,L_m)$ theory of gravity by Harko *et al.* (2015), and the thermodynamic parameter of the string was explicitly obtained. In the article, "cosmology in $f(R,L_m)$ gravity", Jaybhaye *et al.* (2022a) analyzed by utilizing $H(z)$, Pantheon and combining $H(z)+$Pantheon datasets. There, they determined the optimal ranges for model parameters. Additionally, a study was conducted on the variation in cosmological parameters based on the constraints established by these observational datasets. Also, the authors of Jaybhaye *et al.* (2022a) investigated the stability of the obtained model.

Solanki *et al.* (2023) studied $f(R,L_m)$ gravity by considering non-linear models. They obtained the Wormhole solutions by assuming three different cases which are linear barotropic EoS, anisotropic EoS and isotropic EoS, whereas Jaybhaye *et al.* (2022b) discussed about constraints on energy conditions and used cosmographic parameters like mean Hubble parameter, deceleration parameter, jerk parameter and snap parameter. Wang *et al.* (2012) also discussed energy conditions by considering a special model in FRW cosmology and compared with observational astronomical results. Singh *et al.* (2023) studied a constrained cosmological model in $f(R,L_m)$ gravity. Shukla *et al.* (2023) used equation of state parameter and Garg *et al.* (2023) used a linear equation of state parameter to study the expansion of the universe. Lobato *et al.* (2021) investigated Neutron stars with realistic equation of state, Patil *et al.* (2023) analyzed FLRW cosmology with Hybrid scale factor, Pawde *et al.* (2023) studied anisotropic behavior of universe with varying deceleration parameter and Jaybhaye *et al.* (2024) derived bouncing cosmological models in $f(R,L_m)$ gravity.

The cosmic string in $f(R)$ gravity have been studied by Ladke *et al.* (2022) and explored three non-static plane symmetric cosmological models. Carvalho *et al.* (2021) investigated the formation and evolution of cosmic string wakes in $f(R)$ Gravity where they considered a simple model in which baryonic matter flows past a cosmic string. To obtain

Cite as: S.D. Katore, P.R. Agrawal, H.G. Paralikar, A.P. Nile, East Eur. J. Phys. 1, 70 (2025), https://doi.org/10.26565/2312-4334-2025-1-06

the solution Carvalho *et al.* (2021) used Zel'dovich approximation and also explored the propagation of light in $f(R)$ cosmic string. Also, they compared the results with wakes formed by cosmic string solutions obtained in General Relativity and Scalar Tensor Theories of Gravity. Silva *et al.* (2021) studied comic string in modified theories of gravitation. Also, several authors studied $f(R)$ theory of gravity in different content [Adhav *et al.* 2012; Hatkar *et al.* 2018; Agrawal and Nile 2024; Malik 2024].

Bishi *et al.* (2015) studied Bianchi type V string cosmological model with bulk viscosity in $f(R,T)$ Gravity by considering a special form and linearly varying parameter. Dasunaidu *et al.* (2018) examined the kinematical behavior of five dimensional non static spherically symmetric cosmological models in the presence of a massive string in $f(R,T)$ Gravity. Also, Agrawal and Nile (2024); Thakre *et al.* (2024) studied $f(R,T)$ theory of gravity in different content.

Here in the present study, we have studied two models for the flat FLRW metric in the presence of string motivated by the above discussion. The work has been organized as, basic formation of $f(R,L_m)$, metric and field equations, cosmological model-I, cosmological model-II, common physical parameters for Model-I and Model-II and lastly, result and discussion of the paper have been given.

BASIC FORMATION OF $f(R,L_m)$

The following action governs the gravitational interaction in $f(R,L_m)$ gravity.

$$S=\int f(R,L_m)\sqrt{-g}d^4x\,, \tag{1}$$

where $f(R,L_m)$ represents an arbitrary function of the Ricci scalar R and the matter Lagrangian term L_m.
Now the following field equation can be acquired by varying action (1) for the metric tensor g_{uv},

$$f_R R_{\mu\nu}+(g^{\mu\nu}\nabla_\mu\nabla^\nu-\nabla_\mu\nabla_\nu)f_R-\frac{1}{2}(f-f_{L_m}L_m)g_{\mu\nu}=\frac{1}{2}f_{L_m}T_{\mu\nu}\,, \tag{2}$$

were $f_R\equiv\frac{\partial f}{\partial R}$, $f_{L_m}\equiv\frac{\partial f}{\partial L_m}$, $g^{\mu\nu}\nabla_\mu\nabla^\nu$ is the D'Alembertian, and $T_{\mu\nu}$ represents the energy-momentum tensor for the perfect fluid, defined by

$$T_{\mu\nu}=\frac{-2}{\sqrt{-g}}\frac{\delta(\sqrt{-g}L_m)}{\delta g^{\mu\nu}}\,. \tag{3}$$

The relation between the trace of energy momentum tensor T, Ricci scalar R and the Lagrangian density of matter L_m obtained by contracting the field equation (2) is

$$Rf_R+3g^{\mu\nu}\nabla_\mu\nabla_\nu f_R-2(f-f_{L_m}L_m)=\frac{1}{2}f_{L_m}T\,. \tag{4}$$

Here, $g^{\mu\nu}\nabla_\mu\nabla_\nu F=\frac{1}{\sqrt{-g}}\partial_\mu(\sqrt{-g}g^{\mu\nu}\partial_\nu F)$ for any scalar function F
Moreover, one can acquire the following result by taking covariant derivative in equation (2),

$$\nabla^\mu T_{\mu\nu}=2\nabla^\mu\log(f_{L_m})\frac{\partial L_m}{\partial g^{\mu\nu}}\,.$$

The energy momentum tensor for cosmic string is given by (Adhav *et al.* 2011),

$$T_\nu^\mu=\rho u_\mu u^\nu-\lambda x_\mu x^\nu\,, \tag{5}$$

where ρ is rest energy density of strings with particles attached to them, λ is the tension density of strings. Orthonormalization of four velocity vectors u^μ and the x_μ, the direction of anisotropy of strings, obeys the following relation.

$$u_\nu u^\nu=-x_\nu x^\nu=1\,,\qquad u^\nu x_\nu=0$$

Metric and Field Equations in $f(R,L_m)$ Gravity

We consider the flat FLRW metric as

$$ds^2 = -dt^2 + a^2(t)\left[dx^2 + dy^2 + dz^2\right]. \tag{6}$$

Here, $a(t)$ is the scale factor that measures the cosmic expansion at time t.

Using equations (5) and (6), the Friedmann equations that describes dynamics of the universe in $f(R,L_m)$ gravity are read as

$$3\frac{\dot{a}^2}{a^2}f_R + \frac{1}{2}\left(f - f_R R - f_{L_m}L_m\right) + 3\frac{\dot{a}}{a}\dot{f}_R = \frac{1}{2}f_{L_m}\rho\,, \tag{7}$$

$$\frac{\ddot{a}}{a}f_R + 3\frac{\dot{a}^2}{a^2}f_R - \ddot{f}_R - 3\frac{\dot{a}}{a}\dot{f}_R + \frac{1}{2}\left(f_{L_m}L_m - f\right) + 3\frac{\dot{a}}{a}\dot{f}_R = \frac{1}{2}f_{L_m}(\rho - \lambda)\,. \tag{8}$$

Cosmological $f(R,L_m)$. Model-I

Here we consider the following form of $f(R,L_m)$ model as (Harko *et al.* 2014),

$$f(R,L_m) = \frac{R}{2} + L_m^{\eta} + \beta\,, \tag{9}$$

where β and η are free model parameters.

For this particular $f(R,L_m)$ model we take $L_m = \rho$ (Harko *et al.* 2014), the Friedmann equation (7) and (8) becomes

$$3\frac{\dot{a}^2}{a^2} = (2\eta - 1)\rho^{\eta} - \beta\,, \tag{10}$$

$$2\frac{\ddot{a}}{a} = \eta\rho^{\eta-1}\lambda - \rho^{\eta} - \beta\,. \tag{11}$$

Here we have system of two equations as presented in equations (10) and (11) involving three unknowns a, ρ and λ. As a result in order to solve a system of equations, it becomes essential to consider a specific condition for getting deterministic solution. For that we consider two different laws.

i) Power Law

In the available literature, there exists many relations in between a and t. For our analysis, we consider power law (Sharif & Zubair (2012)) as

$$a = \alpha t^{\chi}\,.$$

Using equation (10) the rest energy density ρ is given by

$$\rho = \left[\frac{1}{(2\eta - 1)}\left(\frac{3\chi^2}{t^2} + \beta\right)\right]^{\frac{1}{\eta}}, \tag{12}$$

here the model is valid for $\eta > 0.5$.

Using equation (11), the tension density λ is given by

$$\lambda = \frac{\dfrac{2\alpha\chi(\chi-1)t^2}{\alpha t^{\chi}} + \dfrac{1}{(2\eta-1)}\left(\dfrac{3\chi^2}{t^2} + \beta\right) - \beta}{\eta\left[\dfrac{1}{(2\eta-1)}\left(\dfrac{3\chi^2}{t^2} + \beta\right)\right]^{\frac{\eta-1}{\eta}}}. \tag{13}$$

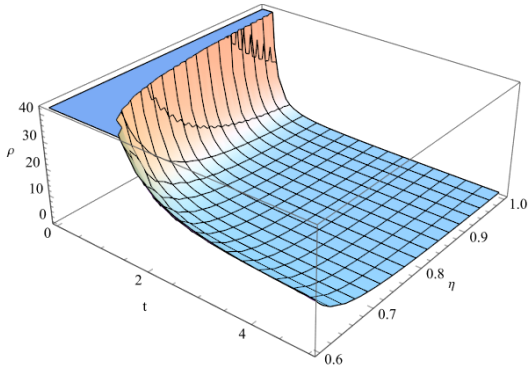

Figure 1. The rest density has been plotted by considering $\alpha = 0.2, \beta = 1, \chi = 0.8$

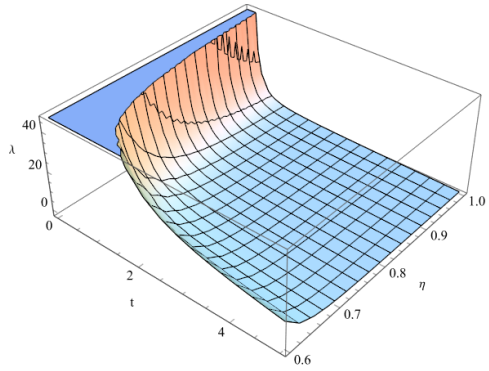

Figure 2. The tension density has been plotted by considering $\alpha = 0.2, \beta = 1, \chi = 0.8$

ii) Hybrid Expansion Law

The hybrid expansion law is given by (Agrawal and Nile 2024)

$$a = te^{mt},$$

where, $m > 0$ be any constant.

Using equation (10) the rest density ρ is given by

$$\rho = \left[\frac{1}{(2\eta - 1)}\left(\frac{3(mt+1)^2}{t^2} + \beta\right)\right]^{\frac{1}{\eta}}. \tag{14}$$

Using equation, the tension density λ is given by

$$\lambda = \frac{\frac{2(2m+m^2t)}{t} + \left[\frac{1}{(2\eta-1)}\left(\frac{3(mt+1)}{t^2} + \beta\right)\right] + \beta}{\eta\left[\frac{1}{(2\eta-1)}\left(\frac{3(mt+1)}{t^2} + \beta\right)\right]^{\frac{\eta-1}{\eta}}}. \tag{15}$$

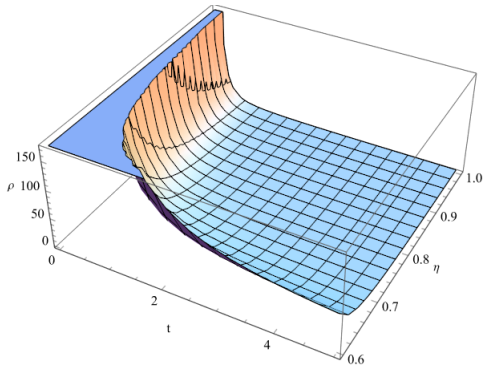

Figure 3. The rest density has been plotted by considering $\alpha = 0.2, \beta = 1, \chi = 0.8, m = 0.5$

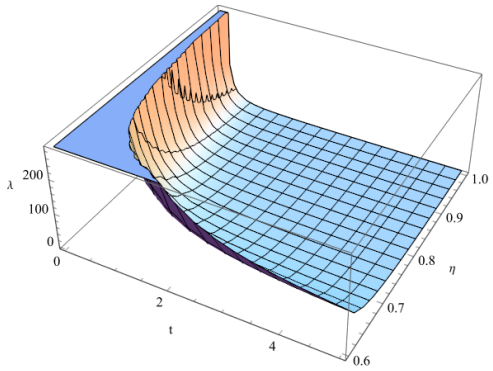

Figure 4. The tension density has been plotted by considering $\alpha = 0.2, \beta = 1, \chi = 0.8, m = 0.5$

Cosmological $f(R, L_m)$. Model-II

Here we consider the anther form of $f(R, L_m)$ model as (Harko *et al.* 2014),

$$f(R, L_m) = \Lambda e^{\frac{R}{2\Lambda} + \frac{L_m}{\Lambda}},$$

where $\Lambda > 0$ is arbitrary constant.

For this particular $f(R, L_m)$ model we take $L_m = \rho$ (Harko *et al.* 2014).

The Friedmann equation (8) and (9) becomes

$$\Lambda-\frac{3\ddot{a}}{a}+\frac{3\dot{a}}{2a\Lambda}=2\rho\,, \tag{16}$$

$$\frac{\ddot{a}}{a}+\frac{3\dot{a}^2}{a^2}-\frac{1}{4\Lambda^2}-\frac{3\dot{a}}{2a\Lambda}-\Lambda=-\lambda\,. \tag{17}$$

The system comprises of two equations (16)-(17), with three unknown variables. To find the solution of this system of equations, it is important to identify a particular condition which guarantees a definite solution.

i) Power Law

By using the power law given by equation (12) and equations (16), we get the rest density as

$$\rho=\frac{1}{2}\left[\Lambda-\frac{3\chi(\chi-1)}{t^2}+\frac{3\chi}{2t\Lambda}\right]. \tag{18}$$

Using the equation (17) the tension density is given by

$$\lambda=\Lambda+\frac{1}{4\Lambda^2}-\frac{\chi(\chi-1)}{t^2}-\frac{3\chi^2}{t^2}+\frac{3\chi}{2t\Lambda}\,. \tag{19}$$

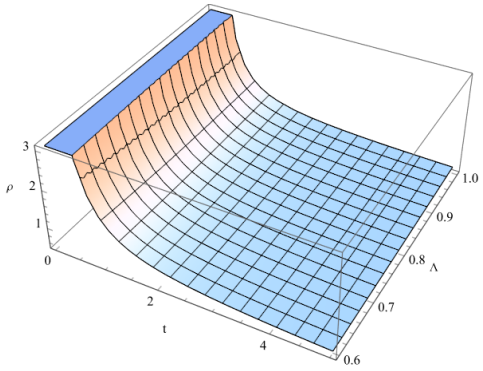

Figure 5. The rest density has been plotted by considering $\chi=0.8,\Lambda=0.1$

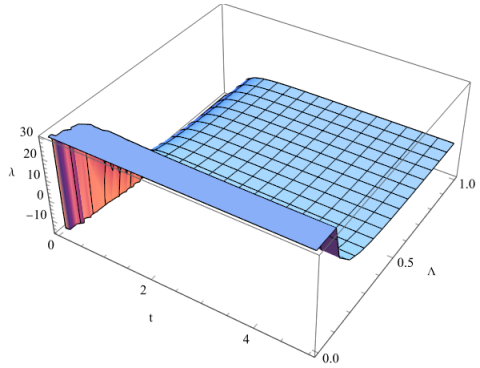

Figure 6. The tension density has been plotted by considering $\chi=0.8,\Lambda=0.1$

ii) Hybrid Expansion Law

By using the hybrid expansion law given by equation (14) and using equations (16), we get the rest density ρ as

$$\rho=\frac{1}{4\Lambda}\left[2\Lambda^2-6\left(m^2+\frac{2m}{t}\right)+3\left(m+\frac{1}{t}\right)\right]. \tag{20}$$

Using equation (17) the tension density λ given by

$$\lambda=\Lambda+\frac{1}{4\Lambda^2}+\frac{3(m+1/t)}{2\Lambda}-\left(m^2+\frac{2m}{t}\right)-3\left(m+\frac{1}{t}\right)^2. \tag{21}$$

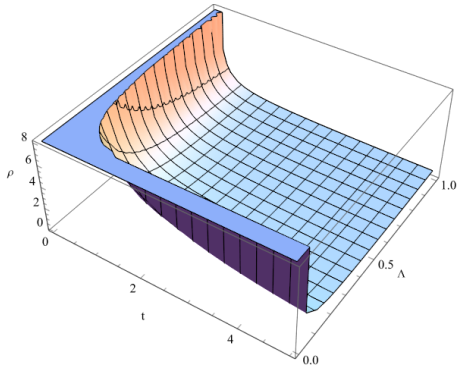

Figure 7. The rest density has been plotted by considering $\chi=0.8,\Lambda=0.1,m=0.5$

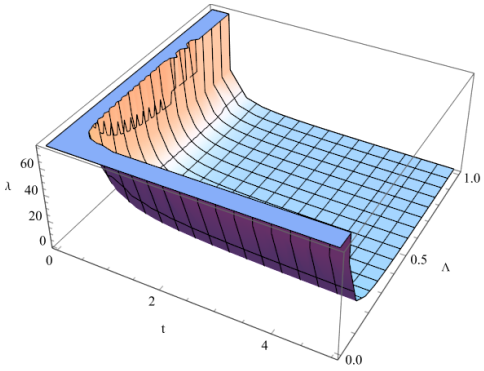

Figure 8. The tension density has been plotted by considering $\chi=0.8,\Lambda=0.1,m=0.5$

Common Physical Parameters for Model-I and Model-II:

Power Law:

We obtained the Hubble parameter and the deceleration parameter in terms of t as

$$H = \frac{\dot{a}}{a} = \frac{\chi}{t}, \tag{22}$$

$$q = \frac{1}{\chi} - 1. \tag{23}$$

The spatial volume is given by

$$V = a^3 = (\alpha t)^3. \tag{24}$$

By using equation (29), we can obtain the Scalar expansion, mean anisotropic parameter and Shear scalar as

$$\theta = 3H = \frac{3\chi}{t}, \tag{25}$$

$$\Delta = \frac{1}{3}\sum_{i=1}^{3}\left(\frac{H_i}{H} - 1\right) = 0, \tag{26}$$

$$\sigma^2 = \frac{3}{2}\Delta H = 0. \tag{27}$$

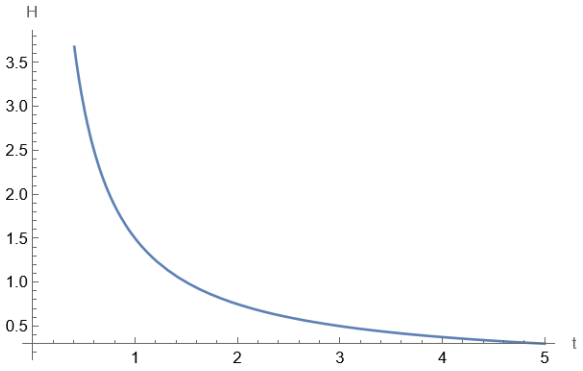

Figure 9. The mean Hubble Parameter has been plotted by considering $\chi = 0.8$

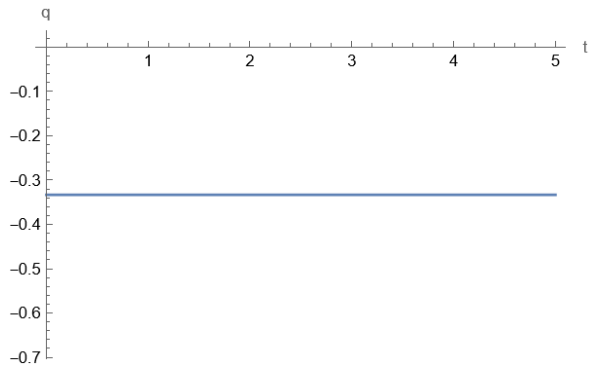

Figure 10. The deceleration parameter has been plotted by considering $\chi = 0.8$

Hybrid Expansion Law:

We obtained the Hubble parameter and the deceleration parameter in terms of t as

$$H = \frac{\dot{a}}{a} = m + \frac{1}{t}, \tag{28}$$

$$q = \frac{1}{(1+mt)^2} - 1. \tag{29}$$

The spatial volume is given by

$$V = a^3 = t^3 e^{3mt}. \tag{30}$$

By using equation (28), we can obtain the Scalar expansion, anisotropic parameter and Shear scalar as

$$\theta = 3H = 3\left(m + \frac{1}{t}\right), \tag{31}$$

$$\Delta = \frac{1}{3}\sum_{i=1}^{3}\left(\frac{H_i}{H} - 1\right) = 0, \tag{32}$$

$$\sigma^2 = \frac{3}{2}\Delta H = 0. \tag{33}$$

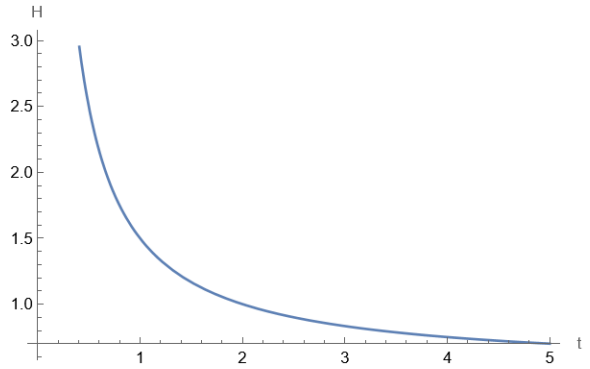

Figure 11. The mean Hubble parameter have been plotted by considering $m = 0.5$

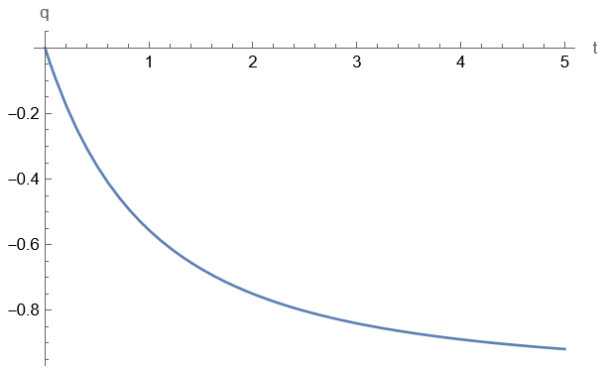

Figure 12. The deceleration parameter has been plotted by considering $m = 0.5$

RESULT AND DISCUSSIONS

In this paper, we have analyzed the FLRW model with cosmic string in the framework of $f(R,L_m)$ gravity considering two different models for two distinct forms of $f(R,L_m)$ gravity such as $f(R,L_m)=\frac{R}{2}+L_m^{\eta}+\beta$ and $f(R,L_m)=\Lambda e^{\frac{R}{2\Lambda}+\frac{L_m}{\Lambda}}$, where η,β and Λ are free model parameters. We obtained the physical and dynamical parameters such as mean Hubble parameter, deceleration parameter etc. specifically we obtained the rest density ρ and the tension density λ for the studied models.

In model-I, it is observed that the rest density for power law and hybrid expansion law is positively decreasing function of cosmic time t and approaches to 0 as depicted in figure-1 & figure-3. Also, the tension density λ for power law and hybrid expansion law is obtained and plotted with respective cosmic time t as shown in figure 2 & Figure-4.

In model-II, it is observed that the rest density for power law and hybrid expansion law is positively decreasing function of cosmic time t and approaches to 0 as $t\to\infty$ as depicted in figure-5 & figure-7. Also, the tension density λ for power law and hybrid expansion law is obtained and plotted against cosmic time t as shown in figure-6 & Figure 8.

This behavior aligns with widely accepted model of an expanding universe, where the energy density of matter, here string, decreases as the universe expands. As cosmic time progresses, the density of the matter, including cosmic strings, diminishes, which indicates the transitioning of universe from a matter-dominated phase to a dark energy dominated phase.

Also, in figure-9 and figure-11, the mean Hubble parameter for the both models shows the occurrence of the expansion of the universe, which is in consistent with the modern-day observations. Figure-10 the deceleration parameter shows the constant expansion. In the figure-12, the deceleration parameter shows the early deceleration to late acceleration of the universe. The shift from deceleration to acceleration is a key feature of modern cosmological models.

CONCLUSION

In conclusion, the analysis of FLRW model with cosmic string within the frame work of $f(R,L_m)$ gravity has provided valuable insights into the universe's expansion dynamics. The results for both Model – I and Model - II demonstrate that the rest and tension densities decrease with cosmic time, reflecting the universe's transition from a matter-dominated phase to a dark energy-dominated phase. The mean Hubble parameter confirms the ongoing expansion of the universe, consistent with current observations (Riess *et al.* (1998); Peebles and Ratra (2003)). Moreover, the behavior of the deceleration parameter, showing a shift from early deceleration to late-time acceleration, aligns with modern cosmological theories. These findings contribute to a deeper understanding of the role of cosmic strings and modified gravity in shaping the universe's evolution.

ORCID

S.D. Katore, https://orcid.org/0000-0003-0521-4334; **P.R. Agrawal,** https://orcid.org/0000-0002-8040-937X
H.G. Paralikar, https://orcid.org/0009-0003-1301-5340; **A.P. Nile,** https://orcid.org/0009-0003-1504-9085

REFERENCES

[1] Adhav, K.S., Gadodia, P.S., Bansod, A.S., "Bianchi Type-I String Cosmological Model in Creation-Field," International Journal of Theoretical Physics, **50**, 2720-2736 (2011). https://doi.org/10.1007/s10773-011-0770-6

[2] Adhav, K.S., "Bianchi Type-III Cosmic Strings Cosmological Model in f(R) Theory of Gravity," Bulgarian Journal of Physics, **39**(3), 197-206 (2012). https://www.bjp-bg.com/papers/bjp2012_3_197-206.pdf

[3] Agrawal, P.R., Nile, A.P., "Accelerating Universe with Wet Dark Fluid in Modified Theory of Gravity," Astronomy and Computing, **48**, 100847 (2024). https://doi.org/10.1016/j.ascom.2024.100847

[4] Agrawal, P.R., Nile, A.P., "Exploring f (R,T) Theory with Polytropic Equation of State," International Journal of Applied and Computational Mathematics, **10**(1), 15 (2024). https://doi.org/10.1007/s40819-023-01642-z

[5] Bishi, B.K., Mahanta, K.L., "Bianchi Type-V Bulk Viscous Cosmic String n Gravity with Time Varying Deceleration Parameter," Advances in High Energy Physics, **2015**, 91403 (2015). https://doi.org/10.1155/2015/491403

[6] Carvalho, G.C., Guimarães, M.E.X., Mesquita, P.O., Neto, J.L., "Formation and Evolution of Wakes in the Spacetime Generated by a Cosmic String in f(R) Theory of Gravity," preprint arXiv:2110.02353, (2021). https://doi.org/10.48550/arXiv.2110.02353

[7] da Silva, M.R., "Cosmic Strings in Modified Theories of Gravity", Master's thesis, Universidade do Porto (Portugal), 2021.

[8] Dasunaidu, K., Aditya, Y., Reddy, D.R.K., "Cosmic Strings in a Five Dimensional Spherically Symmetric Background in f(R,T) Gravity," Astrophysics and Space Science, **363**(7), 158 (2018). https://doi.org/10.1007/s10509-018-3380-4

[9] Garg, R., Singh, G.P., Lalke, A.R., Ray, S., "Cosmological Model with Linear Equation of State Parameter in f(R, L_m) Gravity," preprint arXiv:2310.17340, (2023). https://doi.org/10.48550/arXiv.2310.17340

[10] Harko, T., Lake, M.J., "Cosmic Strings in f(R, L_m) Gravity," The European Physical Journal C, **75**, 60-78 (2015). https://doi.org/10.1140/epjc/s10052-015-3287-y

[11] Harko, T., Lobo, F.S., "f(R,L_m) Gravity," The European Physical Journal C, **70**, 373-379 (2010). https://doi.org/10.1140/epjc/s10052-010-1467-3

[12] Harko, T., Lobo, F.S., "Generalized Curvature-Matter Couplings in Modified Gravity," Galaxies, **2**(3), 410-465 (2014). https://doi.org/10.3390/galaxies2030410

[13] Harko, T., Lobo, F.S., Mimoso, J.P., Pavón, D., "Gravitational Induced Particle Production through a Nonminimal Curvature–Matter Coupling," The European Physical Journal C, **75**, 1-15 (2015). https://doi.org/10.1140/epjc/s10052-015-3620-5

[14] Hatkar, S.P., Gore, S.V., Katore, S.D., "Kasner Type Magnetized String Cosmological Models in f(R, T) Gravity," Serbian Astronomical Journal, (197), 1-11 (2018). https://doi.org/10.2298/SAJ1897001H

[15] Jaybhaye, L.V., Mandal, S., Sahoo, P.K., "Constraints on Energy Conditions in f(R, L_m) Gravity," International Journal of Geometric Methods in Modern Physics, **19**(04), 2250050 (2022b). https://doi.org/10.1142/S0219887822500505

[16] Jaybhaye, L.V., Solanki, R., Sahoo, P.K., "Bouncing Cosmological Models in f(R, L_m) Gravity," Physica Scripta, **99**(6), 065031 (2024). https://doi.org/10.1088/1402-4896/ad4838

[17] Jaybhaye, L.V., Solanki, R., Mandal, S., Sahoo, P.K., "Cosmology in f (R, L_m) gravity," Physics Letters B, **831**, 137148 (2022a). https://doi.org/10.1016/j.physletb.2022.137148

[18] Ladke, L.S., Tripade, V.P., Mishra, R.D., "Non-Static Plane Symmetric Cosmic Strings Cosmological Model in Theory of Gravity," International Journal of Research Publication and Reviews, **3**(2), 432-438 (2022). https://ijrpr.com/uploads/V3ISSUE2/ijrpr2652-non-static-plane-symmetric-cosmic-strings-cosmological-model.pdf

[19] Lobato, R.V., Carvalho, G.A., Bertulani, C.A., "Neutron Stars in f(R, L_m) Gravity with Realistic Equations Of State: Joint-Constrains With GW170817, Massive Pulsars, and the PSR J0030+0451 mass-radius from NICER data," Eur. Phys. J. C, **81**, 1013 (2021). https://doi.org/10.1140/epjc/s10052-021-09785-3

[20] Malik, A., "A Study of Levia-Civita and Cosmic String Solutions in Modified f (R) Gravity," preprint arXiv:2404.10793, (2024). https://doi.org/10.48550/arXiv.2404.10793

[21] Peebles, P.J.E., Ratra, B., "The Cosmological Constant and Dark Energy," Reviews of modern physics, **75**(2), 559 (2003). https://doi.org/10.1103/RevModPhys.75.559

[22] Patil, V., Pawde, J., Mapari, R., Waghmare, S., "FLRW Cosmology with Hybrid Scale Factor in f (R, L_m) Gravity," East European Journal of Physics, (4), 8-17 (2023). https://doi.org/10.26565/2312-4334-2023-4-01

[23] Pawde, J., Mapari, R., Patil, V., Pawar, D., "Anisotropic Behavior of Universe in f(R, L_m) Gravity with Varying Deceleration Parameter," The European Physical Journal C, **84**(3), 320 (2024). https://doi.org/10.1140/epjc/s10052-024-12646-4

[24] Riess, A.G., et al., "Observational Evidence From Supernovae for an Accelerating Universe and a Cosmological Constant," The Astronomical Journal, **116**(3), 1009 (1998). https://doi.org/10.1086/300499

[25] Sharif, M., Zubair, M., "Energy Conditions Constraints and Stability of Power Law Solutions in f(R, T) Gravity," Journal of the Physical Society of Japan, **82**(1), 014002 (2012). https://doi.org/10.7566/JPSJ.82.014002

[26] Singh, J.K., Myrzakulov, R., Balhara, H., "A Constrained Cosmological Model in f(R,L_m) Gravity," New Astronomy, **104**, 102070 (2023). https://doi.org/10.1016/j.newast.2023.102070

[27] Shukla, B.K., Tiwari, R.K., Sofuoğlu, D., Beesham, A., "FLRW Universe in f(R, L_m) Gravity with Equation of State Parameter," East European Journal of Physics, (4), 376-389 (2023). https://doi.org/10.26565/2312-4334-2023-4-48

[28] Solanki, R., Hassan, Z., Sahoo, P.K., "Wormhole Solutions in f(R, L_m) Gravity," Chinese Journal of Physics, **85**, 74-88 (2023). https://doi.org/10.1016/j.cjph.2023.06.005

[29] Thakre, S., Mapari, R. V., Thakare, V.A. "Behaviour of Quark and Strange Quark Matter for Higher Dimensional Bianchi Type-I Universe in f(R, T) Gravity," East European Journal of Physics, (2), 21-35 (2024). https://doi.org/10.26565/2312-4334-2024-2-02

[30] Wang, J., Liao, K., "Energy conditions in f(R, L_m) gravity," Classical and Quantum Gravity, **29**(21), 215016 (2012). https://doi.org/10.1088/0264-9381/29/21/215016

ДИНАМІКА СТРУННОЇ КОСМОЛОГІЧНОЇ МОДЕЛІ У $f(R, L_m)$ ТЕОРІЇ ГРАВІТАЦІЇ

С.Д. Каторе[a], П. Р. Агравал[b], Х. Г. Паралікар[a], А.П. Ніл[b]

[a]*Факультет математики, Університет Сант-Гадж Баба Амраваті, Амраваті 444602, Індія*

[b]*Факультет математики, Науковий коледж Бріджлала Біяні, Амраваті, 444602, Індія*

У цій статті розглядається модель FLRW з космічною струною в рамках гравітації $f(R,L_m)$, розглядаючи дві різні форми гравітації $f(R,L_m)$, такі як $f(R,L_m)=\frac{R}{2}+L_m^{\eta}+\beta$ і $f(R,L_m)=\Lambda e^{\frac{R}{2\Lambda}+\frac{L_m}{\Lambda}}$, де η,β і Λ є вільними параметрами моделі. Розв'язки моделей отримані з використанням як степеневого закону, так і гібридного закону розширення. Отримані фізичні та динамічні параметри моделей аналізуються та представлені у вигляді графічних зображень.

Ключові слова: *гравітація $f(R,L_m)$; струнна космологічна модель; степеневий закон; закон гібридного розширення*

East European Journal of Physics. 1. 79-90 (2025)
DOI:10.26565/2312-4334-2025-1-07 ISSN 2312-4334

EIGEN RADIO FREQUENCY SIGNALS LOCALIZED AT ALFVEN RESONANCES IN A TOKAMAK SCRAPE-OFF LAYER

I. Girka[a]*, O. Trush[a], W. Tierens[b]
[a]*V.N. Karazin Kharkiv National University, Kharkiv, Ukraine*
[b]*Oak Ridge National Laboratory, Oak Ridge, USA*
**Corresponding Author e-mail: igor.girka@ipp.mpg.de*
Received December 12, 2024; revised January 3, 2025; accepted February 1, 2025

Eigen electromagnetic waves with small toroidal wave indices and positive poloidal wave indices are considered in the Ion Cyclotron Range of Frequencies (ICRF) in a tokamak Scrape-Off Layer (SOL). The waves are shown theoretically to exist in the form of the signals localized at the local Alfven Resonances (ARs). The evanescent regions in the direction of lower plasma density are provided by the presence of the wave nonzero poloidal wave indices. The narrow evanescent regions in the direction of higher plasma density are caused by strong plasma variation. The latter regions separate ARs from the high-density SOL and plasma core which are propagating regions for ICRF waves. The dispersion relation of ICRF signals is derived analytically and solved numerically. Possible relevance of the obtained results to experimental measurements is discussed. An exhaustive definition of the signals' excitation sources is out of scope of the present study.
Keywords: *Eigen waves; Ion cyclotron range of frequencies; Alfven resonance; Tokamak scrape-off layer; Asymptotic methods; Dispersion relation*
PACS: 52.35.Bj

INTRODUCTION

Alfven Waves (AWs) were predicted by Hannes Alfven more than eighty years ago [1]. Soon they were experimentally observed by Allen with co-authors [2]. Since then, AWs are extensively studied due to multiple practical applications, in particular, in fusion plasmas and astrophysics.

Plasma non-uniformity both in a laboratory and nature forms preconditions for the propagation of various AW types. For instance, elliptical shape of the fusion device cross-section was shown in [3] to give rise to eigen ellipticity induced Alfven waves (EAEs). AWs with zero toroidal mode number were observed, e.g., in the ellipticity-induced frequency range in JET [4]. Toroidal periodic non-uniformity of fusion plasmas gives rise to toroidal Alfvén eigenmodes (TAEs). An enlarged spectrum of ideal TAEs was demonstrated to exist within a toroidicity-induced Alfvén gap in [5]. Following the experimental observations of TAEs in a counter-current Neutral Beam Injection (NBI) scenario developed in TCV, an in-depth analysis of the impact of such modes on the global confinement and performance was carried out in [6].

The presence of the so-called non-axisymmetric resonances of wave-particle interaction in stellarators which are associated with the lack of axial symmetry of the magnetic configuration were found in [7] to have a strong stabilizing influence through Landau mechanism on TAEs destabilized by the energetic ions. Thermal ions were also reported in [7] to interact with high frequency Alfvén gap modes (helicity-induced Alfvén Eigenmodes and mirror-induced Alfvén Eigenmodes), leading to a considerable damping of these modes at the high pressure attributed to, e.g., a Helias reactor.

Physics of the transverse energy transfer by Alfvén waves in toroidal plasmas was elucidated in [8]. In contrast to the classical Alfvén waves in infinite plasmas, the Alfvén waves in toroidal systems were found to produce plasma compression due to coupling with fast magnetoacoustic waves with providing the energy transfer. The radial group velocities of the traveling waves constituting the Global Alfvén Eigenmodes and TAEs were calculated. The obtained results were applied to explain how Alfvén eigenmodes could provide the spatial energy channeling - the transfer of the energy by these modes from the unstable plasma region to the region where the mode damping dominated.

Non-linear dynamics of multiple infernal Alfvén eigenmodes—a subset of global Alfvén eigenmodes in tokamak plasmas with extended low-shear central core was studied in [9]. The analysis was carried out for a mode triplet with toroidal mode-numbers n = 1, 2, 3. The temporal evolution of the amplitudes and the phase (responsible for the frequency chirping) of the modes was found to exhibit Hopf bifurcations to stable limit cycles. This conclusion was applied for explanation of a synchronous cyclic destabilization of multiple modes in Alfvén avalanches (sudden growth of amplitudes of the mode cluster with different n and approximately equal frequency spacing) in NSTX and bursting modes in MAST.

Comprehensive overview of studying AWs at Institute of Plasma Physics in Kharkiv including the research carried out in collaboration with the research centers of Sweden, Belgium, United Kingdom and Germany was presented in [10]. In particular, various types of Alfvén eigenmodes (AEs) were reported in [11] to be destabilized by fast ions over a broad frequency range in a series of JET experiments in mixed D–3He plasmas. The radial localization of AEs was identified using an X-mode reflectometer, a multiline interferometer and soft x-ray diagnostics. Two different types of Alfvén cascade (AC) eigenmodes were observed originating from the presence of a local minimum of the safety factor. In addition

Cite as: I. Girka, O. Trush, W. Tierens, East Eur. J. Phys. 1, 79 (2025), https://doi.org/10.26565/2312-4334-2025-1-07

to ACs with frequencies below the frequency of TAEs, ACs with frequencies above the TAE frequency were destabilized by energetic ions. Both ACs were localized in the central regions of the plasma.

The deuterium ions accelerated to MeV range in three-ion radio frequency scenario of NBI were shown in [12,13] to produce fusion-born alpha-particles from the D-3He reaction. These alpha-particles were reported to excite EAEs with toroidal mode indices n = −1 and n = 0. The fusion-born alpha-particles rather than accelerated D-ions were shown to interact with EAEs with negative toroidal mode indices. The n = 0 EAEs were found to be excited only if a fast-ion population energy distribution had so-called 'bump-on-tail distribution (where $\partial f/\partial E > 0$).

The identification of TAEs at different radial locations in counter-current NBI scenarios in TCV was presented in [14]. These modes were reported to be significantly different from the ones observed previously in scenarios with co-current off-axis NBI and electron cyclotron heating.

Fourier analyses of the fast-ion loss detector revealed coherent fast-ion losses in the range of the 1...2 MHz in MAST-U [15]. The losses were found to correlate with modes identified as Compressional and Global Alfvén Eigenmodes by the Mirnov coils.

Local Alfven resonance (AR) as a method of plasma heating was first studied in [16]. Comprehensive overview of theoretical research of plasma Alfven heating was presented in [17]. ARs were effectively applied for plasma production and heating in various fusion devices (see, e.g., [18,19]). However, position of ARs is well-known to move to the plasma edge with increase in plasma density which reduces the efficiency of Alfven method of plasma heating and its application for these purposes in modern experiments. Comprehensive overview of the recent studies of AWs and plasma Alfven heating was given e.g. in [20].

Excitation of surface waves with $|k_z| < k_0$ and $\omega > \omega_{ci}$ within Alfven resonance regions by ICRF antenna was numerically demonstrated in [21] with focusing on the cases of DEMO and ITER (here k_z is toroidal wavenumber, k_0 is vacuum wavenumber, $k_0 = \omega/c$, ω is the wave angular frequency, ω_{ci} is ion cyclotron frequency, and c is the speed of light in vacuum). The fast wave field spatial distribution was obtained by the semi-analytic code ANTITER II in plane geometry by summation of Fourier series over the toroidal and poloidal wave indices. A few well radially separated standing (in toroidal direction) wave patterns in edge plasma were clearly demonstrated. This is different from what was is discussed in the present paper. The difference is explained by the fact that the present paper studies the problem of eigen functions and eigen values rather than that of forced oscillations as it was in [21].

In the present paper, the possibility for eigen ICRF signal to be localized in the vicinity of the local AR

$$S \equiv 1 - \frac{\omega_{pi}^2}{\omega^2 - \omega_{ci}^2} = N_z^2, \tag{1}$$

is shown. In (1), S is the component of cold plasma permittivity tensor in Stix notations [22], $N_z = k_z/k_0$ is toroidal refractive index, and ω_{pi} is ion plasma frequency. The wave field spatial distribution is found analytically in the vicinity of the resonance. The distribution corresponds to the localized ICRF signal: the fields decay exponentially with distance from AR (1), both towards the low-density and the high-density plasma. The dispersion relation is analyzed numerically by means of the standard package "Wolfram Mathematica", version 13.1 [23]. Relevance of the numerical results to possible experimental observations is discussed.

The novelty of the present paper is associated with three issues. First, previous analytical studies of AR fine structure were carried out in the framework of models with linear plasma density variation. This assumption was proved by small scale of kinetic and inertial Alfven waves into which large scale magnetohydrodynamic waves converted within ARs. However, plasma density profile in a tokamak SOL can be modelled as exponential decay with the distance from the plasma core. Sufficiently small decay length makes the search of the wave field spatial distribution out of ARs analytically tractable which is realized in the present paper.

Second, no evanescent layer exists between ARs and high-density plasma in the case of smooth plasma density variation and moderate poloidal wave indices. Existence of the layer is the necessary precondition for the ICRF signal localized spatial distribution. Strong exponential variation of the plasma density in a tokamak SOL causes the existence of the layer.

Third, previous studies (analytical and also many of numerical) were carried out with neglecting the toroidal (parallel to external static magnetic field) wave electric field E_z. This is correct due to sufficiently large absolute value of the plasma permittivity component ε_{zz} (P in Stix notations applied below) in ICRF. This issue made it possible to significantly simplify the analysis by reducing Maxwell's system of equations within ARs to the second order ordinary uniform differential equation. Presence of the evanescent layer for E_z between an antenna and ARs causes decay of forced E_z falling on ARs from the antenna side. However, in the case of eigen waves, the same evanescent layer causes decay of E_z with the distance in opposite direction: from ARs to the metal wall. This results in the necessity to consider coupled electromagnetic waves within ARs described by two coupled second order ordinary nonuniform differential equations. These two coupled equations are solved in the present paper to determine the wave field spatial distribution within ARs.

The paper is arranged as follows. The theoretical model is reported in section II with the emphasis on the SOL separation into four regions within which different asymptotic solutions can be applied. Wave field spatial distribution is presented in section III. The dispersion relation is given in section IV. The results of the numerical study of the dispersion properties are presented in section V. The main conclusions and discussions are found in section VI.

II. MODEL DESCRIPTION

The SOL is considered in slab geometry with x axis being perpendicular to the SOL and directed from the low-density to the high-density plasma (opposite to the radial direction). External static uniform magnetic field $\vec{B}_0$ is parallel to the SOL and directed along z axis, $\vec{B}_0||\vec{z}$. SOL is assumed to be uniform along y axis which is chosen such that x, y and z axes form the right triple of vectors (Fig. 1). Plasma electrodynamic properties are described in terms of cold collisionless plasma dielectric permittivity tensor (in Stix notations [22]):

$$\hat{\varepsilon}(x) = \begin{pmatrix} S & -iD & 0 \\ iD & S & 0 \\ 0 & 0 & P \end{pmatrix}. \tag{2}$$

Within the ion cyclotron frequency range, $\omega_{ci} < \omega \ll |\omega_{ce}|$, the tensor components read

$$S = 1 - \frac{\omega_{pi}^2}{\omega^2 - \omega_{ci}^2},\ D = \frac{\omega_{pi}^2 \omega}{\omega_{ci}(\omega^2 - \omega_{ci}^2)},\ P = 1 - \frac{\omega_{pe}^2}{\omega^2}. \tag{3}$$

Hereinafter, ω_{ce} is electron cyclotron frequency, and ω_{pe} is electron plasma frequency.

The wave field spatial distribution is to be found in the form of Fourier harmonic, e.g., the wave toroidal magnetic field

$$\tilde{H_z}(\vec{r}, t) = H_z(x)\exp\left[i\left(k_z z + k_y y - \omega t\right)\right]. \tag{4}$$

In (4), k_y is poloidal wavenumber. Then the wave amplitudes $E_z(x)$ and $H_z(x)$ spatial distribution is governed by two coupled second order ordinary linear differential equations:

$$\frac{1}{k_0^2}\frac{d^2E_z}{dx^2} + \frac{N_z^2}{k_0^2}\frac{d}{dx}\left(\frac{1}{N_\perp^2}\frac{dE_z}{dx}\right) + \frac{N_z^2 N_y}{k_0}E_z\frac{d}{dx}\left(\frac{\mu}{N_\perp^2}\right) + E_z\left[P - N_y^2 - \frac{N_z^2 N_y^2}{N_\perp^2}\right] = -\frac{iN_z}{k_0^2}\frac{d}{dx}\left(\frac{\mu}{N_\perp^2}\frac{dH_z}{dx}\right) - \frac{iN_z N_y}{k_0}H_z\frac{d}{dx}\left(\frac{1}{N_\perp^2}\right) + \frac{iN_z N_y^2 \mu}{N_\perp^2}H_z, \tag{5}$$

$$\frac{1}{k_0^2}\frac{d}{dx}\left(\frac{1}{N_\perp^2}\frac{dH_z}{dx}\right) + H_z\left[1 - \frac{N_y^2}{N_\perp^2} + \frac{N_y}{k_0}\frac{d}{dx}\left(\frac{\mu}{N_\perp^2}\right)\right] = \frac{i}{k_0^2}\frac{d}{dx}\left(\frac{\mu N_z}{N_\perp^2}\frac{dE_z}{dx}\right) - \frac{iN_y^2}{N_\perp^2}\mu N_z E_z + \frac{iN_z N_y}{k_0}E_z\frac{d}{dx}\left(\frac{1}{N_\perp^2}\right). \tag{6}$$

In (5), and (6), $N_y = k_y/k_0$ is poloidal refractive index, $\mu = -D/(S - N_z^2)$, $N_\perp^2 = (R - N_z^2)(L - N_z^2)/(S - N_z^2)$, $R = S + D$, and $L = S - D$.

To derive the dispersion relation, one needs also the expressions for y-components of electrical and magnetic wave fields:

$$E_y = \frac{-1}{N_\perp^2}\{\frac{i}{k_0}\frac{dH_z}{dx} + N_z N_y E_z + \mu[iN_y H_z + \frac{N_z}{k_0}\frac{dE_z}{dx}]\}, \tag{7}$$

$$H_y = \frac{-N_z}{N_\perp^2}\left\{N_y H_z - \frac{iN_z}{k_0}\frac{dE_z}{dx} + \mu\left[-iN_y N_z E_z + \frac{1}{k_0}\frac{dH_z}{dx}\right]\right\} + \frac{i}{k_0}\frac{dE_z}{dx}. \tag{8}$$

These tangential components should be continuous at the interfaces between the regions specified below.

Plasma particle density is assumed to increase exponentially within the SOL [24],

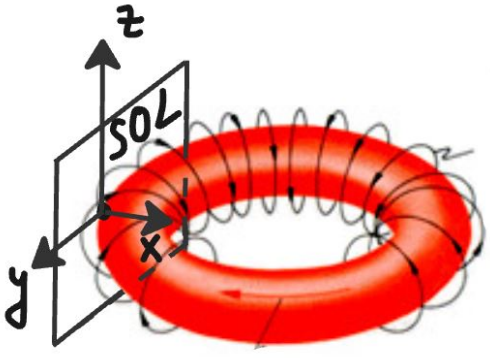

Figure 1. Schematic of the problem

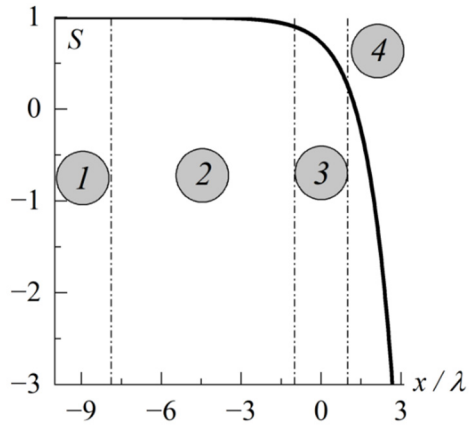

Figure 2. Spatial variation of $S(x)$ (solid curve) and within the low-density SOL. Numbers 1-4 in grey circles indicate the four regions, into which the SOL is separated to make the Maxwell's equations analytically solvable. Dash-dotted vertical lines separate the regions. $n = 3$, $\omega/\omega_{ci} = 5.308$, $R = 2.12\ m$, $\lambda = 0.018\ m$, $B_0 = 2.0\ T$, $n(0) = 8.287 \times 10^{16}\ m^{-3}$)

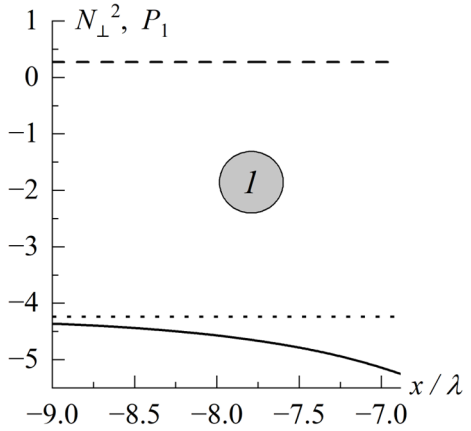

Figure 3. Spatial variation of $N_\perp^2(x)$ (dashed curve), and $P_1(x)$ (solid curve) within the first region. Dotted line corresponds to vacuum value of P_1. The wave and plasma parameters are the same as in Fig. 2

$$n(x) = n_0 \exp\,(x/\lambda). \tag{9}$$

In (9), λ is the decay length, and n_0 is plasma density at $x = 0$ which is considered hereinafter as the position of the local resonance (1). It is the smallness of λ as compared with the tokamak plasma minor radius a which justifies the application of the slab geometry in the present paper, since the studied ICRF signal is shown hereinafter to be localized within the layer with the width of the order of λ.

The components S, D, P (3) of the plasma permittivity tensor, as well as coefficients in Maxwell's equations (5)-(8) vary significantly in low-density SOL. Separation of the SOL into four regions (Fig. 2) according to correlation between the components S, D, and P is explained below. Analytical asymptotic solutions of Eqs. (5)-(6) within these four regions are derived in the next section. The following wave and plasma parameters are applied while calculating the curves in Figs. 2-6: Deuterium single charged ions, toroidal wave index $n = 3$, ratio of the wave frequency to ion cyclotron frequency $\omega/\omega_{ci} = 5.308$, major plasma radius $R = 2.12\ m$, minor plasma radius $a = 0.5\ m$, density decay length $\lambda = 0.018\ m$, the external static uniform magnetic field $B_0 = 2.0\ T$, the plasma density $n(0) = 8.287 \times 10^{16}\ m^{-3}$, and the ion temperature of $T_i = 10.0\ eV$. The electron-ion collision frequency can be estimated for these plasma parameters as $\overline{\nu_{ei}} = 114.0\ kHz$ which is much smaller than ion cyclotron frequency $f_{ci} \approx 14.6\ MHz$. This fact confirms the validity of the collisionless plasma approximation applied in the present paper.

The **first region** (Fig. 3) is determined by the condition that the plasma density is sufficiently small there to provide so-called vacuum conditions:

$$|S - 1| \ll 1, |D| \ll 1, |P - 1| \ll 1. \tag{10}$$

In this region, the wave field spatial distribution can be determined precisely. The wave amplitude is assumed to decay exponentially with the distance from AR (1), $x \to -\infty$. The right boundary x_1 of the first region is determined as

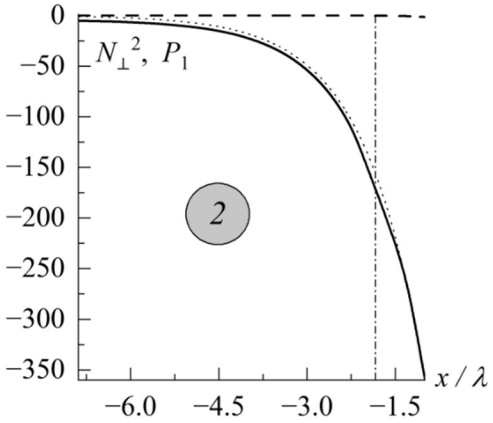

Figure 4. Spatial variation of $N_\perp^2(x)$ (dashed curve), and $P_1(x)$ (solid curve) within the second region. Thin dotted curve demonstrates the asymptotic $P(x)-1$ of $P_1(x)$. Thin vertical dash-dotted line indicates the position of $N_\perp^2(x)=0$. The wave and plasma parameters are the same as in Fig. 2

follows. The factor $P_1 \equiv P - N_y^2 - N_z^2 N_y^2/N_\perp^2$ placed in square brackets in eq. (5) transfers in the vicinity of x_1 from the value $1 - N_y^2 - N_z^2 N_y^2/(1-N_z^2)$, which is inherent for the vacuum, to $P-1$, which is the asymptotic for the larger plasma density, $|P-1| \gg (N_y^2 + N_z^2 - 1)/(1-N_z^2)$:

$$x_1 = \lambda \ln\left(\frac{m_e}{m_i}\frac{\omega^2}{\omega_{ci}^2}\frac{1}{N_A^2(0)}\right). \tag{11}$$

The factor P_1 is shown in Fig. 3 by solid curve. Its maximum deviation from the value $1 - N_y^2 - \frac{N_z^2 N_y^2}{1-N_z^2} \approx -4.237$ given in Fig. 3 by dotted line is observed at $x = x_1$: $P_1(x_1) \approx -5.241$. $N_\perp^2(x)$ is shown in Fig. 3 by dashed curve. It weakly deviates from its vacuum value $N_\perp^2(x \to -\infty) = 1 - N_z^2 \approx 0.276$. Even at the right boundary of the first region, the deviation is smaller than 10^{-4}.

Within the **second region** (Fig. 4), one can neglect plasma particle density, $\omega_{pi}^2 \to 0$, in the expressions for S and D; and must take the difference between P and a unit into account, $|P| \neq 1$. Neglecting the existence of this region would block searching for the solution to the dispersion relation. Comparison of $P_1(x)$ (solid curve in Fig. 4) with its asymptotic $P(x)-1$ presented by thin dotted curve justifies approach to solving eq. (5) presented below. Vertical dash-dotted line indicates the coordinate where $N_\perp^2(x)$ turns to zero and hence, $P_1(x)$ diverges. This divergence is not shown in Fig. 4. Wave fields are known to vary weakly in the vicinity of this coordinate.

The ICRF signal is expected to be localized in the **third region**, where $S \approx N_z^2$ (Fig. 5). Its boundaries can to be determined as follows:

$$-\lambda < x < +\lambda. \tag{12}$$

At the left boundary of the third region, the plasma particle density is sufficiently small to provide the following strong inequalities:

$$|S(-\lambda) - 1| \ll 1, |D(-\lambda)| \ll 1. \tag{13}$$

However, the absolute value of P is already large there, $|P(-\lambda)| \gg 1$. In the particular case, presented in Fig. 5, these quantities are equal: $S(-\lambda) - 1 \approx -0.102$, $D(-\lambda) \approx -0.539$, and $P(-\lambda) \approx -358.543$.

At the right boundary of the third region, the plasma density is sufficiently high, so that μ is almost uniform, $\mu(\lambda) \approx \omega/\omega_{ci}$, and $N_\perp^2$ behaves almost as Alfven refractive index squared, $N_\perp^2(\lambda) \approx N_A^2(\lambda)$ with $N_A \equiv \omega_{pi}/\omega_{ci}$. In the particular case, presented in Fig. 5, $\mu(\lambda) \approx 8.397$, $\omega/\omega_{ci} \approx 5.308$, $N_\perp^2(\lambda) \approx 32.978$, and $N_A^2(\lambda) \approx 20.395$.

The **fourth region** (Fig. 6) lies to the right of the third region,

$$x > +\lambda. \tag{14}$$

In this region, the wave is assumed to decay with the distance from the resonance (1), $x \to +\infty$. The latter boundary condition along with that for $x \to -\infty$ mentioned above provides the localized nature of the ICRF signal under the consideration. Physical essence of the mathematical condition $x \to +\infty$ is that the wave field amplitude decays

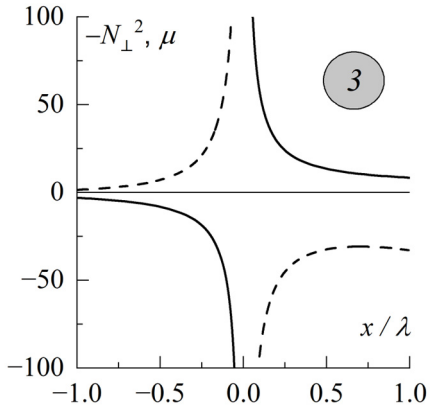

Figure 5. Spatial variation of $\mu(x)$ (solid curve) and $-N_\perp^2(x)$ (dashed curve) within the third region. The wave and plasma parameters are the same as in Fig. 2.

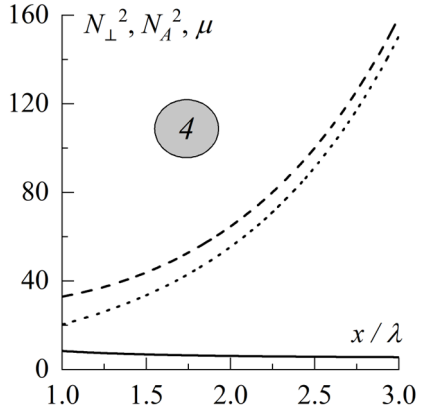

Figure 6. Spatial variation of $\mu(x)$ (solid curve), $N_\perp^2(x)$ (dashed curve), and $N_A^2(x)$ (dotted curve) within the fourth region. The wave and plasma parameters are the same as in Fig. 2

sufficiently before the fast wave reaches the region of its propagation in the high-density plasma. It should be underlined that the $N_\perp^2$ variation in the fourth region approximately follows that of the plasma particle density (9),

$$N_\perp^2 \approx N_A^2(0)\exp(x/\lambda). \tag{15}$$

The latter circumstance significantly simplifies searching the analytical (though approximate) solution to the Maxwell's equations in this region. Note also that μ weakly varies in this region, $\mu \approx \omega/\omega_{ci}$. Weak difference between $N_\perp^2$ and N_A^2 within the fourth region is clearly seen in Fig. 6 where these quantities are shown by dashed and dotted curves respectively. The solid curve in Fig. 6 confirms negligible variation of μ within the fourth region.

III. WAVE FIELD SPATIAL DISTRIBUTION

Within the first region, $-\infty < x < x_1$, both wave field amplitudes $E_z(x)$ and $H_z(x)$ are governed by the same second order uniform differential equations

$$\frac{d^2H_z}{dx^2} + \left(k_0^2 - k_y^2 - k_z^2\right)H_z = 0. \tag{16}$$

Their solutions, which satisfy the boundary condition of the wave field vanishing at $x \to -\infty$, read:

$$H_z = A_1\exp(k_1x),\ E_z = B_1\exp(k_1x). \tag{17}$$

In (17), A_1 and B_1 are the constants of integration, $k_1 = \sqrt{k_y^2 + k_z^2 - k_0^2}$ is assumed to be real observable which physical sense is as follows. The value k_1^{-1} is the spatial scale at which the wave field amplitude decreases by the factor of e. The dependences $E_z(x)$ and $H_z(x)$ within the first region are demonstrated in Fig. 7 by dashed and solid curves respectively to the left of $x_1 \approx -6.885\lambda$. For the plasma parameters applied in calculations for Fig. 7, $k_1 \approx 1.799\ m^{-1}$ is rather small, however, for the wave with $m = 5$, $k_1 \approx 6.0\ m^{-1}$.

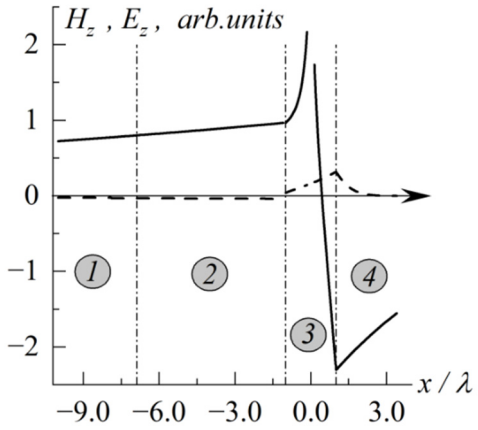

Figure 7. Wave field radial distribution: $H_z(x)$ – solid curves, $E_z(x)$ – dashed curves, $n = 3$, $m = 1$, other data is given in Section V. Vertical dash-dotted lines indicate the boundaries between the regions 1÷4

Within the second region, $x_1 < x < -\lambda$, the wave toroidal magnetic field spatial distribution is governed by the same equation (16) as in the first region unlike that of the wave toroidal electric field which is governed by the following truncated equation:

$$\frac{1}{k_0^2}\frac{d^2E_z}{dx^2} + (P-1)(1-N_z^2)E_z = 0. \tag{18}$$

The solution of eq. (18) can be written in terms of modified Bessel function $I_0(q)$ and McDonald function $K_0(q)$ of the zeroth order:

$$E_z = B_{21}I_0\left(2k_0\lambda\sqrt{(P-1)(N_z^2-1)}\right) + B_{22}K_0\left(2k_0\lambda\sqrt{(P-1)(N_z^2-1)}\right). \tag{19}$$

For the plasma parameters applied in calculations for Fig. 7, the Bessel function arguments in eq. (19) read $0.984\exp(0.5x/\lambda)$.

Within the third region, $-\lambda < x < +\lambda$, one applies the method of narrow layer [16,25] which is generalized in the present report for solving the set of two coupled second order differential equations. Summarizing in brief, the method of narrow layer is appropriate to be applied in the cases opposite to those when the WKB method is applicable one. The wave field spatial distribution within the third region reads

$$H_z = A_{31}\left\{1 - \int_{-\lambda}^{x}[(x+\lambda)k_\perp^2]dx + N_y^2\int_{-\lambda}^{x}\left[k_\perp^2\int_{-\lambda}^{x}\frac{dx}{N_\perp^2}\right]dx - k_y\int_{-\lambda}^{x}\mu dx\right\} - A_{32}\frac{1}{1-N_z^2}\int_{-\lambda}^{x}N_\perp^2 dx$$

$$+iB_{31}\left\{k_zN_y(x+\lambda) - N_y^2N_z\int_{-\lambda}^{x}\left[k_\perp^2\int_{-\lambda}^{x}\frac{\mu dx}{N_\perp^2}\right]dx - \frac{N_zk_y}{1-N_z^2}\int_{-\lambda}^{x}N_\perp^2dx\right\} + iB_{32}N_z\int_{-\lambda}^{x}\mu dx, \tag{20}$$

$$E_z = iA_{31}\left\{N_zk_y^2\int_{-\lambda}^{x}\left[\frac{1}{Q}\int_{-\lambda}^{x}\frac{\mu dx}{N_\perp^2}\right]dx - k_zN_y\int_{-\lambda}^{x}\frac{dx}{QN_\perp^2} + \frac{k_zN_y}{1-N_z^2}\int_{-\lambda}^{x}\frac{dx}{Q}\right\} - iA_{32}N_z\int_{-\lambda}^{x}\frac{\mu dx}{QN_\perp^2}$$

$$+B_{31}\left\{1 - N_z^2k_y\int_{-\lambda}^{x}\frac{\mu dx}{QN_\perp^2} - k_0^2\int_{-\lambda}^{x}\left[\frac{1}{Q}\int_{-\lambda}^{x}\left(P - N_y^2 - \frac{N_z^2N_y^2}{N_\perp^2}\right)dx\right]dx\right\} + B_{32}\frac{1}{1-N_z^2}\int_{-\lambda}^{x}\frac{dx}{Q}. \tag{21}$$

In (20), and (21), the constants of integration A_{31}, A_{32}, B_{31} and B_{32} have clear physical essence. They represent the wave field amplitudes and their derivatives at the left boundary of the region, $x = -\lambda$:

$$A_{31} = H_z(-\lambda),\ A_{32} = \frac{dH_z}{dx}_{|x=-\lambda},\ B_{31} = E_z(-\lambda),\ B_{32} = \frac{dE_z}{dx}_{|x=-\lambda}. \tag{22}$$

In (20), and (21), the following notation is applied

$$Q = \frac{D^2 - S(S-N_z^2)}{D^2 - (S-N_z^2)^2}. \tag{23}$$

The most important benefit from application of Eqs. (20) and (21) is that they connect the values of the wave fields at the opposite sides of the resonance (1).

The problem of electromagnetic energy absorption in the vicinity of the resonance (1) is out of scope of the present paper. Consequently, the wave field distribution shown in Fig. 7 within the third region is discontinuous: no data is presented for $-0.147\lambda < x < 0.147\lambda$. The figure 0.147 corresponds to the characteristic local resonance width, $\Delta x \sim (\rho_{Li}^2 \lambda)^{\frac{1}{3}} \approx 5.3 \times 10^{-3}\ m$ [16,26,27] (here ρ_{Li} is ion Larmor radius). Exclusion of this interval of coordinates from the consideration results in absence of evident resonant behavior of the wave electric field E_z unlike the wave magnetic field H_z which demonstrates resonant growth with approaching to the coordinate $x = 0$. The absence of E_z resonant behavior in Fig. 7 can be explained by different type of the wave field singularity in the cold plasma approximation, in which $H_z \propto \ln|S - N_z^2|$ and $E_z \propto (S - N_z^2)^{-2}$ which means that the resonance of E_z is narrower than that of H_z.

One can note different nature of $H_z(x)$ dependence on opposite sides of the resonant point $x = 0$ presented in Fig. 7. The wave field $H_z(x)$ decays with distance from $x = 0$ to the left ($x < 0$) unlike it crosses the x-axis to the right of the resonant coordinate (at $x \approx 0.44\lambda$). This circumstance agrees with the behavior of $N_\perp^2$ presented in Fig. 5. Since $N_\perp^2 \to +\infty$ for $x \to +0$, the fast wave has a narrow propagation region to the right of the resonant point. It is this region which (in combination with the evanescent region in the fourth region) gives rise to the possibility of the localized ICRF signal studied in the present paper to exist. For $x < 0$, the wave field amplitude $H_z(x)$ decays with the distance from the resonance point but never turns to zero. Within the propagation region, $H_z(x)$ should spatially oscillate which means periodic turning to zero. Since the propagation region is narrow then one observes only one period of such oscillations.

In the fourth region, $x > \lambda$, the coupling between the fast and slow modes can be neglected. To determine the spatial distribution of the wave toroidal magnetic field one can apply eq. (6) which truncated form reads:

$$\frac{1}{k_0^2}\frac{d}{dx}\left(\frac{1}{N_\perp^2}\frac{dH_z}{dx}\right) + \frac{N_y}{k_0}\frac{d}{dx}\left(\frac{\mu}{N_\perp^2}\right)H_z = 0. \tag{24}$$

The term "$H_z \frac{N_y}{k_0}\frac{d}{dx}\left(\frac{\mu}{N_\perp^2}\right)$" in the l.h.s. of eq. (6) appears to be larger by the order of magnitude than "H_z" and "$-N_y^2 H_z/N_\perp^2$ due to strong change of the plasma density (9). This was also confirmed by numerical calculations. Solution of eq. (24) which satisfies the boundary condition of vanishing with going inside the plasma reads

$$H_z = A_4 \exp(-k_4 x). \tag{25}$$

In (25), $k_4 = \frac{\left(\sqrt{1+4\lambda k_y \omega/\omega_{ci}}-1\right)}{2\lambda} \approx \frac{k_y \omega}{\omega_{ci}} > 0$ with k_4^{-1} being the spatial scale at which the wave amplitude decreases by exp. For the plasma parameters applied in calculations for Fig. 7, $k_4 \approx 9.17\ m^{-1}$. It is even larger for the waves with $m = 5$: $k_4 \approx 34.03\ m^{-1}$, which means that the wave amplitude decreases by exp at the distance of $0.024\ m$.

The spatial distribution of the wave toroidal electric field can be found from eq. (5) which can be simplified in the fourth region as follows:

$$\frac{1}{k_0^2}\frac{d^2 E_z}{dx^2} + P E_z = 0. \tag{26}$$

The solution of eq. (26) which satisfies the boundary condition of vanishing with going inside the plasma reads

$$E_z = B_4 K_0\left(2\lambda\omega_{pe}/c\right). \tag{27}$$

For the plasma parameters applied in calculations for Fig. 7, the McDonald function argument in eq. (27) reads $1.872\exp(0.5x/\lambda)$.

IV. DISPERSION RELATION

In Section III, the wave field spatial distribution is derived with ten constants of integration. This means that application of the boundary conditions can result in the dispersion relation in the form of the ten-order determinant equal to zero. Such approach does not cause any numerical problems. However, on one hand, the ten-order determinant contains a lot of zero components. And on the other hand, the constants of integration A_{31}, A_{32}, B_{31} and B_{32} can be easily expressed in terms of A_1, B_1, B_{21}, and B_{22} which makes it possible to reduce the dispersion relation to the form with the six-order determinant equal to zero, $|a_{ij}| = 0$. This conversion does not cause any technical (mathematical) problems. Moreover, even this six-order determinant contains fourteen zero components. The components of the six-order determinant representing the dispersion relation are presented in Annex 1.

V. RESULTS OF NUMERICAL ANALYSIS OF THE DISPERSION RELATION

The dispersion relation is analyzed numerically by means of the standard package "Wolfram Mathematica", version 13.1 [23]. Some results are presented in Table 1. The code input includes the wave toroidal and poloidal indices,

Table 1. Eigen frequencies, Alfven refractive index squared in the resonance (1), $N_A^2(0)$, coefficient of proportionality between $N_A^2(0)$ and $(\omega/\omega_{ci})^2$

Toroidal wave index	Eigen angular frequency, ω/ω_{ci}	Eigen frequency, $\omega/(2\pi)$, MHz	$\frac{\omega_{pi}^2(0)}{\omega_{ci}^2}$	$\frac{N_A^2(0)}{(\omega/\omega_{ci})^2}$
1	1.855	27.063	0.83	0.241
2	3.562	51.959	3.34	0.263
3	5.308	77.437	7.50	0.266
4	7.062	103.026	13.34	0.267
5	8.819	128.653	20.84	0.268
6	10.577	154.301	30.02	0.268

plasma minor and major radii, and the plasma density decay length. ICRF normalized frequency ω/ω_{ci} is the code output.

Numerical solution of the dispersion relation is practically insensitive to the poloidal wave index value. The data for $n = 5{,}6$ is displayed in Table 1. However, the precision of the solutions (20)-(21) is unsatisfactory (44%) for $n = 5$, and it is even worse (76%) for $n = 6$. Assumption of existence of the sufficiently large evanescent region (fourth region) to the right of the resonance (1), where the fast wave decays with the distance from the resonance to the high-density plasma, fails for larger toroidal wave indices.

VI. CONCLUSIONS AND DISCUSSIONS

The following conclusions can be made from the presented analysis. First, the eigen frequencies are approximately proportional to the toroidal wave index, $\omega \propto |n|$. This feature is also known for Alfven waves. Consequently, the frequencies are almost equidistant. The eigen frequencies in Table 1 increase by about $\Delta\omega \approx 1.76\ \omega_{ci}$ with enhancing the toroidal wave index by a unit.

Second, the following question naturally arises when one scrutinizes the figures in Table 1: why the Table does not contain any data concerning the higher toroidal wave indices $n > 6$. The answer is that, first, for larger values of n (higher frequencies) the conditions of applicability of the applied approach worsen. Indeed, the change in the argument of exponential function in eq. (24), $k_4\Delta x$, within the evanescent region should be large. The local resonance (1) shifts to the denser plasma with increase of n, and the change $k_4\Delta x$ decreases. In particular, for chosen plasma parameters, this shift from the resonance position related to $n = 6$ to that related to $n = 3$ is $2.47\ cm$, while the distance between the H_z cut-off [28] position and the resonance position shortens from $7.48\ cm$ in the case of $n = 3$ to $2.71\ cm$ in the case of $n = 6$. And the second, the third term in the l.h.s. of eq. (6) should prevail over the first one to provide applicability of truncated eq. (24) in the fourth region. The following restriction can be derived from the latter condition:

$$\omega^3 \ll c^2\omega_{ci}/(a\lambda). \tag{28}$$

In (28), it is taken into account that $1 - N_z^2 \approx 0.27$ according to the data in Table 1 for all presented values of the toroidal wave indices. For the chosen plasma parameters, the r.h.s. of eq. (28) can be estimated as $\omega^3 \ll c^2\omega_{ci}/(a\lambda) \approx 1.7 \times 10^3\omega_{ci}^3$ or $\omega \ll 12.0\omega_{ci}$.

Third, it is assumed in the present paper that the RF signal is centered in the resonance (1), where

$$N_A^2(0) = (1 - N_z^2)(\omega^2/\omega_{ci}^2 - 1). \tag{29}$$

With taking into account that $\omega \propto |n|$ and hence $N_z^2 \approx Const = 0.72$ as well as $\omega^2 \gg \omega_{ci}^2$ one concludes from eq. (29) that the plasma particle density at the coordinate, where the RF signal is centered, should be almost proportional to the frequency squared, $n(0) \propto \omega^2$ (see the right column in Table 1). On one side, in this respect, numerical results agree with theoretical foresight. On the other side, this means that the coordinate, where the RF signal is predicted to be centered, varies with toroidal wave index n. If this variation is larger than the characteristic local resonance width, $\Delta x \sim (\rho_{Li}^2\lambda)^{\frac{1}{3}} \approx 5.3 \times 10^{-3}\ m$ [16,26,27], one should expect series of ICRF signals in a tokamak SOL, like it was reported in [21]. In the opposite case, ICRF signals spatially overlap and several frequencies should be registered in approximately one position with a nonzero width.

Fourth, the waves with negative poloidal wave indices, $m < 0$, do not contribute to the studied phenomenon. This is explained by the fact that the plasma is propagative for the fast magnetosonic waves with negative poloidal wave indices, $m < 0$, in the fourth region. From mathematical point of view, this conclusion results from the fact that both terms in eq. (24) are of the same sign in this case. This sign coincidence provides propagative character of the solution of eq. (24) which contradicts the initial assumption of the localized nature of the studied RF signal.

The numerical results were explained in [21] based on Fig. 3 in [21] as follows. Surface waves were suggested to arise in the evanescent region bordered by two propagative regions. Such structure is well-known from Quantum Mechanics (see e.g., [29]). The structure is called in Quantum Mechanics as “one-dimensional square potential barrier”. The wave function is well-known to fall from the left propagative region, reflect from the barrier and exponentially decay

within the evanescent region, and then the wave function propagates further into the right propagative region. To get localized increase of the wave amplitude (which is clearly seen in Fig. 13 in [21]), one needs the opposite structure: propagative region should be bordered by two evanescent regions. And just this structure was considered in [21]. The fast wave field spatial distribution was obtained there by the summation of the wave harmonics over k_z and k_y terms. For the wave harmonics with $k_y^2 + k_z^2 > k_0^2$, the left region (vacuum) is the evanescent region. Then a small propagative region takes place near Alfven resonance. And further there is an evanescent region to the right of Alfven resonance before the plasma density becomes sufficiently high and the plasma becomes propagative in the plasma core.

Mechanisms of RF signals' excitation are not discussed in the present paper. The problem of eigen values and eigen functions is considered only. Such signals can be excited either by ICRF antenna, by parametric decay or by energetic ion tails. At the same time, the suggested localized RF signal can still be considered as one of the mechanisms responsible for undesirable ICRF power absorption in the SOL.

Acknowledgement

Two of the authors are very thankful to Ukrainian Armed Forces for being alive. One of the authors is grateful to German people and in particular to IPP for the chance to live and work in Garching. Fruitful discussions with Drs. O. Girka and M. Usoltseva are highly appreciated.

Annex 1.

The components of the determinant a_{ij} which form the dispersion relation of the studied waves read:

$$a_{11} = a_{12} = 0,\ a_{13} = N_4 \equiv k_4/k_0,\ a_{14} = 1.0,\ a_{15} = N_z\omega/\omega_{ci},$$
$$a_{16} = -\omega_{pe}(0)N_z q K_1(q)/\omega_{ci},\ q = 2\lambda\sqrt{e(1-N_z^2)(\omega^2-\omega_{ci}^2)}/c, \quad (30)$$
$$a_{21} = a_{22} = 0,\ a_{23} = N_4 N_z\omega/\omega_{ci},\ a_{24} = a_{15},\ a_{25} = N_A^2(0)e,$$
$$a_{26} = -\omega_{pe}(0)a_{25}qK_1(q)/\omega, \quad (31)$$

$$a_{31} = \frac{N_z N_y}{1-N_z^2} - k_0\lambda N_y^2 N_z I_1,\ a_{32} = \frac{\sigma_1}{N_z^2-1} + \frac{N_z^2 N_y}{a_{25}}\frac{\omega}{\omega_{ci}}\sigma_2 + k_0\lambda\sigma_2 I_2,$$

$$a_{33} = 0,\ a_{34} = -\frac{N_z}{a_{25}}\frac{\omega}{\omega_{ci}},\ a_{35} = -1.0,\ a_{36} = 0, \quad (32)$$

$$a_{41} = -k_0^2\lambda^2 N_z I_3 + \frac{k_z\lambda N_y}{1-N_z^2} I_4 + k_0\lambda N_y N_z I_5 + k_1\lambda N_z I_6,$$

$$a_{42} = \frac{k_0\lambda\sigma_1}{N_z^2-1} I_4 - \sigma_2 - N_z^2 N_y\sigma_2 k_0\lambda I_6 + k_0^2\lambda^2\sigma_2 I_7,$$

$$a_{43} = a_{44} = a_{45} = 0,\ a_{46} = K_0(q), \quad (33)$$

$$a_{51} = 2k_0\lambda + k_0\lambda N_y^2 I_8 + \frac{N_1}{N_z^2-1},\ a_{52} = \frac{N_z N_y\sigma_2}{1-N_z^2} - N_y^2 N_z\sigma_2 k_0\lambda I_1,$$

$$a_{53} = a_{55} = 0,\ a_{54} = 1/a_{25},\ a_{56} = \omega_{pe}(0)N_z K_1(q)\sqrt{e}/(\omega_{ci}a_{25}) \quad (34)$$

$$a_{61} = 1 + k_0^2\lambda^2 I_9 + k_0^2\lambda^2 N_y^2 I_{11} - k_y\lambda I_{12} + \frac{k_1\lambda}{N_z^2-1} I_{13},\ a_{62} = 2N_y\sigma_2 k_z\lambda + N_z\sigma_1 k_0\lambda I_{12} + \frac{N_z k_y\lambda\sigma_2}{1-N_z^2} I_{13} - N_y^2 N_z\sigma_2 k_0^2\lambda^2 I_{14},$$

$$a_{64} = a_{65} = a_{66} = 0,\ a_{63} = -1. \quad (35)$$

The expressions for a_{32}, a_{42}, a_{52}, a_{62} contain the notations $\sigma_{1,2}$:

$$\sigma_1 = \frac{\xi_2}{k_0\lambda}\begin{Bmatrix} 0.5\xi_1[I_1(\xi_2)K_1(\xi_1) - I_1(\xi_1)K_1(\xi_2)] \\ +k_1\lambda[I_1(\xi_2)K_0(\xi_1) + I_0(\xi_1)K_1(\xi_2)] \end{Bmatrix}, \quad (36)$$

$$\sigma_2 = \xi_1[I_1(\xi_1)K_0(\xi_2) + I_0(\xi_2)K_1(\xi_1)] + 2k_1\lambda[I_0(\xi_2)K_0(\xi_1) - I_0(\xi_1)K_0(\xi_2)], \quad (37)$$

where the arguments of the Bessel functions read

$$\xi_1 = 2k_0\lambda\sqrt{\frac{1-N_z^2}{e}},\ \xi_2 = \frac{2\lambda\omega_{ci}}{c}\sqrt{N_A^2(0)\frac{m_i}{m_e}\frac{1-N_z^2}{e}}. \quad (38)$$

In (32)-(35), the definite integrals I_i read

$$I_1 = -\int_{-\lambda}^{\lambda}\frac{\mu}{N_\perp^2}d\left(\frac{x}{\lambda}\right), \quad (39)$$

$$I_2 = \int_{-\lambda}^{\lambda}\left(P - N_y^2 - \frac{N_z^2 N_y^2}{N_\perp^2}\right)d\left(\frac{x}{\lambda}\right), \quad (40)$$

$$I_3 = -\int_{-\lambda}^{\lambda}\left(\frac{1}{Q}\int_{-\lambda}^{x}\frac{\mu}{N_\perp^2}d\left(\frac{x}{\lambda}\right)\right)d\left(\frac{x}{\lambda}\right), \quad (41)$$

$$I_4 = \int_{-\lambda}^{\lambda}\frac{1}{Q}d\left(\frac{x}{\lambda}\right), \quad (42)$$

$$I_5 = -\int_{-\lambda}^{\lambda} \frac{1}{QN_\perp^2} d\left(\frac{x}{\lambda}\right), \tag{43}$$

$$I_6 = -\int_{-\lambda}^{\lambda} \frac{\mu}{QN_\perp^2} d\left(\frac{x}{\lambda}\right), \tag{44}$$

$$I_7 = \int_{-\lambda}^{\lambda} \left(\frac{1}{Q}\int_{-\lambda}^{x} \left(P - N_y^2 - \frac{N_z^2 N_y^2}{N_\perp^2}\right) d\left(\frac{x}{\lambda}\right)\right) d\left(\frac{x}{\lambda}\right), \tag{45}$$

$$I_8 = -\int_{-\lambda}^{\lambda} \frac{1}{N_\perp^2} d\left(\frac{x}{\lambda}\right), \tag{46}$$

$$I_9 = -\int_{-\lambda}^{\lambda} N_\perp^2 (1 + \frac{x}{\lambda}) d\left(\frac{x}{\lambda}\right), \tag{47}$$

$$I_{11} = \int_{-\lambda}^{\lambda} (N_\perp^2 \int_{-\lambda}^{x} \frac{1}{N_\perp^2} d\left(\frac{x}{\lambda}\right)) d\left(\frac{x}{\lambda}\right), \tag{48}$$

$$I_{12} = \int_{-\lambda}^{\lambda} \mu d\left(\frac{x}{\lambda}\right), \tag{49}$$

$$I_{13} = -\int_{-\lambda}^{\lambda} N_\perp^2 d\left(\frac{x}{\lambda}\right), \tag{50}$$

$$I_{14} = \int_{-\lambda}^{\lambda} (N_\perp^2 \int_{-\lambda}^{x} \frac{\mu}{N_\perp^2} d\left(\frac{x}{\lambda}\right)) d\left(\frac{x}{\lambda}\right). \tag{51}$$

All these integrals are dimensionless values. Some of the integrands, like in (47)-(51), are singular. For these integrals, Cauchy principal values should be taken. Imaginary parts of these integrals refer to the wave absorption and damping which are out of scope of the present paper as it is already mentioned above.

It is important to note the following significant difference between the case of exponential variation (9) of the plasma density used in the present paper and a linear one, $n_{lin} = n_0(1 + x/\lambda)$. If the variations of the numerators of the integral functions along x are neglected, the Cauchy principal value of integrals with linear variation of the resonant denominators within the symmetric limits is known to be equal to zero which is not the case for exponential variation of the resonant denominators. Indicated difference explains the absence of the wave field spatial distribution symmetry within the third region and consequently influences the dispersion relation.

ORCID

I. Girka, https://orcid.org/0000-0001-6662-8683; **O. Trush,** https://orcid.org/0000-0001-5105-2335
W. Tierens, https://orcid.org/0000-0002-6979-8140

REFERENCES

[1] H. Alfven, "Existence of electromagnetic – hydrodynamic waves," Nature, **150**(3805), 405–406 (1942). https://doi.org/10.1038/150405d0
[2] T.K. Allen, W.R. Baker, R.V. Pyle, and J.M. Wilcox, "Experimental generation of plasma Alfven waves," Phys. Rev. Letters, **2**(9), 383–384 (1959). https://doi.org/10.1103/PhysRevLett.2.383
[3] R. Betti, and J.P. Freidberg, "Ellipticity induced Alfven eigenmodes," Phys. Fluids B, **3**(8), 1865–1870 (1991). https://doi.org/10.1063/1.859655
[4] H.J.C. Oliver, S.E. Sharapov, B.N. Breizman, L.-J. Zheng, and JET Contributors, "Axisymmetric global Alfvén eigenmodes within the ellipticity-induced frequency gap in the Joint European Torus," Phys. Plasmas, **24**, 122505 (2017). https://doi.org/10.1063/1.5005939
[5] J. Candy, B.N. Breizman, J.W. Van Dam, and T. Ozeki, "Multiplicity of low-shear toroidal Alfvén eigenmodes," Physics Letters A, 215(5-6), 299-304 (1996).
[6] S. Mazzi, M. Vallar, U. Kumar, O. Krutkin, J. Poley-Sanjuan, L. Simons, J. Ball, S. Brunner, S. Coda, J. Garcia, A. Iantchenko, Ye.O. Kazakov, W.H. Lin, J. Ongena, B. Rofman, L. Villard, and the TCV team, "Study of fast-ion-driven toroidal Alfvén eigenmodes impacting on the global confinement in TCV L-mode plasmas," Front. Phys. Sec. Fusion Plasma Physics, **1**, 01-19 (2023). https://doi.org/10.3389/fphy.2023.1225787
[7] Y.I. Kolesnichenko, and A.V. Tykhyy, "Landau damping of Alfvénic modes in stellarators," Plasma Physics and Controlled Fusion, **60**(12), 125004 (2018). https://doi.org/10.1088/1361-6587/aae60a
[8] Ya.I. Kolesnichenko, Yu.V. Yakovenko, and M.H. Tyshchenko, "Mechanisms of the energy transfer across the magnetic field by Alfvén waves in toroidal plasmas," Physics of Plasmas, **25**(12), 122508 (2018). https://doi.org/10.1063/1.5049543
[9] V.S. Marchenko, S.N. Reznik, and Y.I. Kolesnichenko, "Nonlinear dynamics of multiple Alfvén modes driven by trapped energetic ions in tokamaks: A triplet paradigm," Physics of Plasmas, **31**(2), 022507 (2024). https://doi.org/10.1063/5.0186886
[10] V.E. Moiseenko, M.B. Dreval, Yu.V. Kovtun, Yu.S. Kulyk, G.P. Glazunov, Ye. O. Kazakov, J. Ongena, *et al*., "Fusion research in stellarator department of IPP NSC KIPT," PAST, 6, 3–8 (2022). https://doi.org/10.46813/2022-142-003
[11] M. Dreval, S.E. Sharapov, Ye.O. Kazakov, J. Ongena, M. Nocente, R. Calado, R. Coelho, J. Ferreira, A. Figueiredo, M. Fitzgerald, J. Garcia, C. Giroud, N.C. Hawkes, V.G. Kiptily, F. Nabais, M.F.F. Nave, H. Weisen, T. Craciunescu, M. Salewski, Ž. Štancar, and JET Contributors, "Alfvén cascade eigenmodes above the TAE-frequency and localization of Alfvén modes in D-3He plasmas on JET," Nuclear Fusion, **62**, 056001 (2022). https://doi.org/10.1088/1741-4326/ac45a4
[12] V.G. Kiptily, M. Fitzgerald, Ye O. Kazakov, J. Ongena, M. Nocente, S.E. Sharapov, M. Dreval, Ž. Štancar, T. Craciunescu, J. Garcia, L. Giacomelli, V. Goloborodko, H.J.C. Oliver, H. Weisen, and JET Contributors, "Evidence for Alfvén eigenmodes driven by alpha particles in D-3He fusion experiments on JET," Nuclear Fusion, **61**, 114006 (2021). https://doi.org/10.1088/1741-4326/ac26a2
[13] V. Kiptily, Ye. O. Kazakov, M. Nocente, J. Ongena, F. Belli, M. Dreval, T. Craciunescu, J. Eriksson, M. Fitzgerald, L. Giacomelli, V. Goloborodko, M.V. Iliasova, E.M. Khilkevitch, D. Rigamonti, A. Sahlberg, M. Salewski, A.E. Shevelev, J. Garcia, H.J.C. Oliver, S.E. Sharapov, Z. Stancar, H. Weisen, and JET Contributors, "Excitation of Alfvén eigenmodes by fusion-born

alpha-particles in D-3He plasmas on JET," Plasma Physics and Controlled Fusion, **64**, 064001 (2022). https://doi.org/10.1088/1361-6587/ac5d9e
[14] M. Vallar, M. Dreval, B. Duval, M. Garcia-Munoz, S. Sharapov, J. Poley-Sanjuan, A. Karpushov, P. Lauber, and TCV team, "Energetic particle modes in TCV with two neutral beam injectors," in: *Proc. 48th EPS Conference on Plasma Physics*, (2022). https://lac913.epfl.ch/epsppd3/2022/pdf/O4.110.pdf
[15] F. Rivero-Rodriguez, M. García-Muñoz, S. Sharapov, K. McClements, N. Crocker, M. Cecconello, M. Dreval, D. Dunai, M. Fitzgerald, J. Galdon-Quiroga, S. Gibson, C. Michael, J. Oliver, T. Rhodes, D. Ryan, L. Velarde, E. Viezzer, and MAST-U Team, "Experimental observations of fast-ion losses correlated with Global and Compressional Alfvén Eigenmodes in MAST-U," in: *Proc. 48th EPS Conference on Plasma Physics*. (2022). https://lac913.epfl.ch/epsppd3/2022/pdf/O4.109.pdf
[16] V.V. Dolgopolov, and K.N. Stepanov, "Cerenkov absorption of Alfvén waves and of fast magneto-acoustic waves in an inhomogeneous plasma," Nuclear Fusion, **5**, 276-278 (1965). https://doi.org/10.1088/0029-5515/5/4/003
[17] J. Vaclavik, and K. Appert, "Theory of plasma heating by low frequency waves: magnetic pumping and Alfven resonance heating," Nuclear Fusion, **31**(10), 1945-1997 (1991). https://doi.org/10.1088/0029-5515/31/10/013
[18] A.G. Elfimov, E.A. Lerche, R.M.O. Galvao, L.F. Ruchko, A.M.M. Fonseca, R.P. da Silva, and V. Bellintani, "Results of Localized Alfv´en Wave Heating in TCABR," Brazilian Journal of Physics, **34**(4B), 1707-1714 (2004). https://doi.org/10.1590/s0103-97332004000800036
[19] V.E. Moiseenko, Ye.D. Volkov, V.I. Tereshin, and Yu.S. Stadnik, "Alfvén resonance heating in Uragan-2M torsatron," Plasma Physics Reports, **35**(10), 828-833 (2009). https://doi.org/10.1134/S1063780X09100043
[20] I.O. Girka, "Fine structure of the local Alfven resonances in cylindrical plasmas with axial periodic inhomogeneity," in: *Problems of theoretical physics. Scientific works*, Issue 5. edited by V. O. Buts, (V.N. Karazin Kharkiv National University, Kharkiv, 2023). pp. 367-437.
[21] A. Messiaen, and V. Maquet, "Coaxial and surface mode excitation by an ICRF antenna in large machines like DEMO and ITER," Nuclear Fusion, **60**, 076014 (2020). https://doi.org/10.1088/1741-4326/ab8d05
[22] T.H. Stix, *Waves in Plasmas*, (American Institute of Physics, 1992).
[23] S. Wolfram, "Launching Version 13.1 of Wolfram Language & Mathematica," Stephen Wolfram Writings, (2022). https://writings.stephenwolfram.com/2022/06/launching-version-13-1-of-wolfram-language-mathematica/
[24] P.C. Stangeby, *The plasma boundary of magnetic fusion devices*, (Institute of Physics Publishing, 2000).
[25] I.O. Girka, and W. Tierens "Surface wave propagation along a narrow transition layer in a slab Voigt geometry," Physics of Plasmas, **31**, 022106 (2024). https://doi.org/10.1063/5.0182688
[26] I.A. Girka, and K.N. Stepanov, "Absorption and conversion of longwavelength fast magnetosonic waves in the region of local resonance in peripheral plasma," Ukrainian Journal of Physics, **35**, 1680-1688 (1990). (in Russian)
[27] I.A. Girka, V.I. Lapshin, and K.N. Stepanov, "Plasma heating near satellite Alfven resonances in stellarators," Plasma Physics Reports, **23**, 19-27 (1997).
[28] I.O. Girka, O.V. Trush, and W. Tierens, "Three different spatial positions of fast magnetosonic wave component turning points," Problems of Atomic Science and Technology. Series "Plasma Physics", 6, 86-91 (2024). https://doi.org/10.46813/2024-154-014
[29] A. Messiah, *Quantum Mechanics,* vol. 1 (North Holland Publishing Company, 1964).

ВЛАСНІ ВИСОКОЧАСТОТНІ СИГНАЛИ, ЛОКАЛІЗОВАНІ В ОКОЛІ АЛЬФВЕНОВИХ РЕЗОНАНСІВ ЗА ОСТАННЬОЮ МАГНІТНОЮ ПОВЕРХНЕЮ ТОКАМАКА

І. Гірка[a], О. Труш[a], В. Тіренс[b]
[a]Харківський національний університет імені В.Н. Каразіна, Харків, Україна
[b]Оук-Риджська національна лабораторія, Оук-Ридж, США

Розглянуто власні електромагнітні хвилі з малими тороїдними номерами моди та позитивними полоїдними номерами моди в іонному циклотронному діапазоні частот (ІЦДЧ). Теоретично показано, що існують хвилі у формі сигналів, локалізованих поблизу локальних Альфвенових резонансів (АР) за останньою замкненою магнітною поверхнею (ОЗМП) токамака. Просторове загасання в напрямку меншої густини плазми забезпечуються наявністю ненульових полоїдних номерів моди. Вузькі області просторового загасання в напрямку вищої густини плазми викликані сильною неоднорідністю плазми. Ці останні області відокремлюють АР від ОЗМП та центру плазми з високою густиною, який є областю поширення хвиль ІЦДЧ. Дисперсійне рівняння високочастотних сигналів виведено аналітично з застосуванням асимптотичних методів і розв'язано чисельно. Обговорено можливий зв'язок здобутих результатів з експериментальними вимірюваннями. Вичерпне визначення джерел збудження сигналів виходить за межі цього дослідження.

Ключові слова: *власні хвилі; іонний циклотронний діапазон частот; Альфвенів резонанс; остання замкнена магнітна поверхня токамака; асимптотичні методи; дисперсійне рівняння*

EAST EUROPEAN JOURNAL OF PHYSICS. **1.** 91-100 (2025)
DOI:10.26565/2312-4334-2025-1-08 ISSN 2312-4334

GENERATION OF ELECTROMAGNETIC ION CYCLOTRON WAVE BY HOT INJECTION OF ION BEAM FOR RING DISTRIBUTION WITH A.C. ELECTRIC FIELD IN JOVIAN MAGNETOSPHERE

Garima Yadav[a], B.S. Sharma[a], Ankita[b]*
[a]*Department of Physics, Lords University, Alwar-301001, India*
[b]*Department of Physics, Amity Institute of Applied Sciences, Amity University, Sector-125 Noida, Uttar Pradesh, India*
**Corresponding Author e-mail: ankitac@amity.edu*
Received September 11, 2024; revised November 29, 2024; in final form December 20, 2024; accepted January 7, 2025

This paper investigates the electromagnetic ion-cyclotron waves detected by the Ulysses spacecraft within the Jovian magnetosphere. Various types of high-frequency radio emissions resulting from resonant interactions have been identified in this region. The study focuses on the wave-particle interactions between electromagnetic ion-cyclotron waves and fully ionized magnetospheric plasma particles, considering the parallel propagation of these waves. This allows for a detailed evaluation of the dispersion relation with a ring distribution in the presence of a parallel alternating current (AC) electric field within a collisionless magnetosphere of Jupiter. Using a method of characteristics and a kinetic approach, we derive an expression for the relativistic growth rate. Additionally, we analyze injection events recorded by the Galileo spacecraft through its energetic particle detector (EPD) in the Jovian magnetosphere. Following the injection of a hot ion beam, we conduct a parametric analysis of various plasma parameters, such as temperature anisotropy, AC frequency, and relativistic factors, to examine their effects on the growth rate, which is illustrated through plotted graphs.
Keywords: *Electromagnetic ion-cyclotron waves; Ring distribution; Hot ion injection; Jovian magnetosphere*
PACS: 52.35Fp, 94.30Ch, 96.30Pj

1. INTRODUCTION

Electromagnetic ion cyclotron (EMIC) waves, typically left-hand polarized, are generated by the anisotropic temperature distribution of ions, particularly those in the energy range of 10–100 keV [1]. These waves are primarily formed near the magnetic equator of planetary magnetospheres and propagate along magnetic field lines toward higher latitudes [2], [3], [4]. Jupiter, the largest planet in our solar system, is a gas giant with a unique magnetosphere that plays a key role in the planet's dynamic environment. The magnetosphere is primarily shaped by Jupiter's rapid rotation and metallic hydrogen interior, with additional influence from its extensive moon system[4]. In Earth's magnetosphere, EMIC waves are categorized by the gyro frequencies of hydrogen, helium, and oxygen ions, with distinct emissions in the H-band, He-band, and O-band. Previous studies have shown that EMIC waves interact with energetic ions and relativistic electrons, playing a crucial role in the energization of cold ions and the loss of high-energy particles [5], [6], [7], [8]. Particles interacting with EMIC waves can be scattered into the loss cone, leading to precipitation into the upper atmosphere [9]. Observational studies have also shown that EMIC waves can contribute to the heating of He+ ions and electrons [10]. Recent studies have shown that electromagnetic ion cyclotron (EMIC) waves in Jupiter's magnetosphere are generated by anisotropic ions, particularly in regions where ion density and temperature anisotropy are high [11], [12], [13]. For instance, EMIC waves observed in the post-noon to dusk sector are attributed to the thermal anisotropy of strong ions in the current ring region. This suggests that the formation of EMIC waves is closely linked to the presence of ion rings and the cooling of plasma in specific regions of the magnetosphere [14], [15], [16].

The Jovian magnetosphere is an extremely dynamic environment, characterized by intense electromagnetic fields that significantly influence the motion and energy distributions of charged particles. One such phenomenon observed in this environment is the ring distribution, a specific arrangement of particle energies and pitch angles. Ring distributions are often associated with non-thermal electron populations that exhibit an anisotropic energy distribution, commonly seen in the presence of alternating current (A.C.) electric fields. These fields are thought to play a critical role in the acceleration and transport of electrons, facilitating the formation of the ring-like structures [17].

Recent studies have highlighted the significance of wave-particle interactions in the Jovian magnetosphere, which can drive the development of these ring distributions. For instance, the interaction of energetic electrons with electromagnetic waves, particularly those in the ion cyclotron frequency range, can contribute to the formation of these anisotropic distributions. In particular, research using data from the Juno spacecraft has provided insights into the electric field structures in Jupiter's magnetosphere, shedding light on the role of A.C. electric fields in driving such particle dynamics [18]. Understanding these distributions is crucial not only for Jupiter but also for interpreting similar phenomena in other planetary systems and their impact on magnetospheric dynamics.

In this paper, an attempt has been made to study the effect of hot injection on electromagnetic ion-cyclotron instability in Jovian magnetosphere similarly cold beam injection for whistler waves have been studied by [19], [20] at Saturn. Energy exchange processes and plasma injection play an important role in Jupiter's dynamics. Firstly, a detailed

Cite as: G. Yadav, B.S. Sharma, Ankita, East Eur. J. Phys. 1, 91 (2025), https://doi.org/10.26565/2312-4334-2025-1-08

derivation is done for dispersion relation having ring distribution in the presence of parallel AC electric field for ion-cyclotron electromagnetic wave. Also, an expression has been derived from the growth rate in terms of temperature anisotropy and electric field for EMIC waves in anisotropic plasma. Finally, we have calculated the growth rate for Jovian magnetospheric condition at L = 17 R_J and results have been discussed. This approach will be helpful to understand the physics behind the various types of broadband emissions detected in Jovian magnetosphere and ionosphere.

2. DISPERSION RELATION AND GROWTH RATE

The dispersion relation outlines the conditions under which a wave propagates and provides a relation between the wave vector and frequency of the propagating wave on basis of wave particle interaction phenomenon and transfer energy from the particle to waves affect the growth rate of the wave [21]. The dispersion for electromagnetic ion-cyclotron in an infinite magnetosphere of Jupiter for a generalized loss cone type distribution function having anisotropic temperature has been studied. The injection of energetic hot ions (H+) affects the growth rate significantly. To calculate the dispersion relation and growth rate for electromagnetic ion- cyclotron wave in plasma, some certain assumptions are made to the analysis. A spatially homogenous collision-less anisotropic plasma is assumed in the same z direction of ambient magnetic field B and external AC electric field $E = E_o \sin \nu t \hat{e}_z$ to get dispersion relation and considered small inhomogeneity in the interaction zone. Kinetic theory and linearization of Vlasov Maxwell equations are used and after separation of equilibrium and non-equilibrium parts the higher order terms are neglected. Now the general dispersion relation for relativistic case with parallel AC electric field from [20] of equation (9) is written as:

$$\varepsilon_{ij}(k,\omega) = 1 + \sum_s \frac{4e_s^2\pi}{(\beta m_s)^2 \omega^2} \sum_n \sum_p J_p(\lambda_2) \int \frac{\left\| S_{ij}^* \right\| d^3p}{\omega - \frac{k_{||}p_{||}}{\beta m_e} - \frac{k_{||}\Gamma_z}{\beta\nu} + p\nu - \frac{n\omega_c}{\beta}}. \quad (1)$$

Where

$$\left\| S_{ij}^* \right\| = \begin{vmatrix} p_\perp U^* \left(\frac{n}{\lambda_1}\right)^2 J_n^2 & ip_\perp U^* \left(\frac{n}{\lambda_1}\right) J_n J_n' & p_\perp W^* \left(\frac{n}{\lambda_1}\right) J_n^2 \\ ip_\perp U^* \left(\frac{n}{\lambda_1}\right) J_n J_n' & -p_\perp U^* (J_n')^2 & ip_\perp W^* J_n J_n' \\ p_{||} U^* \left(\frac{n}{\lambda_1}\right) J_n^2 & ip_{||} U^* J_n J_n' & p_{||} W^* J_n^2 \end{vmatrix}$$

$$U^* = C - k_{||} D \left(\frac{p}{\lambda_2} - 1\right) + F$$

$$W^* = D \left(\frac{k_\perp n m_e \omega_c}{k_\perp p_\perp}\right) \left(\frac{p}{\lambda_2} - 1\right) - B \left(\frac{n m_e \omega_c}{k_\perp p_\perp}\right) + (\beta m_e \omega) \frac{\partial f_o}{\partial p_{||}}$$

$$B = (\beta m_e) \frac{\partial f_o}{\partial p_{||}} \left(\frac{k_\perp p_\perp}{\beta m_e}\right)$$

$$C = \frac{(\beta m_e)^2}{p_\perp} \frac{\partial f_o}{\partial p_\perp} \left(\omega - \frac{k_{||} p_{||}}{\beta m_e}\right) \frac{p_\perp}{\beta m_e}$$

$$D = \frac{(\beta m_e)^2}{p_\perp} \frac{\partial f_o}{\partial p_\perp} \left(\frac{p_\perp}{\beta m_e}\right) \left(\frac{\Gamma_z}{\beta\nu}\right)$$

$$F = (\beta m_e) \frac{\partial f_o}{\partial p_{||}} \left(\frac{k_{||} p_\perp}{\beta m_e}\right)$$

The Bessel function arguments are defined as

$$J_n'(\lambda_1) = \frac{dJ_n(\lambda_1)}{d\lambda_1}.$$

$$\lambda_1 = \frac{k_\perp v_\perp}{\omega_c m_e} \text{ and } \lambda_2 = \frac{k_{||}\Gamma_z}{\beta\nu^2}$$

Where, β is the relativistic factor and defined as $= 1/\sqrt{1 - \frac{v^2}{c^2}}$. $\Gamma_z = \frac{eE_o}{m_e}$, ν=Angular frequency of A.C. electric field $m_e = \frac{m_s}{\beta}$ and $\omega_c = \frac{eB_o}{m_e}$ = cyclotron frequency of electron; $p_\perp$ and $p_{||}$ denote momenta perpendicular and parallel to the magnetic field. For parallel propagation electromagnetic wave, $\varepsilon_{11} \pm i\varepsilon_{12} = N^2$ where $N^2 = \frac{k^2 c^2}{\omega^2}$.

The general dispersion relation for relativistic case with parallel AC electric field is written as:

$$\frac{k^2c^2}{\omega^2}=1+\sum_s\frac{4e_s^2\pi}{(\beta m_s)^2\omega^2}\sum J_p(\lambda_2)\int\frac{d^3p}{2}p_\perp\left[\begin{array}{l}(\beta m_s)\left(\omega-\frac{k_\parallel p_\parallel}{\beta m_s}\right)\frac{\partial f_o}{\partial p_\perp}\\-k_\parallel(\beta m_s)\frac{\partial f_o}{\partial p_\perp}\frac{\Gamma_z}{\beta\nu}\left(\frac{p}{\lambda_2}-1\right)\\+k_\parallel p_\perp\frac{\partial f_o}{\partial p_\parallel}\end{array}\right]*\left(\frac{1}{\omega-\frac{k_\parallel p_\parallel}{\beta m_s}-\frac{k_\parallel\Gamma_z}{\beta\nu}+p\nu\pm\frac{\omega_c}{\beta}}\right), \tag{2}$$

where, subscript 's' denotes type of species i.e. electrons and ions.

The ring distribution function is assumed to be distribution function of the trapped particles from [10], [20], [22],

$$f(p_\perp,p_\parallel)=\frac{n_s/n}{\pi^{3/2}p_{o\parallel s}p_{o\perp s}^2A}\exp\left[-\frac{(p_\perp-v_o)^2}{p_{o\perp s}^2}-\frac{(p_\parallel^2)}{p_{o\parallel s}^2}\right], \tag{3}$$

$$A=\exp\left(-\frac{v_o^2}{p_{o\perp s}^2}\right)+\sqrt{\pi}\left(\frac{v_o}{p_{o\perp s}}\right)\mathrm{erfc}\left(-\frac{v_o}{p_{o\parallel s}}\right), \tag{4}$$

$p_{o\parallel e}=(k_bT_{\parallel e}/\beta m_e)^{1/2}$, $p_{o\perp e}=(k_bT_\perp/\beta m_e)^{1/2}$, $p_{o\parallel i}=(k_bT_{\parallel i}/\beta m_i)^{1/2}$ and $p_{o\perp i}=(k_bT_{\perp i}/\beta m_i)^{1/2}$ are the associated parallel and perpendicular thermal momenta of ions and electrons.

n_s/n in equation (3) represents the ratio of particle total density captured and characterized by high energy, and erfc(x) in equation (4) is a complementary error function. The drift velocity is represented as v_o.

Substituting $d^3p=2\pi\int_0^\infty p_\perp dp_\perp\int_{-\infty}^\infty dp_\parallel$ and using expression (2) in equation (1) and after solving the integrations, we get the dispersion relation as:

$$\frac{k^2c^2}{\omega^2}=1+\frac{4e_s^2\pi}{(\beta m_s)^2\omega^2}\sum_p J_p(\lambda_2)\frac{(n_s/n)}{A}(\beta m_s)\left[\frac{\beta m_s}{p_{o\parallel s}}\left(\frac{\omega}{k_\parallel}-\frac{\Gamma_{\parallel s}}{\beta\nu}\left(\frac{p}{\lambda_2}-1\right)\right)X_1Z(\xi)+X_2\left(1+\xi Z(\xi)\right)\right]. \tag{5}$$

The above dispersion relation is now approximated in ion cyclotron range of frequencies. In this case electrons temperature $T_{\perp e}=T_{\parallel e}=T_e$ are assumed and magnetized with $|\omega_r+i\gamma|\ll\omega_{ci}$ whereas ions are assumed to have the condition $T_{\perp i}>T_{\parallel i}$ and $|k_\parallel\alpha_{\parallel i}|\ll|\omega_r\pm\omega_{ci}+i\gamma|$, $\frac{\omega_{pe}^2}{\pm\omega_{ce}^2}=\frac{-\omega_{pi}^2}{\pm\omega_{ci}^2}$. So, considering these approximations, equation (5) becomes:

$$D(k,\omega_r+i\gamma)=1-\frac{k^2c^2}{(\omega_r+i\gamma)^2}+\sum_p J_p(\lambda_2)\left[\begin{array}{l}\left(\frac{\omega_{pe}^2}{\omega_{ci}^2}-\frac{\omega_{pe}^2}{(\omega_r+i\gamma)(\pm\omega_{ci})}\right)X_{1e}(\beta m_e)\\+\frac{\omega_{pi}^2}{(\omega_r+i\gamma)^2}\left(\begin{array}{l}X_{1i}\frac{(\beta m_i)}{p_{o\parallel i}}\left(\frac{\omega_r+i\gamma}{k_\parallel}-\frac{\Gamma_{\parallel i}}{\beta\nu}\left(\frac{p}{\lambda_2}-1\right)\right)Z(\xi_i)\\+X_{2i}\left(1+\xi_iZ(\xi_i)\right)\end{array}\right)\end{array}\right]. \tag{6}$$

Where,

$X_{1i}=1+\frac{v_o^2}{p_{o\perp i}^2}-\sqrt{\pi}\frac{v_o}{p_{o\perp i}}$,

$X_{1e}=1+\frac{v_o^2}{p_{o\perp e}^2}-\sqrt{\pi}\frac{v_o}{p_{o\perp e}}$ and

$$X_{2i} = X_{1i} + \frac{p_{o\perp i}^2}{p_{o\|i}^2}\left(1 - \sqrt{\pi}\frac{v_o^3}{p_{o\perp i}^3} erfc\left(\frac{v_{\perp i}^{'}}{p_{o\perp i}}\right) + 3\frac{v_o^2}{p_{o\perp i}^2} - \frac{3}{2}\sqrt{\pi}\frac{v_o}{p_{o\perp i}}\right)$$

After applying the condition $\left|\frac{k^2c^2}{\omega^2} >> 1 + \frac{\omega_{pe}^2}{\omega_{ce}^2}\right|$, the dispersion relation of above equation becomes

$$D(k, \omega_r + i\gamma) = -\frac{k_\|^2 c^2}{\omega_{pi}^2} + \sum_p J_p(\lambda_2)\left[\begin{array}{l} \frac{\omega}{\pm\omega_{ci}}(\beta m_e) X_{1e} \\ +(\beta m_i) X_{1i}\left\{\frac{\beta m_i}{p_{o\|i}}\left(\frac{\omega}{k_\|} - \frac{\Gamma_{\|i}}{\beta\nu}\left(\frac{p}{\lambda_2} - 1\right)\right) Z(\xi_i) + \frac{X_{2i}}{X_{1i}}\left(1 + \xi_i Z(\xi_i)\right)\right\} \end{array}\right]. \quad (7)$$

The function of plasma dispersion is given by

$$Z(\xi) = \frac{1}{\sqrt{\pi}}\int_{-\infty}^{\infty}\frac{e^{-t^2}}{t-\xi}dt,$$

Where

$$\xi = \frac{\beta m_i\omega - k_\|\Gamma_{\|s} m_i / \nu + (\beta m_i) p\nu \pm m_i\omega_c}{k_\| p_{o\|i}};\ \omega_{pi}^2 = \frac{4\pi e^2}{(\beta m_i)^2}\frac{n_i/n}{B}$$

Now, dimensionless parameter wave vector $\tilde{k} = \frac{k_\| p_{o\|i}}{\omega_{ci}}$ is introduced.

In case of Parallel propagation

The expression of growth rate and real frequency for the waves propagating parallel to magnetic field direction becomes:

$$\frac{\gamma}{\omega_{ci}} = \frac{\frac{\sqrt{\pi}}{\tilde{k}}\left(\frac{X_{2i}}{X_{1i}} - k_4\right)k_3^3 \exp\left[-\left(\frac{k_3^2}{\tilde{k}}\right)^2\right]}{1 + \frac{\tilde{k}^2}{2k_3^2} + \frac{\tilde{k}^2}{k_3}\left(\frac{X_{2i}}{X_{1i}} - k_4\right) + \frac{m_e}{m_i}\frac{X_{1e}}{X_{1i}}k_3^2}. \quad (8)$$

The real part of eq. (8) is

$$X_3 = -\frac{\beta\omega_r}{\omega_c} = X_4 + \frac{\tilde{k}^2}{2\beta_1}\left[\frac{X_{2i}}{X_{1i}}\frac{\beta_1}{(1+X_4)} - \frac{(1+X_4)}{\beta X_{1i}}\right]$$

Where

$k_3 = 1 - \beta X_3 + \beta X_4$, $k_4 = \frac{\beta X_3 - \beta X_4}{1 - \beta X_3 + \beta X_4}$ and $\beta_1 = \frac{4\pi\mu_o\varepsilon_o k_b T_{\|i}(n_i/n)}{AB_o^2}$; $X_4 = \frac{k_\|\Gamma_{\|i}}{\beta\nu\omega_c} - \frac{p\nu}{\omega_c}$.

Magnetic field model used is taken from [23], [24], [25]

$$B = B_0\left(\frac{[1+3\sin^2\theta]^{\frac{1}{2}}}{\cos^6\theta}\right),$$

where
B_0 is magnetic field at equator and θ represents the magnetic latitude.

3. PLASMA PARAMETERS

Mauk et al [26] have reported injection events observed by Galileo spacecraft in Jupiter's magnetosphere at the radial distance between 9 and 27 R_J have reported in the energy range above 20 KeV. For the evaluation of growth rate inside Jupiter's magnetosphere to analyze the hot injection effect on electromagnetic ion-cyclotron wave with parallel propagation in Jovian magnetosphere at the radial distance R~17 R_J with B_o = 51 nT [23] the set of background plasma

parameters are considered as number density of cold ions, $n_c = 3\times10^6$ m^{-3}, temperature anisotropy, A_T=2, thermal energy of ions and electrons $K_BT_{||i}$ =1 keV and $K_BT_{||e}$ =200eV, and after injecting warm plasma, parameters are considered as number density of warm ions, $n_w = 3x10^7$ m^{-3}, temperature anisotropy, A_T=1.75, 2, 2.25, thermal energy of ions and electrons $K_BT_{||I}$ =3 keV and $K_BT_{||e}$ =200eV. Where, number density ratio of cold and warm ions, n_c/n_w=1/10. According to the previous study, Clark et al. [27] have reported that the approximate magnitudes of electric field and magnetic field are taken to be 10 mV/m and 51 nT respectively.

4. RESULT AND DISCUSSION

To study the variation of various plasma parameters on growth rate with the effect of hot injection for ring distribution function in the presence of AC electric field, mathematical calculations have been performed.

Figure 1 shows the variation of growth rate (γ/ω_c) with the effect of hot injection on ion-cyclotron wave with respect to increasing $\tilde{k}$ for various values of AC frequency. Ring distribution function is assumed with the beam of energetic particles. Behavior of ion-cyclotron wave is shown in the graph by interaction of wave with hot injected particles in Jovian magnetosphere. AC frequency range has been taken from 2 Hz to 2.2 Hz. The growth rate (γ/ω_c) for υ= 2 Hz is 4.84211×10^{-06} at $\tilde{k}$ =0.35, the growth rate (γ/ω_c) for υ = 2.1 Hz is 0.000011353024571591 at $\tilde{k}$ =0.35 and for υ=2.2 Hz, the growth rate is γ/ω_c = 0.000025023536544779 at $\tilde{k}$ =0.35. It is clearly seen that growth rate increases as the values of AC frequency increases.

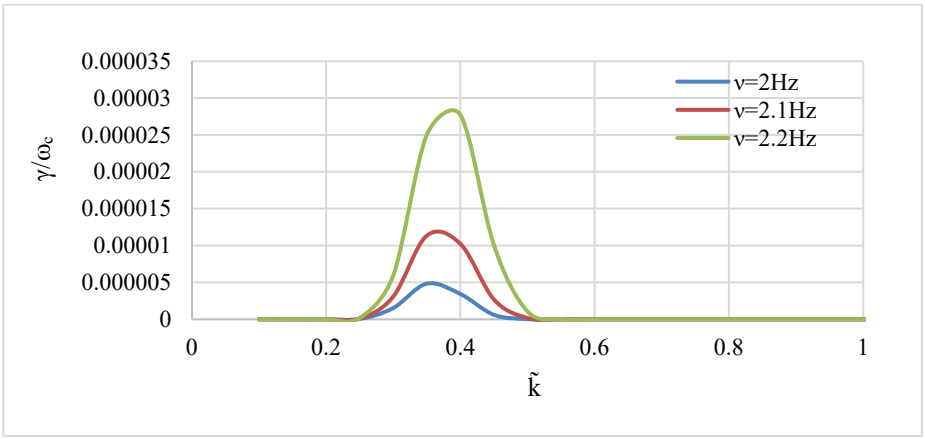

Figure 1. Variation of Growth Rate versus for different values of A.C. frequency at B_o=5.1×10^{-8}T, A_T=1.5, $K_BT_{||i}$=1 keV, $K_BT_{||e}$=200 eV, E_o=0.1 V/m and other fixed parameters of plasma at 17 R_J

In Figure 2, the variation of growth rate (γ/ω_c) with respect to increasing $\tilde{k}$ with the hot injection effect on EMIC for various values temperature anisotropy of cold ions has been plotted. For A_T =1.5, 2 and 2.5, the peak values are observed at $\tilde{k}$ = 0.35, 0.35, 0.35 and the growth rates are γ/ω_c = 3.41842223973875×10^{-06}, 0.0000169021159039714 and 0.0000720765136280518 respectively. Thus, the relativistic growth rate increases as temperature anisotropy of cold plasma increases. Usually the temperature anisotropy of ions is greater than the electron's temperature anisotropy. Hence this condition leads to the wave growth reported by [28].

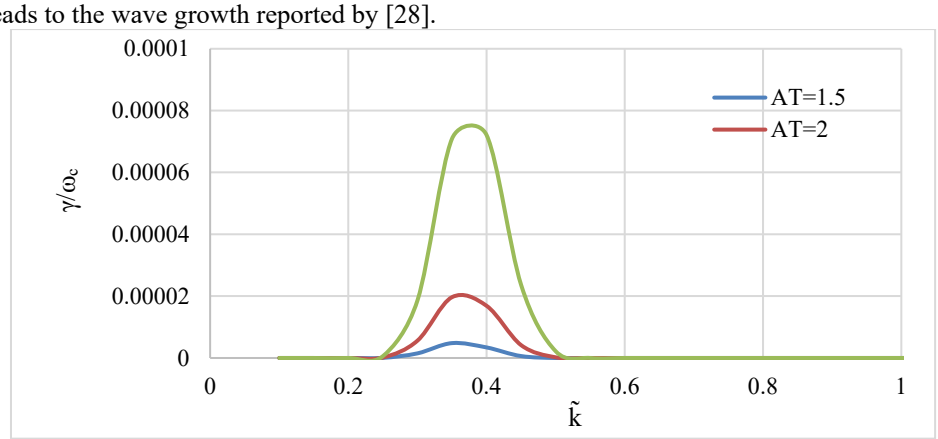

Figure 2. Variation of Growth Rate versus for different values of temperature anisotropy at ν=2 Hz, $K_BT_{||i}$=1 keV, $K_BT_{||e}$=200 eV, B_o=5.1×10^{-8}T, E_o=0.1 V/m and other fixed parameters of plasma at 17 R_J

Using Figure 3, variation of dimensionless growth rate in background plasma on EMIC wave in Jovian magnetosphere with respect to wave number $\tilde{k}$ for different values of number density n_0 at other fixed parameters is shown. For n_0=4×10^6,

the peak value of growth rate is γ/ω_c = 0.00023367 appears at $\tilde{k}$ = 0.4, for $n_0 = 5\times10^6$, growth rate is γ/ω_c = 0.002254457 at $\tilde{k}$ =0.45 and as number density is increasing to $n_0=6\times10^6$, peak value γ/ω_c = 0.009471069 at $\tilde{k}$ =0.5. So, as we increase number density n_0 from 4×10^6 to 6×10^6, growth rate increases, and peaks appear at same wave number $\tilde{k}$.

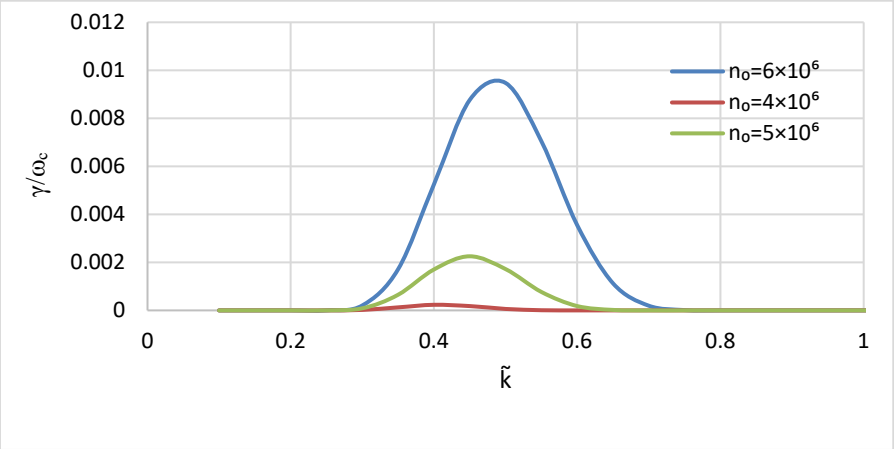

Figure 3. Variation of Growth Rate versus for different values of number density, n_0 at ν = 2 Hz, $K_BT_{||i}$=1 keV, $K_BT_{||e}$=200 eV, $B_o=5.1\times10^{-8}$T, E_o=0.1 V/m and other fixed parameters of plasma at 17 R_J

Figure 4 shows the variation of growth rate (γ/ω_c) with the effect of background on ion-cyclotron wave with respect to increasing $\tilde{k}$ for various values of AC frequency with effect of magnetic field model. Ring distribution function is assumed with the beam of energetic particles. Behavior of ion-cyclotron wave is shown in the graph by interaction of wave with hot injected particles in Jovian magnetosphere. AC frequency range has been taken from 2 Hz to 2.2 Hz. The growth rate (γ/ω_c) for υ = 2 Hz is 6.3028E-09 at $\tilde{k}$ =0.35, the growth rate (γ/ω_c) for υ = 2.1 Hz is 2.2927E-08 at $\tilde{k}$ =0.35 and for υ =2.2 Hz, the growth rate is γ/ω_c = 7.49878E-08 at $\tilde{k}$ =0.35. It is clearly seen that growth rate increases as the values of AC frequency increases.

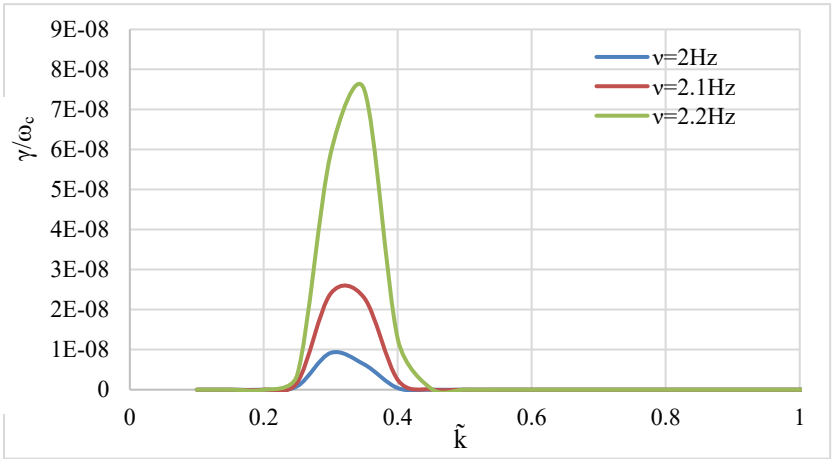

Figure 4. Variation of Growth Rate versus for different values of A.C frequency using magnetic field model at $B_o=5.1\times10^{-8}$T, A_T=1.5, $K_BT_{||i}$=1 keV, $K_BT_{||e}$=200 eV, E_o=0.1 V/m and other fixed parameters of plasma at 17 R_J

In Figure 5, shows the effect of temperature anisotropy on growth rate with the effect of hot injected plasma with effect of magnetic field with respect to $\tilde{k}$ of electromagnetic ion-cyclotron waves using ring distribution function in the Jovian magnetosphere. It can be seen that for A_T=1.5 the maxima occurs at $\tilde{k}$ = 0.3 with γ/ω_c = 9.1863E-09, for A_T=2 the highest peak γ/ω_c = 4.24628E-08 occurs at $\tilde{k}$ =0.3 and for A_T=2.5 the peak value γ/ω_c = 1.77683E-07 appears at $\tilde{k}$ =0.3. It shows that growth increases for parallel propagation of EMIC wave in Jupiter's magnetosphere with increasing the magnitude of temperature anisotropy.

Figure 6 shows the effect of temperature anisotropy on growth rate with the effect of hot injected plasma with respect to $\tilde{k}$ of electromagnetic ion-cyclotron waves using ring distribution function in the Jovian magnetosphere. It can be seen that for A_T=1.5 the maxima occurs at $\tilde{k}$ = 0.55 with γ/ω_c = 0.525446451, for A_T=2 the highest peak γ/ω_c = 0.589756008 occurs at $\tilde{k}$ =0.50 and for A_T=2.5 the peak value γ/ω_c = 0.658963625 appears at $\tilde{k}$ =0.5. It shows that growth increases for parallel propagation of EMIC wave in Jupiter's magnetosphere with increasing the magnitude of temperature anisotropy.

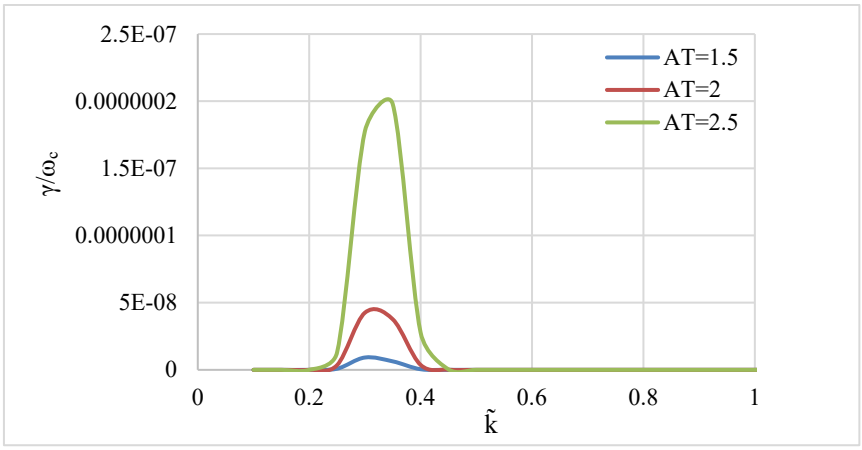

Figure 5. Variation of Growth Rate versus for different values of temperature anisotropy with magnetic field model at ν = 2 Hz, $K_BT_{||i}$=1 keV, $K_BT_{||e}$=200 eV, B_o=5.1×10^{-8}T, E_o=0.1 V/m and other fixed parameters of plasma at 17 R_J

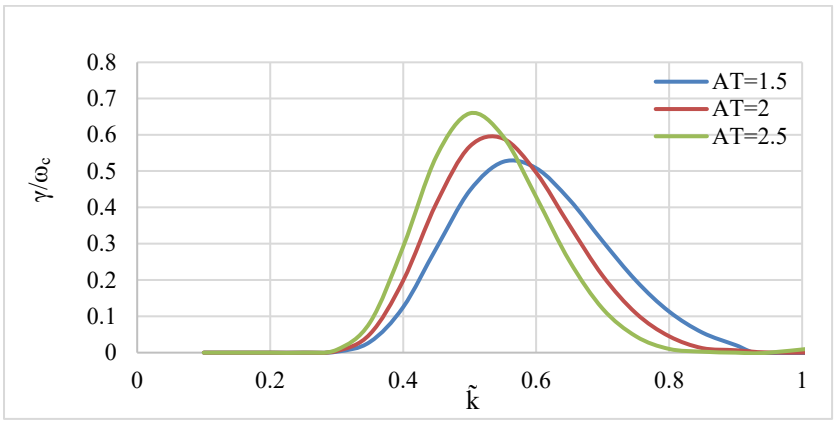

Figure 6. Variation of Growth Rate versus for different values of Temperature Anisotropy with beam at n_c/n_w=1/10, B_o=5.1×10^{-8}T, $K_BT_{||i}$=1 keV, $K_BT_{||ib}$=3 keV, $K_BT_{||e}$=200 eV and other fixed parameters of plasma at 17 R_J

Figure 7 shows the effect of relativistic factor on growth rate with the effect of hot injected plasma with respect to $\tilde{k}$ of electromagnetic ion-cyclotron waves using ring distribution function in the Jovian magnetosphere. It can be seen that for β=0.7 the maxima occurs at $\tilde{k}$ = 0.55 with γ/ω_c = 0.525446451, for β=0.8 the highest peak γ/ω_c = 0.531257736 occurs at $\tilde{k}$ =0.50 and for β=0.9 the peak value γ/ω_c = 0.520711317 appears at $\tilde{k}$ =0.45. It shows that growth rate shifts for higher value of wave number with decrease in the value of relativistic factor for parallel propagation of EMIC wave in Jupiter's magnetosphere with increasing the magnitude of relativistic factor.

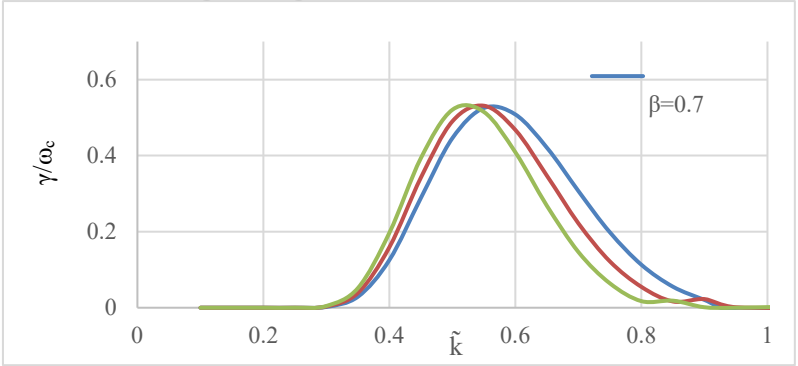

Figure 7. Variation of Growth Rate versus for different values of relativistic factor with beam at n_c/n_w=1/10, B_o=5.1×10^{-8}T, A_T=1.5, $K_BT_{||i}$=1 keV, $K_BT_{||ib}$=3 keV, $K_BT_{||e}$=200 eV and other fixed parameters of plasma at 17 R_J

Figure 8 shows the effect of number density ratio of electrons and ions on growth rate after injecting hot plasma with respect to $\tilde{k}$ of EMIC waves using ring distribution function at Jupiter. It can be observe that for n_c/n_w = 1/10 the maxima occurs at $\tilde{k}$ = 0.55 with γ/ω_c = 0.525446451, for n_c/n_w = 1/20 the highest peak γ/ω_c = 0.529429323 occurs at $\tilde{k}$ =0.55 and for n_c/n_w = 1/30 the peak value γ/ω_c = 0.530342417 appears at $\tilde{k}$ =0.55. It can be concluded that growth increases for parallel propagation of EMIC wave in Jupiter's magnetosphere as the magnitude increases. Thus, number

density of electron does not affect the growth rate in the case of hot injection ion beam as [29], [30] that dependence of dispersive properties of EMIC wave are on density and thermal plasma composition of ions.

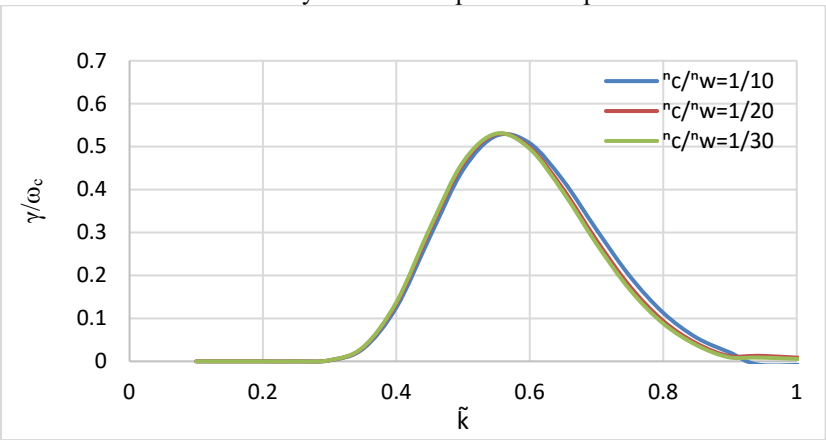

Figure 8. Variation of Growth Rate versus for different values of number density, n_0, for ν = 2 Hz, $K_BT_{||i}$=1 keV, $K_BT_{||ib}$=3 keV, $K_BT_{||e}$=200 eV, B_o=5.1×10^{-8}T, E_o=0.1 V/m and other fixed parameters of plasma at 17 R_J

Using Figure 9, variation of dimensionless growth rate in background plasma with the effect of hot injection on EMIC wave with magnetic field model in Jovian magnetosphere with respect to wave number $\tilde{k}$ for different values of temperature anisotropy at other fixed parameters is shown. For A_T=1.75, the peak value of growth rate is γ/ω_c = 0.522046615 appears at $\tilde{k}$ =0.55, for A_T=2, growth rate is γ/ω_c = 0.59197259 at $\tilde{k}$ =0.55 and as A_T is increasing to 2.25, peak value γ/ω_c = 0.656393317 at $\tilde{k}$ =0.5. So, as we increase temperature anisotropy from 1.5 to 2.5, growth rate increases, and peaks appear to shift towards a lower value of wave number $\tilde{k}$.

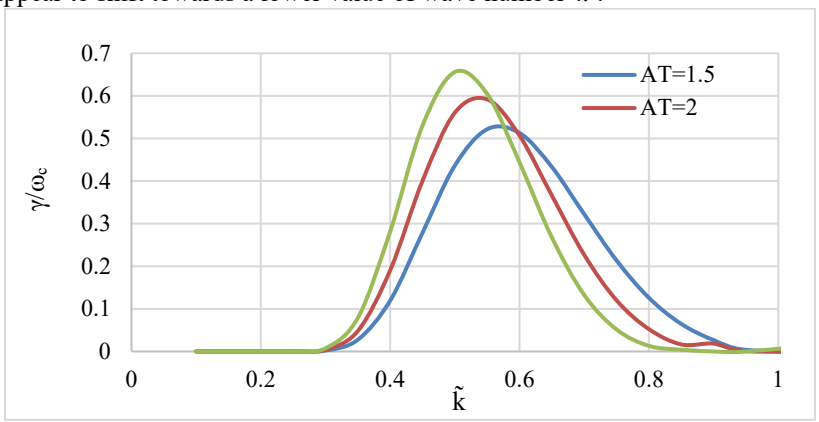

Figure 9. Variation of Growth Rate versus for different values of temperature anisotropy with beam with magnetic field model at nc/nw=1/10, ν=2 Hz, $K_BT_{||i}$=1 keV, $K_BT_{||ib}$=3 keV, $K_BT_{||e}$=200 eV, B_o=5.1×10^{-8}T, E_o=0.1 V/m and other fixed parameters of plasma at 1

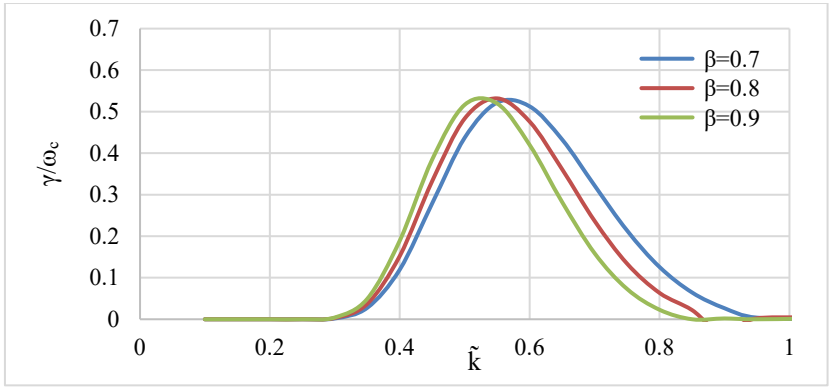

Figure 10. Variation of Growth Rate with relative to different values of relativistic factor with beam with magnetic field model at n_c/n_w=1/10, =2 Hz, A_T=2, B_o=5.1×10^{-8}T, $K_BT_{||i}$=1 keV, $K_BT_{||ib}$=3 keV, $K_BT_{||e}$=200 eV, E_o=0.1 V/m and other fixed parameters of p

Figure 10 shows the effect of relativistic factor on growth rate with the effect of hot injected plasma with respect to $\tilde{k}$ of electromagnetic ion-cyclotron waves using ring distribution function in the Jovian magnetosphere in the presence of external magnetic field model. It can be seen that for β=0.7 the maxima occurs at $\tilde{k}$ = 0.5 with γ/ω_c = 0.437003397,

for β=0.8 the highest peak γ/ω_c = 0.48355298 occurs at $\tilde{k}$ =0.5 and for β=0.9 the peak value γ/ω_c = 0.516484702 appears at $\tilde{k}$ =0.5. It shows that growth increases for parallel propagation of EMIC wave in Jupiter's magnetosphere with increasing the magnitude of relativistic factor.

Figure 11 shows the effect of number density ratio of electrons and ions on growth rate after injecting hot plasma with respect to $\tilde{k}$ of EMIC waves using ring distribution function at Jupiter. It can be observe that for n_c/n_w = 1/10 the maxima occurs at $\tilde{k}$ = 0.55 with γ/ω_c = 0.522046615, for n_c/n_w = 1/20 the highest peak γ/ω_c = 0.52839378 occurs at $\tilde{k}$ =0.55 and for n_c/n_w = 1/30 the peak value γ/ω_c = 0.529800749 appears at $\tilde{k}$ =0.55. It can be concluded that growth increases for parallel propagation of EMIC wave in Jupiter's magnetosphere as the magnitude increases. Thus, number density of electron does not affect the growth rate in the case of hot injection ion beam as [30] reported that dependence of dispersive properties of EMIC wave are on density and thermal plasma composition of ions.

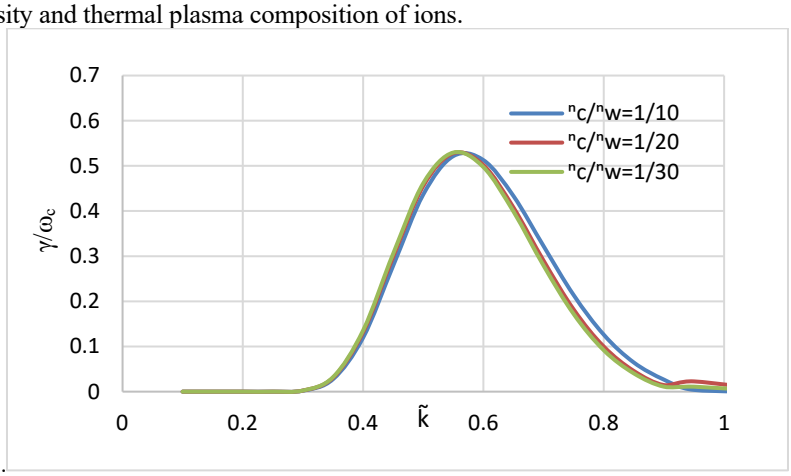

Figure 11. Variation of Growth Rate versus for different values of number density ratio (n_c/n_w) with beam with magnetic field model at =2 Hz, A_T=2, $K_BT_{||i}$=1 keV, $K_BT_{||ib}$=3 keV, $K_BT_{||e}$=200 eV, B_o=5.1×10^{-8}T, E_o=0.1 V/m and other fixed parameters of plasma at 1

5. CONCLUSIONS

In this paper, parallel propagating electromagnetic ion-cyclotron waves have been investigated with the effect of hot injection for ring distribution in the presence of AC electric field in magnetosphere of Jupiter at a radial distance of 17 R_J. To get better efficiency and consistency, kinetic approach has been performed. The detailed expression of dispersion relation, real frequency and growth rate has been derived for the parametric study. To analyze plasma parameters like AC frequency, temperature anisotropy etc., and graphs have been plotted with respect to wavenumber $\tilde{k}$. From the results, it is concluded that ion-cyclotron waves grows at Jupiter with increase in the values of temperature anisotropy, AC frequency and number density. After injecting hot ion beam, growth rate increases with the increasing AC frequency while it decreases as temperature anisotropy increases from 1.5 to 2.5. Graphs show that peak appears at the same value of wavenumber for an individual parameters.

Acknowledgement

We are thankful to our funding agency SERB and Dr. Ashok K. Chauhan (Founder President, Amity University), Dr. Atul Chauhan (President, Amity University) and Dr. Balvinder Shukla (Vice Chancellor, Amity University) for their immense encouragement.

ORCID

Garima Yadav, https://orcid.org/0009-0005-3239-5996; **B.S. Sharma,** https://orcid.org/0000-0002-2327-9396
Ankita, https://orcid.org/0009-0009-2201-6453

REFERENCES

[1] J.M. Cornwall, J. Geophys. Res. **70**(1), 61 (1965). https://doi.org/10.1029/JZ070i001p00061
[2] J.M. Cornwall, F.V. Coroniti, and R.M. Thorne, J. Geophys. Res. **75**(25), 4699 (1970)/ https://doi.org/10.1029/JA075i025p04699
[3] B.J. Fraser, and T.S. Nguyen, J. Atmos. Sol. Terr. Phys. **63**(11), 1225 (2001). https://doi.org/10.1016/S1364-6826(00)00225-X
[4] T.M. Loto'aniu, B.J. Fraser, and C.L. Waters, J. Geophys. Res. Space Phys. **110**(A7), (2005). https://doi.org/10.1029/2004JA010816
[5] E. Kim, and J.R. Johnson, Geophys. Res. Lett. **43**(1), 13 (2016). https://doi.org/10.1002/2015GL066978
[6] Z. Yuan, et al., "In situ evidence of the modification of the parallel propagation of EMIC waves by heated He + ions," J. Geophys. Res. Space Phys. **121**(7), 6711 (2016). https://doi.org/10.1002/2016JA022573
[7] Y. Miyoshi, *et al*., Geophys. Res. Lett. **35**(23), (2008). https://doi.org/10.1029/2008GL035727
[8] K. Hyun, K.-H. Kim, E. Lee, H.-J. Kwon, D.-H. Lee, and H. Jin, J. Geophys. Res. Space Phys. **119**(10), 8357 (2014). https://doi.org/10.1002/2014JA020234
[9] Y. Omura, and D. Summers, J. Geophys. Res. Space. Phys. **111**(A9), (2006). https://doi.org/10.1029/2006JA011600
[10] S. Wu, H. Zhang, C. Zhou, S. Zhu, and X. He, The European Physical Journal D, **68**(7), 208 (2014). https://doi.org/10.1140/epjd/e2014-50161-0

[11] R.C. Allen, *et al*., J. Geophys. Res. Space Phys. **121**(7), 6458 (2016). https://doi.org/10.1002/2016JA022541
[12] A.J. Halford, B.J. Fraser, and S.K. Morley, J. Geophys. Res. Space Phys. **115**(A12), (2010). https://doi.org/10.1029/2010JA015716
[13] D. Wang, *et al*., J. Geophys. Res. Space Phys. **120**(6), 4400 (2015). https://doi.org/10.1002/2015JA021089
[14] R.E. Denton, V.K. Jordanova, and B.J. Fraser, J. Geophys. Res. Space Phys. **119**(10), 8372 (2014). https://doi.org/10.1002/2014JA020384
[15] J.U. Kozyra, T.E. Cravens, A.F. Nagy, E.G. Fontheim, and R.S.B. Ong, J. Geophys. Res. Space Phys. **89**(A4), 2217 (1984). https://doi.org/10.1029/JA089iA04p02217
[16] R.M. Thorne, Geophys. Res. Lett. **37**(22), (2010). https://doi.org/10.1029/2010GL044990
[17] E.H. Annex, R.S. Pandey, and M. Kumar, East Eur. J. Phys. (1), 40 (2022). https://doi.org/10.26565/2312-4334-2022-1-06
[18] F. Bagenal, and P.A. Delamere, J. Geophys. Res. Space Phys. **116**(A5), (2011). https://doi.org/10.1029/2010JA016294
[19] J. Kumari, and R.S. Pandey, Advances in Space Research, **63**(7), 2279 (2019). https://doi.org/10.1016/j.asr.2018.12.013
[20] J. Kumari, R. Kaur, and R.S. Pandey, Astrophys. Space Sci. **363**(2), 33 (2018). https://doi.org/10.1007/s10509-018-3250-0
[21] C. Cheverry, and A. Fontaine, J. Math. Anal. Appl. **466**(2), 1238 (2018). https://doi.org/10.1016/j.jmaa.2018.06.045
[22] S. Kumar, S.K. Singh, and A.K. Gwal, Pramana, **68**(4), 611 (2007). https://doi.org/10.1007/s12043-007-0063-z
[23] S. Agarwal, R.S. Pandey, and C. Jeyaseelan, Astrophys. Space Sci. **364**(8), 133 (2019. https://doi.org/10.1007/s10509-019-3623-z
[24] M.G. Kivelson, and K.K. Khurana, J. Geophys. Res. Space Phys. **107**(A8), (2002). https://doi.org/10.1029/2001JA000249
[25] B. Ni, *et al*., Earth and Planetary Physics, **1**(2), 1 (2018). https://doi.org/10.26464/epp2018001
[26] B.H. Mauk, D.J. Williams, and R.W. McEntire, Geophys. Res. Lett. **24**(23), 2949 (1997). https://doi.org/10.1029/97GL03026
[27] J.T. Clarke, M.K. Hudson, and Y.L. Yung, J. Geophys. Res. Space Phys. **92**(A13), 15139 (1987). https://doi.org/10.1029/JA092iA13p15139
[28] W.C. Feldman, J.R. Asbridge, S.J. Bame, and M.D. Montgomery, J. Geophys. Res. **78**(28), 6451 (1973). https://doi.org/10.1029/JA078i028p06451
[29] D. Summers, and R.M. Thorne, J. Geophys. Res. Space Phys. **108**(A4), (2003). https://doi.org/10.1029/2002JA009489
[30] A.A. Saikin, J.-C. Zhang, C.W. Smith, H.E. Spence, R.B. Torbert, and C.A. Kletzing, J. Geophys. Res. Space Phys. **121**(5), 4362 (2016). https://doi.org/10.1002/2016JA022523

ГЕНЕРАЦІЯ ЕЛЕКТРОМАГНІТНОЇ ІОННОЇ ЦИКЛОТРОННОЇ ХВИЛІ ШЛЯХОМ ГАРЯЧОЇ ІНЖЕКЦІЇ ІОННОГО ПУЧКА ДЛЯ КІЛЬЦЕВОГО РОЗПОДІЛУ З ЕЛЕКТРИЧНИМ ПОЛЕМ ЗМІННОГО ТОКУ В МАГНІТОСФЕРІ ЮПІТЕРА

Гаріма Ядав[a], Б.С. Шарма[a], Анкіта[b]
[a]*Факультет фізики, Університет Лордса, Алвар-301001, Індія*
[b]*Департамент фізики, Інститут прикладних наук Аміті, Університет Аміті, Сектор-125 Нойда, Уттар-Прадеш, Індія*

У цій статті досліджуються електромагнітні іонно-циклотронні хвилі, виявлені космічним кораблем «Улісс» у магнітосфері Юпітера. У цьому регіоні виявлено різні типи високочастотного радіовипромінювання, що є результатом резонансної взаємодії. Дослідження зосереджено на взаємодії хвиля-частинка між електромагнітними іонно-циклотронними хвилями та повністю іонізованими частинками магнітосферної плазми, враховуючи паралельне поширення цих хвиль. Це дозволяє детально оцінити дисперсійне співвідношення з кільцевим розподілом за наявності паралельного електричного поля змінного струму (AC) у магнітосфері Юпітера без зіткнень. Використовуючи метод характеристик і кінетичний підхід, ми отримуємо вираз для релятивістської швидкості зростання. Крім того, ми аналізуємо події інжекції, зафіксовані космічним кораблем Galileo через його детектор енергетичних частинок (EPD) у магнітосфері Юпітера. Після введення гарячого іонного пучка ми проводимо параметричний аналіз різних параметрів плазми, таких як температурна анізотропія, частота змінного струму та релятивістські чинники, щоб дослідити їхній вплив на швидкість росту, що проілюстровано за допомогою нанесених графіків.
Ключові слова: *електромагнітні іонно-циклотронні хвилі; кільцевий розподіл; ін'єкція гарячих іонів; магнітосфера Юпітера*

East European Journal of Physics. 1. 101-111 (2025)
DOI:10.26565/2312-4334-2025-1-09 ISSN 2312-4334

INFLUENCE OF THERMAL RADIATION ON MHD CASSON NANOFLUID FLOW OVER A NON-LINEAR STRETCHING SHEET WITH THE PRESENCE OF CHEMICAL REACTION

P. Raja Shekar*, G. Jithender Reddy†, N. Pothanna
Department of Mathematics, VNR Vignana Jyothi Institute of Engineering and Technology, Hyderabad, 500090, Telangana State, India
**Corresponding Author e-mail: rajoct25@gmail.com; †e-mail: jithendergurejala@gmail.com*
Received November 28, 2024; revised January 16, 2025; accepted January 20, 2025

The focus of this research is to examine how the Casson and chemical reaction parameter impact the variable radiative flow of MHD Nanofluid across a stretching sheet. Through the use of similarity functions, the modelling equations (PDEs) of the motion of fluid are transformed into simple differential equations. The MATLAB tool is adopted to compute the equations numerically. Graphs and descriptions have been provided for velocity, concentration, and temperature outlines, showing the effects of important fluid flow constraints. Different factors are analysed to provide data and explanations for Prandtl, Lewis numbers, slip and chemical decomposition parameters. The current results are in good in good align with existed reports. The viscosity of the fluid and thermal boundary stratum decreases as enhancing of Casson, Magnetic parameter & Prandtl number. Skin friction increasing as enhancing of suction, stretching, magnetic and Casson parameter while decreasing as enhancing of velocity slip quantity. Rate of heat transmission enhancing as increment of thermal radiation and surface temperature while decreasing as enhancing chemical reaction and thermal slip quantities. Rate of mass transfer raising as enhancing of chemical reaction, thermal slip, thermal radiation while decreasing as enhancing of surface temperature parameter.
Keywords: *Nanofluid; Chemical reaction; Thermophoresis; Brownian Motion*
PACS: 47.10.A−, 44.40.+a, 47.11.−j, 52.65.Kj

INTRODUCTION

Boundary stratum flow on a stretched sheet is a noteworthy problem in different industrial developments like paper manufacturing and drawing plastic, glass, fiber & elasticity sheets. This phenomenon can also be observed in the growth of crystals during polymer stretching processes and the cooling of metal sheets in cooling baths. Scientists are focusing on this issue because of its relevance in polymer processing technology, especially in relation to heat transfer applications. Sakiadis [1] made significant contributions to this area by investigating the equations controlling the boundary stratum and flow over an expanding surface moving at a constant velocity. Elbashbeshy and Bazid [2] explored the flow of fluids and heat transmission on a newly explored extended surface by internal heat activation given the importance of these phenomena. Several scholars further developed Crane's work [3] done through the influence of heat & mass transfer by different geometries & shapes, as explored by Abbas et al. [4] and Rosca et al [5].

Base fluids including water, motor oil, and glycerin combined with scattered nanoparticles like carbon nanotubes, copper, silver, and gold make up nanofluid. The idea of utilizing a nanofluid, which is a mixture of a base fluid & nano sized particles, was initially proposed by Choi and Eastman [6]. Solid particles are evenly and durably spread out in the base liquid, such as water, engine oil, pump oil, and ethylene glycol. Nanofluid's are predicted towards the next future of heat transmission fluids because of their ability to greatly improve heat transfer efficiency when compared to pure liquids. Their excellent thermal, chemical, and physical characteristics are highly useful in various industrial and technological applications. Moreover, nanofluids have the potential to enhance abrasion characteristics in comparison with traditional fluid blends. The scattered nanoparticles, often metals or metal oxides, enhance the thermal diffusion of nanofluid's. A variety of thermal applications, including smart fluids, microelectronics, heat exchangers, fuel cells, hybrid-powered generators, pharmaceutical manufacturing, nuclear reactors, industrial cooling, and geothermal power extraction, can benefit from the unique properties of nanofluids. Various researchers have recently finished several studies on nanofluids. Das [7] investigated the behaviour of heat & mass transfer in MHD nanofluid flow across a radiating non-linear permeable extending sheet with changes in thermal & velocity slip. He and his colleagues used the 4th order RK-Fehlberg method along through the shooting method procedure to calculate computational solutions for modelling equations Entropy was investigated by Hayat et al. [8] in a radiative water-based nanofluid between two rotating disks. Wang et al. [9] conducted a computational evaluation of microchannel porous materials by introducing two distinct nanoparticles into a base fluid. Khan and Pop [10] examined nanofluid flow on a flat surface undergoing stretching with Brownian and thermophoresis using an implicit finite-difference method.

In recent years, investigating and describing the advanced properties of composite flows has become a fundamental focus of research. The area of research involving conductive liquids that exhibit magnetic field characteristics is known as magnetohydrodynamics (MHD). Rahman and Eltayeb [11] conducted a computational study on the properties of heat transmission of nanofluid's flowing over a non-linear extending sheet in two dimensions under hydromagnetic natural convection. The study used the mathematical computer program Maple, accounting for the effects of thermal radiation

Cite as: P.R. Shekar, G.J. Reddy, N. Pothanna, East Eur. J. Phys. 1, 101 (2025), https://doi.org/10.26565/2312-4334-2025-1-09

and a convective frontier circumstance. Tausif et al. [12] studied the influence of a magnetic field on nanofluid flow across a non-linear permeable extending sheet boundary layer. Mahantesh et al.'s [13] investigation of MHD fluid flow as well as heat transmission at a point of stagnation took into account non-uniform heating source and sink effects, slip velocity, and thermal leap. The results were reported numerically. Using a two-term perturbation approach, Vedavathi et al. [14] discovered MHD nanofluid circulation on a flat plate while taking radiation absorption, diffusion thermodynamics, and first-order chemical reactions into account. Biswas et al. [15] researched a concentrated nano liquid model over a perpendicular plate. Moreover, in order to finish the project, they utilized an explicit finite difference approach to visually analyse the temperature, concentration, and velocity profiles. Beg et al. [16] examined nanomaterial flow with mixed convection through porous space that starts from an exponentially stretched sheet. However, Al-Mamun et al. [17] inspected the flow of Sisko-nanofluid across an extended nonlinear sheet, taking into the consideration of thermal radiation & the magnetohydrodynamic (MHD) effect. The effects of ion-slip and Hall current on transient magnetohydrodynamic (MHD) flow in a revolving porous medium were studied by Dharmaiah et al. [18]. In a magnetohydrodynamic convective micropolar fluid moving steadily over an inclined radioactive isothermal surface, the interaction amid thermophoresis and heat production and absorption was examined by Shaik Mohammed et al. [19].

Casson fluid, a significant non-Newtonian liquid, is increasingly crucial in our daily lives. Different kinds of sauces, soups & jellies illustrate Casson fluids. In 1959, Casson [20] was the first to develop the modelling equations for Casson fluid and demonstrate the characteristics of different polymers. McDonald [21] highlighted that, the Casson liquid model is characterized by the flow of blood. The class of fluids being discussed has a broad variety of uses in medicine, food industries, biological sciences, and various drilling processes. Because of its significant relevance, numerous researchers in the modern era observe this critical category of fluids in their laboratories. Nagarani et al [22] investigated the movement of Casson liquid in tube with supple ramparts and the spread of solute using peristaltic flow. Vishwanath et al. [23] analyzed the magnetohydrodynamic (MHD) movement of Casson fluid, which is non-Newtonian, on a surface that shrinks exponentially. The surface had both constant and exponentially changing wall temperature with suction. The dynamic behaviour of modelled equations, explaining the motion of micropolar Casson fluid across a sheet was inspected by Nadeem and colleagues [24] with exponential curvature. In their study, Narsimha Reddy and colleagues [25] examined the impact The nanofluid Casson and joules parameter in the varying radiative flow of a stretched sheet with MHD. Reddy and colleagues [26] investigated the flow of a Casson incompressible fluid with heat generation and magnetic field, driven by mixed convective, on a vertically accelerating porous plate.

Among the most crucial process variables for heat & fluid transport in a high temperature thermal system is radiation characteristics. There are several applications for thermal energy in industries as a means of reducing excessive heat emission. One important factor influencing the growth of nuclear energy, steady kit, turbines of gas, satellites, assortment of innovative transformation structures and missiles facilities is thermal radiation, For the determination of analyzing the MHD H_2O-based nanofluid with the effects of significant variables on heat transmission & liquid movement characteristics are inspected by Dharmendra et al. [27]. Nurul et al. [28] highlighted hybrid nanofluids by modelling stagnation point flow in Maxwell fluid. They also studied heat transfer and radiation effects. Analysis of the implications of mixed convection, thermal radiation, and porous media were considered by Abdul Wahed et al. [29]. The goal of Rashad et al.'s work [30] was to develop a computational framework for the MHD Eyring–Powell nanofluid hybrid mixed convection flux when thermal radiation is present. The nano liquid flow between two horizontally infinite plates with a stretchable and permeability lower plate was deliberated by Shaheen [31]. Arulmozhi et al. [32] compare the effects of pure fluid (water) and nanofluid (Cu–H2O) on a moving vertical plate with porosity. By taking into account the nanoparticles' ability to reach thermal equilibrium, the chemical response of this nanofluid with regard to radiation absorption is consider. The effects of radiation and chemical responses on MHD hyperbolic tangent liquid were studied by Athal et al. [33]. The combined effects of radiative heat, thermophoresis, mixed convective heat, Brownian motion, and chemically reactive species were deliberated by Ahmed [34] in relation to magnetohydrodynamic (MHD) flow through the frontier stratum of nanofluid across a non-linear extending a porous medium surface. In the incidence of reactive chemical species and Joule heating, the simultaneous impacts of radiation on the convection of MHD nanofluid across an extensible sheet in permeable medium were examined by Eid and Makinde [35]. Eldabe et al. [36] described the influence of a chemical response on the MHD frontier stratum of an Eyring Powell nanofluid flowing with heat transmission through an extended sheet. Gireesha1 and N. G. Rudraswamy [37] have investigated the effects of chemical processes on stagnation point movement along with heat transmission over an extensible surface of a nano liquid in the incidence of irregular heat source/sink & uniform magnetic field. Anupam Bhandari [38] investigated the stable state of a 2-dimensional incompressible flow of MHD with a micropolar nanofluid across an extended sheet.

Comprehending how nanofluids behave in linear and non-linear stretching situations is important for a range of applications, such as industrial processes, coating applications, material manufacturing, and biomedical uses [39-40]. Investigations in this field help in the comprehension of how nanofluid impact the flow & heat transfer attributes in diverse extending situations, offering valuable information for use in a range of industries. This study addresses various gaps and limitations found in the previously discussed literature. It aims to develop a scientific model to inspect the possessions of radiation on MHD Casson nanofluid movement on a nonlinear extending sheet, incorporating surface temperature & concentration. The inclusion of thermal radiation adds novelty to the problem. The flow is examined under the influence of a nonlinear extending sheet in the existence of a chemical response. This model has practical applications

in areas such as nuclear waste storage, catalytic devices, fire-resistant insulation, & the production of pharmaceuticals, painting, coal-water mixtures and synthetic lubricants.

MATHEMATICAL FORMULATION

The study focused on a non-Newtonian nanofluid movement across an extending surface sheet with a nonlinear boundary layer at the plane $y = 0$. Flow is limited when $y > 0$, with the y axis vertical to the sheet described in Figure 1. It is presumed that the plate is extending along the $x-$ direction, consider a non-linear velocity $u_w = ax^n, a > 0$ $-$ direction where a >0 is a constant number, n is the extending parameter that varies nonlinearly, and x is the co-ordinate along the extending surface. The applied magnetic field $B(x)$ normal to the extending sheet causes the fluid to become electrically conductive, with B_0 being the initial intensity of the field of magnetism. The temperature on the stretching sheet at y=0 is given by $T_w = T_\infty + bx^r$ where the temperature far from the surface is denoted by T_∞ , the surface temperature parameter (STP) is represented by r, and b is a constant that is positive By setting r=0 in certain scenarios, we achieve a consistent temperature across the sheet, known as constant surface temperature (CST). C represents the concentration of nanoparticles, while C_w is the consistent concentration of nanoparticles on the plate's surface, which is higher than the surrounding fluid concentration C_∞ . Additionally, the magnetic Reynolds number is extremely low and can be ignored, resulting in a small induced magnetic field.

The Cauchy stress tensor rheological equation for Casson nanofluid is provided.

$$\tau' = \tau_0 + \mu\gamma \text{ Or } \tau_{ij} = \begin{cases} 2\left(\mu_B + \dfrac{p_y}{\sqrt{2\pi}}\right)e_{ij}, & \pi > \pi_c \\ 2\left(\mu_B + \dfrac{p_y}{\sqrt{2\pi_c}}\right)e_{ij}, & \pi > \pi_c \end{cases}$$

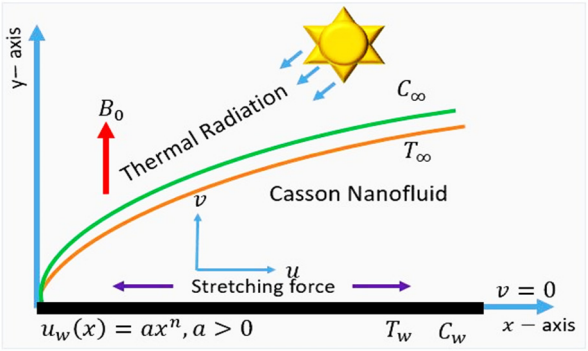

Figure 1. Geometric and physical representation model

In view of the overhead norms and considerations, the PDE models for nanofluid flow in the laminar boundary layer are derived.

$$\frac{\partial u}{\partial x} + \frac{\partial v}{\partial y} = 0, \tag{1}$$

$$u\frac{\partial u}{\partial x} + v\frac{\partial v}{\partial y} = v\left(1 + \frac{1}{\gamma}\right)\frac{\partial^2 u}{\partial y^2} + \frac{\sigma B(x)^2}{\rho_f}u, \tag{2}$$

$$u\frac{\partial T}{\partial x} + v\frac{\partial T}{\partial y} = \alpha\frac{\partial^2 u}{\partial y^2} + \tau\left\{D_B\left(\frac{\partial C}{\partial y}\frac{\partial T}{\partial y}\right)u + \frac{D_T}{T_\infty}\left(\frac{\partial T}{\partial y}\right)^2\right\} - \frac{1}{\rho c_p}\frac{\partial q_r}{\partial y}, \tag{3}$$

$$u\frac{\partial C}{\partial x} + v\frac{\partial C}{\partial y} = D_B\frac{\partial^2 C}{\partial y^2} + \frac{D_T}{T_\infty}\frac{\partial^2 T}{\partial y^2} - k_0(C - C_\infty). \tag{4}$$

Subject to the slip boundary conditions

With boundary condition

$$\left.\begin{array}{c} u = u_s + u_w, v = v_w, T = T_s + T_w, C = C_w \text{ for } y = 0 \\ u = 0, v = 0, T = T_\infty, C = C_\infty \text{ as } y \to \infty \end{array}\right\}. \tag{5}$$

Where u and v are velocity along x and y directions. u_s and T_s are the velocity & thermal slip, v_w is suction or injection, ρ_f is density of the base liquid, σ is electrical conductivity, , ν is kinematic viscosity and $\alpha = \frac{\kappa}{(\rho c)_f}$ is thermal diffusivity of the base liquid. D_B and D_T are Brownian & thermophoretic diffusion constants correspondingly, c_p is the specific heat, k_0 is rate of chemical reaction, $B(x) = B_0 x^{(n-1)/2}$ variable magnetic field, $\tau = \frac{(\rho c)_p}{(\rho c)_f}$ is the ratio of the heat capacity of

the nanoparticles to heat capacity of the base fluid. C is concentration of nanoparticles, C_w is consistent concentration of nanoparticles at surface, greater than the ambient concentration C_∞ .

If we consider an optical thick frontier stratum where the Rosseland estimation, the radioactive heat flux q_r becomes

$$q_r = -\frac{4\ddot{\sigma}}{3\ddot{\kappa}}\frac{\partial T^4}{\partial y}, \tag{6}$$

where $\ddot{\sigma}$ & $\ddot{\kappa}$ are the Stephan–Boltzmann & mean absorption coefficients.
Replacing Eq. (6) in the leading Eq. (3) we get

$$u\frac{\partial T}{\partial x} + v\frac{\partial T}{\partial y} = \alpha\frac{\partial^2 u}{\partial y^2} + \tau\left\{D_B\left(\frac{\partial C}{\partial y}\frac{\partial T}{\partial y}\right)u + \frac{D_T}{T_\infty}\left(\frac{\partial T}{\partial y}\right)^2\right\} + \frac{\nu}{C_p}\left(\frac{\partial u}{\partial y}\right)^2 + \frac{4\ddot{\sigma}}{3\ddot{\kappa}\rho c_p}\frac{\partial}{\partial y}\left(T^3\frac{\partial T^3}{\partial y}\right). \tag{7}$$

The dimensionless measures as

$$\eta = y\sqrt{\frac{a(n+1)}{2\nu}}x^{\frac{n-1}{2}}, u = ax^n f'(\eta), v = \sqrt{\frac{a\nu(n+1)}{2\nu}}x^{\frac{n-1}{2}}\left(f(\eta) + \frac{n-1}{n+1}\eta f'(\eta)\right), \theta(\eta) = \frac{\mathrm{T}-\mathrm{T}_\infty}{\mathrm{T}_w-\mathrm{T}_\infty}, \varphi(\eta) = \frac{\mathrm{C}-\mathrm{C}_\infty}{\mathrm{C}_w-\mathrm{C}_\infty}, \tag{8}$$

here $\psi(x, y)$ is stream function defined by

$$u = \frac{\partial\psi}{\partial y} \text{ and } v = \frac{\partial\psi}{\partial x}. \tag{9}$$

These are satisfying the Eq. (1) and the equations (2)-(5), obtained the equations (10)-(13) as follows

$$\left(1+\frac{1}{\gamma}\right)f''' + ff'' - \left(\frac{2n}{n+1}\right)f'^2 - Mf' = 0 \tag{10}$$

$$\theta'' + Pr\left(f\theta' + Nb\varphi'\theta' + Nt\theta'^2 - \left(\frac{2r}{n+1}\right)f'\theta\right) + \left(\frac{4Pr}{3R}\right)[\{1+(T_r-1)\theta\}^3\theta']' = 0 \tag{11}$$

$$\varphi'' + Lef\varphi' + \frac{Nt}{Nb}\theta'' - krLe\varphi = 0 \tag{12}$$

With boundary conditions as

$$\left.\begin{array}{c} f(0) = f_w,\ f'(0) = 1 + \xi f''(0), \theta'(0) = 1 + \zeta\theta', \varphi(0) = 1 \\ f'(\infty) = 0, \theta(\infty) = 0, \varphi(\infty) = 0 \end{array}\right\}. \tag{13}$$

Here, the dash indicates the derivative with η. f, θ, φ are the similarity function, non-dimensional temperature & concentration of nanoparticle respectively, $Pr = \frac{\nu}{\alpha}, Le = \frac{\nu}{D_B}$ are Prandtl and Lewis number respectively. $Nb = \frac{(\rho c)_p}{(\rho c)_f}\frac{D_B(C_w-C_\infty)}{\nu}$, $= \frac{(\rho c)_p}{(\rho c)_f}\frac{D_T(T_w-T_\infty)}{\nu T_\infty}$, $kr = \frac{k_0\nu}{a^2}$ and $M = \frac{2\sigma B_0^2}{a\rho_f(n+1)}$ are Brownian motion, thermophoresis, Chemical and Magnetic parameters respectively. The parameter for fluid's comparative ratio of temperature at the sheet's surface is $T_r = \frac{T_w}{T_\infty}$, $f_w = v_0\sqrt{\frac{2}{a\nu(n+1)}}$ is suction or injuction, $\xi = s_v\sqrt{\frac{a(n+1)}{2\nu}}$ and $\zeta = s_t\sqrt{\frac{a(n+1)}{2\nu}}$ are the velocity & thermal slips respectively where s_v ands_t are the velocity and thermal factors, The measures of the physical importance are the local skin friction coefficient C_{fx}, the local Nusselt number Nu_x and the local Sherwood number Sh_x which are defined as . $f_w = 0, f_w > 0$, $f_w < 0$ are represents surface is impermeable, suction and injection of the fluid on a porous sheet respectively.

The physical interest's quantities, which are essential for practical reasons

$$C_{fx} = \frac{\mu_f}{\rho U_w^2}\left(\frac{\partial u}{\partial y}\right)_{y=0}, Nu_x = \frac{q_w}{\kappa(T_f-T_\infty)}\left(\frac{4Pr}{3R}\right)[\{1+(T_r-1)\theta\}^3\theta']', Sh_x = \frac{xq_m}{D_B(C_w-C_\infty)}.$$

Where q_w and q_m are the heat and mass flux at the surface, κ is the thermal conductivity of the nanofluid, respectively. The q_w and q_m are given by

$$q_w = -\left(\frac{\partial T}{\partial y}\right)_{y=0} \text{ and } q_w = -D_B\left(\frac{\partial C}{\partial y}\right)_{y=0}$$

The non-dimensional forms of the skin friction, the local Nusselt & the local Sherwood numbers as

$$Re_x^{1/2}C_{fx} = \left(1+\frac{1}{\gamma}\right)f''(0), \frac{Nu_x}{Re_x^{1/2}} = -\left[1+\frac{4}{3R}\{1+(T_r-1)\theta(0)\}^3\right]\theta'(0), \frac{Sh_x}{Re_x^{1/2}} = -\varphi'(0)$$

where $Re_x = xu_w/\nu$ is the local Reynolds number.

DISCUSSION OF FINDING

To calculate the numerical solutions to (10)–(12) with boundary conditions (13), the authors used bvp4c. One of MATLAB's built-in function bvp4c for working with finite difference and collocation polynomials. This technique gives

good agreement results to the other methods which is shown in the Table 1. Numerical calculations are conducted in this part for various parameter values that reflect the flow characteristics, and the outcomes are visually represented.

Code of Validation: Comparison of Nusselt number & Sherwood number tabulated below. The present model is similar of Khan and Pop [10], Rahman and Eltayeb [11] and Das et al [7] when the absence of magnetic, thermal radiation, stretching, suction and surface temperature, Casson and chemical reaction parameters. The present results are good alignment with existed studies by Finite difference (Khan and Pop [10]), Maple software (Rahman and Eltayeb [11]), and RK-Fehlberg method with a shooting method (Das et al [7].

Table 1. The Nusselt and the Sherwood number comparison when $Pr = 2, Le = 2, \eta_\infty = 6$

Nt	**Khan and Pop [10]**		**Rahman and Eltayeb [11]**		**Das et al [7]**		**Present Results**	
	$\boldsymbol{\theta'(0)}$	$\boldsymbol{\varphi'(0)}$	$\boldsymbol{\theta'(0)}$	$\boldsymbol{\varphi'(0)}$	$\boldsymbol{\theta'(0)}$	$\boldsymbol{\varphi'(0)}$	$\boldsymbol{\theta'(0)}$	$\boldsymbol{\varphi'(0)}$
0.1	0.9524	2.1294	0.952376	2.129393	0.95237602	2.12939273	0.95233794	2.12909712
0.2	0.6932	2.2740	0.693174	2.274020	0.69315023	2.27402065	0.69316392	2.27352695
0.3	0.5201	2.5286	0.520079	2.528636	0.52001607	2.52863590	0.52009015	2.52790541
0.4	0.4026	2.7952	0.402581	2.795167	0.40258040	2.79516710	0.40260786	2.79417165

The influence of the Casson fluid parameter (γ) on the velocity outline is portrayed in Figure 2(a). The Casson parameter γ is noted for generating a resistive force in liquid movement. As a consequence, the velocity profile decreases in magnitude with increased values of γ. Increasing γ results in a stronger impact on the temperature field (figure 2(b)). The thickness of the concentration boundary layer will raise as the values of γ increase. The retarding force caused by plastic viscosity contributes to the increased concentration shown in Figure 2(c).

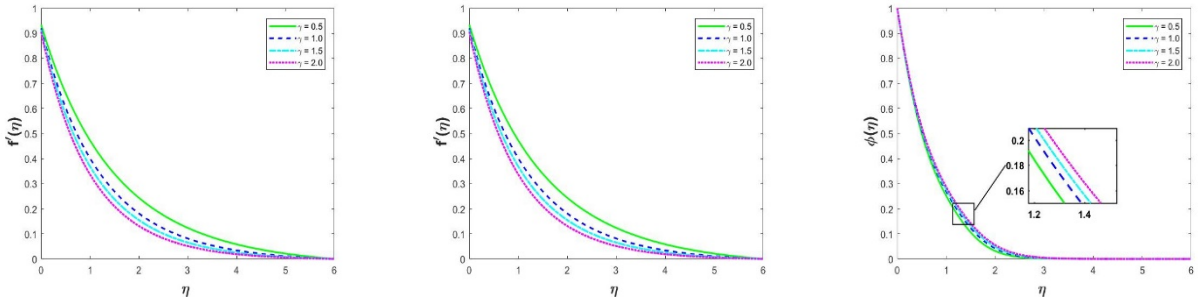

(a) (b) (c)

Figure 2. Impact of Casson parameter on (a) Velocity, (b) Temperature (c) Concentration

The presence of a magnetic field factor leads to an increased distribution of nanoparticles in the boundary layer area. This event is caused by the Lorentz force, which creates a force that goes against the path of fluid movement. Figure 3(b) shows by what means the temperature outlines change with the magnetic field parameter M. It is clear that as M increases, the fluid temperature also increases. The magnetic field makes the magnetic nanoparticles in the nanofluid move and rotate. The drive of the nanoparticles creates friction and crashes, resulting in a rise in temperature by transforming kinetic energy into thermal energy. Additionally, the electrically conducting nanofluid experiences a Lorentz force owing to the functional magnetic field. This energy causes electrical power to transform into warmth, causing the fluid's temperature to rise overall. Therefore, as the magnetic parameter M increases, the thermal boundary layer thickness also increases.

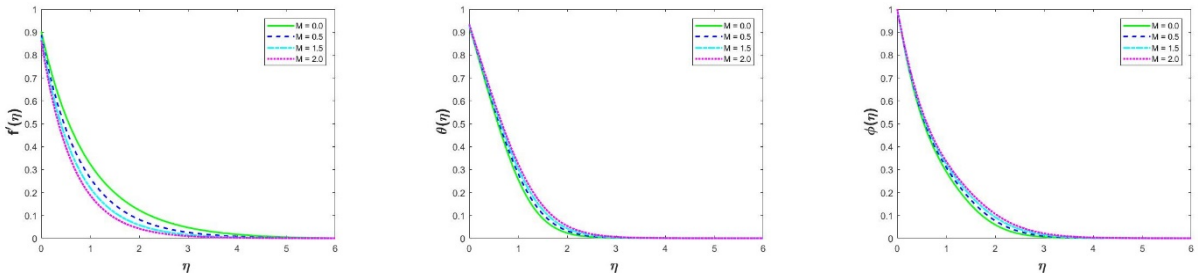

(a) (b) (c)

Figure 3. Impact of M on (a) Velocity, (b) Temperature (c) Concentration

Figure 4(a) demonstrates how the stream-wise velocity varies with different values of the non-linearly stretching sheet parameter n. An increase in this non-linear factor is linked to a decrease in the velocity in the direction of the stream. This suggests that either the stretching process or the parameterization conditions are instigating a deceleration in the movement in the flow path. Consequently, when the parameter n increases, the boundary layer width of impetus decreases. In Figure 4(b), the correlation among temperature variation and parameter n values is illustrated. A greater stretching parameter value means a stronger or more notable extending of the surface. When the surface is stretched more, it adds

extra energy to the fluid movement close to the surface. This extending accomplishment can change the flow outlines, impacting the speed circulation within the boundary sheet. This increases the transmission of momentum and movement of fluids close to the surface, resulting in a thicker boundary layer. Figure 4 illustrates how the nanoparticle concentration profile fluctuations vary with different stretching parameter values, denoted as n. While the effect may be minimal at a constant surface temperature, it is evident that the concentration upsurges as the stretching parameter values upsurge. This happens because the stretching movement can cause improved blending, heightened fluid movement, and changed velocity patterns near the stretched area. This results in increased shear forces in the fluid close to the extended surface. Increased shear stresses improve fluid mixing, resulting in greater transport of species, like substance concentration.

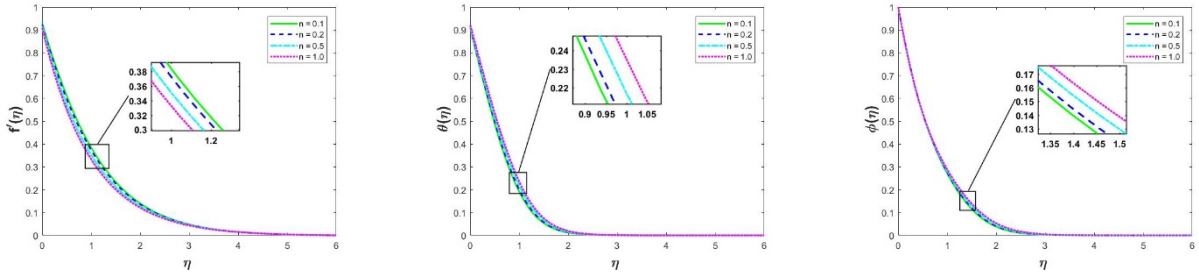

(a) (b) (c)

Figure 4. Impact of n on (a) Velocity, (b) Temperature (c) Concentration

The illustration of how velocity contours behave with dissimilar values of velocity slip parameter ($\boldsymbol{\xi}$) is demonstrated in Fig. 5(a). In general, $\boldsymbol{\xi}$ computes the amount of slip on the cylinder's surface. In this analysis, we examine how fluid speed diminutions with cumulative $\boldsymbol{\xi}$. The cause for this is that $\boldsymbol{\xi}$ primarily hinders the flow of the liquid, which ultimately outcomes in a reduction in overall fluid molecule movement. As the value of $\boldsymbol{\xi}$ increases, it is noted that the concentration and temperature also increase.

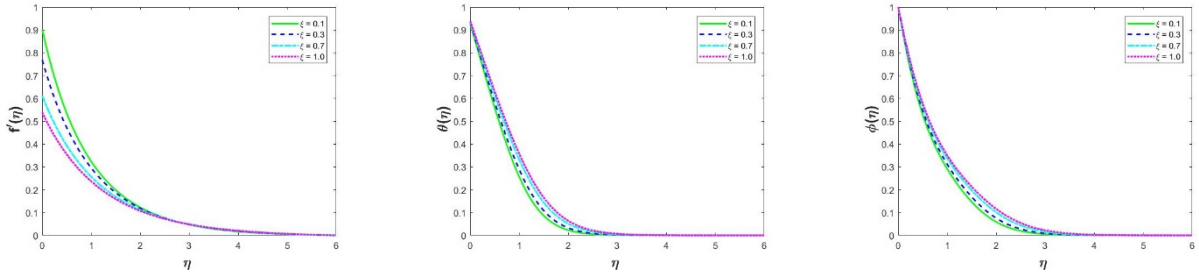

(a) (b) (c)

Figure 5. Impact of velocity slip ξ on (a) Velocity, (b) Temperature (c) Concentration

Figure 6(a) and (b) illustrate how the dimensionless temperature and nanoparticle volume fraction are prejudiced by the thermal slip parameter $\boldsymbol{\zeta}$. Increasing $\boldsymbol{\zeta}$ values clearly reduce temperature and concentration profiles. Even with a modest quantity of heat supplied to the liquid from the sheet, the thermal boundary layer thickness falls with growing thermal slip parameter.

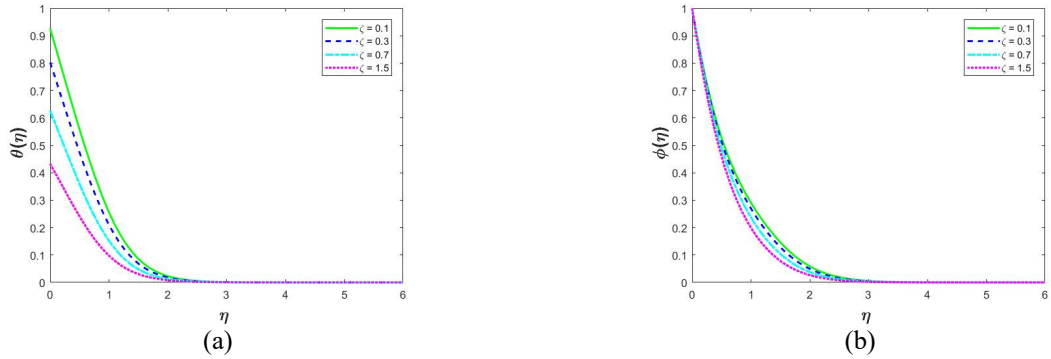

(a) (b)

Figure 6. Impact of thermal slip ζ on (a) Temperature (b) Concentration

Fig. 7(a) shows that the temperature drops with an upsurge in the Prandtl number (Pr). An elevation in Pr could potentially decrease the thermal boundary layer thickness. Pr is the fraction of momentum diffusivity to thermal diffusivity. When dealing with heat transmission matters, the Pr number influences the proportionate growth of the momentum & thermal frontier stratums. When Pr is low, heat spreads rapidly relative to momentum in liquid metals,

resulting in a thermal boundary layer thickness significantly larger than the momentum boundary layer. Liquids with a lesser Pr number exhibit increased thermal conductivities (and thicker frontier stratum structures), allowing for quicker heat diffusion compared to fluids with greater Pr numbers (resulting in thinner frontier stratums) Figure 7(b). Therefore, Pr can be utilized to enhance the rate of cooling in conductive flows.

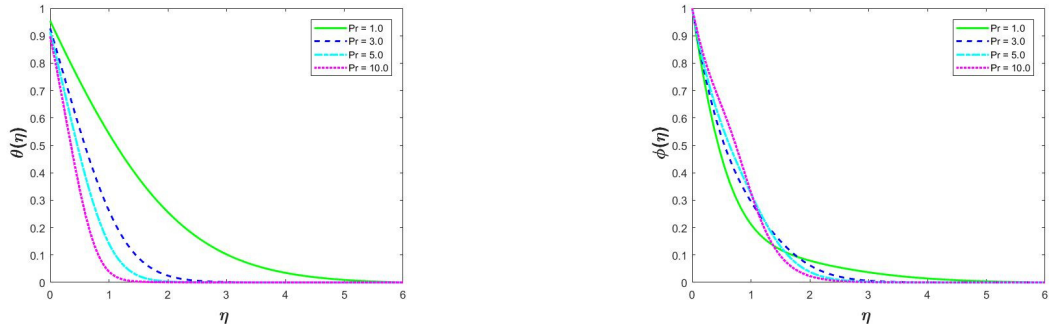

Figure 7. Impact of Pr on (a) Temperature (b) Concentration

Figures 8(a) and 8(b) show how temperature and concentration change with coordinate η for different thermophoretic parameter (Nt) values. The force Nt is caused by the temperature variance among the cold sheet and the hot fluid, leading molecules to move towards the cold sheet. The molecules near the hot stretching sheet are kept warm by the air molecules, resulting in a rapid flow away from the sheet that reduces the temperature difference. This leads to molecules increasing their kinetic energy and temperature. Consequently, the thermophoresis force moved the heated molecules close to the heated contracting surface towards the cold fluid at the surrounding temperature. Thermophoresis causes the momentum boundary layer width to increase, while at the same time thickening the thermal boundary layer width. Graph 8(b) indicates that nanoparticle concentration rises as the thermophoresis parameter increases. Essentially, when a particle exerts a thermophoresis force on another particle, it causes particles to move from a hotter to a colder area, resulting in the fluid moving from a hotter to a colder region, causing the volume proportion of nanoparticles to increase.

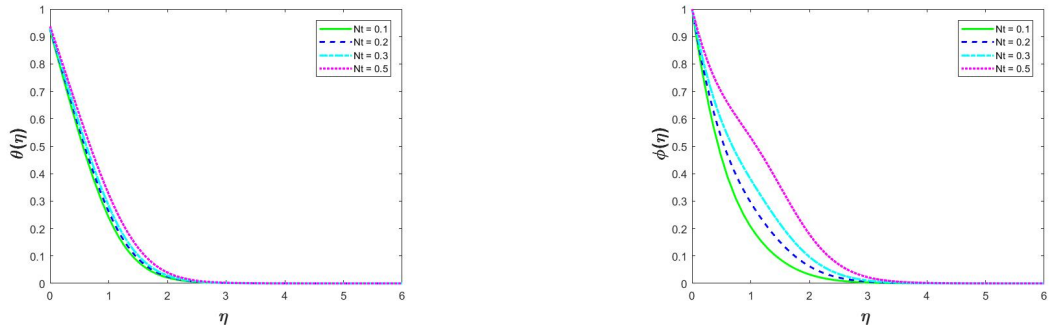

Figure 8. Impact of Nt on (a) Temperature (b) Concentration

The influence of the Brownian diffusion parameter (Nb) on the dimensionless temperature & concentration distributions is demonstrated in Figs 9(a) and 9(b). Brownian diffusion involves the unpredictable movement of nanoparticles suspended in the base liquid, mainly due to the rapid movement of atoms or molecules in the base fluid. It should be noted that Brownian diffusion is connected to the dimensions of nano-particles and frequently appear as clusters and/or clumps. Brownian motion is significantly reduced for larger particles, resulting in Nb having minimal values. As the Nb values increase, the temperature outlines in the frontier stratum region are enhanced (Fig. 9(a)). Nevertheless, the nano particle concentration patterns slow down with increased values of Nb depicted in Fig. 9(b).

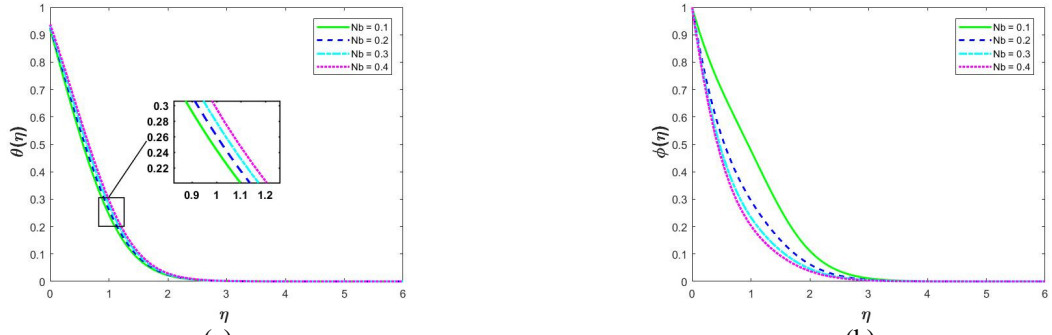

Figure 9. Impact of Nb on (a) Temperature (b) Concentration

Fig. 10(a) displays the temperature distribution for various radiation factor (R) values. It was found that as the R increased, the temperature rose as well. The temperature increased because of the escalation in the conduction effect inside the thermal frontier stratum caused by the rise in R, since the radiation factor was the fraction of conductive heat transfer to radiative heat transfer. This finding may prove useful in directing the ratio of heat transfer properties by means of the thermal radiation mechanism. Fig. 10(b) makes it apparent that when the radiation rises, the fluid's concentration falls.

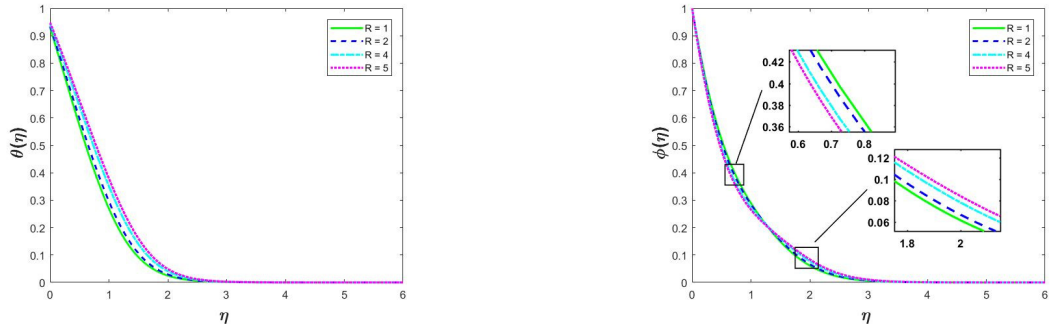

Figure 10. Impact of R on (a) Temperature (b) Concentration

The Lewis number is a unit less parameter that represents the proportion of thermal diffusivity to mass diffusivity and is crucial in the joint impact of heat & mass transfer operations. The relative thermal and concentration boundary layer thicknesses are measured by Le and can also be written as $Le = Sc/Pr$. Reportedly, as Le increases, the temperature decreases sources a lessening in the thickness of the boundary layer fluid. A growth in the parameter slowly enables the fluid to release heat to the external environment or nearby body, resulting in a diminution in the fluid's temperature (Figure 11(a)). Figure 11(b) illustrates how the nanoparticle concentration falls as the Lewis Number (Le) rises. This impact is especially noticeable for smaller Le values. As a result, it is expected that Le will greatly change the concentration frontier stratum. In Figure 12(a) and 12(b), we can see the dimensionless temperature and concentration profile at various values of chemical response. The fluid temperature & concentration declines as the chemical reaction rate rises. The main cause is that the temperature & concentration fields decreases as the kr rises due to thermal conductivity of the particles in the liquid decrease and an upsurge in the number of solute molecules participating in the reaction. Therefore, a harmful chemical reaction greatly declines the thickness of the thermal & concentration frontier stratum.

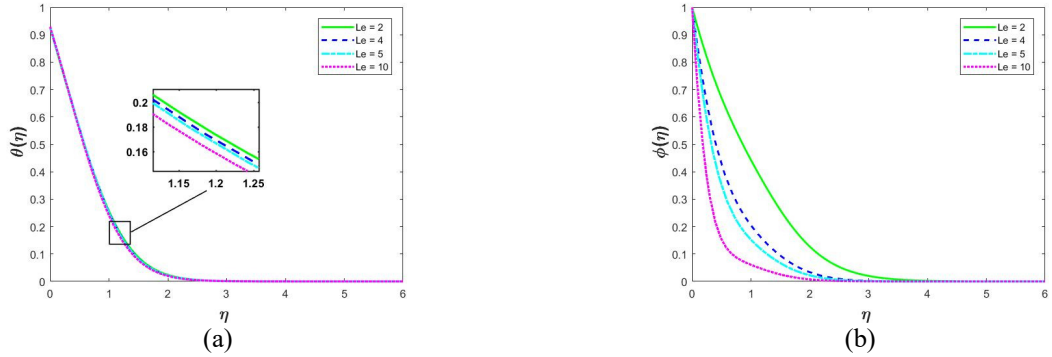

Figure 11. Impact of Le on (a) Temperature (b) Concentration

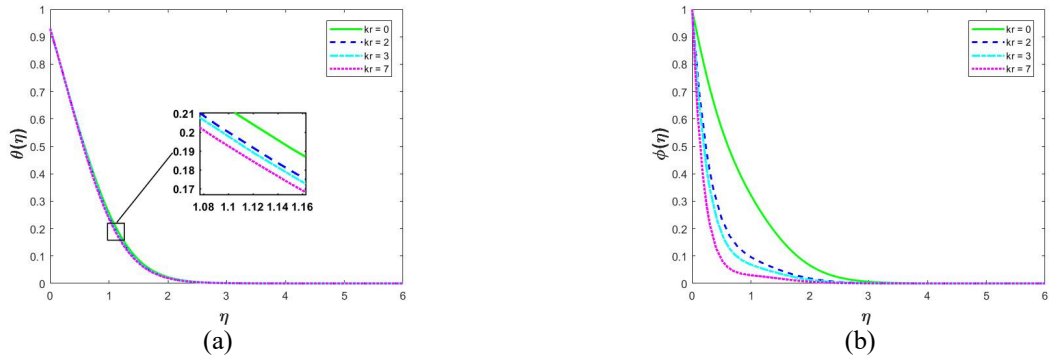

Figure 12. Impact of Kr on (a) Temperature (b) Concentration

The Fig 13. shows the variation of skin friction, Nusselt and Sherwood number with the variation of suction, velocity slip, stretching, magnetic and Casson parameter. Skin friction increases as enhancing of suction, stretching, magnetic and Casson parameter while decreasing as enhancing of velocity slip quantity. Amount of heat transfer improve as enhancing the suction parameter while fall down as enhancing of stretching, velocity slip, magnetic and Casson parameter. Amount of mass transmission raising as suction, stretching parameter while decreasing as enhancing of velocity slip, magnetic and Casson parameter. The Fig 14. Shows the variation of Nusselt & Sherwood number. Proportion of heat transmission enhancing as growing of thermal radiation and surface temperature while decreasing as enhancing chemical reaction and thermal slip quantities. Rate of mass transfer raising as enhancing of chemical reaction, thermal slip, thermal radiation while decreasing as enhancing of surface temperature parameter.

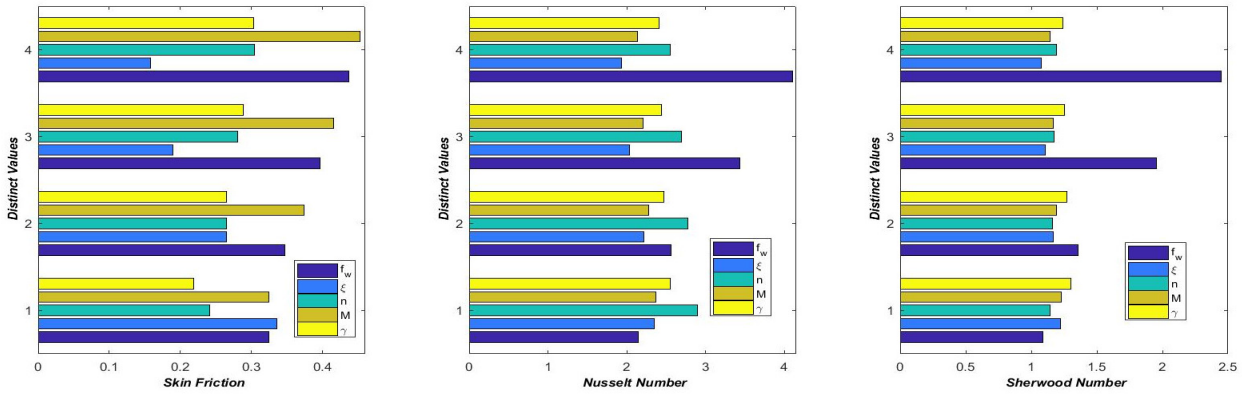

Figure 13. Skin frication, Nusselt and Sherwood number variation with the impact of f_w, ξ, n, M, γ

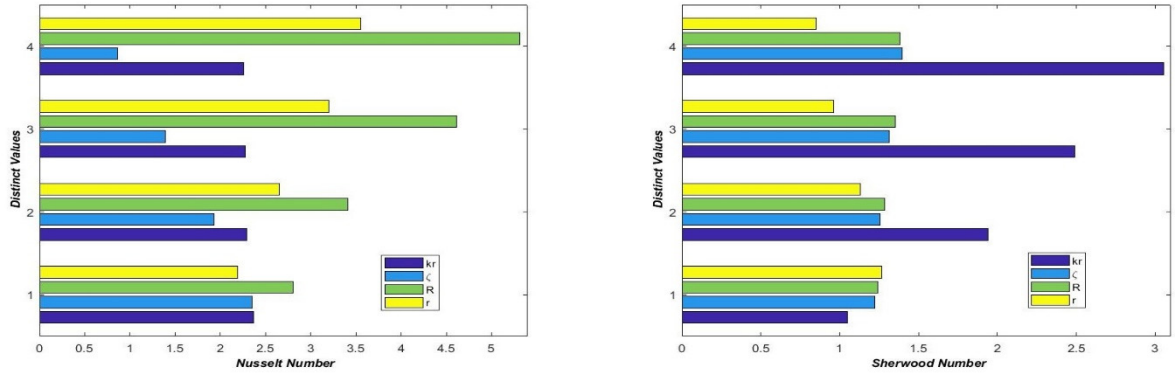

Figure 14. Nusselt and Sherwood number variation with the impact of kr, ζ, R, r

CONCLUSIONS

The purpose of the numerical study is to examine the effect of thermal radiation across a non-linear extending sheet on MHD Casson nano fluid. To solve the resulting ODEs with frontier circumstances and parameter modifications, the numerical schema bvp4c is used. The subsequent decisions are obtained.

- As the Casson, Magnetic parameter, and Prandtl number increase, the fluid's viscosity and that of the thermal frontier stratum decline.
- Lewis number and Brownian diffusion's effects, which are related to the temperature & concentration of reversible fluid flow.
- The temperature & concentration profiles rise with increasing velocity slip value.
- As the thermal slip parameter enhances, the thickness of the thermal frontier stratum falls.
- Temperature of the nanofluid increases while concentration of the fluid decreases with enhancement of the radiation parameter
- Decreases the thickness of the thermal & concentration frontier stratum by enhancing of Chemical decomposition rate.
- Skin friction raises as enhancing of suction, stretching, magnetic and Casson parameter while decreasing as enhancing of velocity slip quantity.
- Rate of heat transfer enhancing as increasing of thermal radiation and surface temperature while decreasing as enhancing chemical reaction and thermal slip quantities.
- Rate of mass transfer raising as enhancing of chemical reaction, thermal slip, thermal radiation while decreasing as enhancing of surface temperature parameter.

- The present results are in good agreement with earlier existed results.
- After discovering all the aforementioned results, we can determine that in several cases industrial production where the surfaces are stretching. Polymer sector when subjected to an external transverse magnetic field effect of several factors. The temperature and density of nanoparticles directly impact the quality of the material. Improving the final product can be achieved by controlling these factors at the period of manufacturing.

ORCID

P. Raja Shekar, https://orcid.org/0000-0003-4028-4688; **G. Jithender Reddy,** https://orcid.org/0000-0002-0103-1146
N. Pothanna, https://orcid.org/0000-0003-3983-3125

REFERENCES

[1] B.C. Sakiadis, "Boundary-layer behaviour on continuous solid surfaces: II. The boundary-layer on a continuous flat surface," AICHE J. 7**, (**1961). https://doi.org/10.1002/aic.690070211
[2] E.M.A. Elbashbeshy, and M.A.A Bazid, "Heat transfer over an unsteady stretching surface with internal heat generation," Appl. Math. Comput. **138**(2), (2003). https://doi.org/10.1016/S0096-3003(02)00106-6
[3] L.J. Crane, "Flow past a stretching plate," Journal of Applied Mathematics and Physics, **21**, (1970). https://doi.org/10.1007/BF01587695
[4] Z. Abbas, S. Rasool, and M. M. Rashidi, "Heat transfer analysis due to an unsteady stretching/shrinking cylinder with partial slip condition and suction," Ain Shams. Eng. J. **6,** (2015). https://doi.org/10.1016/j.asej.2015.01.004
[5] A.V. Rosca, N.C. Rosca, and I. Pop, "Numerical simulation of the stagnation point flow past a permeable stretching/shrinking sheet with convective boundary condition and heat generation," Internat. J. Numer. Methods Heat Fluid Flow, **26,** (2016). http://dx.doi.org/10.1108/HFF-12-2014-0361
[6] S.U. Choi, and J.A. Eastman, in: *Enhancing Thermal Conductivity of Fluids with Nanoparticles*, (Argonne National Lab., IL, United States, 1995), 12. (No. ANL/MSD/ CP-84938; CONF-951135-29).
[7] K. Das, T. Chakraborty, and P. Kumar Kundu, "Slip effects on nanofluid flow over a nonlinear permeable stretching surface with chemical reaction," Proceedings of the Institution of Mechanical Engineers, Part C: Journal of Mechanical Engineering Science. **230**(14), 2473 (2016). https://doi.org/10.1177/0954406215595654
[8] T. Hayat, M.W. Ahmad, S.A. Khan, and A. Alsaedi, "Computational treatment of statistical declaration probable error for flow of nanomaterials with irreversibility," Adv. Mech. Eng. **14,** (2022). https://doi.org/10.1177/16878140211070
[9] J. Wang, Y.P. Xu, R. Qahiti, M. Jafaryar, M.A. Alazwari, N.H. Abu-Hamdeh, and M.M. Selim, "Simulation of hybrid nanofluid flow within a microchannel heat sink considering porous media analyzing CPU stability," J. Petrol. Sci. Eng. **208,** 109734 (2022). http://dx.doi.org/10.1016/j.petrol.2021.109734
[10] W.A. Khan, and I. Pop, "Boundary-layer flow of a nanofluid past a stretching sheet," International Journal of Heat and Mass Transfer, **53,** 2477 (2010). https://doi.org/10.1016/j.ijheatmasstransfer.2010.01.032
[11] M.M. Rahman, and I.A. Eltayeb, "Radiative heat transfer in a hydromagnetic nanofluid past a non-linear stretching surface with convective boundary condition," Meccanica, **48**, 601 (2013). https://doi.org/10.1007/s11012-012-9618-2
[12] Md.T. Sk, K. Das, and P.K. Kundu, "Effect of magnetic field on slip flow of nanofluid induced by a non-linear permeable stretching surface," Applied Thermal Engineering, **104,** 758 (2016). http://dx.doi.org/10.1016/j.applthermaleng.2018.02.089
[13] Mahantesh M. Nandeppanavar, M.C. Kemparaju, and S. Shakunthala, "MHD stagnation point slip flow due to a non-linearly moving surface with effect of non-uniform heat source," Nonlinear Eng. **8,** 270 (2019). http://dx.doi.org/10.1515/nleng-2017-0109
[14] N. Vedavathi, G. Dharmaiah, K.S. Balamurugan, and J. Prakash, "Heat transfer on MHD nanofluid flow over a semi-infinite flat plate embedded in a porous medium with radiation absorption, heat source and diffusion thermo effect," Frontiers in Heat and Mass Transfer, **9,** 38 (2017). https://doi.org/10.5098/hmt.9.38
[15] P. Biswas, S.M. Arifuzzaman, M. Rahman, and M.S. Khan, "Effects of periodic magnetic field on 2D transient optically dense gray nanofluid over a vertical plate: a computational EFDM study with SCA," Journal of Nanofluids, **7**(1), 82 (2018). https://doi.org/10.1166/jon.2018.1434
[16] O.A. Beg, M.S. Khan, I. Karim, M.M. Alam, and M. Ferdows, "Explicit numerical study of unsteady hydromagnetic mixed convective nanofluid flow from an exponentially stretching sheet in porous media," Appl. Nano. sci. **4**, 943 (2014). http://dx.doi.org/10.1007/s13204-013-0275-0
[17] Al-Mamun, S.M. Arifuzzaman, S. Reza-E-Rabbi, P. Biswas, and M.S. Khan, "Computational modelling on MHD radiative Sisko nanofluids flow through a nonlinearly stretching sheet," International Journal of Heat and Technology, **37**(1), 285 (2019). http://dx.doi.org/10.18280/ijht.370134
[18] G. Dharmaiah, W. Sridhar, K.S. Balamurugan, and K.C. Kala, "Hall and ion slip impact on magneto-titanium alloy nano liquid with diffusion thermo and radiation absorption," Int. J. Ambient Energy, **43**, 3507 (2022). https://doi.org/10.1080/01430750.2020.1831597
[19] T.S.R.P. Roja, S.M. Ibrahim, M. Parvathi, G. Dharmaiah, and G. Lorenzini, "Magnetic field influence on Thermophoretic Micropolar fluid flow over an inclined permeable surface: a numerical study," J. Appl. Comput. Mech. **10**(2), 369 (2024). https://doi.org/10.22055/jacm.2024.44739.4265
[20] N. Casson, "A flow equation for pigment-oil suspensions of the printing ink type," Rheology of Disperse Systems, **84,** (1959).
[21] D.A. McDonald, *Blood flow in arteries.* 2nd ed. (Edward Arnold Ltd: Great Britain, 1974).
[22] P. Nagarani, V.M. Job, P.V.S.N. Murthy, "The effect of peristalsis on dispersion in Casson fluid flow," Ain Shams Engineering Journal, **15**, (2024). https://doi.org/10.1016/j.asej.2024.102758
[23] B.V. Awati, A. Goravar, N.M. Kumar, and G. Bognar, "Stability analysis of magnetohydrodynamic Casson fluid flow and heat transfer past an exponentially shrinking surface by spectral approach," Case Studies in Thermal Engineering. **60,** 104810 (2024). https://doi.org/10.1016/j.csite.2024.104810

[24] N. Abbas, W. Shatanawi, and T.A.M. Shatnawi, "Thermodynamic properties of Casson-Sutterby-micropolar fluid flow over exponential stretching curved sheet with impact of MHD and heat generation," Case Studies in Thermal Engineering, **55**, (2024).
[25] B.N. Reddy, and P. Maddileti, "Casson nanofluid and Joule parameter effects on variable radiative flow of MHD stretching sheet," Partial Differential Equations in Applied Mathematics. **7**, 100487 (2023). https://doi.org/10.1016/j.padiff.2022.100487
[26] B.P. Reddy, P.M. Matao, and J.M. Sunzu, "A finite difference study of radiative mixed convection MHD heat propagating Casson fluid past an accelerating porous plate including viscous dissipation and Joule heating effects," Heliyon, **10**, e28591 (2024). https://doi.org/10.1016/j.heliyon.2024.e28591
[27] Y.D. Reddy, and B.S. Goud, "Comprehensive analysis of thermal radiation impact on an unsteady MHD nanofluid flow across an infinite vertical flat plate with ramped temperature with heat consumption," **17**, 100796 (2023). https://doi.org/10.1016/j.rineng.2022.100796
[28] N.A. Zainal, R. Nazar, K. Naganthran, and I. Pop, "The Impact of Thermal Radiation on Maxwell Hybrid Nanofluids in the Stagnation Region," Nanomaterials (Basel), **12**(7), 1109 (2022). https://doi.org/10.3390/nano12071109
[29] A.M.A. Alrashdi, "Mixed convection and thermal radiation effects on non-Newtonian nanofluid flow with peristalsis and Ohmic heating," Front. Mater. **10**, 1178518 (2023). https://doi.org/10.3389/fmats.2023.1178518
[30] A.M. Rashad, M.A. Nafe, and D.A. Eisa, "Heat Generation and Thermal Radiation Impacts on Flow of Magnetic Eyring–Powell Hybrid Nanofluid in a Porous Medium," Arab. J. Sci. Eng. **48**, 939 (2023). https://doi.org/10.1007/s13369-022-07210-9
[31] Y.P. Lv, N. Shaheen, M. Ramzan, *et al*., "Chemical reaction and thermal radiation impact on a nanofluid flow in a rotating channel with Hall current," Sci. Rep. **11**, 19747 (2021). https://doi.org/10.1038/s41598-021-99214-y
[32] S. Arulmozhi, K. Sukkiramathi, S.S. Santra, R. Edwan, U. Fernandez-Gamiz, and S. Noeiaghdam, "Heat and mass transfer analysis of radiative and chemical reactive effects on MHD nanofluid over an infinite moving vertical plate," Results in Engineering, **14**, 100394 (2022). https://doi.org/10.1016/j.rineng.2022.100394
[33] B.H. Athal, A. Sasikala, B.N. Reddy, V. Govindan, P. Maddileti, K. Saritha, B.S. Reddy, *et al*., "Combined impact of radiation and chemical reaction on MHD hyperbolic tangent nanofluid boundary layer flow past a stretching sheet," Modern Physics Letters B, **38**(16), 2341010 (2024). https://doi.org/10.1142/S0217984923410105
[34] A.M. Sedki, "Effect of thermal radiation and chemical reaction on MHD mixed convective heat and mass transfer in nanofluid flow due to nonlinear stretching surface through porous medium," Results in Materials, **16**, 100334 (2022). https://doi.org/10.1016/j.rinma.2022.100334
[35] M. Eid, and O.D. Makinde, "Solar radiation effect on a magneto nanofluid flow in a porous medium with chemically reactive species," Int. J. Chem. React. Eng. **16**(9), 2017012 (2018). http://dx.doi.org/10.1515/ijcre-2017-0212
[36] N.T.M. Eldabe, A.Y. Ghaly, M.A.A. Mohamed, and M.S.H. Mohamoud, "MHD boundary layer chemical reacting flow with heat transfer of Eyring -Powell nanofluid past a stretching sheet," Microsyst. Technol. **24**, 4945 (2018). https://doi.org/10.1007/s00542-018-3915-1
[37] B.J. Gireesha, and N.G. Rudraswamy, "Chemical reaction on MHD flow and heat transfer of a nanofluid near the stagnation point over a permeable stretching surface with non-uniform heat source/sink," International Journal of Engineering, Science and Technology, **6(5)**, 13 (2014). https://doi.org/10.4314/ijest.v6i5.2
[38] A.Bhandari, "Radiation and Chemical Reaction Effects on Nanofluid Flow Over a Stretching Sheet," Fluid Dynamics & Materials Processing, **15**(5), 557 (2019). https://doi.org/10.32604/fdmp.2019.04108
[39] W. Jamshed, V. Kumar, and V. Kumar, "Computational examination of Casson nanofluid due to a non- linear stretching sheet subjected to particle shape factor: Tiwari and Das model," Numerical Methods for Partial Differential Equations **38**(4), 848 (2022). https://doi.org/10.1002/num.22705
[40] I. Ullah, K.S. Nisar, S. Shafie, I. Khan, M. Qasim, and A. Khan, "Unsteady free convection flow of Casson nanofluid over a nonlinear stretching sheet," IEEE Access, **7**, 93076 (2019). https://doi.org/10.1109/access.2019.2920243

ВПЛИВ ТЕПЛОВОГО ВИПРОМІНЮВАННЯ НА МГД ПОТІК НАНОРІДИНИ КАССОНА ЧЕРЕЗ ЛИСТ ЩО НЕЛІНІЙНО РОЗТЯГУЄТЬСЯ З НАЯВНОСТЮ ХІМІЧНОЇ РЕАКЦІЇ

П. Раджа Шекар, Г. Джитендер Редді, Н. Потанна

Кафедра математики, Інженерно-технологічний інститут VNR Віньяна Джьоті, Хайдарабад, 500090, Телангана, Індія

Метою цього дослідження є вивчення впливу параметра Кассона та хімічної реакції на змінний радіаційний МГД потік нанофлюїду через лист, що розтягується. Завдяки використанню функцій подібності рівняння моделювання (PDE) руху рідини перетворюються на прості диференціальні рівняння. Інструмент MATLAB використовується для чисельного обчислення рівнянь. Графіки та описи надані для контурів швидкості, концентрації та температури, що показують вплив важливих обмежень потоку рідини. Аналізуються різні фактори, щоб отримати дані та пояснення чисел Прандтля, Льюїса, параметрів ковзання та хімічного розкладання. Поточні результати є хорошими та добре узгоджуються з наявними звітами. В'язкість флюїду та термічного граничного шару зменшується зі збільшенням Кассона, магнітного параметра та числа Прандтля. Поверхневе тертя збільшується при збільшенні всмоктування, розтягування, магнітного параметра та параметра Кассона, а також зменшується через збільшення швидкісного ковзання. Швидкість передачі тепла збільшується у міру збільшення теплового випромінювання та температури поверхні, одночасно зменшуючись у міру посилення хімічної реакції та теплового ковзання. Швидкість масообміну підвищується за рахунок посилення хімічної реакції, теплового ковзання, теплового випромінювання та зменшується за рахунок збільшення параметра температури поверхні.

Ключові слова: *нанофлюїд; хімічна реакція; термофорез; броунівський рух*

East European Journal of Physics. 1. 112–121 (2025)
DOI: 10.26565/2312-4334-2025-1-10 ISSN 2312-4334

EFFECTS OF HALL CURRENT ON DARCY-FORCHHEIMER MHD MIXED CONVECTIVE FLOW OVER A VERTICAL SURFACE WITH ROTATION IN POROUS MEDIUM

Satyabhushan Roy[a*], **Dipak Sarma**[a], **Ankur Kumar Sarma**[a,b], **Sunmoni Mudoi**[a]
[a] *Department of Mathematics, Cotton University, Guwahati-781001, India*
[b] *Department of Mathematics, Baosi Banikanta Kakati College, Nagaon, Barpeta- 781311, India*
[*] *Corresponding Author e-mail: satyabhushan96@gmail.com*
Received September 30, 2024; revised December 23, 2025; in final form January 14, 2025, accepted January 20, 2025

The analysis of Darcy-Forchheimer MHD flow has been a concern of consideration for research scientists and engineers. This work examines the unsteady hydrodynamic mixed convective flow of an incompressible, viscous, electrically conducting fluid as well as the transfer of heat and mass in a vertical surface with the Hall current, rotation, and Darcy-Forchheimer effect. Through similarity transformation, the dimensionless unstable governing equation is found. Then, using the Matlab method bvp4c, the similarity ordinary differential equation was solved. When the solution and those produced by Elgazery and Stanford were compared to the numerical result for a few exceptional circumstances, there was a fair degree of agreement. Graphs are used to show the temperature, concentration, and fluid velocity. In contrast, skin friction, the Sherwood number, and the Nusselt number are calculated in tabular form.

Keywords: *Hall current; Rotation; Darcy Forchheimer; Mixed convection; Bvp4c*

PACS: 44.25.+f, 44.27.+g, 33.20.Vq, 44.30.+v, 44.40.+a

1. INTRODUCTION

The study of Darcy-Forchheimer magnetohydrodynamic (MHD) flow has become significant in understanding complex fluid dynamics influenced by magnetic fields, rotation, and porous medium. MHD flow involves electrically conducting fluids interacting with magnetic fields, which is particularly relevant in engineering and environmental applications. The Hall current effect, rotation, and Darcy-Forchheimer effects play crucial roles in influencing the velocity, temperature, and concentration of such flows. This study aims to explore the dynamics of unsteady MHD mixed convective flow over a vertical surface, considering the Hall current and rotation in a porous medium, using numerical solutions. The findings can be applied to various practical scenarios, including polymer processing, metal casting, and natural convection in porous media, providing deeper insights into fluid behavior under the influence of electromagnetic forces. Sarma and Sarma (2024) [1] explored unsteady magnetohydrodynamic (MHD) bioconvection Casson fluid flow with gyrotactic microorganisms over a vertically stretched sheet. Samad and Rahman (2006) [2] studied the interaction of thermal radiation with unsteady MHD flow over a vertical porous plate in a porous medium. Mukhopadhyay and Layek (2009)[3] investigated the effects of radiation on forced convective flow and heat transfer over a porous plate within a porous medium. Later, Mukhopadhyay et al. (2012) [4] extended the study to forced convective flow and heat transfer in a Darcy-Forchheimer porous medium in the presence of radiation. Khan et al. (2022) [5] focused on MHD thin-film flow through a porous stretching sheet, considering the impact of thermal radiation and viscous dissipation. Panya et al. (2023) [6] analyzed MHD Darcy-Forchheimer slip flow in a porous medium with variable thermophysical properties. Reddy et al. (2021) [7] examined the chemical reaction impact on MHD natural convection flow through porous media around an exponentially stretching sheet, including the effects of heat sources/sinks and viscous dissipation. Sakiadis (1961)[8] initiated the study of boundary-layer behavior on continuous solid surfaces, forming the foundational equations for two-dimensional and axisymmetric flow. Crane (1970) [9] provided an analytical solution for the boundary layer equation concerning steady two-dimensional flow over a stretched surface in an incompressible fluid. Nayak et al. (2014, 2016)[10][11][12] conducted two studies focusing on the effects of chemical reactions on MHD flow of visco-elastic fluids through porous media and on steady MHD flow and heat transfer with a third-grade fluid during wire coating, considering temperature-dependent viscosity. Vafai and Tien (1982)[13] emphasized boundary and inertia effects on convective mass transfer in porous media. Hong et al. (1987)[14] investigated non-Darcian and non-uniform porosity effects on vertical plate natural convection in porous media. Jumah et al. (2001)[15] examined Darcy-Forchheimer mixed convection heat and mass transfer in fluid-saturated porous media. Chamkha (1997)[16] explored hydromagnetic natural convection from an isothermal inclined surface adjacent to a thermally stratified porous medium. Elgazery (2009)[17] assessed the effects of chemical reactions, Hall and ion-slip currents on MHD flow, considering temperature-dependent viscosity and thermal diffusivity. Kinyanjui et al. (2001)[18] looked at MHD free convection heat and mass transfer of heat-generating fluids past an impulsively started vertical porous plate with Hall current and radiation absorption. Shateyi et al. (2010)[19] examined the effects of thermal radiation, Hall currents, and Soret and Dufour effects on MHD flow over a vertical surface within porous media.

Cite as: S. Roy, D. Sarma, A. Sarma, S. Mudoi, East Eur. J. Phys. 1, 112 (2025), https://doi.org/10.26565/2312-4334-2025-1-10

Singh (1984)[20] analyzed Hall effects on MHD free-convection flow past an accelerated vertical porous plate. Sarma and Pandit (2015)[21] investigated thermal radiation and chemical reaction effects on steady MHD mixed convective flow over a vertical porous plate with induced magnetic fields. Sattar and Kalim (1996)[22] studied the interaction between boundary-layer flow and thermal radiation under unstable free convection past a vertical porous plate. Nandkeolyar et al. (2013) [23] provided exact solutions for unsteady MHD free convection in a heat-absorbing fluid flow over a flat plate with ramped wall temperature. Chamkha (1997)[24] again discussed MHD-free convection from a vertical plate within a thermally stratified porous medium while including Hall effects. Abo-Eldahab and Salem (2004)[25] explored Hall effects on MHD free convection flow of non-Newtonian power-law fluids over a stretching surface. Siddiqa et al. (2013)[26] investigated Hall current effects on magnetohydrodynamic natural convection flow with a strong cross-magnetic field. Seth and Singh (2016) [27] provided a solution for mixed convection hydromagnetic flow in a rotating channel considering Hall and wall conductance effects. Kumar et al. (2020) [28] studied the influence of heat sources/sinks on MHD flow between alternating conducting walls, incorporating Hall effects. Finally, Pandit and Sarma (2017) [29] explored the combined effects of Hall current and rotation on unsteady MHD natural convection flow past a vertical flat plate with ramped wall temperature and heat absorption. This structure highlights the advancements in the field of MHD flow and heat and mass transfer under various conditions, including the effects of magnetic fields, chemical reactions, Hall current, rotation, Darcy-Forchheimer effect and porous media considerations.

Motivated by the above investigations, the influences of the Hall current, soret and Dufour effect with chemical reaction and rotation on Darcy Forchheimer MHD mixed convective flow over a vertical surface are studied. The transformed dimensionless governing equations are solve by bvp4c method. The effect of various physical parameter on velocity, temperature and concentration profile are studied in details. Also the value Skin friction, Nuslet number and sherwood number for different parameters are shown in table.

2. MATHEMATICAL FORMULATION

We examine the dynamics of an unsteady flow in an electrically conducting, viscous fluid that involves mass and heat transfer. The flow passes across a vertical flat plate that is semi-infinite in length, rotated, and immersed in a homogenous porous media. Furthermore, the effect of Hall current is considered. Think of a coordinate system (x,y,z) in which the vertical plate and the x-axis are in line. with the y-axis perpendicular to it and pointing upward. Around the y-axis, the fluid and plate rotate at a constant angular velocity Ω. The front border of the plate and the z-axis line up. A homogeneous transverse magnetic field of intensity B_0 applied in the y direction causes the fluid to become saturated, as shown in Fig 1. The flow is three-dimensional because of the force that the Hall current effect creates in the z direction, which results in a cross flow velocity. Considering Hall currents,

The following is the format of generalized Ohm's law:

$$J = \frac{\sigma}{1+m^2}\left(E + (V \times B) - \frac{1}{\sigma n_e} J \times B\right)$$

The equation includes the magnetic induction vector (B), electric field intensity vector (E), electric current density vector (J), Hall current parameter (m), velocity vector (V), electrical conductivity (σ), and electron density (n_e).

The governing equation in (x,y,z)-coordinates may be expressed as follows under the standard boundary layer and Boussinesq approximations:

$$\frac{\partial u}{\partial t} + 2\Omega w + u\frac{\partial u}{\partial x} + v\frac{\partial u}{\partial y} = \nu\frac{\partial^2 u}{\partial y^2} - \frac{\sigma B_0^2}{\rho(1+m^2)}(u+mw) + g\beta_c(C-C_\infty) + g\beta_t(T-T_\infty) - \frac{\nu}{K_p}u - \frac{K^*}{\sqrt{K_p}}u^2 \quad (1)$$

$$\frac{\partial w}{\partial t} + 2\Omega u + u\frac{\partial w}{\partial x} + v\frac{\partial w}{\partial y} = \nu\frac{\partial^2 w}{\partial y^2} + \frac{\sigma B_0^2}{\rho(1+m^2)}(mu-w) - \frac{\nu}{K_p}w - \frac{K^*}{\sqrt{K_p}}w^2 \quad (2)$$

$$\frac{\partial T}{\partial t} + u\frac{\partial T}{\partial x} + v\frac{\partial T}{\partial y} = \frac{k}{\rho c_p}\frac{\partial^2 T}{\partial y^2} + \frac{D_M K_T}{c_s c_p}\frac{\partial^2 C}{\partial y^2} + \frac{\sigma B_0^2}{\rho c_p(1+m^2)}(u^2+w^2) - \frac{1}{\rho c_p}\frac{\partial q_r}{\partial y} \quad (3)$$

$$\frac{\partial C}{\partial t} + u\frac{\partial C}{\partial x} + v\frac{\partial C}{\partial y} = D\frac{\partial^2 C}{\partial y^2} + \frac{D_M K_T}{T_m}\frac{\partial^2 T}{\partial y^2} \quad (4)$$

The boundary conditions are,

$$\begin{gathered} u(x,0) = U_s = \frac{A_0 x}{1-ct}, \quad v(x,0) = -V_w, \quad w(x,0) = 0, \quad T(x,0) = T_w, \quad C(x,0) = C_w \\ u(x,\infty) = w(x,\infty) = 0 \quad T(x,\infty) = T_\infty \quad C(x,\infty) = C_\infty \end{gathered} \quad (5)$$

Where u,v and w represent the components of fluid velocity along the x-,y-,and z-axes, respectively. The fluid temperature and concentration are represented by T and C, respectively. These variables are commonly used in physics to describe fluid properties: ν represents kinematic viscosity, μ represents dynamic viscosity, ρ represents fluid density, g represents gravitational force due to acceleration, and β_t represents the coefficient of volume expansion. β_c represents the volumetric coefficient of expansion when concentration is taken into account, while B_0 denotes the constant magnetic field. Strength is determined by the coefficient of mass diffusivity D, c_p is the specific heat at constant pressure. c_s is the Concentration susceptibility, T_m represents the average fluid temperature, K_T denotes the thermal diffusion ratio, and k is The fluid's thermal conductivity, K_p is the medium's permeability, and the Hall parameter m, are all important factors to consider.

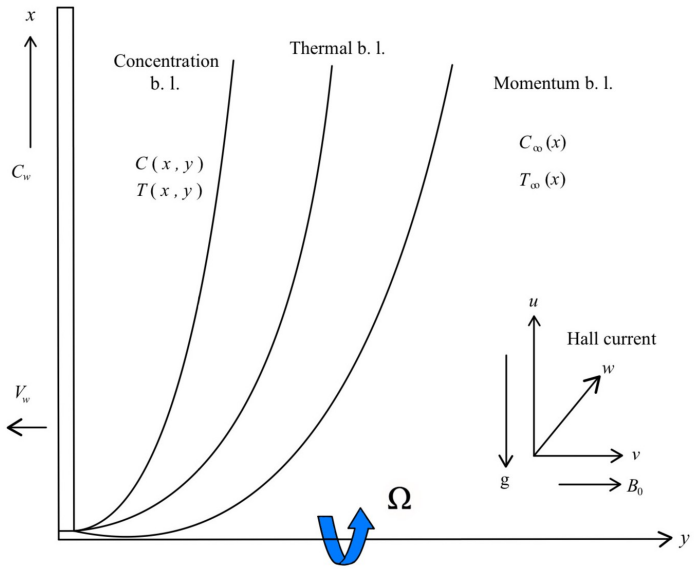

Figure 1. The coordinate system for the physical model of the problem

U_s is the surface velocity, A_0 is a constant with dimension $(time)^{-1}$, V_w, T_w and C_w are suction or injection velocity, temperature and concentration at the plate respectively. By using Rosseland approximation for thermal radiation, the radiative heat flux is modeled as,

$$q_r = -\frac{4\sigma_1}{3k_1}\frac{\partial T^4}{\partial y}$$

where k_1 is the mean absorption coefficient and σ_1 is the Stefan Boltzmann constant. Following Chamkha [16] it is assumed that T^4 can be stated as a linear function of temperature since the temperature difference within the flow are thought to be sufficiently small. This is achieved by omitting higher order terms and expanding T^4 in a Taylor series around T_∞, thus

$$T^4 \approx 4T_\infty^3 T - 3T_\infty^4$$

and thus the gradient of heat radiation term can be expressed as

$$\frac{\partial q_r}{\partial y} = -\frac{16\sigma_1 T_\infty^3}{3k_1}\frac{\partial^2 T}{\partial y^2}$$

Following [17] We nondimensionalize (1)-(4) using the following transformation,

$$\eta = \sqrt{\frac{A_0}{\nu(1-ct)}}y,\quad u = \frac{A_0 x}{(1-ct)}f'(\eta),\quad v = -\sqrt{\frac{A_0\nu}{(1-ct)}}f(\eta),\quad w = \sqrt{\frac{A_0\nu}{(1-ct)}}h(\eta)$$
$$U_s = \frac{A_0 x}{(1-ct)},\quad \theta(\eta) = \frac{T-T_\infty}{T_w-T_\infty},\quad \phi(\eta) = \frac{C-C_\infty}{C_w-C_\infty} \tag{6}$$

where $f(\eta)$,$h(\eta)$,$\theta(\eta)$ and $\phi(\eta)$ are dimensional stream functions, temperature and concentration distribution function respectively.

Substituting (6) into (1)-(4) we get the following similarity equations,

$$U_n(f' + \frac{1}{2}\eta f'') + 2K^2\sqrt{Re}f'^2h + f'^2 - ff'' = f''' - \frac{M}{1+m^2}(f' + \frac{m}{\sqrt{Re}}h) + Gm\phi + Gr\theta - Spf' - Ff'^2 \quad (7)$$

$$\frac{1}{2}U_n(\eta h' + h) - 2K^2Re^{\frac{3}{2}}f'^3 + fh' = h'' + \frac{M}{1+m^2}(mf' - \frac{1}{Re}h) - Sph - F\frac{1}{Re}h^2 \quad (8)$$

$$U_n(\frac{1}{2}\eta\theta' + \theta) + \theta f' - f\theta' = (1 + \frac{4}{3N})\frac{1}{Pr}\theta'' + Du\phi'' + \frac{M}{1+m^2}Ec(f'^2 + \frac{1}{Re}h^2) \quad (9)$$

$$U_n(\frac{1}{2}\eta\phi' + \phi) + \phi f' - f\phi' = \frac{1}{Sc}\phi'' + Sr\theta'' \quad (10)$$

The transformed boundary conditions are as follows,

$$\begin{aligned} f(0) = f_w,\ \ f'(0) = 1,\ \ h(0) = 0,\ \ \theta(0) = 1,\ \ \phi(0) = 1\ \ as\ \ \eta \to 0 \\ f'(\infty) = 0,\ \ h(\infty) = 0,\ \ \theta(\infty) = 0,\ \ \phi(\infty) = 0\ \ \ as\ \ \eta \to \infty \end{aligned} \quad (11)$$

where the primes denote differentiation with respect to η. Where $M = \frac{\sigma B_0^2(1-ct)}{\rho A_0}$ is the magnetic parameter, $Re = \frac{xU_s}{\nu}$ is the Reynolds number, $K^2 = \frac{\nu\Omega}{u^2}$ is the Rotation parameter, $Gr = \frac{g\beta_t(T_w - T_\infty)(1-ct)}{U_s A_0}$ is the Local Grashof number, $Gm = \frac{g\beta_c(C_w - C_\infty)(1-ct)}{U_s A_0}$ is the Local modified Grashof number, $Sp = \frac{\nu(1-ct)}{A_0 Kp}$ is the Permeability parameter, $Pr = \frac{\mu c_p}{k}$ is the Prandtl number, $Ec = \frac{{U_s}^2}{c_p(T_w - T_\infty)}$ is the Eckert number, $Du = \frac{D_M K_T(C_w - C_\infty)}{\nu c_s c_p(T_w - T_\infty)}$ is the Dufour number, $Sc = \frac{\nu}{D}$ is the Schmidt number, $Sr = \frac{D_M K_T(T_w - T_\infty)}{\nu T_m(C_w - C_\infty)}$ is the Soret number.

3. METHOD OF SOLUTION

A MATLAB boundary value problem solver named bvp4c was used to solve the equations (7), (8), (9), and (10) subject to boundary conditions (11). Using bvp4c, almost any BVP may be prepared for solution. The present result for the coefficient of skin friction $-f''(0)$ with different values of $k_p = \frac{1}{S_p}$ are compared with the Elgazery [17] and the Stanford [30] result. It is seen from Table 1, the obtained numerical result using bvp4c method are in an excellent agreement with those published previously. m=Gr=Gm=0, fw = -0.7, and M=1 were used to construct Table 1.

Table 1. Values of the skin friction $-f''(0)$, the present method, result of Elgazery [17] and the Stanford [30]

k_p	Elgazery [17]	Stanford Shateyi[30]	Present work
1	1.4170	1.4170	1.4171
2	1.2694	1.2694	1.2694
5	1.1739	1.1739	1.1740
10	1.1408	1.1408	1.1408
15	1.1295	1.1295	1.1294

4. RESULTS AND DISCUSSION

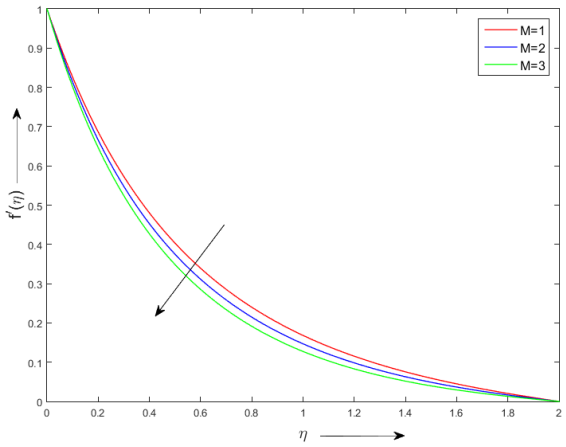

Figure 2
Variation of tangential velocity distribution with increasing Magnetic parameter M.

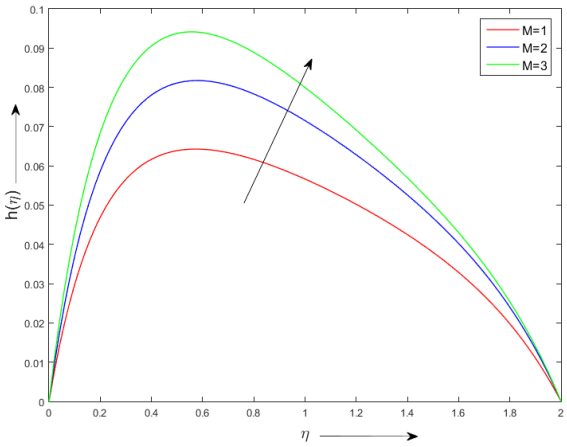

Figure 3
Variation of lateral velocity distribution with increasing Magnetic parameter M..

Figures 2 and 3 show how the magnetic parameter affects tangential and lateral velocity. The tangential velocity falls with increasing magnetic parameter. The Lorentz force causes a reduction in the tangential velocity in the direction of flow. The fluid particles slow down and decrease their sideways speed due to the magnetic field's force, which works at a right angle to the direction of flow. On the other hand, the lateral velocity rises with the magnetic parameter. The Lorentz force causes an increase in the lateral velocity perpendicular to the flow direction. The fluid particles experience lateral deflection due to the magnetic field, which raises their lateral velocity. A magnetic field produces a narrow boundary layer close to the wall, where there is a noticeable velocity gradient, which raises the lateral velocity.

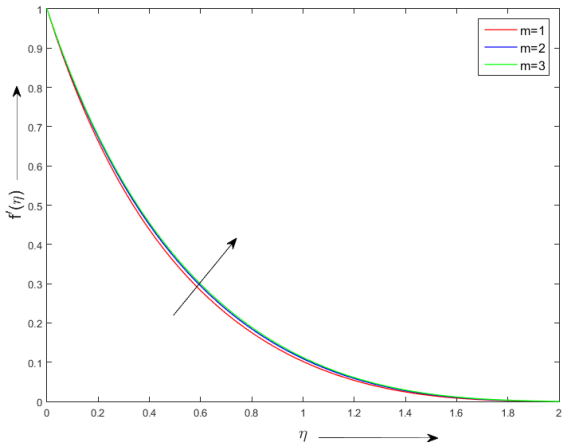

Figure 4
Variation of tangential velocity distribution with increasing Hall parameter m.

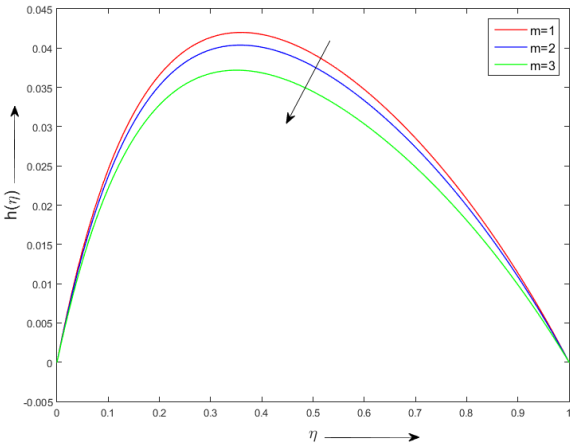

Figure 5
Variation of lateral velocity distribution with increasing Hall parameter m.

Figures 4 and 5 illustrate the effect of the Hall current parameter on tangential and lateral velocity. As the Hall current parameter increases, the tangential velocity also increases. The tangential velocity increases as a result of the force generated by Hall current, which accelerates the fluid particles in the direction of flow. On the other hand, the lateral velocity decreases as a result of the Hall current. Due to the Hall current, the fluid particle is deflected in the opposite direction, resulting in a decrease in lateral velocity.

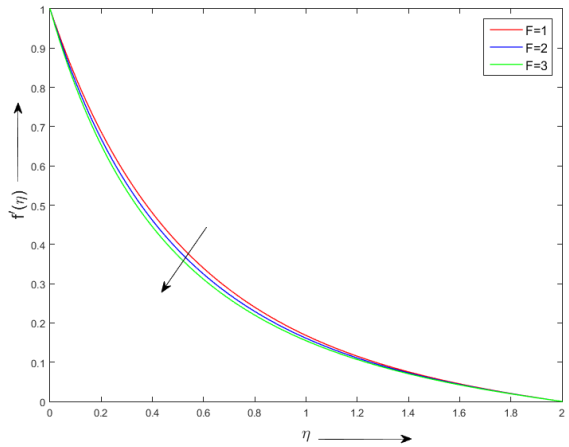

Figure 6
Variation of tangential velocity distribution with increasing Darcy-Forchheimer Parameter.

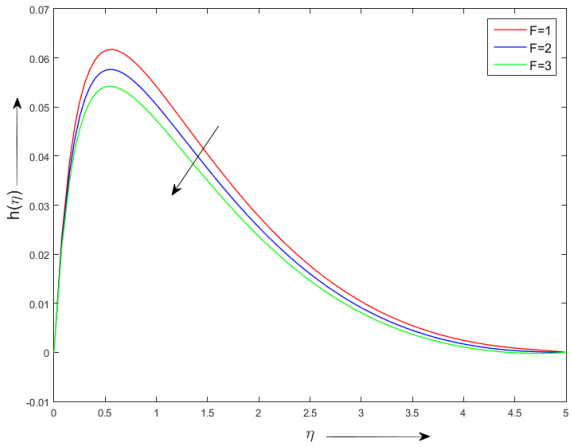

Figure 7
Variation of lateral velocity distribution with increasing Darcy-Forchheimer Parameter.

Figures 6 and 7 demonstrate the impact of the Darcy-Forchheimer number on the tangential and lateral velocity. The Darcy-Forchheimer number plays a significant role in the flow dynamics, causing greater resistance, increased viscous effects, decreased inertial effects, and overall flow stabilization. All of these factors contribute to a reduction in both tangential and lateral velocities.

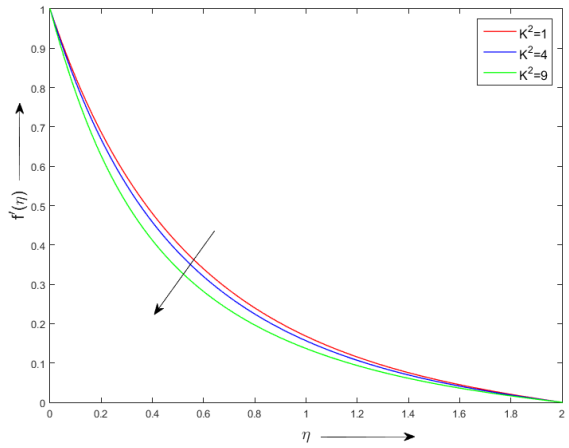

Figure 8
Variation of tangential velocity distribution with increasing Rotation parameter K^2.

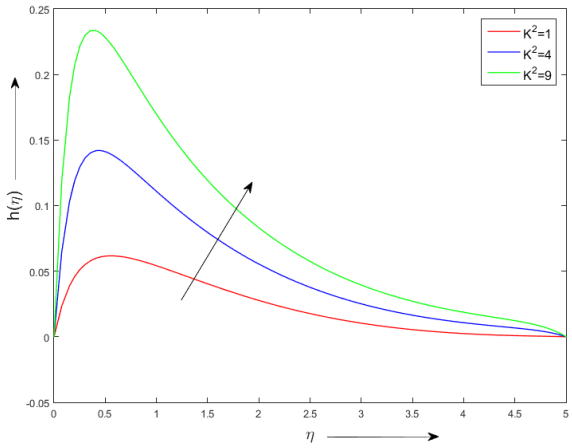

Figure 9
Variation of lateral velocity distribution with increasing Rotation parameter K^2.

Figures 8 and 9 show how the rotation parameter affects tangential and lateral velocity. From figure it is observed that tangential velocity decreases with increasing the rotation parameter whereas lateral velocity increases with increasing the rotation parameter. The coriolis force which results from rotation acts perpendicular to both the direction of motion and axis of rotation. In this fluid flow it tends to deflect the fluid particle away from the original path. As rotation parameter increase, the coriolis force become stronger, deflecting the fluid particles more towards the lateral direction. This results in increase in lateral velocity. The Coriolis force can also oppose the tangential flow, especially near the boundaries. This can lead to decrease in tangential velocities, particularly in the boundary layer region. The coriolis force can significantly affect the boundary layer leading to a thicker boundary layer and reduced tangential velocity.

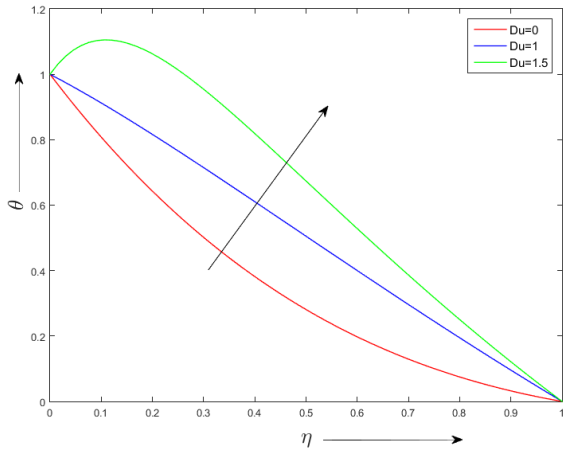

Figure 10
Variation of temperature distribution with increasing Dufour number Du.

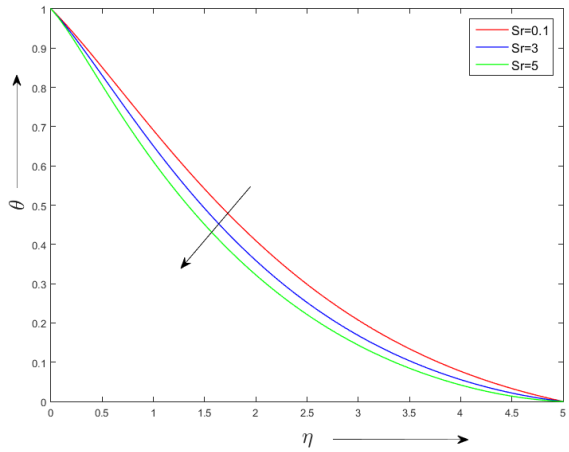

Figure 11
Variation of temperature distribution with increasing Soret number Sr.

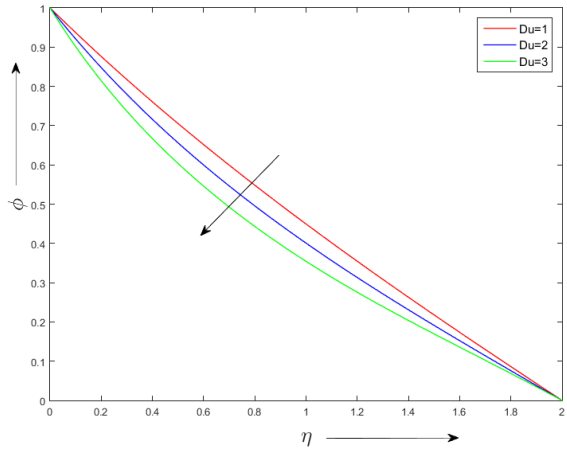

Figure 12
Variation of Concentration distribution with increasing Dufour number Du.

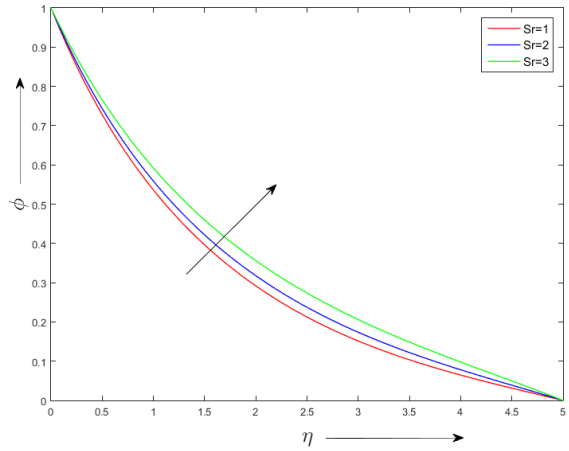

Figure 13
Variation of Concentration distribution with increasing Soret number Sr.

Figures 10 and 12 demonstrate the impact of temperature and concentration as the Dufour number increases. The Dufour effect illustrates how concentration gradients can impact heat transfer. As the Dufour number increases, the heat transfer caused by the concentration gradient becomes more significant, resulting in a rise in temperature. On the other hand, the heightened heat transfer resulting from the Dufour effect causes a reduction in concentration. The heat transfer plays a crucial role in enhancing the diffusion of species, which in turn leads to a reduction in concentration gradients.

Figures 11 and 13 demonstrate the impact of temperature and concentration as soret number rises. The soret effect illustrates the effects of temperature gradient on mass transport. As soret number grows, the mass transfer owing to temperature gradient becomes more substantial, resulting to decrease in temperature. This is because the soret effect promotes the transmission of heat from the system, cooling it down. Conversely the enhanced mass transfer owing to the soret effect leads to an increase in concentration. This is because the soret effect pushes the migration of species towards the colder zone, increasing the concentration gradients.

Table 2 illustrates the influence of M, Pr, m, F, K^2, Du, Sr on the coefficient of skin friction, sherwood number and nuslet number. From the table we observe that as M, Pr, F, K^2 increase the value of skin friction increases but it shows opposite effect with the rise in m, Du and Sr.
Also, Nuslet number rises with enlarged values of Pr and m while it shows opposite result with the increasing value of M, F, K^2, Du, Sr.

Also, it can be seen that Sherwood number rises with enlarged values of M and Du while it shows opposite result with increasing the value of Pr, m, F, K^2 and Sr.

Table 2. Variations of $-f''$,$-\theta'$, $-\phi'$ for different parameters.

M	Pr	m	F	K^2	Du	Sr	$-f''$	$-\theta'$	$-\phi'$
1							1.9434	2.0538	1.1698
2							2.0987	2.0188	1.1708
3							2.2478	1.9867	1.1714
	1						1.9466	2.1022	1.1466
	2						1.9577	2.2856	1.0587
	3						1.9651	2.4944	0.9589
		1					1.9434	2.0538	1.1698
		2					1.8567	2.0746	1.1682
		3					1.8239	2.0825	1.1678
			1				1.9434	2.0538	1.1698
			2				2.1152	2.0430	1.1646
			3				2.2754	2.0333	1.1601
				1			1.9434	2.0538	1.1698
				2			2.0694	2.0404	1.1643
				3			2.3809	2.0118	1.1528
					0.7		1.8953	1.4157	1.4775
					0.8		1.8721	1.0670	1.6446
					0.9		1.8492	0.6936	1.8229
						0.5	1.9434	2.0538	1.1698
						1	1.8591	1.3277	1.1382
						1.5	1.8271	1.0849	1.0980

5. CONCLUSION

In this work, the effect of Hall current, Darcy Forchheimer effect on an unsteady MHD mixed convective flow with rotation in porous medium is investigated. The resulting partial differential equations with boundary condition were transformed to a set of ordinary differential equation by using similarity transformation. The bvp4c method is used to obtain the numerical solution. Graphical results were obtained to illustrate the details of flow and their dependence on some physical parameter.

In conclusion, the magnetic parameter reduces tangential velocity while increasing lateral velocity due to the influence of the Lorentz force. The Hall parameter has a contrasting effect, enhancing tangential velocity while reducing lateral velocity. The Darcy-Forchheimer parameter decreases both tangential and lateral velocities, indicating increased resistance and stabilized flow in the porous medium. The rotation parameter lowers tangential velocity but boosts lateral velocity due to Coriolis force. Furthermore, an increase in the Dufour number leads to a rise in temperature and a reduction in concentration, while an increase in the Soret number decreases temperature but raises concentration. Coefficient of skin friction increases with increasing M, Pr, F, K^2 increase but decreases with increasing m, Du and Sr. With increasing Pr and m, the value of Nuslet number increases but decreases with increasing M, F, K^2, Du, Sr. Sherwood number increases with increasing M and Du but decreases with increasing Pr, m, F, K^2 and Sr. These findings highlight the significant impact of magnetic fields, rotation, and porous medium properties on fluid flow dynamics, temperature, and concentration distributions.

ORCID

Satyabhushan Roy, https://orcid.org/0009-0005-7899-7351; **Dipak Sarma**, https://orcid.org/0009-0007-1463-242X; **Ankur Kumar Sarma**, https://orcid.org/0009-0003-6209-8859; **Sunmoni Mudoi**, https://orcid.org/0009-0000-2170-5235

REFERENCES

[1] A.K.Sarma, and D. Sarma, "Unsteady magnetohydrodynamic bioconvection Casson fluid flow in presence of gyrotactic microorganisms over a vertically stretched sheet," Numerical Heat Transfer, Part A: Applications, 1-24 (2024). https://doi.org/10.1080/10407782.2024.2389338

[2] Md.A. Samad, and M. Mansur-Rahman, "Thermal radiation interaction with unsteady MHD flow past a vertical porous plate immersed in a porous medium," Journal of Naval Architecture and Marine Engineering, **3**(1), 7-14 (2006). https://doi.org/10.3329/jname.v3i1.924

[3] S. Mukhopadhyay, and G.C. Layek, "Radiation effect on forced convective flow and heat transfer over a porous plate in a porous medium," Meccanica, **44**(5), 587-597 (2009). https://doi.org/10.1007/s11012-009-9211-5

[4] S. Mukhopadhyay, et al., "Forced convective flow and heat transfer over a porous plate in a Darcy-Forchheimer porous medium in presence of radiation," Meccanica, **47**, 153-161 (2012). https://doi.org/10.1007/s11012-011-9423-3

[5] Z. Khan, et al., "Magnetohydrodynamic thin film flow through a porous stretching sheet with the impact of thermal radiation and viscous dissipation," Mathematical Problems in Engineering, **2022**(1), 1086847 (2022). https://doi.org/10.1155/2022/1086847

[6] A.L. Panya, O.A. Akinyemi, and A.M. Okedoye, "MHD Darcy–Forchheimer slip flow in a porous medium with variable thermo-physical properties," Zenodo, 10(2), 30-43 (2023). https://doi.org/10.5281/zenodo.7646344

[7] N.N. Reddy, V.S. Rao, and B.R. Reddy, "Chemical reaction impact on MHD natural convection flow through porous medium past an exponentially stretching sheet in presence of heat source/sink and viscous dissipation," Case studies in thermal engineering, **25**, 100879 (2021). https://doi.org/10.1016/j.csite.2021.100879

[8] B.C. Sakiadis, "Boundary-layer behavior on continuous solid surfaces: I. Boundary-layer equations for two-dimensional and axisymmetric flow," AIChE Journal **7**(1), 26–28 (1961). https://doi.org/10.1002/aic.690070108

[9] L.J. Crane, "Flow past a stretching plate," Zeitschrift für angewandte Mathematik und Physik, **21**, 645-647 (1970). https://doi.org/10.1007/BF01587695

[10] M.K.Nayak, G.C. Dash, and L.P. Singh, "Effect of chemical reaction on MHD flow of a visco-elastic fluid through porous medium," J. Appl. Anal. Comput. **4**(4), 367-381 (2014).

[11] M.K.Nayak, G.C. Dash, and L.P. Singh, "Steady MHD flow and heat transfer of a third grade fluid in wire coating analysis with temperature dependent viscosity," International Journal of Heat and Mass Transfer, **79**, 1087-1095 (2014). https://doi.org/10.1016/j.ijheatmasstransfer.2014.08.057

[12] M.K. Nayak, G.C. Dash, and L.P. Singh, "Heat and mass transfer effects on MHD viscoelastic fluid over a stretching sheet through porous medium in presence of chemical reaction," Propulsion and Power Research, **5**(1), 70-80 (2016). https://doi.org/10.1016/j.jppr.2016.01.006

[13] K. Vafai, and C.L. Tien, "Boundary and inertia effects on convective mass transfer in porous media", International Journal of Heat and Mass Transfer, 25(8), 1183–1190 (1982). https://doi.org/10.1016/0017-9310(82)90212-5

[14] J.T. Hong, Y. Yamada, and C.L. Tien, "Effects of non-Darcian and nonuniform porosity on vertical-plate natural convection in porous media," J. Heat Transfer. **109**(2), 356-362 (1987). https://doi.org/10.1115/1.3248088

[15] R.Y. Jumah, A. Fawzi, and F. Abu-Al-Rub, "Darcy-Forchheimer mixed convection heat and mass transfer in fluid saturated porous media," International Journal of Numerical Methods for Heat and Fluid Flow, **11**(6), 600–618 (2001). https://doi.org/10.1108/09615530110399503

[16] A.J. Chamkha, "Hydromagnetic natural convection from an isothermal inclined surface adjacent to a thermally stratified porous medium," International Journal of Engineering Science, **35**(10-11), 975–986 (1997). https://doi.org/10.1016/S0020-7225(96)00122-X

[17] N.S. Elgazery, "The effects of chemical reaction, Hall and ion-slip currents on MHD flow with temperature dependent viscosity and thermal diffusivity," Communications in Nonlinear Science and Numerical Simulation, **14**(4), 1267–1283 (2009). https://doi.org/10.1016/j.cnsns.2007.12.009

[18] M. Kinyanjui, J.K. Kwanza, and S.M. Uppal, "Magnetohydrodynamic free convection heat and mass transfer of a heat generating fluid past an impulsively started infinite vertical porous plate with Hall current and radiation absorption," Energy conversion and management, **42**(8), 917–931 (2001). https://doi.org/10.1016/S0196-8904(00)00115-1

[19] S. Shateyi, S.S. Motsa, and P. Sibanda, "The Effects of Thermal Radiation, Hall Currents, Soret, and Dufour on MHD Flow by Mixed Convection over a Vertical Surface in Porous Media," Mathematical Problems in Engineering, **2010**, 627475 (2010). https://doi.org/10.1155/2010/627475

[20] A.K. Singh, "Hall effects on MHD free-convection flow past an accelerated vertical porous plate," Astrophysics and Space Science, **102**, 213-221 (1984). https://doi.org/10.1007/BF00650168

[21] D. Sarma, and K.K. Pandit, "Effects of thermal radiation and chemical reaction on steady MHD mixed convective flow over a vertical porous plate with induced magnetic field," International journal of fluid Mechanics Research, **42**(4), 315-333 (2015). https://doi.org/10.1615/InterJFluidMechRes.v42.i4.30

[22] M.D.A. Sattar, and H. Kalim, "Unsteady free-convection interaction with thermal radiation in a boundary layer flow past a vertical porous plate," J. Math. Phys. Sci. **30**(1), 25-37 (1996). URL

[23] R. Nandkeolyar, M. Das, and S. Precious, "Exact solutions of unsteady MHD-free convection in a heat-absorbing fluid flow past a flat plate with ramped wall temperature," Boundary Value Problems, **2013**, 1-16 (2013). http://dx.doi.org/10.1186%2F1687-2770-2013-247

[24] A.J. Chamkha, "MHD-free convection from a vertical plate embedded in a thermally stratified porous medium with Hall effects," Applied Mathematical Modeling, **21**(10), 603-609 (1997). https://doi.org/10.1016/S0307-904X(97)00084-X

[25] E.M. Abo-Eldahab, and A.M. Salem, "Hall effects on MHD free convection flow of a non-Newtonian power-law fluid at a stretching surface," International communications in heat and mass transfer, **31**(3), 343-354 (2004). https://doi.org/10.1016/j.icheatmasstransfer.2004.02.005

[26] S. Siddiqa, M.A. Hossain, and R.S.D. Gorla. "Hall current effects on magnetohydrodynamic natural convection flow with strong cross-magnetic field," International journal of thermal sciences, **71**, 196-204 (2013). https://doi.org/10.1016/j.ijthermalsci.2013.04.016

[27] G.S.Seth, and J.K. Singh, "Mixed convection hydromagnetic flow in a rotating channel with Hall and wall conductance effects," Applied Mathematical Modelling, **40**(4), 2783-2803 (2016). https://doi.org/10.1016/j.apm.2015.10.015

[28] D. Kumar, A.K. Singh, and D. Kumar. "Influence of heat source/sink on MHD flow between vertical alternate conducting walls with Hall effect," Physica A: Statistical Mechanics and its Applications, **544**, 123562 (2020). https://doi.org/10.1016/j.physa.2019.123562

[29] K.K. Pandit, and D. Sarma, "Effects of Hall Current and Rotation on Unsteady MHD Natural Convection Flow Past a Vertical Flat Plate with Ramped Wall Temperature and Heat Absorption," in: *Proceedings of the 24th National and 2nd International ISHMT-ASTFE Heat and Mass Transfer Conference (IHMTC-2017)*, (Begel House Inc., BITS Pilani, Hyderabad, India, 2017), pp. 953-969. http://dx.doi.org/10.1615/IHMTC-2017.1340

[30] S. Shateyi, S.S. Motsa, and S. Precious, "The Effects of Thermal Radiation, Hall Currents, Soret, and Dufour on MHD Flow by Mixed Convection over a Vertical Surface in Porous Media," Mathematical Problems in Engineering, **2010**, (2010). https://doi.org/10.1155/2010/627475

ВПЛИВ СТРУМУ ХОЛЛА НА ЗМІШАНИЙ КОНВЕКТИВНИЙ ПОТІК ДАРСІ-ФОРХГЕЙМЕРА ПО ВЕРТИКАЛЬНІЙ ПОВЕРХНІ З ОБЕРТАННЯМ У ПОРИСТОМУ СЕРЕДОВИЩІ

Сатьябхушан Рой[a*], **Діпак Сарма**[a], **Анкур Кумар**[a,b], **Сунмоні Мудоі**[a]

[a] *Математичний факультет, Університет Коттон, Гувахаті-781001, Індія*

[b] *Кафедра математики, Коледж Баосі Баніканта Какаті, Нагаон, Барпета-781311, Індія*

Аналіз МГД-потоку Дарсі-Форхгеймера був предметом занепокоєння вчених-дослідників та інженерів. У цій роботі розглядається нестаціонарний гідродинамічний змішаний конвективний потік нестисливої, в'язкої, електропровідної рідини, а також перенесення тепла та маси у вертикальній поверхні за допомогою струму Холла, обертання та ефекту Дарсі-Форхгеймера. Шляхом перетворення подібності знайдено безрозмірне нестійке керуюче рівняння. Потім за допомогою методу Matlab Bvp4c було розв'язано звичайне диференціальне рівняння подібності. Коли отримані рішення та рішення, отримані Елгазері та Стенфордом, порівняли з чисельним результатом для кількох виняткових обставин, виявилося досить значне збіг. Графіки використовуються для відображення температури, концентрації та швидкості рідини. Навпаки, тертя шкіри, число Шервуда і число Нуссельта розраховуються в табличній формі.

Ключові слова: *струм Холла; обертання; Дарсі Форххаймер; змішана конвекція; bvp4c*

East European Journal of Physics. 1. 122–133 (2025)
DOI: 10.26565/2312-4334-2025-1-11 ISSN 2312-4334

BIOMAGNETO-HYDRODYNAMIC WILLIAMSON FLUID FLOW AND HEAT TRANSFER OVER A STRETCHING SURFACE: A SPECTRAL QUASI-LINEARIZATION APPROACH

Kairavadi Suresh Babu[b], **Vangala Sugunamma**[a], **Vamsi Krishna Narla**[c]
[a] *Sri Venkateswara University, Tirupati, AP, 517502, India*
[b] *Gokaraju Rangaraju Institute of Engineering and Technology, TG, India*
[c] *GITAM Deemed to be University, Department of Mathematics, Hyderabad, 502329, India*
[*] *Corresponding Author e-mail: vnarla@gitam.edu*
Received October 20, 2024; revised December 29, 2024; accepted January 23, 2025

The flow and heat transfer of a Williamson fluid subjected to a magnetic field are analyzed and investigated through the spectral quasi-linearization method (SQLM). The equations concerned with momentum and energy are obtained from the Navier-Stokes equations, accounting for non-Newtonian effects, viscous dissipation, magnetic forces, and the Lorentz force. The electrically conductive fluid's interaction with the magnetic field produces the Lorentz force, which strongly modifies flow behaviour by exerting a resistive force against the fluid's velocity. The method efficiently linearises the non-linear equations, enabling accurate solutions through the spectral method. Numerical results highlight the influence of Williamson fluid parameters, magnetic field intensity, and heat sources on velocity and temperature fields, offering insights into the fluid's behaviour in industrial applications involving non-Newtonian fluids and magnetic fields.

Keywords: *Williamson fluid; Heat source parameter; Magnetic dipole; Lorentz force and Spectral quasi linearization method*

PACS: 47.50.-d; 47.65.Cb; 65.20.Jk; 03.30.+p; 02.70.Hm; 52.75.Fk, 84.60.Lw.

NOMENCLATURE

$\mathbf{S}$	Cauchy stress tensor
b	Specific body force vector
C_f	Skin friction coefficient
H	Magnetic field
Ha	Hartmann number
K	Pyromagnetic coefficient
k	Thermal conductivity
M	Magnetization
Nu	Nusselt number
Pr	Prandtl number
Q_s	Heat source parameter
We	Weissenberg number
a	Distance of magnetic dipole
C_p	Specific heat
T	Temperature
T_c	Curie temperature
T_w	Temperature at surface
u	velocity component of fluid in x direction
v	velocity component of fluid in y direction

Greek Symbols

α	Magnetic field strength
β	Ferromagnetic interaction parameter
ϵ	Dimensionless temperature parameter
η	Similarity variable
Λ	Thermal relaxiation parameter
λ	Dissipation factor,
μ	Dynamic viscosity
μ_0	Magnetic permeability
ϕ	Magnetic scalar potential
ρ	fluid density
σ	Stefan-Boltzmann constant
θ	Dimensionless temperature
ϑ	Kinematic viscosity

1. INTRODUCTION

The study of non-Newtonian fluid dynamics over-stretching sheets has become increasingly significant in recent years, owing to its relevance in numerous industrial and engineering applications, such as plastic films, paper, and glass fibres. The continuous deforming boundary condition that a stretching sheet produces influences the fluid's motion and heat transfer properties. Understanding this

Cite as: K.S. Babu, V. Sugunamma, V. K. Narla, East Eur. J. Phys. 1, 122 (2025), https://doi.org/10.26565/2312-4334-2025-1-11

phenomenon is essential to optimising cooling and stretching processes in materials. A constitutive model explaining the connection between shear stress and shear rate was put forth by Williamson [1] in 1929, and it has subsequently been used to tackle a number of flow-related issues. The fluid model is better suited to describe complex fluids found in extrusion and spinning processes, as well as polymeric solutions, because it takes into account a decreasing viscosity with increasing shear rate. Numerous investigations have focused on the flow of non-Newtonian fluids across stretching sheets, such as Williamson's fluid [2]-[7]. The analysis of flow and heat transfer of ferrofluids across a stretched sheet under the influence of a dipole magnet has significant technical and industrial applications. The unique properties of ferrofluids in a carrier fluid may be controlled by applying external magnetic fields [8, 9, 10]. E.E. Tzirtzilakis developed a model for analysing mathematically the flow of blood, which is induced by magnetic fields [11]. Magnetic forces are incorporated into the Navier-Stokes equations and solved through numerical methods. Magnetic fields substantially influence blood circulation, potentially facilitating targeted magnetic therapy. Daneshvar Garmroodi et al. [12] conducted numerical simulations of free convection in non-Newtonian ferrofluids in a cavity that is porous and elliptical with a non-uniform magnetic field. The presence of a magnetic field markedly enhanced the transfer of heat, particularly when the wire was positioned at the centre of the elliptical walls. Shear-thinning fluids further augmented the average Nusselt number. AbuHamdeh et al. [13] examined the dynamics of magnetic nanoparticles in the context of a magnetic field within non-Newtonian blood vessels. Their research illustrated the significance of considering non-Newtonian fluid characteristics to enhance drug delivery precision. Srinu and Sreerama [14] investigated the influence of thermal slips and velocity on Williamson's fluid flow across a stretching sheet in the presence of a magnetic field that was inclined and radiation. Abbas et al. [15] investigated flow and heat transmission of magnetohydrodynamic Williamson nanofluid across a stretching sheet (non-linear) that was contained in a porous medium. It was found that with a rise in the Williamson fluid parameter, the concentration profile rises and the velocity declines. It was concluded that rising mass concentration and temperature are caused by increasing Eckert number Ec. As Q, the heat-generating parameter rises, the temperature profile rises, and a reduction in concentration is noticed. The results showed that the profiles of both temperature and concentration trended upward with an increase in the magnetic field parameter M, while the velocity field trended downward. Rashid et al. [16] looked at how a generated magnetic force affected Williamson fluid's flow within a curved channel. It was noticed that compared to a viscous fluid, for a Williamson fluid, the rise in pressure is higher, and the generated magnetic field's magnitude is smaller. Further, the velocity was observed to be small in comparison with a Newtonian fluid. M.V. Krishna and B.V. Swarnalathamma, in their work [17], studied the flow of a MHD Williamson's fluid, which was electrically conducting and heat transfer in the planar symmetrical channel. Obalalu et al. [18] in their work addressed the Hall effect on the flow of Williamson's fluid across a channel that was considered inclined and stretching. In addition, their model took into consideration the impacts of solar radiation, chemical reactions, heat generation or absorption, and activation energy. The graphical results indicated that the heat sink exhibits a thermal efficiency ranging from 4.4% to 5.0%, which was lower compared to that of the heat source. The flow of Williamson fluid diminishes in the magnetic field's presence because of Lorentz force acting opposite to flow direction, which can be considered an application in wired technology. Kashif et al. [19] examined the transport of mass and heat of a MHD Williamson's fluid across a stretched permeable layered plate. The study's findings demonstrate that augmenting the parameter for Brownian motion (Nb) and Thermophoresis (Nt) results in elevated local Nusselt number, signifying enhanced heat transfer rates.

Analyzing the influence of nanofluid properties and magnetic fields can deepen the understanding of heat and mass transport characteristics. Such insights can potentially enhance the performance of ferrofluid-based devices across diverse applications. Recent developments have primarily concentrated on creating efficient numerical techniques for resolving complex, nonlinear differential equations that control fluid flow dynamics [20],[21]. The Spectral Quasi-Linearization Method (SQLM) [22] integrates spectral methods with the quasilinearization technique to achieve high accuracy in linearisation and solving nonlinear terms. Numerous fluid flow applications have benefited from the successful application of this technique, such as the study of boundary layer flows in non-Darcy porous media across sheets that are stretching or shrinking (see, [23]-[27]). Tzirtzilakis and Tanoudis [28] have investigated heat transfer and flow of biomagnetic fluid in magnetic fields using the Chebyshev pseudospectral method (CPSM). CPSM is more accurate and efficient than finite difference methods. The study shows that flow characteristics are significantly influenced by the biomagnetic interaction parameter and that CPSM performs well in this application. Some related literatures are cited in references ([29]-[33]).

The ferrofluid flow and heat transfer of a couple of stress fluids are analysed in the present study. The Spectral Quasi-Linearization Method (SQLM) is utilised to solve flow-governing equations numerically, incorporating the effects of couple stresses and magnetic forces. The equations are converted using similarity variables. We systematically examine effects on the profiles of velocity and temperature of important parameters like the couple stress parameter, ferromagnetic interaction parameter, Prandtl number, heat source parameter, and Hartmann number. The findings show how these parameters impact the flow and thermal properties of ferrofluids and offer comprehensive insights into the intricate interactions between them.

2. FLUID MODEL

A problem of fluid flow across a flat, stretchable sheet stretched in x-direction with velocity $u = cx$ is the primary focus of this analysis, where c is a stretching constant as shown in Fig.(1). At a distance $'a'$ from the centre of sheet, a magnetic dipole is located. In Fig.(1), the symbols S and N denote the South and North Poles of the dipole, respectively. Deformation of fluid in y-direction is a result of the flow being magnetised and saturated. The equations for an incompressible Williamson fluid flow given as:

$$\nabla.V = 0 \tag{1}$$

$$\rho \frac{dV}{dt} = \nabla \mathbf{S} + \rho b \tag{2}$$

The following is an expression of the Williamson fluid model's basic equations:

$$\mathbf{S} = -pI + \tau \tag{3}$$

where

$$\tau = \mu_\infty + \left(\frac{\mu_0 - \mu_\infty}{1 - \Gamma\dot{\gamma}}\right)A \tag{4}$$

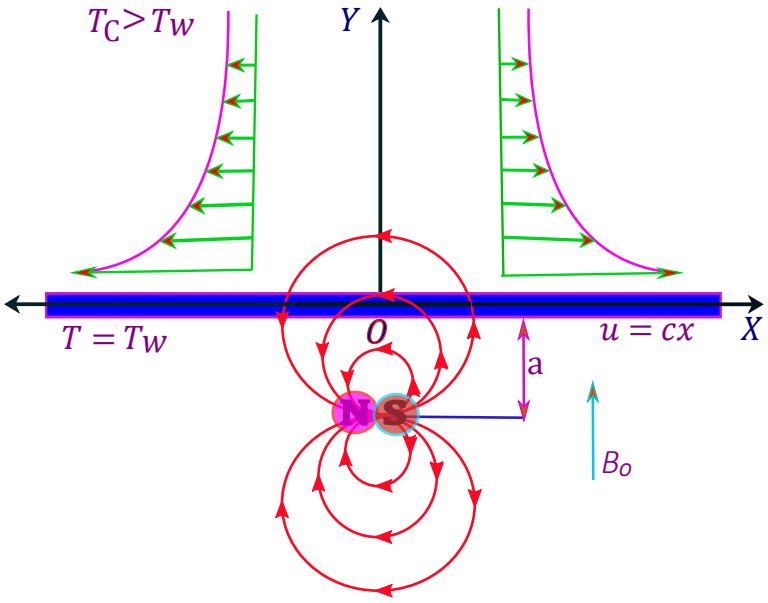

Figure 1. Illustration of physical problem

p stands for pressure, I for identity vector, τ for extra stress tensor, μ_0 and μ_∞ for limiting viscosities at zero and infinite shear rates, respectively, $\Gamma > 0$ for time constant, A for first Rivlin-Erickson tensor. Here $\dot{\gamma}$ is defined as follows:

$$\dot{\gamma} = \sqrt{\frac{1}{2}\pi} \tag{5}$$

$$where \quad \pi = \text{Trace}(A^2), \quad A = \nabla\bar{q} + \nabla\bar{q}^{Tr}$$
$$\nabla\bar{q} = \left[\frac{\partial u}{\partial x} \quad \frac{\partial u}{\partial y}, \quad \frac{\partial v}{\partial x} \quad \frac{\partial v}{\partial y}\right],$$

by substituting in (5), we get:

$$\dot{\gamma} = \left[2\left[\left(\frac{\partial u}{\partial x}\right)^2 + \left(\frac{\partial v}{\partial y}\right)^2\right] + \left(\frac{\partial u}{\partial y} + \frac{\partial v}{\partial x}\right)^2\right]^{\frac{1}{2}} \tag{6}$$

for $\mu_\infty = 0$ and $\Gamma\dot{\gamma} < 1$ and hence, the extra stress tensor takes the form:

$$\tau = \left(\frac{\mu_0}{1 - \Gamma\dot{\gamma}}\right)A \tag{7}$$

by using binomial expansion, we get:

$$\tau = \mu_0\left(1 + \Gamma\dot{\gamma}\right)A \tag{8}$$

When the boundary layer approximations are applied, the continuity, momentum, and energy equations governing the flow take the following form:

$$\frac{\partial u}{\partial x} + \frac{\partial v}{\partial y} = 0 \tag{9}$$

$$\rho\left[u\frac{\partial u}{\partial x} + v\frac{\partial u}{\partial y}\right] = \mu\left(\frac{\partial^2 u}{\partial y^2}\right) + 2\mu\Gamma\frac{\partial u}{\partial y}\frac{\partial^2 u}{\partial y^2} + \mu_0 M\frac{\partial H}{\partial x} - \sigma B_0^2 u \tag{10}$$

$$\begin{aligned}(\rho C_p)\left[u\frac{\partial T}{\partial x} + v\frac{\partial T}{\partial y}\right] + \mu_0 T\frac{\partial M}{\partial T}\left[u\frac{\partial H}{\partial x} + v\frac{\partial H}{\partial y}\right] + \lambda\left[\left(u\frac{\partial u}{\partial x} + v\frac{\partial u}{\partial y}\right)\frac{\partial T}{\partial x}\right.\\ \left.+\left(u\frac{\partial v}{\partial x} + v\frac{\partial v}{\partial y}\right)\frac{\partial T}{\partial y} + u^2\frac{\partial^2 T}{\partial x^2} + v^2\frac{\partial^2 T}{\partial y^2} + 2uv\frac{\partial^2 T}{\partial x \partial y}\right]\\ = k\left[\frac{\partial^2 T}{\partial x^2} + \frac{\partial^2 T}{\partial y^2}\right] + Q(T_c - T) + \sigma B_0^2 u\end{aligned} \tag{11}$$

The assumed boundary conditions for resolving the aforementioned equations are as follows:

$$\begin{aligned}u(x,0) = cx,\ v(x,0) = 0,\ T = T_w \ \text{ at } \ y = 0,\\ u(x,\infty) \to 0,\ T(x,\infty) \to T_c \ \text{ at } \ y \to \infty.\end{aligned} \tag{12}$$

The potential of magnetic dipole can be found by $\phi(x,y) = \frac{\alpha}{2\pi}\left[\frac{x}{x^2+(y+a)^2}\right]$. We arrive at the conclusion $H = [H_x^2 + H_y^2]^{\frac{1}{2}}$ by employing a linear correlation between magnetic body force and the gradient of H. $M = K(T_c - T)$ is a linear equation that approximates the relationship between magnetization M and temperature T.
The equations considered for transformation are

$$(\xi,\eta) = \frac{(x,y)}{\sqrt{\frac{\nu}{c}}},\ \ u = cxf'(\eta),\ \ v = -\sqrt{c\nu}f(\eta)\ \ and\ \ \theta(\xi,\eta) = \frac{T_c - T}{T_c - T_\omega} = \theta_1(\eta) + \xi^2\theta_2(\eta) \tag{13}$$

u, v the components of velocity satisfy the continuity equation (9). By substituting equations (10) and (11) in (13) and equating the coefficients of ξ^0, ξ and ξ^2, the following equations are obtained:

$$f''' + ff'' - (f')^2 + Wef''f''' - \frac{2\beta\theta_1}{(\eta+\bar{d})^4} - Haf' = 0, \tag{14}$$

$$\theta_1'' + Pr[f\theta_1' - Q_s\theta_1] - \lambda\beta(\epsilon - \theta_1)\left[\frac{2f}{(\eta+\bar{d})^3}\right] - \Lambda\Big(ff'\theta_1' + f^2\theta_1''\Big) + 2\theta_2 = 0, \tag{15}$$

$$\begin{aligned}\theta_2'' + Pr[f\theta_2' - 2f'\theta_2 - Q_s\theta_2] + \lambda\beta(\epsilon - \theta_1)\left[\frac{2f'}{(\eta+\bar{d})^4} + \frac{4f}{(\eta+\bar{d})^5}\right] + \frac{2\lambda\beta f\theta_2}{(\eta+\bar{d})^3}\\ +\Lambda\Big(-4f'^2\theta_2 + 3ff'\theta_2' - f^2\theta_2'' + 2ff''\theta_2\Big) - \lambda Haf'^2 = 0.\end{aligned} \tag{16}$$

The following are the transformed boundary conditions:

$$\begin{aligned}f(0) = 0,\ f'(0) = 1,\ \theta_1(0) = 1,\ \theta_2(0) = 0\\ f'(\infty) = 0,\ \theta_1(\infty) = 0,\ \theta_2(\infty) = 0\end{aligned} \tag{17}$$

The remaining non-dimensional variables in the aforementioned converted equations are specified as :

$$\Lambda = \frac{\lambda c\nu}{k},\ \ \beta = \frac{\alpha\mu_0}{2\pi}\frac{\rho K(T_c - T_w)}{\mu^2},\ \ Pr = \frac{(\rho C_p)\vartheta}{k},\ \ We = 2\Gamma x\sqrt{\frac{c^3}{\nu}}$$
$$\lambda = \frac{\mu^2 c}{\rho k(T_c - T_w)},\ \ \epsilon = \frac{T_c}{T_c - T_w}, Ha = \frac{\sigma B_0^2}{\rho c},\ \ Q_s = \frac{Q}{c\rho C_p}.$$

3. SPECTRAL QUASI LINEARIZATION

The spectral quasi-linearization procedure has been applied to obtain the numerical solution of the nonlinear coupled equations (14) to (16), in accordance with the boundary conditions (17). The quasi-linearization technique is applied to equations (14) to (17), yielding the following equations:

$$e_{1,r}f'''_{r+1} + e_{2,r}f''_{r+1} + e_{3,r}f'_{r+1} + e_{4,r}f_{r+1} + e_{5,r}(\theta_1)_{r+1} = S_1, \tag{18}$$

$$e_{6,r}f'_{r+1} + e_{7,r}f_{r+1} + e_{8,r}(\theta_1)''_{r+1} + e_{9,r}(\theta_1)'_{r+1} + e_{10,r}(\theta_1)_{r+1} + e_{11,r}(\theta_2)_{r+1} = S_2, \tag{19}$$

$$e_{12,r}f''_{r+1} + e_{13,r}f'_{r+1} + e_{14,r}f_{r+1} + e_{15,r}(\theta_1)_{r+1} + e_{16,r}(\theta_2)''_{r+1} + e_{17,r}(\theta_2)'_{r+1} + e_{18,r}(\theta_2)_{r+1} = S_3, \tag{20}$$

The boundary conditions are:

$$\begin{aligned}f_{r+1} = 0, f'_{r+1} = 1, (\theta_1)_{r+1} = 1, (\theta_2)_{r+1} = 0\ \text{ at }\ \eta = 0,\\ f'_{r+1} = 0, (\theta_1)_{r+1} = 0, (\theta_2)_{r+1} = 0\ \text{ at }\ \eta \to \infty.\end{aligned} \tag{21}$$

The coefficients are obtained as

$$e_{1,r} = Wef''_r + 1,\quad e_{2,r} = f_r + Wef'''_r,\quad e_{3,r} = -2f'_r - Ha,\quad e_{4,r} = f''_r,\quad e_{5,r} = \frac{-2\beta}{(\eta+\bar{d})^4},$$
$$e_{6,r} = -\Lambda f_r(\theta_1')_r,\quad e_{7,r} = Pr(\theta_1')_r - \frac{2\lambda\beta\epsilon}{(\eta+\bar{d})^3} + \frac{2\lambda\beta(\theta_1)_r}{(\eta+\bar{d})^3} - \Lambda f'_r(\theta_1')_r - 2\Lambda f_r(\theta_1'')_r,$$
$$e_{8,r} = 1 - \Lambda f_r^2,\quad e_{9,r} = Prf_r - \Lambda f_r f'_r,\quad e_{10,r} = \frac{2\lambda\beta f_r}{(\eta+\bar{d})^3} - PrQ_s, e_{11,r} = 2,$$
$$e_{12,r} = 2\Lambda f_r(\theta_2)_r,\quad e_{13,r} = -2Pr(\theta_2)_r + \frac{2\lambda\beta\epsilon}{(\eta+\bar{d})^4} - \frac{2\lambda\beta(\theta_1)_r}{(\eta+\bar{d})^4} - 8\Lambda f'_r\theta_2 + 3\Lambda f_r(\theta_2')_r - 2\lambda Haf',$$
$$e_{14,r} = Pr(\theta_2')_r + \frac{2\lambda\beta(\theta_2)_r}{(\eta+\bar{d})^3} + \frac{4\lambda\beta\epsilon}{(\eta+\bar{d})^5} - \frac{4\lambda\beta(\theta_1)_r}{(\eta+\bar{d})^5} + 3\Lambda f'_r(\theta_2')_r - 2\Lambda f_r(\theta_2'')_r + 2\Lambda f''_r(\theta_2)_r,$$
$$e_{15,r} = \frac{-2\lambda\beta f'_r}{(\eta+\bar{d})^4} - \frac{4\lambda\beta f_r}{(\eta+\bar{d})^5},\quad e_{16,r} = 1 - \Lambda f_r^2,\quad e_{17,r} = Prf_r + 3\Lambda f'_r f_r,$$
$$e_{18,r} = -2Prf'_r - PrQ_s + \frac{2\lambda\beta f_r}{(\eta+\bar{d})^3} - 4\Lambda(f'_r)^2 + 2\Lambda f_r f''_r,$$

$$S_1 = f_r f_r'' - f_r'^2 + We f_r'' f_r''', \quad S_2 = -\Lambda f_r' f_r \theta_r' - \Lambda (f_r)^2 (\theta_1'')_r + Pr f_r (\theta_1')_r + \frac{2\lambda\beta f_r (\theta_1)_r}{(\eta + \bar{d})^3},$$

$$S_3 = -\lambda Ha((f')^2)_r - 2Pr f_r' (\theta_2)_r + Pr f_r (\theta_2')_r + \frac{2\lambda\beta f_r (\theta_2)_r}{(\eta + \bar{d})^3} - \frac{2\lambda\beta f_r' (\theta_1)_r}{(\eta + \bar{d})^4} - \frac{4\lambda\beta (\theta_1)_r f_r}{(\eta + \bar{d})^5} - 3\Lambda f_r' f_r (\theta_2')_r$$
$$- \Lambda (f^2)_r (\theta_2'')_r + 2\Lambda f_r'' f_r (\theta_2)_r - (4(f')^2)_r (\theta_2)_r.$$

Equations (14)–(17) are solved numerically using the pseudo-spectral Chebyshev collocation method. In this framework, initially, the semi-infinite range $\eta \in [0,\ \infty)$ is truncated to $\eta \in [0,\ L_\infty]$, where $L_\infty \in \mathbb{Z}^+$. This range $[0,\ L_\infty]$ is transformed into $[-1,\ 1]$ using the transformation variable $\eta = L_\infty(1 + \zeta)/2$. Using the differential matrix $\mathbf{D}$ for Chebyshev polynomials (see, [27]), the derivatives of the unknown functions $f(\eta)$, $\theta_1(\eta)$, and $\theta_2(\eta)$ are derived at the collocation points of the product matrix vector as follows:

$$\begin{aligned}
\frac{\partial^p f_{r+1}}{\partial \eta^p} &= \left(\frac{2}{L}\right)^p \sum_{i=0}^{N} D_{N,i}^p f_{r+1}(\eta_i) = \mathbf{D}^p F, \\
\frac{\partial^p (\theta_1)_{r+1}}{\partial \eta^p} &= \left(\frac{2}{L}\right)^p \sum_{i=0}^{N} D_{N,i}^p (\theta_1)_{r+1}(\eta_i) = \mathbf{D}^p \Theta_1, \\
\frac{\partial^p (\theta_2)_{r+1}}{\partial \eta^p} &= \left(\frac{2}{L}\right)^p \sum_{i=0}^{N} D_{N,i}^p (\theta_2)_{r+1}(\eta_i) = \mathbf{D}^p \Theta_2.
\end{aligned} \tag{22}$$

The Chebyshev differentiation matrix $\mathbf{D}$ is scaled by $L_\infty/2$. The matrix $\mathbf{D}$ in this instance has a derivative order of p and an order of $(N + 1) \times (N + 1)$. Using $\zeta_j = \cos(\pi j/N)$, $j = 1, 2, \cdots N$, where N denotes number of collocation points, the Gauss-Lobatto points are constructed to characterize nodes in $[-1, 1]$. Substituting Eq. (22) into Eqs. (18)-(21), we obtain

$$[e_{1,r}\mathbf{D}^3 + e_{2,r}\mathbf{D}^2 + e_{3,r}\mathbf{D} + e_{4,r}I] f_{r+1} + e_{5,r}(\theta_1)_{r+1} = S_1, \tag{23}$$

$$[e_{6,r}\mathbf{D} + e_{7,r}I] f_{r+1} + [e_{8,r}\mathbf{D}^2 + e_{9,r}\mathbf{D} + e_{10,r}I](\theta_1)_{r+1} + [e_{11,r}I](\theta_2)_{r+1} = S_2, \tag{24}$$

$$[e_{12,r}\mathbf{D}^2 + e_{13,r}\mathbf{D} + e_{14,r}I] f_{r+1} + e_{15,r}(\theta_1)_{r+1} + [e_{16,r}\mathbf{D}^2 + e_{17,r}\mathbf{D} + e_{18,r}I](\theta_2)_{r+1} = S_3. \tag{25}$$

Applying spectral method on the boundary conditions gives

$$\sum_{k=0}^{N} \mathbf{D}_{N,k} f_{r+1}(\zeta_0) = 0,\ (\theta_1)_{r+1}(\zeta_0) = 0,\ (\theta_2)_{r+1}(\zeta_0) = 0,\ f_{r+1}(\zeta_N) = 0,$$

$$\sum_{k=0}^{N} \mathbf{D}_{N,k} f_{r+1}(\zeta_N) = 1,\ (\theta_1)_{r+1}(\zeta_N) = 1,\ (\theta_2)_{r+1}(\zeta_N) = 0.$$

The above system of equations expressed in matrix form as:

$$\begin{bmatrix} \mathbf{K}_{11} & \mathbf{K}_{12} & \mathbf{K}_{13} \\ \mathbf{K}_{21} & \mathbf{K}_{22} & \mathbf{K}_{23} \\ \mathbf{K}_{31} & \mathbf{K}_{32} & \mathbf{K}_{33} \end{bmatrix} \times \begin{bmatrix} F_{r+1} \\ \Theta_{1r+1} \\ \Theta_{2r+1} \end{bmatrix} = \begin{bmatrix} S_1 \\ S_2 \\ S_3 \end{bmatrix}, \tag{26}$$

The boundary conditions are placed on the separate matrices as follows:

$$\mathbf{K}_{11} = \begin{bmatrix} \mathbf{D}_{0,0} & \mathbf{D}_{0,1} & \cdots & \mathbf{D}_{0,N-1} & \mathbf{D}_{0,N} \\ \hline & & K_{11} & & \\ \hline \mathbf{D_{N-1,0}} & \mathbf{D_{N-1,1}} & \cdots & \mathbf{D_{N-1,N-1}} & \mathbf{D_{N-1,N}} \\ 0 & 0 & \cdots & 0 & 1 \end{bmatrix}, \quad \mathbf{K}_{12} = \begin{bmatrix} 0 & 0 & \cdots & 0 & 0 \\ \hline & & K_{12} & & \\ \hline 0 & 0 & \cdots & 0 & 0 \\ 0 & 0 & \cdots & 0 & 0 \end{bmatrix},$$

$$\mathbf{K}_{13} = \begin{bmatrix} 0 & 0 & \cdots & 0 & 0 \\ \hline & & K_{13} & & \\ \hline 0 & 0 & \cdots & 0 & 0 \\ 0 & 0 & \cdots & 0 & 0 \end{bmatrix}, \mathbf{K}_{21} = \begin{bmatrix} 0 & 0 & \cdots & 0 & 0 \\ \hline & & K_{21} & & \\ \hline 0 & 0 & \cdots & 0 & 0 \end{bmatrix}, \quad \mathbf{K}_{22} = \begin{bmatrix} 1 & 0 & \cdots & 0 & 0 \\ \hline & & K_{22} & & \\ \hline 0 & 0 & \cdots & 0 & 1 \end{bmatrix},$$

$$\mathbf{K}_{23} = \begin{bmatrix} 0 & 0 & \cdots & 0 & 0 \\ \hline & & K_{23} & & \\ \hline 0 & 0 & \cdots & 0 & 0 \end{bmatrix}, \quad \mathbf{K}_{31} = \begin{bmatrix} 0 & 0 & \cdots & 0 & 0 \\ \hline & & K_{31} & & \\ \hline 0 & 0 & \cdots & 0 & 0 \end{bmatrix}, \quad \mathbf{K}_{32} = \begin{bmatrix} 0 & 0 & \cdots & 0 & 0 \\ \hline & & K_{32} & & \\ \hline 0 & 0 & \cdots & 0 & 0 \end{bmatrix},$$

$$\mathbf{K}_{33} = \begin{bmatrix} 1 & 0 & \cdots & 0 & 0 \\ \hline & & K_{33} & & \\ \hline 0 & 0 & \cdots & 0 & 1 \end{bmatrix}, \quad \mathbf{F}_{r+1} = \begin{bmatrix} f_{r+1,0} \\ \hline \vdots \\ \hline f_{r+1,N-1} \\ f_{r+1,N} \end{bmatrix}, \quad \mathbf{\Theta_1}_{r+1} = \begin{bmatrix} \theta_{1r+1,0} \\ \hline \vdots \\ \vdots \\ \hline \theta_{1r+1,N} \end{bmatrix},$$

$$\mathbf{\Theta_{2}}_{r+1} = \begin{bmatrix} \theta_{2r+1,0} \\ \vdots \\ \theta_{2r+1,N} \end{bmatrix}, \quad S_1 = \begin{bmatrix} 0 \\ \mathbf{s_1} \\ 1 \\ 0 \end{bmatrix}, \quad S_2 = \begin{bmatrix} 0 \\ \mathbf{s_2} \\ 1 \end{bmatrix}, \quad S_3 = \begin{bmatrix} 0 \\ \mathbf{s_3} \\ 0 \end{bmatrix},$$

where

$$\begin{aligned}
K_{11} &= [\text{diag}(e_{1,r}) \quad \text{diag}(e_{2,r}) \quad \text{diag}(e_{3,r}) \quad \text{diag}(e_{4,r})][\mathbf{D}^3 \quad \mathbf{D}^2 \quad \mathbf{D} \quad I]^T, \\
K_{12} &= \text{diag}(e_{5,r}), \quad K_{13} = 0, \\
K_{21} &= [\text{diag}(e_{6,r}) \quad \text{diag}(e_{7,r})][\mathbf{D} \quad I]^T, \\
K_{22} &= [\text{diag}(e_{8},r) \quad \text{diag}(e_{9,r}) \quad \text{diag}(e_{10,r})][\mathbf{D}^3 \quad \mathbf{D}^2 \quad \mathbf{D} \quad I]^T, \quad K_{23} = [\text{diag}(e_{11,r})]I, \\
K_{31} &= [\text{diag}(e_{12,r}) \quad \text{diag}(e_{13,r}) \quad \text{diag}(e_{14,r})][\mathbf{D}^2 \quad \mathbf{D} \quad I]^T, \quad K_{32} = \text{diag}(e_{15,r}), \\
K_{33} &= [\text{diag}(e_{16}r) \quad \text{diag}(e_{17,r}) \quad \text{diag}(e_{18,r})][\mathbf{D}^2 \quad \mathbf{D} \quad I]^T,
\end{aligned}$$

where e is (N + 1)×(N + 1) diagonal matrix, I, 0 are (N + 1)×(N + 1) unit matrix and zero matrix, respectively.

4. CONVERGENCE ANALYSIS AND RESULTS

The convergence analysis shows that iterative approach convergence to exact solution of the equations (14) and (15), while considering the boundery conditions (17). The residual error quantifies the proximity of the numerical solution to exact solution. The residual error of equations (14) and (15) is represented below:

$$Res(f) = f''' + ff'' - (f')^2 + Wef''f''' - \frac{2\beta\theta_1}{(\eta + \bar{d})^4} - Haf', \tag{27}$$

$$Res(\theta_1) = \theta_1'' + Pr[f\theta_1' - Q_s\theta_1] - \lambda\beta(\epsilon - \theta_1)\left[\frac{2f}{(\eta + \bar{d})^3}\right] - \Lambda\left(ff'\theta_1' + f^2\theta_1''\right) + 2\theta_2. \tag{28}$$

$\|Res(f)\|_\infty$ and $\|Res(\theta_1)\|_\infty$ measure the largest absolute value of the error throughout the domain.

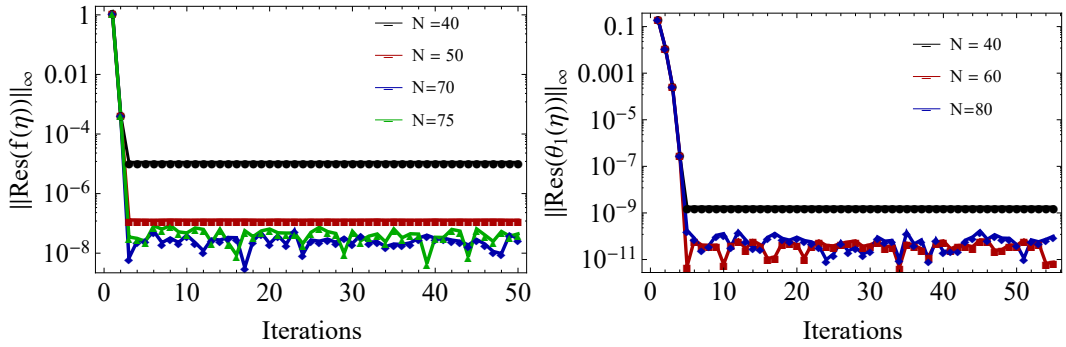

Figure 2. Influence of iterations on $\|Res(f)\|_\infty$ and $\|Res(\theta_1)\|_\infty$ when Pr = 1, λ= 0.01,Q_s=0.5, ϵ=2, β = 1, Λ = 0.5, Ha = 1 and We = 0.01.

The residual error in f over 50 iterations for several numbers of collocation points (N = 65, 70, 75) is displayed in Fig. (2)(a). The figure shows that the best accuracy is achieved in between the collocation points 65 and 75, with residual errors around 10^{-8}. Similarly, The optimal residuals are achieved around 10^{-11} for the residual errors in θ_1 that is shown in Fig. (2)(b). The accuracy gradually reduces beyond this range of collocation points. From the above results, the numerical approach achieved the best accuracy between 65 to 75 collocation points and performance after the seventh iteration in f and the tenth iteration in θ_1.

The resistance that the fluid applies to the surface as a result of shear stresses is measured by C_f, the skin friction coefficient defined as:

$$C_f = \frac{\tau_w}{\rho U_s^2}$$

where τ_w is the wall shear stress at surface (y = 0):

$$\tau_w = \mu\left(1 - \frac{1}{\Gamma\dot{\gamma} + 1}\right)\left(\frac{\partial u}{\partial y}\right)_{y=0}$$

A simplified expression for skin friction coefficient is given as:

$$C_f Re_x^{\frac{1}{2}} = f''(0) + \frac{We}{2} f''(0)^2$$

Table 1. Numerical values of $C_f Re_x^{\frac{1}{2}}$

We	$C_f Re_x^{\frac{1}{2}}$					
	β=0	β=0.1	β=0.2	β=0.3	β=0.4	$\beta = 1$
0	-1.095599662	-1.128912975	-1.162233927	-1.195730434	-1.229308197	-1.432427836
0.001	-1.095382958	-1.128657128	-1.162015567	-1.195459333	-1.228989428	-1.43204273
0.1	-1.073084327	-1.105917857	-1.13882558	-1.171808576	-1.204867949	-1.404893248
0.2	-1.048548562	-1.08079605	-1.113097732	-1.145454265	-1.177866314	-1.373542304
0.3	-1.0213007	-1.052721717	-1.084153148	-1.11559285	-1.147038361	-1.335636773
0.4	-0.990052177	-1.02015071	-1.050134304	-1.079979608	-1.109655784	-1.146034455

The Nusselt number for a Williamson fluid over a stretched sheet quantifies the convective heat transfer at the surface in relation to the conductive heat transfer inside the fluid. The following is the definition of the local Nusselt number Nu_x at a distance x from the leading edge:

$$Nu_x = \frac{q_w x}{k(T_w - T_c)}$$

where $q_w = -k\left(\frac{\partial T}{\partial y}\right)_{y=0}$ is the wall heat flux.
The local Nusselt number becomes:

$$Nu_x = -\theta'(0)\sqrt{Re_x}$$

Table 2. Numerical values of $Nu_x Re_x^{\frac{-1}{2}}$

We	$Nu_x Re_x^{\frac{-1}{2}}$					
	β=0	β=0.1	β=0.2	β=0.3	β=0.4	β=1
0	1.073455819	1.068598579	1.068738038	1.064270995	1.060645959	1.042842363
0.001	1.074442179	1.071432388	1.068411953	1.065378014	1.062332056	1.043801078
0.1	1.067971776	1.064767511	1.06154568	1.058306182	1.055048916	1.03512635
0.2	1.06075601	1.057305343	1.053827978	1.050323504	1.046791495	1.024995014
0.3	1.052633942	1.048854466	1.045030664	1.041160916	1.037243449	1.012610756
0.4	1.04319135	1.038916915	1.034552705	1.030089571	1.025515841	0.993059527

Tables (1) and (2) display variations in coefficient of Skin friction and heat transfer rate for different values of Γ and β. Other parameters are maintained at following values: $d = 1$, $\lambda = 0.01$, $\epsilon = 2$, $Pr = 1$, $\Lambda = 0.5$, $Ha = 0.2$, $Qs = 0.5$. From Table (1) it can be noticed that for a fixed β, the drag coefficient increases with a rise in We. The augmentation of the drag coefficient with a rise in Weissenberg number is attributable to the fluid's shear-thinning characteristics, and increased energy dissipation within the flow. Further, it decreases with a rise in β. This is attributed to the stabilising influence of magnetic field, a decrease in flow instabilities, laminar flow development, or alterations in the velocity gradient and shear stress adjacent to the wall. Table (2) depicts a decrease in heat transfer coefficient with a rise in We and β. Higher values of β intensify the effects of magnet in fluid and speed up heat transfer as a consequence of the interaction between ferromagnetic particles in fluid and magnetic field. Better thermal conductivity and more effective heat transfer are encouraged by this interaction. The effects of β, Pr We, Qs, Γ on profiles of velocity and temperature are depicted in (3)-(10). From Figure (3)(a), one can notice that velocity drops from the highest value near the wall where η=0, towards the free stream value (where $\eta \to \infty$) with the increment of β. This signifies that enhanced magnetic effects lead to a more rapid deceleration of fluid in boundary layer as β levels rise. Figure 3(b) illustrates that as β is increased, it leads to a more pronounced temperature differential near the wall, indicating a reduced thickness of the thermal boundary layer. Increased values of β facilitate the transfer of heat to fluid from the surface.

Figure 4(a) clearly illustrates that the velocity diminishes from its maximum near the wall to the free stream value across different Prandtl numbers Pr. Fluctuations in the Prandtl number exert negligible influence on the thickness of velocity boundary layer, as they do not significantly alter the velocity profile. Figure 4(b) illustrates a reduction in temperature profile as Prandtl number (Pr) increases. This suggests that a higher Pr value results in diminished thermal diffusivity, thereby decreasing the efficiency of heat conduction away from the wall. Consequently, there is an elevated rate of temperature change and a reduced temperature near the surface. Fig. (5)(a) and Fig. (5)(b) illustrate the impact of heat source Q_s on profiles of velocity and temperature. Figure 5(a) demonstrates a more significant velocity gradient near the wall, signifying a reduction in boundary layer thickness as values of Q_s increase. Figure 5(b) shows that elevated values of (Q_s) result in a diminished temperature profile near the wall. The observed phenomena can be attributed to the

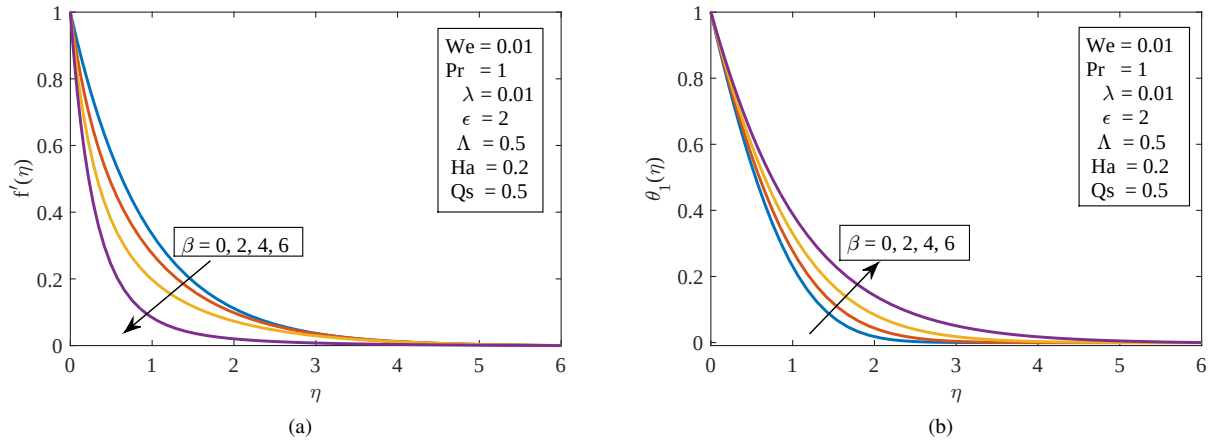

Figure 3. Impact of β on velocity and temperature.

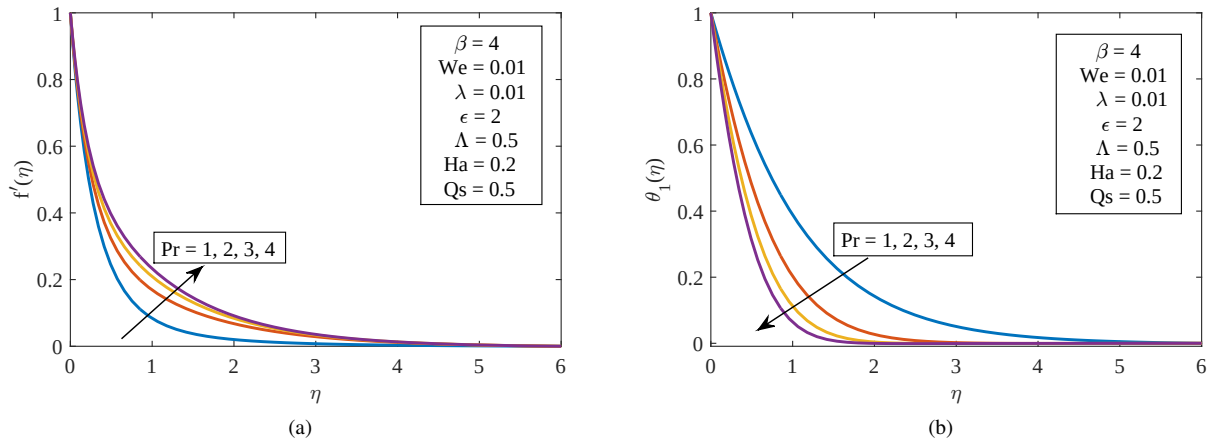

Figure 4. Impact of Pr on velocity and temperature.

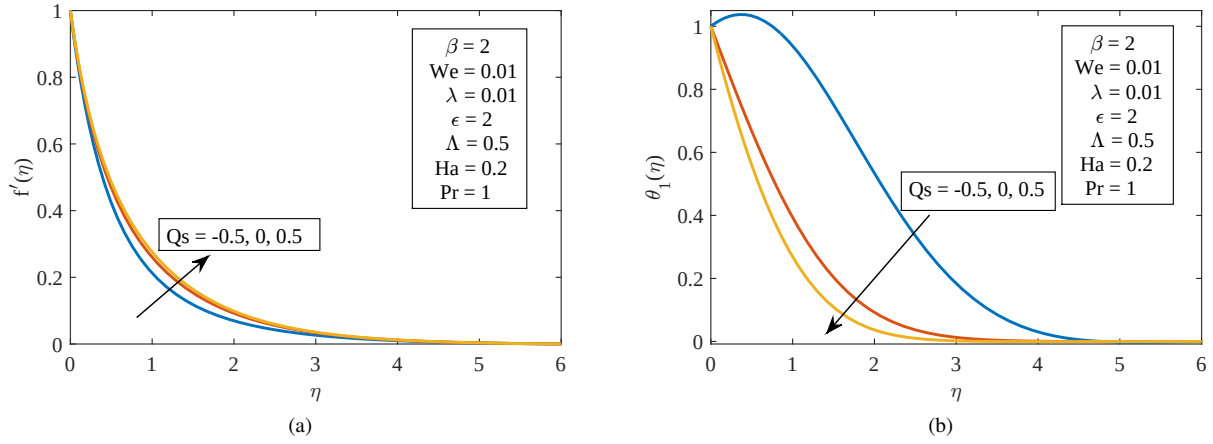

Figure 5. Impact of Qs on velocity and temperature.

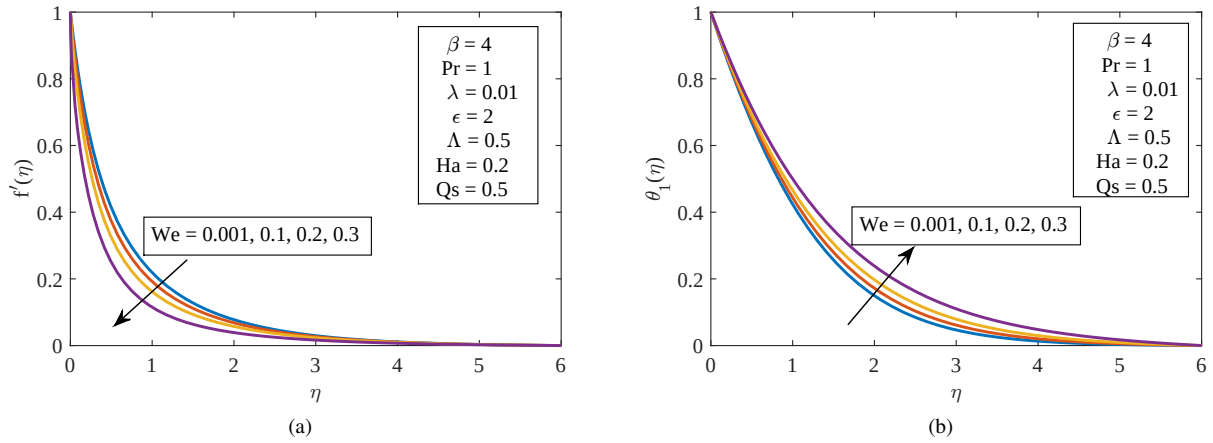

Figure 6. Impact of We on velocity and temperature.

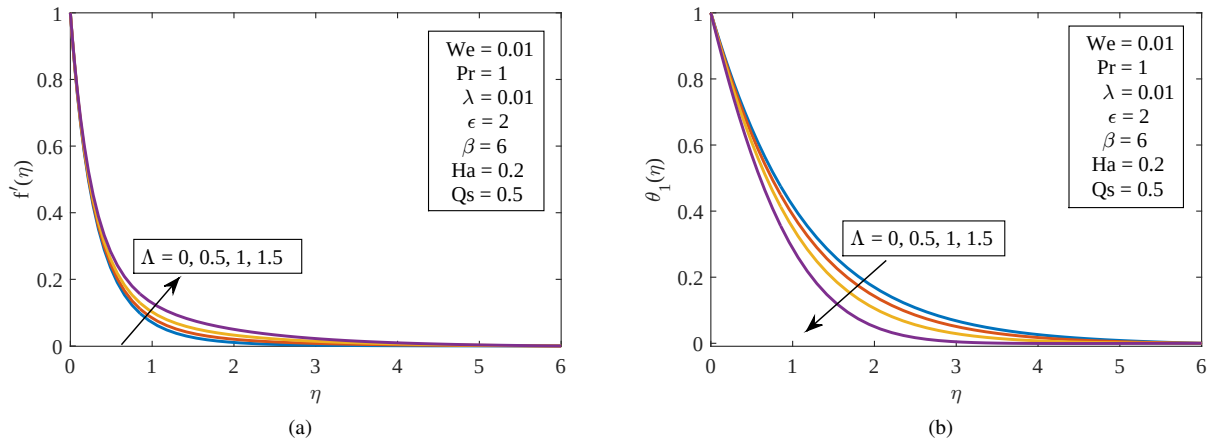

Figure 7. Impact of Λ on velocity and temperature.

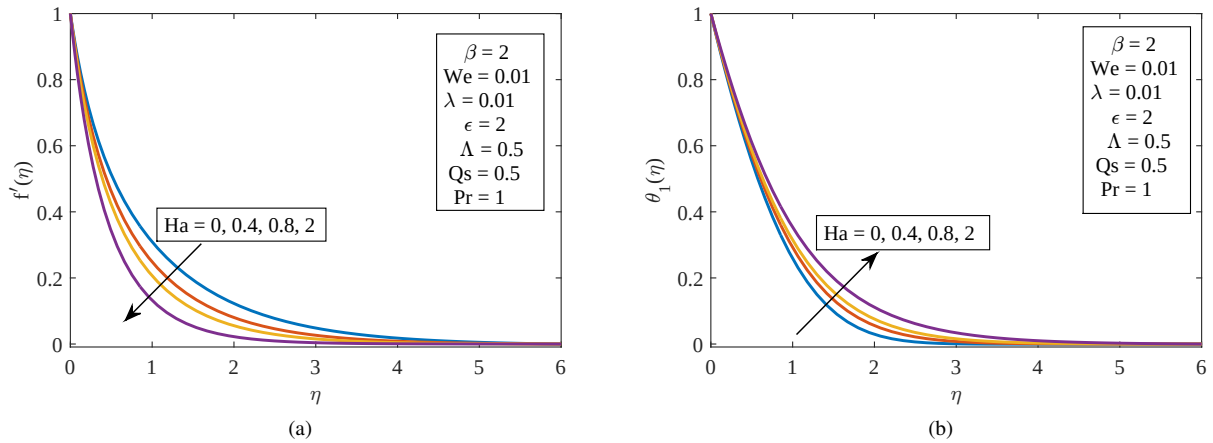

Figure 8. Impact of Ha on velocity and temperature.

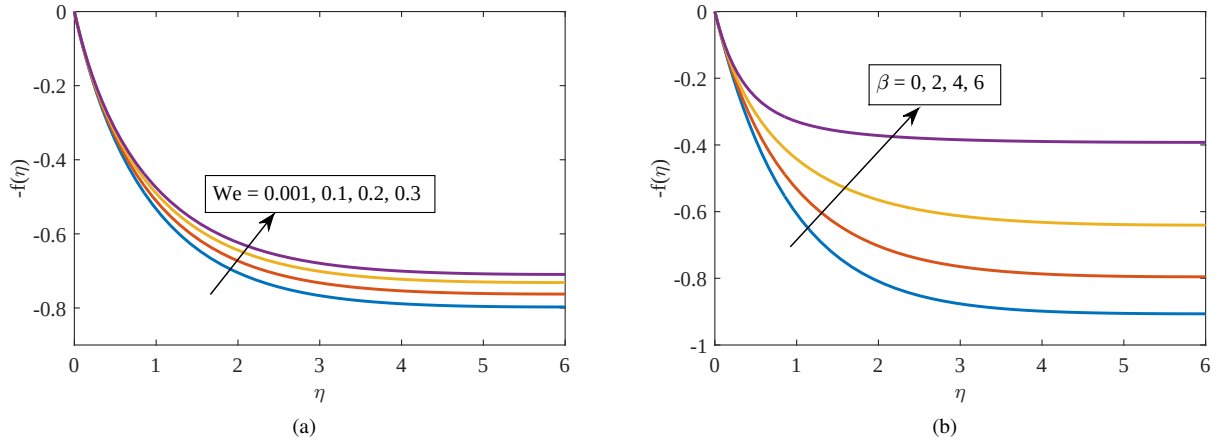

Figure 9. Impact of We and β on transverse velocity $-f(\eta)$.

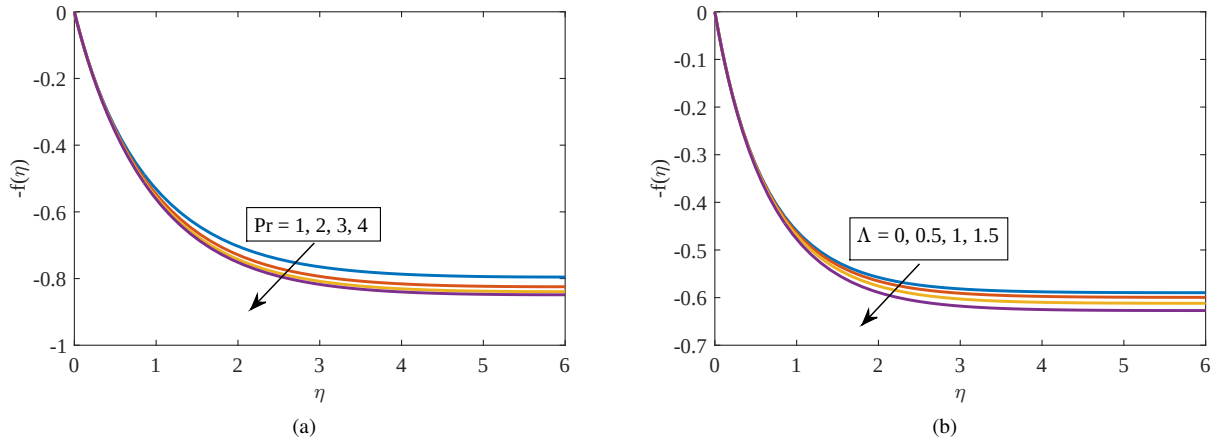

Figure 10. Impact of Pr and Λ on transverse velocity $-f(\eta)$.

increased heat generation in the fluid, which leads to a more uniform distribution of temperature within boundary layer and diminishing temperature variation near the wall.

Fig. (6)(a)-6(b) are depicted to notice the influence of We on profiles of velocity and temperature. Due to the fluid particle's increased relaxation time, the velocity profile decreases as We rises. The thickness of thermal boundary layer decreases as We increases which results in an enhancement in the temperature profile.

Fig. (7)(a) and (7)(b) illustrates a rise in velocity and reduction of temperature as Λ increases. The axial velocity is noticed to increase with a rise Λ due to reduced thermal effects which causes the momentum to increase. With an increase of Λ, a time lag is introduced in the process of heat conduction, which slows the heat diffusion rate due which the reduction in temperature.

Fig. (8)(a) and (8)(b) depict the influence of Ha on profiles of velocity and temperature. A rise in Hartmann number increases the resistive force, leading to reduced flow. The temperature is noticed to increase with a rise in Ha, due to increased viscous dissipation and slowed convective heat transfer. The graphs in figure (9) and (10) are plotted for the values: $\lambda = 0.01$, $\epsilon = 2$, $Pr = 1$, $Ha = 0.2$, β=2, $Qs = 0.5$, We=0.01 and Λ= 0.5.

Fig. (9) (a) and (9)(b) illustrate the impact of We and β on the transverse velocity. With a rise in both We and β, the elastic and magnetic interactions of fluid are enhanced, leading to an increase in transverse velocity. Figures in (10) illustrate the influence of Pr and Λ on transverse velocity.

The decline in transverse velocity with an elevation of Pr and Λ results from the synergistic effects of heightened viscous dissipation, diminished temperature gradients, and alterations in the fluid's responsiveness to thermal fluctuations.

5. CONCLUSIONS

This article examines the flow and heat transfer characteristics of Williamson fluid over a stretched sheet when a magnetic dipole is present. Equations governing fluid flow are transformed to non-linear ordinary differential equations using similarity transformations. These equations are solved numerically through the Spectral Quasi-Linearization Method. A MATLAB program is utilized to generate

graphical results, facilitating a detailed analysis of the influence of various parameters on the velocity and temperature profiles. The conclusions that can be drawn are:

- An increase of β, We and Ha results in a decline of axial velocity and a rise in temperature, and transverse velocity.
- With higher values of the Qs, Prandtl number Pr, and Thermal relaxation parameter Λ, the temperature declines and velocity rises.
- With an increase in We, coefficient of skin friction reduces and rate of heat transfer rises, while both decrease with a rise in β.

Residual errors for velocity and temperature profiles clearly showed rapid convergence, with a significant improvement in accuracy after the fifth iteration. The optimal accuracy required 40-80 collocation points, after which the accuracy gradually decreased. The residual error norms for different parameters ranged from 10^{-5} to 10^{-11}, indicating the numerical scheme's robustness and efficiency.

The results can be applied to simulate blood flow in the presence of a magnetic field, as blood exhibits non-Newtonian behavior similar to Williamson fluids under certain conditions. This is crucial for designing medical devices like magnetic resonance imaging (MRI) systems or improving techniques for controlling blood flow during surgeries.
In industries dealing with non-Newtonian fluids, the results are vital for optimizing processes such as extrusion and stretching of polymer sheets or films. Understanding heat transfer and fluid flow characteristics ensures better quality control and energy efficiency during production.

ORCID

Kairavadi Suresh Babu, https://orcid.org/0000-0003-1538-1072; **Vangala Sugunamma**, https://orcid.org/0000-0001-6815-1540; **Vamsi Krishna Narla**, https://orcid.org/0000-0003-0994-3497

REFERENCES

[1] R.V. Williamson, "The Flow of Pseudoplastic Materials," Industrial and Engineering Chemistry, **21**(11), 1108–1111 (1929). https://doi.org/10.1021/ie50239a035

[2] S. Nadeem, S.T. Hussain, and C. Lee, "Flow of a Williamson fluid over a stretching sheet," Brazilian Journal of Chemical Engineering, **30**(3), 619–625 (2013). https://doi.org/10.1590/S0104-66322013000300019

[3] M.Y. Malik, M. Bibi, F. Khan, and T. Salahuddin, "Numerical solution of Williamson fluid flow past a stretching cylinder and heat transfer with variable thermal conductivity and heat generation/absorption," AIP Advances, **6**(3), o35101 (2016). https://doi.org/10.1063/1.4943398

[4] M.I. Khan, S. Qayyum, T. Hayat, M.I. Khan, and A. Alsaedi, "Entropy optimization in flow of Williamson nanofluid in the presence of chemical reaction and Joule heating," International Journal of Heat and Mass Transfer, **133**, 959–967 (2019). https://doi.org/10.1016/j.ijheatmasstransfer.2018.12.168

[5] I. Zehra, M.M. Yousaf, and S. Nadeem, "Numerical solutions of Williamson fluid with pressure dependent viscosity," Results in Physics, **5**, 20–25 (2015). https://doi.org/10.1016/j.rinp.2014.12.002

[6] K. Subbarayudu, S. Suneetha, and P.B.A. Reddy, "The assessment of time dependent flow of Williamson fluid with radiative blood flow against a wedge," Propulsion and Power Research, **9**(1), 87–99 (2019). https://doi.org/10.1016/j.jppr.2019.07.001

[7] A.M. Megahed, "Williamson fluid flow due to a nonlinearly stretching sheet with viscous dissipation and thermal radiation," Journal of the Egyptian Mathematical Society, **27**(1), 12 (2019). https://doi.org/10.1186/s42787-019-0016-y

[8] R.E. Rosensweig, *Ferrohydrodynamics*, (Cambridge University Press, New York, USA, 1985).

[9] H.I. Andersson, and O.A. Valnes, "Flow of a heated ferrofluid over a stretching sheet in the presence of a magnetic dipole," Acta Mechanica, **128**, 39–47, (1998). https://doi.org/10.1007/BF01463158

[10] B.A. Pasha, G. Sowmya, V. Ramachandramurthy, and H.M. Nagesh, "Influence of Heat Source on Thin Film Flow of Ferrofluid Past an Unsteady Stretching Sheet," Journal of Mines Metals and Fuels, **71**(10), 1518–1525 (2023). https://doi.org/10.18311/jmmf/2023/35812

[11] E.E. Tzirtzilakis, "A mathematical model for blood flow in magnetic field," Physics of Fluids, **17**(7), 077103 (2005). https://doi.org/10.1063/1.1978807

[12] M.R.D. Garmroodi, A. Ahmadpour, M.R. Hajmohammadi, and S. Gholamrezaie, "Natural convection of a non-Newtonian ferrofluid in a porous elliptical enclosure in the presence of a non-uniform magnetic field," Journal of Thermal Analysis and Calorimetry, **141**(5), 2127–2143 (2019). https://doi.org/10.1007/s10973-019-09045-3

[13] N.H. Abu-Hamdeh, R.A.R. Bantan, F. Aalizadeh, and A. Alimoradi, "Controlled drug delivery using the magnetic nanoparticles in non-Newtonian blood vessels," Alexandria Engineering Journal, **59**(6), 4049–4062 (2020). https://doi.org/10.1016/j.aej.2020.07.010

[14] N.S. Anagandula, and N.K.S. Reddy, "Velocity and Thermal Slips Impact on the Williamson Fluid Flow above a Stretching Sheet in the Existence of Radiation and Inclined Magnetic Field," CFD Letters, **16**(7), 118–135 (2024). https://doi.org/10.37934/cfdl.16.7.118135

[15] A. Abbas, M.B. Jeelani, A.S. Alnahdi, and A. Ilyas, "MHD Williamson Nanofluid Fluid Flow and Heat Transfer Past a Non-Linear Stretching Sheet Implanted in a Porous Medium: Effects of Heat Generation and Viscous Dissipation," Processes, **10**(6), 1221 (2022). https://doi.org/10.3390/pr10061221

[16] M. Rashid, K. Ansar, and S. Nadeem, "Effects of induced magnetic field for peristaltic flow of Williamson fluid in a curved channel," Physica a Statistical Mechanics and Its Applications, **553**, 123979 (2020). https://doi.org/10.1016/j.physa.2019.123979

[17] M.V. Krishna, and B.V. Swarnalathamma, "Convective heat and mass transfer on MHD peristaltic flow of Williamson fluid with the effect of inclined magnetic field," AIP Conference Proceedings, **1728**, 020461 (2016). https://doi.org/10.1063/1.4946512

[18] A.M. Obalalu, S.O. Salawu, O.A. Olayemi, O.A. Ajala, and K. Issa, "Analysis of hydromagnetic Williamson fluid flow over an inclined stretching sheet with Hall current using Galerkin Weighted Residual Method," Computers & Mathematics With Applications, **146**, 22–32 (2023). https://doi.org/10.1016/j.camwa.2023.06.021

[19] Y.-X. Li, M.H. Alshbool, Y.-P. Lv, I. Khan, M.R. Khan, and A. Issakhov, "Heat and mass transfer in MHD Williamson nanofluid flow over an exponentially porous stretching surface," Case Studies in Thermal Engineering, **26**, 100975 (2021). https://doi.org/10.1016/j.csite.2021.100975

[20] M. Dhivua, and K. Vajravelu, "Heat transfer characteristics of a Williamson fluid flow through a variable porosity regime," International Journal of Ambient Energy, **44**(1), 2553–2568 (2023). https://doi.org/10.1080/01430750.2023.2258378

[21] M.S. Anwar, M.S. Alqarni, and M. Irfan, "Exploring the marvels of heat transfer: "MHD convection at a stagnation point in non-Newtonian fluid with yield stress and chemical reactions," Chinese Journal of Physics, **89**, 1299-1308 (2024). https://doi.org/10.1016/j.cjph.2024.01.030

[22] L.N. Trefethen, *Spectral Methods in MATLAB*, (Oxford University Mathematical Institute, Oxford, United Kingdom, 2000).

[23] D. Srinivasacharya, and K.H. Bindu, "Entropy generation in a micropolar fluid flow through an inclined channel with slip and convective boundary conditions," Energy, **91**, 72–83 (2015). https://doi.org/10.1016/j.energy.2015.08.014

[24] R.A. Alharbey, H. Mondal, and R. Behl, "Spectral Quasi-Linearization Method for Non-Darcy Porous Medium with Convective Boundary Condition," Entropy, **21**(9), 838 (2019). https://doi.org/10.3390/e21090838

[25] H. Mondal, and S. Bharti, "Spectral Quasi-linearization for MHD Nanofluid Stagnation Boundary Layer Flow due to a Stretching/Shrinking Surface," Journal of Applied and Computational Mechanics, **6**(4), 1058–1068 (2020). https://doi.org/10.22055/jacm.2019.30677.1766

[26] N. Rai, and S. Mondal, "Spectral methods to solve nonlinear problems: A review," Partial Differential Equations in Applied Mathematics, **4**, 100043 (2021). https://doi.org/10.1016/j.padiff.2021.100043

[27] W. Al-Kouz, C.S. Reddy, M.S. Alqarni, and B. Mahanthesh, "Spectral quasi-linearization and irreversibility analysis of magnetized cross fluid flow through a microchannel with two different heat sources and Newton boundary conditions," The European Physical Journal Plus, **136**(6), 645 (2021). https://doi.org/10.1140/epjp/s13360-021-01625-3

[28] E.E. Tzirtzilakis, and G.B. Tanoudis, "Numerical study of biomagnetic fluid flow over a stretching sheet with heat transfer," International Journal of Numerical Methods for Heat & Amp Fluid Flow, **13**(7), 830–848 (2003). https://doi.org/10.1108/09615530310502055

[29] H. Muzara, and S. Shateyi, "Magnetohydrodynamics Williamson Nanofluid Flow over an Exponentially Stretching Surface with a Chemical Reaction and Thermal Radiation," Mathematics, **11**, 2740 (2023). https://doi.org/10.3390/math11122740

[30] A. Srinu, K.S. Reddy and N. Amar, "Radiation and inclined magnetic field effects on Williamson fluid flow above a stretching sheet in the existence of velocity, thermal, and concentration slips", Partial Differential Equations in Applied Mathematics, **9**, 100611 (2024). https://doi.org/10.1016/j.padiff.2023.100611

[31] M. Faizan, M. Ajithkumar, M.V. Reddy, M.A. Jamal, B. Almutairi, N.A. Shah, and J.D. Chung, "A theoretical analysis of the ternary hybrid nano-fluid with Williamson fluid model," Ain Shams Engineering Journal, **15**, 102839 (2024). https://doi.org/10.1016/j.asej.2024.102839

[32] T. Salahuddin, and Muhammad Awais, "Thermal and solutal transport by Cattaneo-Christov model for the magnetohydrodynamic Williamson fluid with joule heating and heat source/sink," Heliyon, **10**, e29228 (2024). https://doi.org/10.1016/j.heliyon.2024.e29228

[33] Z. Liu, S. Li, T. Sadaf, S.U. Khan, F. Alzahrani, M.I. Khan, and S.M. Eldin, "Numerical bio-convective assessment for rate type nanofluid influenced by Nield thermal constraints and distinct slip features", Case Studies in Thermal Engineering, **44**, 102821 (2023). https://doi.org/10.1016/j.csite.2023.102821

БІОМАГНІТО-ГІДРОДИНАМІЧНИЙ ПОТІК РІДИНИ ВІЛЬЯМСОНА ТА ТЕПЛОПЕРЕНОС ЧЕРЕЗ ПОВЕРХНЮ, ЩО РОЗТЯГУЄТЬСЯ: СПЕКТРАЛЬНИЙ КВАЗІЛІНЕАРИЗАЦІЙНИЙ ПІДХІД

Кайраваді Сурeш Бабу[b], **Вангала Сугунамма**[a], **Вамсі Крішна Нарла**[c]

[a] *Університет Шрі Венкатешвара, Тірупаті, АР, 517502, Індія*

[a] *Інженерно-технологічний інститут Гокараджу Рангараджу, TG, Індія*

[c] *GITAM вважається університетом, факультет математики, Хайдарабад, 502329, Індія*

Потік і теплопередача рідини Вільямсона, підданої магнітному полю, аналізуються та досліджуються методом спектральної квазілінеаризації (SQLM). Рівняння, пов'язані з імпульсом і енергією, отримані з рівнянь Нав'є-Стокса з урахуванням неньютонівських ефектів, в'язкої дисипації, магнітних сил і сили Лоренца. Взаємодія електропровідної рідини з магнітним полем створює силу Лоренца, яка суттєво змінює поведінку потоку, застосовуючи силу опору проти швидкості рідини. Метод ефективно лінеаризує нелінійні рівняння, забезпечуючи точні рішення за допомогою спектрального методу. Чисельні результати підкреслюють вплив параметрів рідини Вільямсона, інтенсивності магнітного поля та джерел тепла на поля швидкості та температури, пропонуючи зрозуміти поведінку рідини в промислових застосуваннях, що включають неньютонівські рідини та магнітні поля.

Ключові слова: *рідина Вільямсона; параметр джерела тепла; магнітний диполь; сила Лоренца та метод спектральної квазілінеаризації*

East European Journal of Physics. 1. 134-140 (2025)
DOI:10.26565/2312-4334-2025-1-12 ISSN 2312-4334

NUMERICAL INVESTIGATION OF JOULE HEATING EFFECT ON MICROPOLAR NANOFLUID FLOW OVER AN INCLINED SURFACE IN PRESENCE OF HEAT SOURCE

Keshab Borah[a], Jadav Konch[b,*], Shyamanta Chakraborty[c], Abhijit Konch[b], Salma Akhtar[a]
[a] *Department of Mathematics, Gauhati University, Guwahati-781014, Assam, India*
[b] *Department of Mathematics, Dhemaji College, Dhemaji-787057, Assam, India*
[c] *UGC- MMTTC, Gauhati University, Guwahati-781014, Assam, India*
**Corresponding Author e-mail: jadavkonch@gmail.com*
Received September 30, 2024; revised January 31, 2025; in final form February 6, 2025' accepted February 15, 2025

The MHD boundary layer flow of a micropolar nanofluid across an inclined stretching surface in the presence of a heat source is examined in this paper. This study employs permeable inclined surfaces with energy flow as its primary observation with heat radiation and the Dufour impact. Additionally, the impact of Joule heating, viscous dissipation and heat source on the porous media are considered. This study uses similarity transformations to convert nonlinear partial differential equations that governs the flow to ordinary differential equations. The bvp4c computational technique in MATLAB is used to illustrate the numerical findings. Based on the findings we were able to determine that the velocity and angular velocity of the fluid increases with the angle of inclination, the temperature profile increases with the increasing values of Eckert number whereas the concentration profile decreases with Eckert number. These findings are further illustrated through numerical data presented in table and visual representations in figures. These findings will enable engineers and scientists to better control fluid flow, leading to improvements in complex systems that rely on it.
Keywords: *MHD; Micropolar nanofluid; Joule heating; Inclined sheet; Heat source; Porous medium; Radiation*
PACS: 44.25+g; 44.05.+e; 44.30.+v; 44.40.+a

INTRODUCTION

The dynamics of fluid flows caused by stretching surfaces have received extensive consideration. It is due of their widespread use in designing and industrial processes. The boundary layer flow toward an inclined surface has drawn interest from scientists because of its modern and building applications, such as material fabricated by expulsion, paper making, hot moving, plastic manufacture, and versatile expulsion. Sakiadis [1] initially studied the boundary layer fluid flow of a viscous incompressible fluid on a continuous moving surface. Gupta et al. [2] utilized a similar solution approach to explore heat and mass transfer within the boundary layer of a stretched sheet subjected to blowing or suction. The investigation of micropolar nanofluid flow across an inclined surfaces has been a subject of significant interest in the field of heat transfer and fluid dynamics. Nanofluids, which are a class of engineered fluids containing nanoparticles, have shown great potential in enhancing heat transfer capabilities compared to their base fluids. Moreover, the incorporation of micropolar effects, which account for the rotational motion of fluid particles, adds an additional layer of complexity to the analysis of such flows [3].

An inclined surface is a surface which is neither vertical nor horizontal, but has a slope or angle relative to a reference plane or surface. An inclined surface's geometry may be characterized using the slope, angle of inclination, and surface dimensions. The angle of inclination is the angle formed between an inclined surface and a horizontal plane. Deebani et al. [4] investigate the flow of a 2D micropolar fluid across an inclined linear shrinking/stretching surface under suction, convection, slip, and thermal radiation impact. Roja et al. [5] explored the two-dimensional steady incompressible MHD flow of a micropolar fluid over an inclined permeable surface with natural convection. Suriyakumar et al. [6] observed the combined influences of internal heat generation and suction on mixed convection nanofluid flow across an inclined surface. Meanwhile, Ziaei Rad et al. [7] derived similarity solutions for nanofluid flow within the boundary layer of an inclined surface. Selva Rani et al. [8] conducted an investigation on the convective heat transfer properties of nanofluids flowing over an inclined plate, incorporating the influences of thermal radiation and a variable surface temperature. Rafique et al. [9, 10] studied about the boundary layer flow of micropolar nanofluid over linearly inclined stretching surface under the influence of a magnetic field. Eid et al. [11] conducted a mathematical study on the energy transfer dynamics of micropolar magnetic viscous nanofluid flow over an inclined permeable surface, considering the effects of Dufour phenomenon and thermal radiation. Waleign et al. [12] developed a mathematical model to investigate how various thermal and physical properties influence the behavior of micropolar nanofluid flow near an inclined surface.

Joule heating occurs due to the interactions between the conductor's atomic structure and the flowing electric current. As charged particles collide, some of their kinetic energy converts to heat, causing the conductor's temperature to rise. Several studies have explored the impact of Joule heating on fluid dynamics and heat transfer under various situations, indicating its major effect on magnetohydrodynamic (MHD) flows. Yadav and Sharma [13] examined the impact of Joule heating on magnetohydrodynamic flow induced by an exponentially moving stretching sheet, embedded in porous media. Srinivasacharya et al. [14] conducted a study examining the combined impacts of Hall current and Joule heating on the

Cite as: K. Borah, J. Konch, S. Chakraborty, A. Konch, S. Akhtar, East Eur. J. Phys. 1, 134 (2025), https://doi.org/10.26565/2312-4334-2025-1-12

viscous fluid flow passing over an exponentially stretching sheet. Jayanthi et al. [15] studies MHD nanofluid flow via a stretched vertical surface as impacted by Joule heating, chemical reaction, viscosity dissipation, thermal radiation, and activation energy. Prasad et al. [16] look at the combined effects of Hall current and thermal diffusion on the unsteady MHD free convective rotating flow of nanofluids in a porous media. The study examines flow past a moving vertical semi-infinite flat plate in the presence of a heat source and a chemical reaction.

Motivated by the above works, the objectives of this study is to investigate the Joule heating and heat source effects on magnetohydrodynamic (MHD) micropolar viscous nanofluid flow past over a permeable inclined surface. This is an addition of Joule Heating and Heat source effects to the problem discussed by Eid et al. [11]. The equations that govern the flow are transformed using similarity transformations and solved numerically with MATLAB's bvp4c solver. The impact of key dimensionless parameters on velocity, angular velocity, temperature, solute concentration, and nanoparticle concentration are visualized through graphical representations.

MATHEMATICAL FORMULATION

A two-dimensional (2-D) boundary layer flow of micropolar nanofluid is studied as it moves over an inclined surface that is extending linearly at an angle Ω. The surface and free stream velocities are considered to be $u_w(x) = bx$ and $u_\infty(x) = 0$, respectively, where '*b*' is a constant and *x* is the coordinate along the surface. A transverse magnetic field is placed perpendicularly to the flow direction with negligible induced magnetic field effects. The micropolar nanofluid contains constantly distributed micropolar finite size particles and nanoparticles, allowing for spinning effects and extra space for particles to move before colliding. The analysis includes the impacts of Brownian motion, Dufour, radiation, Joule heating, heat source, and thermophoresis. The temperature and nanoparticle fraction at the wall are held constant at T_w and C_w, while the ambient values for nanofluid mass and temperature fractions (C_∞ and T_∞) are achieved as the distance from the wall (*y*) approaches infinity, as shown in Figure 1.

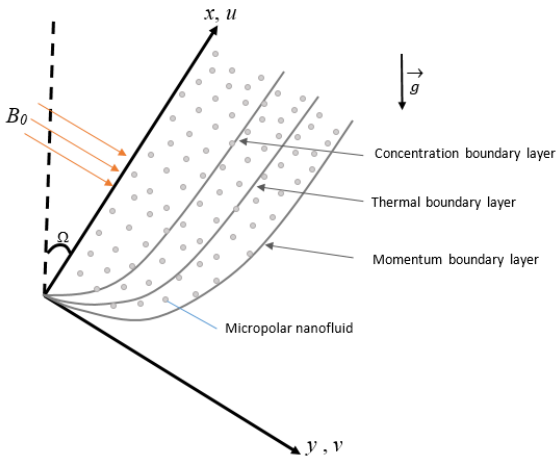

Figure 1. Flow geometry of the problem.

The governing equations of the flow are given as [10, 11]:

$$\frac{\partial u}{\partial x}+\frac{\partial v}{\partial y}=0 \tag{1}$$

$$u\frac{\partial u}{\partial x}+v\frac{\partial u}{\partial y}=\left(\frac{\mu+\kappa}{\rho}\right)\frac{\partial^2 u}{\partial y^2}+\frac{\kappa}{\rho}\frac{\partial N}{\partial y}+g\left[\beta_T\left(T-T_\infty\right)+\beta_C\left(C-C_\infty\right)\right]\cos\Omega-\frac{\sigma B_0^2}{\rho}u-\frac{\upsilon}{K_p'}u \tag{2}$$

$$u\frac{\partial N}{\partial x}+v\frac{\partial N}{\partial y}=\frac{\gamma}{\rho j}\frac{\partial^2 N}{\partial y^2}-\frac{\kappa}{\rho j}\left(2N+\frac{\partial u}{\partial y}\right) \tag{3}$$

$$u\frac{\partial T}{\partial x}+v\frac{\partial T}{\partial y}=\alpha\frac{\partial^2 T}{\partial y^2}-\frac{1}{\rho C_P}\frac{\partial q_r}{\partial y}+\tau\left(D_B\frac{\partial C}{\partial y}\frac{\partial T}{\partial y}+\frac{D_T}{T_\infty}\left(\frac{\partial T}{\partial y}\right)^2\right)+\left(\frac{\mu+\kappa}{\rho C_P}\right)\left(\frac{\partial u}{\partial y}\right)^2+\frac{D_M K_T}{C_S C_P}\frac{\partial^2 C}{\partial y^2}+\frac{Q}{\rho C_P}\left(T-T_\infty\right)+\frac{\sigma B^2 u^2}{\rho C_P} \tag{4}$$

$$u\frac{\partial C}{\partial x}+v\frac{\partial C}{\partial y}=D_B\frac{\partial^2 C}{\partial y^2} \tag{5}$$

The boundary conditions are

$$\left.\begin{array}{l} u = u_w = bx, v = v_w, N = -m\dfrac{\partial u}{\partial y},\ T = T_w,\ C = C_w \ \text{ at } \ y = 0 \\ u \to 0\ , \quad N \to 0, \quad T \to T_\infty, \quad C \to C_\infty \quad \text{ as } \ y \to \infty \end{array}\right\} \tag{6}$$

By using the Rosseland [17] approximation for radiation, radiation heat flux is given by

$$q_r = -\frac{4\sigma^*}{3k^*}\frac{\partial T^4}{\partial y} \tag{7}$$

Where σ^* denotes the Stefan–Boltzmann constant and k^* represents mean absorption coefficient. Considering that the variations in temperature throughout the flow such that the term T^4 may be stated as a linear function of the temperature, and expanding T^4 in a Taylor series about T_∞ and neglecting the higher order terms that are beyond the first degree in $(T - T_\infty)$, then we get

$$T^4 \cong 4T_\infty^3 T - 3T_\infty^4 \tag{8}$$

Using equations (7) and (8), equation (4) can be written as

$$u\frac{\partial T}{\partial x} + v\frac{\partial T}{\partial y} = \alpha\left(1 + \frac{16T_\infty^3\sigma^*}{3k^*\kappa}\right)\frac{\partial^2 T}{\partial y^2} + \tau\left(D_B\frac{\partial C}{\partial y}\frac{\partial T}{\partial y} + \frac{D_T}{T_\infty}\left(\frac{\partial T}{\partial y}\right)^2\right) + \left(\frac{\mu+\kappa}{\rho C_P}\right)\left(\frac{\partial u}{\partial y}\right)^2 + \frac{D_M K_T}{C_S C_P}\frac{\partial^2 C}{\partial y^2} + \frac{Q'}{\rho C_P}(T - T_\infty) + \frac{\sigma B^2 u^2}{\rho C_P} \tag{9}$$

We introduce the following similarity variable and dimensionless functions:

$$\eta = \sqrt{\frac{b}{\upsilon}}y\ ,\ f(\eta) = \frac{\psi}{x\sqrt{b\upsilon}}\ ,\ h(\eta) = \sqrt{\frac{\upsilon}{b}}\frac{N}{bx}\ ,\ \theta(\eta) = \frac{T - T_\infty}{T_w - T_\infty}\ ,\ \phi(\eta) = \frac{C - C_\infty}{C_w - C_\infty}$$

Using the relation $u = \dfrac{\partial\psi}{\partial y}$ and $v = -\dfrac{\partial\psi}{\partial x}$ (where ψ is the stream function), we get

$$u = xbf'(\eta) \ \text{ and } \ v = -\sqrt{b\upsilon}f(\eta).$$

Using the above transformations the equation of continuity (1) is identically satisfied and other equations (2), (3), (5) and (9) reduces to

$$(1+K)f''' - (f')^2 + ff'' + Kh' + (Gr\,\theta + Gc\,\phi)\cos\Omega - \left(M + \frac{1}{Kp}\right)f' = 0 \tag{10}$$

$$\left(1 + \frac{K}{2}\right)h'' + fh' - f'h - K(2h + f'') = 0 \tag{11}$$

$$\frac{1}{\Pr}\left(1 + \frac{4}{3}R\right)\theta'' + f\theta' + N_b\theta'\phi' + N_t(\theta')^2 + (1+K)Ec(f'')^2 + Q\theta + Ec\,M(f')^2 + Df\,\phi'' = 0 \tag{12}$$

$$\phi'' + Le\,f\,\phi' = 0 \tag{13}$$

Where

$$K = \frac{\kappa}{\mu}\ ,\ Gr_x = \frac{g\beta_T(T_w - T_\infty)}{b^2 x}\ ,\ Gc_x = \frac{g\beta_c(C_w - C_\infty)}{b^2 x}\ ,\ M = \frac{\sigma B_0^2}{b\rho}\ ,\ Kp = \frac{bK_p'}{\upsilon}\ ,\ Pr = \frac{\upsilon}{\alpha}\ ,\ R = \frac{16T_\infty^3\sigma^*}{3k^*k},$$

$$N_b = \frac{\tau D_B(C_w - C_\infty)}{\upsilon}\ ,\ N_t = \frac{\tau D_T(T_w - T_\infty)}{\upsilon T_\infty}\ ,\ Ec = \frac{u_w^2}{C_P(T_w - T_\infty)}\ ,\ Q = \frac{Q'}{b\rho C_P}\ ,\ Le = \frac{\upsilon}{D_B}\ ,\ Df = \frac{D_M K_T(C_w - C_\infty)}{\upsilon C_S C_P(T_w - T_\infty)}.$$

The boundary conditions (6) reduce to

$$\left.\begin{array}{l} f(\eta) = f_w,\ f'(\eta) = 1, h(\eta) = -m\,f''(0), \theta(\eta) = 1,\ \phi(\eta) = 1 \ \ at \ \ \eta = 0 \\ f'(\eta) = 0, \quad h(\eta) = 0, \quad \theta(\eta) = 0, \quad \phi(\eta) = 0 \quad as \quad \eta \to \infty \end{array}\right\} \tag{14}$$

Here, to eliminate x-dependence in the local Grashof number (Gr_x), local modified Grashof number (Gc_x), β_t (thermal expansion coefficient) and β_c (concentration expansion coefficient) are required to be directly proportional to x^1. Therefore, assume that [18, 19].

$$\beta_t = nx^1, \beta_c = n_1 x^1 \tag{15}$$

Where n_1 and n signifies constants. Substituting equation (15) into the quantities Gr_x and Gc_x, consequences become

$$Gr = \frac{g\,n(T_w - T_\infty)}{b^2}\ ,\ Gc = \frac{g\,n_1(C_w - C_\infty)}{b^2}$$

The important physical quantities of interest in this problem are the skin friction coefficient (C_f), the Nusselt number (Nu_x) and the Sherwood number (Sh_x) and defined as

$$Nu_x = \frac{xq_w}{k(T_w - T_\infty)},\ Sh_x = \frac{xq_m}{D_B(C_w - C_\infty)},\ C_f = \frac{t_w}{\frac{1}{2}u_w^2\rho}$$

The associated expressions for the skin friction coefficient, the reduced Sherwood number, and the reduced Nusselt Number are as follows:

$$C_{fx} = C_f\sqrt{\mathrm{Re}}\ ,\ -\phi'(0) = \frac{Sh_x}{\sqrt{\mathrm{Re}}}\ ,\ -\theta'(0) = \frac{Nu_x}{\sqrt{\mathrm{Re}}}$$

where $\mathrm{Re} = \frac{u_w x}{\nu}$ represents the Reynolds Number.

RESULTS AND DISCUSSIONS

The boundary value problem represented by the equations (10) to (13) with the initial boundary conditions given by in equation (14) is solved using bvp4c solver by developing suitable codes in MATLAB. Graphs are used to analyze the effects of various dimensionless parameters on velocity, angular velocity, temperature, solute concentration profile. In order to verify the accuracy of applied numerical method, a comparison of numerical results of present study with previous study is presented in table 1, where we have found an excellent agreement. The graphical representation of velocity profile, micro-rotation profile, temperature profile, concentration profile for various parameters that appears in the equations are depicted in Figure 2 to Figure 11.

Table 1 is created to verify the appropriateness and efficacy of the bvp4c approach. The results obtained are in good agreement with the literature in limiting cases, confirming the method's suitability.

Table 1. Comparison of findings of the Nusselt number –θ′ (0) at $Gc = Gr = M = K = R = Df = m = Kp = 0,\ Le = Pr = 10$ *and* $\Omega = 90°$

Nt	Nb	Khan and Pop [20]	Rafique et al. [10]	Eid et al. [11]	Present Study
0.1	0.1	0.9524	0.9524	0.9524	0.9524
0.3	0.3	0.1355	0.1355	0.1355	0.1354
0.5	0.5	0.0179	0.0179	0.0179	0.0177

Figures 2 to 5 demonstrates how increasing values of magnetic parameter (M) influence the fluid velocity, micro-rotation or angular velocity, temperature, and concentricity profile. Figure 2 reveals a significant decrease in the fluid's velocity as the magnetic variable M is increased.

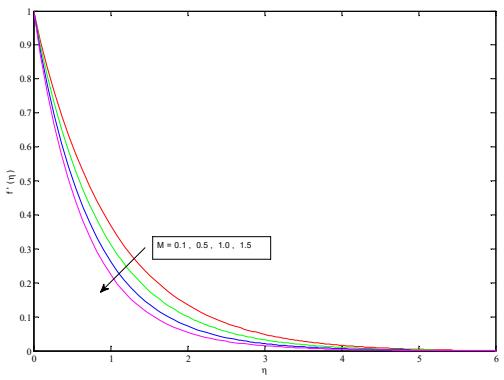

Figure 2. Velocity profile for different M

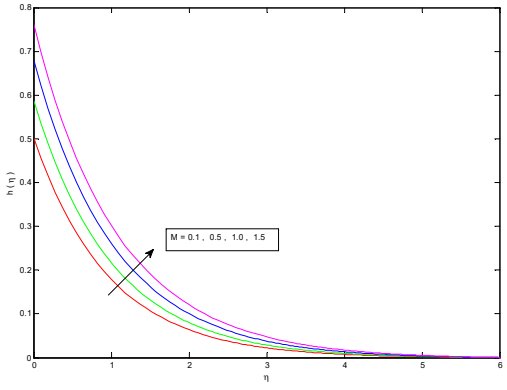

Figure 3. Micro-rotation profile for different M

This phenomenon can be attributed to the Lorentz force, which generates friction and consequently slows down the fluid's movement. Figure 3 shows that the micro-rotation of tiny particles within the fluid exhibits a decreasing trend with the increasing values of *M*.

Figures 4 and 5 shows that temperature $\theta(\eta)$ and concentricity $\varphi(\eta)$ increases with higher values of *M*, as friction generates more heat and mass, leading to increased temperature and concentration.

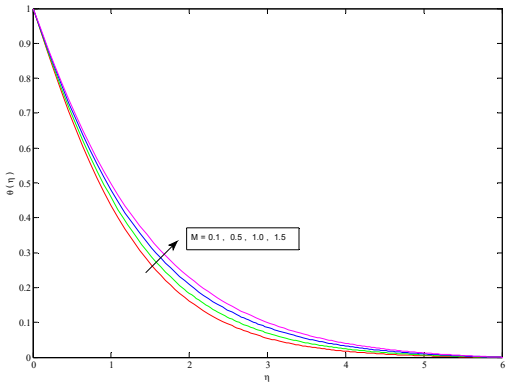

Figure 4. Temperature profile for different *M*

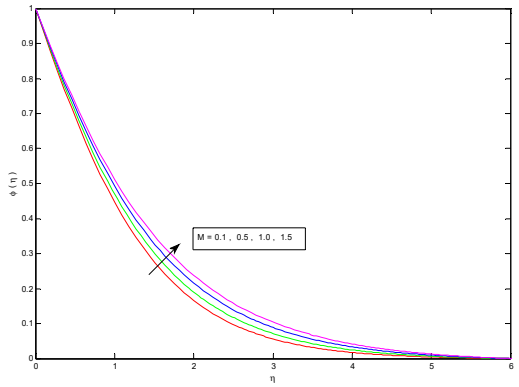

Figure 5. Concentration profile for different *M*

Figures 6 and 7 illustrates the impact of the Eckert number (*Ec*) on the temperature and concentration profiles respectively. Figure 6 reveals a significant relationship between the Eckert number (*Ec*) and temperature. It represents that as Eckert number increases, so does the amount of temperature. Physically, rise in *Ec* increases the fluid friction and fluid particles strike more frequently to each other, consequently they generate the heat energy in the medium. Figure 7 shows that the concentration profile decreases with Eckert number.

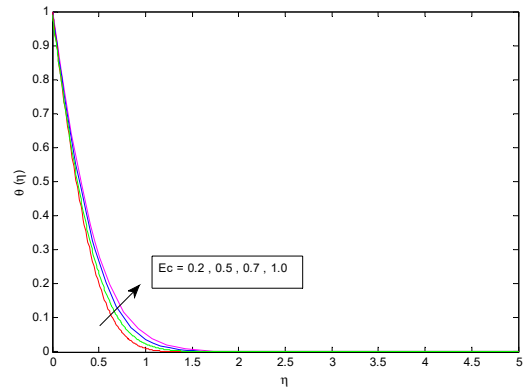

Figure 6. Temperature profile for different *Ec*

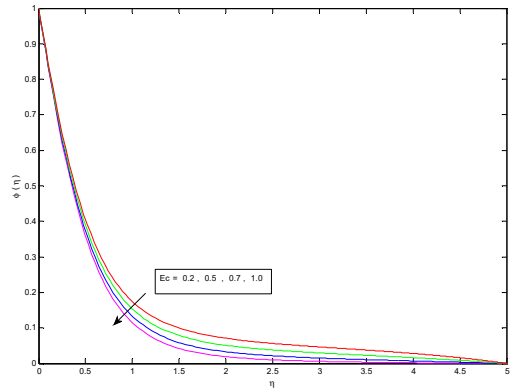

Figure 7. Concentration profile for different *Ec*

Figures 8 and 9 illustrate the impact of the heat source parameter on the temperature and concentration profiles. It is observed that as the heat generation parameter increases, the temperature and concentration profiles increases.

Figures 10 and 11 illustrate the impact of the angle of inclination on the velocity and micro-rotation profiles, which depicts that velocity and angular velocity of the fluid increases as the inclination angle increases. This is due to the increase of buoyancy effect with the inclination angle.

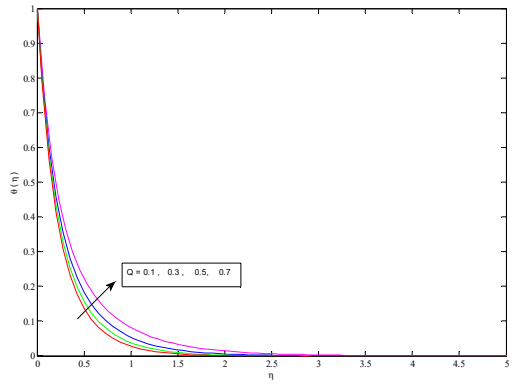

Figure 8. Temperature profile for different *Q*

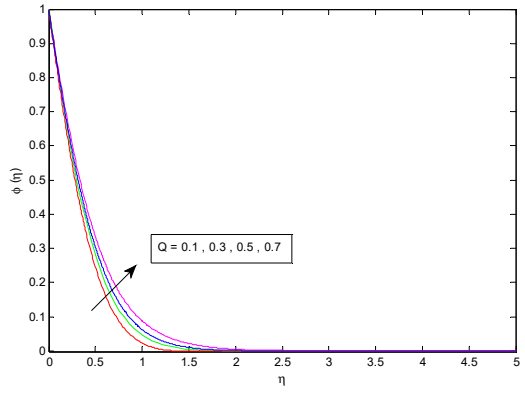

Figure 9. Concentration profile for different *Q*

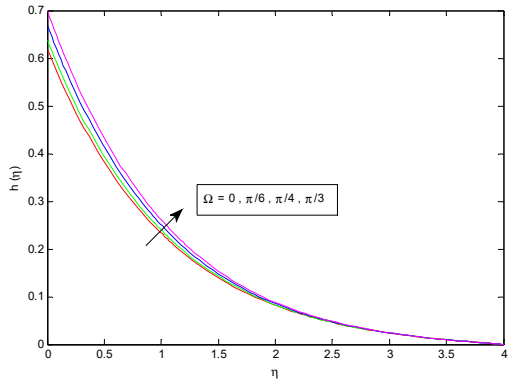

Figure 10. Velocity profile for different Ω

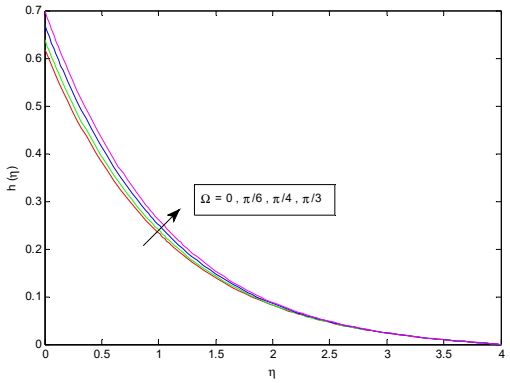

Figure 11. Micro-rotation profile for different Ω

CONCLUSION

In this study, an analysis has been carried out on the effect of magnetic parameter, heat source, Eckert number and angle of inclination on MHD micropolar nanofluid flow past an inclined plate in presence of viscous dissipation, thermal radiation, Dufour effect, Joule heating where it is observed that the parameters have significant influence on the velocity, temperature, concentration and micro-rotation profile. The resulting ordinary differential equations are solved numerically using the bvp4c method. To ensure the accuracy of the computational results obtained in this study, they are compared with findings from previous research. Additionally, the results of the current analysis are presented in a visual format through various graphs, facilitating a clear understanding of the outcomes. Following are some conclusions drawn from the above analysis.

- The velocity and angular velocity of the fluid increases with the angle of inclination.
- The temperature profile increases with the increasing of Eckert number whereas the concentration profile decreases as the Eckert number increases.
- The fluid velocity deceases with the Magnetic Parameter M, whereas micro-rotation, temperature and Nanoparticle concentricity increases with M.

Future scope: Micropolar nanofluids have several uses, including electronic chips, thermal energy retention, polymeric polymers, semiconductor wafers, industrial, and biomedical industries. As a result, in the future, the current analysis will be expanded to include the effects of variable thermal conductivity and viscosity in presence of non-uniform heat source and sink.

Nomenclature

u, v Velocity components along x and y direction
μ Coefficient of dynamic viscosity
κ Coefficient of Vortex viscosity.
ρ Free stream density
υ Coefficient of kinematic viscosity
N Angular velocity or micro-rotation
γ Viscosity of spin gradient.
b Constant.
D_M Chemical molecular diffusivity
D_B Brownian diffusion coefficient,
$\vec{g}$ Acceleration due to gravity.
β_t Thermal expansion coefficient
β_c Concentration expansion coefficient
f_w Suction (injection)
σ^* Stefan–Boltzmann constant
k^* Mean absorption coefficient
C_P Specific heat at constant pressure
u_w Surface velocity
C Concentricity
C_w Species concentration at the surface
C_∞ Fluid concentration outlying the surface
T Temperature
T_w Wall temperature
T_∞ Ambient temperature
Pr Prandtl Number.
Ec Eckert Number.
K Material parameter.
Le Lewis number
ψ Stream function
θ Dimensionless temperature
ϕ Dimensionless concentration
C_f The local skin friction coefficient.
Nu Nusselt number.
S_h Sherwood number.
N_t Thermophoresis parameter
N_b Brownian motion parameter
Gr Local Grashof number
Gc Local modified Grashof number
Ω Angle of inclination
K_p Porosity parameter
R Radiation parameter
Q Heat Source parameter
Df Dufour Number.
M Magnetic parameter.
τ_w Wall shear stress

ORCID

Keshab Borah, https://orcid.org/0009-0005-5486-5784; **Shyamanta Chakraborty,** https://orcid.org/0000-0001-5839-4856
Salma Akhtar, https://orcid.org/0009-0003-1793-001X; **Jadav Konch**, https://orcid.org/0000-0002-6953-3679

REFERENCES

[1] B.C. Sakiadis, "Boundary-layer behavior on continuous solid surfaces: I. Boundary-layer equations for two-dimensional and axisymmetric flow," AIChE J. **7**(1), 26-28 (1961).
[2] P.S. Gupta, and A.S. Gupta, "Heat and mass transfer on a stretching sheet with suction or blowing," Can. J. Chem. Eng. **55**, 744-746 (1977). http://dx.doi.org/10.1002/cjce.5450550619
[3] A. Mitra, "Simulation on Natural Convection of a Nanofluid along an Isothermal Inclined Plate," IOP Conference Series: Materials Science and Engineering, **225**, 012096-012096 (2017). https://doi.org/10.1088/1757-899x/225/1/012096
[4] W. Deebani, L.A. Lund, A.F. Chandio, U. Yashkun, Z. Shah, and A. Alshehri, "Convective micropolar fluid over inclined surface with thermal radiation and velocity slip condition effects: Duality and stability," International Journal of Modern Physics B, **38**(08), 2450114 (2023). https://doi.org/10.1142/s0217979224501145
[5] P. Roja, T.S. Reddy, S.M. Ibrahim, M. Parvathi, G. Dharmaiah, and G. Lorenzini, "Magnetic Field Influence on Thermophoretic Micropolar Fluid Flow over an Inclined Permeable Surface: A Numerical Study," Journal of Applied and Computational Mechanics, **10**(2), 369-382 (2024). https://doi.org/10.22055/jacm.2024.44739.4265
[6] P. Suriyakumar, and S.A. Devi, "Effects of suction and internal heat generation on hydromagnetic mixed convective nanofluid flow over an inclined stretching plate," European Journal of Advances in Engineering and Technology, **2**(3), 51-58 (2015). https://ejaet.com/PDF/2-3/EJAET-2-3-51-58.pdf
[7] M. Ziaei-Rad, A. Kasaeipoor, M.M. Rashidi, and G. Lorenzini, "A similarity solution for mixed-convection boundary layer nanofluid flow on an inclined permeable surface," Journal of Thermal Science and Engineering Applications, **9**(2), 021015 (2017). https://doi.org/10.1115/1.4035733
[8] M. Selva rani, and A. Govindarajan, "Radiative fluid flow of a nanofluid over an inclined plate with non-uniform surface temperature," J. Phys. Conf. Ser. **1000**, 012173 (2018). https://doi.org/10.1088/1742-6596/1000/1/012173
[9] K. Rafique, M.I. Anwar, and M. Misiran, "Numerical Study on Micropolar Nanofluid Flow over an Inclined Surface by Means of Keller-Box," Asian Journal of Probability and Statistics, **4**(4), 1–21 (2019). https://doi.org/10.9734/ajpas/2019/v4i430122
[10] K. Rafique, M.I. Anwar, M. Misiran, and M.I. Asjad, "Energy and mass transport of micropolar nanofluid flow over an inclined surface with Keller-Box simulation," Heat Transfer, **49**(8), 4592-4611 (2020). https://doi.org/10.1002/htj.21843
[11] M.R. Eid, W. Jamshed, B.S. Goud, R.W. Ibrahim, S.M. El Din, A. Abd-Elmonem, and N.S.E. Abdalla, "Mathematical analysis for energy transfer of micropolar magnetic viscous nanofluid flow on permeable inclined surface and Dufour impact," Case Studies in Thermal Engineering, **49**, 103296 (2023). https://doi.org/10.1016/j.csite.2023.103296
[12] T. Walelign, and E. Seid, "Mathematical model analysis for hydromagnetic flow of micropolar nanofluid with heat and mass transfer over inclined surface," International Journal of Thermofluids, **21**, 100541 (2024). https://doi.org/10.1016/j.ijft.2023.100541
[13] R.S. Yadav, and P.R. Sharma, "Effects ff radiation and viscous dissipation on MHD boundary layer flow due to an exponentially moving stretching sheet in porous medium," Asian J. Multidiscip. Stud. **2**(8), 119–124 (2014).
[14] D. Srinivasacharya, and P. Jagadeeshwar, "MHD flow with Hall current and Joule heating effects over an exponentially stretching sheet," Nonlinear Eng. Model. Appl. **6**(2), 101–114 (2017). https://doi.org/10.1515/nleng-2016-0035
[15] S. Jayanthi, and H. Niranjan, "Effects of joule heating, viscous dissipation, and activation energy on nanofluid flow induced by MHD on a vertical surface," Symmetry, **15**(2), 314 (2023). https://doi.org/10.3390/sym15020314
[16] V.R. Prasad, N.U.B. Varma, J. Bodduna, *et al.*, "Effects of hall current and thermal diffusion on unsteady MHD rotating flow of water-based Cu, and TiO2 nanofluid in the presence of thermal radiation and chemical reaction," Multiscale and Multidiscip. Model. Exp. and Des. **8**, 161 (2025). https://doi.org/10.1007/s41939-025-00736-z
[17] S. Rosseland, *Astrophysik und atom-theoretische Grundlagen*, (Springer, 1931). https://doi.org/10.1007/978-3-662-26679-3
[18] F. Shah, and M.I. Khan, "Analytical Investigation on the Combined Impacts of the Soret and Dufour Phenomenon in the Forced Convective Flow of a Non-newtonian Nanofluid by the Movable Riga Device," Waves Random Complex Media, 1-18 (2023). https://doi.org/10.1080/17455030.2022.2154407
[19] K. Rafique, M.I. Anwar, M. Misiran, I. Khan, A.H. Seikh, E.-S.M. Sherif, and K. Sooppy Nisar, "Keller-Box Simulation for the Buongiorno Mathematical Model of Micropolar Nanofluid Flow over a Nonlinear Inclined Surface," Processes, **7**(12), 926 (2019). https://doi.org/10.3390/pr7120926
[20] W. Khan, and I. Pop, "Boundary-layer flow of a nanofluid past a stretching sheet," International Journal of Heat and Mass Transfer, **53**(11-12), 2477-2483 (2010). https://doi.org/10.1016/j.ijheatmasstransfer.2010.01.032

ЧИСЕЛЬНЕ ДОСЛІДЖЕННЯ ВПЛИВУ ДЖОУЛЕВОГО НАГРІВУ НА МІКРОПОЛЯРНИЙ ПОТІК НАНОРІДИНИ ПО НАХИЛІЙ ПОВЕРХНІ ЗА НАЯВНОСТІ ДЖЕРЕЛА ТЕПЛА

Кешаб Борах[a], Джадав Конч[b], Шьяманта Чакраборті[c], Абхіджит Конч[b], Салма Ахтар[a]
[a]Департамент математики, Університет Гаухаті, Гувахаті-781014, Ассам, Індія
[b]Департамент математики, коледж Демаджі, Демаджі-787057, Ассам, Індія
[c] UGC- MMTTC, Університет Гаухаті, Гувахаті-781014, Ассам, Індія

У цій статті досліджено МГД потік мікрополярної нанофлюїду в пограничному шарі через похилу розтягнуту поверхню за наявності джерела тепла. У цьому дослідженні в якості основного спостереження використовуються проникні похилі поверхні з потоком енергії з тепловим випромінюванням і впливом Дюфура. Крім того, розглядається вплив джоулева нагрівання, в'язкої диссипації та джерела тепла на пористі середовища. Це дослідження використовує перетворення подібності для перетворення нелінійних диференціальних рівнянь у частинних похідних, які керують потоком, у звичайні диференціальні рівняння. Для ілюстрації чисельних результатів використовується обчислювальна техніка bvp4c у MATLAB. На підставі отриманих даних ми змогли визначити, що швидкість і кутова швидкість рідини зростає зі збільшенням кута нахилу, температурний профіль зростає зі збільшенням числа Еккерта, тоді як профіль концентрації зменшується зі збільшенням числа Еккерта. Ці висновки додатково ілюструються числовими даними, представленими в таблиці, і візуальними представленнями на малюнках. Ці відкриття дозволять інженерам і вченим краще контролювати потік рідини, що призведе до вдосконалення складних систем, які покладаються на нього.
Ключові слова: *МГД; мікрополярний нанофлюїд; Джоулеве нагрівання; похилий лист; джерело тепла; пористе середовище; випромінювання*

EAST EUROPEAN JOURNAL OF PHYSICS. 1. 141-150 (2025)
DOI:10.26565/2312-4334-2025-1-13 ISSN 2312-4334

PERFORMANCE ENHANCEMENT OF InGaP/GaAs DUAL-JUNCTION SOLAR CELLS THROUGH BSF LAYER OPTIMIZATION AND HETERO-TUNNEL JUNCTION

Ikram Zidani[a]*, Zouaoui Bensaad[a], Loumafak Hafaifa[b,c], Hamza Abid[a], Ahmed Hafaifa[d]
[a]*Applied Materials Laboratory, Djilali Liabes University, Sidi Bel Abbes, Algeria*
[b]*Department of Physics, Faculty of Exact Sciences and Computer Science, Ziane Achour University, 17000 Djelfa, Algeria*
[c]*Physico-Chemistry of Materials and Environment Laboratory, Ziane Achour University, BP 3117, Djelfa, Algeria*
[d] *Applied Automation and Industrial Diagnostics Laboratory, Faculty of Science and Technology, University of Djelfa 17000 DZ, Algeria*
**Corresponding Author e-mail: ikram.zidani@univ-sba.dz*
Received October 9, 2024; revised December 18, 2024; accepted January 5, 2025

This study focuses on the simulation and optimization of an InGaP/GaAs dual-junction solar cells using Silvaco Atlas software, with a special emphasis on the incorporation of a hetero tunnel junction. The hetero-tunnel junction plays a pivotal role in enabling efficient charge carrier transport between the sub-cells, significantly improving the overall cell efficiency. Additionally, a new back-surface field (BSF) layer was integrated into the GaAs bottom sub-cell to further enhance performance. Various material combinations for the hetero-tunnel junction such as GaInP/GaAs, AlGaInP/GaInP, and AlGaInP/GaAs were systematically tested to assess their influence on device efficiency. The optimized structure demonstrated a short-circuit current density of 1.780 mA/cm², an open-circuit voltage of 2.310 V, a fill factor of 86.501%, and a conversion efficiency of 35.57% under AM1.5G illumination at 300 K. Recombination losses were minimized by the BSF layer optimization in the top and bottom cell, particularly with AlGaInP, leading to improved charge collection. Elevated temperatures were found to reduce both the open-circuit voltage and efficiency, highlighting the necessity of thermal management. These optimizations represent significant improvements over prior designs.
Keywords: *InGaP/GaAs DJSCs; Solar cell; BSF; Silvaco-Atlas; Optimization*
PACS: 02.60.Cb, 02.60.Pn, 82.47.Jk, 84.60.Jt, 42.79.Ek, 89.30.Cc

INTRODUCTION

Solar cell technology remains one of the most effective methods for harnessing the sun's vast, renewable, and clean energy potential [1]**.** Photovoltaic conversion is the process by which electromagnetic energy is transformed directly into continuous electrical energy. This is achieved by converting photons from sunlight into electricity. This process is achieved through solar cells (photovoltaic cells) that incorporate optimized optoelectronic devices with reliable models. Solar radiation is the most abundant source of electromagnetic energy [2]. The solar photovoltaic research field is rapidly evolving, with continuous efforts aimed at reducing costs and enhancing efficiency. A notable approach to improving efficiency is spectrum splitting, which broadens the range of light absorbed across the solar spectrum [3]. Dual-junction solar cells (DJSCs), a leading innovation in photovoltaic (PV) technology, offer much higher conversion efficiencies than single-junction cells. This improvement is achieved through their two-layer structure, where each layer is optimized to absorb different parts of the solar spectrum. The top cell, with a higher bandgap, captures high-energy photons, while the bottom cell, with a lower bandgap, absorbs the lower-energy photons that pass through [4–6]. This complementary absorption of a wider range of sunlight boosts overall energy conversion efficiency. DJSCs, which incorporate this technique in a tandem structure, typically utilize III-V semiconductor materials like InGaP, GaAs, and Ge. These materials have different bandgaps, allowing for more efficient absorption across the solar spectrum [7].

In 2017, a study reported a 25.43% efficiency for an InGaP/GaAs hetero-junction solar cell by examining the influence of the window layer on performance at 300 K. The following year, another study achieved 34.44% efficiency by integrating a BSF and a TJ in an InGaP/GaAs structure [8]**.** The following year, another study achieved 34.44% efficiency by integrating a BSF and a TJ in an InGaP/GaAs structure [9]**.** Furthermore, Bin Zhao et al. introduced a thin layer into the structure of InGaP/GaAs DJSCs, improving the stability and performance of the cell's operational dynamics [10]. Tomah Sogabe et al. analyzed the impact of fluctuations in the intermediate band of InAs/GaAs solar cells, optimizing the efficiency and stability of these organometallic cells [11]. More recently, in 2023, optimization of an InGaP/GaAs DJSCs with dual tunnel junctions (TJs) and enhanced BSF layers resulted in an efficiency of 35.15% [12].

This paper aims to improve the efficiency of GaInP/GaAs DJSCs and identify the optimal output parameters of the structure. To achieve this, a DJSC comprising two sub-cells was simulated using Silvaco-Atlas software under standard AM1.5G illumination, with an incident power density of 100 mW/cm² and an ambient temperature of 300 K. First, numerical simulations were conducted to optimize the thickness of the new BSF layer in the bottom cell, aiming for favorable current matching between the upper and lower cells, which is essential for maximizing DJSC efficiency. Additionally, the material composition of the TJ was varied to explore potential improvements in conversion efficiency.

Cite as: I. Zidani, Z. Bensaad, L. Hafaifa, H. Abid, A. Hafaifa, East Eur. J. Phys. 1, 141 (2025), https://doi.org/10.26565/2312-4334-2025-1-13

Finally, the BSF layer in the upper cell was optimized, and the impact of temperature on the cell's performance parameters was investigated.

PARAMETERS FOR SIMULATION MODEL

Physical Models

The Physical modeling and simulation are critical for understanding device behavior and predicting performance, particularly in semiconductor devices like solar cells. Their main advantages cost-effectiveness, easy accessibility, and rapid implementation make them indispensable for optimizing and improving device designs. Among the available tools, Silvaco-Atlas is widely recognized as one of the most prominent simulation programs for solar cell modeling [13]. In this study, the physical models are divided into five core categories: mobility, recombination, carrier statistics, collision ionization, and tunneling. These models were carefully selected to match the material properties of the solar cell, ensuring accurate application throughout the device structure. Key parameters such as Shockley-Read-Hall (SRH) recombination and Band Gap Narrowing (BGN) are incorporated to capture critical mechanisms, including carrier recombination and the influence of heavy doping on the band structure. Operating temperature plays a significant role in device performance, primarily by affecting recombination dynamics. The SRH recombination model is particularly valued for its ability to replicate experimental results accurately, making it a standard approach in numerical simulations of solar cells. [8–10].

For the precise simulation of InGaP/GaAs DJSCs, especially in hetero tunnel junctions, specialized tunneling models are necessary. In this study, the BBT.NONLOCAL model is employed to account for non-local band-to-band tunneling, while the BBT model handles direct band-to-band transitions in regions with high electric fields. To ensure convergence during simulations, particularly when non-local coupling is present, the BBT.NLDERIVS model is recommended. The combination of these models enhances the accuracy and stability of the simulation results [11,12].

Key performance parameters critical to solar cell operation are derived from the *I-V* characteristics, represented by the *I-V* curve. The total current (*I*) in a solar cell consists of the sum of dark current and photocurrent (I_{ph}). This relationship is mathematically described by the Shockley equation [18]:

$$I = I_{ph} - I_0\left(\exp(\frac{qV}{akT}) - 1\right) \tag{1}$$

I is the net current flowing through the solar cell, V is the applied voltage, I_0 represents the saturation reverse current, a is the ideality factor, q denotes the electron charge, k is Boltzmann's constant, T is the absolute temperature.
The I_{SC} is defined as the current through the solar cell when V=0:

$$I_{sc} = I_{ph} \tag{2}$$

Key performance metrics, including the Jsc, Voc, and FF, can be calculated using the following equations:

$$V_{oc} = \frac{E_g}{q} - \frac{akT}{q}\ln(\frac{I_0}{I_{ph}}) \tag{3}$$

$$FF = \frac{P_{\max}}{V_{oc}J_{sc}} \tag{4}$$

Here P_{max} is the maximum power output of the solar cell.
The efficiency (η) of the solar cell is intrinsically linked to these parameters and is expressed as follows:

$$\eta = \frac{P_{max}}{P_{in}} = \frac{V_{oc}I_{sc}FF}{P_{in}} \tag{5}$$

Additionally, the recombination rates within the solar cell are modeled using the SRH mechanism, represented by the equation:

$$R_{n,p} = \frac{\sigma_n\sigma_p v_{th}N_t\left(np - n_i^2\right)}{\sigma_n\left[n + n_i\exp\left(\frac{E_t - E_i}{kT}\right)\right] + \sigma_p\left[p + n_i\exp\left(\frac{E_t - E_i}{kT}\right)\right]} \tag{6}$$

Where n_i is the intrinsic carrier density, v_{th} is the thermal velocity, σ_n and σ_p are the electron and hole capture cross sections, E_i and E_t represent the intrinsic Fermi energy level and trap energy level.

SIMULATED STRUCTURE

The structure of the simulated InGaP/GaAs DJSCs is illustrated in Figure 1, showcasing its intricate design aimed at optimizing both light absorption and charge carrier transport. This dual junction solar cell consists of a upper InGaP

cell and a lower GaAs cell, connected via a Hetero TJ (AlGaInP/GaAs). Each component is carefully engineered to maximize device performance.

The top InGaP cell features a p+/n+ junction, with a P+ InGaP emitter and an n+ InGaP base. With an energy Eg of 1.9 eV, this layer is optimized for capturing high-energy photons. To reduce surface recombination, a P+ AlInGaP window layer is positioned at the front of the top cell, enhancing overall efficiency. A BSF layer of n+ AlInGaP at the rear of the top cell further mitigates recombination by reflecting charge carriers.

The hetero tunnel junction that links the top and bottom cells is essential for seamless charge transport between them. This junction comprises an n+ AlInGaP layer and a p+ GaAs layer. These heavily doped layers facilitate efficient carrier tunneling with minimal resistance, ensuring strong electrical connectivity.

The bottom GaAs cell, with a p-n junction, has a lower energy Eg = 1.42 eV, targeting the absorption of lower-energy photons transmitted by the top cell. Its P+ GaAs emitter and n+ GaAs base are optimized for enhanced photon absorption. A P+ InGaP window layer further reduces surface recombination at the front, while two BSF layers (BSF1 and BSF2) of n+ AlInGaP ensure charge carrier reflection, minimizing recombination losses at the rear.

The entire cell architecture rests on an n+ GaAs substrate [19,20], which provides mechanical stability and enhanced electrical conductivity. A gold (Au) contact is employed at the cathode to facilitate efficient charge collection and conduction.

This meticulously engineered dual-junction configuration, leveraging the higher band-gap of InGaP and the lower band-gap of GaAs, enables efficient utilization of the solar spectrum. The design minimizes recombination losses and promotes effective charge transport, contributing to improved overall conversion efficiency. Additionally, the optical properties of the materials were sourced from the comprehensive SOPRA database available within the Silvaco-Atlas library [21]. All input parameters used in the simulations are presented in Table 1.

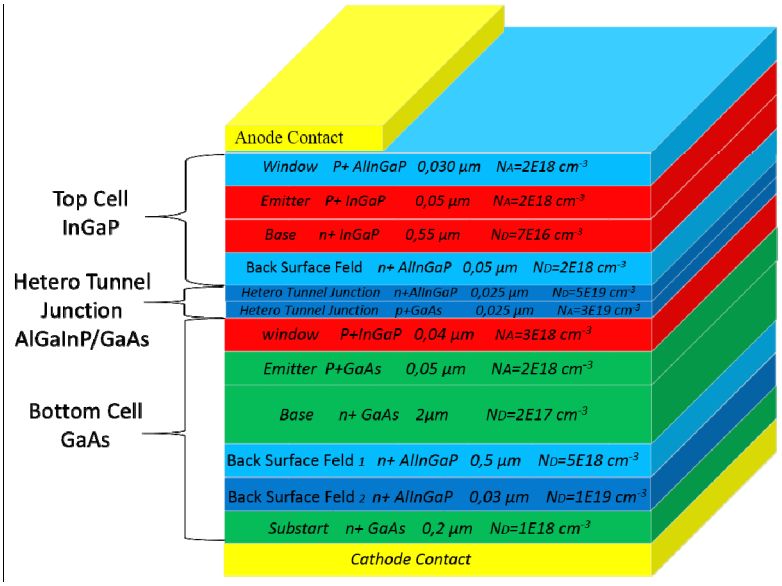

Figure 1. Schematic structure of InGaP/GaAs DJSCs.

Table 1. Summarizes the physical parameters of each material used in this simulation [22–24]**.**

Layer properties	AlGaInP	GaInP	GaAs	AlGaAs
Eg (eV)	2.3	1.9	1.42	1.8
α (Å)	5.56	5.56	5.56	5.64
es/eo	11.7	11.6	11.0	11.0
χ (eV)	4.2	4.16	4.07	4.1
Nc (cm^{-3})	1.2×10^{20}	1.30×10^{20}	4.7×10^{17}	4.35×10^{17}
Nv (cm^{-3})	1.28×10^{19}	1.28×10^{19}	7.0×10^{18}	8.16×10^{18}
MUN(cm^2/Vs)	2150	1945	8800	2000
MUP(cm^2/Vs)	141	141	400	138
τ_n(s)	1.00×10^{-9}	1.00×10^{-9}	1.00×10^{-9}	1.00×10^{-9}
τ_p (s)	1.00×10^{-9}	1.00×10^{-9}	2.00×0^{-8}	2.00×10^{-8}
n_i (per cc)	1	7.43×10^{4}	2.12×10^{6}	1

RESULTS AND DISCUSSION

The InGaP/GaAs DJSCs was simulated using the parameters outlined in Table 1, resulting in the J-V characteristics shown in Figure 2. This figure presents the I-V curves for the DJSCs, which features a GaAs/GaAs TJ. The individual I-V curves for the InGaP upper cell and GaAs lower cell are also depicted for comparison.

Under AM1.5G illumination, the design achieves a Jsc of 1.65×10^{-10}, Voc of 2.31 V, FF of 86.29%, and η of 32.83%. The tandem structure demonstrates efficient current matching between the sub-cells, with the I-V curves reflecting the performance of each junction within the stack.

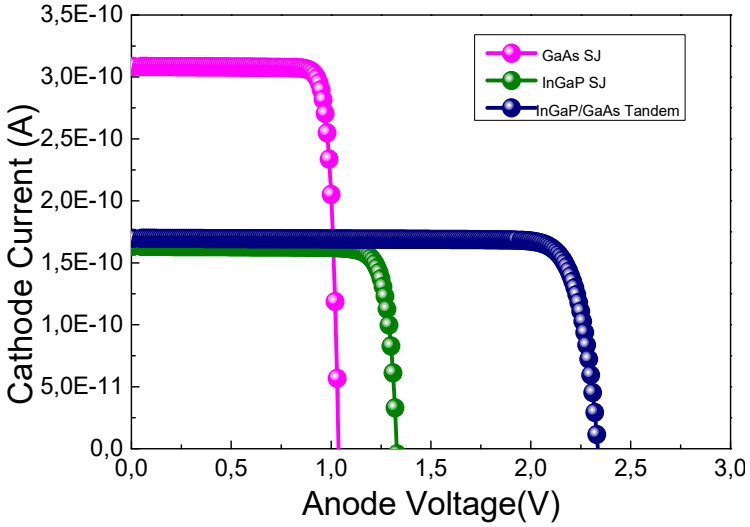

Figure 2. I-V Characteristics of InGaP/GaAs DJSCs

OPTIMIZATION OF THE NEW BSF LAYER IN THE GaAs BOTTOM CELL

The introduction of the quaternary compound AlInGaP as a BSF in the n-p GaAs bottom cell significantly influences the solar cell's performance metrics, as illustrated in Figure 3. The variation in BSF thickness from 0.01 µm to 0.04 µm reveals distinct trends across key parameters such as Jsc, Voc, FF, and η.

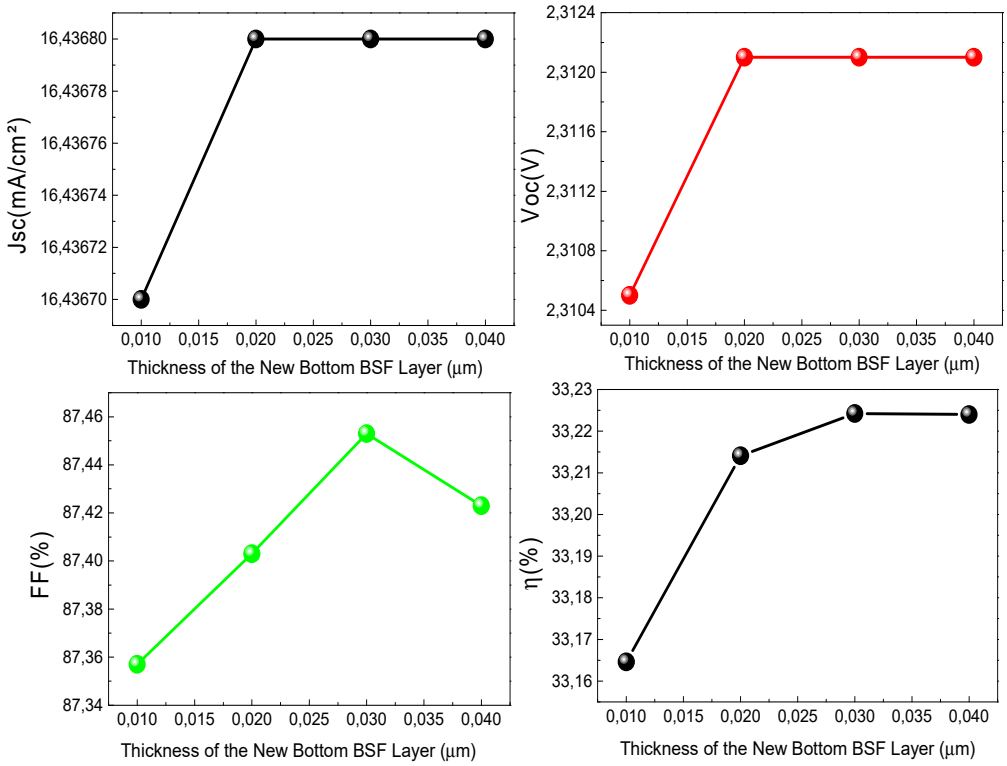

Figure 3. Impact of varying the thickness of the new bottom BSF layer on the η, FF, J_{SC}, and V_{OC} of the InGaP/GaAs DJSCs.

Jsc shows a sharp increase as the new bottom BSF thickness rises from 0.01 µm to 0.02 µm, reaching a stable maximum value of 16.436 mA/cm² beyond this point. Similarly, the Voc also increases with BSF thickness, stabilizing at 2.312 V for thicknesses greater than 0.02 µm.

The FF improves steadily as the new bottom BSF thickness increases from 0.01 µm, peaking at 87.46% at 0.03 µm. However, further increasing the new bottom BSF thickness results in a slight decline in FF, indicating that an overly thick BSF may hinder optimal carrier transport.

The overall efficiency follows a similar pattern, reaching its maximum value of 33.224% at a BSF thickness of 0.03 µm. Beyond this thickness, the efficiency begins to plateau, suggesting that 0.03 µm represents the optimal BSF thickness for this design. At this point, recombination losses are minimized, and photo-generated carrier transport is maximized, leading to the highest observed efficiency [7,12].

In conclusion, the optimal new bottom BSF thickness for this InGaP/GaAs DJSCs is identified at 0.03 µm, where the balance between reduced recombination losses and efficient carrier transport is achieved, as evidenced by the peak in both fill factor and overall efficiency. This highlights the critical role of BSF thickness in fine-tuning device performance for maximum output.

INFLUENCE OF HETERO-TJ MATERIALS ON InGaP/GaAs DJSCs PERFORMANCE

We further examined the impact of different hetero TJ materials by testing combinations of GaAs, AlGaAs, GaInP, and AlGaInP for the InGaP/GaAs DJSCs. The tunnel region facilitates the recombination of electrons and holes between the upper and lower cells, allowing current to flow in the DJSCs [20]. Figures 4 and 5 illustrate the I-V characteristics and conversion efficiency for various hetero TJ materials.

Among the combinations, the AlGaInP/GaAs hetero TJ exhibited the highest efficiency, reaching 34.31%, accompanied by a Jsc of 1.75 mA/cm² (as seen in Figure 5), a Voc of 2.36 V, and an FF of 87.19%. This makes AlGaInP/GaAs the optimal material combination in this study. The superior performance is attributed to the wider band-gap of AlGaInP, which reduces optical absorption compared to other materials, allowing lighter to reach the underlying layers. However, this higher band-gap increases the potential barrier, which slightly reduces the tunneling current in the diode.

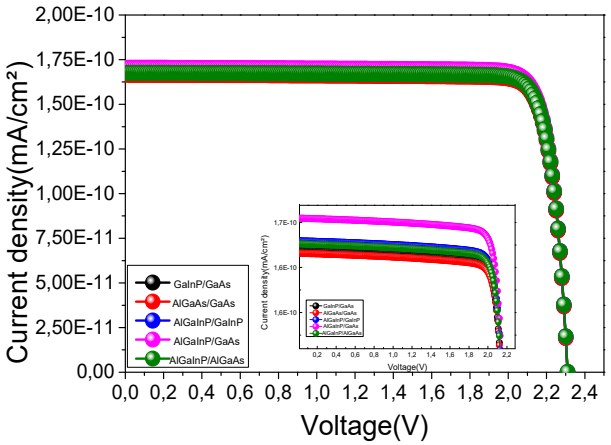

Figure 4. I-V Characteristics of InGaP/GaAs DJSCs with Different Tunnel Junctions

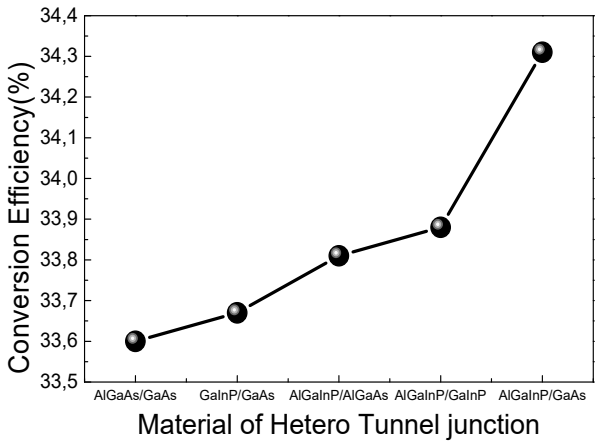

Figure 5. Impact of TJ Material on the Conversion Efficiency of InGaP/GaAs DJSCs

Similar trends were observed for AlGaAs/GaAs, GaInP/GaAs, AlGaInP/AlGaAs, and AlGaInP/GaInP combinations, though with comparatively lower efficiencies. Both the Jsc and η improved with the use of AlGaInP as the anode material in the hetero-tunnel junction, instead of GaAs. These results suggest that optimizing the hetero tunnel junction with AlGaInP can significantly enhance the efficiency of InGaP/GaAs DJSCs, primarily due to its favorable optical and electrical properties [25,26].

1.1. OPTIMIZATION OF BSF THICKNESS IN THE TOP SOLAR CELL

In this analysis, we systematically varied the thickness of the BSF layer in the upper cell while keeping all other parameters constant to assess its effect on the performance of the double-junction solar cell. As shown in Figure 6**,** the Jsc increases proportionally with efficiency as the thickness of the BSF layer grows. Notably, varying the BSF thickness from 0.01 to 0.05 µm has a significant impact on the overall efficiency of the cell.

The Jsc rises logarithmically from 16.61 to 17.805 mA/cm² as the thickness increases from 0.01 to 0.05 µm (Figure 6a). This indicates that the thicker BSF layer enhances carrier collection by minimizing recombination at the rear contact. Figure 6b shows that Voc **r**emains stable, holding at approximately 2.310 V across the range of BSF thicknesses. However, FF (Figure 6c) decreases slightly, reaching 86.5% at the thickest BSF layer. This reduction in FF is likely due to the increased series resistance associated with a thicker BSF layer, which can impede charge extraction.

Figure 6d illustrates that the overall η improves significantly as the BSF thickness increases. The efficiency rises from 33.53% to 35.57% as the thickness is varied from 0.01 to 0.05 µm, reflecting a logarithmic increase in performance. This enhancement can be attributed to better photo-generated carrier transport and reduced recombination, leading to higher current density and improved efficiency.

These findings underscore the importance of optimizing the BSF layer thickness to achieve higher efficiency in DJSCs, with the optimal thickness identified as 0.05 µm in this study. The results are consistent with those reported in previous studies [27,28], further validating the positive impact of a thicker BSF on cell performance.

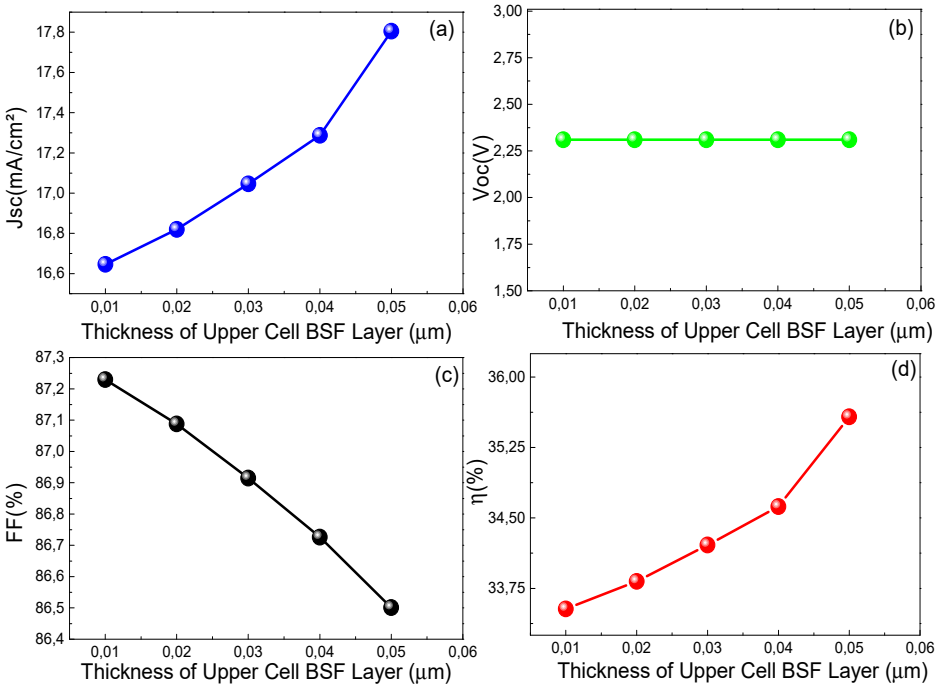

Figure 6. Effect of different BSF thickness of the upper cell on the η, FF, J_{SC}, and V_{OC} of the InGaP/GaAs DJSCs

Figure 7 illustrates the photo-generation rate for the proposed solar cell model, with values varying between 0 and 22.4 $cm^{-3}s^{-1}$. As seen in the figure, the highest photogeneration rates occur primarily in the upper layers of the solar cell, particularly in the InAlGaP and InGaP regions.

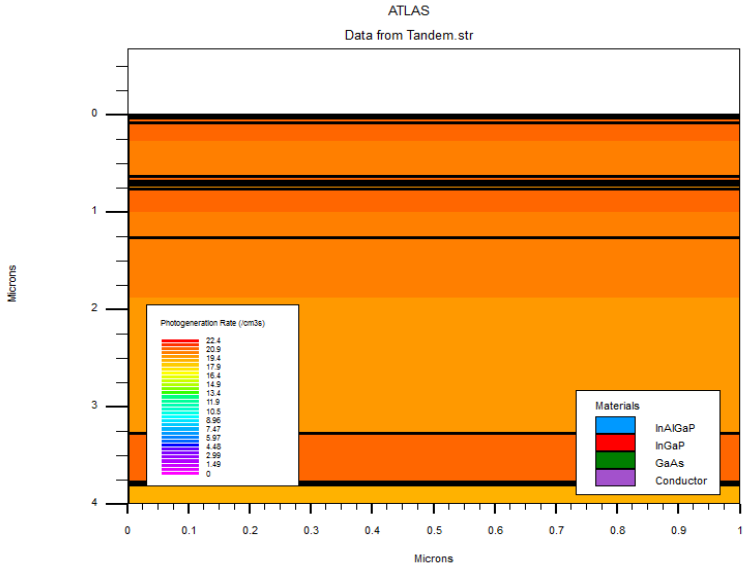

Figure 7. The photo-generation rate across various InGaP/GaAs DJSCs layers.

This is expected, as the majority of photon energy is absorbed near the surface before penetrating into the deeper layers of the device. The InAlGaP layer, in particular, demonstrates a superior photogeneration rate due to its higher absorption coefficient (α) compared to GaAs and InGaP. The increased absorption in this material allows for more efficient generation of electron-hole pairs, contributing significantly to the overall device performance. The highest photogeneration rates, exceeding 20 $cm^{-3}s^{-1}$, are concentrated in the InAlGaP layer, highlighting its critical role in enhancing the cell's optical and electrical performance.

Deeper into the cell, within the GaAs region, the photogeneration rate diminishes as most of the photon energy has already been absorbed in the upper layers. This trend underscores the importance of optimizing the thickness and material composition of the upper layers to maximize light absorption and improve the overall efficiency of the solar cell. These findings align with previous studies that emphasize the importance of material choice in achieving higher conversion efficiencies [20,29].

IMPACT OF TEMPERATURE FLUCTUATIONS

The temperature sensitivity of solar cells is a well-documented phenomenon, typical of semiconductor devices. As temperature increases, the band gap of the semiconductor decreases, which adversely affects the overall performance of the cell. This reduction in band gap is caused by the increased thermal energy within the material . As the temperature rises, less energy is required to break atomic bonds, thereby reducing the bond energy and, subsequently, the band gap. Consequently, higher temperatures result in a narrower energy gap in the solar cell. It is well-established that increasing the operating temperature of a solar cell leads to a reduction in both its efficiency and output power [30–32].

Figure 8(a) shows the variation in Jsc over a T range of 300 K to 400 K. While Jsc begins at 17.805 mA/cm² at 300 K, it gradually decreases to 17.760 mA/cm² at 400 K. This small reduction in Jsc indicates that it is relatively stable over this temperature range, suggesting that the InGaP/GaAs tandem cell's Jsc is less sensitive to temperature compared to other parameters.

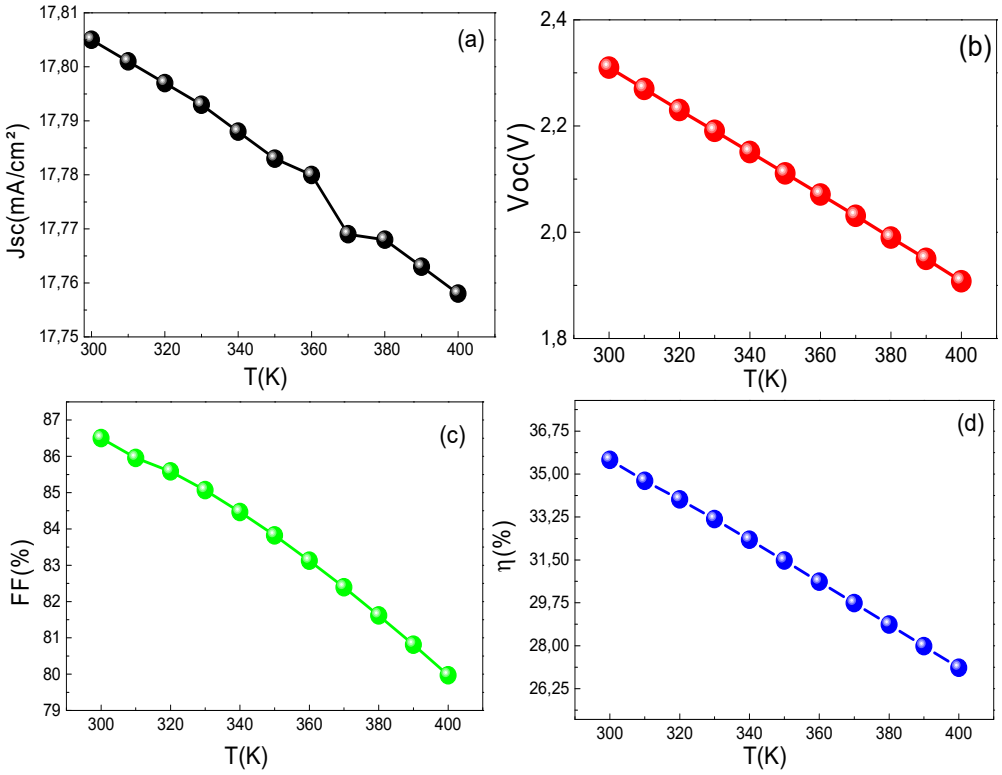

Figure 8. Impact of temperature on the InGaP/GaAs DJSCs performance.

Figure 8(b) highlights the significant impact of temperature on Voc. As the temperature increases from 300 K to 400 K, Voc steadily declines from 2.310 V to 1.908 V, indicating a strong temperature sensitivity. This reduction in Voc, governed by Eq. (3), is the primary factor behind the overall decline in performance parameters. The efficiency decreases markedly at higher temperatures due to this drop in Voc, which can be attributed to the temperature-induced narrowing of the band gap. As the band gap shrinks, the maximum achievable voltage of the cell is reduced, directly affecting its performance.

The FF, as shown in Figure 8(c), also decreases as the temperature increases. FF declines from 86.501% at 300 K to 79.970% at 400 K. This decline reflects a reduced ability of the solar cell to deliver its maximum power as the temperature rises, likely due to increased recombination losses [32,33].

Most critically, Figure 8(d) shows a linear decrease in the η of the solar cell. Efficiency falls from 35.57% at 300 K to 26.253% at 400 K. This significant reduction in efficiency, more than 10 percentage points, highlights the detrimental effect of elevated temperatures on the performance of the solar cell. The efficiency decline is primarily due to increased recombination losses, and reduced Voc at higher temperatures.

In summary, the data presented clearly demonstrate the negative impact of rising temperature on the performance of the InGaP/GaAs DJSCs. As temperature increases from 300 K to 400 K, all key performance metrics Jsc, Voc, FF, and η Experience declines. Notably, the efficiency of the cell peaks at 35.57% at 300 K, corresponding to optimal performance at lower temperatures. This highlights the importance of temperature management in maintaining the efficiency and longevity of solar cells in practical applications.

OPTIMIZED InGaP/GaAs DJSCs

The output parameters of the optimized InGaP/GaAs DJSCs are presented in **Table 2**, offering a comparative analysis of experimental and theoretical values from various studies. Notably, the tandem cell developed in this work

demonstrates strong performance across key metrics, positioning it competitively within the field. The Jsc of the DJSCs in this study is 1.7805 mA/cm², which exceeds both the theoretical values reported in [8,9], and [12], as well as the experimental value of 1.61 mA/cm² from [20]. This higher Jsc indicates an improvement in current collection, likely due to the optimization of the tandem structure, which enhances light absorption and carrier generation.

The η of the tandem cell, at 35.57%, represents a significant improvement over both the experimental result of 32.19% from [20] and the theoretical values from [8,9]. This substantial increase in efficiency highlights the effectiveness of the optimized hetero-tunnel junction design (n-AlInGaP/p-GaAs) used in this work, which minimizes recombination losses and maximizes power output.

Table. 2 Comparative analysis of performance parameters for optimized InGaP/GaAs DJSC structure compared to other designs.

	Jsc (mA/cm^2)	Voc (V)	FF (%)	η (%)
InGaP/GaAs DJSCs (Theoretical) [8]	1.519	2.53	91.32	25.43
InGaP/GaAs DJSCs (Experimental)[20]	1.61	2.39	87.52	32.19
InGaP/GaAs DJSCs (Theoretical) [9]	1.449	2.62	90.68	34.44
InGaP/GaAs DJSCs (Theoretical) [12]	1.613	2.45	88.80	35.15%
Our Simulation	1.780	2.310	86.501	35.57

The I-V characteristics for the GaInP/GaAs DJSCs, displayed in Figure 9**,** compare the performance of the fundamental design with the improved version. The improved cell shows a clear enhancement in both current and voltage stability across the operating range. This improved performance suggests more efficient charge carrier collection and superior voltage retention, leading to higher overall power output.

In conclusion, the optimization strategies applied in this work, particularly the design of the hetero-tunnel junction, have resulted in a significant boost in both Jsc and η, demonstrating that this tandem solar cell outperforms previous designs and represents a notable advancement in the field of high-efficiency DJSCs.

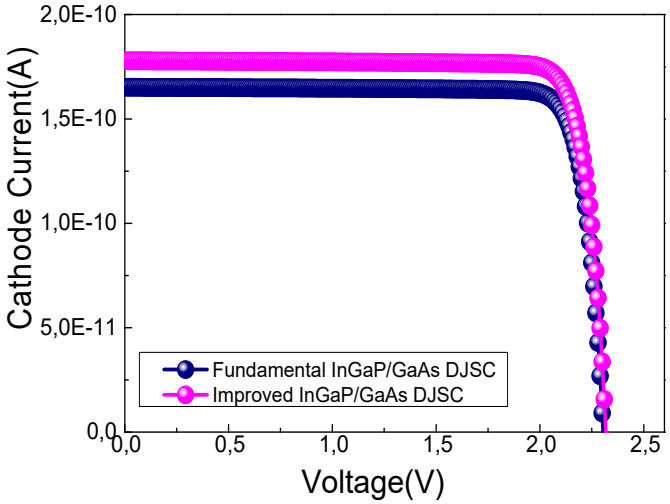

Figure 9. I-V Characteristic of InGaP/GaAs DJSCs.

CONCLUSIONS

This study utilized advanced numerical simulations via Silvaco Atlas to assess and optimize the performance of an InGaP/GaAs dual-junction solar cells. A new BSF layer was incorporated into the bottom cell, and various hetero-tunnel junction materials were systematically evaluated. The results indicated that the optimal performance was achieved with a new bottom BSF layer of 0.03 μm, composed of InAlGaP, resulting in an efficiency of 33.224%. Among the hetero-tunnel junction materials tested, the InAlGaP/GaAs combination demonstrated superior efficiency and overall performance enhancements. Furthermore, optimizing a BSF layer with a thickness of 0.05 μm to the upper cell significantly increased the overall efficiency to 35.57%. The optimized dual-junction structure achieved Jsc of 1.780 mA/cm², Voc of 2.310 V, FF of 86.501%, and η of 35.57% at 300 K. These results highlight the effectiveness of simulation-driven approaches in optimizing multi-junction solar cell designs, offering a cost-effective method to reduce prototyping efforts by focusing experimental validation on a refined set of high-performance configurations.

Acknowledgement

The authors are thankful to the DGRSDT for the provided support to accomplish this research.

ORCID

Ikram Zidani, https://orcid.org/0009-0003-8900-5261; **Loumafak Hafaifa,** https://orcid.org/0009-0000-0900-759X
Ahmed Hafaifa, https://orcid.org/0000-0002-7812-7429

REFERENCES

[1] N. Akter, M.A. Matin, and N. Amin, "High performance $In_xGa_{1-x}N$ Tandem solar cells designed from numerical analysis," in: *CEAT 2013 - 2013 IEEE Conf. Clean Energy Technol*, 2013, pp. 469–472. https://doi.org/10.1109/CEAT.2013.6775678

[2] J.B. Garcia, *Indium Gallium Nitride Multijunction Solar Cell Simulation Using Silvaco Atlas*, Security, 110, (2007)

[3] C. Cornet, M. Da Silva, C. Levallois, and O. Durand, "GaP/Si-based photovoltaic devices grown by molecular beam epitaxy," in: *Molecular Beam Epitaxy*, second edition), (2018), pp. 637–648. https://doi.org/10.1016/B978-0-12-812136-8.00030-X

[4] L. Hafaifa, M. Maache, and M.W. Bouabdelli, "Improving the Performance of CZTS/CZTSSe Tandem Thin Film Solar Cell," J. Nano- Electron. Phys. **16**, 1–6 (2024). https://doi.org/10.21272/jnep.16(2).02018

[5] E. Raza, and Z. Ahmad, "Review on two-terminal and four-terminal crystalline-silicon/perovskite tandem solar cells; progress, challenges, and future perspectives," Energy Reports, **8**, 5820–5851 (2022). https://doi.org/10.1016/j.egyr.2022.04.028

[6] L. Hafaifa, M. Maache, and Y. Djalab, "Performance Enhancement of CGS/CIGS Thin Flm Tandem Solar Cell Using Different Buffer Layers," J. Opt. (2024). https://doi.org/10.1007/s12596-024-02035-1

[7] A. Ghadimi, and H. Arzbin, "Efficiency improvement of ARC less InGaP/GaAs DJ solar cell with InGaP tunnel junction and optimized two BSF layer in top and bottom cells," Optik, **148**, 358–367 (2017). https://doi.org/10.1016/j.ijleo.2017.09.016

[8] F. Djaafar, B. Hadri, and G. Bachir, "Optimal parameters for performant heterojunction InGaP/GaAs solar cell," Int. J. Hydrogen Energy, **42**, 8644–8649 (2017). https://doi.org/10.1016/j.ijhydene.2016.06.139

[9] F. Djaafar, B. Hadri, and G. Bachir, "IV Characteristics of InGaP/GaAs Solar Cell with the presence of a Back Surface Field and a Tunnel junction," J. Electr. Syst. **14**, 64–76 (2018).

[10] B. Zhao, X.-S. Tang, W.-X. Huo, Y. Jiang, Z.-G. Ma, L. Wang, W.-X. Wang, *et al*., "Characteristics of InGaP/GaAs double junction thin film solar cells on a flexible metallic substrate," Sol. Energy, **174**, 703–708 (2018). https://doi.org/10.1016/j.solener.2018.06.099

[11] T. Sogabe, Y. Shoji, N. Miyashita, D.J. Farrell, K. Shiba, H.-F. Hong, and Y. Okada, "High-efficiency InAs/GaAs quantum dot intermediate band solar cell achieved through current constraint engineering," Next Mater. **1**, 100013 (2023). https://doi.org/10.1016/j.nxmate.2023.100013

[12] F.Z. Kharchich, and A. Khamlichi, "Optimizing efficiency of InGaP/GaAs dual-junction solar cells with double tunnel junction and bottom back surface field layers," Optik, **272**, 170196 (2023). https://doi.org/10.1016/j.ijleo.2022.170196

[13] L. Hafaifa, M. Maache, Z. Allam, and A. Zebeir, "Simulation and performance analysis of CdTe thin film solar cell using different Cd-free zinc chalcogenide-based buffer layers," Results Opt. **14**, 100596 (2024). https://doi.org/10.1016/j.rio.2023.100596

[14] J.L. Gray, *Handbook of Photovoltaic Science and Engineering*, Chapter 3, (John Wiley & Sons, Ltd, 2003), pp. 61–112.

[15] M.H. Tsutagawa, and S. Michael, "Triple junction InGaP/GaAS/Ge solar cell optimization: the design parameters for a 36.2% efficient space cell using Silvaco ATLAS modeling & simulation," in: *2009 34th IEEE Photovolt. Spec. Conf. IEEE*, (2009), pp. 1954–1957. https://doi.org/10.1109/PVSC.2009.5411544

[16] J.E. VanDyke, "Modeling laser effects on multi-junction solar cells using Silvaco ATLAS software for spacecraft power beaming applications, PhD Thesis. Monterey, California. Naval Postgraduate School, 2010.

[17] J.B. Lavery, "Quantum tunneling model of a pn junction in Silvaco," PhD Thesis. Monterey, California. Naval Postgraduate School, (2008).

[18] L. Hafaifa, M. Maache, and M.W. Bouabdelli, "Improved performance of CdTe thin-film solar cell through key parameters," J. Theor. Appl. Phys. **18**, 1–10 (2024). https://doi.org/10.57647/j.jtap.2024.1803.35

[19] R.R. King, N.H. Karam, J.H. Ermer, N. Haddad, P. Colter, T. Isshiki, H. Yoon, *et al*., "Next-generation, high-efficiency III-V multijunction solar cells," in: *Conf. Rec. Twenty-Eighth IEEE Photovolt. Spec. Conf. (Cat. No. 00CH37036), IEEE*, 2000, pp. 998–1001. https://doi.org/10.1109/PVSC.2000.916054

[20] K.J. Singh, and S.K. Sarkar, "Highly efficient ARC less InGaP/GaAs DJ solar cell numerical modeling using optimized InAlGaP BSF layers," Opt. Quantum Electron. **43**, 1–21 (2012). https://doi.org/10.1007/s11082-011-9499-y

[21] Atlas User's Manual, SILVACO Inc, Santa Clara, CA 95054, California, USA, 2018.

[22] I. Vurgaftman, J.A.R. Meyer, and L.R. Ram-Mohan, "Band parameters for III–V compound semiconductors and their alloys," J. Appl. Phys. **89**, 5815–5875 (2001). https://doi.org/10.1063/1.1368156

[23] S. Abbasian, and R. Sabbaghi-Nadooshan, "Design and evaluation of ARC less InGaP/AlGaInP DJ solar cell," Optik, **136**, 487–496 (2017). https://doi.org/10.1016/j.ijleo.2017.02.078

[24] G.S. Sahoo, and G.P. Mishra, "Effective use of spectrum by an ARC less dual junction solar cell to achieve higher efficiency: a simulation study," Superlattices Microstruct. **109**, 794–804 v. https://doi.org/10.1016/j.spmi.2017.06.002

[25] G.S. Sahoo, P.P. Nayak, and G.P. Mishra, "An ARC less InGaP/GaAs DJ solar cell with hetero tunnel junction," Superlattices Microstruct. **95**, 115–127 (2016). https://doi.org/10.1016/j.spmi.2016.04.045

[26] S.M. Sze, Y. Li, and K.K. Ng, *Physics of semiconductor devices*, (John wiley & sons, 2021).

[27] M. Verma, and G.P. Mishra, "An integrated GaInP/Si dual-junction solar cell with enhanced efficiency using TOPCon technology," Appl. Phys. A Mater. Sci. Process. **126**, 1–13 (2020). https://doi.org/10.1007/s00339-020-03840-8

[28] S. Bagheri, R. Talebzadeh, B. Sardari, and F. Mehdizadeh, "Design and simulation of a high efficiency InGaP/GaAs multi junction solar cell with AlGaAs tunnel junction," Optik, **199**, 163315 (2019). https://doi.org/10.1016/j.ijleo.2019.163315

[29] H.R. Arzbin, and A. Ghadimi, "Improving the performance of a multi-junction solar cell by optimizing BSF, base and emitter layers," Mater. Sci. Eng. B, **243**, 108–114 (2019). https://doi.org/10.1016/j.mseb.2019.04.001

[30] Y.P. Varshni, "Temperature dependence of the energy gap in semiconductors," Physica, **34**, 149–154 (1967). https://doi.org/10.1016/0031-8914(67)90062-6

[31] H.M. Ali, M. Mahmood, M.A. Bashir, M. Ali, and A.M. Siddiqui, "Outdoor testing of photovoltaic modules during summer in Taxila, Pakistan," Therm. Sci. **20**, 165–173 (2016). https://doi.org/10.2298/TSCI131216025A

[32] L. Hafaifa, M. Maache, S. Rabhi, Z. Allam, Z.I. Gouchida, Y. Benbouzid, A. Zebeir, and R. Adjouz, "Enhanced CZTSSe Thin-Film Solar Cell Efficiency: Key Parameter Analysis," Phys. Status Solidi Appl. Mater. Sci. **222**(2), 2400332 1–8 (2024). https://doi.org/10.1002/pssa.202400332

[33] E.T. Mohamed, A.O.M. Maka, M. Mehmood, Al.M. Direedar, and N. Amin, "Performance simulation of single and dual-junction GaInP/GaAs tandem solar cells using AMPS-1D," Sustain. Energy Technol. Assessments, **44**, 101067 (2021). https://doi.org/10.1016/j.seta.2021.101067

ПІДВИЩЕННЯ ПРОДУКТИВНОСТІ СОНЯЧНИХ ЕЛЕМЕНТІВ З ПОДВІЙНИМ ПЕРЕХОДОМ InGaP/GaAs ЧЕРЕЗ ОПТИМІЗАЦІЮ ШАРУ BSF ТА ГЕТЕРОТУНЕЛЬНИЙ ПЕРЕХІД

Ікрам Зідані[a], Зуауї Бенсаад[a], Лумафак Хафайфа[b,c], Хамза Абід[a], Ахмед Хафайфа[d]

[a]Лабораторія прикладних матеріалів, Університет Джілалі Ліабес, Сіді-Бель-Аббес, Алжир

[b]Кафедра фізики, факультет точних наук і комп'ютерних наук, Університет Зіана Ашура, 17000 Джельфа, Алжир

[c]Лабораторія фізико-хімії матеріалів та навколишнього середовища, Університет Зіан Ашур, BP 3117, Джельфа, Алжир

[d]Лабораторія прикладної автоматизації та промислової діагностики, факультет науки і технологій, Університет Джельфи 17000 DZ, Алжир

Це дослідження зосереджено на моделюванні та оптимізації подвійних сонячних елементів InGaP/GaAs з використанням програмного забезпечення Silvaco Atlas, з особливим акцентом на впровадженні гетеротунельного переходу. Гетеротунельний перехід відіграє ключову роль у забезпеченні ефективного транспортування носіїв заряду між субелементами, значно покращуючи загальну ефективність клітини. Крім того, новий шар поля зворотної поверхні (BSF) був інтегрований у нижню частину GaAs для подальшого підвищення продуктивності. Різні комбінації матеріалів для гетеротунельного переходу, такі як GaInP/GaAs, AlGaInP/GaInP і AlGaInP/GaAs, систематично перевірялися, щоб оцінити їх вплив на ефективність пристрою. Оптимізована структура продемонструвала щільність струму короткого замикання 1,780 мА/см², напругу холостого ходу 2,310 В, коефіцієнт заповнення 86,501% і ефективність перетворення 35,57% під освітленням AM1.5G при 300 K. Втрати на рекомбінацію були мінімізовані оптимізацією шару BSF у верхній і нижній комірках, зокрема з AlGaInP, що сприяє покращенню збору заряду. Виявлено, що підвищені температури знижують як напругу холостого ходу, так і ефективність, що підкреслює необхідність керування температурою. Ці оптимізації представляють значні покращення порівняно з попередніми проектами.

Ключові слова: *InGaP/GaAs DJSCs; сонячна батарея; BSF, Silvaco-Atlas; оптимізація*

East European Journal of Physics. 1. 151-159 (2025)
DOI:10.26565/2312-4334-2025-1-14 ISSN 2312-4334

OPTIMIZATION OF ORGANIC PHOTODETECTORS USING SCAPS-1D SIMULATION: ENHANCING PERFORMANCE OF PBDB-T-2F BASED DEVICES THROUGH LAYER CONFIGURATION AND DOPING ADJUSTMENTS

Ahmet Sait Alali*[a], Murat Oduncuoglu[a], Hmoud Al-Dmour[b], Abdelaal S.A. Ahmed[c]
[a]*Department of Physics, Yıldız Technical University, Istanbul, Turkey*
[b]*Mutah University, Faculty of Science, Department of Physics, 61710, Jordan*
[c]*Chemistry department, Faculty of Science, AlAzhar University, Assuit, 71524, Egypt*
**Corresponding Author email: saitnuclear@gmail.com*
Received October 5, 2024; revised December 12, 2024; accepted January 7, 2025

In this study, we conducted an exploration of the optimization of various parameters of a photodetector using SCAPS-1D simulation to enhance its overall performance. The photodetector structure was modified based on the structure proposed by N.I.M. Ibrahim *et al.* (AMPC, 14(04), 55–65 (2024) by changing the order of the hole transport layer (HTL) and electron transport layer (ETL). Through the optimization of layer thicknesses and doping concentrations, we significantly improved the photovoltaic parameters of our optimized structure (FTO/PFN/PBDB-T-2F/PEDOT/Ag). The optimized device exhibited V_{OC} of 1.02V, J_{SC} of 35.20 mA/cm², FF of 84.61%, and an overall efficiency of 30.40%. Additionally, the device demonstrated a high quantum efficiency (EQ) of over 99% and responsivity peaking at 0.65 A/W, covering a broad spectral region from 300 nm to 900 nm. The results indicate the critical role of meticulous optimization in developing high-performance photodetectors, providing valuable insights into the design and fabrication of devices with superior performance characteristics.
Keywords: *Organic photodetector; SCAPS-1D Simulation; Performance optimization; PBDB-T-2F: BTP-4F; PEDOT: PSS; PFN: Br*
PACS: 84.60. Jt 81.05. Xj 85.60.Jb 73.61.Ph 72.80.Le

1. INTRODUCTION

For the advancement of several applications in biosensing, communication networks, and health monitoring, the organic photodetectors (OPDs) must be enhanced, as the performance enhancement of OPD leads to a higher signal amplification efficiency. It has been reported that the integration of organic field-effect transistors (OFETs) with OPDs significantly boosts the signal-to-noise ratio, which is essential for accurate physiological data extraction from photoplethysmographical (PPG) waveforms [1]. Recent advancements in materials and fabrication techniques, such as using iron-phthalocyanine (FePc) with polyamide-nylon polymer coatings, have shown promising ability to enhance the photoconductivity and the responsivity by several orders of magnitude, making OPDs more effective in UV and visible regions [2]. The development of ultrathin, self-powered OPDs with efficient exciton dissociation and charge extraction processes further enhances the sensitivity and response time, which are critical for high-performance photodetection [3]. Modifying transport layers, such as using N,N′-bis-(1-naphthyl)-N,N′-diphenyl-1,1′-biphenyl-4,4′-diamine (NPB) interfacial layers with MoO_3 can improve charge selectivity and reduce dark current, thereby increasing responsivity and detectivity [4]. Through enhanced polymer-based OPDs, detection capabilities can be extended into the near-infrared (NIR) range, allowing for applications such as real-time pulse oximetry without the need for signal amplification [5]. In addition to optimizing carrier extraction and minimizing dark current, the right thickness of interfacial layers-like SnO_2-can also improve overall device performance [6]. OPDs with upgraded active layers and other parts, such as trans-impedance amplifiers, can greatly improve signal reception and lower bit error rates in visible light communication (VLC) systems [7]. For some applications, it is essential to optimize narrow wavelength selectivity while boosting responsivity and detectivity in *p-n* junction OPDs by utilizing non-fullerene acceptors (NFAs). [8]. Photomultiplication OPDs with materials like PBDB-T and FIrpic produce excellent external quantum efficiency and detectivity, ideal for high-quality imaging without preamplifiers [9]. For efficient photodetection with high detectivity and response speed, it is critical to understand the optoelectronic behavior and address recombination losses in bilayer OPDs [10]. Thus, there is an urgent need to enhance the OPD's overall performance to meet the growing demands of modern technological applications.

In organic photovoltaic systems (OPVs), both PBDB-T-2F and BTP-4F materials are frequently utilized as active layers. These active layers usually comprise a donor and an acceptor substance that aid in the production and movement of charge carriers. For example, in the setting of ternary blending solar cells, a fullerene derivative such as PC61BM is employed as the acceptor, and high-crystallinity P3HT is used as the donor to provide low recombination efficiency and good carrier transport capacity [11]. Comparably, the exciton dissociation efficiency and optical absorption range, which are essential for the overall performance of OPVs, may be increased by using PBDB-T-2F as a donor and BTP-4F as an acceptor. Furthermore, the material characteristics can be further improved by crystallizing active layers using methods like laser irradiation. This is demonstrated in thin-film transistors, where the active layer is heated and crystallized utilizing asymmetric laser profiles [12]. In other applications, such as proton-exchange membrane fuel cells (PEMFC), the active layer comprises

Cite as: A.S. Alali, M. Oduncuoglu, H. Al-Dmour, A.S.A. Ahmed, East Eur. J. Phys. 1, 151 (2025), https://doi.org/10.26565/2312-4334-2025-1-14

perfluoro sulfonate ionomers to improve ion conductivity and performance [13]. Furthermore, developments in materials science emphasize the significance of material attributes like energy conversion efficiency and biocompatibility in a variety of applications, as demonstrated by the creation of biologic piezoelectric layers on Ti substrates [14]. Improved signal-to-noise ratios through the incorporation of optical gain in interferometers highlight the importance of material advancements for improved performance in photonic devices [15]. In general, the integration of PBDB-T-2F and BTP-4F into the active layer of OPV devices is a potentially effective method for attaining enhanced efficiency and performance, drawing upon the concepts and developments noted in several associated domains [16], [17], [18].

PEDOT: PSS (poly(3,4-ethylenedioxythiophene): poly (styrene sulfonate)) is commonly utilized material as a hole transport layer (HTL) in a variety of optoelectronic devices, such as perovskite solar cells (PSCs) and organic solar cells (OSCs). This is because of its advantageous characteristics, which include outstanding wettability, appropriate conductivity, and high optical transparency, making it a great option for improving the overall performance of the device [19]. In addition, PEDOT: PSS has outstanding environmental stability, processability, and thermoelectric qualities. These can be further enhanced by doping with nanomaterials such as carbon nanotubes (CNTs) to raise the material's Seebeck coefficient and conductivity [20]. By doping graphene oxide (GO) into PEDOT: PSS, the work function of HTL significantly improved, which is critical for better hole injection and lessens luminescence quenching at the HTL/emission layer interface, thus increasing luminance and current efficiency in perovskite light-emitting diodes (PeLEDs) [21]. Additionally, PEDOT: PSS can be altered to increase its conductivity and pattern-making capabilities, which qualifies it for flexible electronics applications with high brightness and current efficiency, like flexible PeLEDs [22]. On the other hand, low sheet resistance and high transmittance have been obtained by doping PEDOT: PSS-doped with Ag nanowires (NWs), which are desirable for flexible and transparent devices [23]. Moreover, PEDOT:PSS can promote neural stem cell adhesion, proliferation, and differentiation, suggesting applications in tissue engineering and bioelectronics [24]. However, because of its capacity to increase electron mobility and decrease recombination losses, PFN: Br (poly[(9,9-bis(3'-(N,N-dimethylamino)propyl)-2,7-fluorene)-alt-2,7-(9,9-dioctylfluorene)] bromide) is frequently employed as an ETL, and thus enhancing the overall efficiency of devices [25]. By maximizing charge transport and minimizing energy losses, PEDOT: PSS as HTL and PFN: Br as ETL can work in concert to improve the overall performance of optoelectronic devices.

In this work, we investigate how to greatly improve the performance of photodetectors by optimizing their various parameters using SCAPS-1D simulation. An apparatus called a photodetector transforms light into electrical signals that are utilized in a variety of fields, including communications, imaging, and environmental monitoring. Investigations were conducted into the impacts of temperature variations on device performance as well as the optimization of the thicknesses and doping densities of PBDB-T-2F: BTP-4F, PEDOT: PSS, and PFN: Br layers. Our study builds upon the structure proposed by N. I. M. Ibrahim et al., who reported on a device configuration of ITO/PEDOT: PSS/PBDB/PBDB-T-2F: BTP-4F/PFN: Br/Ag. The power conversion efficiency (PCE) of this configuration was 4.1%, with a V_{OC} of 0.25 V, a J_{SC} of 29.14 mA/cm², and a fill factor (FF) of 56.44%. In our study, the configuration was modified to FTO/PFN: Br/PBDB/PBDB-T-2F: BTP-4F/PEDOT: PSS/Ag, reversing the order of the HTL and ETL. Through meticulous optimization of the layer thicknesses and doping concentrations, we achieved significantly improved outcomes. The optimization process involved varying the thicknesses of HTL, ETL layers, and doping densities for the PFN: Br and PEDOT: PSS layers to achieve the highest efficiency. Our optimized structure exhibited a V_{OC} of 1.02V, a J_{SC} of 35.21 mA/cm², an FF of 84.62%, and an overall efficiency of 30.40%. This study emphasizes how important careful optimization is to create high-performance photodetectors. Through our methodical examination of the impacts of temperature, doping density, and layer thickness, we offer important insights into the design and manufacturing of photodetectors with exceptional performance qualities. The results of this investigation further the field of photodetector technology by providing useful recommendations for optimizing efficiency in practical applications.

2. METHODOLOGY

2.1 Numerical simulation and device structures

The SCAPS-1D software is widely used for numerical simulations to evaluate the optical and electrical properties of various solar cell structures [26], [27]. The SCAPS-1D software utilizes fixed sources and solves three fundamental differential equations: Poisson's equation and the continuity equations for electrons and holes, all under specific boundary conditions. Through the use of self-consistent iteration methods, SCAPS-1D effectively models solar cells, producing simulated results that closely align with experimental data. This reliability makes it an invaluable tool for predicting device performance. Researchers can use SCAPS-1D to optimize various parameters, such as layer thickness, carrier concentration, and defect density, thereby enhancing solar cell efficiency and overall performance. Consequently, SCAPS-1D plays a crucial role in the design and analysis of photovoltaic devices [28], [29], [30].
Poisson's equation for a solar cell device is as follows:

$$\frac{\partial}{\partial x}\left(-\varepsilon(x)\frac{\partial V}{\partial x}\right) = q[p(x) - n(x) + N_D^+(x) - N_D^-(x) + p_t(x) - n_t(x)], \quad (1)$$

And the electron, hole continuity equations are:

$$\frac{\partial n}{\partial x} = \frac{1}{q}\frac{\partial J_n}{\partial x} + G_n - R_n, \tag{2}$$

$$\frac{\partial n}{\partial x} = -\frac{1}{q}\frac{\partial J_n}{\partial x} + G_p - R_p. \tag{3}$$

Where ε is the dielectric permittivity, V is the electric potential, and q is the electronic charge. The variables $p(x)$ and $n(x)$ represent the concentrations of free holes and free electrons, respectively. $ND{+}x$ and $NA{-}x$ are the ionized donor and acceptor concentrations. The terms $pt(x)$ and $nt(x)$ denote the trap densities for holes and electrons. Additionally, $J_{n/p}$ signify the current densities, while $G_{n/p}$ represent the generation rates, and $R_{n/p}$ correspond to the recombination rates for electrons and holes.

The physical parameters for the photodetector components in the SCAPS-1D simulation are listed in **Table 1.** These parameters are FTO, PBDB-T-2F: BTP-4F, PEDOT: PSS, and PFN: Br. Thickness, band gap, electron affinity, dielectric permittivity, effective density of states, mobility, doping densities, and thermal velocities are some of these properties. FTO serves as the transparent electrode, PFN: Br is the ETL, PBDB-T-2F: BTP-4F is the active layer responsible for light absorption and charge generation, and PEDOT: PSS acts as the HTL. The values that are supplied act as a basis for both simulation and optimization.

Table 1. Physical parameters utilized for SCAPS 1D simulation

Material properties	FTO [31]	PFN: Br (ETL)[32]	PBDB-T-2F: BTP-4F (Active layer)[33]	PEDOT:PSS (HTL) [33]
Thickness (nm)	500	5	Variable	40
Band gap (eV)	3.500	2.8	1.27	1.6
Electron affinity (eV)	4.000	4	4.03	3.4
Dielectric permittivity	9.000	5	6.1	3
Conduction band effective density of states, n_c (cm^{-3})	2.20×10^{18}	1×10^{19}	1×10^{19}	1×10^{22}
Conduction band effective density of states, n_v (cm^{-3})	1.80×10^{19}	1×10^{19}	1×10^{19}	1×10^{22}
Electron thermal velocity, V_e (cm/s)	1.00×10^{7}	1.00×10^{7}	1.00×10^{7}	1.00×10^{7}
Hole thermal velocity, V_h (cm/s)	1.00×10^{7}	1.00×10^{7}	1.00×10^{7}	1.00×10^{7}
Electron mobility, μ_e (cm^2/Vs)	20	2.00×10^{-6}	1.70×10^{-3}	4.5×10^{-4}
Hole mobility, μ_h (cm^2/Vs)	10	1.00×10^{-4}	2.96×10^{-4}	9.9×10^{-5}
Shallow uniform donor density, n_D (cm^{-3})	1×10^{19}	9.00×10^{-18}	7.5×10^{16}	2.00×10^{21}
Shallow uniform acceptor density, n_A (cm^{-3})	0	0	0	0

The photodetector and energy band diagram are shown in their entirety in **Figure 1**. Several layers known as FTO, PFN:Br (ETL), PBDB-T-2F:BTP-4F (active layer), PEDOT:PSS (HTL), and Ag within the device are shown in **Figure 1a**. Light is typically allowed in through the FTO light window, electron transport is facilitated by PFN:Br, photons are absorbed and charge carriers are produced by PBDB-T-2F:BTP-4F, hole transport is promoted by PEDOT:PSS, and Ag is the back electrode. **Figure 1b** shows the energy band diagram with conduction band (Ec) and valence band (Ev) energies, indicating efficient charge separation and transport, essential for optimal device performance.

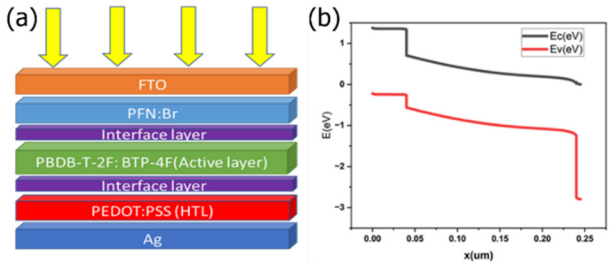

Figure 1. Schematic structure of the device, and (b) energy band diagram

3. RESULTS AND DISCUSSIONS

3.1 Optimal thickness and performance of active layer

Figure 2a depicts the effect of the thickness of the PBDB-T-2F: BTP-4F layer and performance items; open-circuit voltage (V_{OC}), current density (J_{SC}), fill factor (FF), and efficiency (η). As the layer thickness increases from 100 nm to 800 nm, V_{OC} rises steadily from 0.95V to 1.00V, and JSC increases dramatically from 17 mA/cm² to roughly 35 mA/cm². FF indicates a marginal decline from 79.1% to roughly 78.5%. There was a notable increase in overall efficiency from 13.1% to around 27.5%. This shows that the ideal thickness for the PBDB-T-2F: BTP-4F layer is around 800 nm. Nonetheless, a thickness range of 700–800 nm might be chosen for practical reasons to balance production efficiency and performance.

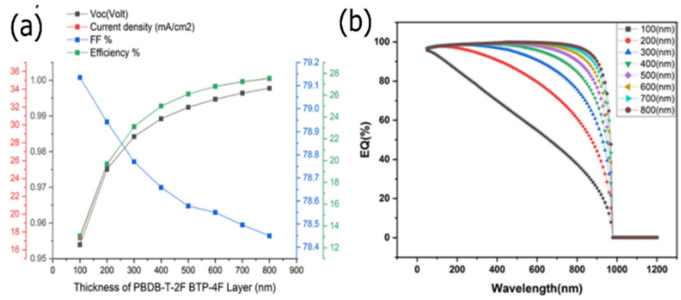

Figure 2. (a) The effect of PBDB-T-2F: BTP-4F layer thickness on photovoltaic parameters (V_{OC}, J_{SC}, FF, and η), and (b) the EQE as a function of wavelength with varying PBDB-T-2F: BTP-4F layer thickness

3.2 Impact of HTL layer thickness on device performance

Figure 3a displays the simulation-based examination of the effect of PEDOT: PSS layer thickness on several performance metrics of the device. As the thickness increases from 50 nm to 600 nm, the V_{OC} shows a tiny increase from 0.97519V to 0.977099V, suggesting a marginally beneficial impact on open-circuit voltage. With a continuous improvement, the JSC goes from 25.5886 mA/cm² to 26.5829 mA/cm². The overall efficiency, which declines little from 19.6797% to 19.4037%, is negatively impacted by the FF, which falls dramatically from 78.8647% to 74.704%. The simulation-based EQE as a function of wavelength for various PEDOT: PSS layer thicknesses is shown in **Figure 3b**. The EQE curves show a comparatively constant spectrum response at different thicknesses, indicating that the device's spectral response is not significantly impacted by the thickness of the PEDOT: PSS layer.

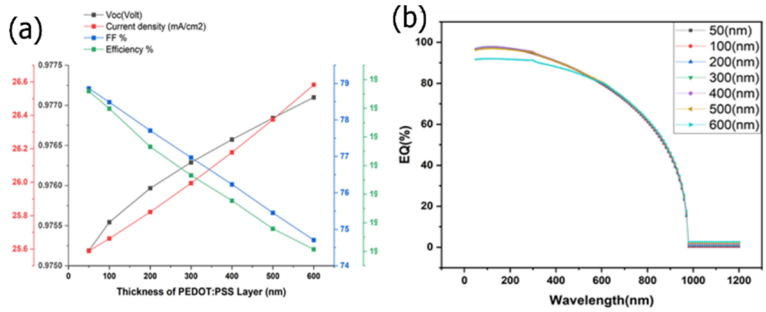

Figure 3. (a) the effect of PEDOT: PSS layer thickness on photovoltaic parameters (V_{OC}, Jsc, FF, and η). (b) the EQE as a function of wavelength for varying PEDOT: PSS layer thicknesses.

3.3 Impact of ETL layer thickness on device performance

The influence of different PFN: Br layer thicknesses on important performance metrics as VOC, JSC, FF, and η is shown by the simulation-based analysis in **Figure 4**. All the performance measures show a decrease with thickness. From **Figure 4a**, the V_{OC} of 0.975086 V, J_{SC} of 25.5741 mA/cm², FF of 78.9427%, and efficiency of 19.6859% are achieved at 5 nm. These measures show that 5 nm is the ideal thickness for the PFN: Br layer because there is a considerable decrease beyond this point. The EQE curves, displayed in panel (**Figure 4b**), further attest to the durability of the performance at the ideal thickness because they hold steady at varying thicknesses.

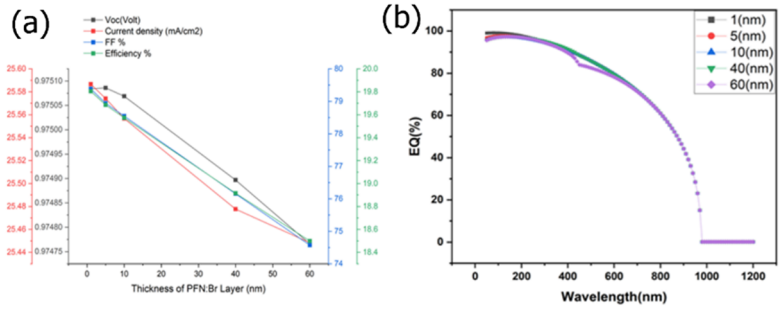

Figure 4. (a) the effect of PFN: Br layer thickness on photovoltaic parameters (V_{OC}, J_{SC}, FF, and η), and (b) the EQE as a function of wavelength for varying PFN: Br layer thicknesses

3.4 Effect of donor density of PFN: Br layer on device performance

The impact of donor density modifications in the PFN: Br layer on device performance metrics, such as VOC, Jsc, FF, and η, is investigated in the simulation-based analysis shown in **Figure 5**. It can be observed that by increases the donor density from $10^{14}cm^{-3}$ to $10^{21}cm^{-3}$, a significant improvement in FF and η, while V_{OC} stabilizes around

$10^{18}cm^{-3}$ as presented in **Figure 5a**. The maximum performance is observed at a donor density of $10^{21}cm^{-3}$ with a V_{OC} of 0.97 V, Jsc of 25.57 mA/cm², FF of 79.53%, and an efficiency of 19.82%. Further confirming the durability of the device performance at the ideal donor density are the EQE curves displayed in panel (**Figure 5b**), which hold true for a range of donor densities.

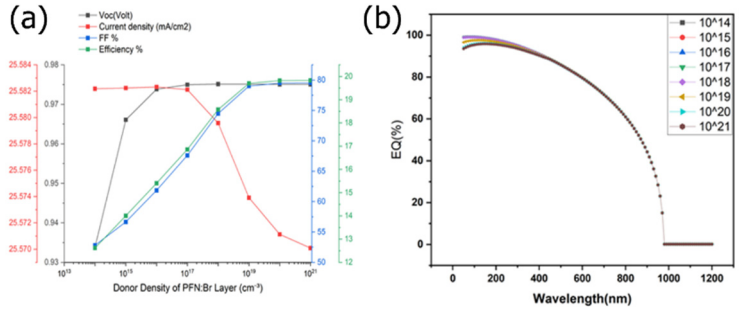

Figure 5. (a) the effect of donor density in the PFN:Br layer on photovoltaic parameters (V_{OC}, Jsc, FF, and η). (b) the EQE as a function of wavelength for varying donor densities in the PFN:Br layer.

3.5 Effect of acceptor density of HTL layer on device performance

The investigation performed using simulation, as illustrated in **Figure 6**, display how different acceptor densities in the PEDOT: PSS layer affect the V_{OC}, J_{SC}, FF, and η parameters. **Figure 6a**, illustrates a clear trend were increasing the acceptor density from $10^{14}cm^{-3}$ to $10^{21}cm^{-3}$ significantly enhances the FF and η. The V_{OC} also shows a steady increase, reaching 1.0058 V at the highest acceptor density. Optimal device performance is observed at an acceptor density of $10^{21}cm^{-3}$ with a V_{OC} of 1.0058 V, Jsc of 25.5714 mA/cm², FF of 85.38%, and an efficiency of 21.96%. It is supported that device performance is robust at greater acceptor densities by the EQE curves shown in panel (**Figure 6b**), which are essentially consistent across a range of acceptor densities.

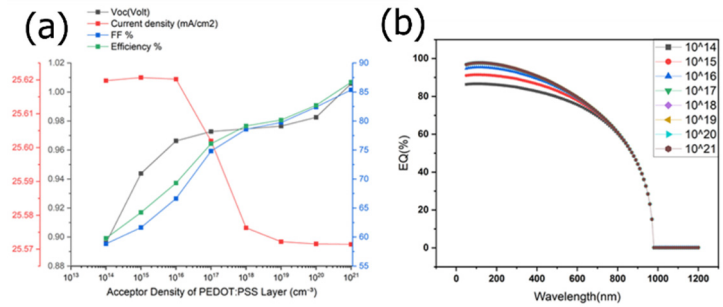

Figure 6. (a) The effect of acceptor density in the PEDOT: PSS layer on photovoltaic parameters (V_{OC}, J_{SC}, FF, and η), and (b) the EQE as a function of wavelength for varying acceptor densities in the PEDOT: PSS layer

3.6 Temperature dependence on device performance

Here, as shown in **Figure 7**, we examine the performance of the device as a function of temperature. From **Figure 7a**, as the temperature rises from 273K to 333K, the V_{OC} decreases steadily from 0.984V at 273K to 0.956V.

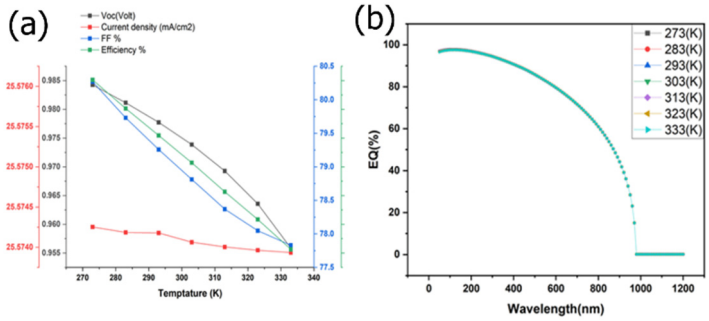

Figure 7. The effect of temperature on the (a) the changes in photovoltaic parameters (V_{OC}, Jsc, FF, and η) with varying temperatures, and (b) the EQE percentages

Similarly, the FF drops from 80.27% to 77.83%, and the overall efficiency of the device falls from 20.21% to 19.03%. The current density exhibits a notable degree of stability throughout the temperature range, suggesting that variations in V_{OC}, FF, and η are not attributable to substantial shifts in the current output. The lowest temperature, 273K, where the maximum values of V_{OC}, FF, and η are measured, is where best performance is observed. As can be seen from

the EQE spectrum in **Figure 7b**, the EQE of the device is largely constant between 273K and 333K. This stability indicates that the capacity of the device to convert photons into electrons over the reported wavelength range is mostly unaffected by temperature fluctuations. This stability in EQE, in contrast to other performance metrics like V_{OC}, FF, and η, suggests that the main photoactive processes are less susceptible to temperature variations than the device's total electrical performance.

4. OPTIMIZED DEVICE

The optimum parameters for our photodetector device are given in **Table 2**. The active layer thickness was set to 800 nm, the PEDOT: PSS HTL to 50 nm, and the PFN:Br ETL to 5 nm. The shallow uniform acceptor density (nA) of the active layer was optimized to $7.5 \times 10^{16} \times cm^{-3}$, while the shallow uniform donor density (nD) of PFN: Br (ETL) and the shallow uniform acceptor density (nA) of PEDOT: PSS (HTL) were both set to $10^{21} \times cm^{-3}$. Our device structure (FTO/PFN:Br/PBDB-T-2F:BTP-4F /PEDOT:PSS/Ag) differs significantly from the structure used in the work by N.I.M. Ibrahim et al. (ITO/PEDOT:PSS/PBDB-T-2F:BTP-4F/PFN/Ag)[33]. By changing the order of the HTL and ETL layers, we were able to achieve superior performance. Specifically, after optimizing layer thickness and doping concentrations.

Table 2. Optimized numerical parameters

Parameters	Value
Thickness of Active layer	800 nm
Thickness of PEDOT: PSS (HTL)	50 nm
Thickness of PFN:Br (ETL)	5 nm
Shallow uniform acceptor density, nA of Active layer	$7.5 \times 10^{16} cm^{-3}$
Shallow uniform donor density, nD of PFN:Br (ETL)	$1 \times 10^{21} cm^{-3}$
Shallow uniform acceptor density, nA of PEDOT: PSS (HTL)	$1 \times 10^{21} cm^{-3}$

The current density-voltage (J-V) characteristics of the photodetector device are displayed in **Figure 8a**, which also shows the dark current density and photocurrent density. A robust photoresponse is indicated by the photocurrent density (black line), which peaks at about 35 mA/cm² slightly below 1 V under illumination. At low voltages, the dark current density (red line) stays low and only begins to climb noticeably at 0.2 V. According to the dark current density statistics, it is modest (between 10^{-18} and 10^{-15} A/cm²) until 0.2 V, at which point it climbs exponentially to 9.18 A/cm² at 1 V. This behavior indicates low leakage current at low voltages, which enhances the stability and efficiency of the device.

The quantum efficiency (QE) and responsivity (R) at wavelengths ranging from 200 nm to 1200 nm are shown in **Figure 8b**. Between 300 and 900 nm, the QE (black line) stays high and nearly 100%, demonstrating the device's remarkable photon-to-electron conversion efficiency. In the same spectral region, the responsivity (red line) peaks at approximately 0.66 A/W, suggesting great sensitivity. Beyond 900 nm, photon energy decreases and QE and responsivity both decreases. According to comprehensive statistics, QE and responsivity peak at 800 nm and then steadily decline from 50 nm to 800 nm. Performance is at its best at 800 nm, where QE is 97.68% and responsivity is 0.63 A/W. These findings highlight the device's excellent sensitivity and efficiency overall, making it appropriate for applications requiring accurate light detection over a wide spectral range.

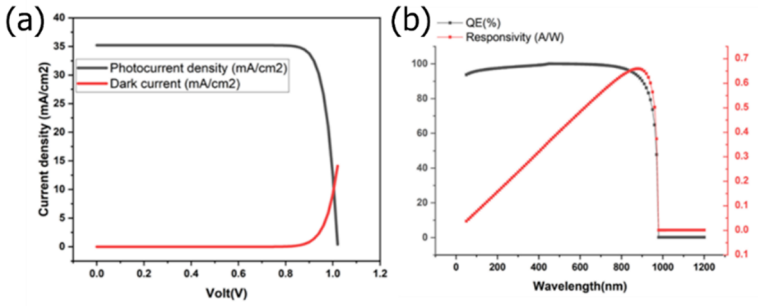

Figure 8. (a) J-V characteristic curve of the optimized photodetector, and (b) QE and responsivity as functions of wavelength.

Table 3. A comparative analysis of the performance of various OPDs from different studies, highlighting the advancements achieved in this work

Active Materials	V_{OC} (V)	Jsc (mA/cm²)	FF (%)	PCE (%)	Ref.
Experimental Results					
PEDOT: PSS/GO/PCDTBT: PC71BM	0.82	10.44	50.0	4.28	[34]
PEDOT: PSS/GO/PCDTBT: PC71BM	0.85	10.82	57.0	5.24	[35]
PEDOT: PSS/PTB7:PC71BM	0.74	14.89	74.08	5.92	[36]
PTB4/PC71BM	0.70	14.80	64.60	7.1	[37]
PEDOT: PSS/PTB7-Th: PC61BM	0.78	17.66	52.41	7.24	[38]

Active Materials	V_{OC} (V)	Jsc (mA/cm^2)	FF (%)	PCE (%)	Ref.
PEDOT: PSS/PBDB-T: ITIC-OE	0.96	16.50	69.75	11.0	[39]
PEDOT: PSS/PBDB-T: ITIC	1.06	16.20	82.95	14.25	[40]
CuI/PBDB-T: ITIC	0.98	20.15	79.59	15.68	[41]
PBD: PFBSA/PBDB-T: N2200	0.85	24.23	71.0	16.2	[42]
Simulation Results					
GO/PBDB-T: ITIC	0.9148	25.71	58.45	13.74	[32]
GO/PTB7:PC71BM	0.9070	18.12	61.30	10.07	[32]
PEDOT: PSS/PBDB-T-2F: BTP-4F/PFN-Br	0.25	29.14	56.44.4	4.1	[33]
PFN-Br /PBDB-T-2F: BTP-4F/ PEDOT: PSS	1.02	35.20	84.61	30.40	This work

CONCLUSIONS

This study highlights the notable enhancements in photodetector performance that may be obtained by carefully adjusting layer thicknesses and doping densities with the use of SCAPS-1D simulations. Through structural modification, we were able to create a significantly higher efficiency device configuration than that suggested by N. I. M. Ibrahim et al. using modifications in the HTL and ETL layers, the optimized structure using FTO/PFN/PBDB-T-2F/PEDOT/Ag shown notable improvements in V_{OC}, J_{SC}, FF, and overall efficiency. Furthermore, the device displayed a high EQ exceeding 99% and responsivity reaching up to 0.65 A/W throughout a broad spectral area from 300 nm to 900 nm. These results pave the way for more effective devices in real-world applications by highlighting the significance of layer arrangement and material qualities in generating high-performance photodetectors.

Acknowledgments

The authors would like to acknowledge that this paper has been submitted in part. fulfillment of the requirements for a PhD degree at Yildiz Technical University.

Funding Declaration: This research received no specific grant from any funding agency in the public, commercial, or not-for-profit sectors.

Competing Interest Declaration: The authors declare that there are no competing interests.

ORCID

Ahmet Sait Alali, https://orcid.org/0000-0002-7750-5571; **Murat Oduncuoglu**, https://orcid.org/0000-0002-3130-5646
Hmoud Al-Dmour, https://orcid.org/0000-0001-5680-5703

REFERENCES

[1] G. Luo, *et al.*, "Boosting the Performance of Organic Photodetectors with a Solution-Processed Integration Circuit toward Ubiquitous Health Monitoring," Advanced Materials, **35**(36), 2301020 (2023). https://doi.org/10.1002/adma.202301020
[2] N.S. Hamzah, and E.K. Hassan, "Fabrication and Enhancement of Organic Photodetectors Based on Iron Phthalocyanine Films, International Journal of Nanoscience, (2024). https://doi.org/10.1142/S0219581X2350028X
[3] J.-W. Qiao, F.-Z. Cui, L. Feng, P. Lu, H. Yin, and X.-T. Hao, "Efficient Ultrathin Self-Powered Organic Photodetector with Reduced Exciton Binding Energy and Auxiliary Föster Resonance Energy Transfer Processes," Advanced Functional Materials, **33**(30), 2301433 (2023). https://doi.org/10.1002/adfm.202301433
[4] W. Liu, Q. Liu, J. Xiao, Y. Wang, L. Yuan, H. Tai, and Y. Jiang, "Performance enhancement of an organic photodetector enabled by NPB modified hole transport layer," IOPscience, **55**, 234001 (2024). https://doi.org/10.1088/1361-6463/ac5990
[5] P. Jacoutot, *et al.*, "Enhanced sub-1 eV detection in organic photodetectors through tuning polymer energetics and microstructure," Science Advances, **9**(23), eadh2694 (2023). https://doi.org/10.1126/sciadv.adh2694
[6] X. Yan, X. Wang, S. Gao, and W. Qiao, "High-Performance Organic Photodetectors Using SnO2 as Interfacial Layer with Optimal Thickness," Physica Status Solidi (a), **220**(1), 2200667 (2023). https://doi.org/10.1002/pssa.202200667
[7] P. Corral, F. Rodriguez-Mas, G.D. Scals, D. Valiente, J.C. Ferrer, and S.F. de Avila, "Improvements of Organic Photodetectors for VLC Using a New Active Layer, Focal Lens, and a Transimpedance Amplifier," Elektronika ir Elektrotechnika, **28**(4), 4 (2022). https://doi.org/10.5755/j02.eie.31292
[8] J. Kang, *et al.*, "Enhanced Static and Dynamic Properties of Highly Miscible Fullerene-Free Green-Selective Organic Photodetectors," ACS Appl. Mater. Interfaces, **13**(21), 25164–25174 (2021). https://doi.org/10.1021/acsami.1c02357
[9] J. Wang, *et al.*, "Enhanced photomultiplication of organic photodetectors via phosphorescent material incorporation," J. Mater. Chem. C, **9**(47), 16918–16924 (2021). https://doi.org/10.1039/D1TC04524E
[10] G. Manzoor, K.K. Sharma, G.K. Bharti, and D. Nath, "Modelling and Performance Analysis of CuPc and C60 Based Bilayer Organic Photodetector," IJEER, **10**(4), 811–816 (2022). https://doi.org/10.37391/ijeer.100408
[11] W. Teng, W. Yanbin, J. Chen, and B. Wang, *Active layer used for ternary blending solar cell and application of active layer*, (2018). [Online Video]. https://typeset.io/papers/active-layer-used-for-ternary-blending-solar-cell-and-2rxfqsnc5q
[12] B.-K. Choo, S. Ahn, B.-Ho Cheong, J.-w. Cho, H.-J. Cho, and H.S. Yeon, Active layer of thin film transistor crystallizing apparatus and the crystallizing method using the same, (2015). [Online Video]. https://typeset.io/papers/active-layer-of-thin-film-transistor-crystallizing-apparatus-j6u2d4hdjw
[13] J. Tard, J. Pauchet, R. Vincent, Formulation of an active layer having improved performances, (2013). [Online Video]. https://typeset.io/papers/formulation-of-an-active-layer-having-improved-performances-39t79hc0se

[14] Y. Zheng, Y. Cheng, L. Li, Active bio piezoelectric ceramic coating layer and method of preparing said coating layer on titanium base body surface, (2006). [Online Video]. https://typeset.io/papers/active-bio-piezoelectric-ceramic-coating-layer-and-method-of-3oleypt5z1
[15] R.-K. Shiu, *et al.*, "Performance Enhancement of Optical Comb Based Microwave Photonic Filter by Machine Learning Technique," Journal of Lightwave Technology, **38**(19), 5302–5310 (2020). https://doi.org/10.1109/JLT.2020.2989210
[16] Y. Wang, *et al.*, "Organic photovoltaics with 300 nm thick ternary active layers exhibiting 15.6% efficiency," J. Mater. Chem. C, **9**(31), 9892–9898 (2021). https://doi.org/10.1039/D1TC02748D
[17] L. Zhan, *et al.*, "Layer-by-Layer Processed Ternary Organic Photovoltaics with Efficiency over 18%," Advanced Materials, **33**(12), 2007231 (2021). https://doi.org/10.1002/adma.202007231
[18] J. Gao, *et al.*, "Over 16.7% efficiency of ternary organic photovoltaics by employing extra PC71BM as morphology regulator," Sci. China Chem. **63**(1), 83–91 (2020). https://doi.org/10.1007/s11426-019-9634-5
[19] T. Kong, *et al.*, "A Newly Crosslinked-double Network PEDOT:PSS@PEGDMA toward Highly-Efficient and Stable Tin-Lead Perovskite Solar Cells," Small, **19**(40), 2303159 (2023). https://doi.org/10.1002/smll.202303159
[20] L. Jin, J. W. Zhang, and S. Ju, "Preparation and Properties of PEDOT:PSS-Based Thermoelectric Thin Films," Materials Science Forum, **1070**, 173–181 (2022). https://doi.org/10.4028/p-pmw1c6
[21] Y. Zhou, *et al.*, "Effects of PEDOT:PSS:GO composite hole transport layer on the luminescence of perovskite light-emitting diodes," RSC Adv. **10**(44), 26381–26387 (2020,). https://doi.org/10.1039/D0RA04425C
[22] L. Liu, H. Yang, Z. Zhang, Y. Wang, J. Piao, Y. Dai, and B. Cai, "Photopatternable and Highly Conductive PEDOT:PSS Electrodes for Flexible Perovskite Light-Emitting Diodes," ACS Appl. Mater. Interfaces, **15**(17), 21344–21353 (2023). https://doi.org/10.1021/acsami.3c03108
[23] H. Fu, *et al.*, "High-performance Ag nanowires/PEDOT:PSS composite electrodes for PVDF-HFP piezoelectric nanogenerators," J. Mater. Sci: Mater. Electron. **32**(16), 21178–21187 (2021). https://doi.org/10.1007/s10854-021-06616-9
[24] A. Pisciotta, *et al.*, "PEDOT: PSS promotes neurogenic commitment of neural crest-derived stem cells," Front. Physiol. **13**, (2022). https://doi.org/10.3389/fphys.2022.930804
[25] S.A. Moiz, M.S. Alzahrani, and A.N.M. Alahmadi, "Electron Transport Layer Optimization for Efficient PTB7:PC70BM Bulk-Heterojunction Solar Cells," Polymers, **14**(17), 3610 (2022). https://doi.org/10.3390/polym14173610
[26] A. Ait Abdelkadir, and M. Sahal, "Theoretical development of the CZTS thin-film solar cell by SCAPS-1D software based on experimental work," Materials Science and Engineering: B, **296**, 116710 (2023). https://doi.org/10.1016/j.mseb.2023.116710
[27] S. Chowdhury, A.S. Najm, M. Luengchavanon, A.M. Holi, C.H. Chia, K. Techato, and S. Channumsin, "Investigating the Effect of Nonideal Conditions on the Performance of a Planar Sb2Se3-Based Solar Cell through SCAPS-1D Simulation," Energy & Fuels, **37**(9), 6722-6732 (2024). https://doi.org/10.1021/acs.energyfuels.2c03593
[28] M. Abdelfatah, A.M. El Sayed, W. Ismail, S. Ulrich, V. Sittinger, and A. El-Shaer, "SCAPS simulation of novel inorganic ZrS2/CuO heterojunction solar cells" Scientific Reports, **13**, 4553 (2024). https://www.nature.com/articles/s41598-023-31553-4
[29] Y. Hairch, Aelmelouky, M. Monkade, and R. Elmoznine, "Investigation of optical and electrical properties of CIGS solar cell using simulation program SCAPS and Impedance spectroscopy," (2023). https://doi.org/10.22541/au.167872056.62172198/v1
[30] Sk.T. Ahamed, A. Basak, and A. Mondal, "Device modeling and investigation of Sb-based low-cost heterojunction solar cells using SCAPS-1D," Results in Optics, **10**, 100364 (2023). https://doi.org/10.1016/j.rio.2023.100364
[31] M. Muzammil, K.N. Naam, M. Fareed, M.S. Hussain, and M. Zulfiqar, "Boosting the performance of PBDB-T/ITIC based organic solar cell: A theoretical analysis utilizing SCAPS-1D," Chemical Physics Impact, **8**, 100407 (2024). https://doi.org/10.1016/j.chphi.2023.100407
[32] G.A. Nowsherwan, *et al.*, "Performance Analysis and Optimization of a PBDB-T:ITIC Based Organic Solar Cell Using Graphene Oxide as the Hole Transport Layer," Nanomaterials, **12**(10), (2022,). https://doi.org/10.3390/nano12101767
[33] N.I.M. Ibrahim, A.M. Elharbi, and A. Albadri, "Study the Effect of Thickness on the Performance of PM6:Y6 Organic Solar Using SCAPS Simulation," AMPC, **14**(04), 55–65 (2024). https://doi.org/10.4236/ampc.2024.144005
[34] S. Rafique, S.M. Abdullah, M.M. Shahid, M.O. Ansari, and K. Sulaiman, "Significantly improved photovoltaic performance in polymer bulk heterojunction solar cells with graphene oxide /PEDOT:PSS double decked hole transport layer," Sci Rep, **7**(1), 39555 (2017). https://doi.org/10.1038/srep39555
[35] S. Rafique, *et al.*, "UV- ozone treated graphene oxide/ PEDOT:PSS bilayer as a novel hole transport layer in highly efficient and stable organic solar cells," Organic Electronics, **66**, 32–42 (2019). https://doi.org/10.1016/j.orgel.2018.12.005
[36] K. Tan, P. Lin, G. Wang, Y. Liu, Z. Xu, and Y. Lin, "Controllable design of solid-state perovskite solar cells by SCAPS device simulation," Solid-State Electronics, **126**, 75–80 (2016). https://doi.org/10.1016/j.sse.2016.09.012
[37] L. Lu, and L. Yu, "Understanding Low Bandgap Polymer PTB7 and Optimizing Polymer Solar Cells Based on It," Advanced Materials, **26**(26), 4413–4430 (2014). https://doi.org/10.1002/adma.201400384
[38] H. Lian, J. Ning, A. Bolag, A. Hexig, N. Gerile, O. Tegus, and S. Lin, "Optimization of PEDOT:PSS Hole Transport Layer Toward the Organic Solar Cells with High Fill Factor," Scientific. Net. 113-118 (2024). https://www.scientific.net/SSP.288.113
[39] K.S. Nithya, and K.S. Sudheer, "Numerical modelling of non-fullerene organic solar cell with high dielectric constant ITIC-OE acceptor," J. Phys. Commun. **4**(2), 025012 (2020). https://doi.org/10.1088/2399-6528/ab772a
[40] W. Abdelaziz, A. Shaker, M. Abouelatta, and A. Zekry, "Possible efficiency boosting of non-fullerene acceptor solar cell using device simulation," Optical Materials, **91**, 239–245 (2019). https://doi.org/10.1016/j.optmat.2019.03.023
[41] K.S. Nithya, and K.S. Sudheer, "Device modelling of non-fullerene organic solar cell with inorganic CuI hole transport layer using SCAPS 1-D," Optik, **217**, 164790 (2020). https://doi.org/10.1016/j.ijleo.2020.164790
[42] T.N.L. Phan, J. Kim, G.-U. Kim, S. Lee, and B.J. Kim, "Aniline-based hole transporting materials for high-performance organic solar cells with enhanced ambient stability," Journal of Materials Chemistry A, (RSC Publishing). (2024). https://pubs.rsc.org/en/content/articlelanding/2021/xx/d1ta03665c/unauth

ОПТИМІЗАЦІЯ ОРГАНІЧНИХ ФОТОДЕТЕКТОРІВ ЗА ДОПОМОГОЮ МОДЕЛЮВАННЯ SCAPS-1D: ПІДВИЩЕННЯ ПРОДУКТИВНОСТІ ПРИСТРОЇВ НА ОСНОВІ PBDB-T-2F ШЛЯХОМ КОНФІГУРАЦІЇ ШАРУ ТА РЕГУЛЮВАННЯ ЛЕГУВАННЯ

Ахмет Саїт Алалі[a], Мурат Одункуоглу[a], Хмуд Аль-Дмур[b], Абделааль С.А. Ахмед[c]

[a]Факультет фізики, Технічний університет Йилдиз, Стамбул, Туреччина

[b]Університет Мута, факультет природничих наук, кафедра фізики, 61710, Йорданія

[c]Кафедра хімії, Факультет природничих наук, Університет Аль-Азхар, Ассуїт, 71524, Єгипет

У цьому дослідженні ми провели дослідження оптимізації різних параметрів фотодетектора за допомогою моделювання SCAPS-1D для підвищення його загальної продуктивності. Конструкцію фотоприймача модифіковано на основі структури, запропонованої H.I.M. Ібрагім та ін. (AMPC, 14(04), 55–65 (2024) шляхом зміни порядку шару транспортування дірок (HTL) та шару транспортування електронів (ETL). Завдяки оптимізації товщини шару та концентрації легування ми значно покращили фотоелектричні параметри нашої оптимізованої структури (FTO/PFN/PBDB-T-2F/PEDOT/Ag). 1,02 В, JSC 35,20 мА/см², FF 84,61 % і загальний ККД 30,40 % Крім того, пристрій продемонстрував високу квантову ефективність (EQ) понад 99 % і чутливість із піком 0,65 А/Вт, охоплюючи широка спектральна область від 300 нм до 900 нм результати вказують на критичну роль ретельної оптимізації при розробці високоефективних фотодетекторів, надаючи цінну інформацію про проектування та виготовлення пристроїв із чудовими характеристиками продуктивності.

Ключові слова: *органічний фотодетектор; моделювання SCAPS-1D; оптимізація продуктивності; PBDB-T-2F: BTP-4F; PEDOT: PSS; PFN: Br*

East European Journal of Physics. 1. 160-169 (2025)
DOI:10.26565/2312-4334-2025-1-15 ISSN 2312-4334

EFFECT OF THE POROSITY OF A PSi SUBSTRATE ON THE CHARACTERISTICS OF CdS NANOPARTICLES PRODUCED BY THE CBD METHOD

F. Saker[a], L. Remache[a], A. Rahmani[b], H. Moualkia[c], M.S. Aida[d], N. Guermit[e], D. Belfennache[f], R. Yekhlef[f], Mohamed A. Ali[g]

[a]*Laboratory of Materials and System Structure and their Reliability, Oum El Bouaghi University, Oum El Bouaghi, 04000, Algeria*
[b]*Laboratory of physico-chemistry of materials LPCM, University of Laghouat, Laghouat, 310081, Algeria*
[c]*Faculty of natural and life sciences, department of material sciences, Oum El Bouaghi University, Oum El Bouaghi, 04000, Algeria*
[d]*Departement of physics, King Abdulaziz University, Jeddah, Makkah Province, Saudi Arabia*
[e]*Larbi Ben M'hidi University, Oum El Bouaghi, 04000, Algeria*
[f]*Research Center in Industrial Technologies CRTI, P.O. Box 64, Cheraga, 16014 Algiers, Algeria*
[g]*School of Biotechnology, Badr University in Cairo (BUC), Badr City 11829, Cairo, Egypt*
**Correspondence Author e-mail: fatima.saker@univ-oeb.dz, belfennachedjamel@gmail.com*
Received November 2, 2024; revised December 11, 2024; accepted December 16, 2024

The motivation for research to study the potential offered by semiconductor materials such as silicon is their use as a substrate for the manufacture of thin films. In this work the chemical bath deposition (CBD) method was used to synthesize Cadmium sulphide (CdS) thin films on glass, silicon (Si), and porous silicon (PSi) substrates. The PSi substrates were prepared by an electrochemical etching method using different current densities at constant etching time of 5 minutes. The obtained results demonstrated that the morphology of the deposited materials was influenced by the porosity of the PSi substrates. The average crystallite dimensions for CdS/glass and CdS/Si were determined to be 46.12 nm and 23.08 nm, respectively. In CdS/PSi structures, the average value of the grain size decreases with increasing porosity. The smallest one is obtained for the CdS/PSi structure with 70% porosity, amounting to 11.55 nm. The measured current-voltage characteristics in coplanar structure on the CdS/PSi/Si sample showed that the photocurrent of the CdS/Si structure is of 3.17 μA and increases up to 600 μA for the CdS/PSi/60% structure.
Keywords: *Chalcogenide semiconductors; Porous silicon; CdS; Thin film; CBD*
PACS: 73.50.-h, 73.50.Pz

1. INTRODUCTION

Semiconductors have attracted considerable attention from researchers in different fields because of their excellent performance capability in optics, electronics, and photonics [1-4]. Historically, metal oxide semiconductors have been recognized to be feasible for optoelectronic devices. Metal chalcogenide nanostructures have also emerged as promising materials due to their specific characteristics and advantages compared with other nanomaterials, related to their low cost, chemical stability, simplicity of synthesis, and superior optoelectronic performance [5, 6].

Cadmium sulfide (CdS) is recognized as one of the most extensively studied materials within the category of chalcogenide semiconductors. Its direct intermediate band gap, which is approximately 2.5 eV, in conjunction with a relatively low work function, high refractive index, and remarkable thermal and chemical stability, renders it highly appealing for various applications [7, 8]. Cadmium sulfide (CdS) has diverse applications across numerous fields, including solar cells, light emitting diodes (LEDs), photodetectors, waveguides, and lasers [7]. Importantly, improvements in synthesis methods have facilitated the precise fabrication of nanostructured CdS with customized dimensions and forms. These nanostructures exhibit intriguing properties such as laser cooling, Franz-Keldysh effect, and quantum confinement due to surface depletion [9–11]. With most reviews copiously focusing on growth techniques and mechanisms [12, 13], cadmium sulfide thin films could be synthesized using PVD and solution growth deposition methods. Indeed, several conventional methods such as chemical bath deposition, sputtering, thermal evaporation, MBE, sol-gel processes, spin coating, electrodeposition, and screen printing have been widely utilized for CdS thin film deposition [14–16]. Among them, the chemical bath deposition is worth mentioning since it's a very user-friendly technique, offering several economic advantages coupled with its steady performance, thereby making it widely popular among other thin film deposition methods. Moreover, the advantage with CBD is the capability for large-area deposition and low-temperature deposition of CdS thin films [17]. The crystallinity of the CdS thin films prepared by CBD is superior, with a lower defect density compared to other alternative deposition techniques. These films exhibit a well uniformity, granularity, continuity, and smoothness, presenting negligible surface roughness [14]. The development of films is dependent on the influencing factors of deposition, including bath concentration, solution temperature, pH, deposition duration, and substrate characteristics [18-21]. The nature and properties of the substrate used will influence the microstructure and adhesion of the resultant film. Thus, the choice of substrates can considerably enhance or alter the general properties of the final products [22].

Cite as: F. Saker, L. Remache, A. Rahmani, H. Moualkia, M.S. Aida, N. Guermit, D. Belfennache, R. Yekhlef, M.A. Ali, East Eur. J. Phys. 1, 160 (2025), https://doi.org/10.26565/2312-4334-2025-1-15

The use of silicon in various technological fields has attracted the attention of many researchers due to its distinctive properties [23-25]. On the other hand, porous silicon becomes a promising material for detection applications because of many reasons: morphology, large specific surface area, low energy consumption, compatibility with silicon-based technologies [26, 27]. In addition, various morphological and structural properties of this material can be achieved in a localized manner by low-cost electrochemical process, which can be integrated on silicon through microtechnological processes [26]. PSi sensitivity is influenced by the morphological properties of pores, such as pore diameter, degree of homogeneity, surface roughness, and layer thickness [28]. Furthermore, its large specific surface area makes it more reactive than bulk silicon. In this context, the variation of porosity can influence the surface roughness and the specific surface area of the PSi substrate. Rahmani *et al.* [29, 30] show that an increase in porosity results in an increase in roughness and also uncover the evolution of PS nanocrystallites. On the other hand, many works shown that the variation in porosity in the range of 50 to 70% yields to a high average specific surface area around 600 cm^2/m^3. [31,32]. Therefore, It has broad use in several environmental and biological detection systems [28,33,34]. In order to manufacture high-performance photodetectors, many studies have reported the improvement in the performance of detector when prepared on porous silicon [16, 28]. Another more attractive way is to deposit nanoparticles of materials into the PSi matrix, hence improving the electrical properties of the elaborated layers and produces sensors with higher and faster response [35]. In the realm of porous silicon, various materials like ZnO, ZnS, TiO_2, and more can be seamlessly integrated into the matrix [36, 37]. Numerous studies focused on incorporating nanoparticles into the porous silicon matrix, including noteworthy materials like CdSe, CdS, ZnS, and ZnO have been carried [38–40]. Hasoon et al. [38] have achieved the deposition of nanostructured CdS thin films on the PSi matrix by the vacuum thermal evaporation method. Sara *et al*. [39] adopted a different path, by preparing a CuS/PSi heterojunction photodetector using the chemical spray pyrolysis route. Khashan [41] succeeded in ZnO nanoparticles incorporating into PSi matrix through chemical method. Similarly, Habubi investigated the response improvement of PSi photodetectors when incorporated with CdSe nanoparticles prepared via laser ablation [42]. Li *et al.* [43] conducted an interesting study on the electronic properties of the CdS/Si nano-hetero structure prepared via chemical bath deposition technique on a silicon nanoporous pillar array. Perillo *et al.* [44] demonstrated the photoresponse performance of CdS thin films, deposited by CBD on glass, through low-temperature thermal treatment.

The novely of this study is to examine the influence of the porosity of a PSi substrate on the characteristics of CdS nanoparticles produced by the CBD method. By comparing the structural, morphological, and optical properties of the CdS layers on the PSi substrate with those on CdS/Si and CdS/glass structures.

2. MATERIALS AND METHODS

2.1. Porous silicon formation

The PSi layers were prepared by the anodization of p-type Boron-doped (100) oriented mono-crystalline silicon (CSi) wafers, with resistivity of 0.015−0.018 Ω cm and thickness of 250 − 300 µm, in a solution composed of hydrofluoric acid and ethanol. The unpolished face of the silicon served as the anode, while a platinum electrode served as the cathode. The silicon wafers were treated before the anodization process by rinsing them with a 2% hydrofluoric acid solution. Electrolyte preparation was performed by mixing 40% hydrofluoric acid with 99.98% ethanol in a 1:1 volumetric ratio. A single-cell configuration was used, connected to a Keithley 2400 generator. The porous layers were prepared at various current densities, namely 5, 30, 60, and 100 mA/cm^2 during 5 min at room temperature, where the porosity of PSi was found to be around 37%, 53%, 60%, and 70%, respectively. Finally, take out the samples and clean them by ethanol and then dry using a hair dryer.

2.2 Synthesis CdS

Glass, Si and PSi substrates were used to deposited thin films using chemic CBD technique. The CdS solution in this work is made by mixing cadmium sulfate ($CdSO_4$), ammonia (NH_4OH), thiourea ($CS(NH_2)_2$), and de-ionized water (DIH_2O). The samples were soaked at 50° for 60 minutes with magnetic stirring in this solution. After that, the samples were retrieved from it, collected, cleaned with de-ionized water, and dried in the air with a hair drier. All the films were yellowish in color, homogeneous, and well-covered on the entire surface. In this study, different structures were considered: CdS nanoparticles deposited on glass (CdS/glass), on silicon (CdS/Si), and on porous silicon prepared at room temperature with current densities of 5 mA/cm^2 (CdS/P Si 37%), 30 mA/cm^2 (CdS/PSi 53%), 60 mA/cm^2 (CdS/PSi 60%), and 100 mA/cm2 (CdS/P Si 70%). The crystallographic structure of the prepared samples was investigated by an ARL-EQUINOX100 X-ray diffractometer using CuKα1 radiation at an operation current of 40 mA and voltage of 40 kV. The optical transmittance of CdS thin films was measured by a JacsoV-30 UV-visible spectrophotometer. The surface morphology of the films was investigated by a scanning electron microscope (SEM) JEOL JSM-7001 F. The atomic percent composition of the thin films was evaluated by energy dispersive X-ray (EDX) analysis.

3. RESULTS AND DISCUSSIONS

3.1 XRD characterizations

Fig.1 shows the X-ray diffraction spectra for the same current densities described above for CBD-CdS films synthesized on glass, silicon, and PSi substrates. The recorded diffraction patterns confirm that indeed the deposited CdS films are polycrystalline in nature. More precisely, it was observed that among all peaks, the intensity of the (002)

peaks were higher; hence, the crystallites exhibit a preferential orientation along the (002) plane perpendicular to the substrate. This observation is in good agreement with the LCDD No. 01-083-5246 that shows a hexagonal (Wurtzite) crystalline structure [45]. Other peaks correspond to reflections from the planes (110) and (112). Such reflections indicate a hexagonal CdS film. Another extra reflection in CdS/Si, CdS/PSi37%, CdS/PSi53%, and CdS/PSi60% attributed to cubic CdS phase (200) also appears beside the hexagonal one. Most frequently, XRD studies of PVD deposited CdS thin films showed that they have a dominant hexagonal structure, and solution growth deposited CdS films showed a dominant hexagonal or dominant cubic or a mixed structure [46–51]. Hexagonal CdS structure is recommended due to its higher stability regarding the cubic one [52].

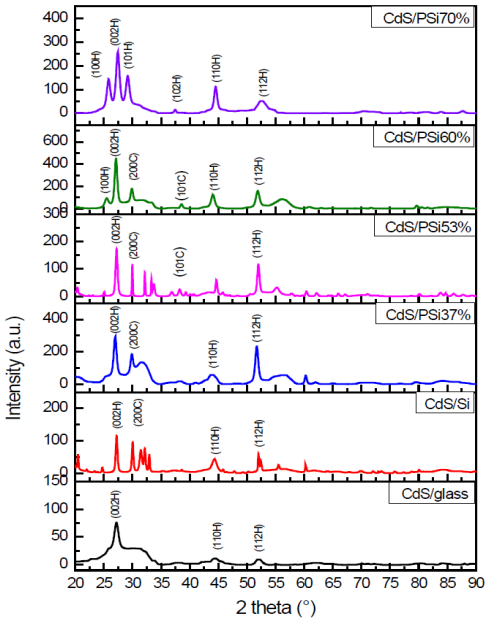

Figure 1. XRD spectra of CdS nanoparticles deposited on glass, silicon and porous silicon

The distinctive peaks (101) and (200), originating from the cubic metastable phase, underwent a remarkable transformation within the domain of the hexagonal stable phase. Specifically, (101) evolved into (102), while (200) transmuted into (101). This interesting observation revealed that CdS/PSi70% has a unique single-phase hexagonal structure, which distinguishes it from the other examined samples. Remarkably, Haque *et al.* [53] obtained similar results to ours but by pre-deposited film heating. In our study we achieved the conversion from a mixed phase to the hexagonal stable phase by manipulating the porosity of the PSi substrate. Additionally, in CdS/PSi(60%) and CdS/PSi(70%) structures, we noted the emergence of an additional peak corresponding to the (101) plane within the hexagonal phase. Further examination of the diffraction spectra shed light on distinct characteristics. When the CdS film was deposited on a glass substrate, the diffraction peaks exhibited reduced intensity, suggesting their lower crystallinity. This result can be attributed to the amorphous nature of the glass substrate [54]. In contrast, the diffraction peaks for the CdS films deposited on PSi substrate became more pronounced and narrower, indicating the film's crystallinity improvement [55]. It is well known that the formation energy required for crystallization is higher when dealing with amorphous substrates like glass compared to crystalline substrates, which promote nucleation. This fundamental distinction explains the lower crystallinity observed in the CdS/glass structure. Notably, the CdS film grown on the PSi substrate exhibit superior crystallinity compared to the other substrates, as demonstrated in Figure 1. This crystalline superiority makes it a remarkable specimen deserving of attention and further exploration.

With the application of Bragg's diffraction condition, the calculation of interplanar spacing (d) for different planes across all XRD patterns is possible [56].

$$2d\cdot\sin\theta = n\cdot\lambda, \tag{1}$$

Where: θ is the angle of diffraction, n gives the order of diffraction, and κ is the wavelength of X-ray radiation from CuKα (λ = 0.154 nm).

Using Bragg's formula for the hexagonal system [57], the 'a' and 'c' lattice parameters are determined from the position of the peaks.

$$\frac{1}{d^2} = \frac{4}{3}\frac{(h^2+hk+k^2}{a^2} + \frac{l^2}{C^2}. \tag{2}$$

The minor deviation from the standard values can be attributed to the strain induced in these samples because of excess Cd interstitials or S vacancies [57].

The crystallite size can be simply determined using the Scherer formula [57] as follows:

$$D = \frac{k\lambda}{\beta cos\theta}. \quad (3)$$

Where:
β represents the full width at half maximum (FWHM in radians) of the peak, adjusted for instrumental broadening.
θ is the diffraction angle mesered in radians
k: Scherer constant (k = 0.9)
λ: Wavelength of X-ray.
The lengths are expressed in [Å] and the angles in radians.
The strain values ϵ can be calculated using the following formula [39]:

$$\varepsilon = \frac{\beta cos\theta}{4} \quad (4)$$

The density of dislocations δ is determined by the Williamson and Smallman's relation [58]:

$$\delta = \frac{1}{D^2} \quad (5)$$

Table 1 presents the lattice parameter values obtained. These values have a good agreement with the published data.

Table 1. Structural parameters for the strongest peaks of CdS nanoparticles deposited on different substrates

Substrats	Structure	(hkl)	I / I_0	2θ (°)	$d_{spasing}$(A°)	Laticeconstante
CdS/ glass	Hex	(002)	100	26.6352	3.3417	
	Hex	(110)	14.76	44.2537	2.0467	a =4.0890
	Hex	(112)	12.07	52.4457	1.7447	c =6.6936
CdS/Si	Hex	(002)	100	27.2090	3.2775	
	Cub	(200)	82.61	30.0070	2.9779	a =4.1986
	Hex	(110)	37.46	44.2794	2.0456	
	Hex	(112)	52.35	51.9987	1.7586	c =6.5550
CdS /PSi37%	Hex	(002)	100	26.8596	3.3193	
	Cub	(200)	62.79	29.7193	3.0061	a =4.1746
	Hex	(110)	19.46	43.9789	2.0589	
	Hex	(112)	78.91	51.7355	1.7670	c =6.6384
CdS /PSi53%	Hex	(002)	100	27.2016	3.2784	
	Cub	(200)	68.84	29.9541	2.9831	a= 4.1726
	Hex	(110)	34.58	44.6292	2.0304	
	Hex	(112)	67.74	51.9526	1.7601	c= 6.5568
CdS /PSi60%	Hex	(100)	19.79	25.4144	3.5047	
	Hex	(002)	100	27.0974	3.2907	a =4.1562
	Cub	(200)	39.66	29.9875	2.9798	
	Hex	(110)	27.66	44.0521	2.0556	c =6.8516
	Hex	(112)	35.24	52.0017	1.7585	
CdS /PSi70%	Hex	(100)	54.50	25.8233	3.4501	
	Hex	(002)	100	27.4168	3.2531	a = 4.0832
	Hex	(101)	60.68	29.2907	3.0491	
	Hex	(110)	79.00	44.4943	3.0362	c =6.5063
	Hex	(112)	35.30	52.0950	1.2792	

Data from X-ray diffraction on FWHM, crystallite size, strain, and dislocation density concerning CdS thin films deposited onto various substrates are presented in Table 2. From the results obtained, crystallite size decreases in films grown on Si and PSi substrates. The smallest value of crystallite size was measured in the largest porosity Psi substrate (70%). Additionally, the strain and dislocation density values are lower in the case of films depoited on glass substrate. By comparing the diffraction pattern of films deposited on glass and of those deposited on Si and PSi substrates for different current densities, we can observe that most peak diffraction shift towards the bigger angles. It is well known that the deformation due to planar stress causes the shift in XRD peaks. Therefore, the values of strain calculated in Table 2 confirm the fact.

Table 2. X-ray diffraction data of 2θ, full width half maximum (FWHM), crystallite size, strain and dislocation density of (002) plan for CdS thin films deposited on glass, silicon and PSi substrates

Substrats	2θ (°)	FWHM (°)	D(nm)	$\varepsilon .10^{-3}$	$\delta .10^{-3}$ (nm^{-2})
CdS/ glass	26.6352	0.1771	46.120	0.751	0.470
CdS/Si	27.2090	0.3542	23.088	1.501	1.875
CdS /PSi37%	26.8596	0.3542	23.071	1.502	1.878
CdS /PSi53%	27.2016	0.4133	19.786	1.752	2.554
CdS /PSi60%	27.0974	0.5314	15.385	2.253	4.224
CdS /PSi70%	27.4168	0.7085	11.554	3.002	7.490

3.2 Morphological study

Fig. 2 shows the SEM images of CdS thin films deposited on glass (a) and on silicon (b) substrates.

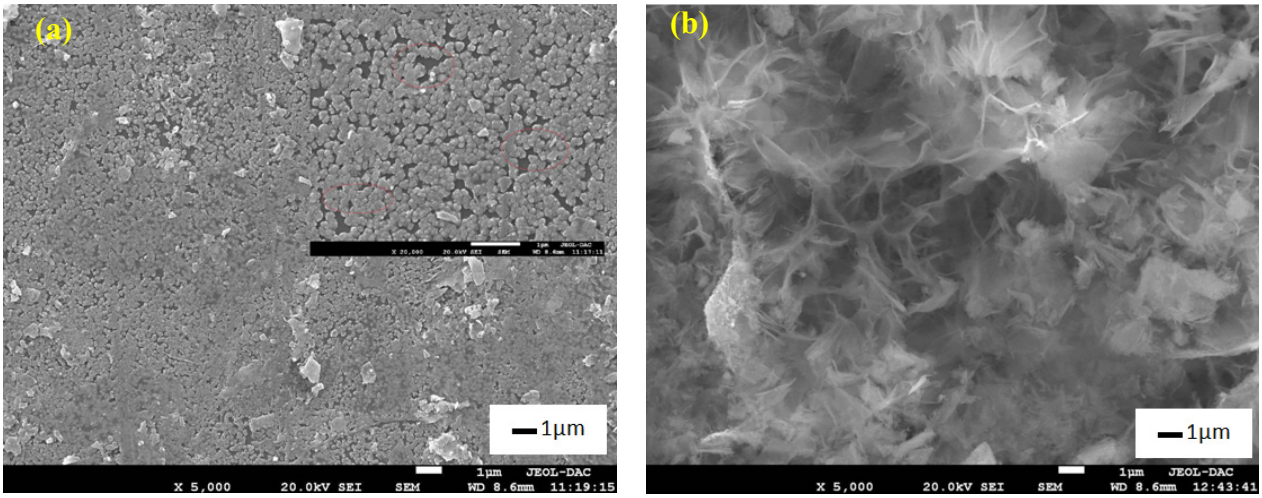

Figure 2. SEM images of (a) CdS/glass, (b) CdS/Si

CdS/glass sample structure show the presence of compact globular structures owing spherical and hexagonal shapes. These structuresare composed of nanoparticles that maintain a uniform size. However, careful observation reveals the existence of voids between the grains, indicating incomplete growth of CdS thin films. It is plausible that the smooth nature of the glass substrate hampers the perfect development of CdS thin films.

In contrast, the SEM image of the CdS/Si structure portrays the formation of micro-flowers, micro-sheets, and micropores on the surface. These micro-features create an environment conducive to the formation of non-spherical nanoparticles within the micropores. This distinct morphology of the nanoparticles can be attributed to the intrinsic roughness of the silicon surface, which provides favorable conditions for the growth of non-spherical CdS nanoparticles in the recesses of the micropores. Moreover, an interesting discrepancy becomes evident when comparing the particle density of the CdS/Si thin films to that of the CdS/glass structure. Remarkably, the particles in the CdS/Si thin films appear to be more densely packed compared to those in the CdS/glass structure. This disparity in particle density becomes visually apparent in Figure 3, which depicts the morphologies of both the porous silicon (PSi) and CdS/PSi structures. This distinction can be ascribed to the distinctive characteristics of the silicon substrate, which likely facilitate a more compact deposition of CdS thin films.

Figure 3 (a) illustrates the SEM image of the porous silicon matrix. The surface clearly consists of semi-circular shaped pores, which are distinctive by their uniform distribution and great density. The size of these pores falls within the range of 20 to 25 nm. Regarding the CdS/PSi structures, the SEM observation of the CdS/PSi37% structure (Fig. 3 (b)) exhibits the formation of micro-flowers, which subsequently generate pores with diameters on the scale of a few micrometers. These pores undergo widening and deepening due to the porous nature of the silicon substrate and the heightened surface roughness. A transition in the sample morphology is observed in the CdS/PSi53% structure (Fig. 3 (c)), where the micro-flowers and pores partially disappear, leading to the emergence of micrometric plates on the surface. Additionally, spherical nanoparticles appear and tend to aggregate, retaining their shape and forming macroscopic hierarchical masses. As the porosity of the silicon substrate increases to a specific threshold (around 60% (Fig 3 (d)), the characteristic flower-like morphology completely vanishes. Instead, of these two distinct types of nanoparticles appear. Firstly, nano plates with dimensions spanning from 300 nm to 1 µm are observed. Secondly, spherical nanoparticles with a striking white appearance reminiscent of snowballs are formed. Notably, upon reaching 70% porosity in the silicon substrate (Figure 3 (e)), the SEM image reveals the complete disappearance of micro-flowers and micro-plates followed by the formation of spherical nanoparticles with dimensions ranging from 10 nm to 50 nm, with a uniform distribution across the entire surface. Furthermore, the agglomeration of nanoparticles with identical dimensions leads to the formation of microspheres with diameters between 500 and 700 nm. Additionally, microspheres characterized by inhomogeneous and low-density structures also emerge through the agglomeration of nanoparticles of similar dimensions.

In summary, the SEM analysis offers valuable information regarding the unique morphological characteristics observed in the CdS/glass and CdS/Si configurations. In the CdS/glass structure, spherical nanoparticles form globular structures, whereas the CdS/Si structures are composed of micro-flowers, micro-sheets, and non-spherical nanoparticles within micropores. Additionally, the CdS/Si thin films exhibit a greater particle density compared to the CdS/glass structure. Furthermore, the investigation of CdS/PSi structures evolves from micro-flowers and pores to micrometric plates and aggregated spherical particles.

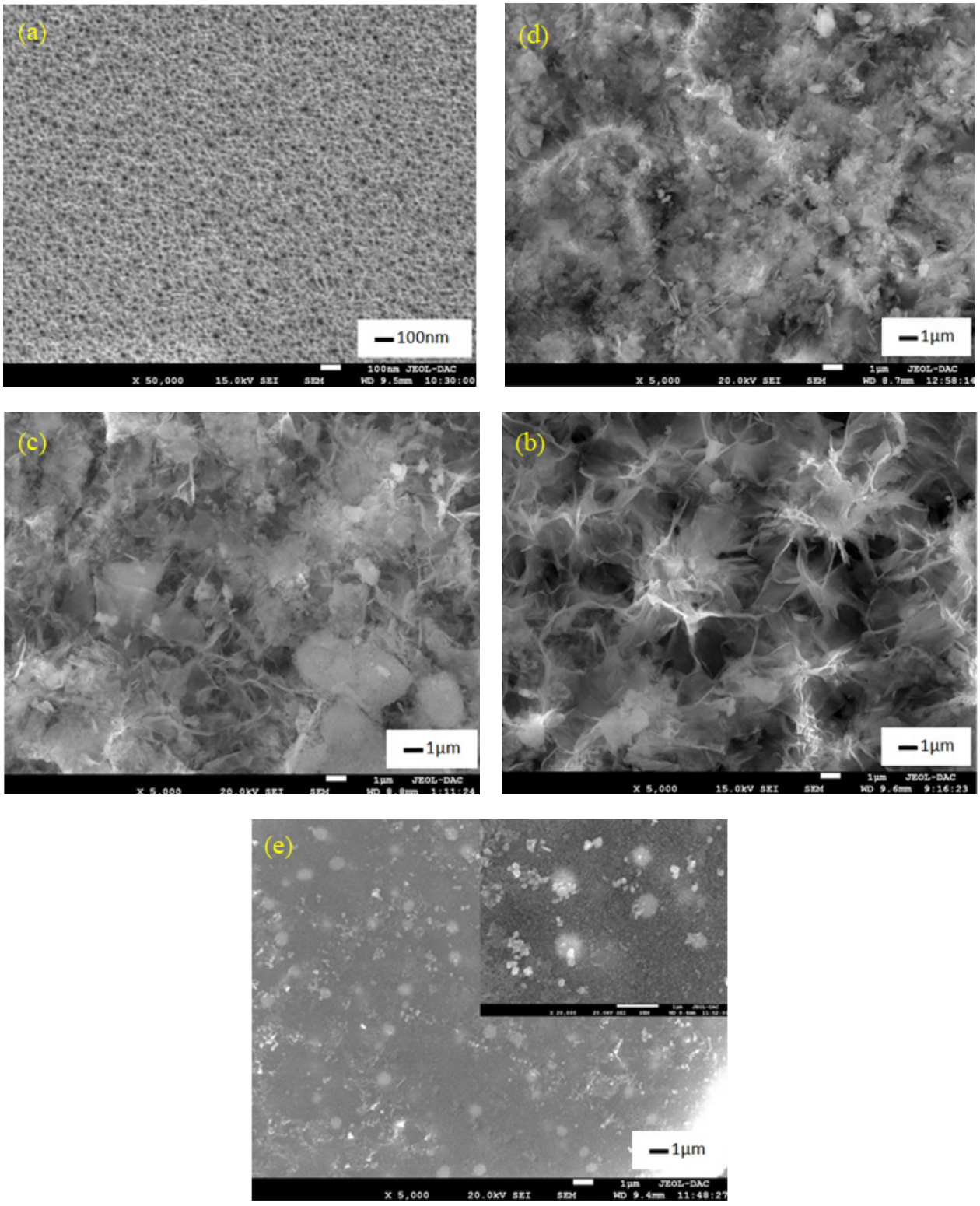

Figure 3. SEM images of (a) PSi60%, (b) CdS/PSi37%, (c) CdS/PSi53%, (d) CdS/PSi60%, and (e) CdS/PSi70%

3.3 Compositional analysis

To determine the element composition and the ratio of atomic percentage of different elements in CdS thin films prepared by CBD, we have used energy-dispersive X-ray (EDX) analysis. In Figure 4, we have reported the recorded EDX spactra in different samples. As seen, high peaks assigned to Sulfur (S) and Cadmium (Cd) element are present in whole spectra confirming the formation with a good purity of CdS thin films. However , we noticed that the percentage of Cd and S elements is higher in the case of the CdS/PSi structure than in the other ones, reflecting better crystallization of CdS on porous silicon.

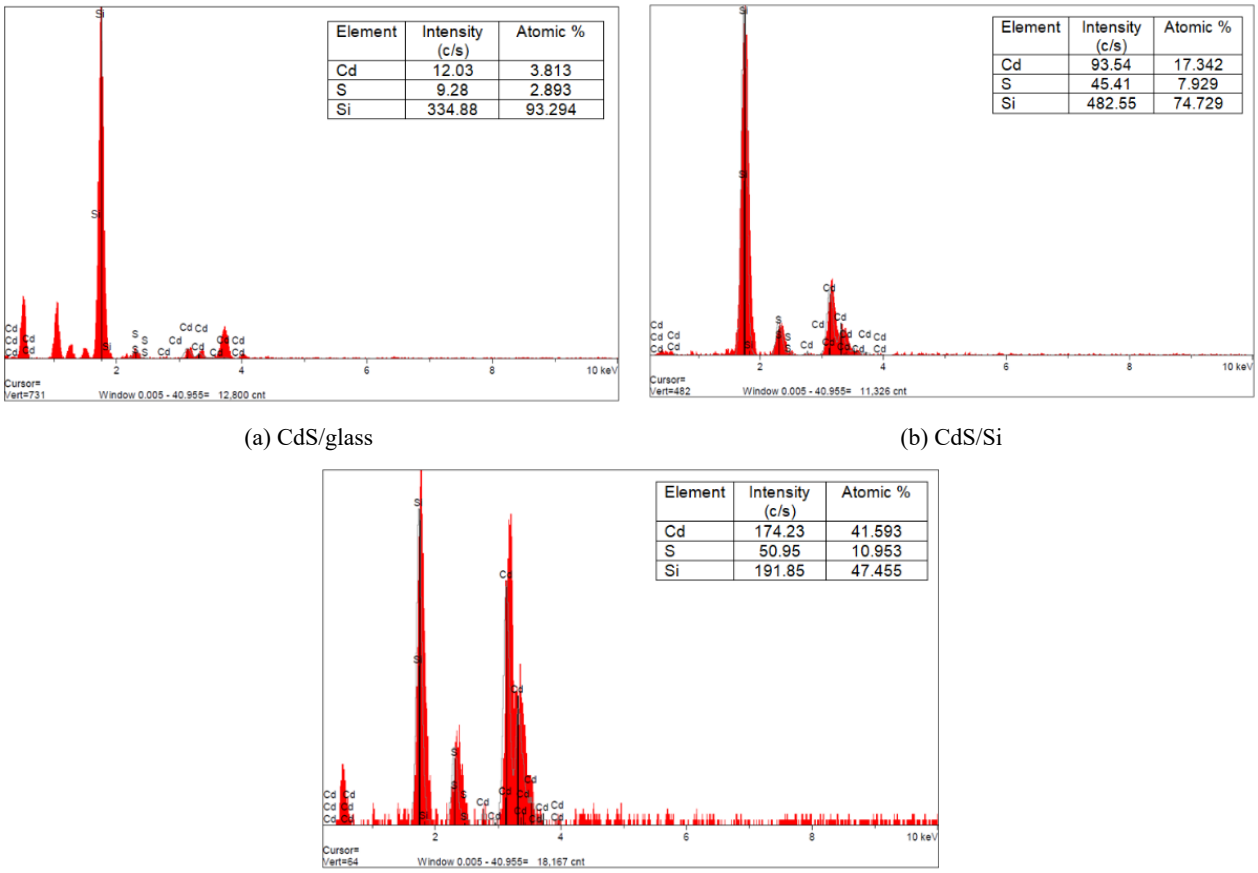

(a) CdS/glass (b) CdS/Si

(c) CdS/PSi60%

Figure 4. EDX spectrum of nanocrystalline CdS thin films

3.4 Optical characterization

In order to study the optical gap of the CdS samples, the optical transmittance spectroscopy, in the Uv visible range, of thin film deposited on glass is used. Figure 5 illustrates the variations in transmittance with respect to wavelength The spectrum exhibited absorption edges at around 500 nm, which indicated the existence of the optical band gap of the CdS thin film. The average transmittance obtained within the visible spectrum is about 55%. It is worth noting that the reduced transmittance of the deposited film could be attributed to the surface roughness resulting from the morphology of clustered CdS thin films.

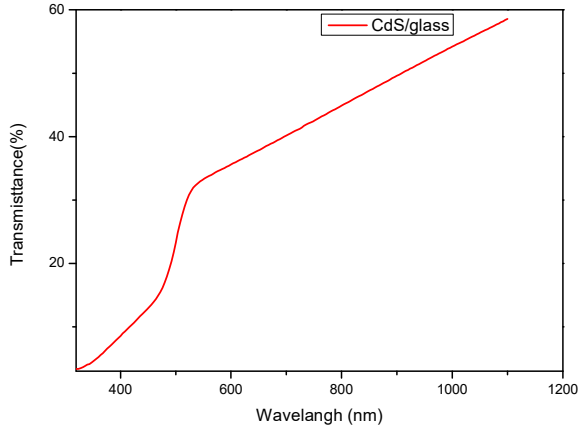

Fig. 5. Optical transmittance spectrum of CdS thin film

The relationship between the energy of the photon and the optical absorption coefficient (α) for direct transitions is expressed by the following Tauc equation [59]:

$$\alpha(h\nu) = (h\nu - E_g)^{\frac{1}{2}}, \tag{6}$$

where: A: Independent energy constant Eg: Optical band-gap of semiconductor (eV) hν: Photon energy

In Figure 6, we have plotted $(\alpha h\nu)^2$ as a function of theenergy of the photon. The optical film's band gap was estimted from the intercept of the linear part of $(\alpha h\nu)^2$ up with the x-axis. The obtained energy band gap of CdS thin film deposited on glass is 2.3 eV. This result is in good agreement with that published in the literature [60].

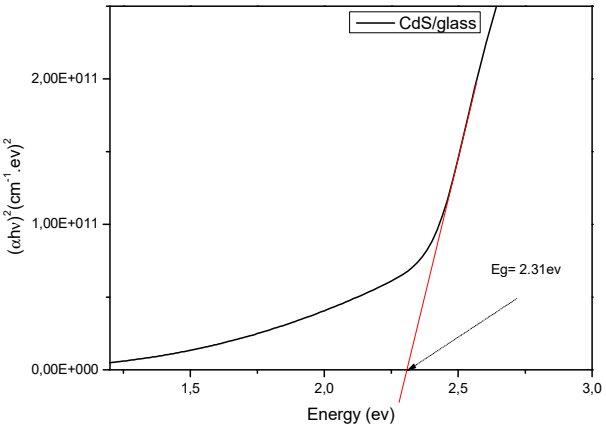

Fig. 6. Determination of the energy gap for the CdS thin film

3.5 Electrical characterization

For the film's electrical characterization, we have measured DC conductivity in a coplanar structure. Two circular silver (Ag) electrodes were placed on the surface to perform electrical conductivity measurements at a distance of 5 mm (Figure 7a). The choice of the distance between the Ag electrodes was intended to guarantee the flow of electric current, taking into account the geometric properties of the electrical contacts used in previous studies [61]. In Figure 7b, we have plotted therecorded current-voltage (I-V) characteristics, measured in total darkness and under illumination. It is evident that as the applied voltage increases, the current values of the CdS films increase significantly, both in dark and illuminated conditions. Moreover, the measured current in illuminated condition is larger than in dark one, this is attributed to the photonconductivity of the prepared CdS films, this suggests their possible application as photodetector. The CdS/Si, Cd/PSi37%, Cd/PSi57%, Cd/PSi60%, and Cd/PSi70% structures present photocurrents of 3.14, 4.63, 58.85, 590.40 and 204.88 µA, respectively at bias voltage of 9V, as illuminated by visible light (Fig. 7a). In addition, the highest photocurrent value is observed for CdS/PSi60% structure. However, the current measured in CdS/PSi70% structure was substantially greater than that of CdS/PSi60%, this suggests the possibility of defects formation within the CdS thin films attributed to the high porosity of the substrate. These defects may behave as recombination centers and consequently reduces the electronic transport.

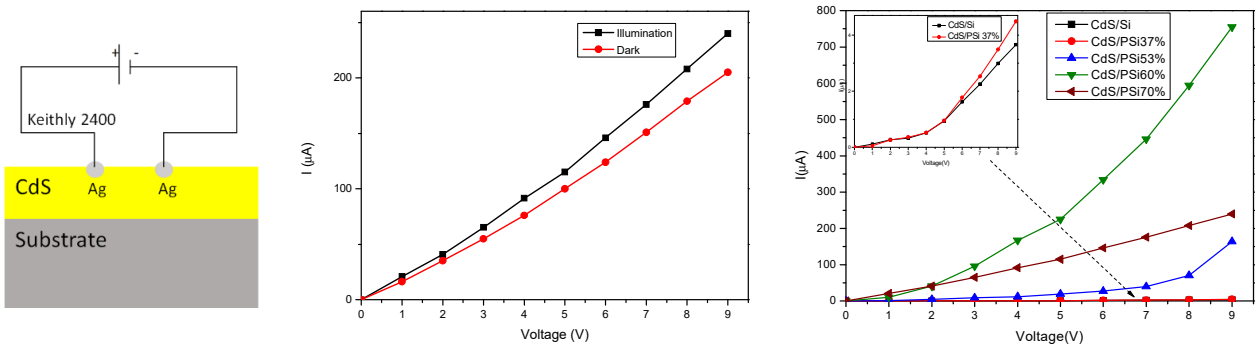

(a) (b) (c)

Figure 7. I–V characteristics
(a) Structure used for I-V characterization; (b) CdS/PSi70%; (c) CdS/Si and CdS/PSi structures under illumination

In conclusion, the electrical characteristics of the produced CdS thin films can be influenced by the surface shape and porosity of the porous silicon substrate. Successful synthesis of CdS thin films was achieved on glass, silicon, and mesoporous silicon substrates using the chemical bath method.

4. CONCLUSIONS

This work has made it possible to meet the objectives set concerning the effect of porosity of mesoporous silicon substrates on CdS thin films deposited by chemical bath deposition. Successful synthesis of CdS thin films was achieved on glass, silicon, and mesoporous silicon substrates using the chemical bath method. Variations in the porosity of the PSi substrate yield to CdS thin films with various morphologies. The impact of PSi porosity on the grain size of CdS was studied.

Indeed, a porosity of around 70% yields to films owing better crystallinity and reduces the size of the CdS grains to less than 12 nm. The DC current measurements showed that the CdS/PSi structure with porosities between 60-70% significantly exibited larger conductivity and photoconductivity, compared to the CdS/glass and CdS/Si structures. Finally, due to the vast complexity of the influence of the porosity of a PSi substrate on the characteristics of CdS nanoparticles. several issues are still open for future investigation in order to fully understand the effect of porosity of silicon substrates on CdS thin films. Hopefully, the results presented in this study gives a contribution to this understanding.

Acknowledgments

This research was funded by the DGRSDT and the laboratory of Materials and System Structure and their Reliability of Oum El Bouaghi university, Algeria.

ORCID

D. Belfennache, https://orcid.org/0000-0002-4908-6058; **Mohamed A. Ali**, https://orcid.org/0000-0002-7390-8592

REFERENCES

[1] Y. Benkrima, D. Belfennache, R. Yekhlef, and A.M. Ghaleb, Chalcogenide Lett. **20**(8), 609 (2023). https://doi.org/10.15251/CL.2023.208.609.
[2] M. Husham, Z. Hassan, and A.M. Selman. Eur. Phys. J. Appl. Phys. **74**(1), 10101 (2016). https://doi.org/10.1051/epjap/2016150414
[3] D. Belfennache, D. Madi, R. Yekhlef, L. Toukal, N. Maouche, M.S. Akhtar, and S. Zahra, Semicond. Phys. Quantum Electron. Optoelectron. **24**(4), 378 (2021). https://doi.org/10.15407/spqeo24.04.378
[4] S. Mahdid, D. Belfennache, D. Madi, M. Samah, R. Yekhlef, and Y. Benkrima, J. Ovonic. Res. **19**(5), 535 (2023). https://doi.org/10.15251/JOR.2023.195.535
[5] P. Priyadarshini, S. Das, and R. Naik, RSC Advances, **12**(16), 9599 (2022). https://doi.org/10.1039/D2RA00771A
[6] A.M. Abu-Dief, Journal of Nanotechnology and Nanomaterials, **1**(1), 5 (2020). https://doi.org/10.33696/Nanotechnol.1.002
[7] Y. Xi, C. Hu, C. Zheng, H. Zhang, R. Yang, and Y. Tian, Mater. Res. Bull. **45**(10), 1476 (2010). https://doi.org/10.1016/j.materresbull.2010.06.007
[8] Y. Ma, X. Li, Z. Yang, H. Yu, P. Wang, and L. Tong, Appl. Phys. Lett. **97**(15), 153122 (2010). https://doi.org/10.1063/1.3501969
[9] J. Zhang, D. Li, R. Chen, and Q. Xiong, Nature, **493**(7433), 504 (2013). https://doi.org/10.1038/nature11721
[10] D. Li, J. Zhang, Q. Zhang, and Q. Xiong. Nano Lett. **12**(6), 2993 (2012). https://doi.org/10.1021/nl300749z
[11] D. Li, J. Zhang, and Q. Xiong, ACS Nano, **6**(6), 5283 (2012). https://doi.org/10.1021/nn301053r
[12] T. Zhai, X. Fang, L. Li, Y. Bando, and D. Golberg, Nanoscale, **2**(2), 168 (2010). https://doi.org/10.1039/B9NR00415G
[13] H. Li, X. Wang, J. Xu, Q. Zhang, Y. Bando, D. Golberg, Y. Ma, and T. Zhai, Adv. Mater. **25**(22), 3017 (2013). https://doi.org/10.1002/adma.201300244
[14] A. Ashok, G. Regmi, A. Romero-Nunez, M. Solis-Lopez, S. Velumani, and H. Castaneda, J. Mater. Sci. Mater. Electron. **31**, 74997518 (2020). https://doi.org/10.1007/s10854-020-03024-3
[15] S. Hariech, J. Bougdira, M. Belmahi, G. Medjahdi, M.S. Aida, and A. Zertal, Bull. Mater. Sci. **45**(2), 78 (2022). https://doi.org/10.1007/s12034-022-02661-0
[16] S. Hariech, M.S. Aida, J. Bougdira, M. Belmahi, G. Medjahdi, D. Gen`eve, N. Attaf, and H. Rinnert, J. Semicond. **39**(3), 034004 (2018). https://doi.org/10.1088/1674-4926/39/3/034004
[17] H. Khallaf, Ph.D. Thesis Dissertations. University of Central Florida, (2009). https://stars.library.ucf.edu/etd/3941
[18] D. Belfennache, N. Brihi, and D. Madi, in: *Proceeding of the IEEE xplore*, 8th (ICMIC) (2016). 7804164 (2017), pp. 497–502. https://doi.org/10.1109/ICMIC.2016.7804164.
[19] D. Belfennache, D. Madi, N. Brihi, M.S. Aida, and M.A. Saeed, Appl. Phys. A, **124**, 697 (2018). https://doi.org/10.1007/s00339-018-2118-z
[20] R. Pribyl, S. Kelarova, M. Karkus, and V. Bursikova, Carbon Trends, **17**, 100416 (2024). https://doi.org/10.1016/j.cartre.2024.100416
[21] S. Morishita, M. Kunihiro, M. Funahashi, and N. Tsurumachi, J. Mol. Liq. 126425 (2024). https://doi.org/10.1016/j.molliq.2024.126425
[22] T.A.-H. Abbas, Diyala journal for pure sciences, **13**(3), 227 (2017). https://doi.org/10.24237/djps.1303.261A
[23] R. Ouldamer, D. Madi, D. Belfennache, in: *Advanced Computational Techniques for Renewable Energy Systems. IC-AIRES 2022I,* edited by M. Hatti, **591**, (Springer, Cham. 2023), pp. 700-705. https://doi.org/10.1007/978-3-031-21216-1_71
[24] E.V. Pasos, B. Wagner, F. Xu, Y. Wang, M. Kim, M. Zachariah, and L. Mangolini, Chem Eng J. **500**, 156997 (2024). https://doi.org/10.1016/j.cej.2024.156997
[25] R. Ouldamer, D. Belfennache, D. Madi, R. Yekhlef, S. Zaiou, and M.A. Ali, J. Ovonic. Res. **20**(1), 45 (2024). https://doi.org/10.15251/JOR.2024.201.45
[26] N. Naderi, and M. Hashim Int. J. Electrochem. Sci. **7**(11), 11512 (2012). https://doi.org/10.1016/S1452-3981(23)16962-8
[27] I. González, R. Nava, M. Cruz-Irisson, J.A. del Río, I. Ornelas-Cruz, J. Pilo, Y.G. Rubo, *et al*., J. Energy Storage, **102,** 114087 (2024). https://doi.org/10.1016/j.est.2024.114087
[28] T. Jalkanen, A. Maattanen, E. Makila, *et al*., Journal of Sensors, 927396 (2015). https://doi.org/10.1155/2015/927396
[29] N. Rahmani, and R.S. Dariani, AIP Advances, **5**, 077112 (2015). https://doi.org/10.1063/1.4926460
[30] N. Rahmani, R.S. Dariani, and M. Rajabi, Appl. Surf. Sci. **366**, 359 (2016) https://doi.org/10.1016/j.apsusc.2016.01.075
[31] A. Halimaoui, "Porous silicon: material processing, properties and applications," in: *Porous Silicon Science and Technology*, edited by J.C. Vial, and J. Derrien, (Centre de Physique des Houches, Springer Berlin Heidelberg, 1995). **1**, pp. 33-52. https://doi.org/10.1007/978-3-662-03120-9_3
[32] M. Du Plessis, Physica Status Solidi (a), **204**(7), 2319 (2007). https://doi.org/10.1002/pssa.200622237
[33] M. Lai, L. Wei, Y-H Huang, X-D Wang, and Z. Yang. ACS Photonics, **11(6)**, 2439 (2024). https://doi.org/10.1021/acsphotonics.4c00335J

[34] A. Jane, R. Dronov, A. Hodges, and N.H. Voelcker, **27**(4), 230 (2009). https://doi.org/10.1016/j.tibtech.2008.12.004
[35] A. Rahmani, L. Remache, M. Guendouz, M.S. Aida, and Z. Hebboul, Appl. Phys. A, **127**(5), 396 (2021). https://doi.org/10.1007/s00339-021-04548-z
[36] C-M. Chou, H-T. Cho, V.K. Hsiao, K-T. Yong, W-C. Law, Nanoscale Res. Lett. **7**, 1 (2012). https://doi.org/10.1186/1556-276X-7-291
[37] B. Meier, L. Egermann, S. Voigt, M. Stanel, H. Kempa, and A.C. Huebler, Thin Solid Films, **519**(19), 6610 (2011). https://doi.org/10.1016/j.tsf.2011.04.225
[38] S.A. Hasoon, I.M. Ibrahim, R. Al-Haddad, and S.S. Mahmood, Int. J. Curr. Eng. Technol. **4**(2), 594 (2014).
[39] S.T. Kassim, H.A. Hadi, and R.A. Ismail, Optik, **221**, 165339 (2020). https://doi.org/10.1016/j.ijleo.2020.165339
[40] A. Rahmani, L. Remache, M. Guendouz, N. Lorrain, A. Djermane, and L. Hadjeris, Surf. Rev. Lett. **29**(03), 2250039 (2022). https://doi.org/10.1142/S0218625X22500391
[41] K.S. Khashan, Int. J. Mod. Phys. B, **25**(02), 277 (2011). https://doi.org/10.1142/S0217979211054744
[42] N.F. Habubi, R.A. Ismail, A.N. Abd, and W.K. Hamoudi, Indian J. Pure Appl. Phys. **53**, 718-724 (2015).
[43] Y. Li, X.Y. Song, Y.L. Song, P.F. Ji, F.Q. Zhou, M.L. Tian, H.C. Huang, and X.J. Li, Mater. Res. Bull. **74**, 507 (2016). https://doi.org/10.1016/j.materresbull.2015.11.023
[44] P.M. Perillo, and D.F. Rodriguez, Physica B: Condensed Matter, **680**, 415828 (2024). https://doi.org/10.1016/j.physb.2024.415828
[45] M. Cao, Y. Sun, J. Wu, X. Chen, and N. Dai, J. Alloys Compd. **508**(2), 297 (2010) https://doi.org/10.1016/j.jallcom.2010.08.066
[46] C. Tsai, D. Chuu, G. Chen, and S. Yang. J. Appl. Phys. **79**(12), 9105 (1996) https://doi.org/10.1063/1.362645
[47] B-S. Moon, J-H. Lee, and H. Jung. Thin solid films, **511**, 299 (2006) https://doi.org/10.1016/j.tsf.2005.11.080
[48] D.W. Niles, and H. Hochst, Phys. Rev. B, **41**(18), 12710 (1990). https://doi.org/10.1103/PhysRevB.41.12710
[49] J. Patel, F. Mighri, A. Ajji, D. Tiwari, and T.K. Chaudhuri, Appl. Phys. A, **117**, 1791 (2014) https://doi.org/10.1007/s00339-014-8659-x
[50] M. Cao, L.Li, B. Zhang, J. Huang, K. Tang, H. Cao, Y. Sun, and Y. Shen, J. Alloys Compd. **530**, 81 (2012). https://doi.org/10.1016/j.jallcom.2012.03.054
[51] Z. Rabeel, M. Abbas, M. Basit, N.A. Shah, I. Ahmad, and M. Hassan, J. Adv Nanomat. **2**(2), 113 (2017). https://dx.doi.org/10.22606/jan.2017.22004
[52] S. A-J. Jassim, A.A.R.A. Zumaila, and G.A.A. Al Waly, Results Phys. **3**, 173 (2013). https://doi.org/10.1016/j.rinp.2013.08.003
[53] S.E. Haque, B. Ramdas, N. Padmavathy, and A. Sheela, Micro & Nano Letters, **9**(10), 731 (2014). https://doi.org/10.1049/mnl.2014.0167
[54] L. Ma, X. Ai, and X. Wu, J. Alloys. Compd. **691**, 399 (2017). https://doi.org/10.1016/j.jallcom.2016.08.298
[55] S. Thanikaikarasan, T. Mahalingam, T. Ahamad, S.M. Alshehri, J. Saudi Chem. Soc. **24**(12), 955 (2020). https://doi.org/10.1016/j.jscs.2020.10.003
[56] N. Maticiuc, and J. Hiie, IOP Conf. Ser.: Mater. Sci. Eng. **49**(1), 012061 (2013). https://doi.org/10.1088/1757-899X/49/1/012061
[57] F. Ouachtari, A. Rmili, B. Elidrissi, A. Bouaoud, H. Erguig, and P. Elies, J. Mod. Phys. **2**(9), 1073 (2011). https://doi.org/10.4236/jmp.2011.29131
[58] V.G. Nair, R. Jayakrishnan, J. John, J.A. Salam, and A.M. Anand, A. Raj, Mater. Chem. Phys. **247**, 122849 (2020). https://doi.org/10.1016/j.matchemphys.2020.122849
[59] D. Komaraiah, E. Radha, Y. Vijayakumar, J. Sivakumar, M.R. Reddy, and R. Sayanna, Modern Research in Catalysis, **5**(4), 130 (2016). https://doi.org/10.4236/mrc.2016.54011; M. Shaban, M. Mustafa, and A. El Sayed, Mater. Sci. Semicond. Process. **56**, 329 (2016). https://doi.org/10.1016/j.mssp.2016.09.006
[60] G. Mani, and J.B.B. Rayappan, Appl. Surf. Sci. **311**, 405 (2014). https://doi.org/10.1016/j.apsusc.2014.05.075

ВПЛИВ ПОРИСТОСТІ ПІДЛОЖКИ PSi НА ХАРАКТЕРИСТИКИ НАНОЧАСТИНОК CdS, ОТРИМАНИХ МЕТОДОМ CBD

Ф. Сакер[a], Л. Ремаш[a], А. Рахмані[b], Х. Муалкіа[c], М.С. Аїда[d], Н. Герміт[e], Д. Бельфенаше[f], Р. Єхлеф[f], Мохамед А. Алі[g]
[a]Лабораторія матеріалів і системної структури та їх надійності, Університет Ум Ель Буагі, Ум Ель Буагі, 04000, Алжир
[b]Лабораторія фізико-хімії матеріалів LPCM, Університет Лагуат, Лагуат, 310081, Алжир
[c]Факультет природничих і природничих наук, кафедра матеріалознавства, Університет Ум Ель Буагі, Ум Ель Буагі, 04000, Алжир
[d]Факультет фізики, Університет короля Абдулазіза, Джидда, провінція Мекка, Саудівська Аравія
[e]Університет Ларбі Бен М'хіді, Ум Ель Буагі, 04000, Алжир
[f]Дослідницький центр промислових технологій CRTI, P.O. Box 64, Черега, Алджер, Алжир
[g]Школа біотехнології, Університет Бадр у Каїрі (BUC), місто Бадр 11829, Каїр, Єгипет

Мотивацією для дослідження потенціалу таких напівпровідникових матеріалів, як кремній, є їх використання як підкладки для виготовлення тонких плівок. У цій роботі метод хімічного осадження (CBD) використовувався для синтезу тонких плівок сульфіду кадмію (CdS) на підкладках зі скла, кремнію (Si) і пористого кремнію (PSi). Підкладки PSi були підготовлені методом електрохімічного травлення з використанням різних густин струму при постійному часі травлення 5 хвилин. Отримані результати продемонстрували, що на морфологію нанесених матеріалів впливала пористість підкладок PSi. Визначено, що середні розміри кристалітів CdS/скло та CdS/Si становлять 46,12 нм та 23,08 нм відповідно. У структурах CdS/PSi середнє значення розміру зерен зменшується зі збільшенням пористості. Найменший отримано для структури CdS/PSi з 70% пористістю, що становить 11,55 нм. Виміряні вольт-амперні характеристики в компланарній структурі на зразку CdS/PSi/Si показали, що фотострум структури CdS/Si становить 3,17 мкА і збільшується до 600 мкА для структури CdS/PSi/60%.
Ключові слова: *халькогенідні напівпровідники; пористий кремній; CdS; тонка плівка; CBD*

East European Journal of Physics. 1. 170-176 (2025)
DOI:10.26565/2312-4334-2025-1-16 ISSN 2312-4334

FAST AND CHEAP SYNTHESIS OF CuO/ZnO THIN FILMS MADE WITH THE SPRAY PYROLYSIS TECHNIQUE

Y. Bellal, A. Bouhank, D. Belfennache*, R. Yekhlef
Research Center in Industrial Technologies CRTI, P.O. Box 64, Cheraga, 16014 Algiers, Algeria
**Correspondence Author e-mail: belfennachedjamel@gmail.com*
Received December 26, 2024; revised January 31, 2025; accepted February 7, 2025

In this paper, CuO/ZnO nanocomposites thin films were elaborated with different combination ratio of precursors (copper chloride, zinc chloride) dissolved in distilled water using the spray pyrolysis method in order to study their physicochemical properties. Nanocomposites were elaborated as thin films deposited on the surface of ordinary glass at 550°C using a cheaper and fast technique. Optical, structural and morphological properties of the latter have been examined by UV-vis, X-ray diffraction (XRD), RAMAN, SEM/EDS and AFM. XRD peaks prove the attendance of the polycrystalline models of CuO and ZnO with preferential orientation. Raman shift spectrum confirms the attendance of CuO and ZnO nanocomposites. SEM/EDS and AFM support that there is same roughness on the surface of the ordinary glass RMS=106 nm, which is suitable for the mechanism of photodegradation. In the visible region, we notice a high absorbance and high optical band gaps (Egap= 4.07 eV) that is suitable for the photodegradation of undesirable substances.
Keywords: *Spray Pyrolysis; CuO/ZnO; Thin Films; Precursor; RAMAN; Photodegradation*
PACS: 73.50.-h, 73.50.Pz

1. INTRODUCTION

Semiconductors attract considerable attention from fundamental and application points of view, due to their widely exploited properties [1-3].Considerable efforts have been focused on semiconducting metal oxides (TiO_2, MgO, ZnO, CuO, SiO_2, etc), have been the subject of numerous research works and they have attracted great interest in the academic and industrial circles because they present a remarkable improvement in the properties of materials compared to conventional micro and macrocomposites [4-8]. The development of these materials is linked to their interesting physical properties and their advantages over other materials (available, stable, non-toxic, low cost, etc.) [9,10]. These materials (oxides) are good candidates for applications in different technological sectors, particularly in photovoltaics and optoelectronics [11-13]. Currently, the association of two oxides cites great attention from researchers because of their various practical applications such as photocatalyst, sensor, fabrication of microelectronic circuits, piezoelectric devices, fuel cell and solar cells [14-17].

In this case, we have many contents with higher amounts of oxides based on zinc (ZnO) and copper (CuO) that act on semi-conductors with more advantages for different applications. The composite nanostructures of these semi-conductors have a large interface and allow for multiple functional functions and a voice to new applications. The ZnO is a semi-conductor type with a large cross-band direct current (3.37 eV) and a strong exciton energy environment of 60 MeV at the ambient temperature and electrical properties. It is necessary to pay attention to large applications with potential in luminescence, photocatalysts, electricity, gas caps, solar cells, hydrocarbon storage and information [18]. Copper oxide is a beneficial semiconductor material due to its cheaper price, most availability from raw materials and the most important is their non-toxicity. They are used in transistors, spintronic devices, super capacitors, gas sensing electro chromic devices and photocatalysis The, with a gap of 1.2eV at low temperature [19]. In the Uv-vis domain, its gap energy is 1.2 to 1.7 eV [19,20] which requires a low energy ($h\upsilon$) for the electron to move from the valence band to the conduction band, but unfortunately it turns out that this gap energy is a little weak to degrade an organic and inorganic pollutants [21]. For that we opt to improve the optical and energetic properties by adding to this semiconductor another n-type semiconductor (ZnO) [21, 22].

This amalgamation can produce interstitial defects which lead the easily passage of the electrons from the valence band to the conduction band by releasing a higher energy to use the oxidation reduction reactions at the semiconductor / pollutant interface (liquid or gas) [21]. The composite nanostructures of these semi-conductors have a large interface and allow for multiple functional functions and a voice to new applications.

Several methods have been used to synthesize ZnO-CuO composites. Among these methods, we can cite Co-precipitation [23], hydrothermal [24]; sol-gel [25] and the Spray Pyrolysis method [26]. The latter offers many manufacturing advantages comparable to the deposition methods, namely the use of available and less expensive equipment, the ability to operate at atmospheric pressure and at low temperature, easy control of manufacturing parameters, compatibility with large deposition surfaces. In this work we study the fast and cheap synthesis of CuO/ZnO thin films made with the spray pyrolysis technique.

Cite as: Y. Bellal, A. Bouhank, D. Belfennache, R. Yekhlef, East Eur. J. Phys. 1, 170 (2025), https://doi.org/10.26565/2312-4334-2025-1-16

2. EXPREMENTAL PROCEDURE

In this work, we have used a simple device for deposition, it is a small spray perfume bottle filled with a desired precursor solution (copper chloride (S_1) zinc chloride (S_2)), prepared with distilled water at different concentration of precursors as follows: C_{Total}= 0.05M and V_{Total}=10ml (Fig. 1). The zinc chloride $ZnCl_2$,$2H_2O$ and copper chloride $CuCl_2$, $2H_2O$ are Sigma-Aldrich products with more than 98% of purity.

In the open air with T_{room} = 25°C and t = 1 hour, the solutions were prepared. The precursor solutions have been sprayed onto ordinary glasses heated at 550°C. Before that; the ordinary glasses are cleaned like the previous protocol [21].

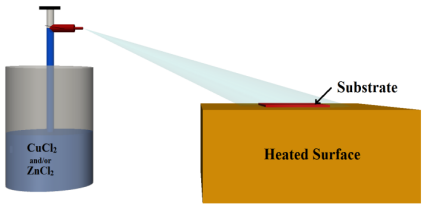

Figure 1. Principle of Spray Pyrolysis

3. RESULTS AND DISCUSSION

3.1 The UV-Visible characterization

ZnO and CuO thin films are n-type and p-type semi-conductors, and the direct result of Zn and Cu gaps in the assembly of the structure leads to the formation of holes in the valence bond. Equations (1) and (2) calculate the gap energy [21].

The optical absorbance spectra of thin films elaborated with different percentage of CuO/ZnO were shown in Figures 2 and 3. The obtained thin films reveal low and strong absorption in the visible region with a= 381.57nm more or less for all thin films. These are the basic characteristics of a solar selective absorber.

In order to determinate the CuO/ZnO band gap energy, the experimental data were extracted and reformed to absorption coefficient (α) as follows [21]:

$$\alpha = \frac{1}{t} ln[\frac{(1-R^2)}{2T} + \sqrt{\frac{(1-R)^4}{4\,T^2} + R^2}] \quad (1)$$

Where
α: Absorption coefficient;
t: Thickness;
R: reflectance;
T: transmittance;
The thickness t is nanometrically scaled Eg and α can be calculated by Tauc eq. (2):

$$\alpha h\upsilon = A(h\upsilon - E_g)^n \quad (2)$$

Where h is the photon energy, A is an independent constant of the energy and n is 2 or 0.5 for the indirect and direct allowed transition respectively, for this reason, the gap energy can be computed by extrapolating the linear part of the plot $(\alpha h\nu)^2$ with respect to hν (Fig. 3) [21]. we can see that the crystallite sizes of the CuO and ZnO are the responsible factors who can give same band gap variation. In this work, the connection between the band gap and crystallite size was investigated previously [27]. As a result, by adding another precursor the crystallite size is increased. Thus, a high crystallite size is, a band gap is. [27]. CuO is 3.7 eV gap energy in water less than what we found in this work, Eg = 4.07 eV for equimolar concentration of precursor solution (50 % $ZnCl_2$; 50%$CuCl_2$). For this reason, we believe that the equi-concentration of the precursor gives the good results for the photdegradation of pollutants.

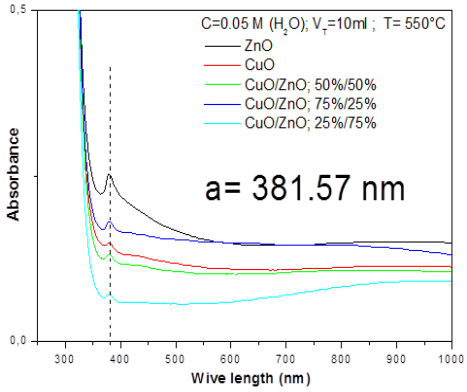

Figure 2. Different optical absorbance of CuO/ZnO nanocomposite thin films

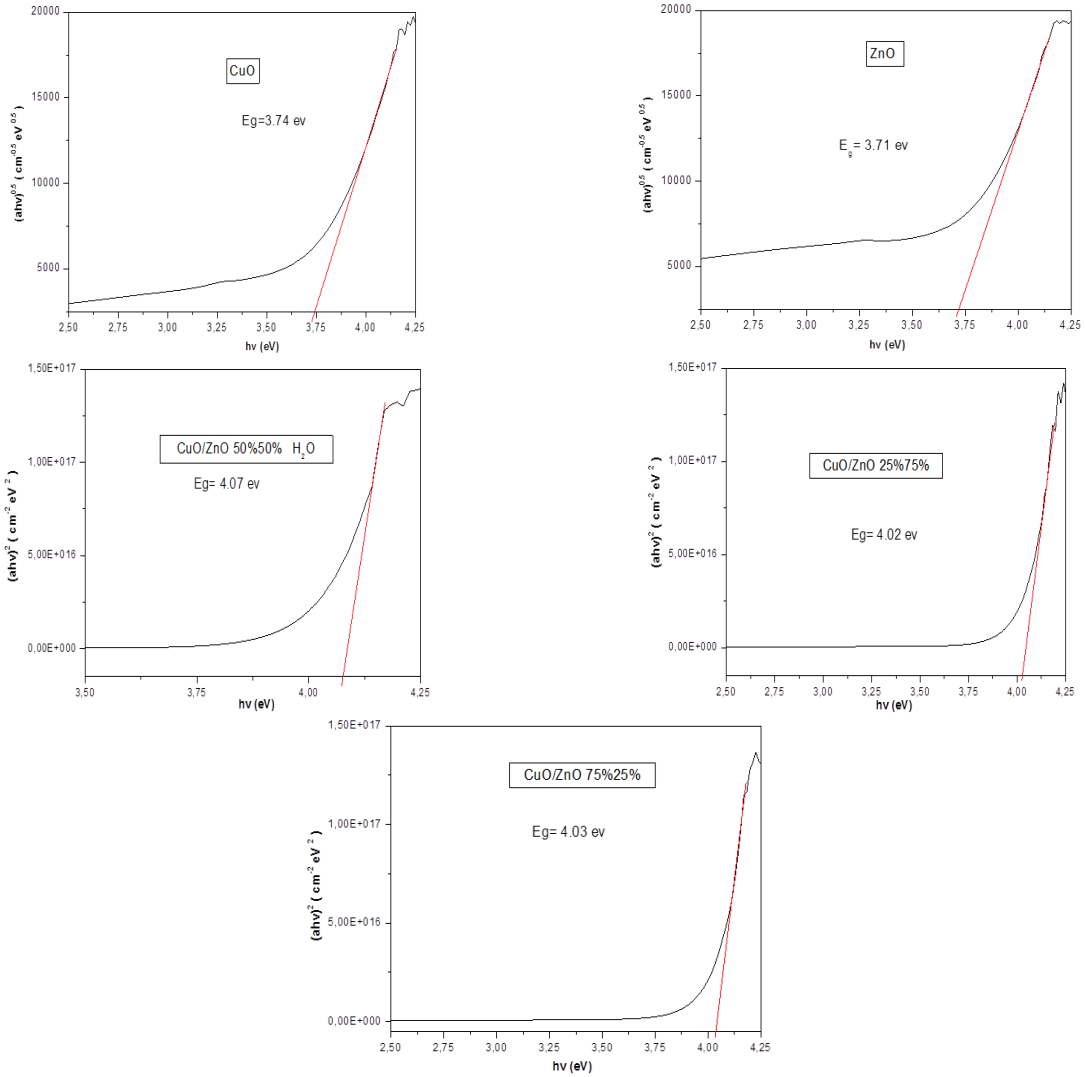

Figure 3. Different Band Gap of CuO/ZnO nanocomposites thin films

3.2. XRD Characterization & Crystallites Sizes Calculation

Fig.4 show the X-ray diffraction spectra for CuO/ZnO nano comoposite film made with the Spray Pyrolysis Technique. while the precursors were added in equi molar concentration, CuO/ZnO nano composites thin films formed show a various intensity of peaks at 2theta: 16.39, 37.51, 41.32, 43.50, 56.39 and 68° corresponding to the diffraction planes of CuO and ZnO with monoclinic crystalline arrangement. This observation is in good agreement with the JCPDS card 89-5899 for monoclinic crystalline structure

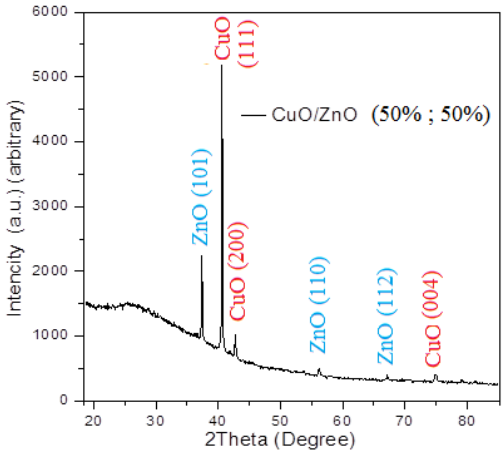

Figure 4. X-ray diffraction of CuO/ZnO thin films at T=550°C

Using Scherrer equation [27, 28]: Crystallite size can be deduced from XRD spectrum from several peaks mentioned below:

$$D = \frac{k\lambda}{W\,cos\theta} \tag{3}$$

Where:
D: Crystallites size
K: shape factor named "Scherrer constant" (K=0.9)
W: Full width at half maximum (FWHM) expressed in radians and θ represents the peak position (radians)
λ: Wavelength of X-ray sources ($Cu_{K\alpha}$ = 1.5406 Å).

We notice that CuO/ZnO grain sizes produced at homogeneous mixture of the precursors solution (copper chloride (S_1) zinc chloride (S_2)) are in nanometric scale with a small increase of 15 to 30 nm unlike CuO/ZnO elaborated independently [29-31]. We can gather the crystallites sizes values calculated by (3) in Table 1.

Table 1. Crystallites sizes values

Peaks (2θ°)	Plane (hkl)	Crystallite size (nm)
37.36	101	27.56
40.58	111	41.76
42.73	200	12.01
56.20	110	12.33
67.18	112	26.12
74.90	004	08.97

3.2 Raman Characterization

Raman characterization of CuO-ZnO nanocomposite thin films is an effective method to study the structural and electronic properties of these materials. Raman spectroscopy allows analyzing the vibration modes of chemical bonds in the material, which can provide information on the phase, purity, and interactions between the different phases of the nanocomposite. Figure 5 shows the Raman shift of CuO/ZnO thin films at T=550°C, it shows the presence of the majority of characteristic bands of CuO and ZnO nanocomposite thin films.

In this case, one can expect to observe characteristic peaks related to each phase, as well as interaction or coupling peaks between the two oxides. The main Raman modes for CuO are generally located around 290 cm^{-1}; 340 and 620 cm^{-1}, while for ZnO the main modes are found around 380 cm^{-1} and 570 cm^{-1}. This is consistent with the results reported in the literatures [21,22].

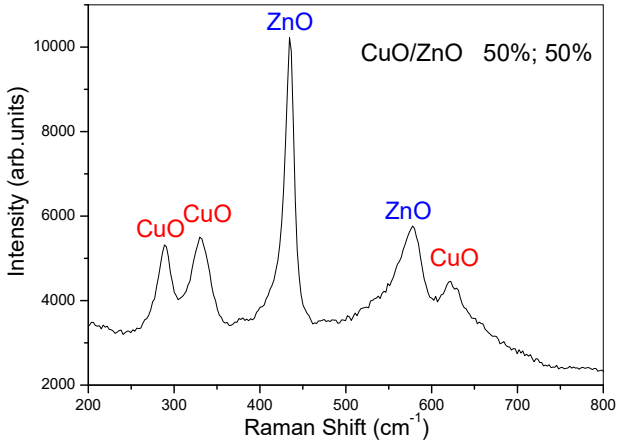

Figure 5. Raman shifts of CuO/ZnO thin films at T=550°C

3.3. Atomic force microscopy (AFM) characterization

In order to better measure the roughness of these samples, we based on the measurement of the factor of roughness RMS to the surface of the software WSxM software [32]. AFM analysis was carried out to observe the surface morphology of CuO/ZnO films. Fig. 6 shows the topographies of the CuO/ZnO thin films at T=550°C, the results of the analysis indicate the presence of islands with different shape, size and number. This is well described according to the "Volmer-Weber" mode i.e. the binding energy between metal ad-atom and substrate atoms is smaller than the binding energy between metal ad-atoms themselves, which leads over potential deposition (OPD) of a 3D metal forming on substrate. For the pulse CuO/ZnO thin films pro-duced with equimolar of precursor shows there is same roughness on the surface of the ordinary glass RMS=106 nm, which is suitable for the mechanism of photdegradation in the visible region (Figure 6). By way of comparison, Bünyamin Şahin et al [33] have obtained a roughness lower than found rms values of 60, and 23 nm for ZnO/CuO nanocomposite thin films synthesized by the SILAR (Successive Ionic Layer Adsorption and Reaction) method.

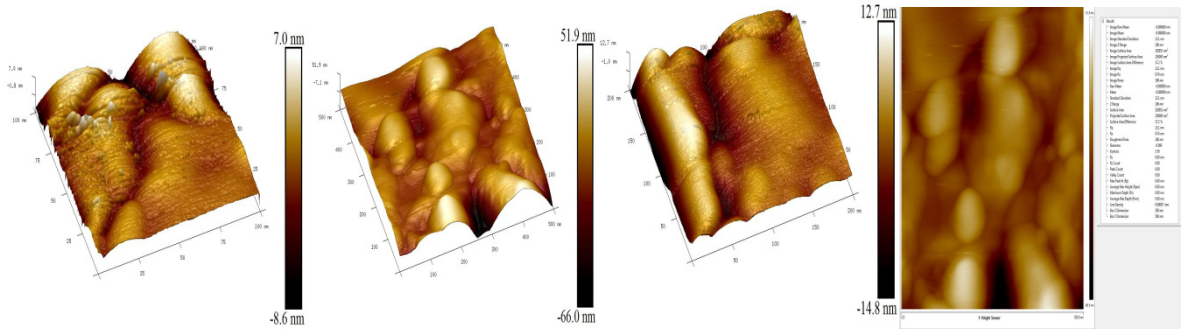

Figure 6. AFM image of CuO/ZnO thin films at T=550°C

3.4 SEM/EDS Characterization

From the Figure 7, we can see that there is a large heterogeneity of deposition on the surface with a nanometrical scale of particle; CuO is spherical form [20] and ZnO is rod with hexagonal form [34] which are suitable for the displacement of the electron from the valance band of CuO to the conductivity band of ZnO that favourite the photodegradation.

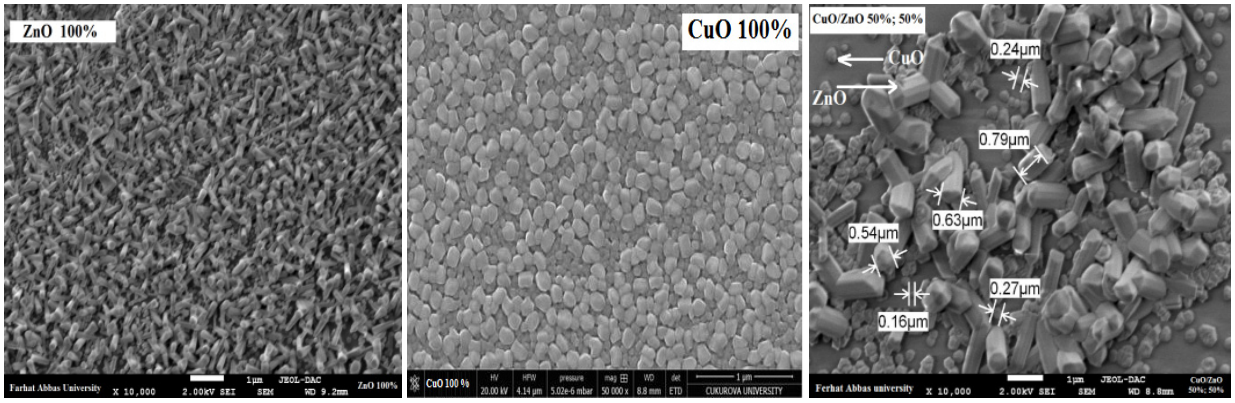

Figure 7. SEM images of CuO/ZnO thin films at T=550°C

In other hand, EDS characterization illustrate that all chemical elements of thin films on the surface of the substrate shows the presence of CuO/ZnO nonocomposite arrangement (Fig.8) [21, 22].

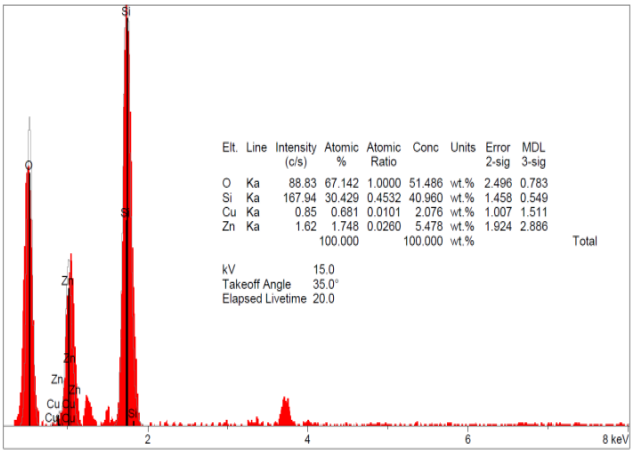

Figure 8. EDS result of CuO/ZnO thin films at T=550°C

4. CONCLUSIONS

This study has made it possible to meet the objectives set concerning the fast and cheap synthesis of CuO/ZnO thin films made with the Spray Pyrolysis Technique. Successful synthesis of thin films samples with the spray pyrolysis technical by different percentage of precursor solution of $CuCl_2$, $2H_2O$ and $ZnCl_2$,$2H_2O$, dissolved in distilled water, from the most important results obtained, it is possible to conclude that:

- The UV-Visible characterization shows that all thin films exhibit ultraviolet optical transmission.
- XRD, SEM/EDS and RAMAN characterization of CuO/ZnO nanocomposites confirm the presence of the various phase of CuO and ZnO and the crystallite size are at the nanometrical scale.

Finally, according to these results and compared with the literature CuO and ZnO are suitable for photodegradation of organic and inorganic pollutants. Several issues are still open for future investigation in order to fully understand the synthesis of CuO/ZnO thin films for photodegradation of pollutants. Hopefully, the results presented in this study gives a contribution to this understanding.

Aknowledgements

The authors gratefully acknowledge the support of the Directorate General for Scientific Research and Technological Development of Algeria (DGRSDT). The authors would like to thank Madame Meriem Nechadi from Laboratory of Energy and Solid-State Electrochemistry (L.E.E.S.), Department of Engineering Pro-cess, Faculty of Technology, Ferhat Abbas University Setif-1, Algeria for her help.

ORCID

Youcef Bellal, https://orcid.org/0000-0002-8280-9967; **Djamel Belfennache,** https://orcid.org/0000-0002-4908-6058

REFERENCES

[1] Z. Wang, J. Fan, Y. Zou, X. Fu, L. Shi, Y. Li, X. Ma, Opt. Commun. **577**, 131425 (2025). https://doi.org/10.1016/j.optcom.2024.131425.
[2] Y. Benkrima, D. Belfennache, R. Yekhlef, A. M. Ghaleb, Chalcogenide Lett. **20**(8). 609-618 (2023). DOI:10.15251/CL.2023.208.609.
[3] C. Cao, Y. He, Y. Liu, H. Huang, F. Zhang,Int. J. Prod. Econ.109496 (2024) https://doi.org/10.1016/j.ijpe.2024.109496.102829
[4] R.S. Foumani, E. Fatehifar, and T. Rajaee, Results in Chemistry. **13**, 101963 (2025), https://doi.org/10.1016/j.rechem.2024.101963
[5] Y. Benkrima, A. Achouri, D. Belfennache, R. Yekhlef, and N. Hocine, East Eur. J. Phys. **2**, 215 (2023), https://doi.org/10.26565/2312-4334-2023-2-23
[6] T.G. Gindose, T.B. Atisme, G. Gebreslassie, A.B. Gebresilassie, and E.A. Zereffa, Materials Advances, **5**(20), 8017 (2024). https://doi.org/10.1039/d4ma00357h
[7] S. Mahdid, D. Belfennache, D. Madi, M. Samah, R. Yekhlef, and Y. Benkrima, J. Ovonic. Res. **19**(5), 535 (2023). https://doi.org/10.15251/JOR.2023.195.535
[8] D. Belfennache, D. Madi, R. Yekhlef, L. Toukal, N. Maouche, M.S. Akhtar, S. Zahra. Semicond. Phys. Quantum Electron. Optoelectron.. **24(4).** 378-389 (2021). https://doi.org/10.15407/spqeo24.04.378
[9] R. Papitha, V. Hadkar, N.K. Sishu, S. Arunagiri, S.M. Roopan, and C.I. Selvaraj, Ceramics International, **50**(20), 39109 (2024). https://doi.org/10.1016/j.ceramint.2024.07.277
[10] S. Zaiou, O. Beldjebli, D. Belfennache, M. Tayeb, F. Zenikheri, and A. Harabi, Digest J. Nanomater. Biostruct. **18**(1), 69 (2023). https://doi.org/10.15251/DJNB.2023.181.69
[11] A. Pandey, P. Yadav, A. Fahad, P. Kumar, and M.K. Singh, Ceramics International, **50**(12)**,** 21417 (2024). https://doi.org/10.1016/j.ceramint.2024.03.253
[12] Z. Yin, Y. Zeng, D. Yang, Y. Jiao, J. Song, P. Hu, H. Fan, and F. Teng, Journal of Luminescence, **257**, 119762 (2023) https://doi.org/10.1016/j.jlumin.2023.119762
[13] R. Ouldamer, D. Madi, and D. Belfennache, in: Advanced Computational Techniques for Renewable Energy Systems. IC-AIRES 2022. edited by M. Hatti, Lecture Notes in Networks and Systems, **591**, 700 (2023). (Springer, Cham). https://doi.org/10.1007/978-3-031-21216-1_71
[14] A. Gebretsadik, B. Kefale, C. Sori, D. Tsegaye, H.C.A. Murthy, and B. Abebe, RSC Advances. **14**(41), 29763 (2024). https://doi.org/10.1039/d4ra05989a
[15] S-M. Lam, J-C. Sin, W.W. Tong, H. Zeng, H. Li, L. Huang, H. Lin, and J-W. Lim, Chemosphere, **344**, 140402 (2023). https://doi.org/10.1016/j.chemosphere.2023.140402
[16] Chitralekha, I. Maurya, T. Gupta, S. Shankar, S. Gaurav, V. Tuli, J. Shah, and R.K. Kotnala, Mater. Chem. Phys. **291**, 126690 (2022). https://doi.org/10.1016/j.matchemphys.2022.126690
[17] R. Ouldamer, D. Belfennache, D. Madi, R. Yekhlef, S. Zaiou, and M.A. Ali, J. Ovonic. Res. **20**(1), 45 (2024). https://doi.org/10.15251/JOR.2024.201.45
[18] C.V. Niveditha, M.J. Fatima, and S. Sindhu, J. Electrochem. Soc. **163**, H426 (2016). https://doi.org/10.1149/2.0971606jes
[19] K.E. Brown, and K.S. Choi, Chem. Commun. **31**, 3311 (2006). https://doi.org/10.1039/b604097g
[20] Y. Bellal, A. Bouhank, H. Serrar, T. Tüken, and G. Sığırcık, MATEC Web Conf. **253**, 03002 (2019). https://doi.org/10.1051/matecconf/201925303002
[21] Y. Bellal, and A. Bouhank, Int. J. Nanosci. **20**(03), 2150029 (2021). https://doi.org/10.1142/S0219581X21500290
[22] X. Zhao, P. Wang, and B. Li, Chemical Communications, **46**(36), 6768 (2010). https://doi.org/10.1039/c0cc01610a
[23] N. Abraham, and S. Aseena, Materials Today: Proceedings, **43**, 3698 (2021). https://doi.org/10.1016/j.matpr.2020.11.406
[24] X. Guo, W. Ju, Z. Luo, B. Ruan, K. Wu, and P. Li, Int. J. Hydrogen Energy, **98,** 1087 (2025). https://doi.org/10.1016/j.ijhydene.2024.12.117
[25] P. Mahajan, A. Singh, and S. Arya, J. Alloys Compd. **814**, 152292 (2020). https://doi.org/10.1016/j.jallcom.2019.152292
[26] M.N. Najah, F.A. Rahmania, I. Cahyanti, M. Hesnaty, S.H. Alias, D. Hartanto, W.P. Utomo, *et al*., Afr. J. Chem. Eng. **51**, 188 (2025). https://doi.org/10.1016/j.sajce.2024.11.009
[27] A. Bouhank, and Y. Bellal, J. Nano Res. **69**, 23 (2021). https://doi.org/10.4028/www.scientific.net/JNanoR.69.23
[28] B.D. Cullity, in: *Elements of X-ray Diffraction*, (Addison and Wesley Publishing Company Inc. Reading, USA). pp. 32-106 (1978).
[29] D. Saravanakkumar, H.A. Oualid, Y. Brahmi, A. Ayeshamariam, M. Karunanaithy, A.M. Saleem, K. Kaviyarasu, *et al*., OpenNano, **4**, 100025 (2019). https://doi.org/10.1016/j.onano.2018.11.001
[30] M. Alrefaee, U.P. Singh, and S.K. Das, J. Phys.: Conf. Ser. **1973**(1), 012069 (2021). https://doi.org/10.1088/1742-6596/1973/1/012069

[31] D.M. Jundale, P.B. Joshi, S. Sen, and V.B. Patil, J. Mater. Sci.: Mater. Electron. **23**, 1492 (2012). https://doi.org/10.1007/s10854-011-0616-2
[32] I. Horcas, R. Fernández, J.M. Gomez-Rodriguez, J. Colchero, J. Gómez-Herrero; and A.M. Baro, Rev. Sci. Instrum. **78**(1), 013705 (2007). https://doi.org/10.1063/1.2432410
[33] B. Şahin, and T. Kaya, Mater. Sci. Semicond. Process, **121**, 105428 (2021). https://doi.org/10.1016/j.mssp.2020.105428
[34] N.D. Dien, Adv. Mater. Sci. **4**, 1 (2019). https://doi.org/10.15761/AMS.1000147

ШВИДКИЙ ТА ДЕШЕВИЙ СИНТЕЗ ТОНКІХ ПЛІВОК CuO/ZnO, ВИГОТОВЛЕНИХ ЗА МЕТОДИКОЮ СПРЕЄВОГО ПІРОЛІЗУ

Ю. Беллал, А. Буханк, Д. Бельфенаше, Р. Єхлеф
Науково-дослідний центр промислових технологій CRTI, Черага, Алджер, Алжир

У цій статті було розроблено тонкі плівки нанокомпозитів CuO/ZnO з різним співвідношенням комбінацій прекурсорів (хлорид міді, хлорид цинку), розчинених у дистильованій воді методом розпилювального піролізу з метою вивчення їх фізико-хімічних властивостей. Нанокомпозити були розроблені у вигляді тонких плівок, нанесених на поверхню звичайного скла при 550°C за допомогою дешевшої та швидкої техніки. Оптичні, структурні та морфологічні властивості останнього були досліджені методами УФ-виділення, дифракції рентгенівських променів (XRD), раманівського розсіювання, SEM/EDS та AFM. XRD-піки доводять присутність полікристалічних моделей CuO та ZnO з переважною орієнтацією. Спектр комбінаційного зсуву підтверджує присутність нанокомпозитів CuO та ZnO. SEM/EDS та AFM підтверджують, що на поверхні звичайного скла є однакова шорсткість RMS=106 нм, яка підходить для механізму фотодеградації. У видимій області ми помічаємо високе поглинання та великі оптичні заборонені зони (Egap= 4,07 еВ), що підходить для фотодеградації небажаних речовин.

Ключові слова: *спрей-піроліз; CuO/ZnO; тонкі плівки; прекурсор; RAMAN; фотодеградація*

EAST EUROPEAN JOURNAL OF PHYSICS. 1. 177-183 (2025)
DOI:10.26565/2312-4334-2025-1-17 ISSN 2312-4334

IMPACT OF RESISTIVITY ON ELECTRICAL CHARACTERISTICS OF Al-DOPED ZnO/p-Si HETEROSTRUCTURES

Fakhriddin T. Yusupov*, Mekhriddin F. Akhmadjonov, Dadakhon Sh. Khidirov, Dilmuhammad Kh. Tolaboyev, Ikhtiyor M. Tursunov
Fergana Polytechnic Institute, Fergana, Uzbekistan
**Corresponding Author e-mail: yusupov.fizika@gmail.com*
Received October 2, 2024; revised December 15, 2024; accepted January 7, 2025

This study investigates the impact of the resistivity of Aluminum-doped Zinc Oxide (AZO) films on the electrical characteristics of AZO/p-Si heterojunctions. AZO films were deposited using a thermal evaporation technique on p-Si substrates, with varying deposition temperatures to control film morphology and resistivity. Comprehensive current-voltage (I-V) and capacitance-voltage (C-V) measurements were conducted to evaluate the diode performance and interface state dynamics. The results show that samples with higher resistivity, particularly those deposited at room temperature (S1 and S2), exhibit MOS-like behavior, indicating higher concentrations of interface states and defects. In contrast, samples deposited at elevated temperatures (S3, S4, and S5) demonstrate improved diode characteristics, with lower resistivity, enhanced carrier mobility, and better crystalline quality. Mott-Schottky and capacitance-frequency (C-f) analyses further reveal the significant role of interface states in determining the heterojunction's electrical response, especially at lower frequencies where charge trapping dominates. Additionally, photoluminescence (PL) spectra confirm the presence of oxygen vacancies in the AZO films, with strong visible emission observed in S1 and S2, linked to deep-level defect states. This work highlights the critical influence of deposition conditions on the resistivity and performance of AZO films in heterojunction-based optoelectronic devices, offering valuable insights into optimizing material properties for improved device efficiency.
Keywords: *AZO films; Resistivity; p-Si heterojunction; I-V characteristics; C-V characteristics; Mott-Schottky analysis; Interface states; Photoluminescence (PL) spectra; Oxygen vacancies; Thermal evaporation; Charge trapping*
PACS: 78.20.-e, 73.61.Ga, 85.60.-q, 68.55.-a

INTRODUCTION

Aluminum-doped Zinc Oxide (AZO) films have garnered significant attention in recent years due to their versatile electrical and optical properties, making them suitable for various optoelectronic applications such as transparent conducting electrodes, photodetectors, and solar cells [1,2]. The combination of low resistivity, high optical transparency, and chemical stability has made AZO a compelling alternative to conventional transparent conductive oxides (TCOs) such as Indium Tin Oxide (ITO), especially considering the abundance and lower cost of zinc compared to indium.

The performance of AZO films in heterojunction-based devices, however, is highly sensitive to their resistivity, which is influenced by deposition conditions, doping concentration, and the film's crystalline quality. In particular, the resistivity of AZO films directly affects the interface properties between the AZO layer and the silicon (p-Si) substrate in heterojunction structures [3]. High-resistivity AZO films tend to introduce more interface states and defects, such as oxygen vacancies, which can trap charge carriers and hinder device performance by promoting non-radiative recombination. Conversely, lower-resistivity films typically result in improved electrical characteristics, including enhanced carrier mobility and reduced recombination losses, making them more suitable for high-efficiency devices.

Previous studies have explored the structural, electrical, and optical properties of AZO films in various device architectures, but limited work has focused on the direct correlation between film resistivity and the electrical behavior of AZO/p-Si heterojunctions. Understanding how resistivity influences the current-voltage (I-V) and capacitance-voltage (C-V) characteristics, as well as the role of interface states, is crucial for optimizing the performance of these heterojunctions.

This study aims to systematically investigate the effects of AZO film resistivity on the I-V and C-V characteristics of AZO/p-Si heterojunctions. By varying the deposition conditions of the AZO films, we were able to tailor their resistivity and evaluate the corresponding changes in electrical behavior. In addition, photoluminescence (PL) spectra were measured to analyze the presence of defect states, particularly oxygen vacancies, which are known to influence the material's optoelectronic properties. The results of this study provide valuable insights into optimizing the deposition process to enhance the performance of AZO-based heterojunctions for advanced optoelectronic applications [2,3].

EXPERIMENTAL DETAILS

Substrate Preparation and Cleaning. The experimental process began with the meticulous preparation of p-type silicon (p-Si) substrates. These substrates were subjected to a rigorous cleaning process involving sequential immersions in deionized water, a mixture of hydrogen peroxide (H_2O_2), and ammonium hydroxide (NH_4OH), followed by a thorough rinse. A second cleaning phase with a solution of hydrogen peroxide and hydrochloric acid (HCl) was applied to ensure

Cite as: F.T. Yusupov, M.F. Akhmadjonov, D.Sh. Khidirov, D.Kh. Tolaboyev, I.M. Tursunov, East Eur. J. Phys. 1, 177 (2025), https://doi.org/10.26565/2312-4334-2025-1-17

the removal of all contaminants [5,7]. This step was critical for achieving a pristine surface, essential for high-quality film deposition and effective heterojunction formation.

Film Deposition. Aluminum-doped Zinc Oxide (AZO) films were deposited using a thermal evaporation technique. A blend of high-purity zinc oxide (ZnO) powder and aluminum (Al), with a doping concentration of 2%, was prepared and placed in a tungsten boat within the evaporation chamber. The chamber was evacuated to a base pressure of 10^{-5} mmHg to ensure a contaminant-free environment. The mixture was then heated to 1753 K, allowing the ZnO and Al to evaporate and deposit on the prepared substrates under a controlled atmosphere of 16 mTorr oxygen. The deposition process was carefully monitored with a quartz crystal microbalance to maintain the film thickness between 100 nm and 150 nm.

Contact Formation and Structural Analysis. Following deposition, aluminum was evaporated onto the reverse side of the p-Si substrates to serve as the bottom contact. On the top side, gold contacts were defined in two areas, 0.01 cm^2 and 0.5 cm^2, to establish the top contacts for the heterojunction. The structural and morphological properties of the AZO films were then characterized using scanning electron microscopy (SEM) and atomic force microscopy (AFM), providing detailed insights into surface topography and film uniformity.

Electrical Characterization. The resistivity, carrier mobility, and concentration of the AZO films were measured using a Hall effect measurement system, which provided detailed insights into the electronic properties of the films. The four-point probe method was utilized to assess the resistivity and doping concentration of the p-Si substrates.

Electrical and Optical Measurements. Comprehensive electrical characterization was performed under dark conditions to avoid light-induced effects. Current-voltage (I-V), capacitance-voltage (C-V), and capacitance-frequency (C-f) measurements were carried out using a semiconductor parameter analyzer. These tests were crucial for evaluating the heterojunction's electrical behavior under various electrical biases, ranging from −5 V to 5 V.

Finally, the optical properties of the AZO films were analyzed using photoluminescence spectroscopy. An Avantes spectrometer, equipped with a 266 nm laser as the excitation source, was used to examine the energy band structure and defect states within the films. This structured approach, employing state-of-the-art techniques, ensured the high fidelity of the data collected, which is essential for understanding the effects of AZO film resistivity on the electrical characteristics of AZO/p-Si heterojunctions.

RESULTS AND DISCUSSION

The electrical and optical properties of the AZO/p-Si heterojunction samples were investigated through I-V, C-V, and photoluminescence (PL) measurements. These analyses allowed for the evaluation of the effects of AZO film resistivity on diode performance and the role of interface states in determining the overall device characteristics. The results, presented below, highlight the significant influence of deposition conditions and material resistivity on the heterojunction behavior [6].

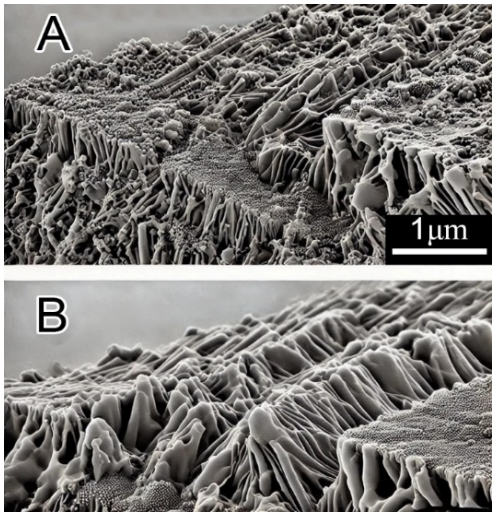

Figure 1. Surface morphology of AZO thin films at different deposition temperatures

Figure 1. Shows the surface morphology of Aluminum-doped Zinc Oxide (AZO) thin films deposited at two distinct substrate temperatures: room temperature and 573 K.

- (A) AZO deposited at room temperature: the surface morphology of the AZO film deposited at room temperature displays a rough surface with relatively smaller grains. The lack of thermal energy limits the mobility of adatoms on the substrate, leading to a highly textured, disordered structure. Grain boundaries are more pronounced, and the overall roughness is higher, reflecting the insufficient crystallinity development at lower temperatures.

- (B) AZO deposited at 573 K: In contrast, the AZO film deposited at 573 K demonstrates a smoother surface with larger, well-defined grains. The increased substrate temperature allows for greater adatom mobility, promoting improved

crystalline growth. This results in larger grain sizes and a more uniform surface morphology, indicative of enhanced crystallization. The smoother surface correlates with a decrease in surface roughness and improved film quality.

Scale bar: each image contains a 1 μm scale bar, providing reference for the relative size of the surface features. The significant difference in grain size and surface smoothness between the two deposition conditions highlights the role of substrate temperature in controlling the physical properties of AZO thin films. At higher temperatures, the films exhibit enhanced structural characteristics, which can influence their electrical and optical performance in semiconductor applications.

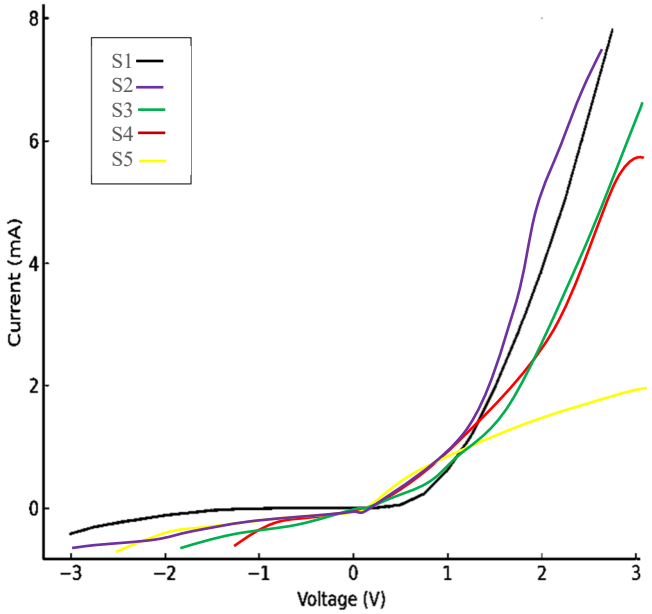

Figure 2. Current-Voltage (I-V) characteristics of AZO/p-Si heterojunction samples S1–S5

The I-V characteristics presented in Figure 2 show case the impact of deposition conditions and resistivity variations in AZO/p-Si heterojunctions for samples S1, S2, S3, S4, and S5. These samples exhibit distinct differences in electrical performance due to the resistivity and morphology of the AZO films, as well as the deposition temperatures used during fabrication. S1 and S2 have significantly higher resistivity compared to S3, S4, and S5. The resistivity ranges from 10^{-3} Ω *cm* for S5 to 10^{-3} Ω *cm* for S1. Higher resistivity in S1 and S2 results from room-temperature deposition, which limits atomic mobility and hinders film crystallinity. In contrast, S3 to S5 were deposited at elevated temperatures, reducing resistivity and improving electrical conductivity due to better atomic arrangement and crystallization. Also, S1 and S2 were deposited at room temperature, leading to higher resistivity and smaller grain size. The lower deposition temperature restricts atomic movement, causing smaller, less ordered grains and higher surface roughness. S3, S4, and S5 were deposited at progressively higher temperatures, reaching up to 573 K. This increase in substrate temperature improves the crystalline quality of the AZO films, leading to larger grain sizes and smoother surfaces. Consequently, their resistivity is lower, and they exhibit better electrical characteristics. Samples S1 and S2 exhibit smaller grain sizes and rougher surfaces, contributing to their higher resistivity and poorer electrical performance. Samples S3, S4, and S5 show larger grains and smoother surfaces due to the higher deposition temperatures. These morphological improvements correlate with lower resistivity and better carrier mobility, resulting in improved diode characteristics [8-10].

The I-V curves (Figure 2.) for S1 and S2 indicate MOS-like behavior, particularly in the reverse-bias region, where the films act as insulating layers. This is due to the higher resistivity of the AZO films in these samples, which inhibits current flow even under forward bias. S3, S4, and S5 exhibit typical p-n junction behavior, with lower resistivity and higher carrier mobility. These samples show a steep increase in current once the forward bias exceeds the built-in potential, indicative of efficient diode behavior. The built-in potential (V_{bi}) varies across the samples, with S3, S4, and S5 showing values closer to typical n-ZnO/p-Si heterojunctions, while S1 and S2 exhibit larger V_{bi} values due to their MOS-like characteristics. The I-V curves (Figure 2.) reveal several distinct characteristics across the five samples:

- S1 and S2 exhibit a delayed onset of current in the forward bias region, indicating higher resistivity and MOS-like behavior. Their reverse current remains near zero, with S1 showing slightly higher leakage current, possibly due to defects or interface states.
- S3, S4, and S5 show more typical p-n junction diode behavior, with lower threshold voltages and steeper slopes in the forward bias region. This reflects lower resistivity and better carrier mobility.
- S5 has the lowest current values in the positive voltage region, indicating it has the highest resistivity among the lower-temperature deposited samples.

The variations in deposition conditions, particularly substrate temperature and laser fluence, directly affect the resistivity, morphology, and I-V characteristics of AZO/p-Si heterojunctions. S1 and S2, deposited at room temperature,

display MOS-like behavior with higher resistivity and poor diode performance, while S3, S4, and S5, deposited at higher temperatures, exhibit better diode characteristics due to lower resistivity, improved film morphology, and higher carrier mobility. These findings highlight the crucial role of deposition conditions in optimizing the performance of AZO-based heterojunctions for semiconductor applications.

The Mott-Schottky analysis, a cornerstone in semiconductor diagnostics, allows for the detailed investigation of junction properties through the assessment of the space charge capacitance across semiconductor interfaces. Figure 3 exemplifies this approach by depicting the inverse square of the capacitance ($1/C^2$) as a function of applied voltage (V), thereby facilitating a quantitative analysis of the semiconductor's doping density and flat-band potential [11]. The capacitance (C) in the depletion region of a semiconductor can be expressed by the equation:

$$C = \frac{\epsilon A}{W}$$

where ϵ-represents the permittivity of the semiconductor, A - the cross-sectional area of the junction, and W - the width of the depletion layer. The Mott-Schottky plot (Figure 3) utilizes this relationship, presenting ($1/C^2$) plotted against the applied voltage for samples S1, S2, and S3, each corresponding to different experimental conditions or semiconductor materials.

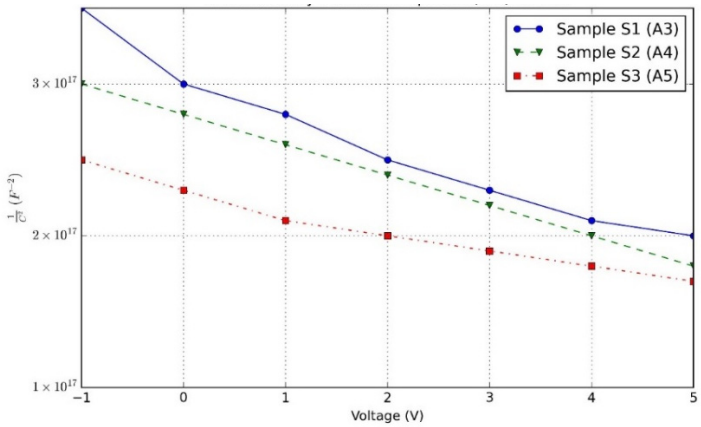

Figure 3. Mott-Schottky analysis of semiconductor junctions: Capacitance-Voltage characteristics for samples S1, S2, and S3

From the slopes and intercepts of these plots, critical semiconductor parameters are derived. For instance, the slope (m) of these plots, calculated from the linear fit to the data, is inversely proportional to the doping concentration (N_D) and is given by:

$$m = \frac{2}{q\epsilon N_D}$$

Here, q denotes the elementary charge (approximately 1.602×10^{-19} Coulombs). Suppose the slope from the plot for Sample S1 is $5\times10^{16}F^{-2}V^{-1}$, applying the semiconductor permittivity for silicon ($\epsilon_{Si} \approx 11.7 \times \epsilon_0$), one can calculate the doping concentration N_D as follows [12]:

$$N_D = \frac{2}{q \times \epsilon_{Si} \times m} \approx \frac{2}{1.602 \times 10^{-19} \times 11.7 \times 8.854 \times 10^{-12} \times 5 \times 10^{16}} \approx 7.38 \times 10^{15} cm^{-3}$$

Additionally, the flat-band potential (V_{FB}) is determined from where the plot intercepts the voltage axis, indicating the voltage at which the semiconductor's internal electric fields are neutralized, leading to no band bending. Accurate determination of is V_{FB} crucial for understanding the intrinsic electronic properties of the material. This detailed characterization using the Mott-Schottky plot not only enhances our understanding of semiconductor physics but also supports the development of semiconductor devices by providing a method to precisely control material properties based on their doping characteristics [13-15].

In AZO/p-Si heterojunctions, the Mott-Schottky analysis helps to assess the quality of the interface and the doping uniformity of the AZO layer. Samples with higher resistivity (such as S1) show more pronounced deviations due to higher defect densities and interface states, while those with lower resistivity (such as S3) demonstrate improved junction properties with lower interface state densities. Figure 3. Mott-Schottky plots ($1/C^2$ vs. V) for AZO/p-Si heterojunction samples S1, S2, and S3. The slopes of the linear regions are inversely proportional to the doping concentrations, revealing that Sample S1 has the lowest doping density while Sample S3 has the highest. The x-intercepts correspond to the flat-band potentials (V_{FB}), indicating variations in built-in potentials due to differences in resistivity and interface state densities. Deviations from linearity in the high-resistivity samples (S1 and S2) suggest a higher concentration of interface states and trap levels, which degrade the junction performance.

Figure 4 illustrates the capacitance-frequency (C-f) characteristics of the AZO/p-Si heterojunction samples (S1 to S5) measured at zero bias, across the frequency range from 1 kHz to 1 MHz. The C-f plot provides insight into the influence of interface states and the overall electrical behavior of the heterojunctions. At lower frequencies (1 kHz), the capacitance density is highest for samples S1 and S2. This can be attributed to the significant contribution of interface states, which are able to follow the low-frequency AC signal. The high capacitance at low frequencies suggests that interface states are readily available and contribute to charge accumulation. As the frequency increases, the ability of these interface states to respond diminishes due to their finite trap times, resulting in a general decrease in capacitance for all samples.

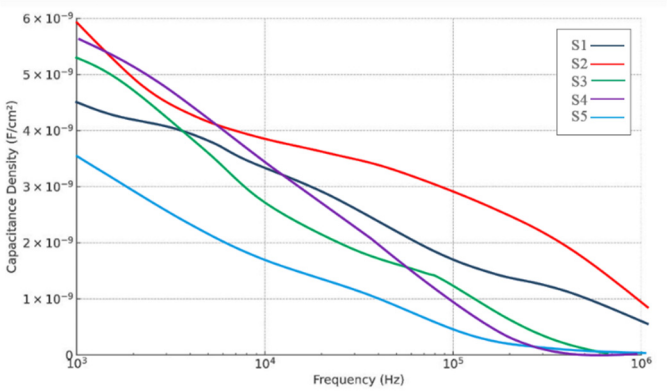

Figure 4. Capacitance-frequency characteristics of AZO/p-Si heterojunctions at Zero Bias

The capacitance decrease is more pronounced in samples S3, S4, and S5, indicating fewer or less responsive interface states. These samples show more typical behavior of a p-n junction, where the depletion capacitance dominates at higher frequencies, and the contribution from interface states becomes negligible. Conversely, samples S1 and S2 exhibit a "shoulder" between 10 kHz and 100 kHz, which points to the presence of faster interface states that can still respond to higher-frequency signals. The distinct behavior of S1 and S2 across the frequency range can be explained by a higher density of interface states with shorter trap times, which are still active at high frequencies. At 1 MHz, these samples retain higher capacitance values compared to S3, S4, and S5. This suggests that even at high frequencies, some interface states in S1 and S2 are still capable of following the AC signal, indicating a high concentration of these states at the AZO/p-Si interface. In contrast, the capacitance of samples S3, S4, and S5 continues to decrease as frequency increases, indicating that these samples are dominated by depletion capacitance at high frequencies, with a minimal contribution from interface states. This is consistent with a lower interface state density, likely due to differences in deposition conditions or structural variations between the samples. The C-f behavior observed in Figure 4 is crucial for evaluating the quality of the AZO/p-Si heterojunctions, particularly in terms of interface state density and their impact on device performance. Interface states can introduce charge trapping and detrapping effects, which influence the overall capacitance, especially at lower frequencies. Therefore, understanding and controlling these states is critical for optimizing the electrical properties of heterojunction-based devices such as photodetectors and solar cells. Samples S1 and S2, which were deposited at room temperature, display higher resistivity and a more pronounced MOS-like response, suggesting higher interface state densities. In contrast, the lower capacitance at higher frequencies for samples S3, S4, and S5 indicates more typical p-n junction behavior with fewer active interface states. These variations in capacitance-frequency characteristics can be correlated with structural differences, such as grain size and resistivity, between the samples. Figure 4 highlights the importance of interface state dynamics in the capacitance response of AZO/p-Si heterojunctions. The observed frequency-dependent behavior provides valuable information for optimizing the deposition process and interface quality in order to enhance the performance of semiconductor devices. By tailoring the interface state density and improving material quality, the electrical properties of heterojunction-based optoelectronic devices can be significantly improved, leading to better device efficiency and reliability.

Figure 5 presents the photoluminescence (PL) spectra of samples S1 through S5, measured in the wavelength range of 300 nm to 700 nm. The intensity of the PL emission provides critical insights into the defect states, optical transitions, and material quality of the samples. The PL spectra for samples S1 and S2 exhibit prominent peaks around 520–550 nm, corresponding to visible luminescence. This emission is typically associated with oxygen-related defects in ZnO or AZO materials, specifically ionized oxygen vacancies (Vo^{+}). These mid-gap states, located within the bandgap, contribute to green luminescence through non-radiative recombination pathways. The higher intensity of these peaks in S1 and S2 suggests a higher concentration of such defects, which act as deep-level traps for charge carriers.

Samples S3, S4, and S5 display much lower PL intensities across the entire wavelength range, with only minor oscillations around a baseline intensity. This indicates a significantly lower defect density in these samples, which results in reduced non-radiative recombination. The weak PL intensity is a sign of improved material quality, particularly in terms of fewer oxygen vacancies or other defects that contribute to visible light emission [16]. The broad green emission centered around 520–550 nm for S1 and S2 aligns with the photon energy of ~2.4 eV, which corresponds to the recombination of electrons and holes trapped at oxygen vacancies. The intensity of this green emission typically reflects

the number of recombination centers in the material. For S3, S4, and S5, the lack of significant visible emission suggests fewer recombination centers and a higher degree of crystallinity.

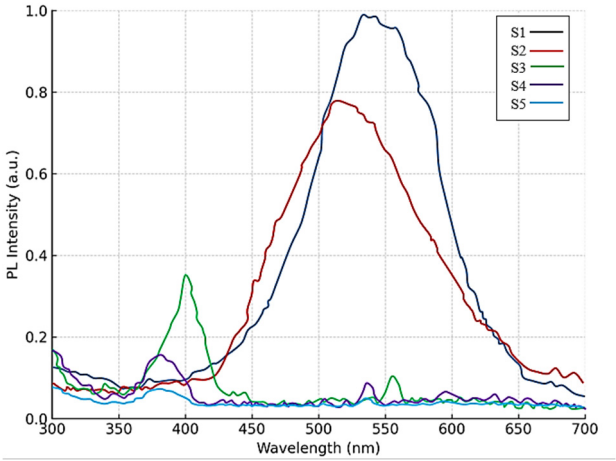

Figure 5. Photoluminescence (PL) spectra of S1 to S5 samples: defect states and optical transitions

The sharp and high-intensity PL peaks in S1 and S2 are indicative of a higher concentration of defect states, which could impair the electrical properties of these samples. In contrast, the lower and more stable PL response in S3, S4, and S5 suggests better crystalline quality, leading to enhanced carrier mobility and fewer trapping events. This makes S3, S4, and S5 more suitable for applications requiring high-quality semiconductor films with fewer defects, such as photodetectors or optoelectronic devices. The visible green emission observed in S1 and S2 is often linked to deep-level defects within the material. Oxygen vacancies, in particular, play a significant role in this emission. These vacancies create defect levels within the bandgap, allowing for non-radiative recombination of charge carriers, which contributes to the green luminescence. The higher defect density in S1 and S2 correlates with lower carrier mobility and higher resistivity, as carriers become trapped at these defect sites. Samples S3, S4, and S5, with their low PL intensity, demonstrate better structural integrity and reduced defect-related recombination. This lower defect density results in improved optoelectronic properties, making these samples more ideal for high-efficiency devices. The PL spectra in this graph highlight the role of defect states, particularly oxygen vacancies, in determining the optical and electronic properties of the samples [17,18]. The strong visible emissions in S1 and S2 suggest a high concentration of defects, while the weak emissions in S3, S4, and S5 point to better material quality. This information is critical for optimizing the performance of ZnO or AZO-based heterojunctions, with S3, S4, and S5 showing greater potential for high-performance optoelectronic applications.

CONCLUSIONS

This study comprehensively analyzed the effects of AZO film resistivity on the electrical and optical properties of AZO/p-Si heterojunctions. Through detailed I-V, C-V, and photoluminescence (PL) measurements, it was demonstrated that the resistivity of the AZO films plays a critical role in determining the diode performance, particularly in terms of carrier transport, interface state density, and defect-related recombination. Samples with higher resistivity, such as S1 and S2, exhibited higher concentrations of interface states and oxygen vacancies, leading to increased leakage currents, higher turn-on voltages, and strong mid-gap emission in the PL spectra. In contrast, samples with lower resistivity, such as S3, S4, and S5, showed improved electrical characteristics with lower turn-on voltages, reduced reverse leakage, and diminished PL intensity, indicating fewer defects and better crystallinity.

The study underscores the importance of optimizing the deposition conditions, particularly the substrate temperature, to control the resistivity and defect density of AZO films. These findings offer valuable insights for the development of high-performance AZO/p-Si heterojunction-based optoelectronic devices, where the careful tuning of film resistivity is essential for enhancing device efficiency and stability [19].

ORCID

Fakhriddin T. Yusupov, https://orcid.org/0000-0001-8937-7944
Mekhriddin F. Akhmadjonov, https://orcid.org/0000-0002-1623-0404
Dadakhon Sh. Khidirov, https://orcid.org/0000-0003-1391-4250
Dilmuhammad Kh. Tolaboyev, https://orcid.org/0000-0001-6248-845X
Ikhtiyor M. Tursunov, https://orcid.org/0009-0009-0864-2204

REFERENCES

[1] R.A. Antwi, I. Nkrumah, F.K. Ampong, M. Paal, R.Y. Tamakloe, R.K. Nkum, and F. Boakye, "Synthesis of Pure and Manganese Doped Zinc Oxide Nanoparticles by a Solution Growth Technique: Structural and Optical Investigation," East European Journal of Physics, (4), 129-136 (2023). https://doi.org/10.26565/2312-4334-2023-4-13

[2] Z.X. Mirzajonov, K.A. Sulaymonov, T.I. Rakhmonov, F.T. Yusupov, D.SH. Khidirov, and J.S. Rakhimjonov, "Advancements in Zinc Oxide (ZnO) thin films for photonic and optoelectronic applications: a focus on doping and annealing processes," E3S Web of Conferences, **549**, 03013 (2024). https://doi.org/10.1051/e3sconf/202454903013
[3] R. Pietruszka, R. Schifano, T.A. Krajewski, B.S. Witkowski, K. Kopalko, L. Wachnicki, and E. Zielony, "Improved efficiency of n-ZnO/p-Si based photovoltaic cells by band offset engineering," Solar Energy Materials and Solar Cells, **147**, 164-170 (2016). https://doi.org/10.1016/j.solmat.2015.12.018.
[4] N. Sultanov, Z. Mirzajonov, and F. Yusupov, "Technology of production and photoelectric characteristics of AlB 10 heterojunctions based on silicon," E3S Web of Conferences, **458**, 01013 (2023). https://doi.org/10.1051/e3sconf/202345801013
[5] N.A. Sultanov, Z.X. Mirzajonov, F.T. Yusupov, and T.I. Rakhmonov, "Nanocrystalline ZnO Films on Various Substrates: A Study on Their Structural, Optical, and Electrical Characteristics," East European Journal of Physics, (2), 309-314 (2024). https://doi.org/10.26565/2312-4334-2024-2-35
[6] K.H. Kong, R. Kek, T.Y. Tou, and S.S. Yap, "Effects of the resistivity of AZO film on the IV and CV characteristics of AZO/p-Si heterojunction," Microelectronic Engineering, **213**, 24-30 (2019). https://doi.org/10.1016/j.mee.2019.04.011
[7] S. Erat, A. Braun, S. Çetinkaya, S. Yıldırımcan, A.E. Kasapoglu, E. Gür, E. Harputlu, K. Ocakoglu, "Solution-Processable Growth and Characterization of Dandelion-like ZnO:B Microflower Structures," Crystals, **12**(1), 11 (2021). https://doi.org/10.3390/cryst12010011
[8] M. Sharmin, and A.H. Bhuiyan, "Modifications in structure, surface morphology, optical and electrical properties of ZnO thin films with low boron doping," Journal of Materials Science: Materials in Electronics, **30**(5), 4867-4879 (2019). https://doi.org/10.1007/S10854-019-00781-8
[9] A. Roy, and M. Benhaliliba, "Investigation of ZnO/p-Si heterojunction solar cell: Showcasing experimental and simulation study," Optik, **274**, 170557 (2023). https://doi.org/10.1016/j.ijleo.2023.170557.
[10] Mohammad-Reza Zamani-Meymian, Nima Naderi, Maryam Zareshahi, Improved n-ZnO nanorods/p-Si heterojunction solar cells with graphene incorporation, Ceramics International, **48**(23), 34948-34956 (2022). https://doi.org/10.1016/j.ceramint.2022.08.084
[11] F.T. Yusupov, T.I. Rakhmonov, M.F. Akhmadjonov, M.M. Madrahimov, and S.S. Abdullayev, "Enhancing ZnO/Si Heterojunction Solar Cells: A Combined Experimental And Simulation Approach," East European Journal of Physics, (3), 425-434 (2024). https://doi.org/10.26565/2312-4334-2024-3-51
[12] D. Das, and L. Karmakar, "Optimization of Si doping in ZnO thin films and fabrication of n-ZnO:Si/p-Si heterojunction solar cells," Journal of Alloys and Compounds, **824**, 153902 (2020). https://doi.org/10.1016/j.jallcom.2020.153902
[13] S. Karakaya, "Effect of fluorine and boron co-doping on ZnO thin films: Structural, luminescence properties, and Hall effect measurements," Journal of Materials Science: Materials in Electronics, **29**, 1628-1638 (2018). https://doi.org/10.1007/s10854-017-8352-x
[14] N.M. Nemma, and Z.S. Sadeq, "Eco-Friendly Green Synthesis and Photocatalyst Activity of Ag-ZnO Nanocomposite," East European Journal of Physics, (3), 271-278 (2023). https://doi.org/10.26565/2312-4334-2023-3-24
[15] M.A. Shafi, S. Bibi, M.M. Khan, H. Sikandar, F. Javed, H. Ullah, L. Khan, and B. Mari, "A Numerical Simulation for Efficiency Enhancement of CZTS Based Thin Film Solar Cell Using SCAPS-1D," East European Journal of Physics, (2), 52-63 (2022). https://doi.org/10.26565/2312-4334-2022-2-06
[16] I. Kanmaz, "Simulation of CdS/p-Si/p+-Si and ZnO/CdS/p-Si/p+-Si heterojunction solar cells," Results in Optics, **10**, 100353 (2023). https://doi.org/10.1016/j.rio.2023.100353
[17] S. Maqsood, Z. Ali, K. Ali, M. Ishaq, M. Sajid, A. Farhan, A. Rahdar, and S. Pandey, "Assessment of different optimized anti-reflection coatings for ZnO/Si heterojunction solar cells," Ceramics International, **49**(23), 37118-37126 (2023). https://doi.org/10.1016/j.ceramint.2023.08.313
[18] S. Maity, and P.P. Sahu, "Efficient Si-ZnO-ZnMgO heterojunction solar cell with alignment of grown hexagonal nanopillar," Thin Solid Films, **674**, 107-111 (2019). https://doi.org/10.1016/j.tsf.2019.02.007
[19] Q. Yu, H. Zhao, and Y. Zhao, "The study of optical-electrical properties of ZnO(AZO)/Si heterojunction," Current Applied Physics, **57**, 111-118 (2024). https://doi.org/10.1016/j.cap.2023.11.008

ВПЛИВ ОПОРУ НА ЕЛЕКТРИЧНІ ХАРАКТЕРИСТИКИ ГЕТЕРОСТРУКТУР Al-ЛЕГОВАНОГО ZnO/p-Si

Фахріддін Т. Юсупов, Мехріддін Ф. Ахмаджонов, Дадахон Ш. Хідіров, Ділмухаммад Х. Толабоєв, Іхтіор М. Турсунов
Ферганський політехнічний інститут, Фергана, Узбекистан

Це дослідження вивчає вплив питомого опору плівок оксиду цинку з домішками алюмінію (AZO) на електричні характеристики AZO/p-Si гетеропереходів. Плівки AZO були осаджені методом термічного випаровування на підкладках з p-Si, причому температура осадження змінювалася для регулювання морфології плівок та їхнього питомого опору. Для оцінки роботи діода та динаміки станів на межі розділу були проведені комплексні вимірювання струмо-напругових (I-V) та ємнісно-напругових (C-V) характеристик. Результати показали, що зразки з вищим питомим опором, особливо ті, що були осаджені при кімнатній температурі (S1 та S2), демонструють поведінку, подібну до МОН-структур, що вказує на підвищену концентрацію станів на межі розділу та дефектів. Натомість зразки, осаджені при підвищених температурах (S3, S4 та S5), демонструють покращені характеристики діода з меншим питомим опором, підвищеною рухливістю носіїв заряду та кращою кристалічною якістю. Аналізи Мотта-Шотткі та ємнісно-частотні (C-f) вимірювання також виявили значну роль станів на межі розділу у визначенні електричного відгуку гетероперехоту, особливо на низьких частотах, де переважає захоплення заряду. Крім того, спектри фотолюмінесценції (PL) підтверджують наявність кисневих вакансій у плівках AZO, з сильним видимим випромінюванням, що спостерігається у зразках S1 та S2, яке пов'язане з глибокими дефектними станами. Ця робота підкреслює критичний вплив умов осадження на питомий опір та продуктивність плівок AZO у гетероструктурних оптоелектронних пристроях, надаючи цінну інформацію для оптимізації властивостей матеріалу з метою підвищення ефективності пристроїв.

Ключові слова: *AZO плівки; питомий опір; p-Si гетероперехід; ВАХ; C-V характеристики; аналіз Мотта-Шотткі; проміжні стани; спектри фотолюмінесценції (ФЛ); кисневі вакансії; термічне випаровування; уловлювання заряду*

East European Journal of Physics. 1. 184-189 (2025)
DOI:10.26565/2312-4334-2025-1-18 ISSN 2312-4334

PHYSICAL AND MAGNETIC PROPERTIES OF SILICON DOPED WITH IMPURITY GERMANIUM ATOMS

Nurulla F. Zikrillaev[a], Feruza E. Urakova[a#], Alisher R. Toshev[b], Giyosiddin A. Kushiev[a]*, Temur B. Ismailov[a], Yoldoshali A. Abduganiev[a], Nemat Norkulov[c]
[a]*Tashkent State Technical University, 100095, University St., 2, Tashkent, Uzbekistan*
[b]*Tashkent State Technical University Almalyk branch, Tashkent, Uzbekistan*
[c]*National University of Uzbekistan named after Mirzo Ulugbek, 100098, University St.4, Tashkent, Uzbekistan*
**Corresponding Author e-mail: #feruzaxonurakova@gmail.com; e-mail: *giyosiddinabdivahobogli@gmail.com*
Received November 7, 2024; revised December 11, 2024; in final form December 20, 2024; accepted December 25, 2024

This paper presents the results of a study of silicon diffusion-doped with germanium impurity atoms. For the diffusion of germanium impurity atoms, the original single-crystal silicon of the KEF-100 brand was used, in which the phosphorus concentration was equal to $Np \approx 5 \cdot 10^{13} cm^{-3}$. The selection of such a concentration of phosphorus impurity atoms was justified by the fact that this concentration of phosphorus atoms has practically no effect on the electrophysical properties of the obtained samples of silicon doped with germanium impurity atoms (Si<Ge>) due to the high solubility of germanium impurity atoms in silicon. As shown by the conducted experimental studies in silicon samples doped by the developed new technology, there are a number of important practical features as well as, the time of the diffusion process of impurity atoms of germanium in silicon according to the developed new technology is reduced by 2-2.5 times, the power consumption during diffusion is reduced by 2 times, the formation of various impurities, silicides, both on the surface and at the surface region of silicon and surface erosion are almost completely eliminated. The study of the electrophysical and magnetic properties of silicon doped with impurity atoms of germanium showed that on the surface and in the near-surface, in addition to the formation of saturated layers of impurity atoms of germanium, binary compounds Ge_xSi_{1-x} are also formed. Based on the X-ray energy dispersive microanalysis, it was determined that the concentration of silicon atoms on the surface is ~44.32%, germanium atoms ~38.11%, oxygen atoms ~15.58% and carbon atoms ~1.98%. These data showed that the number of germanium atoms on the surface is almost half the number of the main silicon atoms. The presence of impurity germanium atoms leads to a strong change in the fundamental parameters of the original silicon. The results of the study showed that in the samples of silicon doped with impurity germanium atoms, ferromagnetic properties are observed at relatively high temperatures (T = 300 K). For the first time in the samples of silicon doped with impurity germanium atoms, galvanomagnetic parameters such as M_s-saturation magnetization, M_r-residual magnetization and H_c-coercive force were determined. It was shown that in samples of silicon doped with impurity atoms of germanium, the fundamental parameters (the value of the width of the forbidden zone, mobility and band structure) of the original silicon change in a wide range, which leads to an expansion of the spectral range of photosensitivity, as well as magnetic properties, i.e. ferromagnetism is observed at relatively high temperatures (T=300 K).
Keywords: *Silicon; Compounds; Diffusion; Germanium; Concentration; Impurity; Physical Mechanism*
PACS: 52.70.La, 68.35.bg, 68.37.Rt, 68.37.Ps, 85.30.-z, 85.70.−w.

INTRODUCTION

The measurement and control of magnetic fields have always been and remain an urgent challenge, attracting significant interest from scientists and specialists. From literary analysis it has been established that the measurement and conversion of the magnetic field value to an electrical signal requires the creation of modern magnetic resistors based on semiconductor materials and structures. To date, semiconductor materials and multilayer structures based on binary compounds have been primarily used for this purpose, often necessitating modern and costly equipment [1-4].

In compensated silicon doped with impurity atoms that create deep electronic levels within the forbidden band, a range of intriguing physical phenomena have been observed. These include high photosensitivity, temperature and infrared quenching of photoconductivity, tensile and magnetic properties, current auto-oscillations, and more [5-8]. Studies on the magnetic properties of silicon doped with isovalent and rare-earth impurity atoms have revealed high magnetosensitivity, both negative and positive magnetoresistance, and transitions to a ferromagnetic state at relatively low temperatures in certain samples [9-10]. This paper presents the results of the study of physical properties of silicon samples doped with impurity germanium atoms.

METHODS

To obtain silicon samples doped with germanium impurity atoms, a two-stage diffusion technique was developed, which enabled a significant increase in the diffusion coefficient of germanium atoms into silicon.

It is well-known that diffusion in semiconductors occurs primarily through the interaction of diffusing impurity atoms with the host atoms and point defects within the crystal lattice of the initial material. The gas-phase diffusion of impurity atoms in semiconductors typically follows Fick's law. However, this approach often fails to fully capture the physical mechanisms of diffusion in semiconductors [11,12].

Cite as: N.F. Zikrillaev, F.E. Urakova, A.R. Toshev, G.A. Kushiev, T.B. Ismailov, Y.A. Abduganiev, N. Norkulov, East Eur. J. Phys. 1, 184 (2025), https://doi.org/10.26565/2312-4334-2025-1-18

For the diffusion of impurity atoms of germanium, the initial single-crystal silicon of the KEF-100 brand was used, in which the phosphorus concentration was equal to $N_p \approx 5 \cdot 10^{13} cm^{-3}$. Such a concentration of impurity atoms of phosphorus has practically no effect on the physical properties of the obtained samples of silicon doped with impurity atoms of germanium (Si<Ge>) due to the high solubility of impurity atoms of germanium in silicon. Powdered germanium with a purity of ~99.999% was used for the diffusion of impurity atoms of germanium. The essence of the developed low-temperature diffusion is as follows. The studied samples of the initial silicon and a diffusant of a certain mass (this is determined by the volume of the ampoule) are in evacuated quartz ampoules (the pressure in the ampoule is $P = 10^{-6}$ mm Hg) and placed in a diffusion furnace at a temperature of T = 300 K. The temperature of the furnace from the quartz ampoule is gradually raised at a rate of 5ºC/min. Then the temperature rises to T = (823 ÷ 973) K and is maintained at this temperature for t = (10 ÷ 20) min, then the furnace temperature rises fairly quickly (T = 423÷ 473 K/min) to a certain temperature (T = 960 ÷ 1050 K) and the samples are maintained at this temperature for t = 3 ÷ 5 hours, after which the ampoules are removed from the furnace and cooled at a rate of 200 ºC/sec. The developed new diffusion technology was carried out dozens of times of diffusion of impurity atoms of germanium from the gas phase. After each diffusion, 5 to 7 samples of silicon were obtained, the surface of which was examined by an electron microscope of the MIM-8 brand. Diffusion was also carried out by the usual high-temperature diffusion method. As the analysis of the obtained results of the study showed, in contrast to the samples obtained by the usual method, in the samples obtained by the developed low-temperature technology no surface erosion was detected, impurities and silicides were not formed, both on the surface and in the surface area. To determine the penetration depth of impurity atoms in the diffusion process, a study of the specific resistance of silicon samples doped with impurity atoms of germanium was carried out by the 4-probe method on the Van der Pauw installation of the Hall Measurements system 7000 brand with the removal of the thickness of the obtained samples, and the concentration of mobility and charge carriers were determined.

EXPERIMENTAL PART

Ferrimagnetic properties were first discovered in silicon doped with germanium impurity atoms at relatively low temperatures (T ≈ 30 K). Studies on the properties of silicon diffusively doped with germanium were conducted at a temperature of T = 300 K, where ferrimagnetic behavior was observed in these samples under specific conditions – a phenomenon not previously documented.

The magnetic properties of the obtained Si<Ge> samples were examined using a magnetic force microscope, the FM-Nanoview 1000. "Magnetic" images of the topography of germanium-doped silicon were obtained at the submicron level, providing detailed visualization of the sample structure (Fig. 1).

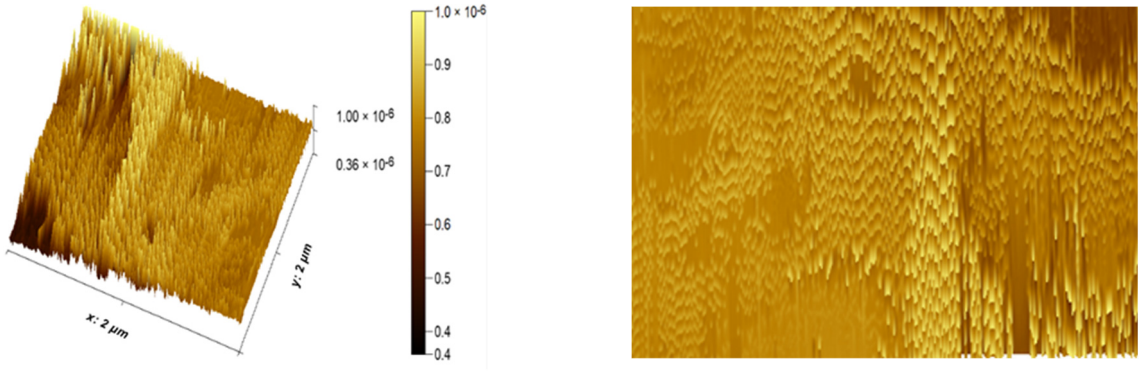

Figure 1. 3D-representation of magnetic domain topography and magnetic topography images in Si<Ge> samples, at T=300 K

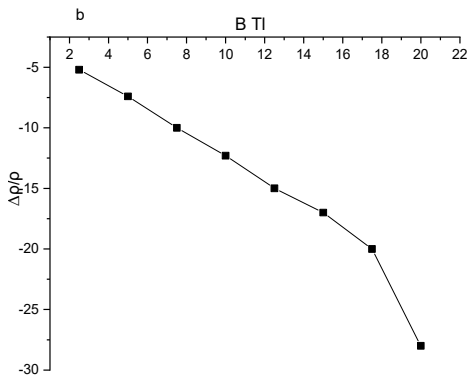

Figure 2. Dependence of negative magneto-resistance on the magnitude of magnetic field in samples p-Si<Ge>, at E =100 V/cm, a) T = 80K, b) T = 300K

These results confirm that silicon samples doped with germanium impurity atoms exhibit ferrimagnetic properties not only at low temperatures ($T_{Ge} \approx 30$ K) but also at relatively high temperatures (T = 300 K). The study of the magnetic properties of Si<Ge> samples demonstrate a significant negative magnetosensitivity in silicon doped with germanium impurity atoms (Fig. 2).

A Scanning Electron Microscope (SEM) provides high-quality imaging and analysis of material surfaces. This technique enhances image quality and resolution by using a stream of high-energy electrons to scan the surface, producing highly detailed images [13,14]. Figures 3a and 3b show the surface topology of a silicon sample doped with germanium impurity atoms, obtained using a JSM-IT 200 SEM. The elemental composition of the silicon surface is presented in Figure 3c.

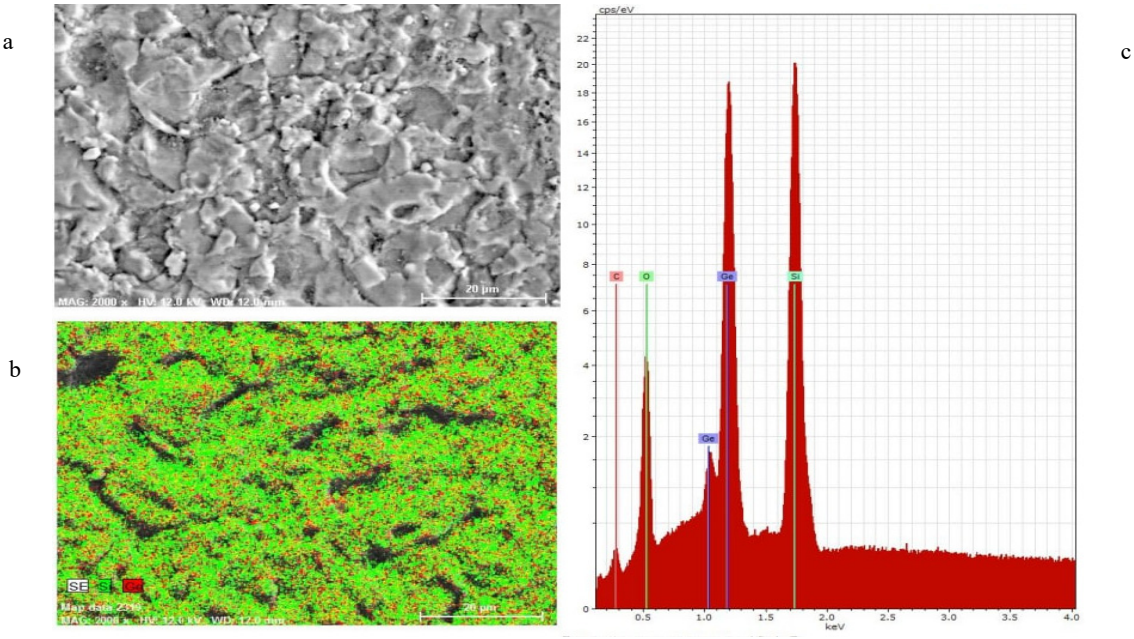

Figure 3. a) and b) surface topology of silicon diffusion-doped with germanium impurity atoms, c) results of micro-X-ray energy-dispersive analysis (scale 20 μm).

Table 1 shows the elemental composition of silicon samples doped with germanium impurity atoms, determined from micro X-ray energy dispersive analysis obtained using a scanning electron microscope.

Table 1. Elemental composition of silicon samples doped with impurity germanium atoms

Element	AN	Series	unn. C {wt}	norm. C {wt.%}	Error {wt}.
Si	14	K	44.45	44.32	1.8
O	8	K	15.63	15.58	1.9
Ge	32	K	38.23	38.11	2.1
C	6	K	1.99	1.98	0.4
Total:			100.29	100.00	

THEORETICAL CALCULATIONS AND RESEARCH RESULTS

Analysis of the study results revealed that after the diffusion of germanium impurity atoms onto the silicon surface, a thin layer forms where germanium-silicon compounds (GeSi) are present. The elemental composition of the silicon surface is shown in Table 1. X-ray energy-dispersive microanalysis indicated that the surface concentrations are approximately 44.32% silicon atoms, 38.11% germanium atoms, 15.58% oxygen atoms, and 1.98% carbon atoms. This data demonstrates that the quantity of germanium atoms on the surface and near-surface layer of silicon is nearly half that of the primary silicon atoms.

Microscopic analysis revealed that a compound layer with an approximate composition of $Ge_{0.38}Si_{0.62}$ and a thickness of 0.5–2 microns formed on the surface and near-surface region of the silicon. Beyond this layer, the concentration of germanium atoms decreases sharply; at a depth of 5–6 microns, the compound composition reaches $Ge_{0.05}Si_{0.95}$. These findings confirm the formation of binary $GeSi_{1-x}$ compounds and heterostructures of the Ge_xSi_{1-x}-Si type on the silicon surface and near-surface region through the diffusion of germanium impurity atoms.

Fig. 4a shows the surface topography of a silicon sample doped with germanium impurity atoms, obtained using a JSM-IT 200 scanning electron microscope (SEM) in secondary electron mode. The X-ray spectrum at point 3 (Fig. 4) indicates a composition of 86% silicon and 14% germanium atoms, corresponding to the binary compound ratio $Ge_{0.14}Si_{0.86}$.

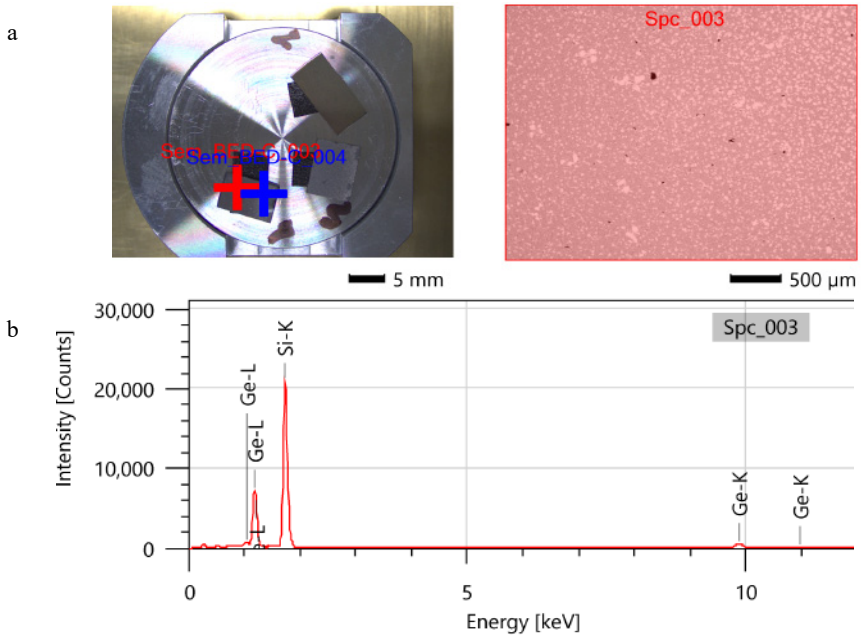

Figure 4. a) Surface topography of silicon sample doped with impurity germanium atoms. b) X-ray energy dispersive microanalysis of silicon samples doped with impurity germanium atoms.

Table 2. Elemental composition of silicon samples doped with impurity germanium atoms

Element	Line	Weight %	Atom %
Si	K	70.34±0.24	85.97±0.3
Ge	K	29.66±0.44	14.03±0.21
Total:		100.00	100.00

Literature data [15] indicate that it is impossible to achieve a uniform distribution of germanium impurity atoms in silicon at concentrations around 80%. In our study, the results can be explained by the fact that, during the additional heat treatment of silicon samples doped with germanium impurity atoms, binary compounds such as Ge_xSi_{1-x} with high concentrations were formed in addition to individual impurity atoms.

To confirm the formation of binary compounds Ge_xSi_{1-x}, silicon samples doped with germanium impurity atoms were examined using an atomic force microscope (FM-Nanoview 1000) (Fig. 5).

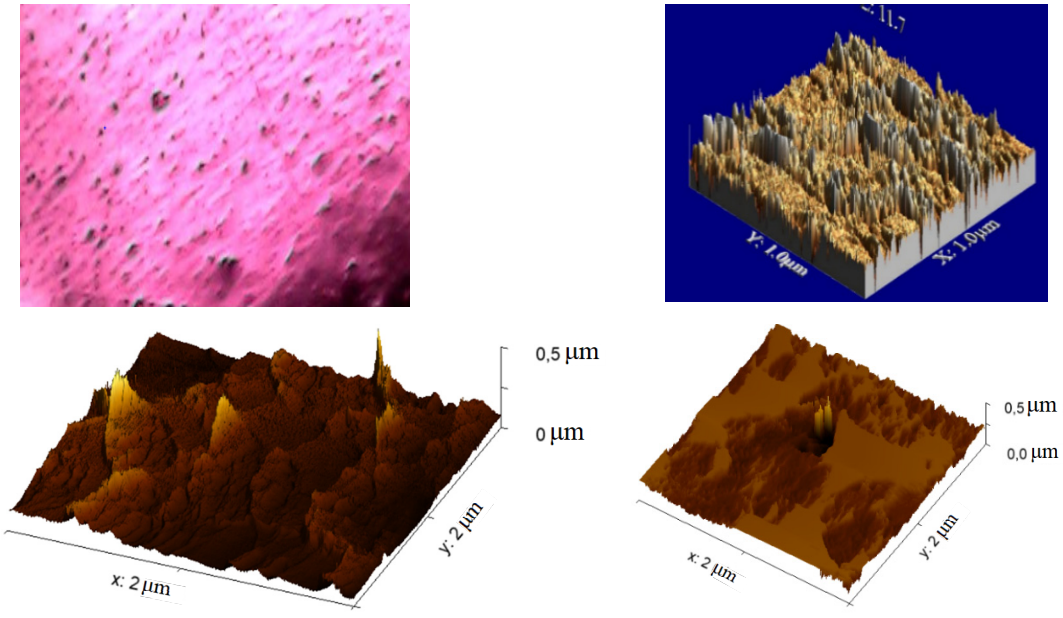

Figure 5. AFM images of the surface of silicon doped with impurity germanium atoms

The results showed the formation of islands on the surface and near-surface regions of the silicon samples, which are key to the formation of Ge_xSi_{1-x} compounds. Further analysis of the silicon samples doped with germanium was conducted

using an IR microscope. The results revealed that the size of the formed silicon-germanium binary compounds reaches up to 1–2 μm, and these compounds were found in large quantities on both the surface and near-surface layer of the silicon.

As shown in Fig. 5, the formation of islands consisting of binary Ge_xSi_{1-x} compounds on the silicon surface leads to an increase in the average roughness size [16]. This indicates that the binary Ge_xSi_{1-x} compounds are forming on the silicon surface due to the impurity germanium atoms, whose electric potential is higher than that of the original silicon.

The experimental results revealed that silicon samples doped with impurity germanium atoms exhibit a ferromagnetic state at a temperature of T = 300 K (Fig. 6).

Studies of the dependence of the magnetic moment of silicon samples doped with impurity atoms of germanium on the specific resistance of the material showed that in high-resistance samples (where the specific resistance is close to the intrinsic conductivity $\rho \geq 10^5$ Ω·cm) and in samples less than with $\rho < 4\times10^4$ Ω·cm, a decrease in the magnetic moment is observed. According to the results of studying the negative magnetoresistance in samples obtained in similar modes, a similar picture of a noticeable decrease in the NMR is observed in silicon samples doped with impurity atoms of germanium at the same specific resistances. On this basis, it can be considered that the NMR phenomena that are observed can be directly related to the presence of magnetic ordering in these samples.

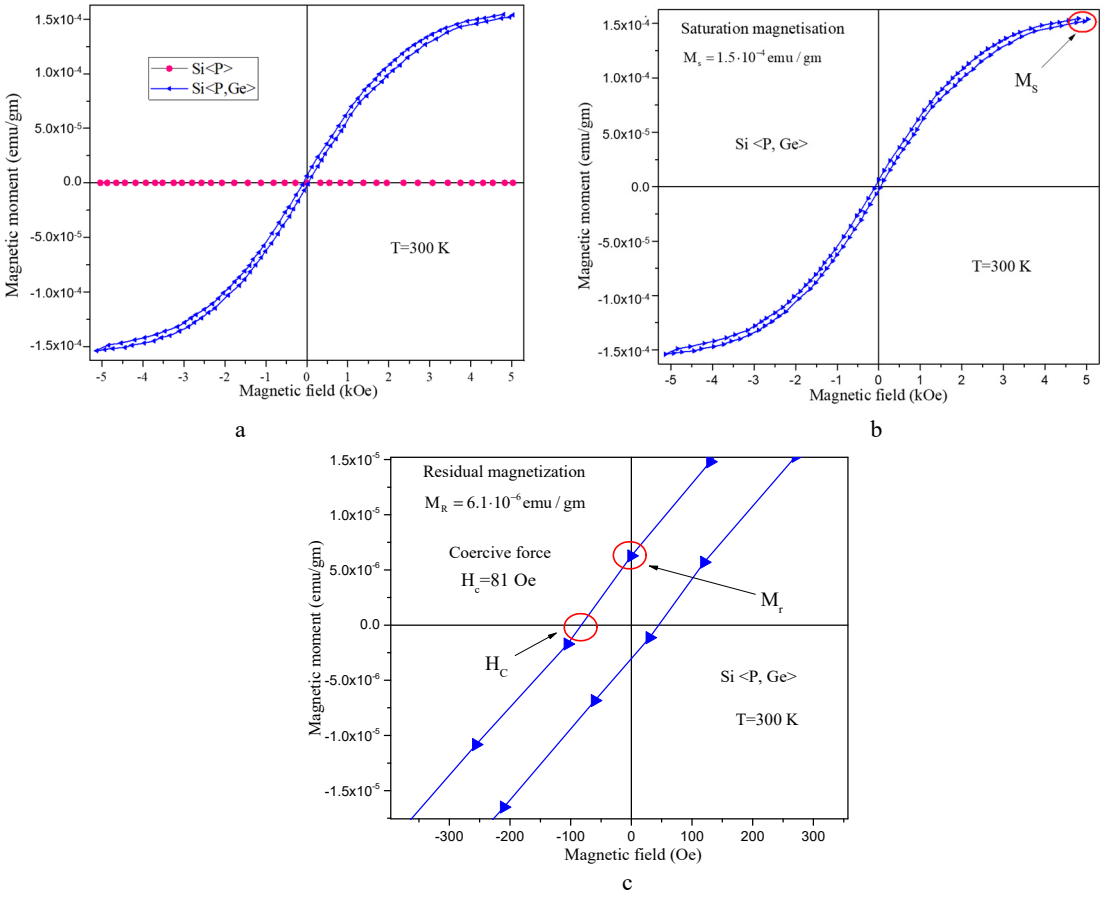

Figure 6. Magnetization dependence on magnetic field of silicon samples doped with impurity germanium atoms at T= 300 K, a) in samples of silicon Si <B, Ge>, $\rho = 4\times10^4$ Ω·cm, *p*-type (blue color) and original silicon (red color), b), v) finding the parameters M_s-saturation of magnetization, M_r-residual magnetization and H_c-coercive force.

DISCUSSIONS

Based on experimental studies, it has been shown that by controlling the parameters of the low-temperature diffusion process, binary compounds of the Ge_xSi_{1-x} type can be obtained with a thickness of up to 5–6 μm, and with germanium atom concentrations on the surface reaching up to 27%.

The formation of Ge_xSi_{1-x} binary compounds in silicon doped with germanium impurity atoms leads to a change in one of silicon's fundamental parameters: the bond dissociation energy. The bond dissociation energy between germanium and silicon atoms is higher than that of the germanium-germanium bond but lower than that of the silicon-silicon bond.

It has been established that, in addition to various combinations of Ge_xSi_{1-x} forming in the silicon crystal lattice, neutral molecular compounds, such as Si_2-Ge_xBrSi_{1-x}, may also form. These compounds consist of tetrahedral clusters of three silicon atoms surrounded by germanium atoms. The formation of such compounds contributes to the creation of heterostructures of the type $GeSi_{1-x}$ -Si on the surface and near-surface regions of silicon.

The results of the study also revealed that silicon samples doped with germanium impurity atoms exhibit ferromagnetic properties at a temperature of T = 300 K.

CONCLUSIONS

Analysis of the study results revealed that in silicon samples doped with germanium impurity atoms, there is a wide range of changes in the fundamental parameters of silicon, such as the width of the bandgap, mobility, and electronic structure. These changes lead to an expansion of the spectral range of photosensitivity and the emergence of magnetic properties, including ferromagnetism at relatively high temperatures (T = 300 K). This makes the doped silicon suitable for the development of sensitive photodetectors, solar cells, and magnetic sensors.

Acknowledgments

The authors are grateful to Uzbek-Japanese Innovation Center of Youth, Institute of Ion Plasma and Laser Technology, Academy of Sciences of the Republic of Uzbekistan, and Tashkent State Technical University for providing to obtain scientific data on the elemental composition of silicon samples doped with impurity germanium atoms using the atomic force microscope FM-Nanoview 1000. A special thanks to Academician of the Academy of Sciences of the Republic of Uzbekistan R.A. Muminov for discussing the obtained results and valuable advice.

ORCID

Nurulla F. Zikrillaev, https://orcid.org/0000-0002-6696-5265; **Feruza E. Urakova,** https://orcid.org/0000-0001-5831-4019
Alisher R. Toshev, https://orcid.org/0009-0000-5283-9498; **Giyosiddin A. Kushiev,** https://orcid.org/0009-0006-5847-6601
Ismailov B. Timur, https://orcid.org/0000-0001-9426-3095; **Yoldoshali A. Abduganiev,** https://orcid.org/0009-0008-1861-3805
Nemat Norkulov, https://orcid.org/0000-0002-6772-9571

REFERENCES

[1] Z. Fan, J. Lian, J.-L. Chen, Y. Pen, and H. Lai, Journal of Materiomics, **9**, 984 (2023). https://doi.org/10.1016/j.jmat.2023.03.004
[2] A.S. Saidov, D.V. Saparov Sh.N. Usmonov, and A. Kutlimratov, J.M. Abdiev, M. Kalanov, A.Sh. Razzakov, *et al*., Advances in Condensed Matter Physics, **2021**, 472487, (2021). https://doi.org/10.1155/2021/3472487
[3] B.A. Akimov, V.A. Bogoyavlenskii, and L.I. Ryabova, Semiconductors. **33**(1), 6 (1999). https://doi.org/10.1134/1.1187637
[4] G.P. Shveikin, and A.I. Gusev. Nanomaterials, Nanostructures, and Nanotechnologies, **42(**6), 696 (2006). https://doi.org/10.1134/S0020168506060215
[5] M.K. Bakhadyrkhanov, S.B. Isamov, and N.F. Zikrillaev. Microelectron. **41(**6), 354 (2012). https://doi.org/10.1134/S1063739712030043
[6] Ch. Etler, P. Senekowitsch, and J. Fabian, Proc. IEEE International Conference on Computational Electronics, **14**, 1 (2010).
[7] Sh.B. Utamuratova, Uzbek Journal of Physics, **19**(4), 12–13 (2017).
[8] M.P. Teplyakov, O.S. Ken, D.N. Goryachev, and O.M. Sreseli, Semiconductors, **52**(9), 1071 (2018).
[9] M.K. Bakhadyrkhanova, Kh.M. Ilieva, G.Kh. Mavlonova, K.S. Ayupova, S.B. Isamova, and S.A. Tachilina, Technical Physics, **64**(3), 385 (2019).
[10] N.F. Zikrillaev, G.H. Mavlonov, L. Trabzon, S.B. Isamov, Y.A. Abduganiev, Sh.N. Ibodullaev, and G.A. Kushiev, Journal of Nano-and Electronic Physics, **15** (6), 06001 (2023). https://doi.org/10.21272/jnep.15(6).06001
[11] A.A. Shklyayev, L. Bolotov, V. Poborchi, T. Tada, and K. Romanyuk, Materials Science in Semiconductor Processing, **83**, 107 (2018).
[12] A.A. Shklyayev, and A.V. Latyshev, Applied Surface Science, **465**, 10 (2019).
[13] T. Ryan, Materials Science in Semiconductor Processing. **4**(1-3), 229 (2001). https://doi:10.1016/s1369-8001(00)00141-4
[14] V.A. Parfenov. News of St. Petersburg Electrotechnical University, LETI, **9**, 61 (2015).
[15] S.B. Erenburg, S.V. Trubina, V.A. Zvereva, V.A. Zinoviev, A.V. Katsyuba, A.V. Dvurechensky, K. Kvashnina, *et al*., JETP, **155**(2), 346 (2019).
[16] H. Groiss, Christian Doppler laboratory for nanoscale Phase Transformation, Center for Surface and Nanoanalytics. 2019.

ФІЗИЧНІ ТА МАГНІТНІ ВЛАСТИВОСТІ КРЕМНІЮ, ЛЕГОВАНОГО ДОМІШКОВИМИ АТОМАМИ ГЕРМАНІЮ

Нурулла Ф. Зікриллаєв[a], Феруза Е. Уракова[a], Алішер Р. Тошев[b], Гіосіддін А. Кушієв[a], Темур Б. Ісмаїлов[a], Йолдошалі А. Абдуганієв[a], Немат Норкулов[c]

[a]Ташкентський державний технічний університет, 100095, вул. Університетська, 2, м. Ташкент, Узбекистан
[b]Алмаликська філія Ташкентського державного технічного університету, м. Ташкент; Узбекистан
[c]Національний університет Узбекистану імені Мірзо Улугбека, 100098, Університетська вул.4. Ташкент, Узбекистан

У даній роботі представлені результати дослідження дифузійно легованого домішками атомів германію кремнію. Для дифузії домішкових атомів германію використовувався вихідний монокристалічний кремній марки КЕФ-100, в якому концентрація фосфору дорівнювала $Np \approx 5 \cdot 10^{13} см^{-3}$. Вибір такої концентрації домішкових атомів фосфору був обгрунтований концентрацією атомів фосфору, яка практично не впливає на фізичні властивості отриманих зразків кремнію, легованого домішковими атомами германію (Si<Ge>) через високу розчинність домішки. атомів германію в кремнії. Дослідженням електрофізичних і магнітних властивостей кремнію, легованого домішковими атомами германію, встановлено, що на поверхні і в приповерхневій зоні крім утворення насичених шарів домішкові атоми германію утворюють також бінарні сполуки Ge_xSi_{1-x}. На основі рентгенівського енергодисперсійного мікроаналізу встановлено, що концентрація атомів кремнію на поверхні становить ~44,32 %, атомів германію ~38,11 %, атомів кисню ~15,58 % і атомів вуглецю ~1,98 %. Ці дані показали, що кількість атомів германію на поверхні становить майже половину кількості основних атомів кремнію. Наявність домішкових атомів германію призводить до сильної зміни фундаментальних параметрів вихідного кремнію. За результатами дослідження встановлено, що в зразках кремнію, легованого домішковими атомами германію, феромагнітні властивості спостерігаються відносно високих температур (T=300 K). Вперше гальваномагнітні параметри, такі як M_s-намагніченість насичення, M_r-залишкова намагніченість і H_c-коерцитивність, були визначені в зразках кремнію, легованих домішковими атомами германію.

Ключові слова: *силікон; компаунд; дифузія; германій; концентрація; домішка; фізичний механізм*

EAST EUROPEAN JOURNAL OF PHYSICS. 1. 190-196 (2025)
DOI:10.26565/2312-4334-2025-1-19 ISSN 2312-4334

STRAIN-RESISTIVE PROPERTIES OF $(Bi_{0.25}Sb_{0.75})_2Te_3$ FILMS AT ONE-SIDED CYCLIC ALTERNATING STRAINS

Rustamjon U. Siddikov, Khusanboy M. Sulaymonov*, Nosirjon Kh. Yuldashev
Fergana Polytechnic Institute, Fergana, Uzbekistan
**Corresponding Author e-mail: husanboy.sulaymonov@gmail.com*
Received August 13, 2024; revised September 21, 2023; in final form October 28; accepted November 5, 2024

The results of a study of the deformation characteristics of polycrystalline films from the $(Bi_{0.25}Sb_{0.75})_2Te_3$ solid solution at one-sided cyclic alternating mechanical stresses is presented. The films were obtained on a polyamide substrate by the method of thermal vacuum condensation of molecular beams and had a columnar porous structure with the dimensions of individual crystalline grains of 2.0-2.5 μm. The effect of static and cyclic deformations on the electrical resistance and volt-ampere characteristics of strain gauge films was studied in order to manufacture strain gauges for fatigue damage accumulation on their basis. It was shown that at room temperature such films have an abnormally high static strain sensitivity $G \approx 10^3$ arb. units and a significant hysteresis of their resistance change was detected at small numbers of alternating deformation cycles. As a result of $N = 5 \cdot 10^5$ deformation cycles, the linear section of the volt-ampere characteristic expands from (0-5) V at $N = 0$ to (0-12) V. And the temperature coefficient of resistance in the range of 293 K-T_{min} changes from $\alpha = -5.6 \cdot 10^{-3} K^{-1}$ to $\alpha = -2.5 \cdot 10^{-4} K^{-1}$. Thecharacteristic value of T_{min}, at which $\alpha = 0$, increases with the growth of N. The studied strain gauge films can be successfully used as a sensor of fatigue stress accumulation in the temperature range of T = 273-413 K and the value of $N = 0 - 5 \cdot 10^5$.
Keywords: *Narrow-gap semiconductor $(Bi_xSb_{1-x})_2Te_3$; Porous polycrystalline films; Strain sensitivity; Cyclic alternating strain; Hysteresis of changes in electrical resistance with strain; Strain gauge of fatigue damage accumulation*
PACS: 62.20.fg, 73.50.Dn, 77.84.-s, 85.50.-n, 91.60.Ba

INTRODUCTION

The strain gauge method for studying the properties of semiconductor materials is one of the most common and informative methods for studying thin-film structures, which are widely used to manufacture electrical sensors [1-4], pressure and displacement sensors [5-7]. From the point of view of the technical application of thin semiconductor films as a strain-sensitive element, the current-voltage characteristic (CVC) plays a special role, in particular, it allows us to judge their energy capabilities and suitability for strain gauge measurement. An important parameter is the maximum permissible power consumption of the strain gauge under specified operating conditions. This is due to the fact that semiconductor films are very sensitive to various types of radiation and temperature changes, and when passing high currents through film samples, their excess Joule heating may occur, which is reflected accordingly in their operating parameters. Thus, it can lead to a nonlinear CVC and, thus, to an increase in the error in the instrument readings. In addition, to ensure safe operation of structures such as aircraft and prevent their destruction during operation, it is necessary to know the number of deformation cycles that a given structure has experienced. In this regard, film strain gauges of fatigue damage accumulation (FDA) based on narrow-band semiconductors [5-10] are successfully used, changing their characteristics with an increase in the number of deformation cycles acting on them.

As is known [7-11], the main electrophysical characteristics of strain gauges are the initial values of electrical resistance R_0, strain sensitivity G_0 and their changes under the influence of external factors, such as cyclic mechanical deformation ε, temperature T, frequency of the supply alternating voltage f etc. Recently, due attention has been paid to the study of the features of low- and high-cycle fatigue of strain gauges made of low-dimensional structures at different deformation amplitudes [12-16]. It should be noted that the authors and their colleagues have recently obtained interesting results in the study of the strain gauge properties of thin polycrystalline films of narrow-band semiconductors [17-21]. Although it has been shown [9-11] that the nature of the anomalously high strain sensitivity $G \approx 10^4\ arb.units.$ of porous films $(Bi_xSb_{1-x})_2Te_3$ is associated with the formation of microcracks at high deformation amplitudes $\varepsilon \approx 10^{-3}$, however, the mechanisms of cyclic deformations at arbitrary amplitudes and amounts of stresses still remain unclear.

This work is devoted to the study of the influence of the number of cycles N and the amplitude ε of alternating deformation on the characteristics of films from a solid solution $(Bi_xSb_{1-x})_2Te_3$ according to the change in the value of its electrical resistance and the strain gauge coefficient (SGC), determined by the expression

$$G = \frac{\Delta R}{R_0 \cdot \varepsilon}, \tag{1}$$

where $\varepsilon = \Delta\ell/\ell_0$ and $\Delta\ell = \ell(\varepsilon) - \ell_0$ are the values of relative and absolute strain, $\Delta R = R(\varepsilon) - R_0$, and R_0 are the electrical resistance of the sample at $\varepsilon = 0$.

Cite as: R.U. Siddikov, Kh.M. Sulaymonov, N.Kh. Yuldashev, East Eur. J. Phys. 1, 190 (2025), https://doi.org/10.26565/2312-4334-2025-1-19

The current-voltage characteristic and temperature dependence of the resistance of $(Bi_{0.25}Sb_{0.75})_2Te_3$ strain gauge films under the action of static and cyclic alternating deformations (CAD) are considered with the aim of manufacturing FDA based on them. It is shown that as a result of the action of $N = 5 \cdot 10^5$ strain cycles, the linear section of the current-voltage characteristic expands from (0-5) *V* at $N = 0$ to (0-12) *V*. The studied films can be successfully used as FDA in the temperature range of $T = 273 - 413\ K$ and the value of $N \le 5 \cdot 10^5$.

TECHNOLOGY AND MEASUREMENT METHODS

Polycrystalline films of $(Bi_xSb_{1-x})_2Te_3$ with an area of $5 \times 20\ mm^2$ were obtained by thermal evaporation in a vacuum with a residual vapor pressure of $(1-3) \cdot 10^{-2}$ *P*a from a mixture of powders Bi_2Te_3 and Sb_2Te_3 in a ratio of x и $(1 - x)\ mol$ %. The temperature of the substrate made of polyamide PM-1 varied in the range of $T_S = 323 - 423\ K$, and the growth rate of the films was $- W = 150 - 450\ \overset{0}{A}/c$. The most strain-sensitive ($G \approx 10^3\ arb.units.$) films with optimal performance characteristics were obtained at thicknesses of $d \approx 3 - 5\ \mu m$, $T_S = 363\ K$, $W = 200\ \overset{0}{A}/c$ and at a value of $x = 0.25$. The method for measuring the deformation characteristics of the films was chosen in the same way as in [1, 7-9]. The samples were not subjected to preliminary heat treatment. The freshly prepared films had an unstable SGC, caused by the presence of strong nonequilibrium internal mechanical stresses (IMS) [11]. With an increase in the N number of CAD, the value of G decreases monotonically, which indicates the possibility of using the manufactured films as FDA. Electron microscopic and X-ray structural studies [3, 7] showed that the grown $(Bi_{0.25}Sb_{0.75})_2Te_3$ layers had a polycrystalline columnar and porous structure. The sizes of individual crystalline grains were $2 - 2.5\ \mu m$.

To measure the deformation characteristics (DC), the studied films from $(Bi_{0.25}Sb_{0.75})_2Te_3$ were glued to a beam of equal resistance made of titanium alloy. The deformation of the films was carried out by bending the beam. In this case, the value of the relative deformation ε was calculated by the magnitude of the bending of the cantilever-fixed beam according to the known expression [1]

$$\varepsilon = 3ab\Delta x/\ell^3, \tag{2}$$

where *a* is the distance from the neutral axis of the cantilever beam to the film, *b* is the distance from the point of application of the force to the middle of the film sample, *Δx* is the bending of the free end of the plate at the point of application of the force, ℓ is the length of the plate between the support point and the point of application of the force. The deformation value varied in the range from $\varepsilon = +2 \cdot 10^{-3}$ to $\varepsilon = -2 \cdot 10^{-3}$ arb. units.

Strain measurements were made at different temperature ranges of the environment. In order to reduce the measurement error, it is necessary to manufacture strain gauges with minimum temperature coefficients of resistance and strain sensitivity.

$$\alpha = dR/R^0dT,\ \alpha' = dG/G^0dT, \tag{3}$$

where R^0 and G^0 are the resistance and *SGC* at a temperature of $T_0 = 273^0\ K$ in a given mechanical state of the films. The study of these parameters of semiconductor strain gauges will to a certain extent help to explain the nature of the physical processes occurring in such a heterogeneous structure as a porous polycrystalline film subjected to mechanical deformation [7, 8].

The temperature dependence of the tensometric parameters of the films $(Bi_{0.25}Sb_{0.75})_2Te_3$ produced was investigated in the range 293-455 *K*. It turned out that at high substrate temperatures $T_s \approx 413\ K$ and high condensation rates $W \approx 400\ \overset{0}{A}/c$ denser films with a small SGC are obtained. The resistance of such films has a metallic dependence with temperature ($\alpha = 0.85 \cdot 10^{-4}K^{-1}$) and it remained practically unchanged after exposure CAD.

RESULTS OF THE EXPERIMENT AND THEIR DISCUSSIONS

1. The region of small values of N.

Here we first present the results of the study of the absolute $\Delta R = R(\varepsilon) - R_0$ and relative $\Delta R(\varepsilon)/R_0$ changes in the resistance of freshly prepared samples with a small number of cycles of mechanical loading with a change not only in value but also in sign. For example, at the first stage, we will consider the region of tensile deformation from $\varepsilon = 0$ to $\varepsilon = \varepsilon_0$, at the second stage we will obtain in the direction of deformation removal, i.e. when changing ε from ε_0 to 0, at the third and fourth stages we radiate the region of compression deformations, first from $\varepsilon = 0$ to $\varepsilon = -\varepsilon_0$, and then from $\varepsilon = -\varepsilon_0$ to $\varepsilon = 0$ and complete one cycle of alternating deformations. The strain-sensitive films made from $(Bi_{0.25}Sb_{0.75})_2Te_3$ withstood quite large numbers CAD before noticeable mechanical destruction. It is obviously of interest to study DC films in extremely small and large quantities *N* CAD.

Fig. 1 shows DC at small values of *N*, and here the change in *R* film was first studied only at 4-x cycles of tensile deformation ($0 \le \varepsilon \le 0.9 \cdot 10^{-2} arb.units.$), and then at 4-x cycles of compressive deformation ($-0.9 \cdot 10^{-2} \le \varepsilon \le 0$). It is seen that when we first smoothly increase the load to ε_0 and then also smoothly remove it to 0, we observe a residual

change in the relative resistance of $\Delta R^0_{res}(N)/R_0$. This value is different for stretching and compression, which reflects the presence of IMS in the film. It is seen that in this case IMS is negative (compressed $\varepsilon_0 < 0$), in addition, it decreases monotonically with the growth of *N*.

Thus, in films $(Bi_{0.25}Sb_{0.75})_2Te_3$, a significant hysteresis of resistance change $R_N(\varepsilon)$ is observed with one CAD ($N = 1$) with an unclosed end. The following hysteresis loops directly continue the previous one and shift to the region of large values *R*, and the absolute value of the vertical displacement ΔR for the next loop decreases monotonically (Fig. 2).

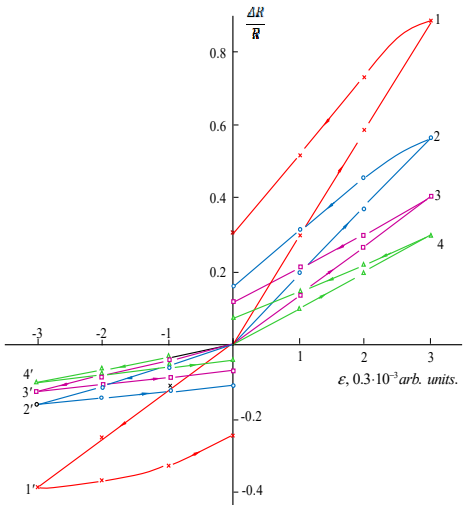

Figure 1. Deformation characteristics of freshly prepared film $(Bi_{0.25}Sb_{0.75})_2Te_3$ under 4-x cycles of tensile deformation (curves 1-4 with arrows indicating the direction of loading) and compression (curves 1′-4′) at room temperature

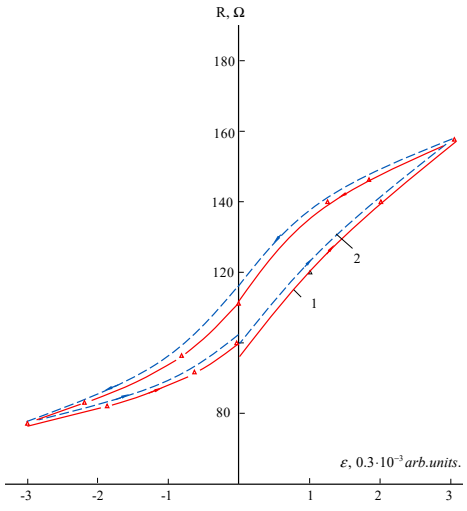

Figure 2. Hysteresis of the change in resistance of the film from $(Bi_{0.25}Sb_{0.75})_2Te_3$ under the influence of CAD. The open hysteresis with dashed lines corresponds to the second CAD (*N*=1)

Fig. 3 shows the dependence of the change in resistance and SGC on the number CAD in the region $1 \leq N \leq 4$. It is evident that the value of G decreases sharply, and R increases, with an increase in the number CAD at low N, and then passes to a smooth monotonic decline. Apparently, the initial sections of the dependence $R_\varepsilon(N)$ and $K_\varepsilon(N)$ are due to strongly nonequilibrium IMS films $(Bi_{0.25}Sb_{0.75})_2Te_3$ without preliminary heat treatment.

2. The region of large values of the number of deformation cycles. Stabilization of the strain gauge parameters of films.

Figure 4 shows the static deformation characteristics of the films before and after exposure to cyclic alternating loads in large quantities ($N \gg 1$). It can be seen that before exposure to deformation cycles, the film resistance increases almost linearly under the action of tensile deformation, while the dependence of the resistance on compressive deformation is nonlinear, and the value of the strain-sensitivity coefficient under compressive deformation is noticeably less than under tensile deformation (curve 1).

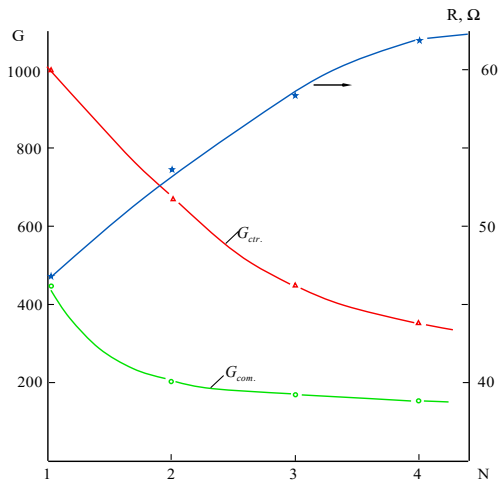

Figure 3. Change in resistance *R* and SGC with the growth of the number CAD in the area of $1 \leq N \leq 4$

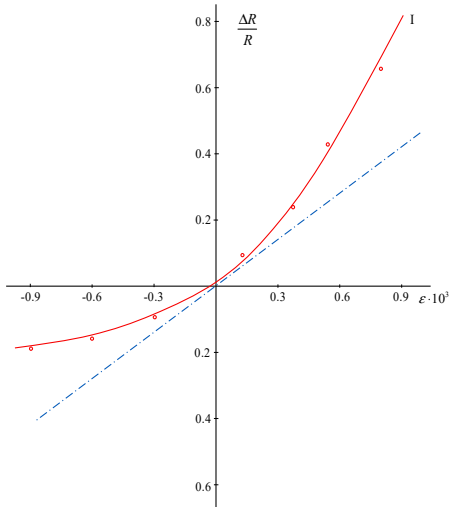

Figure 4. Deformation characteristic of the relative change in resistance of films from $(Bi_{0.25}Sb_{0.75})_2Te_3$ before (curve 1) and after (2) cyclic deformation. For curve $N = 5 \cdot 10^5$

After exposure to deformation cycles ($N \cong 5 \cdot 10^5$), the nonlinearity of the static DC film decreases, its strain sensitivity increases during compression deformation, and decreases during tension (curve 2), i.e. the asymmetry practically disappears.

Fig. 5 and Fig. 6 show the dependence of the relative change in resistance $\Delta R/R_0$ and the strain-sensitivity coefficient G on the number of deformation cycles at different deformation amplitudes ε. It is evident that with an increase in the number of alternating deformation cycles and its amplitude, the relative change in resistance increases, while their strain-sensitivity G decreases, and at values ($N = 5 \cdot 10^5$) in the dependences $R(N), G(N)$, a tendency toward saturation is observed.

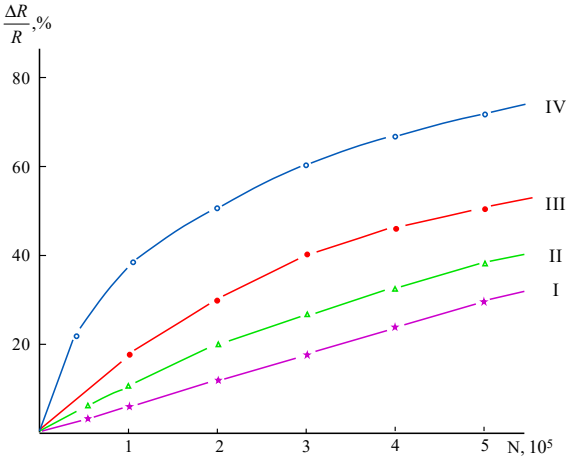

Figure. 5. Relative change in the resistance of strain films $(Bi_xSb_{1-x})_2Te_3$ from the number of cycles of alternating deformations N, at different deformation amplitudes $\varepsilon \cdot 10^{-3}$: I - ± 0.25, II - ± 0.5, III - ± 0.75 and IV - ± 1.0

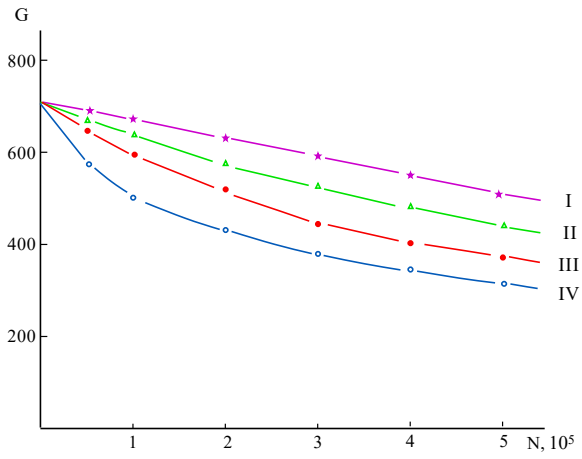

Figure 6. Dependence of G films on the number of deformation cycles at relative deformation amplitudes of $\varepsilon \cdot 10^{-3}$: I - ± 0.25, II - ± 0.5, III - ± 0.75 and IV - ± 1.0.

In our opinion, the experimental facts obtained here can be explained on the basis of a model of the film as a system of microcontacting conducting grains, the dielectric gap between which changes with deformation. Indeed, after the action of the required number of cycles of alternating deformation, the width of the gap between the crystalline grains increases as a result of abrasion of the contacting surfaces of the grains, leading to an increase in the film resistance and the removal to one degree or another of the preliminary IMS. The latter, in turn, determines the tendency toward a linear and symmetrical form DC of the film under the action of deformation cycles.

Therefore, it can be assumed that in the manufactured films $(Bi_{0.25}Sb_{0.75})_2Te_3$, high values of resistance and strain-sensitivity coefficient are correlated with the value of IMS, the dielectric gap and the size of the crystallites. The action of CAD leads to an increase in the change in the value of resistance and strain-sensitivity coefficient under compression, and to a decrease in the value of G under tension, as well as a change in the shape of the static deformation characteristic.

3. Effect of cyclic deformations on the temperature dependence of film resistance.

The temperature dependence of the electroresistance of the polycrystalline film $(Bi_{0.25}Sb_{0.75})_2Te_3$ and the influence of the current CAD can be qualitatively described on the basis of the linear model of microcontacting [7,8,11,21], according to which the resistance of the film is represented as the sum of the connected resistance of the intercrystalline interface $R_{por.i}$ and the individual crystalline levels $R_{cr.i}$

$$R_{film} = R_{cr} + R_{por} = \sum_i \left(R_{cr.i} + R_{por.i} \right) \ . \tag{4}$$

Here R_{cr} is the film resistance due to the volume of crystalline grains and depends on the temperature as

$$R_{cr} = R_{cr}^0 \left[1 + \alpha_{cr} \left(T - T_0 \right) \right] , \tag{5}$$

characteristic of metal resistors made of massive monocrystalline material, R_{cr}^0 - the resistance of a dense film at $T_0 = 273\ K$. We believe that the film resistance, caused by the presence of pores (interface potential barriers), will change with temperature as

$$R_{por} \approx R_{por}^0 \cdot exp\left(E_{por} / kT \right) \ , \tag{6}$$

where R_{por}^0 is some characteristic resistance of the porous film, weakly dependent on temperature, E_{por} is the height of the micropotential barrier, k is the Boltzmann constant.

Then, for the temperature coefficient of electrical resistance of the porous film, from (3-6) we obtain the phenomenological expression

$$\alpha_{film} = \frac{\alpha_{cr} \cdot R_{cr}^0 - \frac{E_{por}}{kT^2} \cdot R_{por}(T)}{R_{cr}^0 + R_{por}^0} \,. \tag{7}$$

From this it is clear that if at the value $T = T'$ the condition $\alpha_{cr} R_{cr}^0 < \frac{E_{por}}{kT'^2} \cdot R_f(T')$ is satisfied, then the porous film initially has a negative value of the temperature coefficient of resistance and at some $T = T_{\min} > T'$ it turns to zero, and then changes sign (i.e. acquires a metallic character of electrical conductivity). From (7) we find that $T_{\min}$ can be roughly estimated by the formula

$$T_{\min} = \sqrt{\frac{E_{por}}{k\alpha_{cr}} \cdot \frac{R_{por}(T_0)}{R_{cr}^0}} \,. \tag{8}$$

In practice, it can be assumed that E_{por} , α_{cr} , R_{cr}^0 weakly depend on CAD, and the interface resistance $R_{por}(T_0)$ increases with increasing *N*, then in accordance with formula (8), the value of $T_{\min}$ grows like $T_{\min} \sim \sqrt{R_{por}(T_0, N)}$ and at large $N \sim 5 \cdot 10^5$ experiences a tendency to saturation, which is observed in the experiment [11].

4. Effect of cyclic deformations on the current-voltage characteristics of films.

The effect of static deformation on CVC films was studied by us [13] in the range of relative deformation values up to $0.9 \cdot 10^{-3} arb.units.$, the corresponding curves are shown in Fig. 7. They show that CVC of the samples is linear in the region of low stresses. With increasing stress, the linearity of the current-voltage dependence is disrupted, which occurs, for example, in the undeformed state at *U=5 V* (curve 4). This stress, at which nonlinearity CVC occurs, depends significantly on the sign and level of deformation.

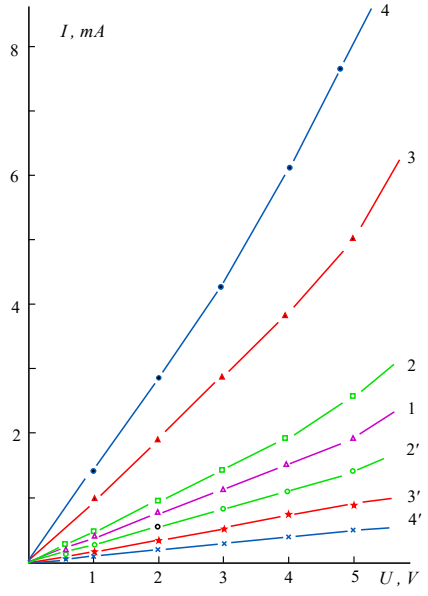

Figure 7. Volt-ampere characteristic of film $(Bi_{0.25}Sb_{0.75})_2Te_3$ on polyimide substrate ПМ-I, under the action of static deformation: ε=0 (curve 1), ± 0.3·10^{-3} (2,2′), ± 0.6 (3,3′), ±0.9 (4,4′). Curves 2-4 were taken under compression, and 2′-4′- under tension

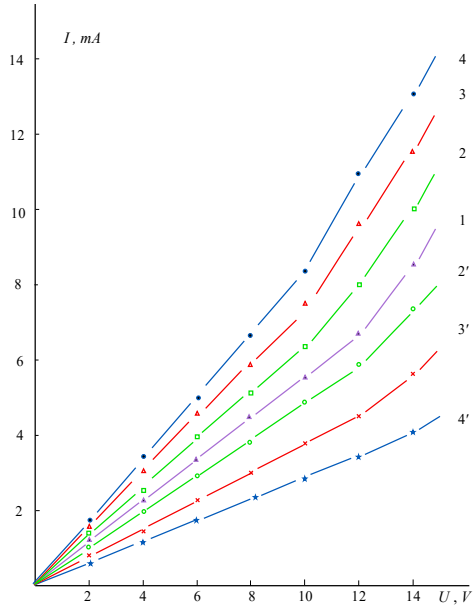

Figure 8. Volt-ampere characteristic of film $(Bi_{0.25}Sb_{0.75})_2Te_3$ after exposure to $N = 5 \cdot 10^5$ cycles of alternating loading. Curves 1-4 and 2′-4′ correspond to curves 1-4 and 2′-4′.

Studies of the current-voltage characteristics (CVC) of films $(Bi_{0.25}Sb_{0.75})_2Te_3$ subjected to CAD are shown in Fig. 8. It is evident from the figure that the CVC of the film change significantly after exposure to cyclic deformations $(= 5 \cdot 10^5)$. All curves taken at different values of relative deformation ε clearly reflect increases in film resistance. The action of $N = 5 \cdot 10^5$ cycles of alternating deformations leads to an increase in the voltage drop across the film with a constant source of almost 10 V, i.e., two-fold.

Since the distances between them increase under the action of cyclic deformations as a result of abrasion of the contacting surfaces of the crystalline grains, this leads to the expansion of the linear section CVC of the film. It is known that strain gauge measurements must be made in the linear region CVC. In this case, it is necessary to take into account the possibility of an error associated with the fact that a fairly large current can flow in the devices, which heats up the strain gauge and also causes the appearance of a nonlinear section CVC. In this case, not the nominal resistance is measured, but the static resistance corresponding to a certain point CVC. To reduce the current through the strain gauge,

an additional resistance can be included, previously measured with sufficient accuracy. The measuring current through the strain gauge in this case should be an order of magnitude lower than the current causing a change in the electrical conductivity mechanism in the film or heating of the strain gauge body. The magnitude of this current can be roughly determined by CVC. Usually this is the current value where CVC begins to deviate from the linear dependence.

CONCLUSIONS

The changes in the resistance value of SGC porous films with increasing number of deformation cycles can be explained by the growth of the dielectric gap between crystallites and micro-wear of their contacts. The model describing the electrical conductivity through micro-contacting surfaces of crystallites, based on the theory of percolation, explains the high values of SGC films and the nonlinearity of their static deformation characteristics. The polycrystalline films of narrow-gap ternary compound $(Bi_{0.25}Sb_{0.75})$ studied here, obtained by thermal evaporation in a vacuum at the above-mentioned optimal process parameters, can be successfully used as FDA for testing and monitoring the parameters of aircraft structures in the temperature range of $T = 273 - 413\ K$ and the value of CAD $N \le 5 \cdot 10^5$.

ORCID

Rustamjon U. Siddikov, https://orcid.org/0009-0009-8324-1275
Husanboy M. Sulaymonov, https://orcid.org/0000-0003-0790-1584
Nosirjon Kh. Yuldashev, https://orcid.org/0000-0003-0226-3528

REFERENCES

[1] E.A. Abdullaev, and N.Kh. Yuldashev, *The effect of piezoresistance in lead and bismuth chalcogenides*, Part 1, ("Fan", Tashkent, 1989).
[2] I.H. Kazi, P.M. Wild, and T.M. Moore, "Characterization of sputtered nichrome (80/20 wt.%) films for strain guage applications," Thin Solid Films, **515**(4), 2602-2606 (2006). https://doi.org/10.1016/j.tsf.2005.10.077
[3] I.M. Pazukha, Z.M. Makukha, Y.M. Shabelnyk, and I.Y. Protsenko, "Tensoresistive properties of thin film systems based on Ag and Co," Journal of Nano- and Electronic Physics, **4**(3), 3020 (2012). https://jnep.sumdu.edu.ua/en/component/content/full_article/826
[4] A.Yu. Gerasimenko, L.P. Ichkitidze, V.M. Podgaetsky, and S.V. Selishchev, "Layers with the Tensoresistive Properties and their Possible Applications in Medicine," Materials Physics and Mechanics, **37**, 153-158 (2018). http://dx.doi.org/10.18720/MPM.3722018_7
[5] L. Elbrecht, and J. Binder, "The Mechanical Properties of Thin Polycrystalline Silicon Films as Function of Deposition and Doping Conditions," Sensors and Materials, **11**(3), 163-179 (1999). https://sensors.myu-group.co.jp/sm_pdf/SM363.pdf
[6] O.O. Mamatkarimov, S.Z. Zaynabidinov, A. Abduraimov, R.Kh. Khamidov, and U.A. Tuychiev, "Dynamic strain gauge characteristics of Schottky barrier diodes under pulsed hydrostatic pressure," Semiconductors, **34**(1), 67 (2000). https://doi.org/10.1134/1.1187960
[7] E.A. Abdullaev, and N.Kh. Yuldashev, *Effect of piezoresistance in lead and bismuth chalcogenides*, Part 2, (Technika, Fergana, 2008). (in Russian)
[8] H.M. Sulaymonov, "Effect of cyclic deformation on the electrical conductivity of p-$(Bi_{0.3}Sb_{0.7})_2Te_3$ films on alternating current," Journal of Technical Physics, **87**(3), 471-472 (2017). (in Russian)
[9] S.Sh. Abdullaev, N.Kh. Yuldashev, Kh.M. Sulaymonov, "Tensoresistive Properties of Thin Polycrystalline $(Bi_{0.3}Sb_{0.7})_2Te_3$ Films at Static and Cyclic Deformations," International Journal of Modern Physics and Application, **3**(4), 52-56 (2016).
[10] H.M. Sulaymonov, M.G. Umarov, and N.Kh. Yuldashev, "Tenzochuvstvitelnost polikristallicheskix poristix plenok". Aktualniye problemi sovremennoy nauki-Rossiya, (4), 149-151 (2015). (in Russian)
[11] H.M. Sulaymonov, and N.K. Yuldashev, "Effect of internal stresses on the static strain characteristics of p-$(Bi_{0.3}Sb_{0.7})_2Te_3$ composite films," Journal of Surface Investigation. X-ray, Synchrotron and Neutron Techniques, **10**(4), 878-882 (2016). https://doi.org/10.1134/S1027451016040364
[12] Z. Xu, C. Huang, C. Tan, M. Wan, Y. Zhao, J. Ye, and W. Zeng, "Influence of microstructure on cyclic deformation response and micromechanics of Ti–55531 alloy," Materials Science and Engineering: A, **803**, 140505 (2021). https://doi.org/10.1016/j.msea.2020.140505
[13] C. He, Y. Wu, L. Peng, N. Su, X. Li, K. Yang, Y. Liu, *et al*., "Cyclic Deformation and Correspondent Crack Initiation at Low-Stress Amplitudes in Mg–Gd–Y–Zr Alloy," Materials, **11**(12), 2429 (2018). https://doi:10.3390/ma11122429
[14] P. Wang, T. Takagi, T. Takeno, and H. Miki, "Early fatigue damage detecting sensors. A review and prospects," Sensors and Actuators A: Physical. **198**, 46-60 (2013). https://doi.org/10.1016/j.sna.2013.03.025
[15] A.A. Koryakin, E.D. Leshchenko, and V.G. Dubrovsky, "Effect of elastic stresses on the formation of axial heterojunctions in three-component AIIIBV nanowires," Physics of the Solid State, **61**, 2437-2441 (2019). (in Russian)
[16] I.P. Buryk, S.I. Vorobyov, and L.V. Odnodvorets, "Strain resistive properties of film materials based on Ni and Mo or Cr," PSE, **7**(1,2), 115 (2009). http://dspace.nbuv.gov.ua/handle/123456789/7962 (in Russian)
[17] N.K. Yuldashev, D.T. Mamadieva, O.R. Nurmatov, T.I. Raxmonov, and X.M. Sulaymonov, "The effect of mechanical deformation on the photovoltaic properties of semiconductor polycrystalline film structures CdTe: Sn," Scientific-technical journal, **23**(3), 9-14 (2019).
[18] Kh.M. Sulaymonov, and N.Kh. Yuldashev, "The deformation properties of films under the influence of unilateral cyclic sign-variable pressure," in: *The Third European Conference on Physics and Mathematics*, 12th September, (Vienna, Austria, 2015). pp. 1926.
[19] T.I. Rakhmonov, "Photosensitivity Spectra of Thin Films from a $CdSe_xS_{1-x}$ Solid Solution," Journal of Applied Mathematics and Physics, **10**(12), 3676-3683 (2022). https://doi.org/10.4236/jamp.2022.1012245
[20] T.I. Rakhmonov, D.T. Mamadiyeva, and N.Kh. Yuldashev, "Photoelectric phenomena in thin Polycrystalline CdTe, CdSe, CdS films under mechanical deformation," European Science Review, (11-12), 40-49 (2021). https://doi.org/10.29013/ESR-21-11.12-40-49

[21] O. Nurmatov, T. Rahmonov, Kh. Sulaymonov, and N. Yuldashev, “Phototenzoelectric properties of polycrystalline films of chalcogenides of cadmium and zinc, produced by portional evaporation in vacuum,” Euroasian Journal of Semiconductors Science and Engineering, **2**(5), 40-45 (2020). https://uzjournals.edu.uz/semiconductors/vol2/iss5/10/

ТЕНЗОРЕЗИСТИВНІ ВЛАСТИВОСТІ ПЛІВОК $(Bi_{0.25}Sb_{0.75})_2Te_3$ ПРИ ОДНОСТОРОННІХ ЦИКЛІЧНИХ ЗНАКОЗМІННИХ ДЕФОРМАЦІЯХ

Рустамжон У. Сіддіков, Хусанбой М. Сулаймонов, Нозіржон Х. Юлдашев

Ферганський політехнічний інститут, Фергана, Узбекистан

Наводяться результати дослідження деформаційних характеристик полікристалічних плівок з твердого розчину $(Bi_{0,25}Sb_{0,75})_2Te_3$ при односторонніх циклічних знакозмінних механічних напруг. Плівки виходили на поліамідній підкладці методом термовакуумної конденсації молекулярних пучків і мали стовпчасту пористу структуру з розмірами окремих кристалічних зерен 2,0-2,5 мкм. Вивчався вплив статичних та циклічних деформацій на електричний опір та вольт амперні характеристики тензорезистивних плівок з метою виготовлення на їх основі тензодатчиків накопичення втомних ушкоджень. Показано, що при кімнатній температурі такі плівки мають аномально високу статичну тензочутливість $G \approx 10^3$ відн. од. і виявляється суттєвий гістерезис зміни їхнього опору при малих кількостях циклів знакозмінних деформацій. В результаті дії $N = 5 \cdot 10^5$ циклів деформацій лінійна ділянка вольтамперної характеристики розширюється від (0-5) при $N = 0$ до (0-12) В. Температурний коефіцієнт опору в інтервалі 293 K-T_{min}змінюється від $\alpha = -5{,}6 \cdot 10^{-3} K^{-1}$ до $\alpha = -2{,}5 \cdot 10^{-4} K^{-1}$. Характерне значення T_{min}, при якому $\alpha = 0$, збільшується зі зростанням N. Досліджені тензорезистивні плівки з успіхом можуть бути використані як датчик накопичення втомних напруг в інтервалі температур $T = 273 - 413\ K$ і значенні $N = 0 - 5 \cdot 10^5$.

Ключові слова: *вузькозонний напівпровідник $(Bi_xSb_{1-x})_2Te_3$; пористі полікристалічні плівки; тензочутливість; циклічна знакозмінна деформація; гістерезис зміни електричного опору з деформацій; тензодатчик накопичення втомних ушкоджень*

EAST EUROPEAN JOURNAL OF PHYSICS. 1. 197-203 (2025)
DOI:10.26565/2312-4334-2025-1-20 ISSN 2312-4334

OPTICAL INVESTIGATION OF ZnS/GaAs and $CuGaS_2$/GaP SYSTEMS

Kh.N. Ahmadova[a,b,c], M.A. Musayev[b], N.N. Hashimova[b]
[a]*Institute of Physics, Ministry of Science and Education of the Republic of Azerbaijan, Baku, AZ-1143, Azerbaijan*
[b]*Azerbaijan State Oil and Industry University, Baku, AZ-1010, Azerbaijan*
[c]*Khazar University, Baku, AZ 1096, Azerbaijan*
**Corresponding Author e-mail: khuramanahmadova85@gmail.com*
Received October 10, 2024; revised January 4, 2025; accepted January 6, 2025

ZnS and $CuGaS_2$ are materials with a wide range of applications in modern optoelectronics. These materials are used for IR windows as well as lenses in the thermal band, where multispectral maximum transmission and lowest absorption are required. Precisely because of these characteristics, extensive and accurate optical research is necessary. This work has developed an ellipsometric approach for ZnS/GaAs and $CuGaS_2$/GaP film/substrate systems to address direct ellipsometry tasks. The proposed approach enables us to determine the effects of lattice mismatch on the optical indicatrix of the stressed film being considered through ellipsometric parameters.
Keywords: *Lattice mismatch; Thin film; Ellipsometry*
PACS: 42.25. p

INTRODUCTION

In modern optoelectronics, ZnS and CuGaS2 materials are widely used for IR windows, as well as lenses in the thermal band, where multispectral maximum transmission and lowest absorption are required. It is these properties that require extensive and precise optical studies of the materials.

In recent two decades ellipsometric approach has gained a worldwide recognition as the most correct approach for description of light wave [1-5]. The ellipsometry method accurately studies the optical parameters of multilayer systems both theoretically and experimentally. At the same time, it can provide extensive information about the optical parameters of two different liquids [6-8]. Applications of are nowadays very numerous and are spread out from *in-sity* control in planar technologies to precise determination of optical function of solids. Ellipsometry is well known as one of the powerful methods to control thin film and surface parameters [9-12]. A huge variety of problems which are or could be solved by ellipsometric study is very persuasive and has provoked our present trial to explore a possibility of ellipsometric investigation of the photo-elastic effect which should take place in thin film/substrate systems because of lattice mismatch.

In this work ellipsometric approach have been developed for ZnS/GaAs and $CuGaS_2$/GaP film/substrate systems to solve direct ellipsometry task. The proposed approach allows to finding through ellipsometric parameters the lattice mismatch effect on optical indicatrix of the considered stressed film.

1. PHOTOELASTIC EFFECT IN STRESSED FILM

The photoelastic effect due to stress (t) or deformation (r) which corresponds to this stress is written in matrix form as

$$\Delta\eta_{ij} = \pi_{ijkl}t_{kl} = p_{ijkl}r_{kl}, \text{ in tensor form, } \Delta\eta_m = \pi_{mn}t_n = p_{mn}r_n$$

where $\pi_{mn} = \pi_{ijkl,}$ n = 1,2,3; $\pi_{mn} = 2\pi_{ijkl,}$ n = 4,5,6; and $p_{mn} = p_{ijkl}$, n = 1,2,3; $p_{mn} = 2p_{ijkl}$, n = 4,5,6. Here Δ is the change of the polarization constant η_m due to stress or deformation, π_{mn} and p_{mn} are the piezooptic and photoelastic coefficients, correspondingly; t_n and r_n are the stress and deformation, correspondingly.

To write down the equation of the photoelastic effect in the stressed film it is necessary to know symmetries of the film and substrate, as well as their orientation. For the sake of certainty, let us consider ZnS $(\bar{4}3m)$/GaAs$(\bar{4}3m)$ and $CuGaS_2(\bar{4}2m)$/GaAs$(\bar{4}3m)$ [13] systems with interface surface perpendicular to [001] direction (z-direction) in both cases.

1.1. ZnS/GaAs system

Before stress, in a coordinate system where z is directed perpendicular to the interface and x and y axes lie in the plane of interface, the equation for polarization constants in the film can be written as

$$\eta\,(x^2+y^2+z^2) = 1 \qquad (1)$$

After the stress, t, due to the lattice mismatch is applied along x and y directions, we have

Cite as: Kh.N. Ahmadova, M.A. Musayev, N.N. Hashimova, East Eur. J. Phys. 1, 197 (2025), https://doi.org/10.26565/2312-4334-2025-1-20

$$\begin{bmatrix} & t & t & 0 & 0 & 0 & 0 \\ \Delta\eta_1 & \pi_{11} & \pi_{12} & \pi_{12} & 0 & 0 & 0 \\ \Delta\eta_2 & \pi_{12} & \pi_{11} & \pi_{12} & 0 & 0 & 0 \\ \Delta\eta_3 & \pi_{12} & \pi_{12} & \pi_{11} & 0 & 0 & 0 \\ \Delta\eta_4 & 0 & 0 & 0 & \pi_{44} & 0 & 0 \\ \Delta\eta_5 & 0 & 0 & 0 & 0 & \pi_{44} & 0 \\ \Delta\eta_6 & 0 & 0 & 0 & 0 & 0 & \pi_{44} \end{bmatrix} \quad (2)$$

and

$$[\eta+(\pi_{11}+\pi_{12})t]x^2+[\eta+(\pi_{12}+\pi_{11})t]y^2+[\eta+(2\pi_{12})t]z^2 = 1 \quad (3)$$

Taking into account the relationship for r_0 [8] and that η equals $1/N^2$ (N is the refractive index) and supposing that everywhere $\Delta\eta<<\eta$, we have for optical indicatrix that

$$\frac{x^2+y^2}{N^2\left(1-N^2\frac{(p_{11}+p_{12})r}{2}\right)^2}+\frac{z^2}{N^2\left(1-N^2p_{12}r\right)^2}=1 \quad (4)$$

i.e., initially optically isotropic film turned into optically uniaxial film with optical axis **C** along the normal to the interface. The ordinary and extraordinary refractive indexes of the last film are

$$N_0 = N\left(1-N^2\frac{(p_{11}+p_{12})r}{2}\right) \quad (5)$$

and

$$N_e = N\left(1-N^2p_{12}r\right) \quad (5^*),$$

respectively.

1.2. $CuGaS_2$/GaP system

CuGaSe film is a uniaxial film, and the equation for polarization constants before stress can be written as $\eta_o(x^2+y^2)+\eta_e z^2=1$.

Stress induced by the lattice mismatch along x and y and the $\Delta\eta_i$ are related as

$$\begin{bmatrix} & t & t & 0 & 0 & 0 & 0 \\ \Delta\eta_1 & \pi_{11} & \pi_{12} & \pi_{13} & 0 & 0 & 0 \\ \Delta\eta_2 & \pi_{12} & \pi_{11} & \pi_{13} & 0 & 0 & 0 \\ \Delta\eta_3 & \pi_{31} & \pi_{31} & \pi_{33} & 0 & 0 & 0 \\ \Delta\eta_4 & 0 & 0 & 0 & \pi_{44} & 0 & 0 \\ \Delta\eta_5 & 0 & 0 & 0 & 0 & \pi_{44} & 0 \\ \Delta\eta_6 & 0 & 0 & 0 & 0 & 0 & \pi_{66} \end{bmatrix} \quad (6)$$

and

$$[\eta_o+(\pi_{11}+\pi_{12})t]x^2+[\eta_o+(\pi_{11}+\pi_{12})t]y^2+[\eta_e+(2\pi_{31})t]z^2=1 \quad (7)$$

For optical indicatrix we then have

$$\frac{x^2+y^2}{N_0^2\left(1-N_0^2\frac{(p_{11}+p_{12})r}{2}\right)^2}+\frac{z^2}{N_e^2\left(1-N_e^2p_{31}r\right)^2}=1 \quad (8)$$

i.e the film is again uniaxial with the same orientation of the principal axes. However, refractive indexes of ordinary and extraordinary beams are changed to

$$N_0^{new} = N_0\left(1-N_0^2\frac{(p_{11}+p_{12})r}{2}\right) \text{ and } N_e^{new} = N_e\left(1-N_e^2p_{31}r\right) \quad (9)$$

2. ELLIPSOMETRIC APPROACH FOR ZnS/GaAs AND $CuGaS_2$/GaP SYSTEMS

In anizotropic systems we have the most general relationship between p- and s- components of the complex amplitude of the reflected (r) and incident (i) waves [14]

$$E_p^r = R_{pp}\ E_{p+}^i \quad R_{sp}E_s^i \quad (10)$$

$$E_s^r = R_{sp}E_p^i + R_{ss}E_s^i \quad (10^*)$$

or

$$\frac{E_p^r}{E_s^r}=\frac{\left(\frac{R_{pp}}{R_{ss}}\right)\frac{E_p^i}{E_s^i}+\left(\frac{R_{ps}}{R_{ss}}\right)}{\left(\frac{R_{sp}}{R_{ss}}\right)\frac{E_p^i}{E_s^i}+1}, \qquad (11)$$

where Rpp/Rss, Rps/Rss and Rsp/Rss are the relative coefficients of reflection, which we have to be determine by solving Wave Equation [9]

$$\Delta E\text{-graddiv}E+(2\pi/\lambda)^2 D=0. \qquad (12)$$

It follows from section 1 (see 1.1 and 1.2) that we shall consider an isotropic substrate and a uniaxial film on, with the same z axis for the film and film/substrate system. It follows from Eq. (12) that in this case the x- and y-components of the electrical vector obey the following equations:

$$\varepsilon_e\frac{\partial^2 E_x}{\partial z^2}+\varepsilon_0\left[\left(\frac{2\pi}{\lambda}\right)^2\varepsilon_e-k_x^2\right]E_x=0 \text{ , and } \frac{\partial^2 E_y}{\partial z^2}+\left[\left(\frac{2\pi}{\lambda}\right)^2\varepsilon_0-k_x^2\right]E_y=0 . \qquad (13)$$

Where, k_x=const= $(2\pi/\lambda)\sin\varphi$, and $\varepsilon_o=(n_o-ik_o)^2$ and $\varepsilon_e=(n_e-ik_e)^2$ are the complex diagonal components of the dielectric function tensor. Now let us consider s-component of the incident wave. In this case Ey=Es;Ex=Ez=0; Hy=0. Using the Abbeles method, from solutions of the Eq. (8) the following matrix of tangential components of electric and magnetic field can be constructed:

$$M_s(0,d)=\begin{pmatrix} m_{s11}m_{s12}\\ m_{s21}m_{s22}\end{pmatrix}=\begin{pmatrix} \frac{1}{2}\left[e^{-i\delta_0}+e^{-i\delta_0}\right]\frac{1}{2g_0}\left[e^{-i\delta_0}-e^{i\delta_0}\right]\\ \frac{g_0}{2}\left[e^{-i\delta_0}-e^{-i\delta_0}\right]\frac{1}{2}\left[e^{-i\delta_0}+e^{i\delta_0}\right]\end{pmatrix}, \qquad (14)$$

where $\delta_0=\frac{2\pi}{\lambda}d\sqrt{\varepsilon_0-\sin^2\phi}$ and $g_0=\sqrt{\varepsilon_0-\sin^2\phi}$.

Now tangential components in the interfaces between the film and ambient and between the film and substrate can be connected through matrix

$$Q_s(0)=\begin{pmatrix} E_s(0)\\ H_x(0)\end{pmatrix}=M_s(0,d)\begin{pmatrix} E_s(d)\\ H_x(d)\end{pmatrix} \qquad (15)$$

Hereafter let us distinguish between thick and thin substrate. In the thick or absorptive substrate, we have no waves reflected from the interface between substrate and ambient and this case, as it will be seen afterwards, corresponds to the situation in ZnS/GaAs system. In the thin substrate, we have waves reflected from its bottom boundary and this will modify the total reflected field. (This case will correspond to the experimental situation in $CuGaS_2$/GaP system).

2.1. Thick substrate

$$R_{ss}=\frac{-\left(m_{s21}+gm_{s22}\right)+g_{sub}\left(m_{s11}+gm_{s12}\right)}{\left(m_{s21}-gm_{s22}\right)-g_{sub}\left(m_{s11}-gm_{s12}\right)}e^{-2ik_z d}, \qquad (16)$$

where:

$$g=\cos\phi \text{, and } g_{sub}=\sqrt{\varepsilon_{sub}-\sin^2\phi}. \qquad (17)$$

2.2. Thin substrate

In this case R_{ss} will be given by the relation (9)

$$M_s\left(0,d_{sub}+d\right)=\begin{pmatrix} m_{s11} & m_{s12}\\ m_{s21} & m_{s22}\end{pmatrix}=M\left(d_{sub},d\right)M\left(0,d_{sub}\right). \qquad (18)$$

Here M (d_{sub},d) is the same as matrix (14), matrix (0, d_{sub}) has the form similar to that of matrix (14) in which δ_0 and g_0 must be replaced by δ_{sub} and g_{sub}, respectively, i.e.

$$M_S\left(0,d_{sub}\right)=\begin{pmatrix}\frac{1}{2}\left[e^{-i\delta_{sub}}+e^{i\delta_{sub}}\right] & \frac{1}{2g_{sub}}\left[e^{-i\delta_{sub}}-e^{i\delta_{sub}}\right]\\ \frac{g_{sub}}{2}\left[e^{-i\delta_{sub}}-e^{i\delta_{sub}}\right] & \frac{1}{2}\left[e^{-i\delta_{sub}}+e^{i\delta_{sub}}\right]\end{pmatrix}, \tag{19}$$

where $\delta_{sub}=\frac{2\pi}{\lambda}d_{sub}\sqrt{\varepsilon_{sub}-\sin^2\phi}$ and $g_{sub}=\sqrt{\varepsilon_{sub}-\sin^2\phi}$

Similary to R_{ss} it is easy to show that R_{pp} can be written in both cases (thin and thick substrate) so as it is shown in the next subsection.

2.3. Thick substrate

$$R_{pp}=\frac{-\left(m_{p21}-gm_{p22}\right)-\frac{g_{sub}}{\varepsilon_{sub}}\left(m_{p11}-gm_{p12}\right)}{\left(m_{p21}+gm_{p22}\right)+\frac{g_{sub}}{\varepsilon_{sub}}\left(m_{p11}+gm_{p12}\right)}e^{-2ik_z d} \tag{20}$$

$$M_p\left(0,d\right)=\begin{pmatrix}\frac{1}{2}\left[e^{-i\delta_e}+e^{i\delta_e}\right] & -\frac{\varepsilon_e}{2g_e}\left[e^{-i\delta_e}-e^{i\delta_e}\right]\\ -\frac{g_e}{2\varepsilon_e}\left[e^{-i\delta_e}-e^{i\delta_e}\right] & \frac{1}{2}\left[e^{-i\delta_e}+e^{i\delta_e}\right]\end{pmatrix}, \tag{21}$$

where,

$$\delta_e=\frac{2\pi}{\lambda}d\sqrt{\varepsilon_0-\left(\frac{\varepsilon_0}{\varepsilon_e}\right)\sin^2\phi}\ \text{ and }\ g_e=\sqrt{\varepsilon_e-\left(\frac{\varepsilon_0}{\varepsilon_e}\right)\sin^2\phi} \tag{22}$$

2.4. Thin substrate

In this case $M_p(d_{sub},d)$ equals

$$M_p\left(0,d_{sub}\right)=\begin{pmatrix}\frac{1}{2}\left[e^{-i\delta_{sub}}+e^{i\delta_{sub}}\right] & -\frac{\varepsilon_{sub}}{2g_{sub}}\left[e^{-i\delta_{sub}}-e^{i\delta_{sub}}\right]\\ -\frac{g_{sub}}{2\varepsilon_{sub}}\left[e^{-i\delta_{sub}}-e^{i\delta_{sub}}\right] & \frac{1}{2}\left[e^{-i\delta_{sub}}+e^{i\delta_{sub}}\right]\end{pmatrix} \tag{23}$$

The ratio of $g_{sub}/\varepsilon_{sub}$ must be replaced by $g=\cos\varphi$. The coefficients m can then be obtained from

$$M_p\left(0,d_{sub}+d\right)=\begin{pmatrix}m_{p11} & m_{p12}\\ m_{p21} & m_{p22}\end{pmatrix}=M_p\left(d_{sub},d\right)M_p\left(0,d_{sub}\right). \tag{24}$$

3. DIRECT ELLIPSOMETRY TASK FOR ZnS/GaAs AND $CuGaS_2$/GaP

Direct ellipsometry task implies a computation of ellipsometric angles ψ and Δ of the system under consideration using analytic expressions obtained in Section 2. Our main target is the photoelastic effect in stressed film/substrate system. To calculate the magnitude of the effect in ψ-and Δ-units we will do the following. First, we will calculate ψ and Δ for unstressed film/substrate systems at different thicknesses of the film d. After that we will calculate ψ and Δ for stressed film/substrate system with above values of the thicknesses and different values (p_{mn}r, r is known) of the photoelastic effect. In both cases we will constract Δ=f(ψ) dependencies and will estimate the smallest value of the photoelastic effect, which we are still be able to detect.

3.1. Unstressed ZnS/GaAs system

ZnS/GaAs system presents an isotropic film/substrate system for which the principal equation of the ellipsometry ($\tan\psi e^{i\Delta}=R_p/R_s$) is very well known and given by

$$\tan\psi\times e^{i\Delta}=\frac{r_{01p}+e^{-2\delta_2}e^{-2i\delta_1}r_{12p}}{1+e^{-2\delta_2}e^{-2i\delta_1}r_{01p}r_{12p}}\times\frac{1+e^{-2\delta_2}e^{-2i\delta_1}r_{01s}r_{12s}}{r_{01s}+e^{-2\delta_2}e^{-2i\delta_1}r_{12s}}, \tag{25}$$

$$r_{12s}=\frac{\sqrt{\varepsilon_{film}-\sin^2\phi}-\sqrt{\varepsilon_{sub}-\sin^2\phi}}{\sqrt{\varepsilon_{film}-\sin^2\phi}+\sqrt{\varepsilon_{sub}-\sin^2\phi}},\ r_{12p}=\frac{\sqrt{\varepsilon_{sub}-\frac{\varepsilon_{sub}\sin^2\phi}{\varepsilon_{film}}}-\sqrt{\varepsilon_{film}-\frac{\varepsilon_{film}\sin^2\phi}{\varepsilon_{sub}}}}{\sqrt{\varepsilon_{sub}-\frac{\varepsilon_{sub}\sin^2\phi}{\varepsilon_{film}}}+\sqrt{\varepsilon_{film}-\frac{\varepsilon_{film}\sin^2\phi}{\varepsilon_{sub}}}},\ r_{01s}=\frac{\cos\phi-\sqrt{\varepsilon_{film}-\sin^2\phi}}{\cos\phi+\sqrt{\varepsilon_{film}-\sin^2\phi}},$$

$$\delta_1=\frac{\sqrt{2}\pi}{\lambda}\times d\times\sqrt{\sqrt{a^2+b^2}+a},\ \delta_2=\frac{\sqrt{2}\pi}{\lambda}\times d\times\sqrt{\sqrt{a^2+b^2}-a},$$

$$a=n_{film}^2-k_{film}^2-\sin^2\phi,\ \varepsilon_{film}=n_{film}^2-k_{film}^2-i2n_{film}k_{film},\ \varepsilon_{sub}=n_{sub}k_{sub}^2-i2n_{sub}k_{sub}.$$

Let us select the experimental wavelength in region where sensitivity of a Jobin-Ivon spectroscopic ellipsometer is high and the substrate is absorptive enough to avoid formation of the reflected beam from the bottom boundary of the substrate.

3.2. Unstressed $CuGaS_2$/GaP system

There exists a possibility to simplify the problem by selecting the experimental wavelength at λ=6400 Å where $N_0=N_e$ (isotropic point) and uniaxial optical idicatrix turns into sphere. It is easy to show that in this case,

$$\tan\psi\times e^{i\Delta}=\frac{r_{01p}+e^{-2\delta_2^{film}}e^{-2i\delta_1^{film}}r_{12p}+e^{-2\delta_2^{sub}}e^{-2i\delta_1^{sub}}r_{01p}r_{12p}r_{23p}+e^{-2(\delta_2^{film}+\delta_2^{sub})}e^{-2i(\delta_1^{film}+\delta_1^{sub})}r_{23p}}{1+e^{-2\delta_2^{film}}e^{-2i\delta_1^{film}}r_{01p}r_{12p}+e^{-2\delta_2^{sub}}e^{-2i\delta_1^{sub}}r_{12p}r_{23p}+e^{-2(\delta_2^{film}+\delta_2^{sub})}e^{-2i(\delta_1^{film}+\delta_1^{sub})}r_{01p}r_{23p}}\times$$
$$\times\frac{1+e^{-2\delta_2^{film}}e^{-2i\delta_1^{film}}r_{01s}r_{12s}+e^{-2\delta_2^{sub}}e^{-2i\delta_1^{sub}}r_{12s}r_{23s}+e^{-2(\delta_2^{film}+\delta_2^{sub})}e^{-2i(\delta_1^{film}+\delta_1^{sub})}r_{01s}r_{23s}}{r_{01s}+e^{-2\delta_2^{film}}e^{-2i\delta_1^{film}}r_{12s}+e^{-2\delta_2^{sub}}e^{-2i\delta_1^{sub}}r_{01s}r_{12s}r_{23s}+e^{-2(\delta_2^{film}+\delta_2^{sub})}e^{-2i(\delta_1^{film}+\delta_1^{sub})}r_{23s}}. \quad (26)$$

The other coefficients are given by

$$r_{23p}=\sqrt{1-\frac{\sin^2\phi}{\varepsilon_{sub}}}-\sqrt{\varepsilon_{sub}}\cos\phi\Big/\sqrt{1-\frac{\sin^2\phi}{\varepsilon_{sub}}}+\sqrt{\varepsilon_{sub}}\cos\phi,\ r_{23s}=\frac{\sqrt{\varepsilon_{sub}-\sin^2\phi}-\cos\phi}{\sqrt{\varepsilon_{sub}-\sin^2\phi}+\cos\phi},$$

$$\delta_1^{film(sub)}=\frac{\sqrt{2}\pi}{\lambda}\times d_{film(sub)}\times\sqrt{\sqrt{a_{film(sub)}^2+b_{film(sub)}^2}+a},\ \delta_2^{film(sub)}=\frac{\sqrt{2}\pi}{\lambda}\times d_{film(sub)}\times\sqrt{\sqrt{a_{film(sub)}^2+b_{film(sub)}^2}-a},$$

$$a_{film(sub)}=n_{film(sub)}^2-k_{film(sub)}^2-\sin^2\phi,\ b_{film(sub)}=2n_{film(sub)}k_{film(sub)}.$$

3.3. Selection of experimental angle of incidence

The change of polarization angles due to the change of the dielectric constant of the film is observable if the following conditions is fulfilled:

$$\delta\psi_{\min}=\left|\delta n_{film,\min}^{(\psi)}\left(\frac{\partial\psi}{\partial n_{film}}\right)-\delta\psi_{el}\right|>0,$$

and

$$\delta\Delta_{\min}=\left|\delta n_{film,\min}^{(\Delta)}\left(\frac{\partial\Delta}{\partial n_{film}}\right)-\delta\Delta_{el}\right|>0 \quad (27)$$

Where $\delta_{film\,\min}^{(\psi,\Delta)}$ are the minimal value of the change of the dielectric constant of the film, $\partial\psi/\partial n_{film}$ and $\partial\Delta/\partial n_{film}$ are the first derivatives, $\delta\psi_{el}$ and $\delta\Delta_{el}$ are the threshold sensitivities of the employed ellipsometer. As seen from Fig.1, the optimum sensitivity for ψ and Δ is attained at around pseudo-Brewster angle for all considered systems. It is natural (Fig.1) that the higher the film thickness the larger response of the ellipsometric angles is.

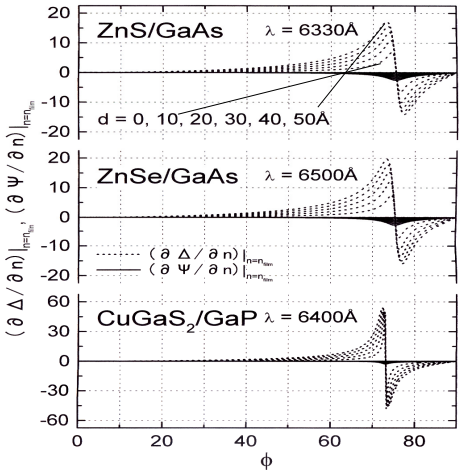

Figure 1. First derivatives of the ellipsometric parameters as function of incidence angle ϕ at various film thicknesses d

3.4. ZnS/GaAs after stress

It follows from Sections 2.3 and 2.4 that after stress the principal ellipsometry equation can be rewritten as

$$\tan\psi e^{i\Delta} = \frac{\left(\cos\phi - \frac{g_{sub}}{\varepsilon_{sub}}\right)\cos\delta_e + i\left(\frac{g_{sub}}{\varepsilon_{sub}}\frac{\varepsilon_e}{g_e} - \frac{g_e}{\varepsilon_e}\right)\sin\delta_e}{\left(\cos\phi + \frac{g_{sub}}{\varepsilon_{sub}}\right)\cos\delta_e + i\left(\frac{g_{sub}}{\varepsilon_{sub}}\frac{\varepsilon_e}{g_e} + \frac{g_e}{\varepsilon_e}\right)\sin\delta_e} \times \frac{(\cos\phi + g_{sub})\cos\delta_0 + i\left(g_0 + \frac{g_{sub}}{g_0}\right)\sin\delta_0}{(\cos\phi - g_{sub})\cos\delta_0 + i\left(g_0 - \frac{g_{sub}}{g_0}\right)\sin\delta_0}. \quad (28)$$

Here

$$\delta_e = \frac{2\pi}{\lambda} d_{eff}\sqrt{\varepsilon_0 - \left(\frac{\varepsilon_0}{\varepsilon_e}\right)\sin^2\phi}\,,\ \delta_0 = \frac{2\pi}{\lambda} d_{eff}\sqrt{\varepsilon_0 - \sin^2\phi}\,, \quad (29)$$

and

$$\varepsilon_e = n_{film}^2(1 - n_{film}^2 p_{12} r_{eff})^2 \quad , \quad \varepsilon_0 = n_{film}^2\left(1 - n_{film}^2 \frac{p_{11} + p_{12}}{2} r_{eff}\right)^2. \quad (30)$$

In similar way the principal ellipsometry equation is obtained for a stressed $CuGaS_2$/GaP system.

4. CONCLUSIONS

The ellipsometric description of the lattice parameter mismatch effect consists of the results of solving the ellipsometric straight problem for ZnS/GaAs and $CuGaS_2$/GaP semiconductor systems. The photoelastic effect resulting from the elastic deformation of materials with different lattice parameters in contact with each other (at the atomic level) is described in this work. The thicknesses of dislocation-free layers in which the photoelastic effect is observed due to the mismatch of the lattice parameters (pure photoelastic effect occurs only in such layers due to the mismatch of the lattice parameters) were evaluated. Amplitude coefficients of reflection from (ZnS/GaAs or $CuGaS_2$/InP) internal boundary and (vacuum/ZnS or $CuGaS_2$) external boundary were determined. The relationship between the optical anisotropy and the optical parameters of the initially isotropic ZnS layer after straining was studied in detail. Analogously, the relationship between the new value of the optical anisotropy of the $CuGaS_2$ layer, which was initially uniaxial, but retained the uniaxial character of the optical anisotropy even after applying the voltage, and the variable parameters of the system was found. The calculated photoelastic effect and its dependence on the thickness of the layers are given in the ellipsometric image, which is more convenient for conducting an ellipsometric experiment.

ORCID

Kh.N. Ahmadova, https://orcid.org/0000-0001-5974-5400

REFERENCES

[1] A. Kitano, Y.G. Shim, K. Wakita, Kh. Khalilova, N. Mamedov, A. Bayramov, E. Huseynov, and I. Hasanov, "Optical characterization of non-annealed CdS:O films for window layers in solar cells," Phys. Status Solidi C, **10**, 1107-1110 (2013). https://doi.org/10.1002/pssc.201200834

[2] Kh. Khalilova, Y.G. Shim, I. Hasanov, R. Asaba, K. Wakita, and N. Mamedov, "Spectroscopic ellipsometry studies of as-prepared and annealed CdS:O thin films," Physica Status Solidi C, **12**, 592-595 (2015). https://doi.org/10.1002/pssc.201400272

[3] Kh.N. Ahmadova, and S.H. Jabarov, "Obtaining of Al nanosized thin layers and their structural properties," Arabian Journal for Science and Engineering, **48**, 8083-8088 (2023). https://doi.org/10.1007/s13369-022-07449-2
[4] Kh.N. Ahmadova, S.H. Jabarov, Y.I. Aliyev, Sh.N. Aliyeva, A.V. Trukhanov, S.V. Trukhanov, and M.N. Mirzayev, "Design, production and investigation of structural singularities of layered metal-oxide nanostructures," International Journal of Nanoscience, (2024). https://doi.org/10.1142/S0219581X24500157
[5] Kh.N. Ahmadova, and S.H. Jabarov, "Obtaining of Al nanolayers and crystal structure," International Journal on Technical and Physical Problems of Engineering, **52**, 116-120 (2022). https://www.iotpe.com/IJTPE/IJTPE-2022/IJTPE-Issue52-Vol14-No3-Sep2022/16-IJTPE-Issue52-Vol14-No3-Sep2022-pp116-120.pdf
[6] Kh.N. Ahmadova, "Spectroscopic ellipsometric investigation of optical parameters of oil-water thin multiple systems," International Journal of Modern Physics B, **34**, 2050058 (2020). https://doi.org/10.1142/S0217979220500587
[7] T.K. Nurubeyli, and Kh.N. Ahmadova, "The role of the spectral matrix effect in the element analysis of biological fluids in ICP-MS," Modern Physics Letters B, **35**, 2150094 (2021). https://doi.org/10.1142/S0217984921500949
[8] Kh.N. Ahmadova, "The new innovative optic complete method of identification of oil and its fraction," International Journal of Modern Physics B, **35**, 2150241 (2021). https://doi.org/10.1142/S0217979221502416
[9] D. Datta, V. Tripathi, P. Gogoi, S. Banerjee, and S. Kumar, "Ellipsometric studies on thin film CuPC: C60 blends for solar cell applications," Thin Solid Films, **516**, 7237 (2008). https://doi.org/10.1016/j.tsf.2007.12.043
[10] Y. Shim, H. Hasegawa, K. Wakita, and N. Mamedov, "$CuAl_{1-x}In_xSe_2$ solid solutions. Dielectric function and inter-band optical transitions," Thin Solid Films, **517**, 1442 (2008). https://doi.org/10.1016/j.tsf.2008.09.013
[11] Y. Shim, W. Okada, K. Wakita, and N. Mamedov, "Refractive indices of layered semiconductor ferroelectrics $TlInS_2$, $TlGaS_2$ and $TlGaSe_2$ from ellipsometric measurements limited to only layer-plane surfaces," J. Appl. Phys. **102**, 083537 (2007). https://doi.org/10.1063/1.2800827
[12] H. Fujiwara, *Spectroscopic Ellipsometry: Principles and Applications*, (John Wiley & Sons, Ltd, 2007), https://doi.org/10.1002/9780470060193
[13] S. Iida, H. Icinokura, Y. Toyama, and A. Kato, "Photoluminescence of site-selectively Zn-doped $CuGaS_2$/GaP epitaxial layers," Journal of Physics and Chemistry of Solids, **64**(9-10), 2017-2020 (2017). https://doi.org/10.1016/S0022-3697(03)00093-3
[14] U. Rossow, "Spectroscopic Ellipsometry," in: *Epioptics. Esprit Basic Research Series*, edited by J.F. McGlip, D. Weaire, and C.H. Patterson, (Springer, Berlin, Heidelberg, 1995). pp. 39-76. https://doi.org/10.1007/978-3-642-79820-7_3

ОПТИЧНІ ДОСЛІДЖЕННЯ СИСТЕМ ZnS/GaAs ТА CuGaS2/GaP

Х.Н. Ахмадова[a,b,c], М.А. Мусаєв[b], Н.Н. Хашімова[b]
[a]Інститут фізики Міністерства науки і освіти Азербайджанської Республіки, Баку, AZ-1143, Азербайджан
[b]Азербайджанський державний університет нафти та промисловості, Баку, AZ-1010, Азербайджан
[c]Хазарський університет, Баку, AZ 1096, Азербайджан

ZnS і $CuGaS_2$ є матеріалами з широким спектром застосування в сучасній оптоелектроніці. Ці матеріали використовуються для ІЧ-вікон, а також для лінз у тепловому діапазоні, де потрібне багатоспектральне максимальне пропускання та найменше поглинання. Саме через ці характеристики необхідні обширні та точні оптичні дослідження. У цій роботі розроблено еліпсометричний підхід для систем плівка/підкладка ZnS/GaAs і $CuGaS_2$/GaP для вирішення завдань прямої еліпсометрії. Запропонований підхід дозволяє через еліпсометричні параметри визначити вплив неузгодженості ґрат на оптичну індикатрису напруженої плівки.

Ключові слова: *неузгодженість решітки; тонка плівка; еліпсометрія*

East European Journal of Physics. 1. 204-210 (2025)
DOI:10.26565/2312-4334-2025-1-21 ISSN 2312-4334

ANALYTIC ANALYSIS OF THE FEATURES OF GaAs/Si RADIAL HETEROJUNCTIONS: INFLUENCE OF TEMPERATURE AND CONCENTRATION

Jo'shqin Sh. Abdullayev[a]*, Ibrokhim B. Sapaev[a,b]
[a] *National Research University TIIAME, Department of Physics and Chemistry, Tashkent, Uzbekistan*
[b] *Western Caspian University, Baku, Azerbaijan*
**Corresponding Author e-mail: j.sh.abdullayev6@gmail.com*
Received November 7, 2024; revised January 6, 2025; accepted January 8, 2025

In this article, we analytically study the electrophysical features of the p-Si/n-GaAs radial heterojunction (RHJ) over a temperature range of 50 K to 500 K, in increments of 50 K while considering various doping concentrations. The analysis encompasses band gap narrowing (BGN), the differences in the band gap between GaAs and Si as a function of temperature, and the built-in potential relative to temperature. In particular, we focus on core p-Si with a radius of 0.5 μm and shell n-GaAs with a radius of 1 μm within the structure. Our findings indicate that the thickness of the depletion region in the p-Si/n-GaAs (RHJ) increases with rising temperature. The band gap difference between GaAs and Si is 0.31 eV at 300 K in our model, which is in good agreement with the experimental results. Additionally, the conduction band offset ΔE_C=0.04 eV and the valence band offset ΔE_V=0.27eV were calculated at 300 K. When the doping concentration changes from $2\cdot10^{15}$ to $2\cdot10^{18}$ band gap narrowing (BGN) decreases by 2 meV. Additionally, the built-in potential of the p-Si/n-GaAs (RHJ) decreases by 76 mV with increasing temperature.
Keywords: *Radial p-n junction; Light trap; External factors; Volt-farad; Heterostructures; Radial heterojunction (RHJ); Band gap narrowing (BGN); Cryogenic temperatures*
PACS: 73.40. Lq, 73.61.Cw, 73.61.Ey, 72.20.Jv

INTRODUCTION

The rapid progress in semiconductor electronics research has led to substantial advancements in the design, optimization, and functionality of modern devices. Key innovations, such as two-dimensional transistors [1], nanowires [2], and notably, radial p-n junction structures [3,4], have expanded the potential for nanoscale applications. Among these, radial p-n junctions offer distinct advantages over conventional planar configurations, particularly in submicron nanowires [5,6]. Over the past two decades, these structures have gained prominence due to their superior optical and electronic characteristics, making them highly suitable for applications in photodiodes, optical sensors [7], thermal detectors, photovoltaic detectors [8], and solar cells [9]. By optimizing light absorption and carrier collection, radial p-n junctions reduce optical losses, thereby enhancing energy conversion efficiency. Their perpendicular orientation for light absorption and carrier transport further supports high-frequency applications, including high-speed electronics and wireless communication. Radial junctions also play a critical role in high-speed photodetectors [10], avalanche photodiodes [11], photovoltaic devices, gamma-ray detectors [12], and infrared sensors [13,14], where their structure provides outstanding efficiency, speed, and sensitivity essential for advanced semiconductor applications. Given the broad application range of these junctions, a detailed investigation of their electrophysical properties particularly ionization processes and performance across diverse temperatures is crucial. Both theoretical modeling and experimental validation are necessary to achieve the high reliability and accuracy required for these devices. While radial p-n and p-i-n junctions have been widely explored, heterojunction structures are less extensively studied. Despite the development of new semiconductor materials, GaAs remain the primary material for optoelectronic devices, while Si continues to be the most widely used material due to its advanced technological development and abundance on the Earth's surface. From this perspective, the p-Si/n-GaAs (RHJ) has been selected for this study. This work addresses this gap by focusing on the p-Si/n-GaAs (RHJ) structure, analyzing its electrophysical properties through theoretical and analytical methods. We apply mathematical modeling to investigate the behavior of the p-Si/n-GaAs (RHJ) under varying temperatures and external voltages, offering insights into its performance characteristics and potential for future applications.

METHODS AND MATERIAL

We have selected a core of p-Si with a radius of 0.5 μm and a shell of n-GaAs with a radius of 1 μm within the structure as the object of this work. Based on the operating temperature of semiconductor devices made from Si and GaAs, the temperature range was selected to be between 50 K and 500 K, in steps of 50 K. The interval $d_{p-n} = r_p < r < r_n$ represents the depletion region and this depends on temperature and external voltage and is represented by the expression (1):

$$d_{p-n} = \sqrt{\frac{2(\varepsilon_{GaAs} N_A + \varepsilon_{Si} N_D)(\varphi_{bi}(T) - U)}{q\varepsilon_{Si}\varepsilon_{GaAs}\varepsilon_0 N_A \cdot N_D}} \quad (1)$$

Cite as: J.Sh. Abdullayev, I.B. Sapaev, East Eur. J. Phys. 1, 204 (2025), https://doi.org/10.26565/2312-4334-2025-1-21

where, $\varepsilon_{Si}, \varepsilon_{GaAs}$ are and dielectric constant of the Si and GaAs respectively, $\varepsilon_0 = 8.85 \cdot 10^{-12}\ F \cdot m^{-1}$ electrical constant. Many articles have conducted theoretical work without considering the dependence of effective mass on temperature and electric field. To address these shortcomings, we calculated the dependence of the effective mass of electrons and holes on temperature using expression (2).

$$m^*_{(e,h)} = m(\theta) \cdot \left(1 + \beta_{(e,h)} \cdot (T - \theta)\right) \tag{2}$$

Where, $m(\theta)$ is mass , $\beta_{(e,h)}$ is the temperature coefficient of the effective mass (which can be determined experimentally or from theoretical models). θ_{GaAs} and θ_{Si} are Debye temperature GaAs and Si respectively.

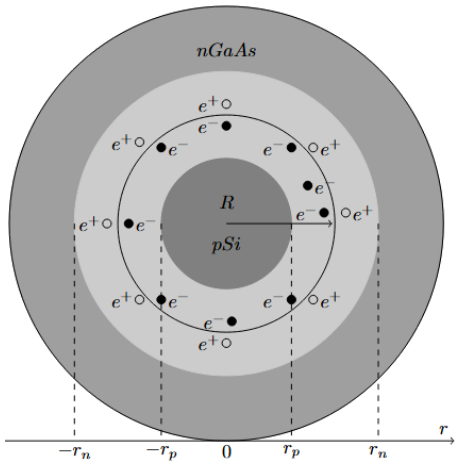

Figure 1. This figure shows a 2D cross-section of the submicron radial p-n junction structures. The light gray area represents the n-type GaAs region, the dark gray area represents the p-type Si region, and the very light gray area denotes the depletion region

Figure 1 shows the cross-sectional view of the selected p-Si/n-GaAs (RHJ) sample, cut along the Z-axis. Where r denotes the radial dimension, $\circ e^+$ and $\bullet e^-$ represents the densities of ionized N_D^+ donor and N_A^- acceptor atoms respectively, at the interface of the radial p-n heterojunction within the depletion region. If full ionization case $N_D^+ = N_D$, $N_A^- = N_A$. In Figure 1, the interval $0 < r < r_p$ represents the p-type quasi-neutral region (QNR), the interval $r_p < r < r_n$ represents the depletion region in the radial p-n heterojunction junction, the interval $r_n < r < 2R$ represents the n-type quasi-neutral region (QNR). In heterojunctions, there are differences in the conduction band ΔE_C and valence band ΔE_V at the interface, and these differences change with temperature and concentration. As a result, there is a difference in the band gap between Si and GaAs, as described by expression (3).

$$\Delta E_g(T, n, p) = \Delta E_g(T) - \Delta E_{BGN}(n, p) \tag{3}$$

Where, $\Delta E_g(T)$ is the term that depends on temperature, and $\Delta E_{BGN}(n,p)$ represents band gap narrowing, which is influenced by concentration, as described by expression (4).

$$\Delta E_{BGN}(n, p) = A \cdot \sqrt[3]{N} + B \cdot \sqrt[4]{N} + C \cdot \sqrt{N} + D \cdot \sqrt{N} \tag{4}$$

where A, B, C, and D are material-dependent semi-empirical coefficients [15]; the values for Si and GaAs are provided in Table 1. The influence of temperature and concentration on electron affinity was also examined, as expressed by equation (5).

$$\chi(T, n, p) = \chi_0 - \alpha \cdot (T - T_0) + \lambda \cdot \ln\left(\frac{(n, p)}{N_{eff}}\right) \tag{5}$$

The energy levels ΔE_C and ΔE_V are influenced by temperature. For instance, as temperature increases, the band gap can change, affecting the thermal generation of charge carriers and the performance of devices like diodes and transistors.

$$\Delta E_V(T) = \Delta E_V(0) + T \cdot \left(\gamma_{GaAs} - \gamma_{Si}\right) \tag{6a}$$

$$\Delta E_C(T) = \Delta E_V(T) + \Delta E_g(T) \tag{6b}$$

Here, γ is a coefficient that describes how the valence band shifts with temperature. $\gamma_{GaAs}, \gamma_{Si}$ are -0.006 and -0.001 eV/K respectively.

Table 1. Coefficients A, B, C, D for Si and GaAs materials

Symbol	Si		GaAs		Unit
A	n-type	p-type	n-type	p-type	eVcm
	$1.02 \cdot 10^{-8}$	$1.11 \cdot 10^{-8}$	$1.65 \cdot 10^{-8}$	$9.77 \cdot 10^{-9}$	
B	$4.15 \cdot 10^{-7}$	$4.79 \cdot 10^{-7}$	$2.38 \cdot 10^{-7}$	$3.87 \cdot 10^{-7}$	$eVcm^{3/4}$
C	$1.45 \cdot 10^{-12}$	$3.23 \cdot 10^{-12}$	$1.83 \cdot 10^{-11}$	$3.41 \cdot 10^{-12}$	$eVcm^{3/2}$
D	$1.48 \cdot 10^{-12}$	$1.81 \cdot 10^{-12}$	$7.25 \cdot 10^{-11}$	$4.84 \cdot 10^{-13}$	$eVcm^{3/2}$

The electrostatic potential difference in the p-Si/n-GaAs (RHJ) varies with changes in the external source voltage, which can be expressed as follows (7):

$$\varphi_{bi}(T) = \Delta E_g(T) - \frac{kT}{q} \cdot \ln\left(\frac{N_A \cdot N_D}{n_{iGaAs} \cdot n_{iSi}}\right) \tag{7}$$

Here, k is the Boltzmann constant, T is the absolute temperature in Kelvin, q is the charge of an electron, N_A and N_D are acceptor and donor concentrations respectively, n_{iSi} and n_{iGaAs} are intrinsic carrier concentrations of Si and GaAs respectively. The results obtained using the formulas and material parameters outlined above are presented in the Results and Discussion section, where the findings are analyzed in relation to the initial expectations.

RESULTS AND DISCUSSION

The effective mass significantly influences the movement of electrons and holes within the crystal. It varies with temperature, affecting their behavior. Figure 2 illustrates the changes in the effective mass of electrons and holes in Si and GaAs materials.

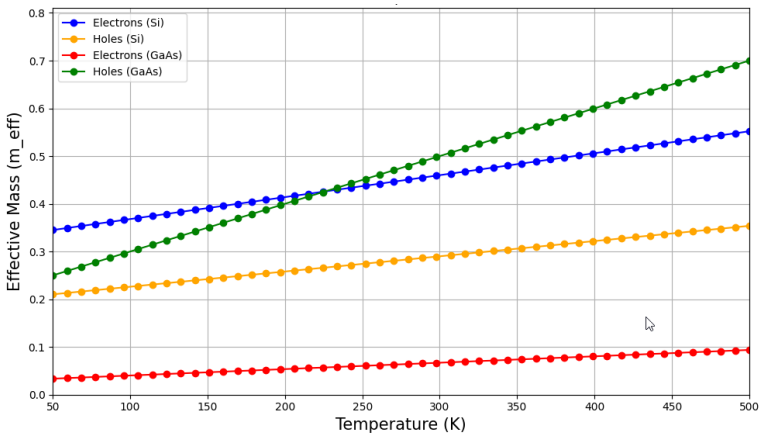

Figure 2. Effective mass of electrons and holes in Si and GaAs as a function of temperature

The plot illustrates the temperature dependence of effective masses for electrons and holes in silicon (Si) and gallium arsenide (GaAs) over a range from 50 K to 500 K. The effective mass of both carriers in each material increases slightly with temperature. In Si, electron effective mass starts at approximately $0.46m_e$ and hole mass at $0.29\ m_e$, both rising gradually. For GaAs, electrons have a lower effective mass, starting around $0.067m_e$, while holes begin at $0.5m_e$ and exhibit a more pronounced increase with temperature.

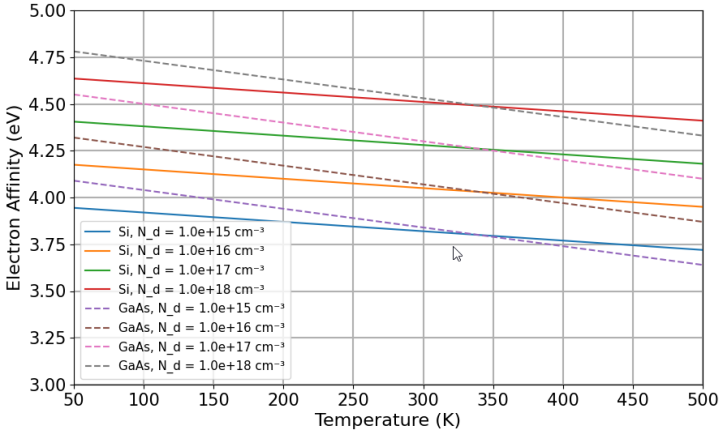

Figure 3. Electron affinity of p-Si and n-GaAs as a function of temperature.

Figure 3 illustrates that the electron affinity of both Si and GaAs decreases with varying doping concentrations over a temperature range of 50 K to 500 K. The electron affinity of GaAs is higher than that of Si up to 350 K, but beyond this temperature, the electron affinity of GaAs becomes lower than that of Si. Understanding the temperature- and doping-dependent electron affinity of Si and GaAs is essential for optimizing band alignment, carrier transport, and device stability in semiconductor applications. This knowledge enables the precise design of heterojunctions, doping profiles, and materials selection, improving the performance and reliability of devices such as transistors, solar cells, and optoelectronic components. These trends reflect material-specific characteristics, with GaAs showing a significant mass disparity between electrons and holes, benefiting high-mobility and optoelectronic applications. Understanding these variations is critical for optimizing electronic and optical device performance across a range of temperatures.

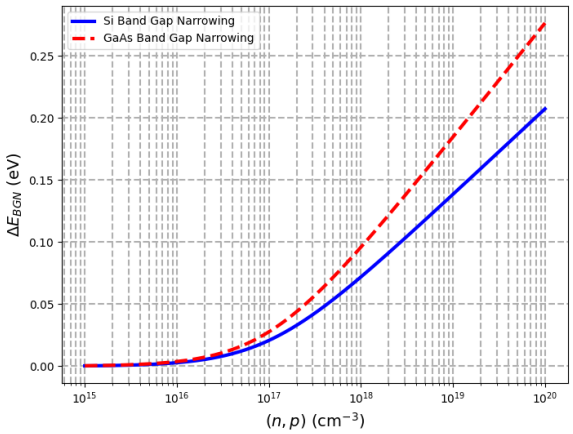

Figure 4. Band gap narrowing in Si and GaAs as a function of temperature.

Figure 4 illustrates the conduction and valence band energies as functions of temperature for Si $\Delta E_{BGN}Si(p)$ and $\Delta E_{BGN}GaAs(n)$. The blue curve represents $\Delta E_{BGN}Si(p)$, which increases from approximately 10^{15} to 10^{20} cm^{-3} as hole concentration p rises. In contrast, the red dashed line represents $\Delta E_{BGN}GaAs(n)$, which follow a similar upward trend with electron concentration n. This comparison highlights the distinct energy characteristics of Si and GaAs across a broad range of carrier concentrations, providing crucial insights into their performance in semiconductor applications.

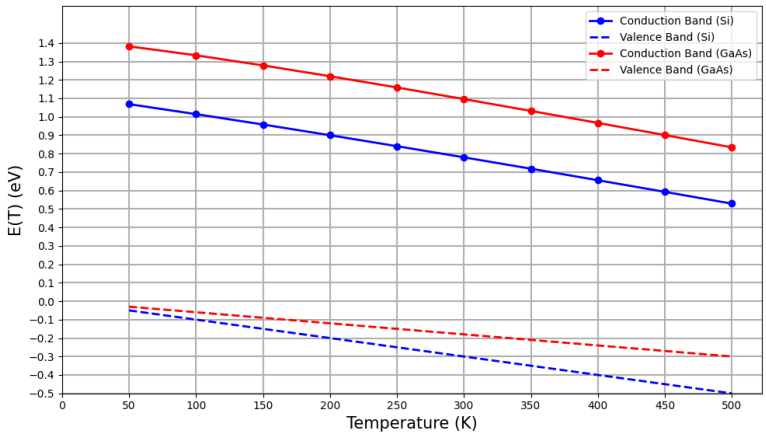

Figure 5. Conduction and valence band energies of Si and GaAs as a function of temperature.

Figure 5 illustrates the temperature dependence of conduction and valence band energies in Si and GaAs over the range of 50 K to 500 K, showing a decrease in both energy levels with increasing temperature. These changes significantly impact electronic properties, including band alignment and carrier dynamics. Understanding these variations is crucial for designing temperature-sensitive semiconductor devices, such as diodes, transistors, and heterojunctions, to ensure optimal performance across wide temperature ranges. The energies of the conduction and valence bands in Silicon and Gallium Arsenide exhibit a distinct dependence on temperature. Grasping these relationships is crucial for the effective design and optimization of semiconductor devices. Figure 6 demonstrates that the band gap and built-in potential of Si and GaAs decrease with increasing temperature, with GaAs showing a steeper decline in the band gap. These changes, influenced by material-specific properties, play a crucial role in the temperature-dependent behavior of semiconductor devices. These trends underscore the importance of temperature considerations in semiconductor device design. As both the band gap and built-in potential decrease, it becomes crucial for engineers to optimize device performance, especially in power electronics and optoelectronics, where thermal stability is vital.

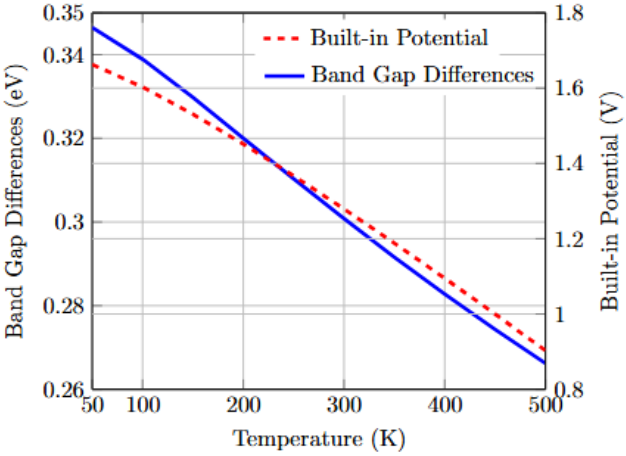

Figure 6. Differences of Band Gap and Built-in Potential as a function of Temperature

Figure 6 highlights the interplay between the band gap and built-in potential as a function of temperature, revealing their critical role in determining the electrical behavior of semiconductor devices. This understanding is vital for optimizing the performance of temperature-sensitive components like p-n junctions, LEDs, and solar cells. Our model indicates a band gap difference of 0.31 eV between GaAs and Si at 300 K, consistent with experimental data. The conduction band offset ΔE_C is calculated at 0.04 eV, while the valence band offset ΔE_V is 0.27 eV at the same temperature. The plot illustrates how temperature affects two critical semiconductor parameters: Band Gap Differences and Built-in Potential. As temperature rises from 50 K to 500 K, both the band gap and built-in potential decrease: Band Gap Differences, the band gap narrows from approximately 0.35 eV to 0.26 eV due to increased lattice vibrations and thermal excitation, which reduce the energy needed for electron transitions. A narrower band gap can increase intrinsic carrier concentrations, enhancing conductivity but also potentially causing unwanted leakage currents in high-temperature devices. Built-in Potential, the built-in potential decreases from about 1.66 V to 0.9 V, indicating a weakening of the internal electric field. This change suggests that thermal effects significantly influence charge carrier dynamics, potentially reducing the efficiency of devices reliant on strong potential barriers, such as diodes and transistors, in high-temperature applications.

This analysis highlights the need for further research into the mechanisms behind these temperature effects and their implications for specific device architectures. Figure 7 shows how the band gap for silicon (Si) and gallium arsenide (GaAs) changes with temperature from 40 K to 500 K. GaAs start with a higher band gap of 1.52 eV at 40 K, decreasing to about 1.35 eV at 500 K, indicating greater thermal sensitivity than Si. This temperature dependence in GaAs can affect its performance at high temperatures but still makes it ideal for optoelectronic applications due to its direct band gap, which benefits devices like LEDs and laser diodes. Overall, understanding these thermal properties helps in designing reliable devices optimized for Si's stability or GaAs's high-frequency and optical capabilities.

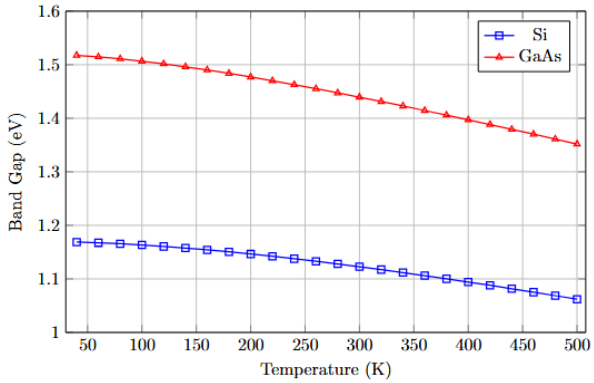

Figure 7. Band gaps of Si and GaAs as a function of temperature

Figure 8 shows that the intrinsic carrier concentration, for Si and GaAs rises exponentially from 50 K to 500 K due to thermal generation of carriers. GaAs, with its narrower band gap, reaches higher $n_i(T)$ values, indicating greater thermal sensitivity compared to Si. Here, majority carrier concentration $p_p = n_n = N_A = N_D = 2 \cdot 10^{16} cm^{-3}$, minority carrier concentration $p_n = n_i^2 / N_D$ and $n_p = n_i^2 / N_A$. Here, $n_i = 1.7 \cdot 10^6 cm^{-3}$ is the intrinsic concentration, for *GaAs*, $n_i = 1.5 \cdot 10^{10} cm^{-3}$ for *Si* at 300 K. This temperature-dependent behavior impacts conductivity, with higher temperatures

potentially affecting device stability. Si's stability is ideal for general electronics, while GaAs's thermal sensitivity and direct band gap make it well-suited for optoelectronic and high-frequency applications, especially in controlled settings. These insights are essential for optimizing device design across different thermal conditions.

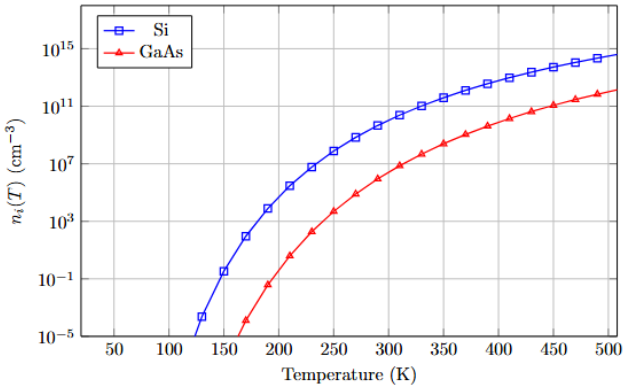

Figure 8. Intrinsic carrier concentration of Si and GaAs as a function of temperature.

CONCLUSIONS

In conclusion, our analytical study of the p-Si/n-GaAs radial heterojunction, specifically with a core radius of 0.5 μm and a shell radius of 1 μm, provides significant insights into its electrophysical features over a temperature range of 50 K to 500 K. We observed that the thickness of the depletion region increases with rising temperature, reflecting the complex dynamics within the heterojunction. At 300 K, the band gap difference between GaAs and Si was determined to be 0.31 eV, which aligns closely with experimental data, while the conduction band offset was calculated at $\Delta E_C = 0.04$ eV and the valence band offset at $\Delta E_V = 0.27$ eV. Additionally, our analysis showed that band gap narrowing (BGN) decreases by 2 meV as doping concentrations increase from $2{\cdot}10^{15}$ to $2{\cdot}10^{18}$. Moreover, we found that the built-in potential of the p-Si/n-GaAs heterojunction decreases by 76 mV with an increase in temperature. These quantitative findings highlight the importance of considering both the geometric parameters and doping concentration in the design and optimization of radial heterojunctions, providing a solid foundation for future advancements in semiconductor device applications.

ORCID

Jo'shqin Sh. Abdullayev, https://orcid.org/0000-0001-6110-6616
Ibrokhim B. Sapaev, https://orcid.org/0000-0003-2365-1554

REFERENCES

[1] R. Elbersen, R.M. Tiggelaar, A. Milbrat, G. Mul, H. Gardeniers, and J. Huskens, Advanced Energy Materials, **5**(6), 1401745 (2014). https://doi.org/10.1002/aenm.201401745.
[2] E. Gnani, A. Gnudi, S. Reggiani, and G. Baccarani, IEEE Trans. Electron Devices, **58**(9), 2903 (2011). https://doi.org/10.1109/TED.2011.2159608.
[3] Abdullayev, J. Sh., & Sapaev, I. B. (2024). Optimization of The Influence of Temperature on The Electrical Distribution of Structures with Radial p-n Junction Structures. East European Journal of Physics, (3), 344-349. https://doi.org/10.26565/2312-4334-2024-3-39
[4] Abdullayev, J. Sh., Sapaev, I. B. (2024). Оптимизация влияния легирования и температуры на электрофизические характеристики p-n и p-i-n переходных структур. Eurasian Physical Technical Journal, 21(3(49), 21–28. (https://doi.org/10.31489/2024No3/21-28).
[5] O.V. Pylypova, A.A. Evtukh, P.V. Parfenyuk, I.I. Ivanov, I.M. Korobchuk, O.O. Havryliuk, and O.Yu. Semchuk, Opto-Electronics Review, **27**(2), 143 (2019). https://doi.org/10.1016/j.opelre.2019.05.003.
[6] R. Ragi, R.V.T. da Nobrega, U.R. Duarte, and M.A. Romero, IEEE Trans. Nanotechnol. **15**(4), 627 (2016). https://doi.org/10.1109/TNANO.2016.2567323.
[7] Abdullayev, J., & Sapaev, I. B. (2024). Factors Influencing the Ideality Factor of Semiconductor p-n and p-i-n Junction Structures at Cryogenic Temperatures. *East European Journal of Physics*, (4), 329-333. https://doi.org/10.26565/2312-4334-2024-4-37
[8] R.D. Trevisoli, R.T. Doria, M. de Souza, S. Das, I. Ferain, and M.A. Pavanello, IEEE Trans. Electron Devices, **59**(12), 3510 (2012). https://doi.org/10.1109/TED.2012.2219055.
[9] N.D. Akhavan, I. Ferain, P. Razavi, R. Yu, and J.-P. Colinge, Appl. Phys. Lett. **98**(10), 103510 (2011). https://doi.org/10.1063/1.3559625.
[10] A.V. Babichev, H. Zhang, P. Lavenus, F.H. Julien, A.Y. Egorov, Y.T. Lin, and M. Tchernycheva, Applied Physics Letters, **103**(20), 201103 (2013). https://doi.org/10.1063/1.4829756.
[11] D.H.K. Murthy, T. Xu, W.H. Chen, A.J. Houtepen, T.J. Savenije, L.D.A. Siebbeles, *et al*., Nanotechnology, **22**(31), 315710 (2011). https://doi.org/10.1088/0957-4484/22/31/315710.
[12] B. Pal, K.J. Sarkar, and P. Banerji, Solar Energy Materials and Solar Cells, **204**, 110217 (2020). https://doi.org/10.1016/j.solmat.2019.110217.
[13] Abdullayev, J. and Sapaev, I. 2024. Modeling and calibration of electrical features of p-n junctions based on Si and GaAs. *Physical Sciences and Technology*. 11, 3-4 (Dec. 2024), 39–48. https://doi.org/10.26577/phst2024v11i2b05.

[14] I. Aberg, G. Vescovi, D. Asoli, U. Naseem, J.P. Gilboy, C. Sundvall, and L. Samuelson, IEEE Journal of Photovoltaics, **6**(1), 185 (2016). https://doi.org/10.1109/JPHOTOV.2015.2484967.
[15] S. C. Jain and D. J. Roulston, "A Simple Expression for Band Gap Narrowing (BGN) in Heavily Doped Si, Ge, GaAs and Ge_xSi_{1-x} Strained Layers," Solid-State Electronics, vol.34, no. 5, pp. 453–465, 1991.

АНАЛІТИЧНИЙ АНАЛІЗ ОСОБЛИВОСТЕЙ РАДІАЛЬНИХ ГЕТЕРОПЕРЕХОДІВ GaAs/Si: ВПЛИВ ТЕМПЕРАТУРИ ТА КОНЦЕНТРАЦІЇ

Джошкін Ш. Абдуллаєв[a], Іброхім Б. Сапаєв[a,b]
[a]Національний дослідницький університет ТІІАМЕ, фізико-хімічний факультет, Ташкент, Узбекистан
[b]Західно-Каспійський університет, Баку, Азербайджан

У цій статті ми аналітично досліджуємо електрофізичні особливості радіального гетеропереходу p-Si/n-GaAs у діапазоні температур від 50 К до 500 К з кроком 50 К, враховуючи різні концентрації легування. Аналіз охоплює звуження енергетичної щілини, різницю в енергетичній щілині між GaAs і Si як функцію температури, а також вбудований потенціал залежно від температури. Зокрема, ми зосереджуємо увагу на ядрі з p-Si з радіусом 0,5 мкм та оболонці з n-GaAs з радіусом 1 мкм у структурі. Наші результати показують, що товщина області збіднення в p-Si/n-GaAs збільшується зі зростанням температури. Різниця енергетичної щілини між GaAs і Si становить 0,31 еВ при 300 К у нашій моделі, що добре узгоджується з експериментальними результатами. Крім того, зсув зони провідності ΔE_C=0,04 еВ та зсув валентної зони ΔE_V=0,27 еВ були обчислені при 300 К. При зміні концентрації легування від $2\cdot10^{15}$ до $2\cdot10^{18}$ звуження енергетичної щілини зменшується на 2 меВ. Додатково, вбудований потенціал p-Si/n-GaAs зменшується на 76 мВ зі збільшенням температури.

Ключові слова: *радіальний p-n перехід; світлова пастка; зовнішні фактори; вольт-фарад; гетероструктури; радіальний гетероперехід; звуження енергетичної щілини; кріогенні температури*